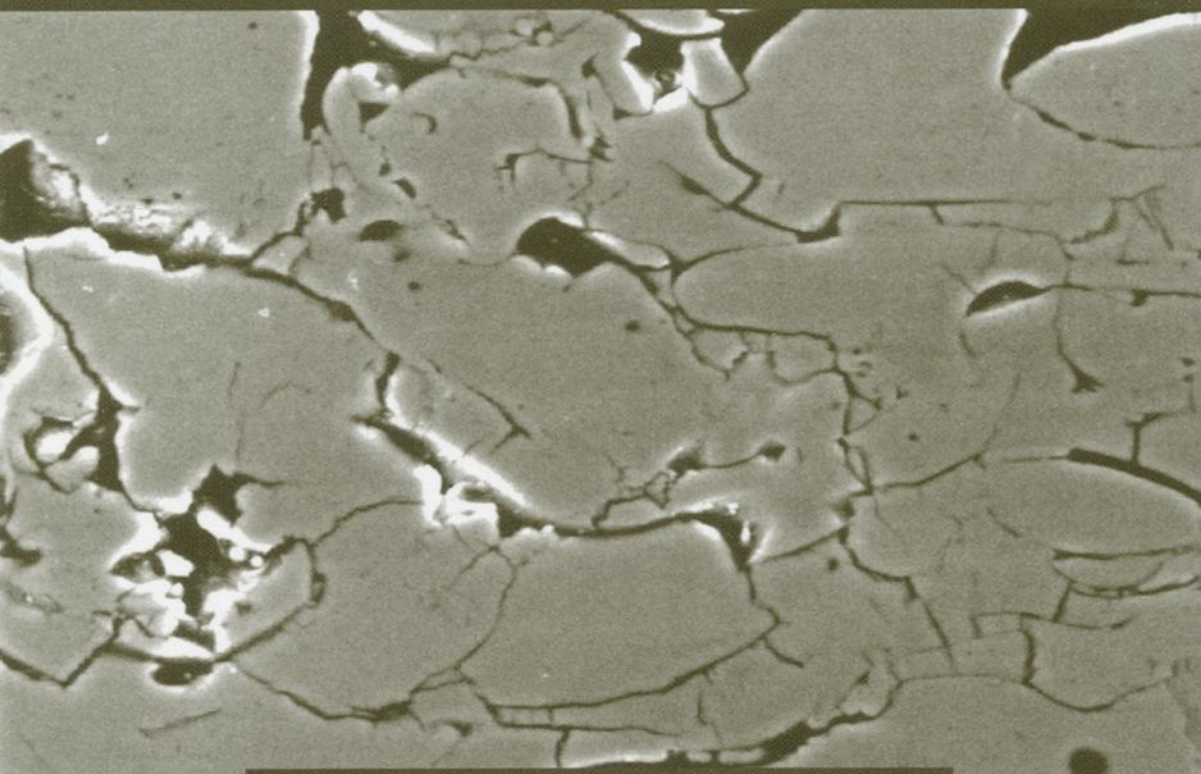
Fatigue and Fracture Mechanics

31st Volume



Gary R. Halford and
Joseph P. Gallagher, editors

ASTM STP 1389

STP 1389

Fatigue and Fracture Mechanics: 31st Volume

Gary R. Halford and Joseph P. Gallagher, editors

ASTM Stock Number: STP1389

ASTM
PO Box C700
100 Barr Harbor Drive
West Conshohocken, PA 19428-2959

Printed in the U.S.A.

ISBN: 0-8031-2868-1
ISSN: 1040-3094

Copyright © 2000 AMERICAN SOCIETY FOR TESTING AND MATERIALS, West Conshohocken, PA. All rights reserved. This material may not be reproduced or copied, in whole or in part, in any printed, mechanical, electronic, film, or other distribution and storage media, without the written consent of the publisher.

Photocopy Rights

Authorization to photocopy items for internal, personal, or educational classroom use, or the internal, personal, or educational classroom use of specific clients, is granted by the American Society for Testing and Materials (ASTM) provided that the appropriate fee is paid to the Copyright Clearance Center, 222 Rosewood Drive, Danvers, MA 01923, Tel: 508-750-8400; online: http://www.copyright.com/.

Peer Review Policy

Each paper published in this volume was evaluated by two peer reviewers and at least one editor. The authors addressed all of the reviewers' comments to the satisfaction of both the technical editor(s) and the ASTM Committee on Publications.

The quality of the papers in this publication reflects not only the obvious efforts of the authors and the technical editor(s), but also the work of the peer reviewers. In keeping with long-standing publication practices, ASTM maintains the anonymity of the peer reviewers. The ASTM Committee on Publications acknowledges with appreciation their dedication and contribution of time and effort on behalf of ASTM.

Printed in Chelsea, MI
December 2000

Foreword

This publication, *Fatigue and Fracture Mechanics, 31st Volume,* contains papers presented at the symposium of the same name held in Cleveland, Ohio, on 21-24 June 1999. The symposium was sponsored by ASTM Committee E08 on Fatigue and Fracture. The symposium co-chairmen were Gary R. Halford, NASA Glenn Research Center at Lewis Field, Cleveland, OH, and Joseph P. Gallagher, University of Dayton Research Institute, Dayton, OH.

Contents

Overview ix

SWEDLOW MEMORIAL LECTURE

An Overview and Discussion of Basic Methodology for Fatigue— N. E. DOWLING AND S. THANGJITHAM 3

KEYNOTE TRIBUTES TO GEORGE IRWIN

Irwin's Stress Intensity Factor—A Historical Perspective—J. C. NEWMAN 39

The Contributions of George Irwin to Elastic-Plastic Fracture Mechanics Development—J. D. LANDES 54

CYCLIC STRESS-STRAIN AND FATIGUE RESISTANCE

A New Incremental Fatigue Method—C.-C. CHU 67

Biaxial Fatigue of Stainless Steel 304 under Irregular Loading—K. S. KIM, B. L. LEE, AND J. C. PARK 79

Fatigue Life Estimation Under Cumulative Cyclic Loading Conditions— S. KALLURI, M. A. McGAW, AND G. R. HALFORD 94

Assessments of Low Cycle Fatigue Behavior of Powder Metallurgy Alloy U720—T. P. GABB, P. J. BONACUSE, L. J. GHOSN, J. W. SWEENEY, A. CHATTERJEE, AND K. A. GREEN 110

Computer Aided Nondestructive Evaluation Method of Welding Residual Stresses by Removing Reinforcement of Weld (Proposal of a New Concept and Its Verification)—K. KUMAGAI, H. NAKAMURA, AND H. KOBAYASHI 128

Bulk Property Evaluation of a Thick Thermal Barrier Coating—E. F. REJDA, D. F. SOCIE, AND B. P. NUEL 143

ELASTIC-PLASTIC FRACTURE MECHANICS

Application of the Two-Parameter J-A_2 Description to Ductile Crack Growth—Y. J. CHAO, X. K. ZHU, P.-S. LAM, M. R. LOUTHAN, AND N. C. IYER 165

The Technical Basis for ASTM E 1820-98 Deformation Limits on J_c—M. T. KIRK AND R. G. LOTT 183

Variations of Constraint and Plastic Zone Size in Surface-Cracked Plates Under Tension or Bending Loads—C. R. AVELINE, JR. AND S. R. DANIEWICZ 206

A Strip-Yield Model for Part-Through Surface Flaws Under Monotonic Loading—S. R. DANIEWICZ AND C. R. AVELINE 221

Application of the Weibull Methodology to a Shallow-Flaw Cruciform Bend Specimen Tested Under Biaxial Loading Conditions—P. T. WILLIAMS, B. R. BASS, AND W. J. MCAFEE 242

Local Approach to Dynamic Fracture Toughness Evaluation—F. MINAMI, T. OCHIAI, T. HASHIDA, K. ARIMOCHI, AND N. KONDA 271

Transition Fracture Toughness Testing with Notched Round Bars (NRB)—C. D. WILSON AND J. D. LANDES 305

Dislocation Mechanics Basis and Stress State Dependency of the Master Curve—M. E. NATISHAN, M. WAGENHOFER, AND M. T. KIRK 318

CRACK ANALYSES AND APPLICATION TO STRUCTURAL INTEGRITY

Investigation of a New Analytical Method for Treating Kinked Cracks in a Plate—S. C. TERMAATH AND S. L. PHOENIX 331

Calculation of Stress Intensity Factors for Cracks of Complex Geometry and Subjected to Arbitrary Nonlinear Stress Fields—G. GLINKA AND W. REINHARDT 348

Stress Intensity Predictions with ANSYS for Use in Aircraft Engine Component Life Prediction—D. C. SLAVIK, R. D. MCCLAIN, AND K. LEWIS 371

Fracture Parameters of Surface Cracks in Compressor Disks—W. Z. ZHUANG AND B. J. WICKS 391

Prediction of Time-Dependent Crack Growth with Retardation Effects in Nickel Base Alloys—R. H. VAN STONE AND D. C. SLAVIK 405

The Effect of Low Cycle Fatigue Cracks and Loading History on High Cycle Fatigue Threshold—M. A. MOSHIER, T. NICHOLAS, AND B. M. HILLBERRY 427

Fatigue Crack Growth Threshold Stress Intensity Determination via Surface Flaw (Kb Bar) Specimen Geometry—K. R. BAIN AND D. S. MILLER 445

Fatigue Strength of Weld Repair Specimens Under Simulated Program Loading of an Overhead Traveling Crane—Y. KITSUNAI, Y. MAEDA, E. YOSHIHISA, T. HONDA, AND S. G. SUNDARA RAMAN 457

Modeling Crack Growth in Thin Sheet Aluminum Alloys—T. SIEGMUND AND W. BROCKS 475

Residual Strength Analyses of Riveted Lap-Splice Joints—B. R. SESHADRI AND J. C. NEWMAN 486

Damage Repair Simulation of a Tension Panel and Pressurized Cylindrical Shell Using Adhesively Bonded Patches—T. J. CURTIN AND R. A. ADEY 505

Effect of Moisture on Fracture Toughness of Composite/Wood Bonded Interfaces—P. QIAO, J. F. DAVALOS, AND B. S. TRIMBLE 526

Indexes 545

Overview

The Thirty-First National Symposium on Fatigue and Fracture Mechanics sponsored by ASTM Committee E08 on Fatigue and Fracture was held in Cleveland, Ohio, June 21-24, 1999. Papers were solicited in several broad subject areas:

- advances in analysis and predictive capability
- behavior of new and emerging materials
- design tools and approaches to control failures
- accelerated testing involving interactions
- assessment of the risk and remaining durability of aging systems
- integrity and durability in a range of industrial applications

Twenty-nine papers were accepted for publication in this volume. They represent a wide range of fatigue- and fracture-related topics. In addition to the contributions from the United States, papers were also contributed from Japan, Korea, Germany, Australia, and Canada. Half of the papers came from universities, while the other half were divided between industry and government.

Following the **Jerry Swedlow Memorial Lecture,** given this year by Professor Norman E. Dowling of Virginia Polytechnic Institute and State University, Blacksburg, the ensuing papers are arranged into four sections: **Keynote Tributes to George Irwin, Cyclic Stress-Strain and Fatigue Resistance, Elastic-Plastic Fracture Mechanics,** and **Crack Analyses and Application to Structural Integrity.**

Professor Dowling's paper addresses the undergraduate educational needs in the area of fatigue and fracture. Rather than rely on standard information presented in material science courses (e.g., Goodman curves and knock-down factors), Dowling suggests that the educator should provide a better introduction to all the modern methods that an engineer must use to attack typical mechanical failure problems.

Dr. James C. Newman, Jr. and Professor John D. Landes provided **Keynote Tributes to George Irwin.** Their papers summarize some of the most important contributions of Dr. George R. Irwin, the father of modern fracture mechanics, who passed away in October 1998. The papers recognize Dr. Irwin's vision and wisdom along with a description of his attempts to develop and gain technical acceptance for understanding the conditions that controlled fracture behavior using the concepts of similitude of the local crack tip conditions and a crack tip stress model. The authors also remember this scientist, educator, and practitioner as a gentle and generous man.

The **Cyclic Stress-Strain and Fatigue Resistance** section consists of a half dozen papers, each providing experimental or analytical insight into approaches for the evaluation of the cyclic durability resistance of engineering materials. Among the issues addressed are: (a) multiaxiality of stress-strain states and how to track cycles and damage accumulation under generalized or specific loading conditions; (b) correlation and evaluation of the influences of primary metallurgical processing variables on the low-cycle fatigue crack initiation and growth resistance of a powder metallurgy gas turbine disk alloy; (c) an analytical technique for computing welding residual stress based on use of eigenstrain distributions following nondestructive removal of weld reinforcement; and (d) experimental evaluation and analytical modeling of the non-linear cyclic stress-strain response of anisotropic porous ceramics such as used in thick thermal barrier coatings for high-temperature turbine components.

In the section on **Elastic-Plastic Fracture Mechanics** (EPFM), eight papers make substantial contributions to our understanding of how best to apply this technology to low-

strength structural materials used in most civil, oceanographic, power plant, and automotive applications. The papers cover topics that: (a) expand the application of analytical methods to stable crack tearing; (b) provide justification for changing the size requirements in ASTM Standard E-1820; (c) identify the level of constraint associated with surface flaw cracks; (d) extend the application of the slice synthesis technique to estimate elastic-plastic behavior by using a strip yield model; (e) develop a procedure for using uniaxially loaded crack data to predict the behavior of shallow surface flaws subjected to biaxial loading conditions; (f) adapt a time-temperature model for crack tip stresses to estimate fracture initiation behavior under dynamic loading conditions; (g) develop a scheme for removing notch root radius bias from apparent fracture toughness estimates generated using non-precracked notched round bar specimens; and (h) present a physics-based understanding of the fracture behavior of pressure vessel steels, respectively.

In the section on **Crack Analyses and Application to Structural Integrity,** twelve papers provide information on advances in crack analyses, fatigue crack growth behavior, and structural applications. The first three papers provide advances in crack analysis methods for non-self similar and branching cracks, for Greens Functions for arbitrary-shaped internal flaws, and for finite element methods used to characterize complex cracks, respectively. The next four papers focus on fatigue crack growth behavior and address: (a) the growth of cracks in compressor disks, (b) models for time-dependent retardation at high temperature, (c) the influence of stress history on the fatigue crack growth rate threshold, and (d) accelerated test methods for generating fatigue crack growth rate threshold data using surface flaw specimens. The final five papers in this section focus primarily on applications. These application papers discuss: (a) approaches to establishing the fatigue strength of weld repairs to an overhead crane, (b) a cohesive zone model for describing thin sheet aluminum alloy fracture behavior for aircraft fuselage structure, (c) a crack tip opening angle (CTOA) model for determining the residual strength of a typical aircraft fuselage riveted joint when multiple site damage (MSD) is present, (d) modeling parameters associated with bonded repairs of fuselage structure, and (e) effects of moisture on the durability of adhesively bonded joints constructed from wood and composite materials.

Cash prizes for the two best student papers were awarded to Stephanie TerMaath of Cornell University, Ithaca, and Ed Rejda of the University of Illinois at Urbana-Champaign. Thanks go to judges Drs. John Landes, Mike Mitchell, Bob Van Stone, Ravi Chona, and Jim Newman.

The efforts of the authors, manuscript reviewers, session chairs, and Robert "Jim" Goode of the Committee on Publications are greatly appreciated. The staff of ASTM must also be recognized for their untiring contributions to making the symposium and this volume a professional success. In particular, the valued assistance of Dorothy Savini, Eileen Gambetta, Bode Buckley, Kathy Dernoga, Helen Mahy, and Hanna Sparks is greatly appreciated.

Gary R. Halford
NASA Glenn Research Center at Lewis Field;
Cleveland, OH; Symposium Chairman and Editor

Joseph P. Gallagher
University of Dayton Research Institute,
Dayton, OH; Symposium Chairman and Editor

Swedlow Memorial Lecture

Norman E. Dowling[1] *and Surot Thangjitham*[1]

An Overview and Discussion of Basic Methodology for Fatigue

REFERENCE: Dowling, N. E. and Thangjitham, S., **"An Overview and Discussion of Basic Methodology for Fatigue,"** *Fatigue and Fracture Mechanics: 31st Volume, ASTM STP 1389,* G. R. Halford and J. P. Gallagher, Eds., American Society for Testing and Materials, West Conshohocken, PA, 2000, pp. 3–36.

ABSTRACT: This paper broadly reviews the stress-based, strain-based, and crack growth approaches to fatigue life prediction, and it attempts to suggest some choices and variations of these that might enhance their inclusion in undergraduate education and their more routine use by practicing engineers. For the stress-based approach, emphasis should shift toward the use of data on actual components, and it should be recognized that damage below the usual fatigue limit may occur. Also, evaluation of mean stress effects by the modified Goodman diagram should be replaced by other methods. The usefulness of the strain-based approach for simple situations may be extended by adding empirical adjustments for surface finish and size. It may also be desirable to lower the long-life end of the strain-life curve to obtain agreement with limited component test data, producing a *component-specific strain-life curve.* Use of the crack growth approach is hampered by the lack of a widely accepted set of materials constants for describing da/dN versus ΔK curves. It is recommended that this situation be remedied by representing the intermediate growth rate region with a Paris-type exponent, an associated coefficient, and a third constant that characterizes the sensitivity to R-ratio according to the equation of Walker. Limits or asymptotic behavior for the low and high growth rate regions should then be handled separately.

KEYWORDS: stress, strain, crack growth, fatigue of materials, life prediction, testing, mean stress, *S-N* curves, strain-life curves, da/dN versus ΔK curves

Introduction

For design and troubleshooting related to service failures in machines, vehicles, and structures, there are three major approaches for estimating fatigue lives of components. The first is the *stress-based* approach, which employs stress versus life curves and mean stress adjustments from modified Goodman diagrams or related methods. Geometric notches, that is, stress raisers such as holes, fillets, or grooves, are considered based on elastic stress analysis and empirical correction factors. Nominal (average) stress is often the variable employed for notched members, and stress-life (*S-N*) curves may be estimated, or they may be based on data from unnotched or notched members. The stress-based approach has been in use for more than 150 years, and its major concepts were all in nearly their present form 40 years ago [*1,2*].

The *strain-based* approach analyzes the effects of local yielding at notches, often by approximate methods such as Neuber's rule. Life estimates are based on materials properties from tests on unnotched, axially loaded specimens, specifically, strain versus life curves and

[1] Professor and associate professor, respectively, Engineering Science and Mechanics Department, Mail Code 0219, Virginia Tech, Blacksburg, VA.

Copyright© 2000 by ASTM International www.astm.org

cyclic stress-strain curves. Due to cycle-dependent hardening or softening, the latter may differ considerably from a given material's ordinary tension-test stress-strain curve. Analysis of local yielding permits the effects of prior severe loading events to be evaluated, as they affect the local mean stresses that occur during subsequent cycling at low levels. Development of this approach began in the late 1950s in work by Coffin [*3*] and Manson [*4*] and continues to the present time. One current research topic is the development of methods for handling complex out-of-phase combined loadings [*5,6*]. Another is the evaluation of cycles below the apparent fatigue limit, but which nevertheless cause fatigue damage [*7*].

Stress intensity factors, K, from fracture mechanics may be employed to estimate fatigue lives as limited by crack growth. Values of K as a function of crack length are needed for the particular geometry of interest, as from handbooks or numerical analysis. These are then combined with materials data in the form of a da/dN versus ΔK relationship, with mean stress effects included according to the ratio $R = S_{min}/S_{max}$. Occasional high loads may introduce residual stresses ahead of the crack that affect the subsequent crack growth. Methods for including this effect have been developed, but it is often useful to simplify the analysis by neglecting the usually beneficial overload interaction effects. Development of this approach began in the early 1960s and continues to the present time [*8,9*]. One area of current research is the special behavior of small cracks [*10*] and another is the interaction and combination of crack growth due to both cyclic loading and hostile environmental effects [*11*].

Now consider undergraduate education in engineering as it relates to the above areas of technology. Design books in mechanical engineering [*12,13*] currently include significant treatment of only the stress-based approach and even then generally offer a version of this that is perhaps not the optimum choice. Students in other disciplines, such as civil, aeronautical, and materials engineering, may or may not receive significant instruction in fatigue and fracture. Coverage of the strain-based and crack growth approaches in any degree of detail is generally found only in elective courses. In general, for many engineering undergraduates, there appears to be a large and unnecessary gap between what is typically taught in this area and the technology available.

In this paper, we will broadly review the three approaches to fatigue and attempt to suggest some choices and variations of these that might enhance their inclusion in undergraduate education, and hence their use by engineers after graduation.

Stress-Based Approach

In mechanical design books, the stress-based approach is usually presented in terms of estimated *S-N* curves and modified Goodman diagrams. A *fatigue limit,* S_{er}, that is, a safe stress below which no fatigue failure occurs, is generally assumed to exist.

Below, in this section of the paper, we will first summarize procedures for estimating fatigue limits and *S-N* curves, and then we will discuss the limitations of these methods. Next, we consider equations for estimating mean stress effects for unnotched and notched members, and finally we discuss these and reach some conclusions as to which are the best to use.

Fatigue Limit and S-N *Curve Estimates*

The fatigue limit is often estimated from the ultimate strength σ_u from a tension test.

$$S_{er} = \frac{m\sigma_u}{k_f}, \qquad m = m_e m_t m_d m_s \tag{1}$$

where m is the multiplicative combination of various empirical adjustment factors. The quan-

tity m_e is an empirical constant for estimating the fatigue limit of polished bending specimens, such as $m_e = 0.5$ for steels. Other factors are also applied, such as m_t for type of loading (bending, axial, or torsion), m_d for size effect, and m_s for surface finish. The design books of Juvinall [*12*] and Shigley [*13*] present such an approach and give details for evaluating the various empirical factors.

To account for the stress raiser effect of the notch, the stress may be lowered by a fatigue notch factor k_f. The latter is obtained from the elastic stress concentration factor k_t, the notch radius ρ, and an empirical curve or material constant, such as the equation of Peterson [*14*] with its material constant α.

$$k_f = 1 + \frac{k_t - 1}{1 + \alpha/\rho} \tag{2}$$

For estimating *S-N* curves, the details of the procedure vary in different design books. Two estimated *S-N* curves are compared with corresponding test data in Fig. 1. Typically, a straight line on a log-log plot is employed between a point at $N_f = 10^3$ cycles, and a long life point at $N_f = N_e$ cycles, where the latter is 10^6 cycles for steels.

$$(S_{ar}, N_f) = \left(\frac{m'\sigma_u}{k'_f}, 10^3\right) \text{ and } (S_{er}, N_e) \tag{3}$$

The stress variable S_{ar} is the amplitude (half range) for the completely reversed case, that is, for zero mean stress, $S_m = 0$. The variable S corresponds to a nominal or average stress, defined consistently with k_t for a notched member. For the point at $N_f = 10^3$ cycles, m' is an empirical factor close to unity, such as $m' = 0.9$ in Shigley [*13*], or $m' = 0.9$ or 0.75 for bending or axial load, respectively, in Juvinall [*12*]. For torsion, σ_u is replaced by an ultimate shear strength τ_u.

The quantity k'_f in Eq 3 accounts for the notch effect at 10^3 cycles. For example, Shigley [*13*] uses $k'_f = 1$. In Juvinall [*12*], the notch effect is not included directly in the *S-N* curve, but is employed separately in a manner equivalent to applying $k'_f = k_f$, giving a very different estimate, as seen in Fig. 1. However, note that an earlier book by Juvinall [*16*] has empirical

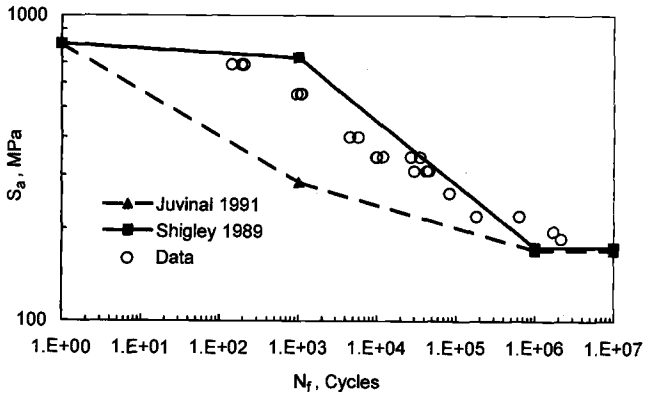


FIG. 1—S-N *curves estimated according to two different authors and corresponding test data for double-edge-notched axial specimens* ($k_t = 2.15$) *made of AISI 4130 steel with* $\sigma_u = 807$ *MPa. (Data from Grover [15].)*

curves that give a value in the range $k'_f = 1$ to k_f, depending on the strength σ_u of the material.

Beyond N_e, the curve is assumed to be flat, at least for steels. For lives shorter than 10^3 cycles, no estimate is provided by Juvinall [*12*] or Shigley [*13*], but it would be consistent with the spirit of these estimates to employ a second line segment that extends to σ_u at $N_f = 1$ cycle, as is done by Norton [*17*]. Within the $N_f = 10^3$ to 10^6 interval, the use of a straight line on a log-log plot gives an equation of the form

$$S_{ar} = AN_f^B \tag{4}$$

where the values of A and B can be calculated from the two points given by Eq 3.

Discussion of Estimated S-N *Curves*

As for the example of Fig. 1, estimated *S-N* curves often deviate drastically from actual behavior, and there is no agreement among various design books as to the details of the procedure. The experimental basis of the estimates is weak, as various assumptions, such as the multiplicative combination of the various factors in Eq 1, appear to have never been thoroughly investigated. Current editions of older design books, as well as new design books, repeat and sometimes modify the empirical factors and procedure, but there has been no major reevaluation based on experimental data for 30 years or more. Early sources on estimating *S-N* curves, such as Noll [*18*], Marin [*19*], and Juvinall [*16*], were more detailed and more cautious than recent treatments, and they have a closer link to experimental data.

The estimates are severely limited by being based mainly on empirical data for steels and cast irons. For these, estimates of fatigue limits are often reasonably accurate. But specific experimental data, not included in current design books, are needed to make corresponding estimates for other alloys. Aluminum and magnesium alloys are included to an extend by Juvinall [*12*], but even for these, not all needed empirical parameters are available. The estimates are certainly not applicable to nonmetals, such as plastics or composite materials.

Alternatives to estimated *S-N* curves do exist. First, data for the specific component of interest may be generated. Such tests may be complex and expensive, and sometimes only a few tests can be conducted. However, component *S-N* curves may already be available, as found in design codes for welded structural members. Another possibility is to employ data from tests on unnotched axially loaded specimens of the material. Constants describing stress-life curves fitted to such data are becoming available for a variety of metals, as in the collections of Boller and Seeger [*20*] and SAE [*21*]. A standard form is often used.

$$\sigma_a = \sigma'_f (2N_f)^b \qquad (\sigma_m = 0) \tag{5}$$

where σ'_f and b are materials constants for completely reversed loading, and σ_a is stress amplitude. Note that the symbol σ is used to indicate actual stress, as at a point, as distinguished from nominal stress S.

Direct application of Eq 5 is appropriate only where stresses are known at the likely failure location in the engineering component. Note that this is usually the case only if the stress, including the local stress at a notch, $\sigma = k_t S$, is below the material's yield strength. This arises from the fact that stresses determined from ordinary stress formulas, and from most finite element analyses, assume elastic behavior of the material. A further complication is that the yield strength may decrease due to the effect of cyclic loading, which occurs in many steels. This limitation to cases of no yielding can be overcome by employing a strain-based approach as described later. Note that the strain-based approach employs a limited set

of materials constants, including σ'_f and b, and can be employed to estimate notched member *S-N* curves for various situations of component geometry and mean stress.

Discussion of Fatigue Limits

The concept of a fatigue limit needs to be treated with some caution. If the stress history is such that the fatigue limit is never exceeded, then the concept can be applied. However, occasional severe stress cycles can cause subsequent cycles below the apparent fatigue limit to contribute to fatigue damage. Experimental data illustrating this are shown in Fig. 2. This effect is caused by the severe cycles initiating fatigue damage in the microstructure of the material, specifically, damage that would otherwise not be able to initiate if the stress never exceeded the fatigue limit. A corrosive environment may also have a similar effect.

One approach to this situation is to simply extrapolate the *S-N* curve below the fatigue limit by extending a straight line on a log-log plot, as suggested by the dashed line in Fig. 2. Other strategies include lowering but not eliminating the fatigue limit and providing a shallow slope to the *S-N* curve beyond N_e. Such modifications to *S-N* curves are in fact employed in design codes for welded members, such as those of AASHTO [*24*], API [*25*], and BSI [*26*]. Recent research [*7,27*] suggests that there is a true fatigue limit around half of the apparent value for several metals studied.

Mean Stress Effects

The traditional approach to handling mean stress effects for unnotched material is to plot the stress amplitude σ_a versus the mean stress σ_m on a modified Goodman diagram as shown in Fig. 3. The stresses plotted correspond to either the fatigue limit or to a particular value of life, N_f. This method has its origins with the early work of John Goodman [*28*], and the manner of presentation shown follows the *modification* due to J. O. Smith [*29*]. A straight line is drawn to the materials ultimate strength σ_u, so that the line corresponds to

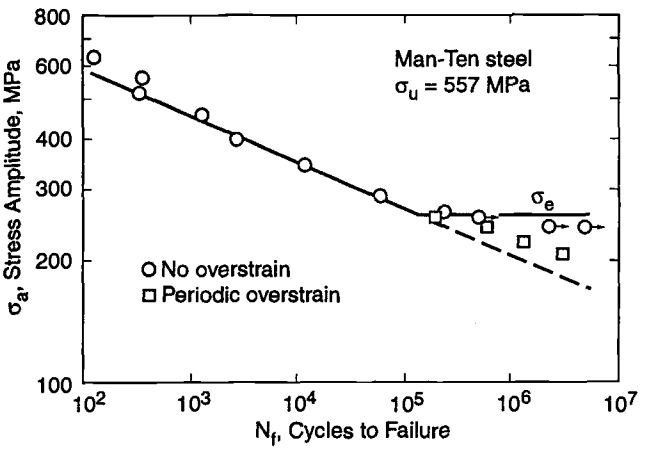


FIG. 2—*Stress-life data for a low strength steel showing the effect of overstrains applied at intervals of 10^5 cycles and corresponding to a summation of cycle ratios not exceeding a few percent. (From Dowling [22], p. 409, as based on data from Brose [23]; © 1999 by Prentice Hall, Upper Saddle River, NJ; reprinted with permission.)*

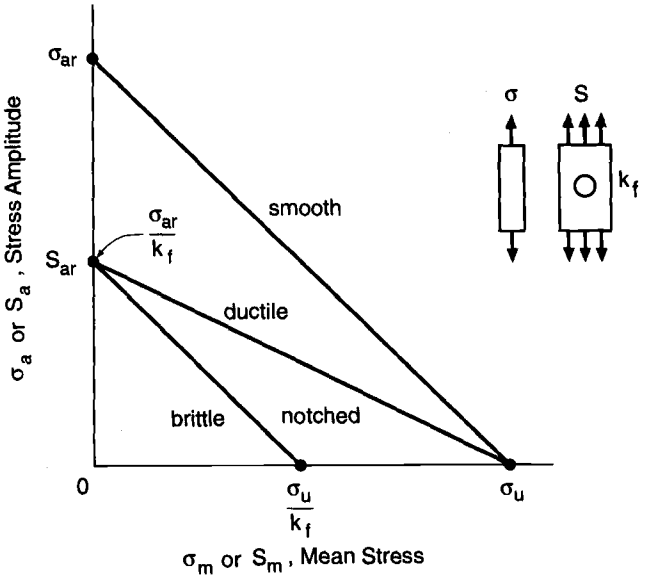


FIG. 3—*Modified Goodman diagram for unnotched (smooth) and notched members. (From Dowling [22], p. 436; © 1999 by Prentice Hall, Upper Saddle River, NJ; reprinted with permission.)*

$$\sigma_{ar} = \frac{\sigma_a}{1 - \frac{\sigma_m}{\sigma_u}} \tag{6}$$

The quantity σ_{ar} may be thought of as an *equivalent completely reversed stress amplitude* that has the same effect as a stress amplitude σ_a applied at a mean stress σ_m. The use of this equation can be justified by noting that most data scatter above the line, so that if one starts with a σ_a versus N_f curve for the completely reversed ($\sigma_m = 0$) case, that is, a σ_{ar} versus N_f curve, it provides conservative estimates.

For notched members, a similar line is drawn from the completely reversed nominal stress, $S_{ar} = \sigma_{ar}/k_f$, giving

$$S_{ar} = \frac{S_a}{1 - \frac{S_m}{\sigma_u}} \tag{7}$$

The same mean stress intercept σ_u is employed, as the static strength of ductile metals is not significantly reduced by the presence of a notch. (This would not be the case for a relatively brittle material, in which case the intercept would also be reduced by the notch factor k_f.)

A wide variety of other equations for handling mean stresses have been proposed. A paper by Morrow [*30*] suggests that σ_u be replaced with the coefficient σ'_f of Eq 5 and further that this quantity is often approximately equal to the true fracture strength, $\tilde{\sigma}_f$. Note that $\tilde{\sigma}_f$ is the load at fracture in a tension test divided by the final area. Hence, an equation is obtained that may be used in either of two forms.

$$\sigma_{ar} = \frac{\sigma_a}{1 - \frac{\sigma_m}{\sigma'_f}}, \qquad \sigma_{ar} = \frac{\sigma_a}{1 - \frac{\sigma_m}{\tilde{\sigma}_f}} \qquad \text{(a, b)} \tag{8}$$

As seen for some data on an alloy steel in Fig. 4, either of the above options may give a line that more accurately represents the data than does Eq 6. Note that the σ_a axis of Fig. 3 is changed in Fig. 4 to the normalized form σ_a/σ_{ar}, so that values for any life can be shown on the same plot.

Another frequently used relationship is that of Smith, Watson, and Topper [*32*], abbreviated SWT.

$$\sigma_{ar} = \sqrt{\sigma_{max}\sigma_a} = \sigma_{max}\sqrt{\frac{1 - R}{2}} \qquad (\sigma_{max} > 0) \tag{9}$$

where $\sigma_{max} = \sigma_m + \sigma_a$, and the life is assumed to be infinite if $\sigma_{max} \leq 0$. The second form is equivalent and is convenient when the mean stress level is expressed in terms of the ratio $R = \sigma_{min}/\sigma_{max}$, in which $\sigma_{min} = \sigma_m - \sigma_a$. This relationship does not form a single curve on a plot of the Fig. 4 type and so is not shown. The SWT relationship may also be employed with nominal stresses for notched members, providing an alternative to Eq 7.

$$S_{ar} = \sqrt{S_{max}S_a} = S_{max}\sqrt{\frac{1 - R}{2}} \qquad (S_{max} > 0) \tag{10}$$

An additional approach that may be applied to notched members is that of Walker [*33*].

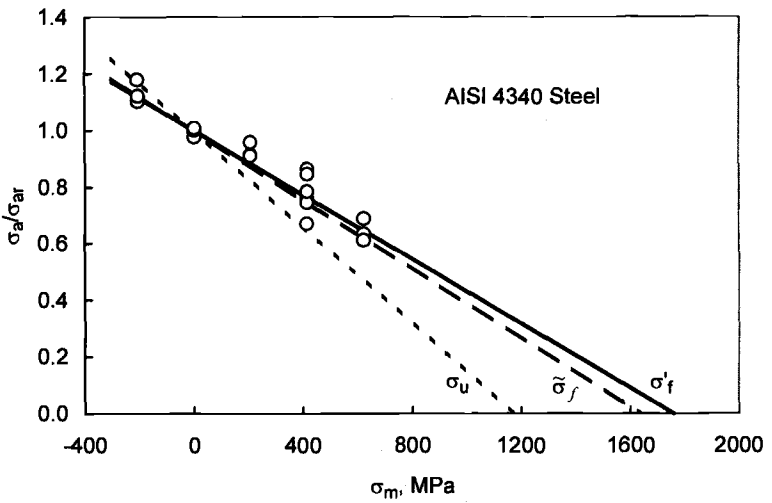


FIG. 4—*Normalized amplitude-mean plot for axial specimens of AISI 4340 steel with* σ_u = *1172 MPa. (Data from Dowling [31].)*

$$S_{ar} = S_{\max}^{1-\gamma} S_a^{\gamma} = S_{\max} \left(\frac{1-R}{2}\right)^{\gamma} \quad \text{(a)}$$

$$\overline{\Delta S} = S_{\max}^{1-\gamma} \Delta S^{\gamma} = S_{\max} (1-R)^{\gamma} \quad \text{(b)} \qquad (S_{\max} > 0) \qquad (11)$$

The second form gives an equivalent zero-to-maximum stress range, which is convenient where the baseline data are for the $R = 0$ case. Note that the two equivalent stresses are related by $\overline{\Delta S} = 2^{\gamma} S_{ar}$. The constant γ is an additional fitting constant that is a measure of how sensitive the life is to mean stress, that is, to R ratio. Note that Eq 11(a) reduces to Eq 10 for the special case of $\gamma = 0.5$.

For a given set of fatigue data including various mean stresses S_m, or stress ratios R, assume that a relationship of the form of Eq 4 applies, but with A and B to be obtained from fitting the data. By combining this with Eq 11(a), the values of A, B, and γ may all be determined in a single fitting procedure.

$$A N_f^B = S_{\max} \left(\frac{1-R}{2}\right)^{\gamma}, \qquad N_f = \left(\frac{S_{\max}}{A} \left(\frac{1-R}{2}\right)^{\gamma}\right)^{1/B} \quad \text{(a, b)}$$

$$\log N_f = \frac{1}{B} \log S_{\max} + \frac{\gamma}{B} \log \frac{1-R}{2} - \frac{1}{B} \log A \quad \text{(c)} \qquad (12)$$

Form (c) provides the basis for a linear least-squares fit, with independent variables x_1 and x_2, and dependent variable y, as follows:

$$y = a_1 x_1 + a_2 x_2 + c \qquad (13)$$

where $y = \log N_f$, $x_1 = \log S_{\max}$, $x_2 = \log \frac{1-R}{2}$

Discussion of Mean Stress Equations

It is useful to consider the above mean stress equations from the viewpoint of the accuracy that they provide in estimated life. In particular, plotting a successful equivalent stress σ_{ar} or S_{ar} versus life should cause fatigue life data for various mean stresses to all fall along the same line, specifically the S-N curve for zero mean stress ($R = -1$).

Using the modified Goodman relationship, Eq 6, the data of Fig. 4 are plotted in this manner in Fig. 5*a*. The correlation is poor, but the estimates are generally conservative, as the data do mostly lie beyond the $R = -1$ fitted line, which is of the form of Eq 5. As expected from Fig. 4, using the Morrow approach gives a much improved correlation, which is shown in Fig. 5*b*, specifically using Eq 8(a). The SWT relationship, Eq 9, gives a correlation of intermediate quality as seen in Fig. 5*c*. Note that the SWT approach is seen to give a nonconservative estimate for compressive mean stresses.

In some cases, particularly for aluminum alloys, fatigue data fitted to Eq 5 may give a coefficient σ'_f that is substantially larger than the true fracture strength $\tilde{\sigma}_f$. In these cases, the Morrow approach works best in the form of Eq 8(b) with $\tilde{\sigma}_f$. Such a case is shown in Fig. 6, where using σ'_f would clearly not give a satisfactory result. For this set of data, the correlation for the Eq 8(b) form is shown in Fig. 7*a*, and for the SWT equation in Fig. 7*b*. The latter is clearly superior for this aluminum alloy.

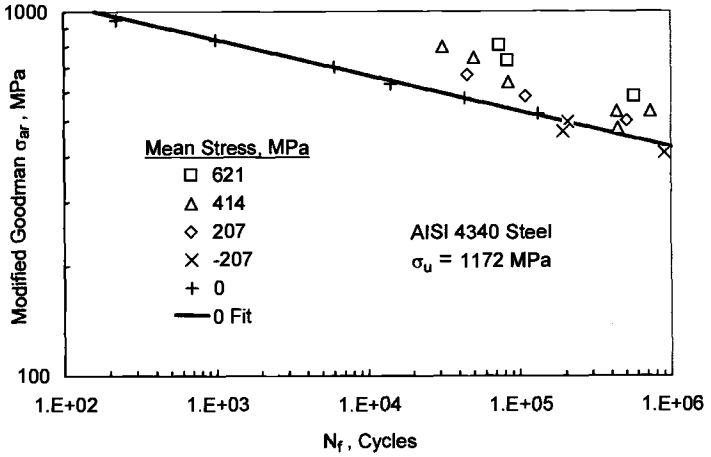


FIG. 5*a*—*Equivalent completely reversed stress from the modified Goodman equation versus life for the data of Fig. 4.*

From the published literature, and from analysis of various additional sets of data, we reach the following general conclusions for unnotched material: The modified Goodman equation is inaccurate but conservative for tensile mean stress. The Morrow equation works well for steels, but it should not be used in the form of Eq 8(a) for nonferrous alloys unless it can be confirmed that σ'_f is reasonably close to $\tilde{\sigma}_f$. The SWT approach seems to be especially accurate for aluminum alloys, and gives reasonable results in general, although for some steels it may not be as accurate as Morrow. For compressive mean stress, both Goodman and SWT tend to be nonconservative.

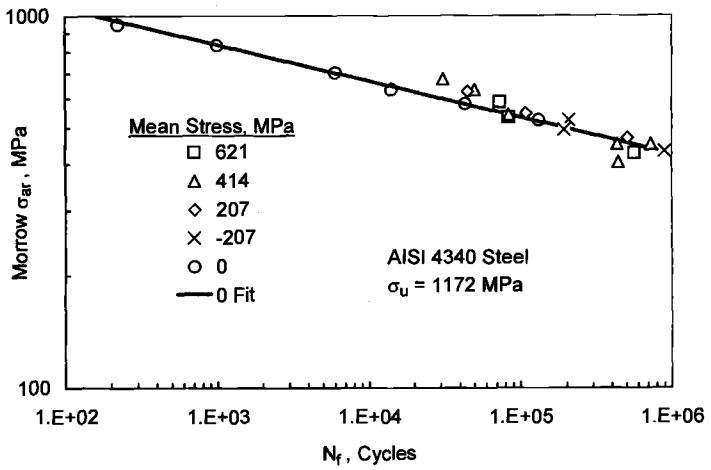


FIG. 5*b*—*Equivalent completely reversed stress from the Morrow equation with σ'_f versus life for the data of Fig. 4.*

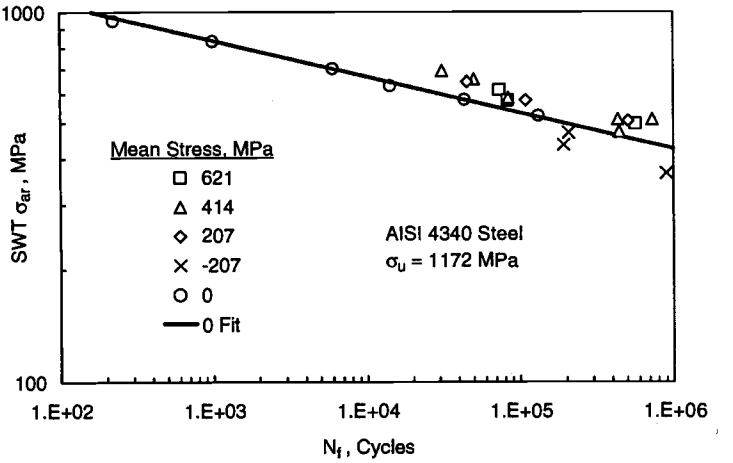


FIG. 5*c*—*Equivalent completely reversed stress from the Smith, Watson, and Topper equation versus life for the data of Fig. 4.*

Now consider notched members. For a notched member of an aluminum alloy, attempted correlations are shown in Figs. 8*a*, 8*b*, and 8*c* for the modified Goodman, SWT, and Walker methods, specifically using Eqs 7, 10, and 11(a), respectively. The correlation for Goodman is poor, that for SWT is intermediate, and that for Walker is quite good. Obviously, the opportunity with the Walker approach to vary the additional parameter γ permits a better fit, in this case with $\gamma = 0.733$. Fitting the Walker equation often gives a value closer to $\gamma = 0.5$, and in such cases the SWT and Walker methods give similar results. (See MIL-HDBK-5G [*35*] for a variety of *S-N* curves fitted to the Walker equation.)

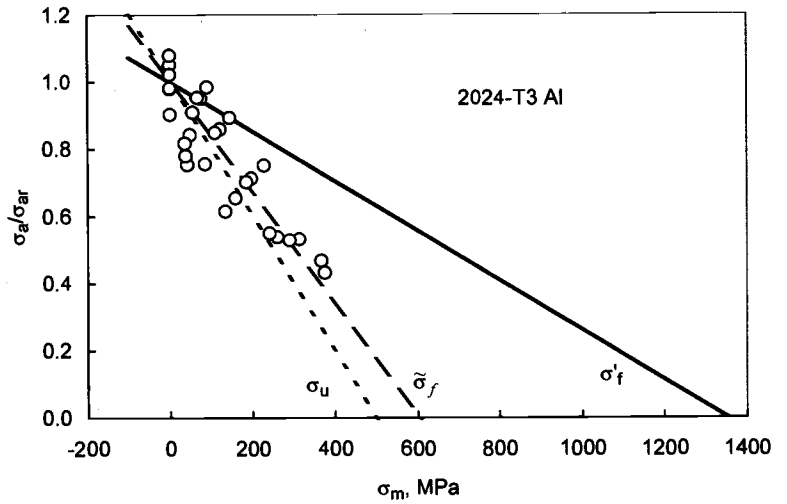


FIG. 6—*Normalized amplitude-mean plot for unnotched axial specimens of 2024-T3 aluminum. (Data from Grover [34].)*

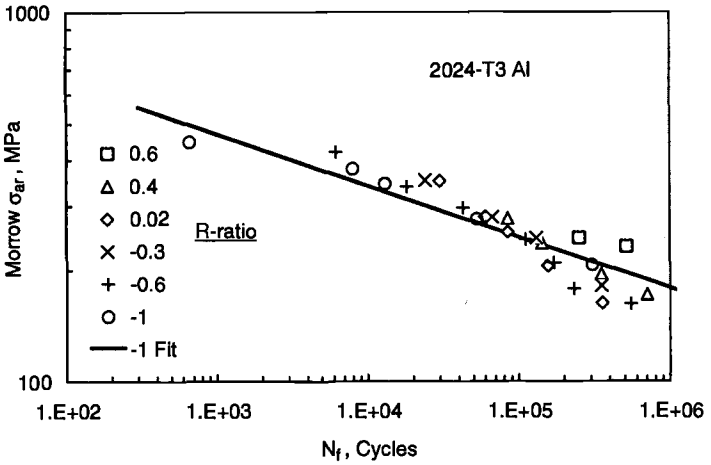


FIG. 7*a*—*Equivalent completely reversed stress from the Morrow equation with* $\tilde{\sigma}_f$ *versus life for the data of Fig. 6.*

Applying the modified Goodman approach to notched members presents a subtle but important difficulty. In particular, for many real engineering components of complex geometry, there is no obvious way to define nominal stress S. However, whatever arbitrary choice is made will affect the numerical values of S, so that the ratio of S_m to σ_u in Eq 7 will change. Thus, different definitions of S will cause the relative adjustment of S_a for mean stress to vary. The SWT and Walker equations contain no ratios of S to materials properties and so give results that are independent of the arbitrary definition of S. In fact, for these it is unnecessary to even define a nominal stress, and they may be applied directly to an applied load P or bending moment M, such as

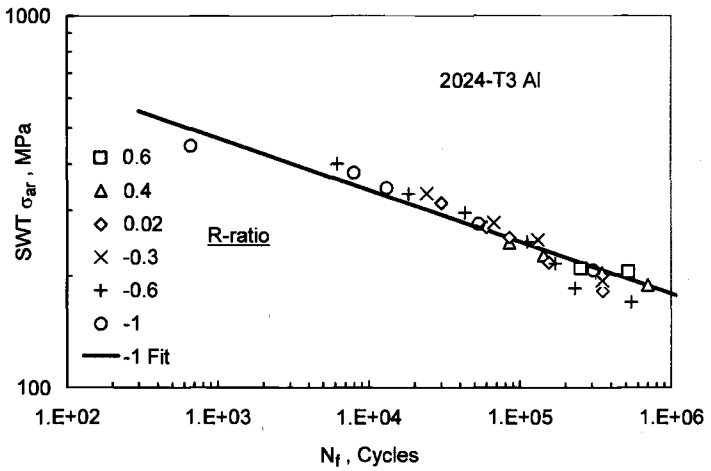


FIG. 7*b*—*Equivalent completely reversed stress from the Smith, Watson, and Topper equation versus life for the data of Fig. 6.*

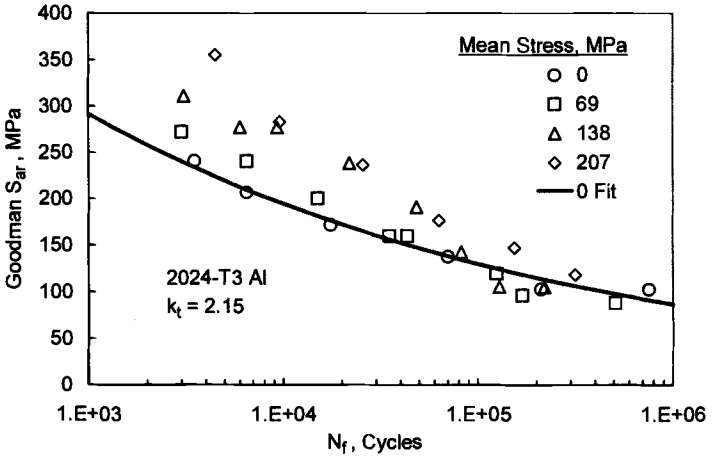


FIG. 8*a*—*Equivalent completely reversed nominal stress from the modified Goodman equation for double-edge-notched axial specimens of 2024-T3 aluminum. (Data from Grover [15].)*

$$P_{ar} = \sqrt{P_{\max} P_a} \qquad \text{(a)}$$

$$P_{ar} = P_{\max}^{1-\gamma} P_a^{\gamma} \qquad \text{(b)} \tag{14}$$

for SWT and Walker, respectively.

Thus, the modified Goodman diagram is not recommended for notched members. The SWT equation should be chosen where limited data are available. The Walker approach should be used where data for more than one mean stress S_m or stress ratio R permit determination of the adjustable parameter γ. If the data are limited to only two different S_m or R values, these values should be widely separated, ideally spanning the range of interest in the application, to provide the most accurate possible value of γ.

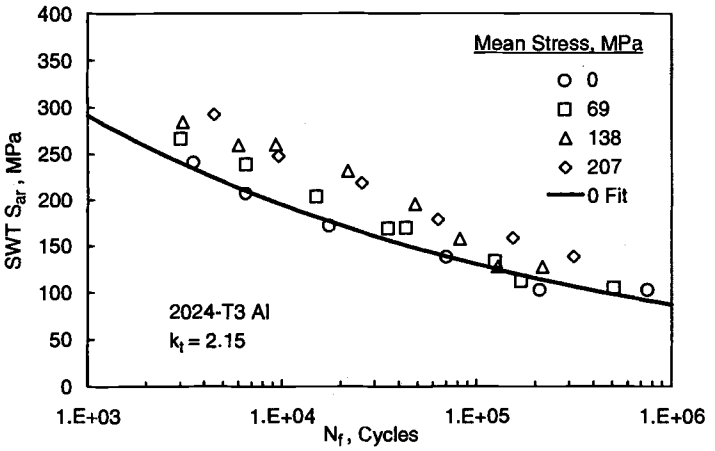


FIG. 8*b*—*Equivalent completely reversed nominal stress from the Smith, Watson, and Topper equation for double-edge-notched axial specimens of 2024-T3 aluminum. (Data from Grover [15].)*

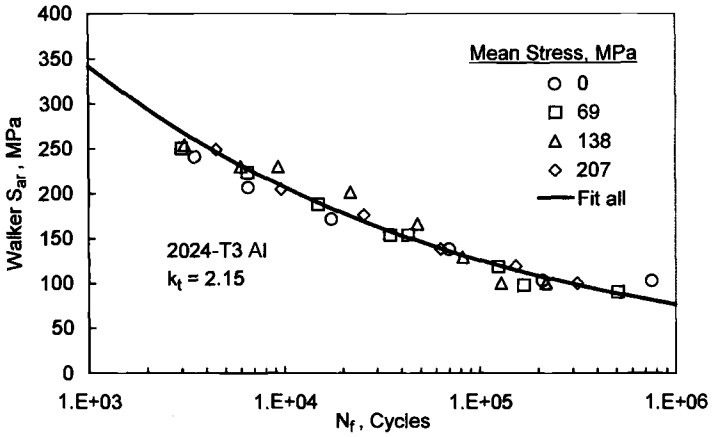


FIG. 8*c*—*Equivalent completely reversed nominal stress from the Walker equation for double-edge-notched axial specimens of 2024-T3 aluminum. The curve is a fit to Eq 12(b) with* $\gamma = 0.733$. *(Data from Grover [15].)*

Strain-Based Approach

The strain-based approach employs a strain versus life curve, and it specifically considers local yielding at notches as illustrated in Fig. 9. Mean stress adjustments are made based on values of local mean stress σ_m at the notch. Materials properties are needed in the form of a cyclic stress-strain curve and a strain-life curve.

$$\varepsilon_a = \frac{\sigma_a}{E} + \left(\frac{\sigma_a}{H'}\right)^{1/n'} \tag{15}$$

$$\varepsilon_a = \frac{\sigma'_f}{E}(2N_f)^b + \varepsilon'_f(2N_f)^c \tag{16}$$

Both of these equations involve the summation of terms corresponding to elastic and plastic strain. The quantities σ_a and ε_a are the amplitudes of stress and strain, respectively, E is the elastic modulus, and H', n', σ'_f, b, ε'_f, and c are fitting constants that are considered to be materials properties. Values of these for various materials are tabulated in Refs *20* and *21*. The yield strength of the cyclic stress-strain curve of Eq 15 may differ considerably from that for an ordinary tension test due to the effects of cycle-dependent hardening or softening. Equation 16 arises from separately fitting stress amplitude σ_a and plastic strain amplitude ε_{pa} to log-log straight lines as shown in Fig. 10. Noting that the elastic strain amplitude is $\varepsilon_{ea} = \sigma_a/E$, summing the elastic and plastic parts then gives the total strain amplitude, $\varepsilon_a = \sigma_a/E + \varepsilon_{pa}$. Hence, Eq 16 includes Eq 5 in its first term.

Life estimates for notched members may be made by employing these equations along with the results of elastic stress analysis, as adjusted for local yielding. The elastic stress analysis can be in the form of a stress concentration factor k_t, or other elastic stress analysis, such as finite element analysis.

In this section of the paper, we will first summarize the procedure for life predictions by the strain-based approach. Some discussion then follows. Finally, a method will then be suggested for adapting this approach to obtain an adjusted *component-specific strain-life*

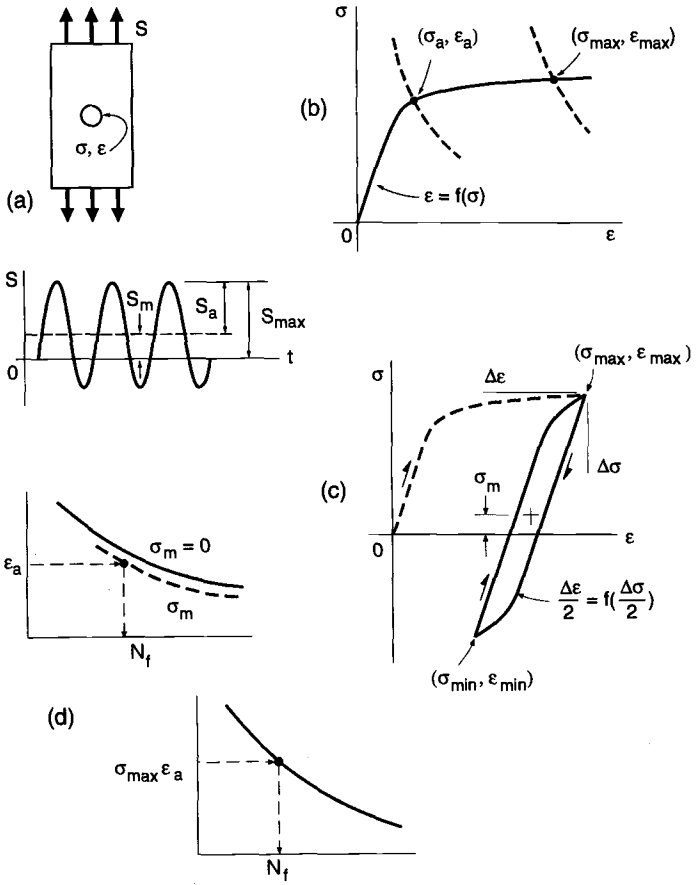


FIG. 9—*Procedure for strain-based life prediction for a notched member under constant amplitude loading. (Adapted from Dowling [22], p. 675; © 1999 by Prentice Hall, Upper Saddle River, NJ; reprinted with permission.)*

curve that includes effects such as surface finish and interaction of high and low load levels in irregular load histories.

Life Estimates for Notched Members

Neuber's rule or similar methods are often employed to extrapolate elastic analysis so that stresses and strains can be estimated that do include the effects of local yielding. For yielding that is confined to the local region of the notch, that is, for cases where there is no general yielding over the entire cross section, Neuber's rule takes the form

$$\sigma\varepsilon = \frac{(k_t S)^2}{E} \tag{17}$$

The quantities σ and ε are the local stress and strain at the notch, and their product is a

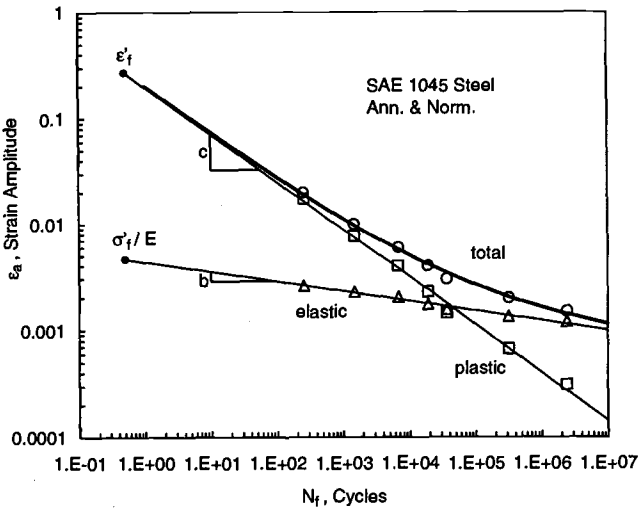


FIG. 10—*Elastic, plastic, and total strain versus life curves for a plain carbon steel. The quantities* ε'_f *and* σ'_f/E *are intercepts at* $N_f = 0.5$ *cycle, and* c *and* b *are slopes on the log-log plot. (Data from Leese [36].)*

function of the quantity $\sigma_{elas} = k_t S$, which is the stress from elastic analysis. Where finite element analysis with a sufficiently fine mesh at the expected failure site is available, σ_{elas} can be taken directly as the result of such analysis, so that a nominal stress S and corresponding elastic stress concentration factor k_t need never be defined.

The stress and strain must also obey the stress-strain curve, here assumed to fit the form of Eq 15.

$$\varepsilon = \frac{\sigma}{E} + \left(\frac{\sigma}{H'}\right)^{1/n'} \tag{18}$$

Combining the above two equations and solving for S gives

$$S = \frac{1}{k_t}\sqrt{\sigma^2 + \sigma E\left(\frac{\sigma}{H'}\right)^{1/n'}} \tag{19}$$

Given S, it is first necessary to solve Eq 19 for σ, which requires a trial and error or numerical solution. Once σ is obtained, substitute this into Eq 18 to obtain ε. The solution of Eqs 17 and 18 to obtain local notch stress and strain may be thought of as the intersection of a hyperbola with the σ-ε curve as shown in Fig. 9*b*. A slight modification to express Eq 19 in terms of $\sigma_{elas} = k_t S$ allows this quantity to be employed.

For application to a notched member under constant amplitude cyclic loading, first enter Eq 19 with the maximum nominal stress S_{max} and solve for σ_{max}. Then substitute the latter into Eq 18 to obtain ε_{max}. Next, take the nominal stress amplitude S_a and follow the same procedure to obtain σ_a and ε_a. Once this is done, additional stresses and strains that are of interest may be computed.

$$\begin{aligned} \sigma_{min} &= \sigma_{max} - 2\sigma_a \qquad \text{(a)} \\ \varepsilon_{min} &= \varepsilon_{max} - 2\varepsilon_a \qquad \text{(b)} \\ \sigma_m &= \sigma_{max} - \sigma_a \qquad \text{(c)} \end{aligned} \tag{20}$$

The stress-strain response at the notch may then be plotted as shown in Fig. 9*c*. Let Eq 18 be represented as $\varepsilon = f(\sigma)$. This path is followed to the point $(\varepsilon_{max}, \sigma_{max})$. The subsequent cyclic loading may then be approximated as repeatedly forming a stress-strain hysteresis loop as shown, where the loop curves follow the base stress-strain curve as scaled up by a factor of two, $\Delta\varepsilon/2 = f(\Delta\sigma/2)$, with $\Delta\varepsilon$ and $\Delta\sigma$ being the changes relative to each loop tip.

To obtain the estimated life from these stresses and strains, the strain-life curve of Eq 16 needs to be adjusted to reflect the effect of the mean stress σ_m. One method of doing so is to assume that the effect of σ_m on life is given by Eq 8(a). On this basis, the strain-life relationship, Eq 16, should be modified as follows:

$$\varepsilon_a = \frac{\sigma'_f}{E}(2N^*)^b + \varepsilon'_f(2N^*)^c, \qquad N_f = N^* \left(1 - \frac{\sigma_m}{\sigma'_f}\right)^{-1/b} \tag{21}$$

The life N^* is calculated from ε_a as if there were no effect of mean stress, and then the value is adjusted to reflect σ_m by calculating the actual N_f from the second expression. A modification of Eq 21 is often employed where the σ_m adjustment is dropped from the second term of the strain-life equation

$$\varepsilon_a = \frac{\sigma'_f}{E}\left(1 - \frac{\sigma_m}{\sigma'_f}\right)(2N_f)^b + \varepsilon'_f(2N_f)^c \tag{22}$$

The above equation roughly compensates for the fact that the value of σ_m as calculated above tends to be too large at short lives. This occurs as a result of some of the mean stress being lost due to relaxation toward zero, which is caused the relatively large plastic strain at short lives. Recalling the earlier discussion of Eqs 8(a) and 8(b), and for cases where σ'_f is not close to $\tilde{\sigma}_f$, the ratio σ_m/σ'_f in Eqs 21 and 22 should be replaced by $\sigma_m/\tilde{\sigma}_f$, but σ'_f left unmodified where it appears alone.

The SWT approach is also often applied in strain-based life estimates by taking the quantity $\sigma_{max}\varepsilon_a$ as the variable that controls the life. This quantity is related to the life N_f by taking the product of Eqs 5 and 16, which gives

$$\sigma_{max}\varepsilon_a = \frac{(\sigma'_f)^2}{E}(2N_f)^{2b} + \sigma'_f\,\varepsilon'_f(2N_f)^{b+c} \tag{23}$$

The product $\sigma_{max}\varepsilon_a$ is available from the estimated stresses and strains, determined from Eqs 18 and 19 as described above. Note that calculating the life from any of Eqs 21 to 23 requires a trial and error or numerical solution. This final step is also illustrated in Fig. 9*d*.

Life estimates made by this procedure for notched members of an aluminum alloy are compared with test data in Fig. 11. The comparison is made for both $S_m = 0$ and for one additional tensile S_m value, with Eq 23 being employed for the latter. Smooth curves are shown that connect estimates made at a number of different stress levels, and these are seen to be in reasonable agreement with the test data points. Since the strain-life curve corresponds to failure of axially loaded specimens of fairly small diameter, typically around 7 mm, the

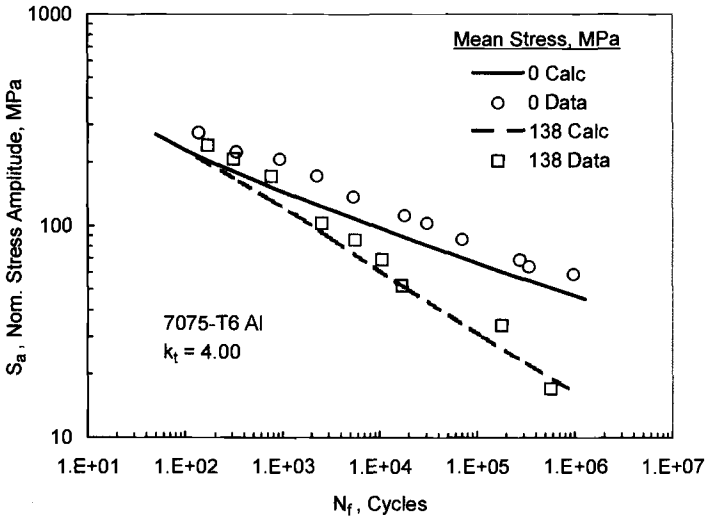


FIG. 11—*Lives calculated by the strain-based approach compared with test data for double-edge-notched specimens of 7075-T6 aluminum. Neuber's rule, Eq 17, was employed to estimate local stresses and strains, and lives were obtained from Eq 23. (Data from Grover [15], Illg [37], and Naumann [38].)*

lives estimated correspond to the initiation of a crack of length around 1 to 2 mm. Additional crack growth to failure in these notched members at least partly explains why the actual lives are somewhat longer than the estimates.

Life Estimates Extended to Irregular Loading Histories

The procedure just described for constant amplitude loading can be extended to irregular variation of load with time as summarized by Fig. 12. The stress-strain behavior follows hysteresis loops as shown, with the closing of these being controlled by the *memory effect.* In particular, the stress-strain paths after each change in the direction of loading can be approximated as following $\Delta\varepsilon/2 = f(\Delta\sigma/2)$. However, at points such as B', a hysteresis loop closes when it reaches the point of prior unloading where the loop started, such as B. At such points, the memory effect acts, and the previously established path, such as *A-B-D*, is continued. For each loop, such as *B-C*, and for the range locating its beginning, such as *A-B*, the half ranges $\Delta\varepsilon/2$ and $\Delta\sigma/2$ are analyzed using Eqs 18 and 19. Such analysis for the entire history allows the stresses and strains to be determined for all points in the history. In addition to *A-B* and *B-C*, the following ranges need to be analyzed for this example: *A-D*, *D-E*, *E-F*, *F-G,* and *E-H*. Also, the starting point *A* needs to be established in the same manner as the S_{max} point for the constant amplitude loading in Fig. 9.

Each closed hysteresis loop, such as *B-C*, *F-G*, *E-H,* and *A-D* in Fig. 12, corresponds to a cycle as identified by the *rain flow cycle counting method* [ASTM Standard E 1049, Cycle Counting in Fatigue Analysis]. The life N_{fj} corresponding to each can be determined, as from its strain amplitude, $\varepsilon_a = \Delta\varepsilon/2$, and its mean stress, σ_m, applied to Eq 22. The life for the variable amplitude loading can then be estimated from the Palmgren-Miner rule. If a sequence of irregular loading is assumed to be repeated until failure occurs, this rule takes the form

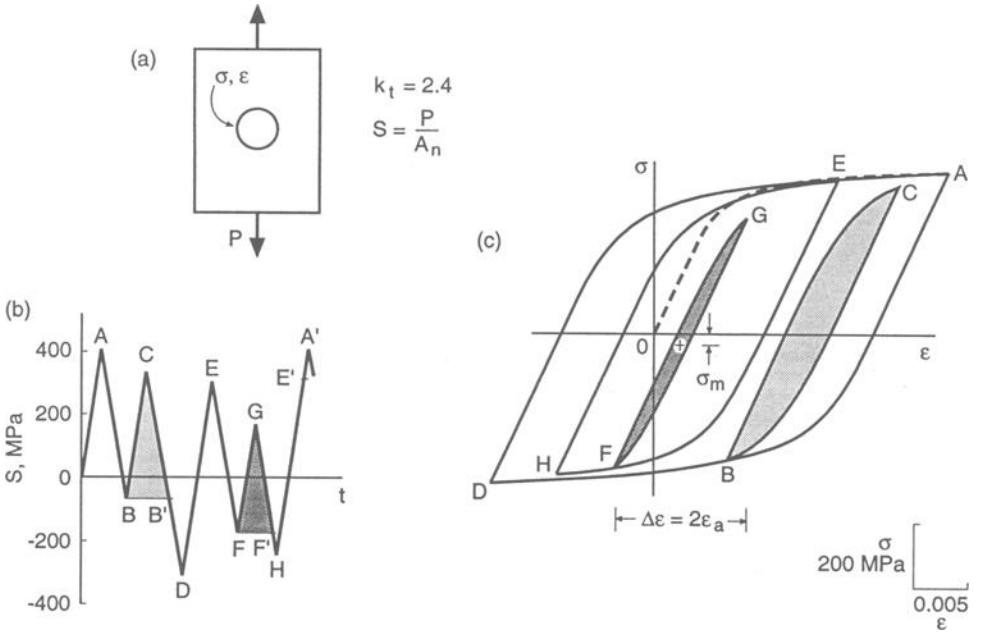


FIG. 12—*Analysis of a notched member subjected to an irregular load versus time history. Notched member* (a)*, made of 2024-T4 aluminum, is subjected to load history* (b)*. The estimated local stress-strain response at the notch is shown in* (c)*. (From Dowling [22], p. 677; © 1999 by Prentice Hall, Upper Saddle River, NJ; reprinted with permission.)*

$$B_f \left[\sum \frac{N_j}{N_{fj}} \right]_{\substack{\text{one} \\ \text{rep.}}} = 1 \tag{24}$$

The summation is performed for one repetition of the history. The N_j are the numbers of times each loop occurs in one repetition of the history, and the N_{fj} are the corresponding numbers of cycles to failure. Once the summation is done, one can solve for B_f, which is the estimated number of repetitions of the history to failure.

A more detailed description of this procedure is given in Section 14.5 of Dowling [22]. Also described there, and in more detail in Ref *39*, is a simplified method for irregular histories that results in upper and a lower bounds on the life being calculated.

Discussion of the Strain-Based Approach

Compared to estimated *S-N* curves as discussed earlier, the strain-based approach is seen to require fewer empirical adjustments. Application of the method to a number of different stress levels in fact provides an estimated *S-N* curve, as in Fig. 11. The effects of different component geometries and of localized yielding explain the need for m' in Eq 3 and the trend of a reduced notch factor k'_f at short lives. Since the strain-based approach includes these effects in its analysis in a more fundamental way, m' and k'_f become unnecessary.

Considering the factors in Eq 1, k_f is sometimes used in place of k_t in strain-based analysis, as in Neuber's rule, Eq 17. However, a large adjustment of k_t to obtain k_f, as from Eq 2, is

mainly needed for quite sharp notches where crack growth dominates the life. We suggest retaining k_t in the strain-based analysis and analyzing the crack growth dominated behavior in very sharply notched members by the methods of fracture mechanics. See Refs *40* and *41* for more detail and discussion on this point.

If the strain-life curve is based on data that extend to long lives, m_e in Eq 1 becomes unnecessary. However, strain-life curves extended to long lives will exhibit the same fatigue limit as seen in *S-N* curves. As discussed previously, this limit should not be considered to be a safe level, below which no fatigue damage occurs, if it is exceeded even occasionally in the actual service loading. Note that the strain-life curve in the form of Eq 16 does not include a fatigue limit. Use of this at arbitrarily long lives is equivalent to the dashed line extension in Fig. 2.

The factor m_t in Eq 1 is used in part to account for the slightly lower *S-N* curves observed for axial loading as compared to bending. This effect is due to the differing stress gradients in the two situations and is related to a weakest link type of size effect. Since the strain-based approach employs axial specimen data, it is conservative with respect to this effect when applied to bending situations. The other use of m_t is to include the state-of-stress effect for the shear stresses that occur in torsion. In the strain-based approach, this can be handled by employing cyclic stress-strain and strain-life curves that correspond to the case of pure shear. See SAE publication AE-14 [*42*] for details and for additional information on strain-based analysis of multiaxial loading.

This leaves the size effect factor m_d and the surface finish factor m_s. The need for these continues for the strain-based approach. Specific data to allow evaluation of these is widely available only for steels, so that special tests may be required where their evaluation is truly needed. The surface finish effect is largest at long lives, so that a reasonable method of including it is to lower the slope constant b of Eqs 5 and 16, while leaving the remaining constants unchanged. Hence, in Fig. 10, the elastic strain line will still have the same intercept σ'_f/E, but it will have a steeper slope, and so will be increasingly lower at longer lives, as will the overall strain-life curve. The estimated effect of a machined surface finish on an alloy steel is shown in Fig. 13. If a reduction factor m_s is applied at a long life of N_e cycles, such as 10^6 cycles for steel, the modified slope is

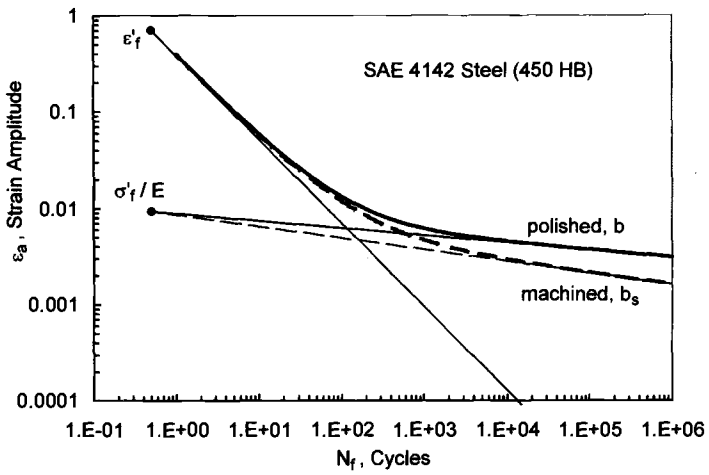


FIG. 13—*Strain-life curve from an alloy steel with* σ_u = *1757 MPa, and also the curve adjusted for a machined surface finish, using* m_s = *0.52 from Juvinall [16].*

$$b_s = \frac{\log[m_s(2N_e)^b]}{\log(2N_e)} \tag{25}$$

In a study of size effect in large shafts of carbon and low-alloy steels, Placek [*43*] recommends modifying the strain-life curve by lowering the intercept constants σ'_f and ε'_f by a common size factor, giving new values of

$$\sigma'_{fd} = m_d\sigma'_f, \qquad \varepsilon'_{fd} = m_d\varepsilon'_f \tag{26}$$

For a shaft of diameter d, the data of that particular study suggest a reduction factor of

$$m_d = \left(\frac{d}{25.4 \text{ mm}}\right)^{-0.093} \tag{27}$$

Note that some computer programs calculate the cyclic stress-strain constants, H' and n' in Eq 15, from the constants for the strain-life curve, Eq 16, rather than using values fitted to the actual stress-strain test data. This practice is not recommended, especially where the strain-life constants are modified as in Eqs 25 and 26.

Component-Specific Strain-Life Curves

For fatigue-critical engineering components, a few tests are sometimes run, but not generally a sufficient number to generate an entire *S-N* curve. Such tests have the advantage of automatically including effects such as those of size, surface finish, and fabrication detail. If a variable amplitude loading history similar to the expected service loading is applied in these tests, the results also include interaction effects between the high and low load levels. In particular, occasional severe stress levels have two effects.

First, the severe cycles affect the local mean stresses for lower level cycles. This effect is included if the strain-based approach is employed as described above for the variable amplitude loading of interest. In particular, the local mean stresses for lower level cycles, such as σ_m for cycle *F-G* in Fig. 12, are affected by the local yielding during the more severe loading events in the history.

Second, the more severe cycles may initiate physical damage in the material such that the lower level cycles have a greater effect than expected from constant amplitude test data. If a distinct fatigue limit exists, this is likely to be lowered or eliminated as already discussed. Even for materials with no distinct fatigue limit, the material may behave as if the strain-life curve were lower at relatively long lives, the effect being qualitatively similar to that of surface finish as in Fig. 13. One approach to dealing with this situation is to apply several cycles at a high strain level prior to testing the strain-life specimens under constant amplitude loading. This provides a lowered strain-life curve and thus more accurate life estimates for notched members under variable amplitude loading. However, strain-life curves from *prestrained* samples are often not available.

Consider a situation where some component *S-N* data are available from tests under variable amplitude loading, and assume that a strain-life curve is available, but not one that includes the prestrain effect. The following procedure is suggested: Adjust the strain-life curve, primarily by changing b in Eq 16, to give a lower curve at long lives, until agreement is obtained between the *S-N* data and life estimates from the strain-based approach. The resulting *component-specific strain-life curve* would then be expected to give improved life estimates for similar situations, such as load histories or geometries that differ only modestly

from the case applied in the component *S-N* tests. Note that any surface finish effects, and perhaps also size effects, will be automatically included in the new strain-life curve.

An illustration of this process is given in Fig. 14. The data points shown correspond to notched plates subjected to the standard helicopter loading spectrum Felix [*44*]. Denoting the peak nominal stress in the spectrum as the 100% level, the spectrum contains occasional ground-air-ground cycles that range between −28 and 100%, or slightly below, in each simulated flight. There are numerous additional cycles at lower levels, averaging about 16,300 in number per flight, with most of these having a relatively high tensile mean stress. A strain-life curve for the titanium 6A1-4V material [*39*] had a value of $b = -0.0763$ for Eq 16. However, this gave nonconservative life estimates. Changing to $b = -0.095$, while leaving σ'_f, ε'_f, and c unchanged, gives better agreement on an average basis. Alternatively, $b = -0.100$ gives calculated lives at the lower limit of the test data. The component-specific strain-life curve with the latter b value is found to be similar to that for prestrained material as given in Boller [*20*] Part D, pp. 136–138.

Crack Growth Approach

Life of engineering components may be estimated based on crack growth using the principles of *fracture mechanics*. This is appropriate in situations where cracks are known to occur, or where safety concerns require the conservative assumption that cracks might be present. In either case, it is necessary to establish an initial crack size a_i that can be reliably found by inspection. Since a crack just below this size might actually occur, the crack growth life is then calculated with a_i as the starting point.

The accuracy of life estimates by the stress- or strain-based approaches can also be improved by employing stress-life or strain-life curves that correspond to the life N_i required

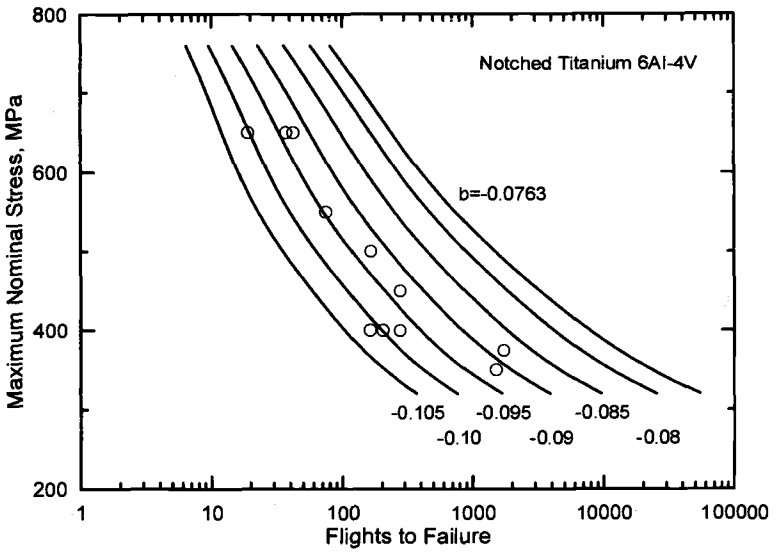


FIG. 14—*Strain-based life estimates using Eq 23 for the standard helicopter load spectrum Felix applied to plates with round holes* ($k_t = 2.5$) *of mill-annealed titanium 6A1-4V. The constant* b = *−0.0763 from strain-life data on similar material gives nonconservative life estimates, but the strain-life curve adjusted with a value around* b = *−0.095 gives better agreement. (Notched specimen data from Edwards [44] and original strain-life curve from Dowling [39].)*

to initiate a crack of a specific relatively small size. This crack size is then taken as the initial size a_i in calculating the number of cycles N_{if} for crack growth to failure. The total life N_f for crack initiation and growth to failure is then the sum.

$$N_i + N_{if} = N_f \tag{28}$$

Combining crack initiation and growth phases to obtain total life is discussed in detail in Refs *40* and *45*.

In analyzing crack growth, the concept of a *stress intensity factor*, K, is employed. This quantity combines the geometry, stress, and crack length to obtain a single variable that characterizes the severity of the crack situation. It is usually expressed mathematically in one of two forms.

$$K = FS\sqrt{\pi a}, \qquad K = F_P \frac{P}{t\sqrt{b}} \qquad \text{(a, b)} \tag{29}$$

For the first form, a, is crack length, S is a conveniently defined nominal stress, and F is a dimensionless factor that depends on geometry and the ratio a/b of crack length to a length characterizing the member width, b. For the second form, P is the applied load, t is the member thickness, and F_P is a different geometry function of a/b. The first form is used more frequently than the second, but the second is sometimes convenient.

Several excellent books provide detailed information on fracture mechanics concepts and applications, such as Anderson [*46*], Broek [*47*], and Ewalds [*48*]. Also, F or F_P can be evaluated from extensive information available in various handbooks and papers, such as Murakami [*49*], Tada [*50*], and Newman [*51*].

Crack Growth Life Estimates

The overall approach for estimating crack growth life is illustrated Fig. 15. Tests are conducted on material specimens that contain cracks intentionally introduced by starting them from a slot with a sharp end. Crack growth rates per cycle, da/dN, are measured and plotted versus the cyclic range of K, which is determined from the cyclic range of either S or P.

$$\Delta K = F\,\Delta S\sqrt{\pi a}, \qquad \Delta K = F_P \frac{\Delta P}{t\sqrt{b}} \qquad \text{(a, b)} \tag{30}$$

The da/dN versus ΔK data may form a straight line on a log-log plot, so that the behavior may be represented by an equation of a form first employed by Paris.

$$\frac{da}{dN} = C(\Delta K)^m \tag{31}$$

The crack growth rate is also affected by the mean level of the cyclic loading, as characterized by the ratio $R = S_{\min}/S_{\max}$. Hence, this effect needs to be included in the test data.

As suggested by Fig. 15, the life for crack growth in an engineering component can be estimated by combining Eqs 30 and 31, where the exact version of the former now corresponds to the component case. In some cases, F for Eq 30(a) is approximately constant during most of the crack growth life, in which case the life is given by

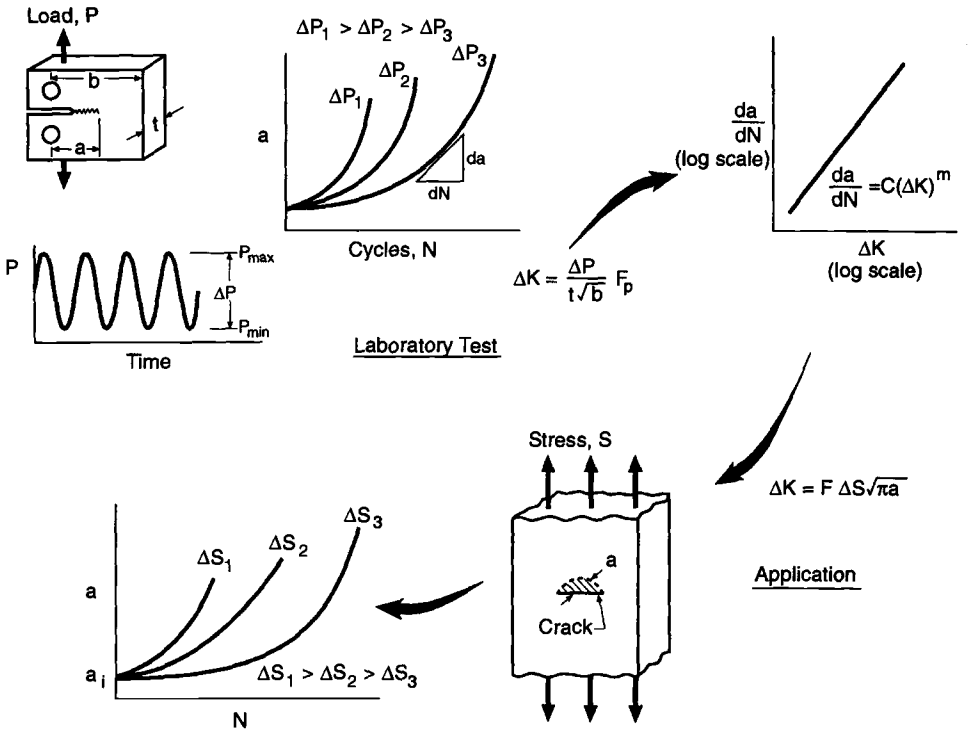


FIG. 15—*Steps in obtaining* da/dN *versus* ΔK *data and using it for an engineering application. (Adapted from Clark [52]; reprinted from* Experimental Mechanics *with the permission of the Society for Experimental Mechanics, Inc., Bethel, CT.)*

$$N_{if} = \frac{a_f^{1-m/2} - a_i^{1-m/2}}{C(F\,\Delta S\sqrt{\pi})^m(1 - m/2)} \tag{32}$$

The final crack length a_f is controlled by either brittle fracture at the *fracture toughness* K_c corresponding to the member thickness, or by fully plastic yielding, depending on the geometry and materials properties. If F varies considerably, or if a da/dN versus ΔK relationship of more complex form than Eq 31 is needed, then a numerical integration will usually be required to calculate N_{if}.

Representing da/dN *Versus* ΔK *Behavior*

If the da/dN versus ΔK behavior is measured over a wide range of growth rates, fairly complex behavior is observed as seen for an aluminum alloy in Fig. 16. At high values of ΔK, the behavior deviates from Eq 31, as the growth rates accelerate toward an asymptote determined by $K_{max} = K_c$, the fracture toughness. However, for tough but low-strength materials, the asymptote may be controlled by $P_{max} = P_o$, where P_o is the fully plastic limit load for the cross section remaining beyond the crack, as affected by the material's yield strength. And at low values of ΔK, the growth rates again depart from Eq 31 and approach an asymptote associated with a threshold value ΔK_{th} below which crack growth does not

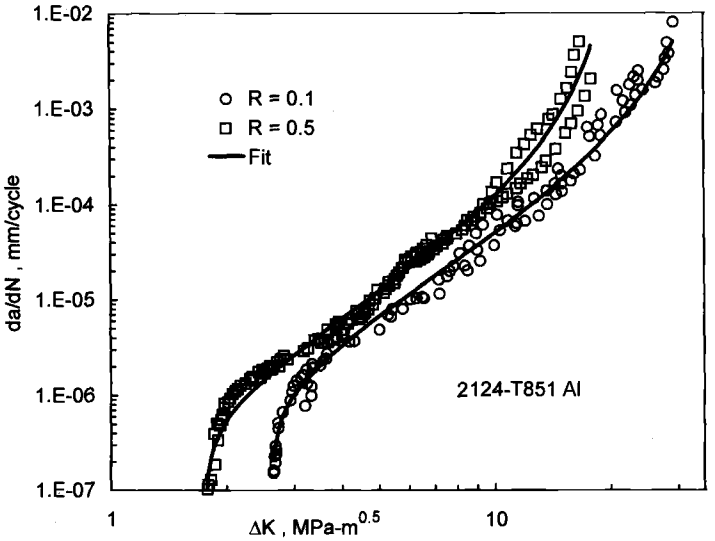


FIG. 16—*Fatigue crack growth rate data for 2124-T851 aluminum at two different* R *ratios for 9.5-mm-thick material. (Data from Ruschau [53], courtesy of J. P. Gallagher, University of Dayton Research Institute, Dayton, OH.)*

ordinarily occur. The value of ΔK_{th} is usually more sensitive to R ratio than would be expected from the behavior at higher growth rates.

This complexity has led to numerous equations being proposed for fitting da/dN versus ΔK data over a wide range, as described by Forman [*54*], Walker [*33*], and Miller [*55*]. There is no consensus in the technical community as to which equation is best. As a result, tabulations of materials constants for fatigue crack growth are not widely available, and this has in turn made it more difficult for engineers to apply crack growth analysis. Therefore, we will further discuss da/dN versus ΔK relationships, and we will make some specific recommendations as to equations that might be used as a basis for tabulating materials properties.

First, consider the region of intermediate growth rates where it is reasonable to apply Eq 31, which is often called the *Paris region.* Metals vary in their sensitivity to R ratio, so that some means of characterizing these different sensitivities is needed. The Walker relationship as in Eq 11b appears to work well. Applied to K, this takes the form

$$\overline{\Delta K} = K_{\max}\,(1 - R)^{\gamma}, \qquad \overline{\Delta K} = \frac{\Delta K}{(1 - R)^{1-\gamma}} \qquad \text{(a, b)} \tag{33}$$

where $\overline{\Delta K}$ is an equivalent zero-to-maximum ΔK that causes the same growth rate as the actual $K_{\max}$ and R combination, or, for the second form, the same ΔK and R combination. The second form arises from the first by invoking the definition of R to obtain $\Delta K = K_{\max}\,(1 - R)$, and then using this to eliminate $K_{\max}$. The value of γ employed is obtained specifically from crack growth data.

If the particular value of C in Eq 31 for $R = 0$ is denoted as C_1, and if $\overline{\Delta K} = \Delta K$ is noted to apply for this $R = 0$ case, combining Eqs 31 and 33 gives

$$\frac{da}{dN} = C_1(\overline{\Delta K})^m, \qquad \frac{da}{dN} = C_1\left(\frac{\Delta K}{(1-R)^{1-\gamma}}\right)^m \qquad \text{(a, b)} \tag{34}$$

Form (b) is equivalent to Eq 31, with C depending on R according to

$$C = \frac{C_1}{(1-R)^{m(1-\gamma)}} \tag{35}$$

Hence, if da/dN versus ΔK data representing several different R ratios are plotted on log-log coordinates, a family of parallel straight lines is expected. The data shown in Fig. 17*a* for a stainless steel approximately follow such a trend. Alternatively, one can plot da/dN versus $\overline{\Delta K}$, and all of the data should fall along a single straight line corresponding to C_1, as shown in Fig. 17*b* for the same set of data.

Using Eq 34, the constants C_1, m, and γ can all be obtained in a single least-squares fit of a set of data including several different R ratios. The procedure is parallel to that of Eqs 12 and 13, with there again being two independent variables, in this case, $\log(\Delta K)$ and $\log(1-R)$, and with $\log(da/dN)$ now being the dependent variable.

We have analyzed da/dN versus (ΔK, R) data in the Paris region for several metals, or confirmed fits done by others, and find that Eq 34 generally fits the data well. (See Ref *22*, p. 506 for some tabulated constants.) Values approaching $\gamma = 1$ correspond to low sensitivity to R ratio, and values around $\gamma = 0.5$ or less indicate a considerable sensitivity. It is necessary to fit data separately for $R < 0$, that is, for cases involving compression. For relatively high-strength metals, $\gamma = 0$ works well for $R < 0$, as this corresponds to the compressive portion

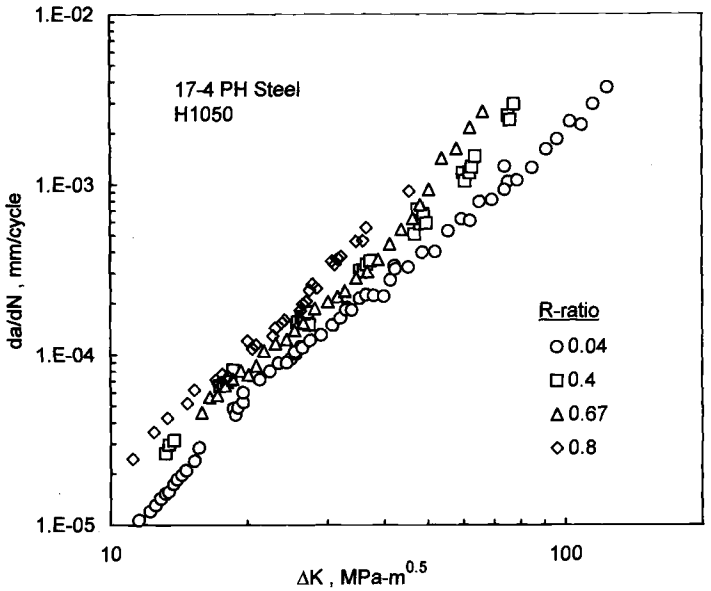


FIG. 17*a*—*Fatigue crack growth rate data at various* R *ratios for a stainless steel. (Data from Crooker [56].)*

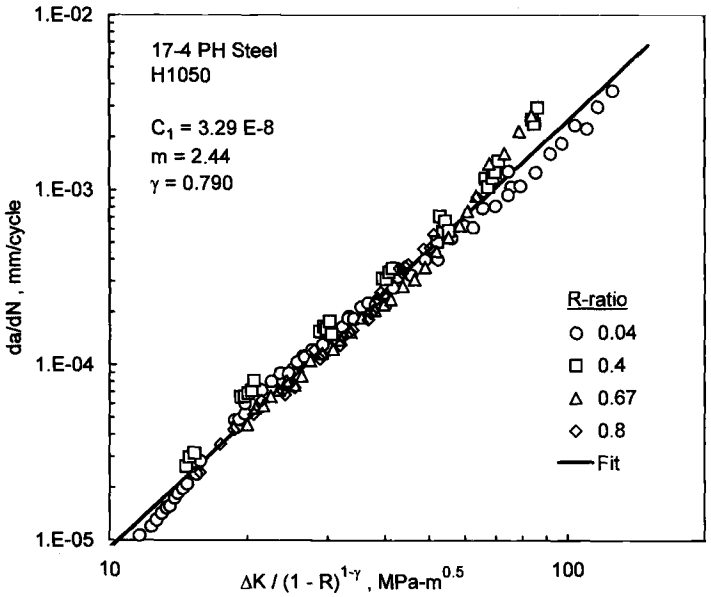


FIG. 17*b*—*Crack growth rate versus* $\overline{\Delta K}$, *the equivalent zero-to-maximum stress intensity factor from the Walker equation, for the data of Fig.* 17a.

of the cyclic load having no effect. But for relatively low-strength metals, a nonzero γ for $R < 0$ may be needed, and this value will differ from the value for $R \geq 0$.

Therefore, we recommend that the Walker relationship be seriously considered by the fracture mechanics community as a standard equation for representing the Paris region, and that values of C_1, m, and γ be tabulated as materials properties. Where this is done, one approach to handling the asymptotes is to replace them with vertical lines as shown in Fig. 18. That is, sudden failure is assumed to occur when either $K_{max} = K_c$ or $P_{max} = P_o$ is reached, and growth rates are taken to be zero where ΔK is below ΔK_{th}. However, caution is needed in assuming that an absolute threshold exists, as ΔK_{th} may be lowered by overload interaction effects, and ΔK_{th} for small cracks may be lower than for long cracks. One conservative option is to ignore the threshold as suggested by the dashed line.

Where threshold values are employed, some relationship for representing the effect of R ratio on ΔK_{th} is needed, such as

$$\Delta K_{th} = \overline{\Delta K}_{th}(1 - R)^{1-\gamma_{th}} \tag{36}$$

This is a separate application of the Walker equation, with $\overline{\Delta K}_{th}$ being the value for $R = 0$. The value of γ_{th} characterizes the sensitivity of the threshold to R and will generally have a different value than γ for the Paris region. Other analogous equations could be used.

Fitting Over a Wide Range of da/dN *Versus* ΔK

It will sometimes be desirable to more accurately represent the da/dN versus ΔK data by continuous curves. One option is to employ an equation of the following form:

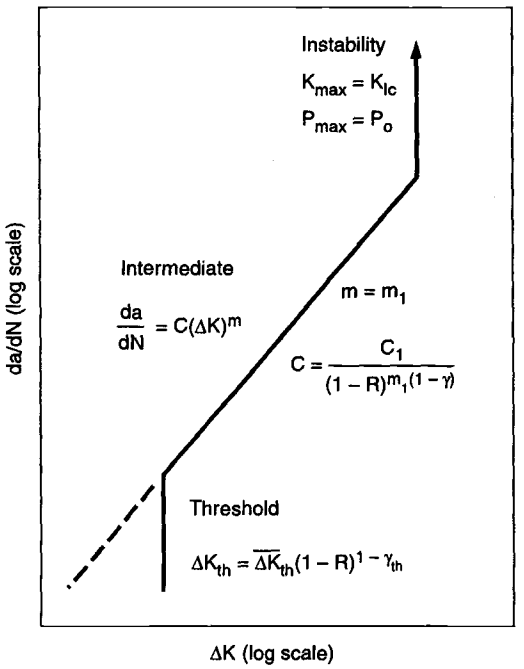


FIG. 18—*Approximate representation of* da/dN *versus* ΔK *behavior with the Walker equation and with asymptotes replaced by vertical lines. (From Dowling [22], p. 511; © 1999 by Prentice Hall, Upper Saddle River, NJ; reprinted with permission.)*

$$\frac{da}{dN} = C_2 \left(\frac{\Delta K}{(1-R)^{1-\gamma_2}} \right)^{m_2} \frac{\left(1 - \frac{\Delta K_{th}}{\Delta K}\right)^p}{\left(1 - \frac{\Delta K}{(1-R)K_c}\right)^q} \tag{37}$$

The first element above is based on the Walker relationship as in Eq 34 and again provides a means of adjusting the sensitivity to R. However, when fitted in this equation, C_2, m_2, and γ_2 will differ considerably from the corresponding values for Eq 34. The quotient element is the same as employed by Henkener [*57*]. Its numerator gives the lower asymptote at ΔK_{th}, and its denominator gives the upper asymptote at $\Delta K/(1-R) = K_{max} = K_c$. When used with a relationship such as Eq 36 that gives the R dependence of ΔK_{th}, all constants can be determined in a single least-squares fit with four independent variables, which correspond to the logarithms of the numerators and denominators of the two elements of Eq 37.

The curves shown in Fig. 16 for 2124-T851 aluminum result from a fit to Eq 37. Prior to fitting, K_c was evaluated for the 9.5-mm thickness based on data in Ref *58*, and the parameters for Eq 36 were estimated from the lower asymptotes, with some judgment being required. These values and the fitted constants are

$$\begin{aligned} K_c &= 42.5, \quad \overline{\Delta K}_{th} = 2.83, \quad \gamma_{th} = 0.320, \quad C_2 = 2.23 \times 10^{-7} \\ m_2 &= 2.15, \quad \gamma_2 = 0.827, \quad p = 0.498, \quad q = 1.91 \end{aligned} \tag{38}$$

where the units are MPa$\sqrt{\text{m}}$ for K and mm/cycle for da/dN.

A disadvantage of Eq 37 or other continuous fits is that it is difficult to change the asymptotes without disturbing the curves in the Paris region. However, it will often be desirable to alter the upper asymptote, as K_c is dependent on the member thickness. (Note that the plane strain fracture toughness K_{Ic} is the minimum value for thick members.) There are also two additional difficulties: First, in at least some steels, the fracture toughness is altered by the severe cyclic loading just prior to fracture [*59,60*], so that K_c values from the usual static tests do not apply. Second, the final unstable behavior may be controlled by fully plastic yielding, so that it does not depend on K_c at all. As to the lower asymptote, it may be desirable to lower or eliminate the threshold to accommodate the special behavior of small cracks. Considering all of these difficulties with the asymptotes, it seems unwise to allow them to affect the constants for the Paris region.

Hence, it is advantageous to employ a discontinuous fit, using the Walker relationship, Eq 34, in the Paris region, and separate equations above and below. This is illustrated in Fig. 19. The da/dN values at points A and B are selected as a matter of judgment as the ends of the Paris region. Hence, for any particular R ratio, these correspond to ΔK values of

$$\Delta K_A = \left(\frac{(da/dN)_A}{C}\right)^{1/m}, \qquad \Delta K_B = \left(\frac{(da/dN)_B}{C}\right)^{1/m} \tag{39}$$

where C depends on R according to Eq 35. It is also useful to note that points A and B correspond to particular values of $\overline{\Delta K}$, which are related to the corresponding da/dN values by Eq 34(a). Equations of the following form are suggested below A and above B:

$$\frac{da}{dN} = \left(\frac{da}{dN}\right)_A \left(\frac{\Delta K}{\overline{\Delta K_A}}\right)^{\alpha} \left(\frac{\Delta K - \Delta K_{th}}{\Delta K_A - \Delta K_{th}}\right)^{\beta} \qquad (\overline{\Delta K} \le \overline{\Delta K_A}) \quad \text{(a)}$$

$$\frac{da}{dN} = \left(\frac{da}{dN}\right)_B \left(\frac{\Delta K}{\overline{\Delta K_B}}\right)^{\delta} \left(\frac{K_c(1 - R) - \Delta K_B}{K_c(1 - R) - \Delta K}\right)^{\phi} \qquad (\overline{\Delta K} \ge \overline{\Delta K_B}) \quad \text{(b)} \tag{40}$$

As before, ΔK_{th} is dependent on R, as from Eq 36 or another analogous relationship. Equation (a) passes through point A and approaches an asymptote at ΔK_{th}, and (b) passes through point B and approaches an asymptote at $\Delta K = K_c(1 - R)$, that is, at $K_{max} = K_c$. The exponents β and ϕ can be determined from least-squares fitting, in which case α and δ should be chosen to require tangency at A and B, respectively, giving

$$\alpha = m - \beta\left(\frac{\Delta K_A}{\Delta K_A - \Delta K_{th}}\right), \qquad \delta = m - \phi\left(\frac{\Delta K_B}{K_c(1 - R) - \Delta K_B}\right) \tag{41}$$

Due to Eqs 36 and 39, the values of α and δ are seen to vary with R.

This discontinuous fit was applied to the same set of data on 2124-T851 aluminum, and the result is shown as Fig. 20. Also, the curves alone are those shown in Fig. 19. The particular values of the constants are

$$\begin{aligned} &C_1 = 3.85 \times 10^{-8}, \quad m = 3.03, \quad \gamma = 0.565, \quad (da/dN)_A = 1.20 \times 10^{-6} \\ &\beta = 0.938, \quad (da/dN)_B = 1.80 \times 10^{-4}, \quad \phi = 4.10 \end{aligned} \tag{42}$$

with the values of K_c, $\overline{\Delta K_{th}}$, and γ_{th} being the same as before. Compared to the continuous fit, the total number of materials constants is increased by two, and there is additional complexity in the equations involved.

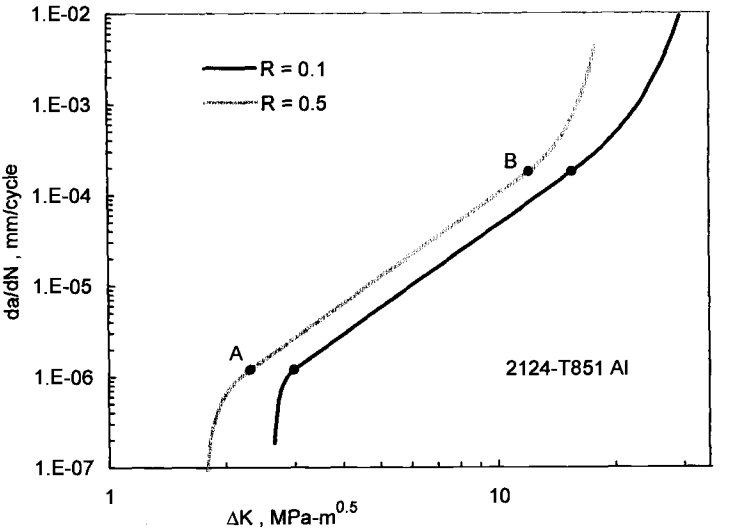


FIG. 19—*Discontinuous* da/dN *versus* ΔK *curves represented by the Walker equation between* A *and* B, *and by equations with asymptotes below* A *and above* B.

We have applied the discontinuous fitting procedure with Eq 40 to only the single set of data illustrated. Further study is needed, which may result in improved equations or procedures for fitting the upper and lower ends. However, the idea of a discontinuous fit using the Walker equation for the Paris region is valid regardless of the details of the fitting for the upper and lower ends.

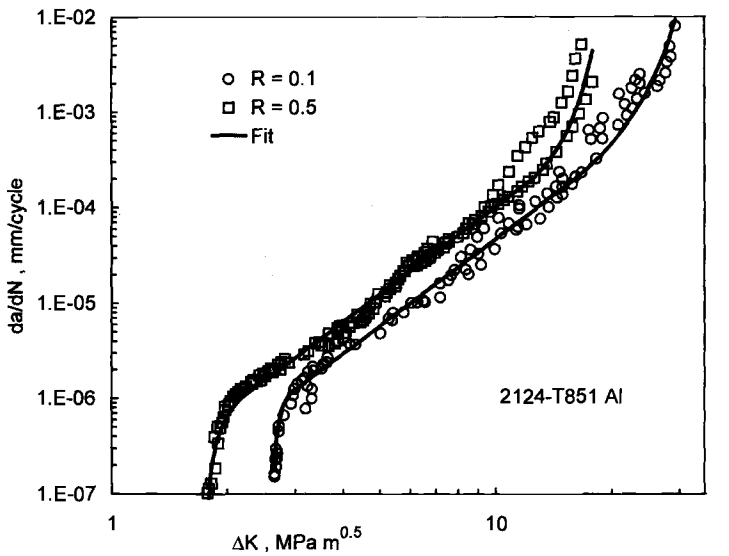


FIG. 20—*Discontinuous fit to the data of Fig. 16.*

Conclusions and Recommendations

We will now state some conclusions and make some recommendations that summarize the considerable discussion that has been given above on the three major approaches for handling fatigue of materials. These comments will be directed particularly toward indicating what variations of these approaches are most appropriate for inclusion in undergraduate engineering education and for use in situations where fairly simple analysis is appropriate. The principal conclusions and recommendations below are given in italics, often followed by statements not in italics that provide additional detail.

Stress-Based Approach

For the stress-based approach, estimated S-N curves, fatigue limits, and modified Goodman diagrams should be de-emphasized. Estimated *S-N* curves may be highly inaccurate at finite lives. Although estimation of fatigue limits may provide reasonable values, the empirical data widely available to support the estimates are limited mainly to steels. For adjusting materials data for mean stress, the Morrow equation, and the Smith, Watson, and Topper (SWT) relationship, are more accurate than the modified Goodman equation.

The very concept of a fatigue limit has severe limitations. Cycles below this presumably safe level may contribute to fatigue damage if there are occasional stress cycles above this level, or if a corrosive environment is present. A crude estimate for variable amplitude loading is to assume that the actual fatigue limit is half the value from constant amplitude tests.

S-N data from tests on actual components should be emphasized. Such an approach avoids the use of inaccurate estimated *S-N* curves. It also avoids the direct use of fatigue data from unnotched specimens, which is significant, as such use in a stress-based approach is limited to situations where there is little or no yielding, even locally at stress raisers, and also where local stresses are well known. Component *S-N* data are often available in industry from tests on critical components, and for welded structural members *S-N* curves are available from design codes.

For handling mean stresses with component S-N curves, use of the modified Goodman equation should be discontinued in favor of the SWT or Walker methods. The Goodman equation is often inaccurate and has the major disadvantage of giving results that are affected by the arbitrary choice of a definition of nominal stress. The optimum approach is to obtain *S-N* data for at least two contrasting levels of mean stress so that the constant γ for the Walker equation can be evaluated for the specific case of interest.

Strain-Based Approach

The strain-based approach should be considered for use where the major concern is the initiation of fatigue cracks as affected by local yielding at notches. This approach employs materials properties in the form of cyclic stress-strain and strain-life curves, which are obtained from tests on unnotched axial specimens. Constants describing these curves have definitions that are widely accepted, and tabulated values for a variety of metals are becoming available.

Effects related to member geometry and local yielding at notches, which require empirical factors in estimated S-N curves, are handled by this approach in a more fundamental manner. Hence, fewer empirical adjustments are needed. Strain-based life estimates done over a range of applied load values in fact produce an estimated *S-N* curve for the component analyzed.

The strain-based approach does not directly account for surface finish and size effects, and so empirical adjustments for these are still needed.

For irregular load versus time histories, the smaller cycles may cause more fatigue damage than would be expected from a constant amplitude S-N curve or strain-life curve. This interaction effect can be accounted for to some extent in the strain-based approach by employing a strain-life curve obtained from testing specimens that are initially or periodically overstrained. Another option is to conduct a limited number of tests on actual components using an irregular load history that is similar to what is expected in service. The strain-life curve can then be adjusted so that strain-based life estimates are brought into agreement with the component data. The adjustment is made primarily by lowering the slope b in Eq 16, which gives a lower strain-life curve at long lives. Such a *component-specific strain-life curve* then automatically includes surface finish, size, and load interaction effects. This curve could then be used to analyze related cases of interest, such as a modestly altered component design or a somewhat different load history.

The strain-based approach should be included in the undergraduate engineering curriculum in basic courses on mechanical and structural design.

Crack Growth Approach

Crack growth analysis based on fracture mechanics is needed where intrinsic cracks are known to commonly occur, where safety considerations dictate that cracks should be assumed to be present, or where it is desired to add the life for crack growth to that estimated for crack initiation.

An impediment to more widespread use of a crack growth approach has been the lack of a generally accepted set of materials constants for describing da/dN versus ΔK curves, and therefore a lack of widely available tabulations of materials constants. This situation seems to have arisen from the complexities involved with including asymptotes at low and high growth rates. For example, in the low growth rate region, the ΔK_{th} is lowered or eliminated for small cracks. In the high growth rate region, the fracture toughness K_c varies with member thickness, and its value for a cyclic loading situation may be different from the results of the usual static tests.

It is recommended that the details of fitting the asymptotes not be allowed to affect the data representation in the intermediate (Paris) region of the da/dN versus ΔK curve. The Walker equation, employed in the form of Eq 34, is recommended as the basis for three standard materials constants, C_1, m, and γ, which represent the Paris region. The value of γ characterizes the sensitivity to the mean stress level, as expressed by the R ratio. Such an adjustable constant is crucial, as the sensitivity to R varies considerably for different metals. For handling the low and high growth rate regions, one of two options is recommended. The first is to assume an abrupt transition to zero growth rate for the lower end, and abrupt failure for the upper end, as controlled by either brittle fracture or fully plastic yielding. The second option is to employ a discontinuous fit with separate equations on each end, while retaining the Walker constants in the Paris region.

Crack growth analysis should also be included in the undergraduate engineering curriculum in courses on mechanical and structural design, especially for those involved with large civil structure or with aircraft structure.

Final Comments

The discussion in this paper is related mainly to straightforward engineering application of the established methodology of fatigue analysis. Recent research on such topics as com-

plex out-of-phase combined loading, damage below the fatigue limit, crack closure, and small crack effects is certainly important, and these results will in time lead to improve engineering methodology that is widely applied. However, the latest advanced methods are not always needed, and even where these might be helpful, their use may not be feasible due to limited resources, limited time, or limited educational background of the engineers who will do the work. As to the latter, there currently exists a large gap between what the typical engineer with an undergraduate education can do and the most advanced methods. The intermediate level of complexity needs some serious attention, and it is hoped that this paper will be helpful at such a level.

References

[1] Mann, J. Y., "The Historical Development of Research on the Fatigue of Materials and Structures," *The Journal of the Australian Institute of Medals,* November 1958, pp. 222–241.

[2] Sines, G. and Waisman, J. L., *Metal Fatigue,* McGraw Hill, New York, NY, 1959.

[3] Coffin, L. F., Jr., and Tavernelli, J. F., "The Cyclic Straining and Fatigue of Metals," *Transactions of the Metallurgical Society of AIME,* Vol. 215, Oct. 1959, pp. 794–807.

[4] Manson, S. S. and Hirschberg, M. H., "Fatigue Behavior in Strain Cycling in the Low and Intermediate Cycle Range," *Fatigue—An Interdisciplinary Approach,* J. J. Burke, N. L. Reed, and V. Weiss, Eds., Syracuse University Press, 1964, pp. 133–178.

[5] McDowell, D. L. and Ellis, R., Eds., *Advances in Multiaxial Fatigue, ASTM STP 1191,* American Society for Testing and Materials, West Conshohocken, PA, 1993.

[6] Chu, C.-C., "Fatigue Damage Calculation Using the Critical Plane Approach," *Journal of Engineering Materials and Technology,* ASME, Vol. 117, 1995, pp. 41–49.

[7] DuQuesnay, D. L., Pompetzki, M. A., and Topper, T. H., "Fatigue Life Prediction for Variable Amplitude Strain Histories," Paper No. 930400, *Fatigue Research and Applications,* Pub. No. SP-1009, Society of Automotive Engineers, Warrendale, PA, 1993, pp. 175–185.

[8] Barsom, J. M., Ed., *Fracture Mechanics Retrospective: Early Classic Papers* (1913–1965), RPS-1, American Society for Testing and Materials, West Conshohocken, PA, 1987.

[9] Paris, P. C., "The Fracture Mechanics Approach to Fatigue," *Fatigue—An Interdisciplinary Approach,* J. J. Burke et al., Eds., *Proceedings of the 10th Sagamore Army Materials Research Conference,* Syracuse University Press, Syracuse, NY, 1964, pp. 107–127.

[10] Newman, J. C., Jr., Phillips, E. P., and Swain, M. H., "Fatigue-Life Prediction Methodology Using Small-Crack Theory," *International Journal of Fatigue,* Vol. 21, No. 2, 1999, pp. 109–119.

[11] Wei, R. P. and Gangloff, R. P., "Environmentally Assisted Crack Growth in Structural Alloys: Perspectives and New Directions," *Fracture Mechanics: Perspectives and Directions (Twentieth Symposium, ASTM STP 1020,* R. P. Wei and R. P. Gangloff, Eds., American Society for Testing and Materials, West Conshohocken, PA, 1989, pp. 233–264.

[12] Juvinall, R. C. and Marshek, K. M., *Fundamentals of Machine Component Design,* 2nd ed., John Wiley, New York, NY, 1991.

[13] Shigley, J. E. and Mischke, C. R., *Mechanical Engineering Design,* 5th ed., McGraw-Hill, New York, NY, 1989. See also J. E. Shigley and L. D. Mitchell, 1993 reprint of the 4th edition.

[14] Peterson, R. E., "Notch-Sensitivity," *Metal Fatigue,* G. Sines and J. L. Waisman, Eds., McGraw-Hill, New York, NY, 1959, pp. 293–306.

[15] Grover, H. J., Bishop, S. M., and Jackson, L. R., "Fatigue Strengths of Aircraft Materials: Axial Load Fatigue Tests on Notched Sheet Specimens of 24S-T3 and 75S-T6 Aluminum Alloys and of SAE 4130 Steel with Stress-Concentration Factors of 2.0 and 4.0," NACA TN 2389, National Advisory Committee for Aeronautics, Washington, DC, June 1951.

[16] Juvinall, R. C., *Stress, Strain, and Strength,* McGraw-Hill, New York, NY, 1967.

[17] Norton, R. L., *Machine Design: An Integrated Approach,* Prentice Hall, Upper Saddle River, NJ, 1996.

[18] Noll, G. C. and Lipson, C., "Allowable Working Stresses," *Proceedings of the Society for Experimental Stress Analysis,* Vol. 3, No. 2, 1945, pp. 89–109.

[19] Marin, J., *Mechanical Behavior of Engineering Materials,* Prentice Hall, Upper Saddle River, NJ, 1962.

[20] Boller, C. and Seeger, T. *Materials Data for Cyclic Loading,* 5 vols., Elsevier Science Pubs., Amsterdam, 1987. See also *Supplement 1,* 1990, by A. Baumel and T. Seeger.

[21] "Technical Report on Fatigue Properties: SAE J1099," *1997 SAE Handbook, Vol. 1, Materials, Fuels, Emissions, and Noise,* Society of Automotive Engineers, Warrendale, PA, 1997, pp. 3.153 to 3.162. (See the current year's *SAE Handbook* for latest update.)

[22] Dowling, N. E., *Mechanical Behavior of Materials: Engineering Methods for Deformation, Fracture, and Fatigue,* 2nd ed., Prentice Hall, Upper Saddle River, NJ, 1999.

[23] Brose, W. R., Dowling, N. E., and Morrow, J., "Effect of Periodic Large Strain Cycles on the Fatigue Behavior of Steels," Paper No. 740221, Society of Automotive Engineers, Automotive Engineering Congress, Detroit, MI, February 1974.

[24] *AASHTO LRFD Bridge Design Specifications,* American Association of State Highway and Transportation Officials, Washington, DC, 1994.

[25] *Recommended Practice for Planning, Designing, and Constructing Fixed Offshore Platforms,* API RP-2A-LRFD or RP-2A-WSD, American Petroleum Institute, Washington, DC, 1993.

[26] *Code of Practice for Fatigue Design and Assessment of Steel Structures,* BS 7608, British Standards Institution, London, 1993.

[27] Heuler, P. and Seeger, T., "A Criterion for Omission of Variable Amplitude Loading Histories," *International Journal of Fatigue,* Vol. 8, No. 4, 1986, pp. 225–230.

[28] Goodman, J., *Mechanics Applied to Engineering,* Longmans, Green and Co., London, 1919, pp. 631–636.

[29] Smith, J. O., "The Effect of Range of Stress on the Fatigue Strength of Metals," Bulletin No. 334, University of Illinois, Engineering Experiment Station, Urbana, IL, Feb. 1942. See also Bulletin No. 316, Sept. 1939.

[30] Morrow, J., "Fatigue Properties of Metals," Section 3.2 of *Fatigue Design Handbook,* Pub. No. AE-4, Society of Automotive Engineers, Warrendale, PA, 1968. Section 3.2 is a summary of a paper presented at a meeting of Division 4 of the SAE Iron and Steel Technical Committee, 4 Nov. 1964.

[31] Dowling, N. E., "Fatigue Life and Inelastic Strain Response under Complex Histories for an Alloy Steel," *Journal of Testing and Evaluation,* ASTM, Vol. 1, No. 4, July 1973, pp. 271–287.

[32] Smith, K. N., Watson, P., and Topper, T. H., "A Stress-Strain Function for the Fatigue of Metals," *Journal of Materials,* ASTM, Vol. 5, No. 4, December 1970, pp. 767–778.

[33] Walker, K., "The Effect of Stress Ratio During Crack Propagation and Fatigue for 2024-T3 and 7075-T6 Aluminum," *Effects of Environment and Complex Load History on Fatigue Life, ASTM STP 462,* American Society for Testing and Materials, West Conshohocken, PA, 1970, pp. 1–14.

[34] Grover, H. J., Bishop, S. M., and Jackson, L. R., "Fatigue Strengths of Aircraft Materials: Axial-Load Fatigue Tests on Unnotched Sheet Specimens of 24S-T3 and 75S-T6 Aluminum Alloys and of SAE 4130 Steel," NACA TN 2324, National Advisory Committee for Aeronautics, Washington, DC, March 1951.

[35] *Military Handbook: Metallic Materials and Elements for Aerospace Vehicle Structures,* MIL-HDBK-5G, 2 Vols., U.S. Dept. of Defense, MIL-HDBK-5 Coordination Activity, Wright-Patterson AFB, OH, 1994.

[36] Leese, G. E. and Morrow, J., "Low Cycle Fatigue Properties of a 1045 Steel in Torsion," *Multiaxial Fatigue, ASTM STP 853,* K. J. Miller and M. W. Brown, Eds., American Society for Testing and Materials, West Conshohocken, PA, 1985, pp. 482–496.

[37] Illg, W., "Fatigue Tests on Notched and Unnotched Sheet Specimens of 2024-T3 and 7075-T6 Aluminum Alloys and of SAE 4130 Steel with Special Consideration of the Life Range from 2 to 10,000 Cycles," NACA TN 3866, National Advisory Committee for Aeronautics, Washington, DC, 1956.

[38] Naumann, E. C., Hardrath, H. F., and Guthrie, D. E., "Axial Load Fatigue Tests of 2024-T3 and 7075-T6 Aluminum Alloy Sheet Specimens Under Constant and Variable Amplitude Loads," NASA TN D-212, National Aeronautics and Space Administration, Washington, DC, 1959.

[39] Dowling, N. E. and Khosrovaneh, A. K., "Simplified Analysis of Helicopter Fatigue Loading Spectra," J. M. Potter and R. T. Watanabe, Eds., *Development of Fatigue Loading Spectra, ASTM STP 1006,* American Society for Testing and Materials, West Conshohocken, PA, 1989, pp. 150–171.

[40] Dowling, N. E., "Notched Member Fatigue Life Predictions Combining Crack Initiation and Propagation," *Fatigue of Engineering Materials and Structures,* Vol. 2, No. 2, 1979, pp. 129–138.

[41] Dowling, N. E. and Wilson, W. K., "Geometry and Size Requirements for Fatigue Life Similitude Among Notched Members," *Advances in Fracture Research,* D. Francois et al., Eds., Pergamon Press, Oxford, UK, 1981, pp. 581–588.

[42] Leese, G. E. and Socie, D., Eds., *Multiaxial Fatigue: Analysis and Experiments, SAE Pub. No. AE-14, Soc. of Automotive Engineers, Warrendale, PA, 1989.*

[43] Placek, R. J., Williams, R. A., Adams, S. L., and Klufas, O., "Determination of Torsional Fatigue Life of Large Turbine Generator Shafts," Report No. EL-3083, Project 1531-1, Electric Power Research Institute, Palo Alto, CA, 1984.

[44] Edwards, P. R. and Darts, J., "Standardized Fatigue Loading Sequences for Helicopter Rotors (Helix and Felix), Parts 1 and 2," Report Nos. TR84084 and TR84085, Royal Aircraft Establishment, Ministry of Defense, Farnborough, Hants, England (also ICAF Document No. 1442), 1984.

[45] Socie, D. F., Dowling, N. E., and Kurath, P., "Fatigue Life Estimation of Notched Members," *Fracture Mechanics: Fifteenth Symposium, ASTM STP 833,* American Society for Testing and Materials, West Conshohocken, PA, 1984, pp. 284–299.

[46] Anderson, T. L., *Fracture Mechanics: Fundamentals and Applications,* 2nd ed., CRC Press, Boca Raton, FL, 1995.

[47] Broek, D., *Elementary Engineering Fracture Mechanics,* 4th ed., Kluwer Academic Publishers, Dordrecht, The Netherlands, 1986.

[48] Ewalds, H. L. and Wanhill, R. J. H., *Fracture Mechanics,* Edward Arnold Pubs., London, 1984.

[49] Murakami, Y., Ed., *Stress Intensity Factors Handbook,* Vols. 1 and 2, 1987, and Vol. 3, 1993, Pergamon Press, Oxford, UK.

[50] Tada, H., Paris, P. C., and Irwin, G. R., *The Stress Analysis of Cracks Handbook,* 2nd ed., Paris Productions, Inc., St. Louis, MO, 1985.

[51] Newman, J. C., Jr. and Raju, I. S., "Stress-Intensity Factor Equations for Cracks in Three-Dimensional Finite Bodies Subjected to Tension and Bending Loads," *Computational Methods in the Mechanics of Fracture,* S. N. Atluri, Ed., Elsevier Science Publishers, New York, NY, 1986.

[52] Clark, W. G., Jr., "Fracture Mechanics in Fatigue," *Experimental Mechanics,* Society for Experimental Mechanics, Inc., Vol. 11, No. 9, September 1971, pp. 421–428.

[53] Ruschau, J. J., "Complete Fatigue Crack Growth Rate Curves for Aluminum Alloy 2124-T851 Including Typical Crack Growth Models," Report No. AFML-TR-78-155, Air Force Materials Laboratory, Wright-Patterson AFB, OH, Nov. 1978.

[54] Forman, R. G., Kearney, V. E., and Engle, R. M., "Numerical Analysis of Crack Propagation in Cyclic-Loaded Structures," *Journal of Basic Engineering, Transactions of ASME,* September 1967, pp. 459–464.

[55] Miller, M. S. and Gallagher, J. P., "An Analysis of Several Fatigue Crack Growth Rate (FCGR) Descriptions," S. J. Hudak, Jr., and R. J. Bucci, Eds., *Fatigue Crack Growth Measurement and Data Analysis, ASTM STP 738,* American Society for Testing and Materials, West Conshohocken, PA, 1981, pp. 205–251.

[56] Crooker, T. W., Hasson, D. F., and Yoder, G. R., "A Fracture Mechanics and Fractographic Study of Fatigue Crack Propagation Resistance in 17-4 PH Stainless Steels," NRL Report 7910, Naval Research Laboratory, Washington, DC, 1975.

[57] Henkener, J. A., Lawrence, V. B., and Forman, R. G., "An Evaluation of Fracture Mechanics Properties of Various Aerospace Materials," R. Chona, Ed., *Fracture Mechanics: Twenty-Third Symposium, ASTM ATP 1189,* American Society for Testing and Materials, West Conshohocken, PA, 1993, pp. 474–497.

[58] Skinn, D. A., Gallagher, J. P., Berens, A. F., Huber, P. D., and Smith, J., "Compilers," *Damage Tolerant Design Handbook,* 5 vols., CINDAS/USAF CRDA Handbooks Operation, Purdue University, West Lafayette, IN, 1994.

[59] Dowling, N. E., "Fatigue-Crack Growth Rate Testing at High Stress Intensities," *Flaw Growth and Fracture, ASTM STP 631,* American Society for Testing and Materials, West Conshohocken, PA, 1977, pp. 139–158.

[60] Troshchenko, V. T., Pokrovsky, V. V., and Prokopenko, A. V., "Investigation of the Fracture Toughness of Constructional Steels in Cyclic Loading," *Fracture 1977: Proceedings of the 4th Int. Conference on Fracture, Vol. 3,* D. M. R. Taplin, Ed., University of Waterloo Press, Waterloo, Ontario, Canada, 1977, pp. 683–686.

Keynote Tributes to George Irwin

James C. Newman, Jr.[1]

Irwin's Stress Intensity Factor—A Historical Perspective

REFERENCE: Newman, J. C., Jr., **"Irwin's Stress-Intensity Factor—A Historical Perspective,"** *Fatigue and Fracture Mechanics: 31st Volume, ASTM STP 1389,* G. R. Halford and J. P. Gallagher, Eds., American Society for Testing and Materials, West Conshohocken, PA 2000, pp. 39–53.

ABSTRACT: This paper is written to honor Dr. George R. Irwin and reviews several key developments in fracture mechanics based on his "stress-intensity factor" concept. The early development of two fundamental crack solutions, (1) an edge crack in a semi-infinite body and (2) the surface crack, are highlighted. Applications of Irwin's early concepts by other researchers to characterize fatigue-crack growth and brittle fracture of metallic materials are presented. The stress-intensity factor is the cornerstone of the damage-tolerance and durability design concepts used by the aerospace community around the world. The stress-intensity factor concept, crack-closure mechanics, and the observation that "fatigue is crack propagation" in many engineering materials has led to a merger of fatigue and fracture mechanics analysis methodologies. Irwin's recognition of the importance of the normal stress parallel to the crack (now referred to as the T-stress) in fracture led many to propose a two-parameter characterization for fracture. The importance of constraint on crack-tip yielding has been further advanced by the use of high-powered computers to calculate a normal-stress constraint parameter following his ideas. The father of fracture mechanics has left a legacy that will endure and provide safer and more reliable structures in the future.

KEYWORDS: cracks, fatigue, fatigue crack growth, fracture mechanics, stress-intensity factor, crack closure, plasticity, constraint

This paper was presented at the 31st National Symposium on Fatigue and Fracture Mechanics to honor Dr. George R. Irwin, the "father of fracture mechanics," whose photo is shown in Fig. 1. The National Symposium series began in the late 1960s, by Drs. Paul Paris and George R. Irwin to foster the rapidly growing field of fracture mechanics. Today, fracture mechanics is a very mature field and is used in many different industries. In the last few years, the fracture community around the world has reflected on the influence that Dr. Irwin has had on the field of fracture. A superb historical treatment is presented in "Fracture Research in Retrospect—An Anniversary Volume in Honour of George R. Irwin's 90th Birthday." [*1*]. The current paper reviews several key developments in fracture mechanics based on Irwin's "stress-intensity factor" concept. In particular, the elastic stress analyses of two key crack configurations, fatigue-crack propagation theories, and brittle fracture are briefly reviewed. In a second paper. Landes [2] reviews the contributions of Dr. Irwin that influenced the development of elastic-plastic fracture mechanics.

In the late 1950s, Irwin's "stress-intensity factor" concept initiated an era in the rational engineering treatment of crack behavior in metallic materials. During the next decades, the calculation of crack-tip stress and strain fields under tensile and shear loading by Irwin [*3,4*]

[1] Senior scientist, NASA Langley Research Center, MS 188E, Hampton, VA 23681-2199.

Copyright© 2000 by ASTM International www.astm.org



FIG. 1—*George Rankin Irwin (1907–1998).*

and many others [*5,6*], and the applications of the concept to fatigue-crack propagation and brittle fracture provided the naval, nuclear, and aerospace industries with the analytical tools required to manage the life and strength of damaged structures.

This paper will briefly review three areas: (1) stress analyses of cracked bodies, (2) fatigue-crack propagation, and (3) brittle fracture, and demonstrate how the stress-intensity factor has advanced our understanding of crack propagation mechanics. The early development of two particular crack solutions by Irwin, (1) an edge crack in a semi-infinite body and (2) the surface crack, are highlighted. Irwin recognized very early that the majority of cracks initiate at edges or surfaces, which are susceptible to inadvertent damage and the environment, and that these crack solutions would provide fundamental solutions. These solutions could then be used to estimate stress-intensity factors for many other crack configurations. Application of Irwin's stress-intensity factor concept to characterize fatigue-crack propagation by Paris, Gomez, and Anderson [*7*] revolutionized the way fatigue cracks were analyzed. The stress-intensity factor is the cornerstone of the damage-tolerance [*8*] and durability [*9*] design concepts used by aerospace communities around the world. His stress-intensity factor concept combined with the discovery of fatigue-crack closure by Elber [*10*] began to explain many of the mysteries of crack propagation under variable-amplitude loading. The observation that "fatigue is crack propagation" for many engineering materials [*11,12*] and the use of the stress-intensity factor concept has led to a merger of fatigue and fracture mechanics analysis methodologies. Characterization of brittle fracture with stress-intensity factor analyses spawned the development of the "plane-strain fracture toughness, K_{Ic}" testing method [*13*] for high-strength, brittle materials. In the early days, many of the fracture criteria proposed for analyzing fracture of thin-sheet, ductile materials involved modifications of the stress-intensity factor and plastic yielding at the crack tip. Covering these fracture criteria is beyond the scope of this paper. However, some of these developments in non-linear fracture mechanics will be covered by Landes [*2*]. Irwin's recognition of the importance of the normal

stress parallel to the crack (now referred to as the T-stress) in fracture [*4*] led many to propose a two-parameter characterization for fracture [*14–16*]. Two-parameter fracture mechanics will only be briefly discussed because many of these approaches involve non-linear fracture mechanics and this paper is restricted to linear-elastic behavior. The importance of constraint on crack-tip yielding has been further advanced by the use of computers to calculate a normal-stress constraint parameter following Irwin's ideas. Here, a recent application of the critical stress-intensity factor $(K_\Phi)_{Ic}$ and a local crack-front constraint parameter α_h will be presented on Irwin's favorite crack configuration, the surface crack, under tension and bending loads on a high-strength, brittle steel [*17*].

Stress Analyses of Cracked Bodies

Griffith [*18*] made use of the stress solution provided by Inglis [*19*] for an elliptical hole in an infinite plate under uniform tension to generate a solution for a sharp crack. But Griffith did not have the knowledge of stress fields near a crack and, thus, he devised an energy-balance analysis for a crack in a brittle material. Sneddon [*20*] was the first to use stress-field expansions for a crack, but Irwin [*3,4*] and Williams [*21*] both recognized the general applicability of the field equations for cracks in linear-elastic bodies. Under these conditions, the crack-tip stresses are:

$$\sigma_{ij}(r, \theta) = K_I(2\pi r)^{-1/2} f_{ij}(\theta) + A_2 g_{ij}(\theta) + A_3 h_{ij}(\theta) r^{1/2} + \ldots \quad (1)$$

where K_I is the Mode I stress-intensity factor; r and θ are the radius and polar angle measured from the crack tip and crack plane, respectively, as shown in Fig. 2. A_i are constants, $f_{ij}(\theta)$, $g_{ij}(\theta)$, and $h_{ij}(\theta)$ are dimensionless functions of θ. By 1965, Paris and Sih [*22*] set the stage for determining stress-intensity factors for a vast number of crack configurations. After some 35 years, the stress-intensity factors for a large number of crack configurations have been generated and collated into several handbooks, see for example, Tada et al. [*5*] and Murakama [*6*]. The strict interpretation of K_I given by Eq 1 remains meaningful only when the plastic zone at the crack tip remains vanishingly small.

One must be alert to "The Story of π" when looking at stress-intensity factors in the literature. In the early Irwin papers, the stress-intensity factor was denoted as a script $\mathcal{K}$, which did not include the $\sqrt{\pi}$ in the stress-field equations; whereas today, the general nomenclature is the symbol K, which has the $\sqrt{\pi}$ in its definition. Thus, some of the early works on stress analyses of cracks and fatigue-crack growth studies used the script $\mathcal{K}$ (or lower case k) definition. As the story goes, two groups of researchers, one studying stress fields and the other energy-balance relations, did not want to carry π in their equations. But

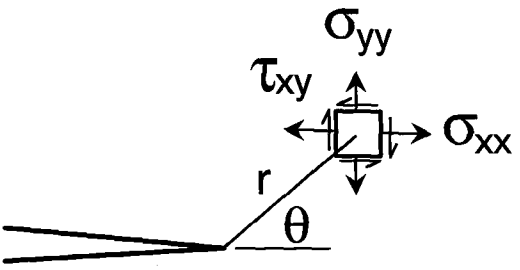


FIG. 2—*Stresses near a crack tip in an elastic body.*

from physics, someone had to win and the other lose. After some time, the well-known relation between the stress-intensity factor (K) and the strain-energy release rate (G) became $K = \sqrt{(EG)}$ and note that the $\sqrt{\pi}$ is in Eq 1. As the old saying goes, "Twos and π's are thrown around at a fracture mechanics meeting like roses at a bull fight." Therefore, the stress analysts will forever have to carry the $\sqrt{\pi}$ around as extra baggage (or as a badge of honor) from Dr. Irwin. As pointed out by many others, Dr. Irwin wanted to honor those who had had a hand in the birth of modern fracture mechanics. Thus, G was used to honor, Dr. A. A. Griffith, and K to honor Dr. Joe Kies.

Edge-Cracked Plate

Irwin [*23*] recognized that the edge crack in a plate under remote tension was an important crack configuration because most cracks in structures initiate at edges or surfaces. He was the first to apply the alternating method to solve a finite-boundary crack problem using the Westergaard [*24*] stress-function approach. Figure 3 shows the two crack configurations that were used in an alternating sense to solve for the stress-intensity factor for an edge crack in a plate under remote tension. One crack configuration had a pair of forces (q) applied to the crack surfaces (Fig. 3*a*) and the other had a pair of forces (p) applied to the free boundary (Fig. 3*b*). The dashed lines show, respectively, the location of the boundary and crack that would be approximately freed of normal stresses. Using only the first approximation, the boundary-correction factor was found to be 1.0947. Thus, the stress-intensity factor is given by the now famous equation, $K = 1.1\ S\ \sqrt{(\pi c)}$. Years later, Gross and Srawley [*25*] used the boundary-collocation method to determine a value of 1.12. Thus, Irwin's solution was within about 2% of the correct solution. Smith [*26*] carried on Irwin's use of the alternating method to solve the surface-crack problem which will be discussed in the next section.

Figure 4 illustrates how the edge-crack solution can now be used to estimate the stress-intensity factors for small cracks emanating from other types of boundaries, such as a pin-loaded hole. Knowing only the normal stresses $\sigma_{\theta\theta}$ at the edge of the hole, the stress-intensity factor is given by $K = 1.12\sigma_{\theta\theta}\ \sqrt{(\pi c)}$. This solution is basically the limiting K solution as the crack length, c, approaches zero. As will be shown later, the fatigue behavior of many metals is controlled by the growth of very small cracks at the edge of a hole or plate, so that the edge-crack solution would be operational over a very large percentage of the fatigue life.

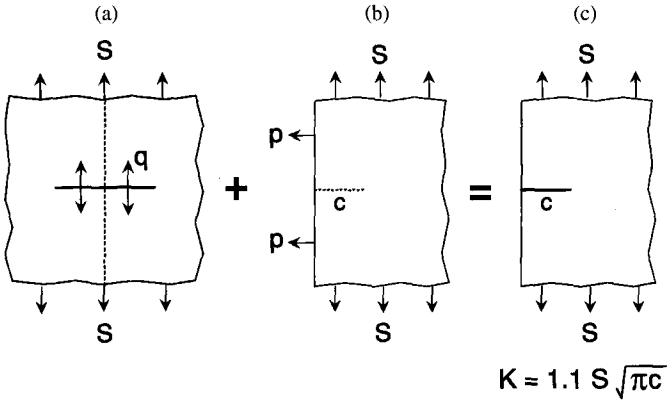


FIG. 3—*Alternating method used to solve an edge crack in semi-infinite plate.*

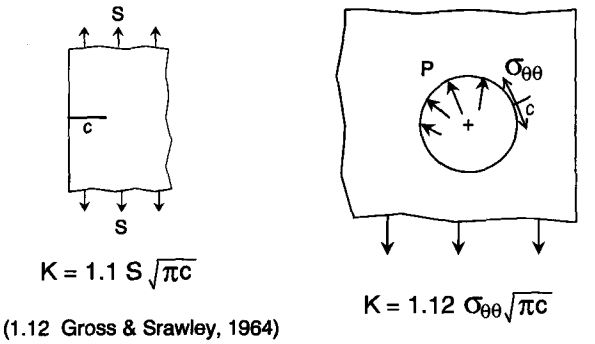


FIG. 4—*Application of edge-crack solution for small crack at stress concentration.*

Surface Crack Configuration

Irwin [*27*] derived an exact expression for the Mode I stress-intensity factor around an elliptical crack in an infinite elastic solid subjected to remote uniform tension (Fig. 5*a*) based on the exact stress analysis by Green and Sneddon [*28*]. The stress-intensity factor was given by

$$K = S\sqrt{(\pi a/Q)}\, f(\phi, a/c) \tag{2}$$

where Q is the square of the complete elliptical integral of the second kind and $f(\phi, a/c)$ is a function of the parametric angle ϕ and the a/c ratio. Years, later, Tada and Paris [*29*] found that Eq 2 could be replaced with

$$K = S\sqrt{(\pi \ell/Q)} \tag{3}$$

where the crack length ℓ is the length of the normal to the ellipse. The observation made by

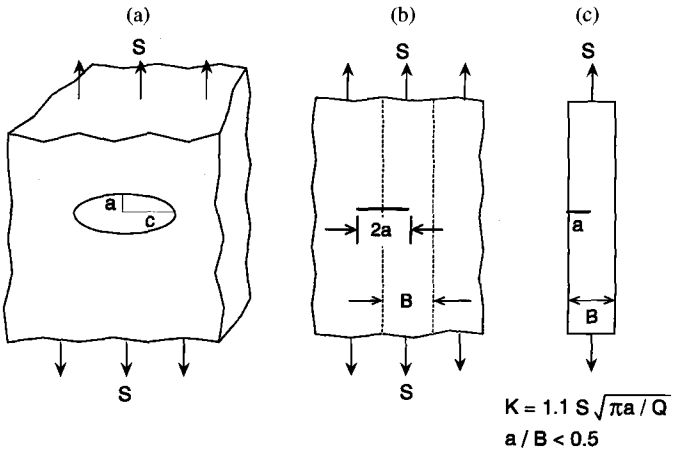


FIG. 5—*The surface crack problem.*

Tada and Paris provides a very useful estimation procedure for stress-intensity factors for arbitrarily shaped cracks in infinite bodies. However, the influence of various shaped boundaries on stress-intensity factors, such as free surfaces and holes, must still be obtained from rigorous numerical or analytical treatment. But most numerical analyses have only considered circular- or elliptical-shaped cracks in finite bodies. The proposed estimation procedure could be very useful in modifying the elliptical-crack solutions in finite bodies to obtain estimates for arbitrarily shaped cracks in the same finite body. This would greatly reduce the computational efforts required to obtain stress-intensity factors for arbitrarily shaped cracks in the neighborhood of boundaries.

In 1962, Irwin used engineering judgment and his previous edge-crack solution to estimate the stress-intensity factor for a surface crack in a finite body under remote tension. By slicing the infinite body with the embedded elliptical crack, as shown in Fig. 5*b*, he estimated the K solution for the surface crack in a plate under tension (Fig. 5*c*) as

$$K = 1.1\ S\ \sqrt{(\pi a/Q)}\ f(\phi, a/c) \tag{4}$$

where the edge-correction factor of 1.1 accounted for the front surface but the a/B ratio was restricted to less than 0.5. He did not estimate the influence of the back surface on stress-intensity factors.

In 1979, Newman [*30*] reviewed the stress-intensity factors for the surface crack in a finite-thickness plate under remote tension and made an assessment of their accuracy in correlating fracture data on a brittle epoxy material tested by Smith [*26*]. A comparison on numerous K solutions from the literature for a semi-elliptical surface crack are shown in Fig. 6. For low a/B ratios, all solutions tend to merge with Irwin's estimate for the maximum depth ($\phi = \pi/2$) location; but for larger a/B ratios, the large variation in the K solutions for the same crack problem was very disturbing. The methods used to generate the various

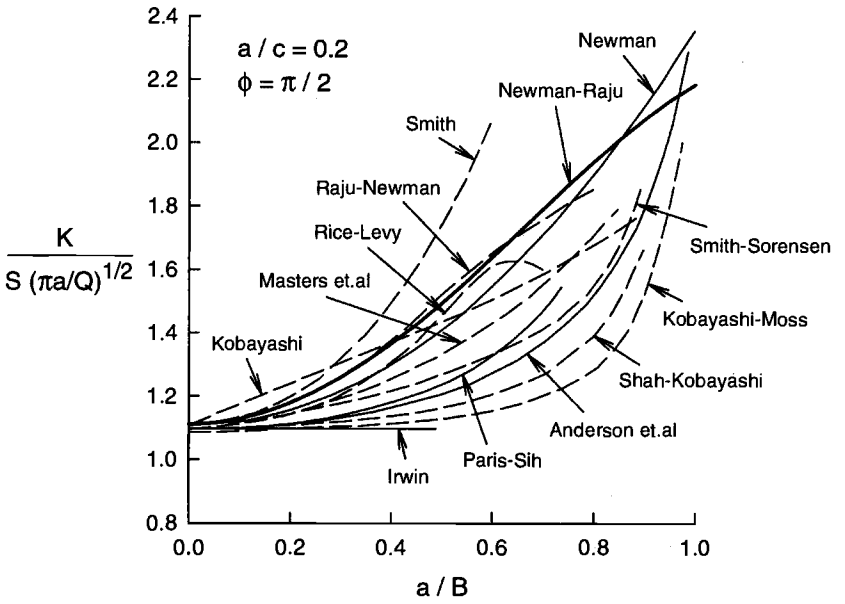


FIG. 6—*Stress-intensity factors for semi-elliptical surface crack in a plate under remote tension.*

solutions and the reasons for the large differences will not be discussed (see Ref *30* for more details). But based on the original fracture assessment and 20 years of additional stress analyses and test data, the stress-intensity factors from Raju and Newman [*31*,*32*], using three-dimensional finite-element analyses, appear to be more accurate solutions.

Fatigue-Crack Propagation

In the mid-1950s, the failure of two Comet jet aircrafts in-flight spurred the rapid development of various fatigue-crack propagation theories. Numerous empirical forms of stress to a power times crack length to a power were proposed to correlate with fatigue-crack growth rates. Out of this early research, however, two rational methods of treating fatigue-crack growth emerged. One was based on notch analyses [*33*] and the other was based on Irwin's stress-intensity factor [*7*]. But the elegance and simplicity of the stress-intensity factor won the favor of many in the technical community and the rest is history.

Rational Analytic Theory of Fatigue

In 1961, Paris, Gomez, and Anderson [*7*] proposed to use Irwin's stress-intensity factor to correlate fatigue-crack growth rates. This approach showed vast promise when test data from various crack configurations fell onto the same K-against-da/dN curve. In the Paris et al. [*7*] paper, a profound statement was made: "using an effective initial imperfection (crack) size makes it possible to calculate . . . the complete S-N curve for a material at any stress level from a single (crack growth) specimen." In order to achieve this goal, however, several key developments had to be made: (1) improved stress analyses of surface- and corner-crack configurations (as illustrated in the last section), (2) discovery of the crack-closure mechanism in the late 1960s, (3) an understanding of small- or short-crack growth behavior (only recognized in the late 1970s), and (4) advances in non-linear fracture mechanics. This paper will briefly review some of these areas and demonstrate the fulfillment of the statement made by Paris, Gomez, and Anderson.

Plasticity-Induced Fatigue Crack Closure

In 1968, Elber observed that fatigue-crack surfaces contact with each other even during tension-tension cyclic loading. Many state that crack-surface closure was observed much earlier in the literature, but it was Elber [*10*] who recognized the significance of the crack-closure concept. This contact is due to residual plastic deformation that is left in the wake of the advancing crack and contacts during unloading, as will be illustrated later. It is surprising that the significance of this observation appeared so many years after crack growth was first studied. But this simple observation and the explanation of the crack-closure mechanism (or more properly crack-opening behavior) began to explain many crack-growth characteristics almost immediately. Since the discovery of plasticity-induced closure, several other closure mechanisms, such as roughness- and oxide/corrosion/fretting product-induced closure, have been identified. But a discussion of these other closure mechanisms is beyond the scope of the present paper.

Hudson [*34*] produced fracture-crack growth-rate data on 2024-T3 and 7075-T6 aluminum alloy sheet material over a very wide range of stress ratios ($R = S_{min}/S_{max} = -1$ to 0.8) and stress-intensity factor ranges. Later, Phillips [*35*] generated crack-growth data in the near-threshold regime for the same alloys, and Dubensky [*36*] conducted tests at extremely high remote stress levels (0.6 to 1.0 times the yield stress of the material). These tests produced crack-growth-rate data over 8 orders of magnitude in rates, as shown in Fig. 7. Using Irwin's

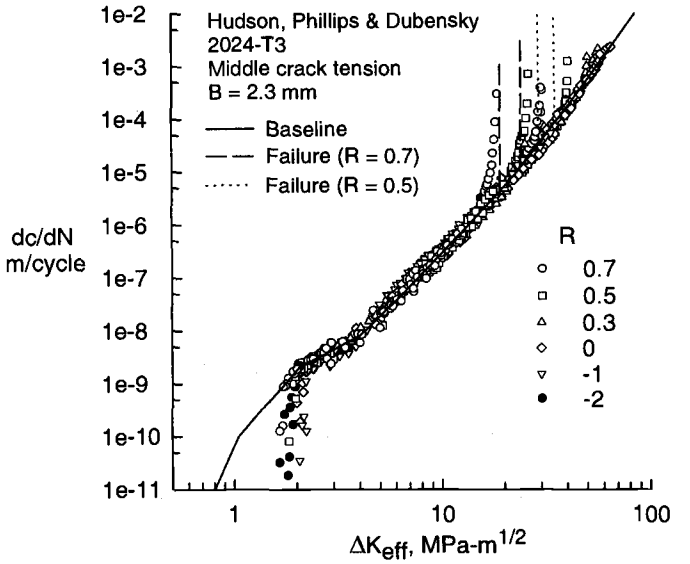


FIG. 7—*Effective stress-intensity factor range against crack-growth rate.*

stress-intensity factor and crack-closure theory to calculate Elber's effective stress-intensity factor range, ΔK_{eff}, crack-growth rate data on the 2024-T3 alloy collapsed into a narrow band except at extremely high rates. (Elber [*10*] had postulated that only the range when the crack tip was fully open would cause damage to the material). The solid line is the baseline relation. At the extremely high rates, the vertical lines indicate where the high stress ratio (R) test would have been predicted to fail based on the two-parameter fracture criterion (to be discussed later). In the low crack-growth rate regime, the large-crack threshold data has been neglected because the threshold test procedure has been shown to induce additional closure not included in the crack-closure model [*37*]. The baseline relation (solid curve) near the large-crack threshold was estimated from small-crack data [*38*].

Small-Crack Growth Behavior

The next example is to use fatigue-crack-growth rate behavior (accounting for small-crack effects) to predict the *S-N* curve for an aluminum alloy over a wide range in applied stress levels from a single crack-growth rate curve, as postulated by Paris et al. [*7*]. Landers and Hardrath [*39*] conducted fatigue tests on 2024-T3 aluminum alloy sheet material with specimens containing a central hole. The results at two stress ratios are shown in Fig. 8 as symbols. Both elastic and elastic-plastic fatigue-crack growth analyses were performed. The solid and dashed curves show predictions using large-crack growth rate data (ignoring the large-crack threshold) and an initial crack size based on an average inclusion particle size that initiated cracks [*38*]. (The elastic-plastic analyses using ΔJ_{eff} were based on a cyclic plastic-zone corrected stress-intensity factor, similar to Irwin's plastic stress-intensity factor. This approach will be discussed by Landes [*2*].) Both predictions agreed near the endurance limit but differed substantially as the applied stress approached the flow stress of the material (σ_o = 425 MPa). Above a stress level of about 250 MPa, the results from the elastic and elastic-plastic analyses differ substantially, but the elastic-plastic analyses agreed well with

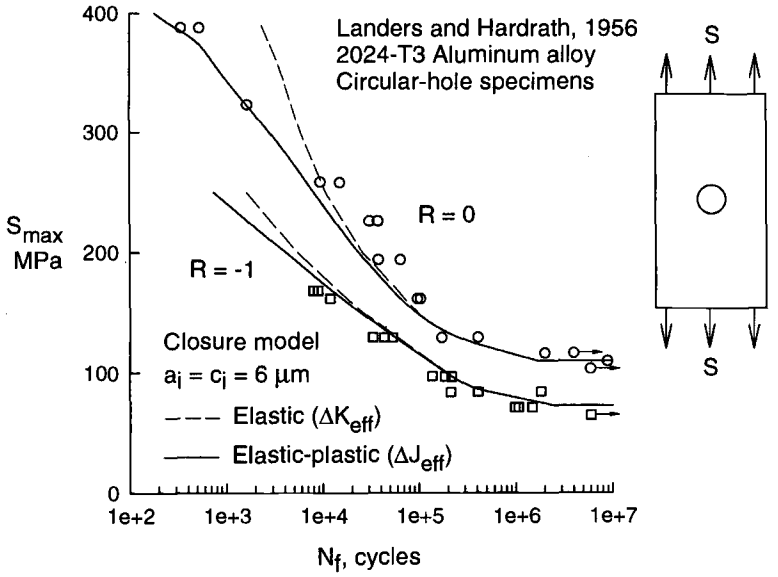


FIG. 8—*Stress-intensity factors used to predict* S-N *behavior.*

the test data and substantiated the use of the cyclic plastic-zone corrected effective stress-intensity factor range (or ΔJ_{eff}).

The author has been amazed over the years as to how well the elastic stress-intensity factor range works for fatigue-crack growth rate analyses. Part of this success can be traced to the plastic-zone sizes under monotonic and cyclic loading, as shown in Fig. 9. For a stationary crack, the cyclic plastic zone ω is about 1/4 of the plastic-zone size, ρ. Whereas for a moving crack, the cyclic plastic zone (accounting for crack closure) is only about 1/10 of the plastic-zone size under $R = 0$ fatigue loading. The plastic-wake contacts and protects the crack tip from reverse yielding. Thus, the cyclic plastic zone corrected stress-

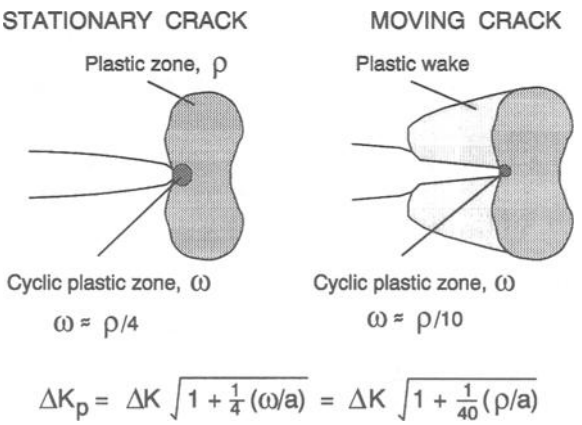


FIG. 9—*Plastic yielding at stationary and moving cracks.*

intensity factor range ΔK_p is very nearly equal to the elastic stress-intensity factor range, ΔK, except at extremely high-stress levels, as shown by the equations on Fig. 9. The application of Irwin's stress-intensity factor analyses to correlate and predict fatigue-crack propagation from micro-cracks to failure is, perhaps, the primary reason for the merger of fatigue and fracture mechanics concepts [*40*].

Fracture

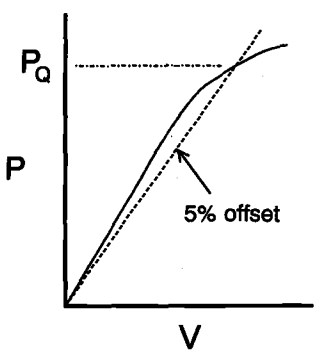
This review, in the area of fracture, will be restricted to linear-elastic fracture mechanics using Irwin's stress-intensity factor to characterize brittle fracture. The influence of the T-stress and constraint on fracture, however, will be briefly discussed and a recent example of fracture of surface-crack specimens made of a high-strength brittle steel under tension and bending loads will be presented.

Plane-Strain Fracture Toughness

In the early 1960s, ASTM Committee E24 was formed and the committee began to develop the plane-strain fracture toughness K_{Ic} test method for metallic materials [*13*]. This method was based on Irwin's stress-intensity factor, K_I. The test method uses the load-displacement (*P-V*) record to determine a 5% offset load, P_Q, as shown in Fig. 10. Extensive test programs on steels, aluminum, and titanium alloys demonstrated that for K_{Ic} to provide a configuration independent measure of fracture toughness, the crack length (a) and thickness (B) had to be greater than 2.5 $(K_{Ic}/\sigma_{ys})^2$. And the P_{max}/P_Q ratio had to be equal to or less than 1.1. This procedure ensures that the plastic zone at fracture does remain vanishingly small relative to a or B; however, selection of the constant value 2.5, needed for materials with low E/σ_{ys} ratios, caused severe limitations on testing of ordinary structural and pressure vessel steels.

Two-Parameter Fracture Mechanics

In 1957, Irwin [*4*] stated "stresses near the end of the crack may be expressed in terms of two parameters." One was the stress-intensity factor K and the other was the so-called T-stress. By the early 1970s, many researchers had realized the inadequacy of a single fracture parameter, such as K, to correlate fracture over a wide range of crack configurations, crack



ASTM E-399 Standard:

$$K_{Ic} = K_Q = (P_Q / BW)\sqrt{\pi a}\ F$$

$$a \text{ and } B \geq 2.5\ (K_{Ic}/\sigma_{ys})^2$$

$$P_{max} / P_Q \leq 1.1$$

FIG. 10—*Plane-strain fracture toughness.*

lengths, specimen sizes, and loading conditions. At this point, "two-parameter" fracture mechanics began to evolve with the second parameter describing "constraint." Most often constraint has been expressed indirectly using the next term(s) in the series expansion of the elastic or elastic-plastic crack-tip stress fields (i.e., the *T*-stress). Larsson and Carlsson [*14*], in 1973, demonstrated that the *T*-stress, had a significant effect on the shape and size of the plastic zone. Since then, several researchers have used a *K-T* fracture locus to explain configuration effects on fracture [*41*].

In 1973, Newman [*15*] proposed the two-parameter fracture criterion (TPFC) which used the additional term in the local elastic-plastic stress equation for a sharp notch or a crack. The TPFC equation, $K_F = K_{Ie}/(1 - mS_n/\sigma_u)$ for $S_n < \sigma_{ys}$, was derived using two approaches. (K_F and m are the two fracture parameters; K_{Ie} is the elastic stress-intensity factor at failure; S_n is the net-section stress; and σ_u is the ultimate tensile strength.) The first approach combined the stress-concentration factor for an ellipsoidal cavity with Neuber's equation [*42*] to derive a relation between the local elastic-plastic stresses and strains and remote loading. This is similar to the way in which Kuhn and Figge [*43*] used the Hardrath-Ohman notch equation many years earlier. The TPFC equation was derived by assuming that fracture occurs when the notch-root stress and strain equal the fracture stress and strain (σ_f and ε_f), and that a crack has a critical notch-root radius, ρ^*. The second parameter, m, arises from the "unity" term in the stress-concentration equation.

The second approach employs the elastic stress field equation for a crack (Eq 1) and Neuber's equation to relate the elastic stresses to the elastic-plastic stresses and strains at a crack tip. In this approach, it is again assumed that fracture occurs at a critical distance, r^*, ahead of the crack tip when the local stress and strain reach the fracture stress and strain. The second parameter, m then, is taken from the next term in the stress-field expansion. When m approached zero, the TPFC equation reduced to Irwin's stress-intensity factor, and when m approached unity, the TPFC equation reduced to the Kuhn-Figge equation.

On the basis of test data and the TPFC, the fracture locus in terms of the elastic stress-intensity factor at failure (K_{Ie}) as a function of the nominal failure stress (S_n) and thickness (B) is illustrated in Fig. 11. This three-dimensional diagram shows how the experimental values of K_{Ie} vary as a function of nominal failure stress and plate thickness [*44*]. The elastic K_{Ie} value is computed from the remote applied stress and the initial crack length in the crack

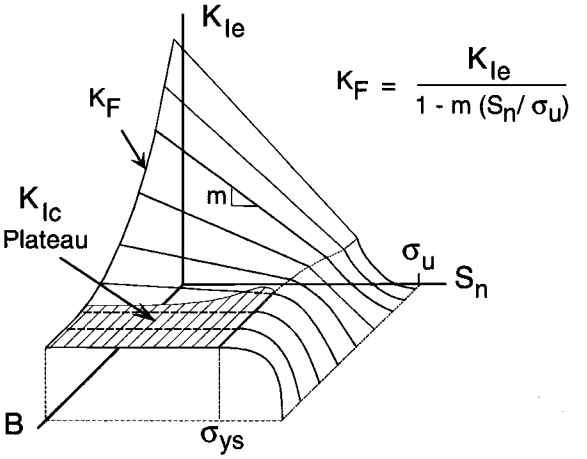


FIG. 11—*Fracture locus from two-parameter fracture criterion.*

configuration and the nominal stress is the net-section stress computed from the loading applied to the uncracked ligament. The "plane-strain" plateau shows the region where the elastic stress-intensity factor at failure, K_{Ic}, is constant. For thin-sheet materials and failure stresses less than the yield stress of the material, K_{Ie} varies almost linearly with S_n. Because K_{Ie} is based on the initial crack length, the relationship between K_{Ie} and S_n includes both plasticity and stable crack growth effects. The results for thin-sheet materials and for high failure stresses (plane-stress fracture regime) are reminiscent of the "two-criteria" approach of Dowling and Townley [*16*], from which the Failure Assessment Diagram evolved.

Surface Crack Configuration

The importance of constraint in the failure analysis of cracked bodies has long been recognized by many investigators. Strain gradients near a crack front led to restrictions of local deformations by the surrounding material. This constraint produces multiaxial stress states that influence the micro-scale separation processes of fracture. The level of constraint depends upon crack configuration and crack location relative to boundaries, thickness, type, and magnitude of applied loading, and the stress-strain properties. In the last few years, a concerted effort (see Blauel and Schwalbe [*45*], Hackett et al. [*46*], and Kirk and Bakker [*47*]) has been undertaken to quantify the influence of constraint on fracture. To evaluate various constraint parameters, two- and three-dimensional (3D) stress analyses have been used to determine stress and deformation states for cracked bodies. The constraint parameters now widely used include the: (1) normal stress, (2) mean stress, (3) T-stress, and (4) Q-stress. In 1960, Irwin [*48*] employed an elevation of the "normal" stress to develop an equation for small-scale yielding at a crack tip using only the K solution. McClintock [*49*] and Rice and Tracey [*50*] considered the influence of the mean stress, $\sigma_m = (\sigma_1 + \sigma_2 + \sigma_3)/3$, on void growth to predict fracture by initiation of ductile tearing. Other mean stress parameters are currently being used in conjunction with 3D, elastic-plastic, finite-element analyses to characterize the local constraint at 3D crack fronts for surface cracks, see Sommer and Aurich [*51*].

As pointed out by Merkle [*52*], in the Fifth Swedlow Lecture, ". . . estimation of constraint effects is best accomplished with three-dimensional analyses." With this in mind, Newman, Reuter, and Aveline [*17*] conducted 3D elastic-plastic, finite-element analyses for surface-cracked plates under tension and bending loads to study a local "normal" stress constraint parameter, α_h. The constraint parameter denotes the average normal-stress-to-flow-stress ratio for yielded material along the surface-crack front. It was postulated that the location that maximizes the product of constraint and stress-intensity factor would indicate the most likely location for brittle fracture to initiate.

Reuter et al. [*53*] conducted fracture tests on surface cracks in a high-strength brittle D6AC steel under remote tension or bending. Figure 12 shows the plane-strain fracture toughness $(K_\phi)_{Ic}$ at the critical location (ϕ) from test data on both surface cracks under tension and bending loads, and at the center-line of a three-point bend specimen. The critical values are plotted against the local constraint parameter. These results show that surface cracks under tension and bending fall together with the three-point bend specimen results within ± 20%. Surface cracks with high critical constraint parameters fail at lower stress-intensity factors than specimens with lower local constraint. These results demonstrate that Irwin's stress-intensity factor and a local "normal stress" constraint parameter can be used to correlate and predict the failure of surface crack in brittle material under combined loading.

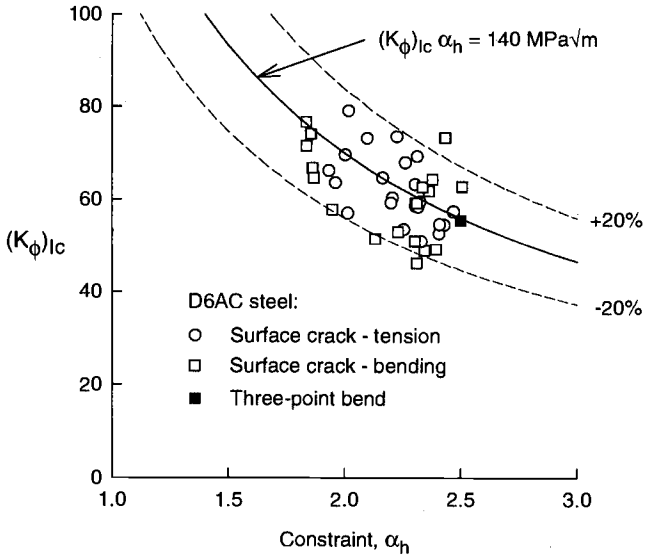


FIG. 12—*Fracture of surface crack under tension and bending loads.*

Concluding Remarks

This paper was written to honor Dr. George Irwin, the founder of modern fracture mechanics, and to reflect on the many contributions that he has made in the understanding of the fracture process in metals. His "stress-intensity factor" concept revolutionized the treatment of both fatigue-crack growth and fracture, and has supported the aerospace, nuclear, and many other industries in the development of design practices to ensure safe operating conditions. Many of his concepts have been adopted and extended to provide more accurate crack-tip stress and strain solutions. During his distinguished career, fracture mechanics had advanced from single-parameter to multi-parameter approaches including the influence of crack-front constraint that he recognized very early as a key issue. Dr. Irwin has been a guiding light and inspiration to many young engineers who have chosen to work in his "field of fracture mechanics." The present author is indebted to Dr. Irwin's kindness and the generous sharing of his thoughts and ideas to advance fracture mechanics principles. The father of fracture mechanics has left a legacy that will endure and provide safer and more reliable structures in the future.

References

[1] Rossmanith, H. P., Ed., "Fracture Research in Retrospect—An Anniversary Volume in Honour of George R. Irwin's 90th Birthday," A. A. Balkema, Rotterdam/Brookfield, 1997.

[2] Landes, J. D., "The Contributions of George Irwin to Elastic-Plastic Fracture Mechanics Development," *Proceedings, 31st National Symposium on Fatigue and Fracture Mechanics,* Cleveland, OH, June 1999.

[3] Irwin, G. R., "Relation of Stresses near a Crack to the Crack Extension Force," *Proceedings of the 9th International Congress on Applied Mechanics,* Brussels, 1956, pp. 245–251.

[4] Irwin, G. R., "Analysis of Stresses and Strains near the End of a Crack Traversing a Plate," *Journal of Applied Mechanics,* Vol. 24, 1957, pp. 361–364.
[5] *The Stress Analysis of Cracks Handbook,* H. Tada, P. C. Paris, and G. R. Irwin, Eds., Del Research Corporation, Bethlehem, PA, 1985.
[6] *Stress Intensity Factors Handbook,* Y. Murakami, Ed., Pergamon Press, Tokyo, Japan, 1987.
[7] Paris, P. C., Gomez, M. P., and Anderson, W. E., "A Rational Analytic Theory of Fatigue," *The Trend of Engineering,* Vol. 13, No. 1, January 1961, pp. 9–14.
[8] Gallagher, J., Giessler, F., Berens, A., and Engle, R., "USAF Damage Tolerance Design Handbook: Guidelines for the Analysis and Design of Damage Tolerant Aircraft Structures," AFWAL-TR-82-3073, 1984.
[9] Manning, S. D. and Yang, J. N., "USAF Durability Design Handbook: Guidelines for the Analysis and Design of Aircraft Structures," AFWAL-TR-83-3027, 1984.
[10] Elber, W., "The Significance of Fatigue Crack Closure," *Damage Tolerance in Aircraft Structures, ASTM STP 486,* 1971, pp. 230–242.
[11] *Short-Crack Growth Behaviour in Various Aircraft Materials,* AGARD Report No. 767, P. R. Edwards and J. C. Newman, Jr., Eds., 1990.
[12] Newman, J. C., Jr., Wu, X. R., Venneri, S. L., and Li, C. G., "Small-Crack Effects in High-Strength Aluminum Alloys—A NASA/CAE Cooperative Program," NASA RP-1309, 1994.
[13] *Plane Strain Crack Toughness Testing of High Strength Metallic Materials, ASTM STP 410,* W. F. Brown, Jr. and J. E. Srawley, Eds., 1967.
[14] Larsson, S. G. and Carlsson, A. J., "Influence of Nonsingular Stress Terms and Specimen Geometry on Small-Scale Yielding at Crack Tips in Elastic-Plastic Materials," *Journal of Mechanics and Physics of Solids,* Vol. 21, 1973, pp. 263–278.
[15] Newman, J. C., Jr., "Fracture Analysis of Surface- and Through-Cracked Sheets and Plates," *Engineering Fracture Mechanics,* Vol. 5, 1973, pp. 667–689.
[16] Dowling, A. R. and Townley, C. H. A., "The Effects of Defects on Structural Failures: A Two-Criteria Approach," *International Journal of Pressure Vessel and Piping,* Vol. 3, 1975, p. 77.
[17] Newman, J. C., Jr., Reuter, W. G., and Aveline, C. R., "Stress and Fracture Analyses of Semi-Elliptical Surface Cracks," *Proceedings, 30th National Symposium on Fatigue and Fracture Mechanics,* St. Louis, MO, June 1998.
[18] Griffith, A. A., "The Phenomena of Rupture and Flow of Solids," *Philosophical Transactions of Royal Society,* Vol. A-221, 1920, p. 163.
[19] Inglis, C. E., "Stresses in a Plate Due to the Presence of Cracks and Sharp Corners," *Proceedings, Institute of Naval Architects,* Vol. 60, 1913.
[20] Sneddon, I. N., "The Distribution of Stress in the Neighborhood of a Crack in an Elastic Solid," *Proceedings, Royal Society of London,* Vol. A-187, 1946, pp. 229–260.
[21] Williams, M. L., "On the Stress Distribution at the Base of a Stationary Crack," *Journal of Applied Mechanics,* Vol. 24, 1957, pp. 109–114.
[22] Paris, P. C. and Sih, G. C., "Stress Analysis of Cracks," *Fracture Toughness Testing and its Applications, ASTM STP 381,* 1965, pp. 30–83.
[23] Irwin, G. R., "The Crack-Extension-Force for a Crack at a Free Surface Boundary," NRL Report 5120, April 1958.
[24] Westergaard, H. M., "Bearing Pressures and Cracks," Transactions, American Society Mechanical Engineers, *Journal of Applied Mechanics,* 1939.
[25] Gross, B. and Srawley, J. E., "Stress-Intensity Factors for Single-Edge Notch Specimen by Boundary Collocation of a Stress Function," NASA TN D-2395, 1964.
[26] Smith, F. W., "The Elastic Analysis of the Part-Circular Surface Flaw Problem by the Alternating Method," *The Surface Crack: Physical Problems and Computational Solutions,* J. L. Swedlow, Ed., 1972, pp. 125–152.
[27] Irwin, G. R., "The Crack Extension Force for a Part Through Crack in a Plate," *Journal of Applied Mechanics,* Vol. 29, No. 4, 1962, pp. 651–654.
[28] Green, A. E. and Sneddon, I. N., "The Stress Distribution in the Neighborhood of a Flat Elliptical Crack in an Elastic Solid," *Proceedings, Cambridge Philosophical Society,* Vol. 46, 1950, pp. 159–164.
[29] Tada, H. and Paris, P. C., "Discussion on Stress-Intensity Factors for Cracks," *Part-Through Crack Fatigue Life Prediction, ASTM STP 687,* J. B. Chang, Ed., 1979, pp. 43–46.
[30] Newman, J. C., Jr., "A Review and Assessment of the Stress-Intensity Factors for Surface Cracks," *Part-Through Crack Fatigue Life Prediction, ASTM STP 687,* J. B. Chang, Ed., 1979, pp. 16–42.
[31] Raju, I. S. and Newman, J. C., Jr., "Stress Intensity Factors for a Wide Range of Semi-Elliptical Surface Cracks in Finite-Thickness Plates," *Engineering Fracture Mechanics Journal,* Vol. 11, 1979, pp. 817–829.

[32] Newman, J. C., Jr. and Raju, I. S., "Analysis of Surface Cracks in Finite Plates under Tension and Bending Loads," NASA TP-1578, National Aeronautics and Space Administration, 1979.
[33] McEvily, A. J. and Illg, W., "The Rate of Crack Propagation in Two Aluminum Alloys," NACA TN-4394, September 1958.
[34] Hudson, C. M., "Effect of Stress Ratio on Fatigue Crack Growth in 7075-T6 and 2024-T3 Aluminum Alloy Specimens," NASA TN D-5390, 1969.
[35] Phillips, E. P., "The Influence of Crack Closure on Fatigue Crack Growth Thresholds in 2024-T3 Aluminum Alloy," *Mechanics of Fatigue Crack Closure, ASTM STP 982,* 1988, pp. 505–515.
[36] Dubensky, R. G., "Fatigue Crack Propagation in 2024-T3 and 7075-T6 Aluminum Alloys at High Stress," NASA CR-1732, 1971.
[37] Newman, J. C., Jr., "A Crack Closure Model for Predicting Fatigue Crack Growth under Aircraft Spectrum Loading," *Methods and Models for Predicting Crack Growth Under Random Loading, ASTM STP 748,* 1981, pp. 53–84.
[38] Newman, J. C., Jr. and Edwards, P. R., "Short-Crack Growth Behaviour in an Aluminum Alloy—An AGARD Cooperative Test Programme," AGARD Report No. 732, 1988.
[39] Landers, C. B. and Hardrath, H. F., "Results of Axial-Load Fatigue Tests on Electropolished 2024-T3 and 7075-T6 Aluminum Alloy Sheet Specimens with Central Holes," NACA TN-3631, 1956.
[40] Newman, J. C., Jr., "The Merging of Fatigue and Fracture Mechanics Concepts: A Historical Perspective," *Progress in Aerospace Sciences,* Vol. 34, No. 5–6, 1998, pp. 345–388.
[41] Chao, Y. J. and Reuter, W. G., "Fracture of Surface Cracks Loaded in Bending," *Fatigue and Fracture Mechanics: 28th Volume, ASTM STP 1321,* J. Underwood, B. Macdonald, and M. Mitchell, Eds., 1997, pp. 214–242.
[42] Neuber, H., "Theory of Stress Concentration for Shear-Strained Prismatical Bodies with Arbitrary Nonlinear Stress-Strain Law," *Journal of Applied Mechanics,* Vol. 28, 1961, pp. 544–550.
[43] Kuhn, P. and Figge, I. E., "Unified Notch-Strength Analysis for Wrought Aluminum Alloys," NASA TN D–1259, 1962.
[44] Newman, J. C., Jr., "Fracture Analysis of Various Cracked Configurations in Sheet and Plate Materials," *Properties Related to Fracture Toughness, ASTM STP 605,* 1976, pp. 104–123.
[45] *Defect Assessment in Components—Fundamentals and Applications,* ESIS/EGF 9, J. G. Blauel and K. Schwalbe, Eds., Mechanical Engineering Publication Ltd., 1991.
[46] *Constraint Effects in Fracture, ASTM STP 1171,* E. Hackett, K. Schwalbe, and R. Dodds, Eds., 1993.
[47] *Constraint Effects in Fracture—2nd Volume, ASTM STP 1244,* M. Kirk and A. Bakker, Eds., 1995.
[48] Irwin, G. R., "Plastic Zone near a Crack and Fracture Toughness," *Proceedings of 7th Sagamore Conference,* Vol. IV, 1960, pp. 63–76.
[49] McClintock, F. A., "A Criterion for Ductile Fracture by the Growth of Holes," *Journal of Applied Mechanics,* June 1968, pp. 363–371.
[50] Rice, J. and Tracey, D. M., "On the Ductile Enlargement of Voids in Triaxial Stress Fields," *Journal of Mechanics and Physics of Solids,* Vol. 17, 1969, pp. 201–217.
[51] Sommer, E. and Aurich, D., 1991. "On the Effect of Constraint on Ductile Fracture," *Defect Assessment in Components—Fundamentals and Applications,* ESIS/EGF 9, 1991, pp. 141–174.
[52] Merkle, J. G., "Patterns and Perspectives in Applied Fracture Mechanics," *Fracture Mechanics: 26th Volume, ASTM STP 1256,* W. Reuter, J. Underwood, and J. Newman, Eds., 1995, pp. 3–40.
[53] Reuter, W., Elfer, N., Hull, D., Newman, J., Munz, D., and Panontin, T., "Fracture Toughness Results and Preliminary Analysis for International Cooperative Test Program on Specimens Containing Surface Cracks," *Fatigue and Fracture Mechanics: 28th Volume, ASTM STP 1321,* J. Underwood, B. Macdonald, and M. Mitchell, Eds., 1997, pp. 146–166.

John D. Landes[1]

The Contributions of George Irwin to Elastic-Plastic Fracture Mechanics Development

REFERENCE: Landes, J. D., **"The Contributions of George Irwin to Elastic-Plastic Fracture Mechanics Development,"** *Fatigue and Fracture Mechanics: 31st Volume, ASTM STP 1389,* G. R. Halford and J. P. Gallagher, Eds., American Society for Testing and Materials, West Conshohocken, PA, 2000, pp. 54–63.

ABSTRACT: George Irwin, the father of fracture mechanics (FM), is well known for his contributions to linear elastic fracture mechanics, especially the development of the crack-tip field approach and the use of the crack tip stress intensity factor, K. During the early years of FM he was well aware that the limits on the use of K restricted its application to high-strength and low-toughness materials. He encouraged the development of new concepts that would be able to extend the use of FM to the more usual engineering materials, materials that might reach yield stress before fracture toughness on a typical structural component. Concern with that area of FM later led to the development of the technology called elastic-plastic fracture mechanics (EPFM). Besides the encouragement he gave, there are several areas where he contributed technical ideas that helped with the development of the EPFM technology. These ideas include use of crack tip field parameters, the energy and crack tip parameter equivalence, the R-curve approach to fracture toughness evaluation and the concern about constraint effects on fracture behavior.

This paper takes a historical look at these developments in elastic-plastic fracture mechanics and the role that George Irwin played. An important observation that will be made is that the approach originally proposed by Irwin gave the correct direction in each case considered in this paper. The original ideas merely needed further development to become mature technical concepts in the EPFM approach.

KEYWORDS: crack-tip field approach, elastic-plastic fracture mechanics, stress intensity factor

The younger generation often have little interest in their past. They are so interested in what is going on now and what they will become that they do not bother to learn about the past lives of their parents and the events that shaped their own lives. However, an interest in the past often develops with maturity, around middle age. Sometimes this interest comes too late and memories of the past are lost before historical events can be explored adequately.

Fracture mechanics is somewhat like this. Several years ago it was in its youth and was concerned only about present and future developments. Now it has passed its 40th year and is reaching middle age in terms of human longevity. Interest is increasing in the history of fracture mechanics and the events the influenced its development over the past 40 years. With the passing of George Irwin in 1998, fracture mechanics has experienced the loss of a parent. Some memories of past events have already been lost, so now is an important time to begin looking at the historical events before all memories of the past are gone.

[1] University of Tennessee, Knoxville, TN.

Copyright© 2000 by ASTM International www.astm.org

This paper is written as a tribute to George Irwin, the "father of fracture mechanics." But, in a greater sense, it is part of the new interest to preserve the history of fracture mechanics. It looks at the fracture mechanics technology as developed by Dr. Irwin and his generation of fracture mechanics researchers. This paper is part of a series of three, one by P. C. Paris [*1*], a second by J. C. Newman [*2*], and the last by myself, all presented at the 31st National Symposium on Fatigue and Fracture Mechanics, in Cleveland, Ohio, in June 1999. The presentation of Paris [*1*] looks at the events that occurred before and leading up to the birth of modern FM. The paper of Newman [*2*] is about that FM birth period concentrating on Irwin's development of the crack-tip stress intensity factor. This paper looks at how the events of that birth time influenced the later development of elastic-plastic fracture mechanics (EPFM). It looks at the original technical views of Irwin and colleagues that directly influenced the manner in which EPFM was developed. It also connected these to the present to see how those ideas are being used today. In that light it makes a bridge from the birth of fracture mechanics up to present day usage.

The format of the paper is as follows. The presentation of the ideas in this paper follows a fairly regular pattern. There are four basic areas discussed that were original ideas of Irwin and that are important influences in the development of EPFM. They are (1) development of crack-tip parameters; (2) crack energy and crack-tip stress field equivalence; (3) R-curves for fracture toughness characterization; (4) constraint effects on fracture behavior. These ideas are discussed relative to the (1) basic idea proposed by Irwin, (2) how that idea influenced the early EPFM development, (3) how that idea has influenced what is being used today in fracture mechanics technology.

Development of Crack-Tip Parameters

The birth of the modern fracture mechanics is often credited as beginning with the 1957 *Journal of Applied Mechanics* paper of Dr. Irwin [*3*]. In that paper two ideas were presented that have an important influence on EPFM. They are the equivalence of a crack-tip stress field parameter with an energy release parameter and the idea that the crack-tip stress field parameters give the best approach for characterizing fracture behavior. The latter will be discussed first. The Irwin-Williams crack-tip stress field approach showed that around the crack tip there is a unique distribution of stresses and strains that can be characterized in magnitude by a single parameter. That parameter, the crack-tip stress intensity factor, K, became the one parameter to characterize the fracture behavior in the newly developed fracture mechanics technology. In this original Irwin paper [*3*], the classical crack tip stress field equations were written in the form,

$$\sigma_{yy} = \left(\frac{EG}{\pi}\right)^{1/2} \frac{\cos \theta/2}{\sqrt{2r}} \left(1 - \sin\frac{\theta}{2} \sin\frac{3\theta}{2}\right) \tag{1}$$

where E is the elastic modulus, G is the Griffiths energy release rate, and r and θ are crack-tip position coordinates. An interesting part of history is that this paper, Ref *3*, is often quoted as being the first mention of the K parameter, but it does not use K for the crack-tip stress field magnitude or even mention K. Rather the form EG/π is used. $EG = K^2$ is an expression of the energy and stress field equivalence.

What is somewhat a mystery is why K was used in a 1956 paper of Irwin [*4*] and a 1957 Boeing report of Paris [*5*] but is not in this 1957 Irwin paper. Part of the mystery may be explained by a discussion of Chona [*6*]. He learned from discussions with Irwin that this paper, which contained somewhat radical ideas for that time, was in the review and revision

process for a long time. In fact, it was in danger of not being published. When it finally was accepted and published, it was a long time after it had been submitted. Although this paper was a September 1957 publication, it had been submitted in February 1956. Therefore, it was then essentially 1955 work and could well have predated most of Irwin's 1956 publications.

Early in the development of a *K*-based approach, Irwin realized the importance of extending the use of the *K* parameter beyond the limits of a linear-elastic approach. He, in fact, developed an extension of the *K* with the plastic zone correction. The idea of using the plastic zone to extend the physical crack length was first presented by Paris [*5*]. Irwin later developed this into his plastic zone corrected *K* parameter [*7*], which gave a way to account for small amounts of plasticity (Fig. 1).

Later Wells [*8*] suggested an alternate parameter, the crack-opening displacement, COD, as a way to extend the *K* approach for larger-scale plasticity. This again was in the context of a crack-tip characterizing parameter. The crack opening displacement is now called crack-tip opening displacement, CTOD, and is used as a crack-tip characterizing parameter for EPFM fracture toughness determination.

The concept of using a crack-tip stress parameter was influential when the idea of using *J* [*9*] to extend linear-elastic fracture mechanics to elastic-plastic was first proposed [*10*]. The use of *J* to characterize fracture was taken in the format of a crack-tip parameter stress parameter and not an energy-based parameter. This was important to the success of this approach. The idea that there could be a unique crack-tip stress and strain field for plasticity was first proposed by the work of Hutchinson [*11*] and Rice and Rosengren [*12*] in 1968. They gave evidence of a unique singular form of the crack-tip field that made an analogy to the linear-elastic crack-tip stress field. This work was based on a non-linear elastic stress field analysis and was appropriate so long as unloading did not occur. McClintock [*13*] wrote these crack-tip field equations in terms of *J* for power-hardening materials,

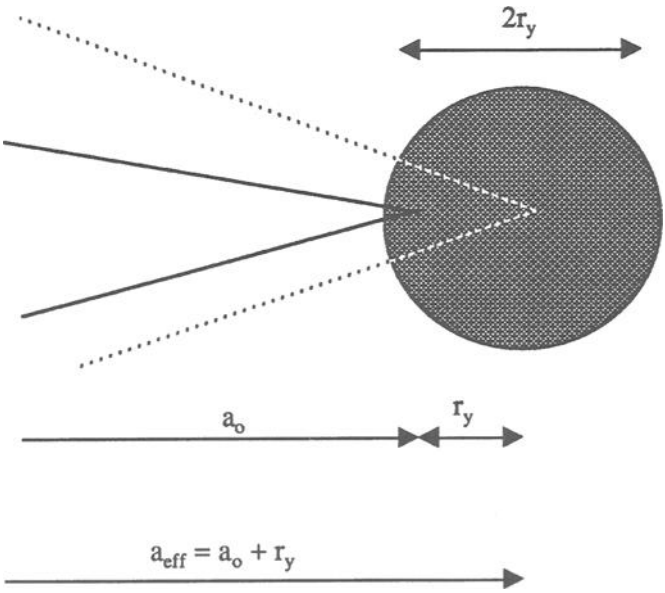


FIG. 1—*Plastic zone adjustment to crack length.*

$$\sigma_{ij} = \left(\frac{J}{\sigma_O I_n r}\right)^{1/n+1} f_{ij}(\theta) \tag{2}$$

where σ_o and I_n are parameters related to the stress strain behavior, σ_o is a flow stress, and I_n a constant that depends on hardening exponent and stress state, and r and θ are crack-tip coordinates. The use of the crack-tip stress equation makes J an extension of the linear-elastic field approach using K or G. The ideas of characterizing fracture behavior with a crack-tip field parameter rather than an energy term was an important one. In the development of EPFM technology, suggestions involving energy parameters were sometimes made. These seemed to have failed, whereas the crack tip parameter approach succeeded. The precedent set by Irwin with the idea of characterizing fracture behavior with a crack-tip parameter rather than an energy parameter was influential here.

In the modern usage of fracture mechanics, K and J [*14*] continue to be used as crack-tip parameters. Some of the other approaches for characterizing fracture behavior used today include, the crack-tip opening displacement, CTOD [*14,15*] and the crack-tip opening angle, CTOA [*16*]. These are both related to the crack-tip field approach and not energy approaches. Although CTOD and CTOA are not related directly to the crack-tip stress field, they indirectly relate to that field and are not energy parameters. Hence, the original idea of Irwin of using crack-tip characterizing parameters continues to be the dominant approach used today.

Energy Release and Crack-Tip Stress Equivalent

Showing the equivalence between the crack-tip stress parameter, K, and the energy release rate, G, was an important step that helped begin the modern fracture mechanics era [*3*]; $G = K^2/E'$, where E' is E for plane stress and $E/(1 - \nu^2)$ for plane strain. This equivalence of the crack-tip field stresses and the energy release rate was the step that showed that the original Griffith energy approach [*17*] was identical to a crack-tip field approach. One of the problems encountered in using an energy-based approach was that the parameter G could be determined only for a few simple geometries of cracked bodies. Of course this was well before the era of numerical evaluation of stress and strain parameters. However, crack-tip stress field analysis had been done for more than a decade before the 1957 Irwin paper [*3*]. The work of Westergaard [*18*], Sneddon [*19*], and Williams [*20*] gave methods for determining the crack-tip field parameters.

The J parameter provided a similar possible two-method approach in that it could be viewed as an energy approach or a crack-tip field approach. Fortunately, the irreversibility of plasticity gave a good reason for not considering it as an energy parameter but rather as a crack-tip field parameter as Irwin had earlier done with K.

The equivalence of the energy and stress field gave a reason for using J as a parameter that can be converted to K in the limit of linear elastic behavior. Originally, the J was used as a parameter to measure fracture toughness in a test with small specimens. The test might have too much plasticity to determine a valid K_{Ic}, but it could be analyzed using J. However, in the application to structural analysis the K and J equivalence, $J = G = K^2/E'$, could be used. This is illustrated in Fig. 2. The approach assumed that the structure being analyzed was large enough to maintain essentially linear-elastic stress conditions. Since the development of EPFM was largely driven by the nuclear power generation industry in the early days, the kinds of structural components involved were usually large.

The use of J for testing to get a fracture toughness result and then converting to K for analysis is still used today, most notably in the transition fracture toughness regime. The master curve [*21*] of ASTM test Method E 1921 to determine the reference temperature, T_o,

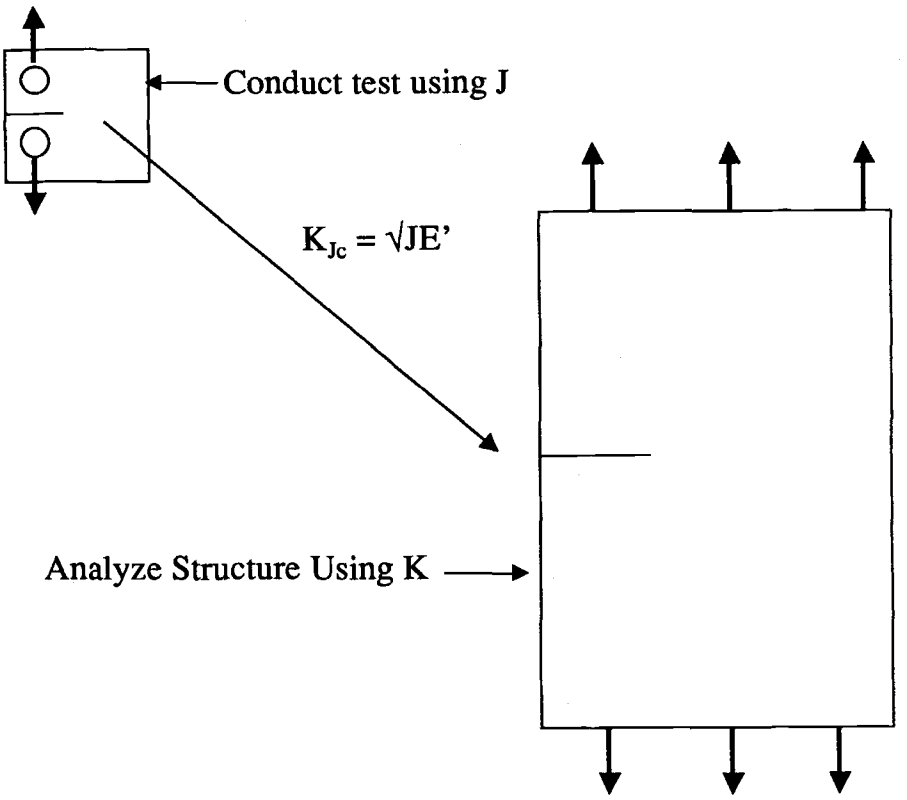


FIG. 2—*Use of* J *and* K *equivalence.*

characterizes a K_{Jc} toughness that has originally been measured by a fracture toughness test using a J_c value, a critical J for brittle fracture. A K_{Jc} value is determined from J_c using the plane stress energy equivalence $K_{Jc} = \sqrt{(J_c E)}$. K_{Jc} is used in the Weibull statistical approach of the new ASTM method E 1921 [*21*] where a median value, $K_{Jc(med)}$ is determined and used in the master curve evaluation of the transition fracture toughness for steels (Fig. 3).

Although the fracture toughness in terms of J can be applied directly to structural evaluation using such things as the *EPRI Handbook* [*22*] to evaluate J for the structural geometry, the conversion to a K value is still used in many applications. A primary reason is that the linear approach allows the superposition of multiple stress fields, whereas for EPFM this superposition cannot be used. Therefore, the energy release and crack-tip field parameter equivalence remains today as an important concept and is used in a way derived from the idea originally proposed by Irwin.

R-Curves for Fracture Toughness

The use of the crack growth resistance curve, or R curve, to describe ductile fracture was one of the earliest concepts that was used, predating the conventional FM birth. An original R curve concept came from a 1954 paper of Irwin and Kies [*23*] that stated ". . . strain energy release rate and fracturing work rate must be equal at the onset of instability. . . ."

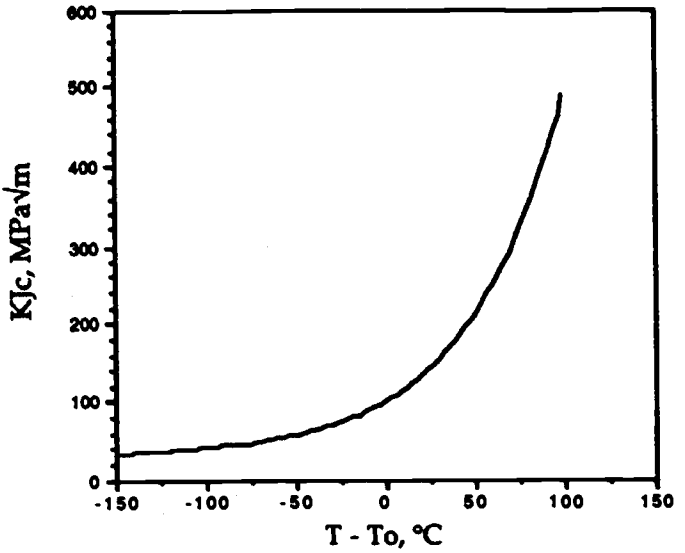


FIG. 3—*Master curve of transition fracture toughness.*

This concept is illustrated in Fig. 4*a*. Some of the important steps in the development of the *R* curve concept include the work of Krafft [*24*] in 1961 that showed a rising *R* curve with an instability point, and the work of Srawley and Brown [*25*] in 1965 that showed geometry effects on *R* curve behavior. The original concept of the *R* curve shape in 1954 [*23*] and how that was modified in 1959 [*26*] is illustrated in Fig. 4*a* and 4*b*. The original 1954

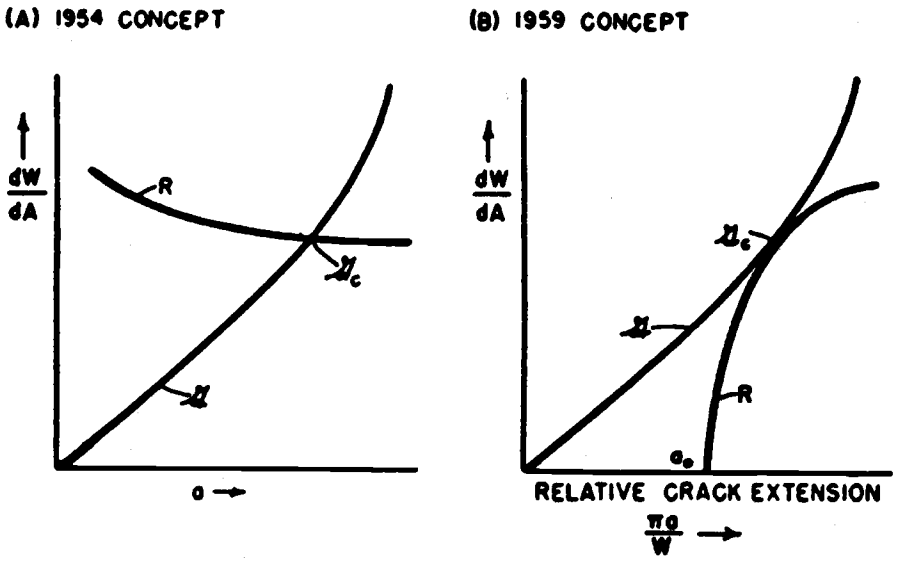


FIG. 4—*Original* R *curve concepts.*

concept on fracture resistance was that it remained essentially constant with increased loading. However, studies of this behavior showed that the *R* curve was rising. The 1959 concept attributed this rise first to shear lip development and later to the development of plasticity [*27*].

The most definitive work on the use of *R* curves came from McCabe and Heyer [*27*] where the *K-R* curve test methods were developed including test specimens like the crack-line-wedge-loaded CLWL specimen. Their work ultimately led to the standardization of the *K-R* curve approach for fracture toughness characterization of thin sheet materials as given in ASTM standard practice E 561 [*28*].

The use of *J* for characterizing fracture toughness originally used the concept of a single fracture toughness measurement point in a manner similar to K_{Ic} [*10,29*], but later it was realized that the ductile fracture behavior can only be adequately characterized by an *R* curve [*30*]. The *R* curve approach for all ductile fracture toughness behaviors still remains today as the best way to characterize ductile fracture toughness and is used in most EPFM test methods.

Examples of the use of an *R* curve concept in the modern EPFM include: the evaluation of a J_{Ic} value that uses an *R* curve to define a point near the initiation of ductile tearing [*14*], the tearing modulus and *J-T* diagram approach to evaluate ductile instability during ductile tearing [*31,32*], and the direct evaluation of structural behavior in the presence of a crack-like defect using the ductile fracture methodology, DFM [*33*]. The *R* curve approach for characterizing ductile fracture, which was originally a contribution of George Irwin, is still very much the accepted method for characterizing ductile fracture behavior.

Constraint Effects

The idea of considering constraint effects in the crack-tip field region was first suggested by Irwin as an influence on the plastic zone size [*7*]. The plastic zone size equation was given as

$$r_y = K^2/\alpha\pi\sigma_{ys}^2 \tag{3}$$

where α is 2 for plane stress and approximately 6 for plane strain. This equation is still used today; however, study of the issue of constraint and its influence on fracture behavior has gone far beyond this original concept. In fact, much of the work on FM in the 1990s has centered on the constraint issue. The original concern with constraint considered mainly the thickness effect. The more modern work is concerned with the effects of planar constraint and considers the influence of constraint on geometry and loading mode differences in fracture behavior [*34*].

Some of the areas that have arisen in FM today that concern constraint are the use of two-parameter fracture mechanics to evaluate fracture [*35–37*], constraint-based adjustment to the fracture parameter [*34*], and scaling to small-scale yield conditions. These have become important in finally rationalizing the fracture behavior of different sizes and geometries. The two-parameter *FM* uses a *K* and *T* approach for linear behavior [*35*] and a *J* and *Q* for EPFM [*36,37*]. The second parameter, *T* or *Q*, is the difference between an actual crack tip stress field as evaluated numerically and the stresses determined by a single singular term as given by Eqs 1 and 2. The two-parameter approach can be used in a correlative manner or for developing modeling approaches [*38*]. The crack-tip adjustment approaches to constraint evaluation uses the relationship between a *J* value for actual loading and one that could be determined in an infinite body that would have small-scale yield conditions. For

every geometry the actual J in that geometry and the equivalent small-scale yield J can be related is a way that allows a transfer of the fracture toughness value measured in the laboratory to the evaluation of that structural geometry [*34*].

The final step needed to transfer laboratory measurements of fracture behavior from specimen geometries to component sizes and geometries is dependent on the understanding of these constraint effects. Often the use of a single crack-tip field parameter to characterize fracture toughness must be modified with considerations developed from a mechanistic-based model of the fracture behavior [*39,40*].

All of the present constraint-based work is dependent on numerical modeling of the stress and strain behavior and could not have been accomplished during the early days of fracture mechanics. However, the work of Irwin that identified constraint as an important consideration in evaluating fracture behavior led the way for the modern efforts.

Summary

The original work of George Irwin, "the father of fracture mechanics," influenced work that led to the development of elastic-plastic fracture mechanics (EPFM). Four important suggestions of Irwin were incorporated into EPFM. They are (1) development of crack-tip parameters; (2) crack energy versus crack-tip stress field equivalence; (3) R-curve for fracture toughness characterization; (4) constraint effects on fracture behavior. These four ideas not only provided input important to the early development of EPFM but provided the approaches that are essentially applied today in the fracture mechanics methods used 40 years after their birth. These concepts all gave the correct direction in their original formulation and are used today in a format that extended the original idea but did not change it to an extent.

References

[*1*] Paris, P. C., "Irwin's Contributions to Fracture Mechanics (The Early Times—1948 to 1957+)," presented at the 31st National Symposium on Fatigue and Fracture Mechanics, Cleveland, OH, 22 June 1999.

[*2*] Newman, J. C., "Irwin's Stress Intensity Factor—A Historical Perspective," *Proceedings,* 31st National Symposium on Fatigue and Fracture Mechanics, Cleveland, OH, 23, June 1999.

[*3*] Irwin, G. R., "Analysis of Stresses and Strains Near the End of a Crack Traversing a Plate," *Journal of Applied Mechanics, Transactions of ASME,* Vol. 24, 1957, pp. 361–364.

[*4*] Irwin, G. R., "Relation of Stresses Near a Crack to the Extension Force," *Proceedings,* 9th Structural Congress on Applied Mechanics, Brussels, Vol. 18, 1956, pp. 245–251.

[*5*] Paris, P. C., "The Boeing Documents of Paul C. Paris 1955 and 1957," Document No. D-17867, Boeing Aircraft Company, Seattle, WA.

[*6*] Chona, R., private communication, June 1999.

[*7*] Irwin, G., "Plastic Zone Near a Crack and Fracture Toughness," *Proceedings,* 7th Sagamore Conference, Vol. IV, 1961, pp. 63–76.

[*8*] Wells, A. A., "Unstable Crack Propagation in Metals: Cleavage and Fast Fracture," *Proceedings,* Crack Propagation Symposium, Vol. 1, Paper 84, Cranfield, UK, 1961, pp. 210–230.

[*9*] Rice, J. R., "A Path Independent Integral and the Approximate Analysis of Strain Concentrations by Notches and Cracks," *Journal of Applied Mechanics,* Vol. 35, 1968, pp. 379–386.

[*10*] Begley, J. A. and Landes, J. D., "The J-Integral as a Fracture Criterion," *Fracture Toughness, Proceedings of the 1971 National Symposium on Fracture Mechanics Part II, ASTM STP 514,* American Society for Testing and Materials, West Conshohocken, PA, 1972, pp. 1–26.

[*11*] Hutchinson, J. W., "Singular Behavior near the End of a Tensile Crack Tip in a Hardening Material," *Journal of the Mechanics and Physics of Solids,* Vol. 16, 1968, pp. 13–31.

[12] Rice, J. R. and Rosengren, G. F., "Plane Strain Deformation Near a Crack Tip in a Power Hardening Material," *Journal of the Mechanics and Physics of Solids*, Vol. 16, 1968, pp. 1–12.
[13] McClintock, F. A., "Plasticity Aspects of Fracture," in *Fracture*, H. Liebowitz, Ed., Vol. 3, Academic Press, New York, 1971, pp. 47–225.
[14] ASTM E 1820, Standard Test Method for Measurement of Fracture Toughness, *ASTM, Annual Book of Standards*, Vol. 03.01.
[15] ASTM E 1290, Standard Test Method for Crack-Tip Opening Displacement (CTOD) Fracture Toughness Measurement, *ASTM Annual Book of Standards*, Vol. 03.01.
[16] Dawicke, D. S., Sutton, M. A., Newman, J. C. Jr., and Bigelow, C. A., "Measurement and Analysis of Critical CTOA for an Aluminum Alloy Sheet," *Fracture Mechanics: 25th Volume, ASTM STP 1220*, F. Erdogan, Ed, American Society for Testing and Materials, 1995, pp. 358–379.
[17] Griffith, A. A., "The Phenomena of Rupture and Flow in Solids," *Philosophical Transactions*, Series A, Vol. 221, 1920, pp. 219–241.
[18] Westergaard, H. M., "Bearing Pressures in Cracks," *Journal of Applied Mechanics*, Vol. 6, 1939, pp. 49–53.
[19] Sneddon, I. N., "The Distribution of Stresses in the Neighborhood of a Crack in an Elastic Solid," *Proceedings, Royal Society of London*, Vol. A-187, 1946, pp. 229–260.
[20] Williams, M. L., "On the Stress Distribution at the Base of a Stationary Crack," *Journal of Applied Mechanics*, Vol. 24, 1957, pp. 109–114.
[21] ASTM E 1921, Standard Test Method for Determination of Reference Temperature, T_o, for Ferritic Steels in the Transition Range, *ASTM Annual Book of Standards*, Vol. 03.01.
[22] Kumar, V., German, M. D., and Shih, C. F., "An Engineering Approach for Elastic-Plastic Fracture Analysis," NP 1931, EPRI Project 1237-1, July 1981.
[23] Irwin, G. R. and Kies, J. A., *Welding Research Supplement*, Vol. 19, April 1954, pp. 193–198.
[24] Krafft, J. J. M., Sullivan, A. M., and Boyle, R. W., *Proceedings*, Crack Propagation Symposium, College of Aeronautics, Vol. 1, Cranfield, England, 1961, pp. 8–26.
[25] Srawley, J. E. and Brown, W. F., "Fracture Toughness Test Methods," *Fracture Toughness Testing and Its Applications, ASTM STP 381*, American Society for Testing and Materials, 1965, pp. 133–198.
[26] ASTM Special Committee on Fracture Testing of High Strength Materials, *ASTM Bulletin*, January 1960, pp. 29–40.
[27] McCabe, D. E. and Heyer, R. H., "R-Curve Determination Using a Crack-Line-Wedge-Loaded (CLWL) Specimen," *Fracture Toughness Evaluation by R-Curve Methods, ASTM STP 527*, American Society for Testing and Materials, 1973, pp. 17–35.
[28] ASTM E 561, "Standard Practice for R-Curve Determinations," *ASTM Annual Book of Standards*, Vol. 03.01.
[29] Landes, J. D. and Begley, J. A., "The Effect of Specimen Geometry on J_{Ic}," *Fracture Toughness, Proceedings of the 1971 National Symposium on Fracture Mechanics, Part II, ASTM STP 514*, American Society for Testing and Materials, 1972, pp. 24–39.
[30] Landes, J. D. and Begley, J. A., "Test Results from J-Integral Studies: An Attempt to Establish a J_{Ic} Testing Procedure," *Fracture Analysis, ASTM STP 560*, American Society for Testing and Materials, 1974, pp. 170–186.
[31] Paris, P. C., Tada, H., Zahoor, A., and Ernst, H. A., "The Theory of Instability of the Tearing Mode of Elastic-Plastic Crack Growth," *Elastic Plastic Fracture, ASTM STP 668*, J. D. Landes, J. A. Begley, and G. A. Clarke, Eds., ASTM, 1979, pp. 5–36.
[32] Paris, P. C. and Johnson, R. E., "A Method of Application of Elastic-Plastic Fracture Mechanics to Nuclear Vessel Analysis," *Elastic-Plastic Fracture: Second Symposium, Volume I—Inelastic Crack Analysis, ASTM STP 803*, C. F. Shih and J. P. Gudas, Eds., ASTM, 1983, pp. II-5–II-40.
[33] Landes, J. D. Zhou, Z., and Brown, K. H., "An Application Methodology for Ductile Fracture Mechanics," *Fracture Mechanics: Twenty-Third Symposium, ASTM STP 1189*, Ravinder Chona, Ed., ASTM, 1993, pp. 229–264.
[34] Anderson, T. L. and Dodds, R. H., "Specimen Size Requirements for Fracture Testing in the Transition Region," *Journal of Testing and Evaluation, JTEVA*, American Society for Testing and Materials, Vol. 19, 1991, pp. 123–134.
[35] Hancock, J. W., Reuter, W. G., and Parks, D. M., "Constraint and Toughness Parameterized by T," *Constraint Effects in Fracture, ASTM STP 1171*, E. M. Hackett, K.-H. Schwalbe, and R. H. Dodds, Eds., American Society for Testing and Materials, 1993, pp. 21–40.
[36] O'Dowd, N. P. and Shih, C. F., "Family of Crack-Tips Fields Characterized by a Triaxiality Parameter: Part I—Structure of Fields," *Journal of the Mechanics and Physics of Solids*, Vol. 39, 1991, pp. 989–1015.

[*37*] O'Dowd, N. P. and Shih, C. F., "Family of Crack-Tip Fields Characterized by a Triaxiality Parameter: Part II—Fracture Applications," *Journal of the Mechanics and Physics of Solids,* Vol. 40, 1992, pp. 939–963.

[*38*] Shih, C. F., O'Dowd, N. P., and Kirk, M. T., "A Framework for Quantifying Crack Tip Constraint," *Constraint Effects in Fracture, ASTM STP 1171,* E. M. Hackett, K.-H. Schwalbe, and R. H. Dodds, Eds., American Society for Testing and Materials, 1993, pp. 2–20.

[*39*] Landes, J. D., "A J-Q Model for Predicting Fracture in the Ductile-Brittle Transition," *Fatigue and Fracture of Engineering Materials and Structures,* Vol. 19, No. 7, 1996, pp. 869–877.

[*40*] Ruggieri, C. and Dodds, Jr., R. H., "Probabilistic Modeling of Brittle Fracture Including 3-D Effects on Constraint Loss and Ductile Tearing," *Proceedings,* International Conference on Local Approach to Fracture (MECAMAT 96), Fontainbleau, France, 1996.

Cyclic Stress-Strain and Fatigue Resistance

C.-C. Chu[1]

A New Incremental Fatigue Method

REFERENCE: Chu, C.-C., **"A New Incremental Fatigue Method,"** *Fatigue and Fracture Mechanics: 31st Volume, ASTM STP 1389,* G. R. Halford and J. P. Gallagher, Eds., American Society for Testing and Materials, West Conshohocken, PA, 2000, pp. 67–78.

ABSTRACT: By analyzing the material's strain-life data differentially, this paper brings to light the generally overlooked incremental damage concept which underlies the conventional uniaxial rainflow counting algorithm and the strain-based fatigue method. This incremental damage concept not only allows the uniaxial rainflow program to be logically extended to multiaxial problems, it also forms the basis for a new incremental fatigue damage accumulation method. Several simple examples, including a multiaxial rainflow algorithm, are given to illustrate how the new approach can be applied to general multiaxial problems and how it can be formulated so that any chosen uniaxial model using the traditional parametric approach can be closely reproduced.

KEYWORDS: fatigue damage event, rainflow, multiaxial rainflow, incremental damage, incremental damage accumulation rate, flow stress, damage parameter, out-of-phase, in-phase, mean stress effect

The traditional rainflow counting method [*1*], commonly used to identify fatigue damage events, was developed based on the material's cyclic stress-strain behavior observed under uniaxial or proportional loadings. This method identifies each closed hysteresis loop in the stress-strain plot as a fatigue event, and the damage caused by such an event is assumed to be a function of an attribute, such as the strain amplitude of the event. Although multiaxial fatigue behavior is generally much more complicated, and the hysteretic behavior can no longer be observed on the stress and strain component level, fatigue analysts nevertheless try to rainflow count, for example, the normal strain component on a potential failure plane in order to determine damage events as if the loading were uniaxial. Such an approach ignores the complex interaction between various stress and strain components. A more recent multiaxial method proposed in Ref *2* essentially rainflowed the equivalent strain history to take into account the material's overall deformation, but it did not address a more fundamental question: What is the mechanism that causes fatigue damage to accumulate in a continuous fashion during an identified fatigue event that generally is comprised of disjointed loading segments?

In this paper, an incremental damage concept is first reviewed as the basis of the conventional rainflow counting method. Then by using flow stress, as in most yield surface based plasticity models, to unite three-dimensional stress states with uniaxial ones, the incremental damage concept is generalized to the equivalent stress-strain behavior. A multiaxial rainflow method based on the variation of flow stress, which represents the 'equivalent' hysteretic behavior under multiaxial loading, is subsequently proposed.

[1] Staff Scientist, Manufacturing Systems Dept., Ford Research Lab, MD3135 SRL, P.O. Box 2053, Dearborn, MI 48121-2053.

Copyright© 2000 by ASTM International www.astm.org

Finally, a general incremental fatigue method is outlined, which has three important features: (1) When the loading is uniaxial or proportional, the method reduces to the conventional strain-based fatigue approach; (2) the fatigue damage analysis can be performed together with the stress-strain analysis, thus eliminating the traditional practice of a separate post-stress analysis rainflow routine to prepare for fatigue analysis; (3) the incremental method allows fatigue damage to be accumulated continuously, that is, the amount of damage accumulated up to any point in the history can be calculated, unlike in the traditional method where the total damage is determined after the loading history is rainflow counted.

Uniaxial Rainflow Method

For materials that cyclically stabilize, an arbitrary uniaxial loading shown in Fig. 1*a* results in a hysteretic stress-strain behavior displayed in Fig. 1*b*. Conventionally, the local strain-based fatigue life approach assumes that each of the closed hysteresis loops in Fig. 1*b* is a fatigue event, and the total fatigue damage of the block history shown in Fig. 1*a* is the sum of damages from all (four) fatigue events, or hysteresis loops. If the stress amplitude is the assumed damage parameter, then the material's stress amplitude versus fatigue life curve is used to determine the damage caused by individual events as illustrated in Fig. 1*c*.

The traditional rainflow counting method was developed to take advantage of the fact that the fatigue events, or the hysteresis loops, of a uniaxial variable amplitude loading can be extracted from the stress (or strain) histogram without resorting to the hysteretic stress-strain plots. This is illustrated in Fig. 1*a* where the shaded damage events can be identified without referring to Fig. 1*b*.

Because of its simplicity and broad usage in analyzing uniaxial problems, the more mechanically oriented background of the rainflow counting method is frequently overlooked. This background, which has strong implications on how the uniaxial rainflow method can be extended to general three dimensional problems, is reemphasized in the following.

Incremental Damage Accumulation Rate

Without loss of generality, let us consider the simple Basquin's equation as the material's fatigue property,

$$\wp = \sigma_a = \sigma'_f(2N_f)^b = \sigma'_f D^{-b} \tag{1}$$

Here the stress amplitude σ_a is assumed to be the damage parameter $\wp$; $2N_f$ denotes the crack initiation life in half cycles; σ'_f and b are material constants, and D denotes the amount of damage per half cycle which is defined as $1/2N_f$. The traditional usage of such fatigue properties is to determine the amount of damage for a completed fatigue event of which the stress amplitude is known. However, a valuable although often neglected piece of information concerning incremental damage is also provided by the above equation. This information can be obtained by differentiating both sides of Eq 1

$$d\wp = d\sigma_a = -b\sigma'_f D^{-b-1}\, dD$$

The incremental damage accumulated rate, which is defined here as the amount of damage caused by a unit damage parameter increase, and from here one denoted by h, can then be expressed by

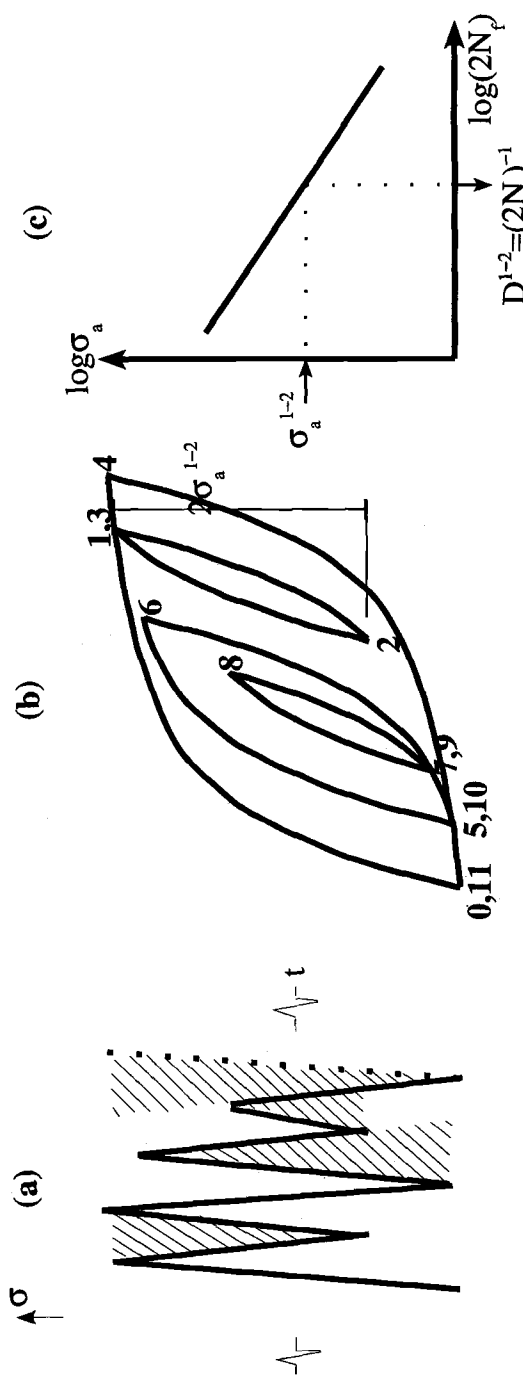


FIG. 1—*A uniaxial example* (a) *stress history,* (b) *its corresponding stress-strain, and* (c) *the material fatigue curve to assess damage.*

$$h = \frac{dD}{d\wp} = \frac{D^{b+1}}{b\sigma'_f} = -\frac{1}{b}(\sigma'_f)^{1/b}\sigma_a^{-1-(1/b)} \tag{2}$$

Note that the last part of the above equation is achieved by using the inverse of Eq 1. An example of the incremental damage accumulation rate is plotted against the damage parameter, stress amplitude, in Fig. 2*a*. The figure shows a typical dependence of the incremental damage accumulation rate on the damage parameter level.

Applying this incremental damage concept to the uniaxial loading in Fig. 1*b*, the fatigue damage accumulates in a fashion described below, and is schematically represented in Fig. 2*b*. From State 0 to 1, the stress amplitude increases from 0 to $\sigma_a^{0\text{-}1}$. Referring to Fig. 2*a*, the fatigue damage accumulates at a rate increasing from 0 at the beginning of the event to h_1 at stress amplitude $\sigma_a^{0\text{-}1}$. Reverse loading at State 1 suspends the (0-1) event and starts a new (1-2) event. During the (1-2) event the stress amplitude decreases from 0 to $\sigma_a^{1\text{-}2}$ and the fatigue damage accumulates at a rate increasing from 0 at the beginning of the event to h_2 at stress amplitude $\sigma_a^{1\text{-}2}$. At State 2, reverse loading terminates event (1-2) and starts a new event (2-3). In the current simple uniaxial example, event (2-3) has the same stress amplitude variation (from 0 to $\sigma_a^{2\text{-}3} = \sigma_a^{1\text{-}2}$) and damage accumulation rate variation (from 0 to h_2) as those of event (1-2). At State 3, the material reaches a previously suspended stress state and is observed to resume the suspended deformation pattern, that is, the deformation rate is that of a much higher stress amplitude level, $\sigma_a^{0\text{-}1}$, than that achieved at the end of event (2-3). As a result, from State 3 to 4, fatigue damage accumulates at a rate increasing from the resumed rate h_1 to h_4 at stress amplitude $\sigma_a^{0\text{-}4}$. Loading paths 0-1 and 3-4, although interrupted, are therefore grouped together as one single fatigue event.

As shown in the sketch in Fig. 2*b*, this analysis can be performed and thus fatigue damage summed up for the complete history. More systematically, the above analysis and damage accumulating procedure can be carried out for any complicated uniaxial history by following two rules: (1) a loading reversal always suspends the current fatigue event and starts a new event; that is, a loading reversal suspends the current damage accumulation rate and resets it to start from 0 for a new event; (2) during a fatigue event, if an earlier suspended deformation state is reached, first the current fatigue event is concluded, then the suspended event with its corresponding damage accumulation rate is resumed.

As displayed by lines of various styles, Fig. 2*b* shows eight fatigue events resolved by the above-mentioned procedures. These are the same as those obtained by examining the hysteretic stress-strain behavior in Fig. 1*b*, or by using the uniaxial rainflow counting method shown in Fig. 1*a*. (Note here that with the current incremental damage algorithm, a single fatigue event identified by the conventional rainflow method is defined as two events.)

According to the incremental damage concept the total fatigue damage can be integrated along the complete loading path as

$$D = \int dD = \int h \cdot d\wp \tag{3}$$

If the damage accumulation rate h is solely a function of $\wp$, (for example h is solely a function of σ_a in Eq 2), then the above equation can be integrated into a unique relationship between D and $\wp$, such as the Basquin equation. In such a case, instead of integrating damage along the loading path, the damage parameter of event i, denoted by $\wp^{(i)}$, can be accumulated for each event, and the $D - \wp$ relationship can be used to look up the fatigue caused by individual events. The total damage is then

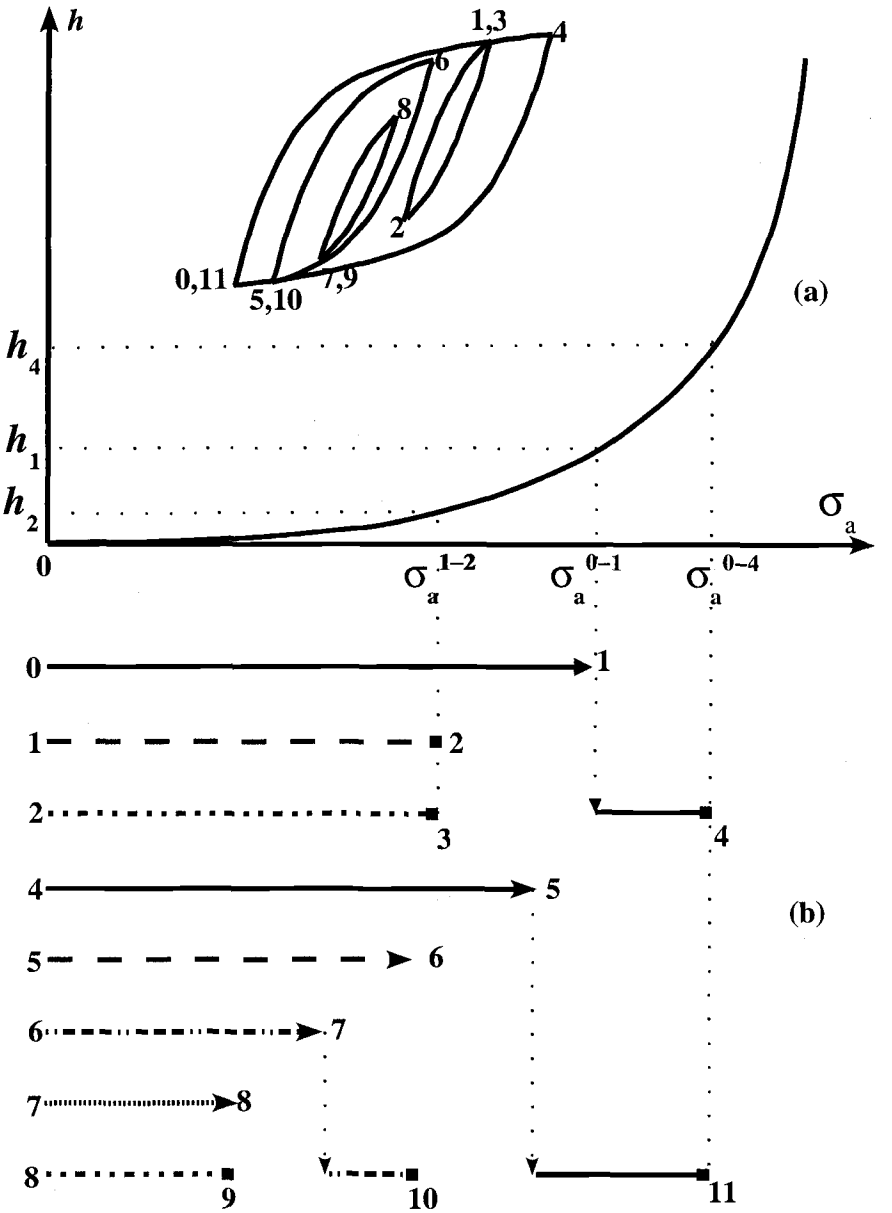


FIG. 2—*Incremental damage accumulation rate and fatigue events for loading in Fig. 1.*

$$D = \sum_i D^{(i)} = \sum_i D[\varphi^{(i)}] = \sum_i D\left[\int_i d\varphi\right]$$

This then results in the common fatigue method where the material's strain-life curve

serves as the D-$\mathcal{P}$ relationship, and the rainflow counting method determines how the parameter should be accumulated. The uniaxial rainflow counting method and the material's fatigue curve, both operated on the final values of the $\mathcal{P}$'s and D's of fatigue events, have traditionally obliterated the underlying incremental damage concept.

Multiaxial Rainflow Method

The above-mentioned incremental damage-based fatigue event identification method, in particular, the two established rules to determine the onset and completion of fatigue events, can now be extended to multiaxial problems by using any yield surface based material model. This is accomplished by plotting the flow stress variation history, as shown in Fig. 3, the same way as the stress amplitude variation history in Fig. 2*b*. Note here that the specific definition for flow stress depends on the cyclic stress-strain model adopted. For example, in a Mróz type of stress-strain model [*3*], it is defined as $\sqrt{3/2}\,(\underline{s} - \underline{\alpha}) \cdot (\underline{s} - \underline{\alpha})$, where $\underline{s}$ and $\underline{\alpha}$ are the deviatoric stress tensor and the center of the active yield surface, respectively.

It is important to first point out that flow stress is proposed here because it is almost universally used to equate a general multiaxial stress state with a uniaxial stress state. Furthermore, in most cyclic stress-strain models, conditions determining whether a stress increment causes continuous loading or unloading are directly related to the variation of flow stress.

A fatigue event, which is defined as loading sequence(s) during which damage accumulates at a continuously increasing rate, can thus be identified using flow stress variations. To help illustrate the procedures, shown in Fig. 3 is an arbitrary flow stress variation similar to the stress amplitude variation in Fig. 2*b*. During a continuous loading path, the flow stress level increases, as indicated by the length of horizontal lines in Fig. 3. The horizontal lines always

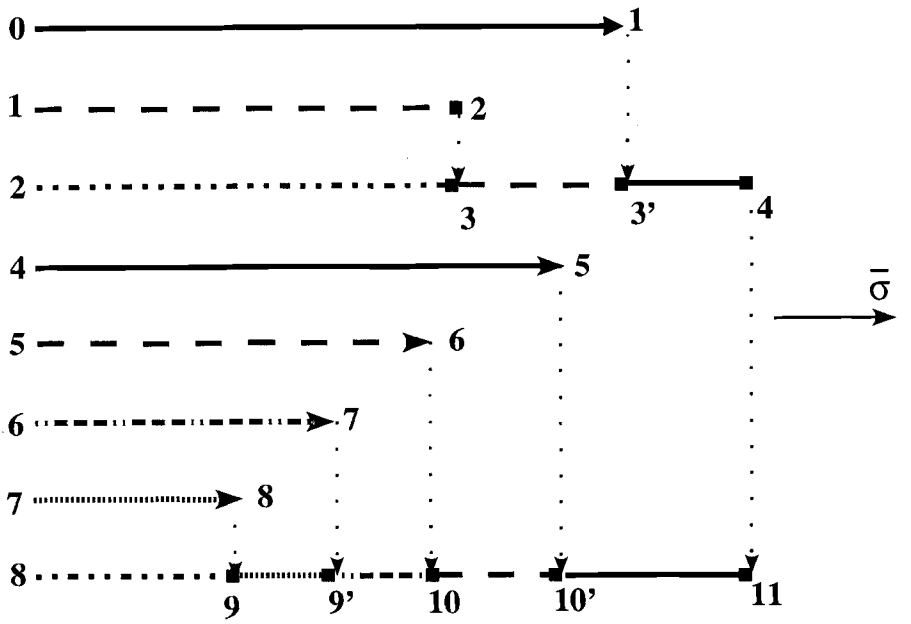


FIG. 3—*Variation of flow stress and resolved fatigue events.*

end at an unloading point, at which the flow stress increment is suspended, and its current value and associated loading state are stored in the material memory. The flow stress is then set to 0 and a new fatigue event (a new flow stress line in Fig. 3) begins. During a continuous loading path, whenever the flow stress reaches a previously suspended level, the current fatigue event ends and the earlier suspended path as well as its corresponding damage accumulation rate is resumed. (Note that once an earlier suspended path is resumed, its record in the material memory is erased.) Using the continuous path 2 to 4 in Fig. 3 as an example, at Point 3 the flow stress increases to the level suspended earlier at unloading Point 2. It thus concludes event (2-3). (The end of an event is marked by a filled square symbol in Fig. 3.) The damage accumulation pattern of event (1-2) is then resumed until the flow stress reaches another level suspended earlier at unloading Point 1. Event (1-2,3-3′) is thus completed and the damage accumulation pattern of event (0-1) is resumed until unloading occurs or another previously suspended state is reached. Carrying out these procedures for the whole history in Fig. 3 results in eight fatigue events. Note that Fig. 3 is almost identical to Fig. 2*b* because for uniaxial loading the flow stress value is the same as stress amplitude value. The major difference between the two figures lies where Points 3 and 3′, 9 and 9′, and 10 and 10′ are. For complex multiaxial loadings the two points are generally different stress states, as shown in Fig. 3. For uniaxial or proportional loading of cyclically stabilized material, however, they coincide. As a result, flow stress jumps at the 'resumption points,' such as State 3, 9, and 10 in Fig. 1*b*; and event (1-2,3-3′) in Fig. 3 degenerates to simply (1-2) in uniaxial loading in Fig. 2*b*.

More specific examples of the above fatigue event identification method can be found in Ref *4* using a generalized Mróz model. Since the Mróz model is based on the stabilized hysteretic stress-strain behavior, Ref *4* also shows that the current multiaxial rainflow method reduces to the conventional rainflow method when applied to uniaxial or proportional loadings.

Incremental Damage Accumulation for Multiaxial Loading

Unlike uniaxial loading cases, the fatigue events under random multiaxial loading generally are comprised of loading segments disjointed in the stress and strain space, although continuous in the flow stress variation. Nevertheless, Eq 3 can be straightforwardly applied to integrate for total fatigue damage if the damage parameter increment $d\wp$, and the instantaneous damage accumulation rate, h, are known. Again, if h is solely a function of $\wp$, then a total D versus $\wp$ relationship exists. That is, fatigue damage accumulated in an event can also be obtained by accumulating $\wp$ and use the D-$\wp$ relationship to look up the damage corresponding to the final accumulated value of $\wp$.

Here it is proposed that the incremental method can be made more general in the following way. First we realize that the flow stress based fatigue event identifying method introduced earlier strongly suggests a flow stress dependent, or deformation state dependent, damage accumulation rate. If we assume that the damage accumulation rate is a function of the instantaneous flow stress level during the fatigue event, then $dD = h[\bar{\sigma}]d\wp$. Using the same Basquin's equation as an example, now the damage accumulation rate is modified to

$$h[\bar{\sigma}] = -\frac{1}{b}(\sigma'_f)^{1/b}(\bar{\sigma})^{-1-(1/b)}. \tag{4}$$

This will thus invalidate a unique total damage versus parameter relationship, unless the flow stress happens to be a function of $\wp$, as in the uniaxial case.

Once h is assumed to be dependent on more variables than simply $\mathcal{P}$, the instantaneous damage accumulation rate can be enhanced to include other factors supported by experimental evidence. For example, as will be shown later, the instantaneous accumulate rate can be made additionally dependent on the current stress level to result in mean stress dependent damage phenomenon.

While a specific function of the general approach outlined above requires much more correlation with available experimental data, two examples are used below to illustrate how the incremental approach may hold some promise.

Out-of-Phase Loading

Figure 4 shows loading paths of various out-of-phase-ness in the deviatoric stress space. The straight path (1) is the proportional, or in-phase path; the circular path (3) is the neutral loading, or the extreme out-of-phase path. Here the Mróz model with von Mises yield criterion is used for its relative simplicity to help explain flow stress variation along loading paths between $\underline{S}_1$ and $\underline{S}_2$. The mutually tangent circles denote positions of yield surfaces at deviatoric stress state $\underline{S}_1$. The flow stress along any loading path from $\underline{S}_1$ to $\underline{S}_2$ is determined by the size of the yield surface encountered by the path. For example, at the same amplitude Δs-distance from $\underline{S}_1$, as indicated by the dotted line in Fig. 4, paths (1), (2), and (3) encounter yield surface $F_{(1)}$, $F_{(2)}$, and $F_{(3)}$, respectively; and therefore have flow stress $\bar{\sigma}_{(1)}$, $\bar{\sigma}_{(2)}$, $\bar{\sigma}_{(3)}$, respectively. If we assume Δs, the stress range in the proportional direction $\underline{S}_1 \rightarrow \underline{S}_2$, to be the damage parameter, it can be seen that at any given parameter level the flow stress value for the neutral loading path (3), which in fact stays constant along the entire loading path, is always higher than that for path (2), which is in turn higher than that for in-phase path (1). That is, $\bar{\sigma}_{(3)} > \bar{\sigma}_{(2)} > \bar{\sigma}_{(1)}$. Since the incremental damage rate is higher for higher flow

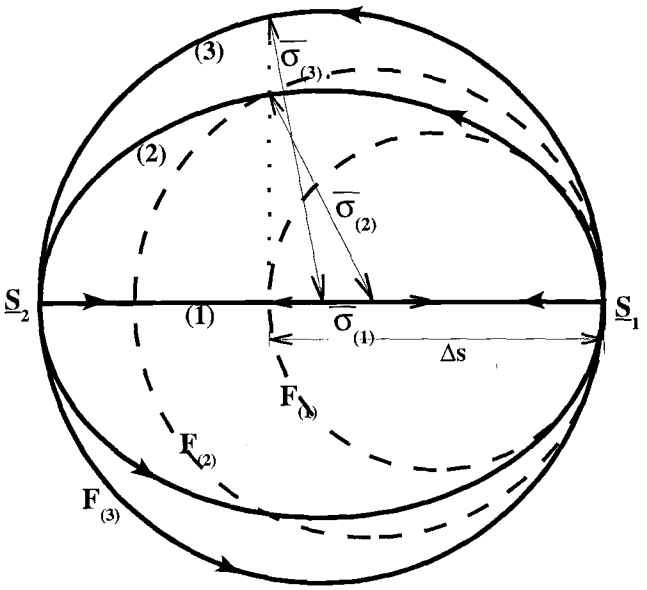


FIG. 4—*Effect of phase on the flow stress at the same damage parameter level.*

stress level, this means that $h[\bar{\sigma}_{(3)}] > h[\bar{\sigma}_{(2)}] > h[\bar{\sigma}_{(1)}]$ and hence more damage can be expected from out-of-phase paths.

Mean Stress Effect

Here an example is given to show how the Goodman type of mean stress correction may be achieved using the incremental damage method. It is assumed that the incremental damage accumulation rate increases/decreases with the current tensile/compressive stress state σ by a multiplying factor of $(1 - (\sigma/\sigma_u))^{1/b}$, where σ_u denotes the material's ultimate strength. When this is used to analyse uniaxial constant amplitude problems with different mean stress values, the effect of mean stress on damage, plotted in the factor $D_{w.\text{mean}}/D_{w/o.\text{mean}}$, is shown in Fig. 5. As will be shown in the Appendix, an asymptotic closed-form solution identical to that of Goodman's correction formula (of which the result is shown as the dotted line in Fig. 5) can be obtained when the stress value throughout the loading path is significantly smaller than σ_u.

Discussion and Conclusion

As mentioned before, it has been a common practice in the analysis of multiaxial problems to apply the uniaxial rainflow counting method to one stress or strain component on the potential crack plane for identifying fatigue damage events. One major difficulty with this simple approach lies in the fact that the change of direction on a stress or strain component is very likely to be different from the loading/unloading condition of the material.

The more recent technique by Wang and Brown through the usage of the equivalent strain measure failed to establish a relationship between "fatigue damage event" and the material's stress-strain behavior. Additionally, the Wang and Brown method, like the traditional rainflow method, requires an examination of the complete history to determine fatigue events. This is equivalent to saying that knowledge of future loading to assess fatigue damage induced by a current event is required. The adoption of the incremental method on the other hand allows fatigue damage to be accumulated as loading proceeds.

The present multiaxial rainflow method identifies fatigue events using the flow stress variation and its corresponding loading/unloading conditions. It emphasizes the incremental damage accumulation concept behind the common rainflow counting method. Depending on the adopted incremental damage accumulation rate, the current method is shown to be readily expandable to take into account stress/strain based fatigue damage mechanisms such as mean stress effect. If the total damage of a fatigue event can be written completely in terms of a damage parameter, then the integration for total fatigue damage can be carried out by accumulating the damage parameter during a fatigue event, followed by looking up the total damage from the damage versus parameter table or formula. The integration of a damage parameter thus reduces to the rainflow counting method used in the most common uniaxial approach.

It should be pointed out that incremental fatigue damage methods have been proposed before. Wetzel in Refs *5* and *6* for example predicted fatigue life by associating various amounts of damage with discretized elements of a uniaxial stress-strain model. Ott et al. [*7*] embedded in their plastic work based fatigue method the incremental damage concept by noting that plastic work done by different segments of the stress-strain curve causes different amount of damage.

In this paper the incremental damage concept is identified to have been the backbone of the common uniaxial rainflow counting method, and is then further generalized to three

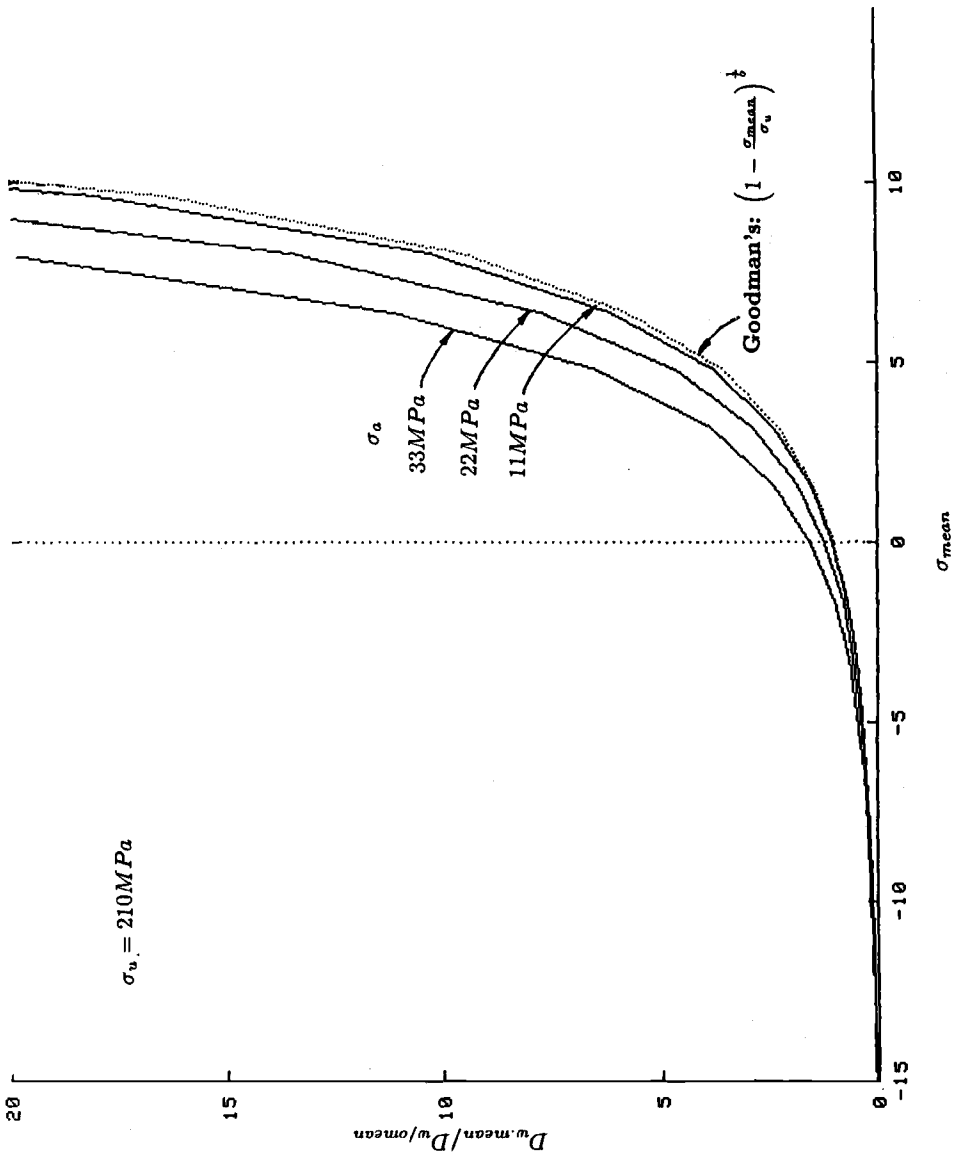


FIG. 5—*Effect of mean stress value on damage, as predicted by an assumed incremental damage rate and by the Goodman correction method.*

dimensional problems without being tied to a particular material model or a particular damage criterion. The main features of the current concept include: (1) The method degenerates to the common uniaxial fatigue method when applied to problems with proportional loadings. (2) The fatigue events, during which damage accumulates in a continuously increasing rate, are identified from the variation of flow stress defined by the adopted plasticity model. Since the flow stress variation for a given history is uniquely determined, so are the fatigue events. (3) The incremental damage accumulation method, being closely related to the material's stress-strain behavior, is most efficiently implemented during, rather than after, the stress analysis. (4) Two examples have been given in this paper to show the new method's promising capability in predicting out-of-phase loading effects and mean stress effects on fatigue damage. (5) By assuming an incremental damage accumulation rate to be dependent on instantaneous values of stress or strain, the method is also shown to be general enough to take into account experimentally observed fatigue damage mechanisms.

Appendix

For constant amplitude test with stress amplitude σ_a, the damage caused by each half cycle can be calculated by inserting the incremental damage accumulation rate in Eq 4 into Eq 3,

$$D = \int_0^{\sigma_a} -\frac{1}{b}(\sigma'_f)^{1/b}(\bar{\sigma})^{-1-(1/b)}d\bar{\sigma}$$

$$= \left(\frac{\sigma_a}{\sigma'_f}\right)^{-(1/b)}.$$

This is simply the original Basquin's equation from which h is derived.

If the incremental damage accumulation rate is assumed to be also influenced by the current stress state,

$$h = -\frac{1}{b}(\sigma'_f)^{1/b}(\bar{\sigma})^{-1-(1/b)}\left(1 - \frac{\sigma}{\sigma_u}\right)^{1/b}$$

the damage per cycle can be calculated as follows. First the current stress σ can be expressed by $(\sigma_{\min} + 2\bar{\sigma})$ and $(\sigma_{\max} - 2\bar{\sigma})$ for the loading and unloading branch, respectively. It is worth noting here that unlike the traditional damage parameter approach, the two halves of a full cycle, as modeled here, accumulate different amounts of damage.

$$D = \int_0^{\alpha_a} -\frac{1}{b}(\sigma'_f)^{1/b}(\bar{\sigma})^{-1-(1/b)}\left(1 - \frac{\sigma_{\min} + 2\bar{\sigma}}{\sigma_u}\right)^{1/b}d\bar{\sigma}$$

$$+ \int_0^{\alpha_a} -\frac{1}{b}(\sigma'_f)^{1/b}(\bar{\sigma})^{-1-(1/b)}\left(1 - \frac{\sigma_{\max} - 2\bar{\sigma}}{\sigma_u}\right)^{1/b}d\bar{\sigma}$$

$$\approx \int_0^{\sigma_a} -\frac{1}{b}(\sigma'_f)^{1/b}(\bar{\sigma})^{-1-(1/b)}\left(1-\frac{\sigma_{\min}}{b\sigma_u}-\frac{2\bar{\sigma}}{b\sigma_u}\right)d\bar{\sigma}$$

$$+\int_0^{\sigma_a} -\frac{1}{b}(\sigma'_f)^{1/b}(\bar{\sigma})^{-1-(1/b)}\left(1-\frac{\sigma_{\max}}{b\sigma_u}+\frac{2\bar{\sigma}}{b\sigma_u}\right)d\bar{\sigma}$$

$$=\left(\frac{\sigma_a}{\sigma'_f}\right)^{-1/b}\left(1-\frac{\sigma_{\min}}{b\sigma_u}-\frac{2\sigma_a}{b(1-b)\sigma_u}\right)$$

$$+\left(\frac{\sigma_a}{\sigma'_f}\right)^{-1/b}\left(1-\frac{\sigma_{\max}}{b\sigma_u}+\frac{2\sigma_a}{b(1-b)\sigma_u}\right)$$

$$=2\left(\frac{\sigma_a}{\sigma'_f}\right)^{-1/b}\left(1-\frac{\sigma_{\text{mean}}}{b\sigma_u}\right)$$

$$\approx 2\left(\frac{\sigma_a}{\sigma'_f}\right)^{-1/b}\left(1-\frac{\sigma_{\text{mean}}}{\sigma_u}\right)^{1/b}$$

$$=2\left(\frac{\sigma_a}{\sigma'_f\left(1-\frac{\sigma_{\text{mean}}}{\sigma_u}\right)}\right)^{-1/b}$$

Note here that the approximation above is carried out assuming that the stress value throughout loading is relatively small compared to σ_u, and σ_{mean} is defined as $\frac{1}{2}(\sigma_{\max} + \sigma_{\min})$. The last line of the equations is indeed the damage caused by the stress amplitude corrected with Goodman's formula.

References

[1] Matsuishi, M. and Endo, T., "Fatigue of Metals Subjected to Varying Stress," Paper presented at Japanese Society of Mechanical Engineers, Fukuoka, Japan, March 1968.

[2] Wang, C. H. and Brown, M. W., "Life Prediction Techniques for Variable Amplitude Multiaxial Fatigue—Part 1: Theories," *Journal of Engineering Materials and Technology, ASME Transactions,* Vol. 118, 1996, pp. 367–370.

[3] Chu, C.-C., "The Analysis of Multiaxial Cyclic Problems with An Anisotropic Hardening Model," *International Journal of Solids and Structures,* Vol. 23, No. 5, 1987, pp. 569–579.

[4] Chu, C.-C., "A 3-D Rainflow Method: Using Plasticity Model to Define Damage Events," *Proceedings of Plasticity '99,* 1999, pp. 885–888.

[5] Wetzel, R. M., "A Method of Fatigue Damage Analysis," Ph.D. thesis, Department of Civil Engineering, University of Waterloo, Ontario, Canada, 1971.

[6] Landgraf, R. W., Richards, F. D., and LaPointe, N. R., "Fatigue Life Predictions for a Notched Member under Complex Load Histories," *SAE Paper No.* 750040, 1975.

[7] Ott, W., Baumgart, O., Trautmann, K.-H., and Nowack, H., "A New Crack Initiation Life Prediction Method for Arbitrary Multiaxial Loading Considering Mean Stress Effect," *Proceedings of the Sixth International Fatigue Congress,* 1996, pp. 1007–1112.

K. S. Kim,[1] *B. L. Lee,*[2] *and J. C. Park*[3]

Biaxial Fatigue of Stainless Steel 304 under Irregular Loading

REFERENCE: Kim, K. S., Lee, B. L., and Park, J. C., **"Biaxial Fatigue of Stainless Steel 304 under Irregular Loading,"** *Fatigue and Fracture Mechanics: 31st Volume, ASTM STP 1389,* G. R. Halford and J. P. Gallagher, Eds., American Society for Testing and Materials, West Conshohocken, PA, 2000, pp. 79–93.

ABSTRACT: Fatigue tests are performed on tubular specimens of stainless steel 304 under variable amplitude, irregular axial-torsional loading. Three parameters are chosen for correlating fatigue life: the Smith-Watson-Topper (SWT) parameter for normal fracture, Fatemi-Socie (FS), and Kandil-Brown-Miller parameters (KBM) for shear fracture. A life computation procedure is employed in which rainflow cycle counting on normal (SWT) or shear (FS, KBM) strain history and the Miner-Palmgren rule are used. It is found that, while the life calculation procedure appears to be viable and each parameter yields acceptable results for most loading conditions, there are cases for which correlation is poor. The SWT parameter performed well except for torsion-dominated cycles, where it overpredicted lives. The FS and KBM parameters did better than the SWT parameter in torsion, but showed poor performance in some other loading conditions.

KEYWORDS: biaxial fatigue, variable amplitude loading, rainflow cycle counting, stainless steel 304, Miner-Palmgren rule

The uniaxial fatigue under complex loading history is well studied, and a number of cycle-counting algorithms are available [*1*]. Fatigue analysis under multiaxial, variable amplitude, irregular loading has been receiving significant attention only lately, although there has been much earlier work under constant amplitude, out-of-phase tension-torsion loading and some other simple non-proportional loading conditions. Bannantine and Socie (BS) [*2*] proposed to use either the Smith-Watson-Topper (SWT) [*3*] parameter or the Fatemi-Socie (FS) [*4*] parameter in accordance with the failure mechanism and to use the maximum damage plane as the critical plane. Wang and Brown (WB) [*5*] applied the Kandil-Brown-Miller (KBM) [*6*] parameter to variable amplitude tension-torsion loading with the maximum shear strain range plane as the critical plane. They reported satisfactory correlation for a number of materials. In the above two papers (BS, WB), rainflow cycle counting was implemented either on the shear strain history (BS, WB) or on the normal strain history (BS) depending on the failure mode. Wang and Brown [*7,8*] proposed a cycle counting method for multiaxial applications and verified the method with experiments. Kim et al. [*9*] used a similar approach as in Ref *5* to predict fatigue life under variable amplitude tension-torsion loading for a material that exhibits shear fracture and concluded that either the maximum shear strain

[1] Professor, Department of Mechanical Engineering, Bohang University of Science and Engineering, Pohang, Korea.
[2] Engineer, Dastek Co., Seocho-dong, Seocho-ku, Seoul, Korea 137-070.
[3] Research engineer, Research Dept. II, Hyundai Space and Aircraft Co., Ltd., Seosan, Chungnam, Korea 356-850.

Copyright© 2000 by ASTM International www.astm.org

TABLE 1—*Chemical composition of the test material.*

Element	C	Si	Mn	P	S	Ni	Cr	Mo	Cu	N
wt%	0.038	0.497	1.16	0.031	0.014	7.99	18.05	0.171	0.313	0.013

plane or the maximum damage plane can be employed as the critical plane. Kim et al. [*10*] extended the work with the FS parameter and obtained similar results.

This paper is aimed at studying the fatigue behavior of stainless steel 304 under variable amplitude, proportional, and nonproportional tension-torsion loading by employing similar concepts as found in other papers [*2,5–8,9–10*]. Three parameters (SWT, FS, and KBM) will be examined for their ability to correlate fatigue lives.

Fatigue Parameters

The fatigue parameters and their relations to life to be used in this paper are given as follows:

1. *SWT parameter*

$$\text{SWT} = \frac{\Delta\varepsilon_n}{2}\sigma_n^{\max} = \frac{\sigma_f'^2}{E}(2N_f)^{2b} + \sigma_f'\varepsilon_f'(2N_f)^{b+c} \tag{1}$$

2. *FS parameter*

$$\text{FS} = \Delta\gamma/2(1 + k\sigma_n^{\max}/\sigma_y) = \frac{\tau_f'}{G}(2N_f)^b + \gamma_f'(2N_f)^c \tag{2}$$

3. *KBM parameter*

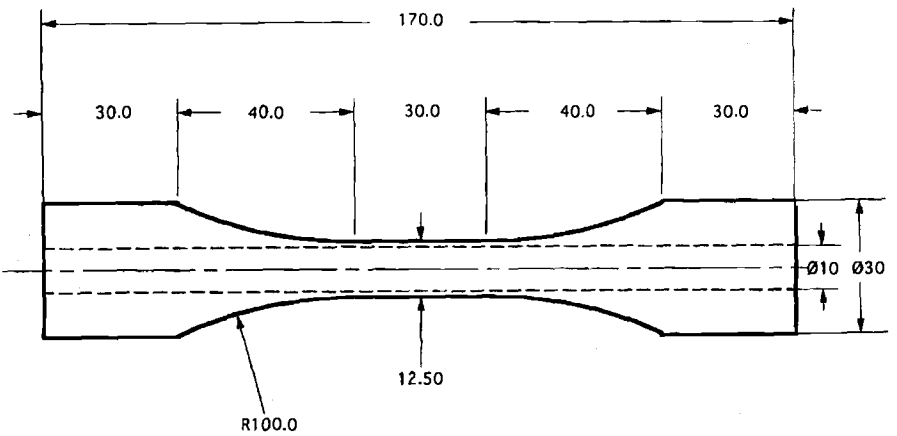


FIG. 1—*Geometry of the biaxial fatigue specimen.*

TABLE 2—*Constant amplitude axial and torsional fatigue tests.*

Test Group	Specimen No.	$\Delta\varepsilon/2$, $\Delta\gamma/2$	$\Delta\varepsilon_e/2$, $\Delta\gamma_e/2$	$\Delta\varepsilon_p/2$, $\Delta\gamma_p/2$	$\Delta\sigma/2$, $\Delta\tau/2$, MPa	σ_o, τ_o, MPa	N_f, cycle
Axial	AF01	0.008	0.002725	0.005275	450.25	−6.85	534
	AF02	0.006	0.00255	0.00345	423.05	−10.25	2 176
	AF03	0.01025	0.002325	0.0077	437.6	−5.9	462
	AF04	0.015	0.0028	0.0122	442.75	−5.05	187
	AF05	0.00295	0.00189	0.00106	326.95	−20.65	81 525
	AF06	0.00343	0.00207	0.00136	352.75	−23.75	38 374
	AF07	0.00217	0.00174	0.00043	311.5	−43	>1400 736
Torsional	TF01	0.0102	0.0057	0.0045	366.5	1.5	6 235
	TF02	0.00755	0.00415	0.0034	251.9	3.2	17 809
	TF02R	0.00789	0.00421	0.00368	252.2	4.67	20 386
	TF03	0.0154	0.0057	0.0097	331.55	1.35	1 273
	TF05	0.0174	0.0056	0.0118	312.4	0.3	1 278
	TF06	0.00635	0.00305	0.0033	200.55	0.15	139 821
	TF07	0.00499	0.00402	0.00097	253.27	0.21	366 294
	TF07R	0.00507	0.00312	0.00195	196.61	9.37	225 500

$$\text{KBM} = \Delta\gamma/2 + s\varepsilon_n^* = [1 + \nu + (1 - \nu)s]\frac{\sigma_f' - 2\sigma_n^o}{E}(2N_f)^b + (1.5 + 0.5s)\varepsilon_f'(2N_f)^c \quad (3)$$

In the above equations, $\Delta\varepsilon_n$ is the normal strain range, $\sigma_n^{\max}$ is the maximum normal stress, $\Delta\gamma$ is the shear strain range, ε_n^* is the normal strain excursion [5], σ_n^o is the mean normal stress, N_f is the number of cycles to failure, σ_y is the yield stress, E is the elastic modulus, ν is the Poisson's ratio, G is the shear modulus, and σ_f', ε_f', τ_f', γ_f', b, c, k, and s are fatigue properties of the material that are determined from axial and torsional fatigue tests. The stress and strain quantities in these equations are determined on the critical plane. The critical plane is assumed to be the plane where the maximum value of $\Delta\varepsilon_n$ is attained for the SWT parameter and where the maximum value of $\Delta\gamma$ is attained for the FS and KBM parameters. It is noted that Eq 1 and Eq 3 can be derived from the equivalence of uniaxial fatigue life to that obtained from the Coffin-Manson equation. The fatigue properties σ_f', ε_f', b, and c are, in principle, identical to those of the Coffin-Mansion equation, although their determination in this study is based on both axial and torsional fatigue data. It is also noted that the KBM and FS parameters are the same for pure torsion since $\sigma_n^{\max}$ and ε_n^* vanish. If one enforces the same fatigue lives from these two parameters, the result is that the exponents b and c are the same between Eq 2 and Eq 3, and that τ_f' and γ_f' can be expressed in terms of σ_f', ε_f', ν, and s [*10*].

Material and Specimen

The material used in this investigation is a stainless steel 304 produced by a local company. The material was purchased in the form of round bar with a diameter of 32 mm. The chemical composition of this material is given in Table 1. The material had the following tensile properties: elastic modulus = 171 GPa, yield strength = 405 MPa, ultimate tensile strength = 754 MPa, shear modulus = 66 GPa, and Poisson's ratio = 0.3.

The specimen had a tubular geometry with an outer diameter of 12.5 mm and an inner diameter of 10 mm at the gage section (Fig. 1). The bar was cut to the specimen length

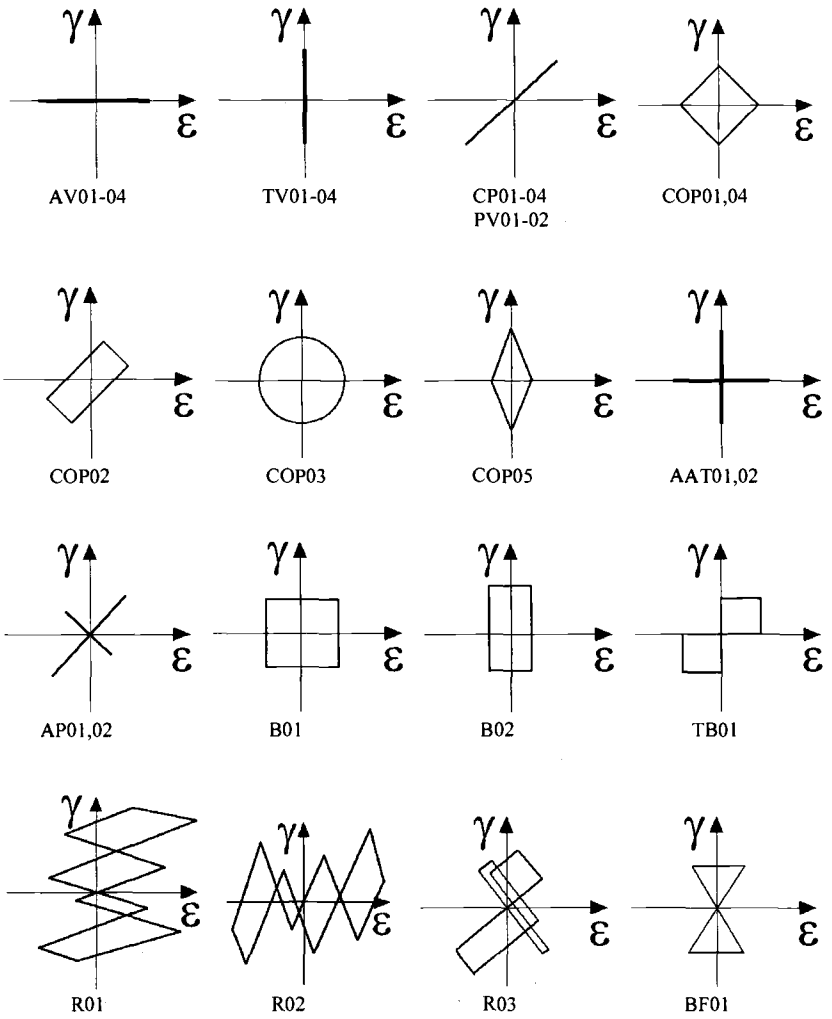


FIG. 2—*Schematics of strain paths in the* (ε,γ) *plane used for variable amplitude/irregular loading fatigue tests.*

first. Then the inner hole was gun-drilled and honed through the center of the bar. The external surface was machined. Finally, the gage section was ground and polished with alumina powder.

Experiment

Tests performed in this study include monotonic tensile and torsion tests, axial fatigue tests, torsional fatigue tests, and variable amplitude/irregular loading axial-torsional fatigue tests. All tests except monotonic tension tests were performed with the same type of specimen described above. Fatigue tests were conducted using an MTS tension-torsion machine under strain control through a biaxial extensometer mounted on the outside of the specimen gage

TABLE 3—*Variable amplitude/irregular path fatigue tests.*

Specimen No.		Strain Peaks in sequence, (ε, γ)(%)											
AV	01	-0.8	0.8	-0.6	0.6	-0.8							
	03	-0.48	0.48	-0.36	0.36	-0.48							
	04	-0.4	0.3	-0.2	0.4	-0.3	0.2	-0.4					
	05	-1.2	1	-1	1.2	-0.6	0.6	-1.2					
TV	01	-1	1	-0.8	0.8	-1							
	02	-1.5	1.2	-0.65	1.5	-1.2	0.65	-1.5					
	03	-0.76	0.76	-0.6	0.6	-0.76							
	04	-0.9	0.3	-0.65	0.9	-0.3	0.65	-0.9					
CP	01	(0, 0)		(0.9, 0.818)		(-0.9, -0.818)		(0, 0)					
	02	(0, 0)		(0.7, 0.64)		(-0.7, -0.64)		(0, 0)					
	03	(0, 0)		(0.42, 0.76)		(-0.42, -0.76)		(0, 0)					
	04	(0, 0)		(0.6, 0.273)		(-0.6, -0.273)		(0, 0)					
PV	01	(-0.8, -0.727) (0.4, 0.364)		(0.6, 0.545) (-0.8, -0.727)		(-0.6, -0.545)		(0.8, 0.727)		(-0.4, -0.364)			
	02	(-0.384, -0.873) (0.384, 0.873)		(0.288, 0.655) (-0.384, -0.873)		(-0.192, -0.436)		(0.192, 0.436)		(-0.288, -0.655)			
COP	01	(0,-0.458)		(0.504,0)		(0,0.458)		(-0.504,0)		(0,-0.458)			
	02	(-0.35,-0.64)		(0.7,0.32)		(0.35,0.64)		(-0.7,-0.32)		(-0.35,-0.64)			
	03	(0,-0.458)		(0.504,0)		(0,0.458) Sinusoidal wave form		(-0.504,0)		(0,-0.458)			
	04	(0,-0.64)		(0.7,0)		(0,0.64)		(-0.7,0)		(0,-0.64)			
	05	(0,-0.66)		(0.36,0)		(0,0.66)		(-0.36,0)		(0,-0.66)			
AAT	01	(0,0) (0,-0.545)		(0.6,0) (0,0)		(-0.6,0)		(0,0)		(0,0.545)			
	02	(0,0) (0,0)		(0.36,0) (0,0.6545)		(-0.24,0) (0,-0.4363)		(0,0.4363)		(0.24,0) (0,-0.6545)		(-0.36,0) (0,0)	
AP	01	(0,0) (-0.8,0.7272)		(0.8,0.7272) (0,0)		(-0.8,-0.7272)		(0,0)		(0.8,-0.7272)			
	02	(0,0) (-0.432,0.393)		(0.6,0.545) (0,0)		(-0.6,-0.545)		(0,0)		(0.432,-0.393)			
B	01	(-0.504,-0.4581)		(0.504,-0.4581)		(0.504,0.4581)		(-0.504,0.4581)		(-0.504,-0.4581)			
	02	(-0.202,-0.458)		(0.202,-0.458)		(0.202,0.458)		(-0.202,0.458)		(-0.202,-0.458)			
TB	01	(0.6,0) (-0.6,0)		(0.6,0.545) (0.6,0)		(0,0.545)		(0,-0.545)		(-0.6,-0.545)			
R	01	(0,0) (0.3,-0.16)		(0.4,0.15) (-0.6,-0.5)		(-0.36,0.42) (-0.28,-0.61)		(0.16,0.61) (0.5,-0.33)		(0.6,0.45) (-0.2,-0.08)		(-0.4,0.09) (0.0)	
	02	(0,0) (-0.13,0.31)		(0.12,0.43) (-0.38,-0.61)		(0.34,-0.37) (-0.48,-0.27)		(0.48,0.15) (-0.27,0.51)		(0.35,0.61) (-0.06,-0.23)		(0.07,-0.43) (0.0)	
	03	(0,0) (-0.3,0.365)		(0.3,0.365) (-0.24,0.44)		(0.06,0.655) (0.2,-0.397)		(-0.2,0.342) (-0.26,-0.66)		(0.4,-0.402) (-0.4,-0.167)		(0.36,-0.44) (0,0)	
BF	01	(0,0)		(0.5,0.46)		(-0.5,0.46)		(0.5,-0.46)		(-0.5,-0.46)		(0,0)	

section. Input strains and output stresses were recorded in the personal computer using an automated data acquisition system. The wave shape used for fatigue tests was triangular except for one case where a sinusoidal wave was used. All tests were conducted at room temperature. The frequency for constant amplitude tests varied between 0.5 and 2 Hz, with lower frequency being applied to high amplitude tests. Similar loading rates were used in variable amplitude tests. The deformation-induced temperature rise was significant in high amplitude tests. However, it was verified by air-cooling the specimen that fatigue life was

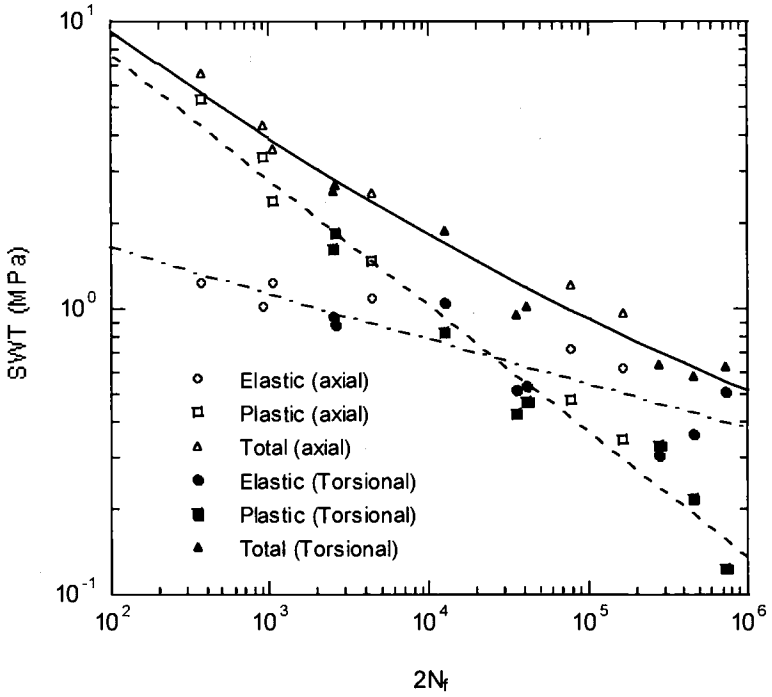


FIG. 3—*The SWT parameter versus fatigue life curve.*

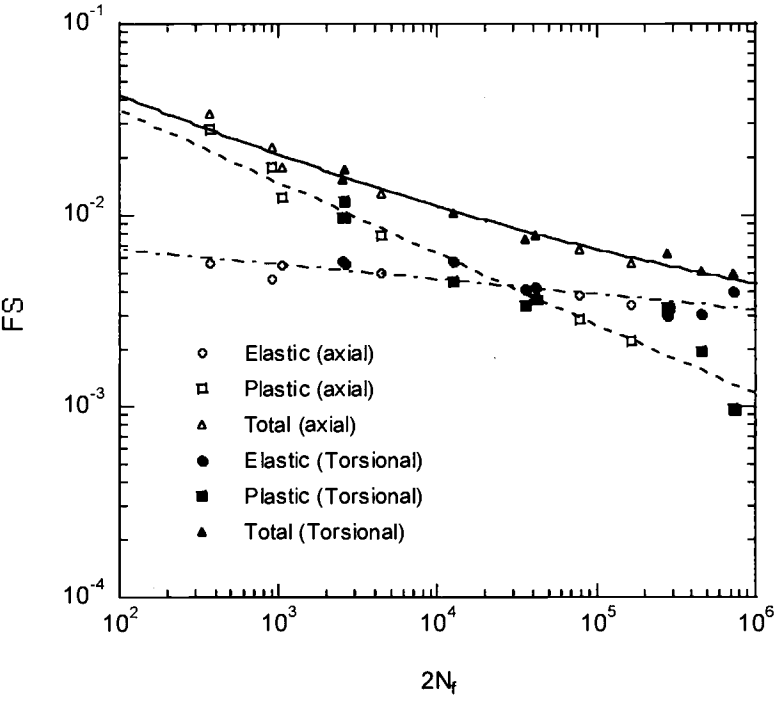


FIG. 4—*The FS parameter versus fatigue life curve.*

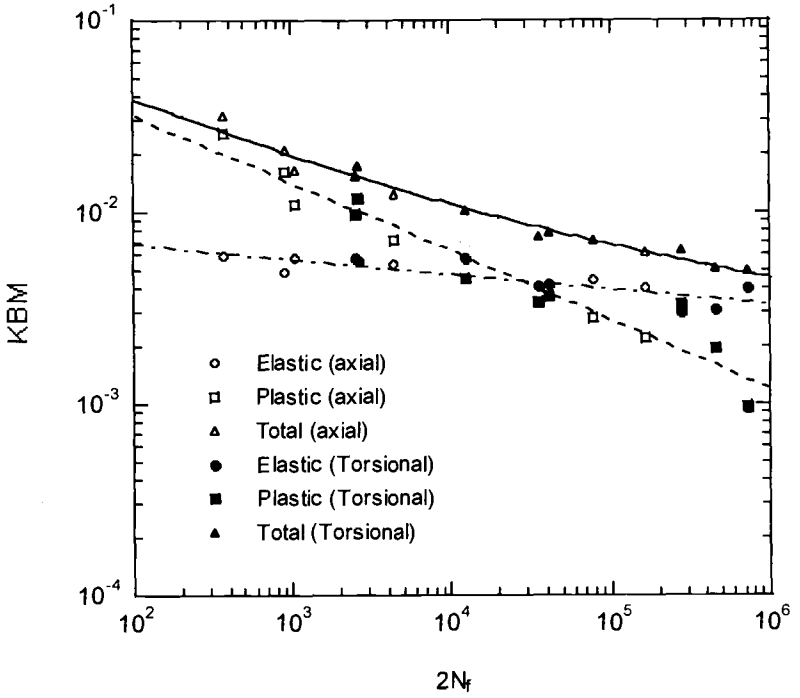


FIG. 5—*The KBM parameter versus fatigue life curve.*

not affected significantly by this temperature rise. Failure was defined as a drop of 10% in axial load for axial tests and axial-torsional tests and a drop of 10% in torque for torsion-only tests.

The constant strain amplitudes used in axial tests and torsion tests are shown in Table 2. Strain paths in the ε-γ plane used in irregular loading tests are illustrated schematically in Fig. 2, and the details of strain history are given in Table 3. These tests consist of four variable amplitude axial tests (AV), four variable amplitude torsion tests (TV), four constant amplitude proportional path tests (CP), two variable amplitude proportional path tests (PV), five constant amplitude out-of-phase tests (COP), two alternating tension-torsion tests (AAT), two alternating proportional path tests (AP), two box path tests (B), a two-box path test (TB), three pseudo-random loading tests (R), and a butterfly path test (BF). The first four groups (AV, TV, CP, PV) belong to proportional loading tests, and the rest to non-proportional loading tests.

TABLE 4—*Fatigue properties of the test material.*

SWT	KBM	FS
σ'_f = 760 MPa	σ'_f = 795 MPa	τ'_f = 627 MPa
ε'_f = 0.0763	ε'_f = 0.0778	γ'_f = 0.193
b = −0.079	b = −0.0777	b = −0.078
c = −0.36	c = −0.354	c = −0.369
	s = 1.162	k = 1.022

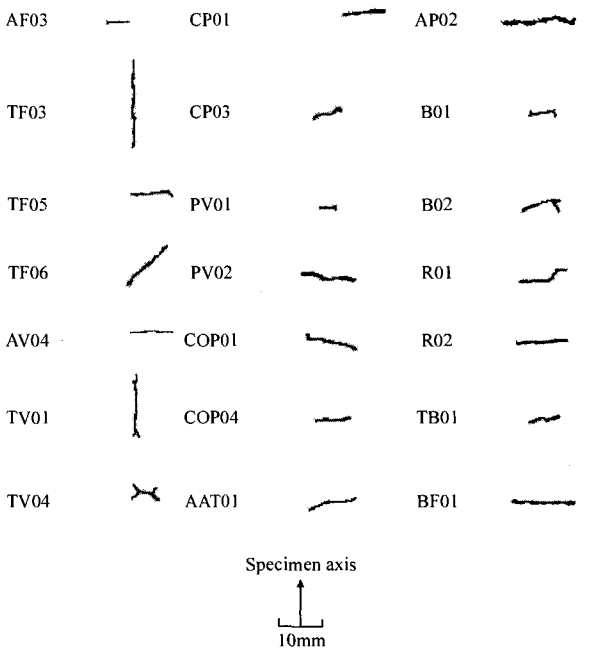


FIG. 6—*Orientation of failure cracks.*

Fatigue Analysis

The fatigue properties appearing in Eqs 1, 2, and 3 were obtained by splitting shear and normal strains into elastic and plastic parts and relating the individual parts to the terms on the right side of these equations. To determine k of Eq 2 and s of Eq 3, fatigue curves were first generated from torsion test data. Then, these constants were determined for each axial test such that the data point falls on the torsion fatigue curve. The average was then taken for all axial tests. The fatigue curves after regression over all axial and torsional data points are given in Figs. 3 to 5. The fatigue properties associated with these curves are listed in Table 4. Notice that the fatigue properties σ'_f, ε'_f, b, and c do not agree precisely among parameters. Ideally they are supposed to represent the same properties found in the Coffin-Manson equation. If uniformity of these properties is enforced among the parameters, by averaging, for instance, slight reduction in the accuracy of predicted lives may occur since they no longer represent best fit for individual fatigue curves.

The analysis of irregular loading fatigue proceeded as follows. First, the axial and torsional hysteresis loops at approximately half-life were determined. Using these data, the shear and normal stress-strain history for a given block of loading is constructed at any plane whose normal vector has an angle θ, positive counter-clockwise, with the specimen axis. In computation of strains the effective Poisson's ratio, which accounts for both elastic and plastic deformation, was set equal to 0.4 for approximation [5]. It is noted that the effect of stress gradient through the thickness of the specimen was assumed to be small and ignored in analysis. Once stress and strain profiles are generated, rainflow cycle counting is performed on the normal strain history for the SWT parameter and on the shear strain history for the FS and KBM parameters. Closed cycles are determined, and fatigue damage is computed for each loop using the fatigue curve. The Miner-Palmgren rule is employed to compute the

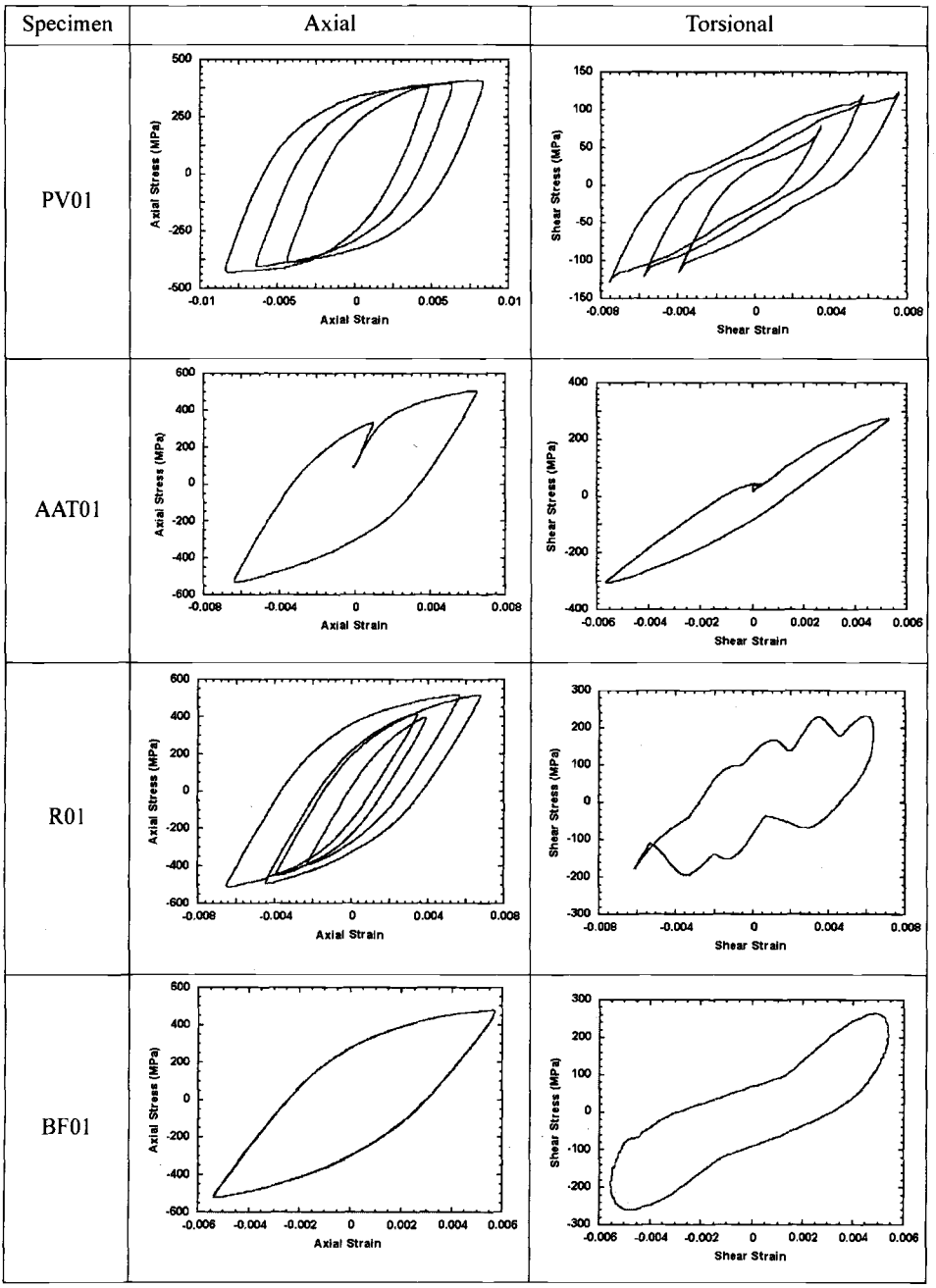


FIG. 7—*Applied axial and torsional hysteresis loops at half-life.*

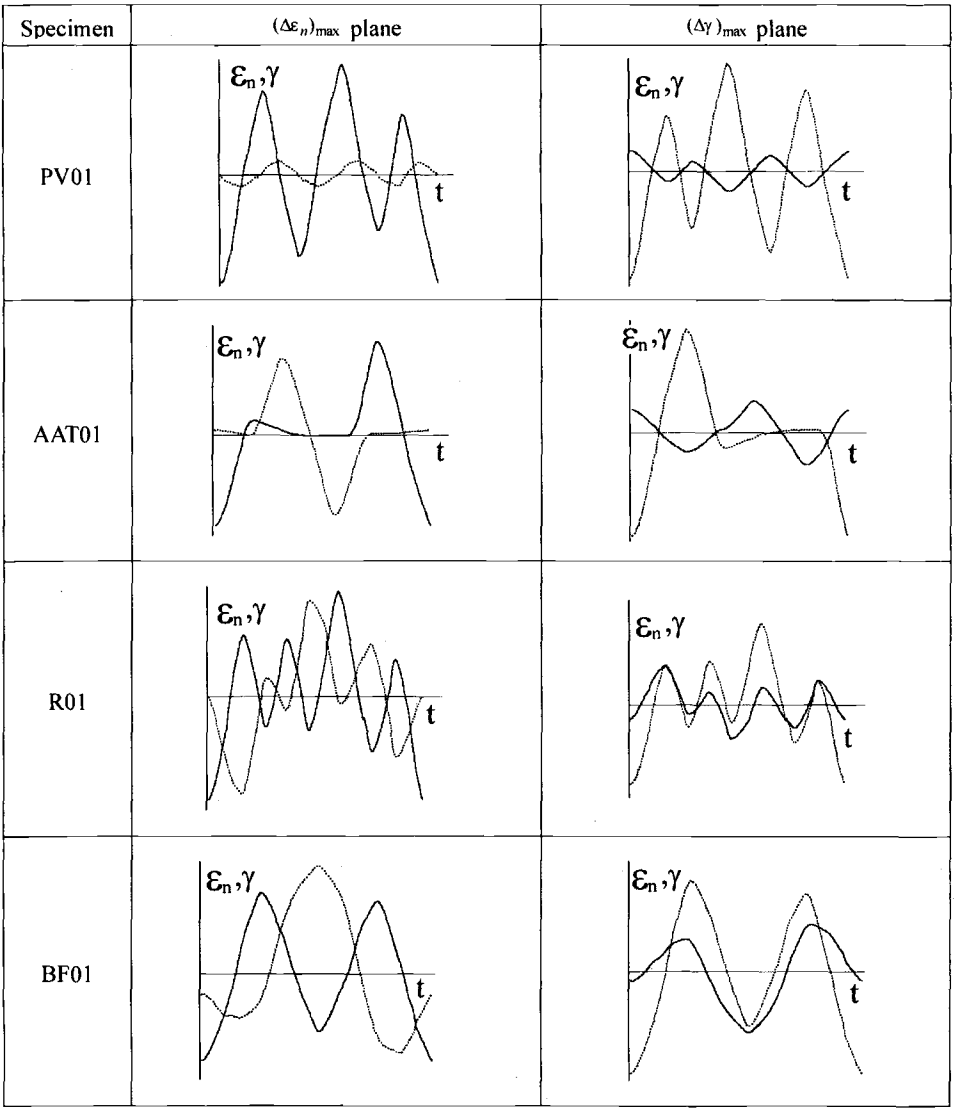


FIG. 8—*Strain profiles on the critical plane* (—ε_n, ·····γ).

total damage in the loading block. The number of blocks to failure is then calculated for this particular plane. In order to keep track of the critical plane, the largest strain range in the pertinent strain history is saved in conjunction with the computed life. The procedure is repeated for $-90° \leq \theta \leq 90°$ with an interval of 1°. The plane where the maximum strain range is encountered among all planes examined is the critical plane, and the life on this plane is the life of the specimen. This process was automated in a computer program.

In the above analysis it was assumed that fatigue failure occurs on the plane where the largest strain range, either shear or normal depending on the parameter, is found. This assumption, while consistent with experimental observations of the fracture behavior [*11–16*],

TABLE 5—*Predicted and experimental fatigue lives.*

Test Group	Specimen No.	Predicted life (Npre)			Experimental Life (Nexp)
		SWT	KBM	FS	
AV	01	564	678	700	338
	03	3686	6484	6402	4934
	04	9936	16330	18084	5192
	05	105	128	124	110
TV	01	7704	4575	4594	3215
	02	2119	937	1015	896
	03	42103	16794	15744	25367
	04	28516	10164	9985	8151
CP	01	302	336	242	446
	02	732	860	685	867
	03	2466	2546	2197	2622
	04	1544	2083	1803	2243
PV	01	277	369	270	372
	02	1133	1283	962	2231
COP	01	1463	1900	1861	2545
	02	497	695	465	763
	03	1118	1142	1124	1186
	04	529	578	502	544
	05	4811	1249	1542	2478
AAT	01	852	1213	1063	1546
	02	8611	1997	2503	3692
AP	01	199	65	138	142
	02	578	344	369	515
B	01	817	533	718	1116
	02	15006	3888	4894	10163
R	01	533	353	397	587
	02	1496	669	535	2603
	03	2417	889	1226	1385
TB	01	533	602	435	927
BF	01	926	418	718	1010

possesses a controversy in that the maximum value of damage could be attained on some other plane. Kim et al. [*9,10*] examined this aspect for a material exhibiting shear fracture by comparing fatigue lives computed from the fatigue curves constructed based on the maximum values of shear strain range and fatigue parameter. It was found that both the maximum shear strain range and the maximum damage approaches provided acceptable life estimates. For the SWT parameter used in this study, the fatigue curve is the same between the two approaches since the maximum normal strain range and the maximum value of the parameter are found on the same plane in axial and torsional fatigue. The fatigue lives predicted from the two approaches again did not produce significant differences for all loading conditions shown in Fig. 2. For these reasons, the maximum damage approach was not considered further in this study.

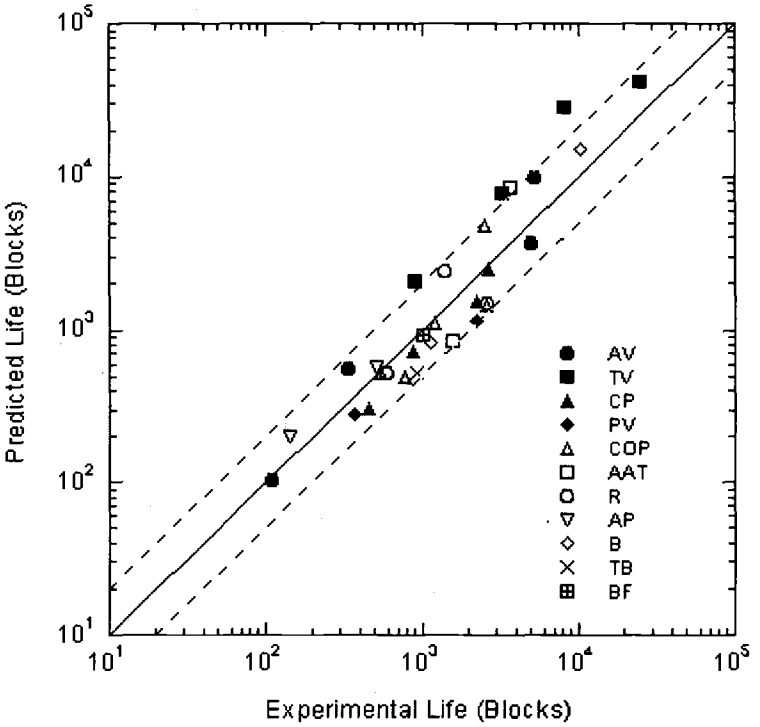


FIG. 9—*Comparison of predicted and experimental lives for the SWT parameter.*

Results and Discussion

The pattern of the failure crack was coincident with other studies [*11,12*] for axial fatigue and torsional fatigue, as found in Fig. 6. It is seen that the crack path is normal to the principal strain direction for axial tests and at relatively long lives in torsion, but is in the direction of the maximum shear strain for low cycle fatigue in torsion. The crack path was jagged, and in the majority of specimens there were little jumps from one plane to another, which are indications of the coalescence of multiply initiated cracks. The orientation of failure cracks did not agree well with the predicted direction of Stage II crack growth in tension-torsion tests, perhaps because the crack path is shifted as the crack interacts with minor cracks.

The stress-strain response showed a mixed cyclic hardening and softening behavior both in axial and torsional tests. Softening occurred at smaller strain amplitudes and hardening occurred at larger strain amplitudes. At small amplitudes in torsion, the material showed slight hardening after initial softening, the overall effect being softening. Additional hardening in 90° out-of-phase loading (COP04) over in-phase loading (CP02) was substantial, but somewhat less than that of a similar material in Socie [*12*]. The hysteresis loops at half-life are given for four axial-torsional specimens in Fig. 7. Figure 8 illustrates the shear and normal strain histories on the critical plane for these specimens at half-life. Minor disturbances from the intended strain paths in Table 3 can be traced in Fig. 7 and Fig. 8, but their effects on life are negligible.

A summary of predicted lives and experimental lives is given in Table 5, and these are compared in Figs. 9 to 11 for the three parameters. The solid lines in these figures represent

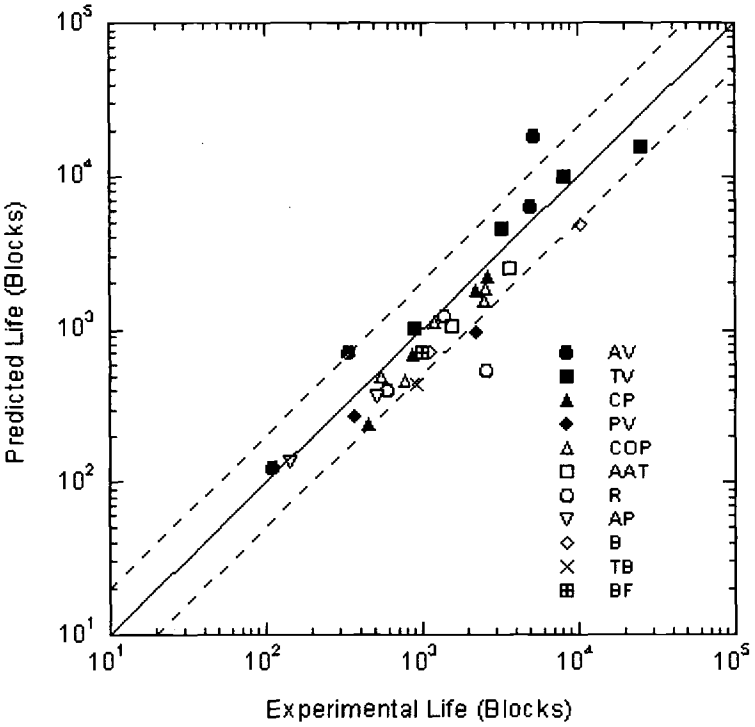


FIG. 10—*Comparison of predicted and experimental lives for the FS parameter.*

perfect correlation and the dotted lines are for the factor-2 band. The prediction will be deemed satisfactory in the following if the point falls within the factor-2 band. The SWT parameter correlated experimental lives satisfactorily except in variable amplitude torsion (TV) and in an alternating axial/torsional loading case (AAT02). For TV specimens, the crack propagated in shear mode except for TV03. Therefore it is not surprising that the performance of this parameter is relatively poor. Notice that the predicted lives are nonconservative in these cases. For an AAT02 specimen, the level of input shear strain is much larger than that of axial strain. The results of analysis again indicate that the nonconservatism of the predicted life is related to the influence of shear strain. The critical plane where the largest normal strain range is found is normal to the axis of the specimen in this case. The maximum shear strain plane is also normal to the axis. Since axial and torsional loading is alternately applied and the shear strain amplitude (0.64%) is substantially larger than the normal strain amplitude (0.34%) on the critical plane, it is expected that the damage due to shear strain cycles may not be overlooked. The SWT parameter, however, does not have the ability to accommodate it, which perhaps resulted in overestimation of life for this specimen. The orientation of failure surface of this specimen was actually normal to the specimen axis.

The performance of shear-strain-based parameters looks similar. They gave satisfactory life estimates for the majority of test conditions and did well with variable amplitude torsion fatigue. They also improved the life of AAT02 into the factor-2 band. This is because both KBM and FS parameters include a measure of treating normal stress/strain effects as well as shear strain effects. There are loading conditions, however, where these parameters performed poorly. A few points are found outside of the factor-2 band in Fig. 10 and Fig. 11.

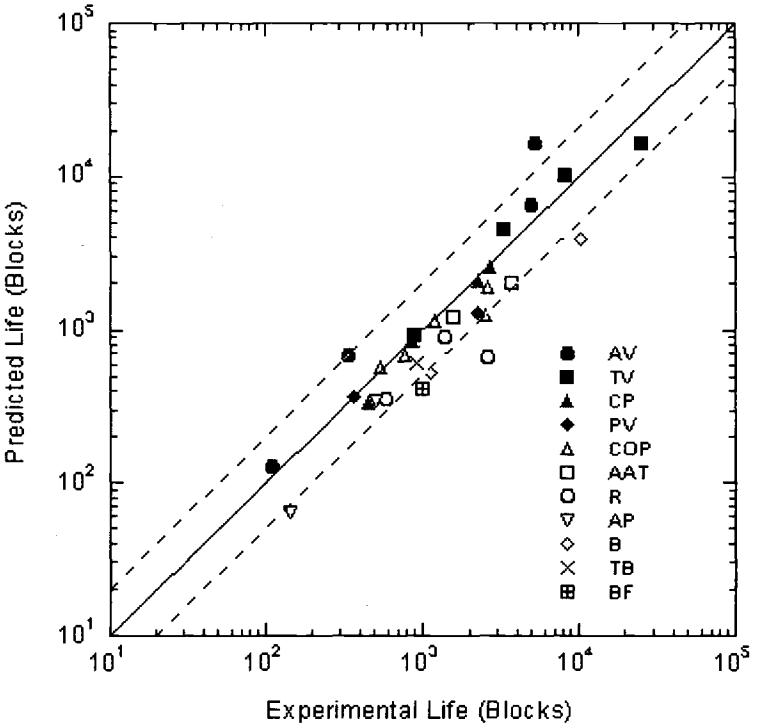


FIG. 11—*Comparison of predicted and experimental lives for the KBM parameter.*

Overall, it can be said that the three parameters yielded satisfactory results for the majority of loading conditions tested; nonetheless, none of them were found satisfactory for all loading conditions. It seems desirable that both shear and normal quantities are considered in the parameter when the mode of failure varies with loading conditions. It is unknown at this time how these quantities should be represented in the parameter for best life prediction. Further investigation is certainly needed in this regard. For the sake of conservatism in practical applications with the current form of parameters, it will be expedient to take the smaller of the two lives computed from the SWT parameter and from either one of the FS/KBM parameters, as remarked earlier by Socie [*12*].

Conclusions

The Smith-Watson-Topper (SWT) parameter for normal fracture and the Fatemi-Socie (FS) and Kandil-Brown-Miller (KBM) parameters for shear fracture were applied to predict fatigue life of stainless steel 304 under variable amplitude, irregular tension-torsion loading. The following conclusions can be drawn from the results:

1. The procedure of multiaxial fatigue life computation used in this paper appears to yield acceptable results. In this procedure the critical plane for the SWT parameter is taken to be the plane where the maximum normal strain range is encountered in the whole spectrum of loading. For the FS and KBM parameters the maximum shear strain range

plane is the critical plane. Rainflow cycle counting on normal or shear strain history, depending on the parameter, together with the Miner-Palmgren rule is used for damage computation under variable amplitude loading.

2. The SWT parameter yields satisfactory life estimates for most loading conditions used in this study. This parameter tends to overpredict fatigue life for torsion-dominated cycles. The FS and KBM parameters gave acceptable life estimates for the majority of loading conditions. Their performance was better in torsion but worse in some other loading conditions compared with the SWT parameter.

Acknowledgment

The authors gratefully acknowledge financial support for this research from Korea Science and Engineering Foundation under Project 971-1004-026-2.

References

[1] Dowling, N. E., "Fatigue Failure Predictions for Complicated Stress-Strain Histories," *Journal of Materials,* Vol. 7, No. 1, 1972, pp. 71–87.

[2] Bannantine, J. A. and Socie, D. F. "A Variable Amplitude Multiaxial Fatigue Life Prediction Method," *ESIS10* (edited K. Kussmaul, D. McDiarmid, and D. Socie), Mechanical Engineering Publications, London, 1991, pp. 35–51.

[3] Smith, R. N., Watson, P., and Topper, T. H., "A Stress Strain Function for the Fatigue of Metal," *Journal of Materials JMLSA,* Vol. 5, No. 4, 1970, pp. 767–778.

[4] Fatemi, A. and Socie, D. F., "A Critical Plane Approach to Multiaxial Fatigue Damage Including Out-of-Phase Loading," *Fatigue and Fracture in Engineering Materials and Structures,* Vol. 11, No. 3, 1988, pp. 149–165.

[5] Wang, C. H. and Brown, M. W., "A Path-Independent Parameter for Fatigue under Proportional and Non-proportional Loading," *Fatigue and Fracture in Engineering Materials and Structures,* Vol. 16, No. 12, 1993, pp. 1285–1298.

[6] Kandil, F. A., Brown, M. W., and Miller, K. J., "Biaxial Low-Cycle Fatigue Fracture of 316 Stainless Steel at Elevated Temperatures," *Book 280,* The Metals Society, London, 1982, pp. 203–210.

[7] Wang, C. H. and Brown, M. W., "Life Prediction Techniques for Variable Amplitude Multiaxial Fatigue—Part 1: Theories," *Journal of Engineering Materials and Technology,* Vol. 18, 1996, pp. 367–370.

[8] Wang, C. H. and Brown, M. W., "Life Prediction Techniques for Variable Amplitude Multiaxial Fatigue—Part 2: Comparison with Experimental Results," *Journal of Engineering Materials and Technology,* Vol. 18, 1996, pp. 371–374.

[9] Kim, K. S., Park, J. C., and Lee, J. W., "Multiaxial Fatigue Under Variable Amplitude Loads," *Journal of Engineering Materials and Technology,* Vol. 121, July 1999, pp. 286–293.

[10] Kim, K. S. and Park, J. C., "Shear Strain Based Multiaxial Fatigue Parameters Applied to Variable Amplitude Loading," *International Journal of Fatigue,* Vol. 21, 1999, pp. 475–483.

[11] Socie, D., "Critical Plane Approaches for Multiaxial Fatigue Damage Assessment," *Advances in Multiaxial Fatigue; ASTM STP 1191,* D. L. McDowell and R. Ellis, Eds., 1993, pp. 7–36.

[12] Socie, D., "Multiaxial Fatigue Damage Models," *Journal of Engineering Materials and Technology,* Vol. 109, 1987, pp. 293–298.

[13] Hua, C. T. and Socie, D. F., "Fatigue Damage in 1045 Steel under Constant Amplitude Biaxial Loading," *Fatigue and Fracture in Engineering Materials and Structures,* Vol. 7, 1984, pp. 165–179.

[14] Hua, C. T. and Socie, D. F., "Fatigue Damage in 1045 Steel under Variable Amplitude Biaxial Loading," *Fatigue and Fracture in Engineering Materials and Structures,* Vol. 8, 1985, pp. 101–114.

[15] Bannantine, J. A. and Socie, D. F., "Observations of Cracking Behavior in Tension and Torsion Low Cycle Fatigue," *Low Cycle Fatigue, ASTM STP 942,* H. D. Solomon, G. R. Halford, L. R. Kaisand, and B. N. Leis, Eds., American Society for Testing and Materials, Philadelphia, 1988, pp. 899–921.

[16] Okawa, I., Takahashi, H., Moriwaki, M., and Misumi, M., "A Study on Fatigue Crack Growth Under Out-of-Phase Combined Loadings," *Fatigue and Fracture in Engineering Materials and Structures,* Vol. 20, No. 6, 1997, pp. 929–940.

Sreeramesh Kalluri,[1] *Michael A. McGaw,*[2] *and Gary R. Halford*[3]

Fatigue Life Estimation Under Cumulative Cyclic Loading Conditions

REFERENCE: Kalluri, S., McGaw, M. A., and Halford, G. R., **"Fatigue Life Estimation Under Cumulative Cyclic Loading Conditions,"** *Fatigue and Fracture Mechanics: 31st Volume, ASTM STP 1389,* G. R. Halford and J. P. Gallagher, Eds., American Society for Testing and Materials, West Conshohocken, PA, 2000, pp. 94–109.

ABSTRACT: The cumulative fatigue behavior of a cobalt-base superalloy, Haynes 188, was investigated at 760°C in air. Initially, strain-controlled tests were conducted on solid cylindrical gage section specimens of Haynes 188 under fully reversed, tensile and compressive mean strain-controlled fatigue tests. Fatigue data from these tests were used to establish the baseline fatigue behavior of the alloy with (1) a total strain range type fatigue life relation and (2) the Smith-Watson-Topper (SWT) parameter. Subsequently, two load-level multi-block fatigue tests were conducted on similar specimens of Haynes 188 at the same temperature. Fatigue lives of the multi-block tests were estimated with (1) the linear damage rule (LDR) and (2) the nonlinear damage curve approach (DCA) both with and without the consideration of mean stresses generated during the cumulative fatigue tests. Fatigue life predictions by the nonlinear DCA were much closer to the experimentally observed lives than those obtained by the LDR. In the presence of mean stresses, the SWT parameter estimated the fatigue lives more accurately under tensile conditions than under compressive conditions.

KEYWORDS: cumulative fatigue, cyclic hardening, damage curve approach, life prediction, linear damage rule, mean strain, mean stress

Nomenclature

b, c	Exponents of elastic and inelastic strain range-life relations
g, h	Exponents in the Smith-Watson-Topper parameter-life relation
n	Number of applied cycles at a load level in a cumulative fatigue test
B, C	Coefficients of elastic and inelastic strain range-life relations
D	Damage
E	Modulus of elasticity
G, h	Coefficients in the Smith-Watson-Topper parameter-life relation
N	Number of cycles in a single load-level test or blocks in a two load-level test
R	Ratio of minimum value to maximum value in a cycle
ε	Engineering strain
Δ	Denotes range of a variable
σ	Stress

[1] Senior research engineer, Ohio Aerospace Institute, Brookpark, OH.
[2] President, McGaw Technology, Inc., Lakewood, OH.
[3] Senior scientific technologist, Research and Technology Directorate, NASA Glenn Research Center, Cleveland, OH.

Copyright© 2000 by ASTM International www.astm.org

Subscripts

1	First load-level in a two load-level cumulative fatigue test
2	Second load-level in a two load-level cumulative fatigue test
B	Blocks
f	Failure
el	Elastic
in	Inelastic
k	Number of blocks at failure in a multi-block fatigue test
m	Mean
max	Maximum
t	Total

Introduction

The determination of fatigue life under cyclically interactive loading conditions is necessary to assess the durability of many engineering components routinely used in terrestrial and aerospace applications. Limitations on the durability of components subjected to cumulative fatigue loading can severely restrict their usage both due to cost and safety considerations. Fatigue life prediction models capable of estimating accurately the durability of engineering components under cumulative loading conditions (involving two or more cyclic loads) are required to avoid unnecessary overdesign as well as underdesign that can potentially lead to catastrophic failures.

Many cumulative fatigue investigations conducted in the past involve mainly two load-level single-block tests [*1–12*]. In such tests, mean stresses and strains are typically avoided at both load levels by careful design of the experiments. The fatigue lives obtained from the single-block (i.e., "one-step") tests are commonly utilized to document the ordering effects (high/low or low/high) in cumulative damage studies. By comparison cumulative fatigue studies under two load-level, multi-block loading conditions that include mean stresses at one or both load levels are fewer in number [*13–16*]. Fatigue life predictions under cumulative fatigue loading conditions that include mean stresses are difficult tasks because they must consider (1) the influence of mean stress (either tensile or compressive) on the material's fatigue behavior and (2) the accumulation of fatigue damage from different load levels and the associated damage interaction.

The objective of the present investigation was to estimate the cumulative fatigue life of a wrought cobalt-base superalloy, Haynes 188, in the presence of mean stresses (either tensile or compressive) under two load-level, multi-block loading conditions. Haynes 188 has applications as a combustor liner material in aeronautical propulsion system components and as a cryogenic oxygen-carrying tube material in the main injector of the reusable space shuttle main engine. The tensile ductility of this material exhibits a minimum around 760°C [*17*]. Since low-cycle fatigue life of a material is predominantly governed by ductility, this temperature was selected for the present investigation to obtain a lower bound on life over the temperature range of application. Two load-level, single-block tests were previously conducted at 760°C by Bizon et al. on Haynes 188 [*7*]. They reported significant cumulative fatigue damage interaction in the high/low type of two load-level single-block tests. In the present study, initially strain-controlled fatigue tests were conducted at three different mean strain conditions (fully reversed, tensile, and compressive) at 760°C on cylindrical specimens machined from Haynes 188. The fatigue data generated from these tests were used to characterize the baseline strain-controlled fatigue behavior of Haynes 188 and the influence of

mean strain on fatigue life. Subsequently, two load-level multi-block cyclic loading experiments were conducted to evaluate the influences of both tensile and compressive mean stresses and strains under cumulative fatigue conditions. The fatigue lives of the specimens tested in cumulative fatigue were estimated by the linear damage rule (LDR) [*1,18,19*] and the nonlinear damage curve approach (DCA) [*4,8*] both with and without the consideration of the tensile and compressive mean stresses generated during the multi-block tests. The results from the experimental program on Haynes 188 superalloy and a comparison of the predictive capabilities of the LDR and DCA methods are discussed.

Material and Specimens

Wrought cobalt-based superalloy, Haynes 188, was supplied by a commercial vendor in the form of bars with a nominal diameter of 19.1 mm. The bars were hot-rolled, centerless ground, and solution-annealed by the manufacturer (heat number: 1880-8-1742). The chemical composition of the superalloy in weight percent was as follows: <0.002 S, 0.002 B, 0.012 P, 0.1 C, 0.4 Si, 0.034 La, 0.75 Mn, 1.24 Fe, 13.95 W, 21.84 Cr, 22.43 Ni, with the balance being cobalt. Solid, cylindrical fatigue specimens with a nominal gage section diameter of 6.4 mm were machined from the bars. The final machining step involved mechanically polishing the gage section of every specimen along the longitudinal direction.

Experimental Details

All the tests were conducted in a servohydraulic rig equipped with hydro-collet grips. The specimens were heated to the test temperature of 760°C in air within a three-coil induction heating fixture. A commercially available, water-cooled extensometer with a gage length of 12.7 mm was used to measure displacement within the gage section of each specimen. The temperature of the specimen in the gage section was monitored with a noncontacting optical temperature measurement system. Temperature control was accomplished by chromel-alumel (Type K) thermocouples spot-welded on the shoulders of the specimen. Test control and data acquisition for baseline mean strain-controlled tests and the two load-level multi-block tests were performed with control-tree based software [*20*]. The software version used in this study [*21*] was executed on a personal computer that contained the necessary analog to digital and digital to analog converters and was interfaced with the servocontroller. In all of the fatigue tests, a cyclic frequency of 0.1 Hz was used and failure was defined either as a 50% drop in tensile load from the maximum value or separation of the specimen into two pieces, whichever occurred first.

Results

Baseline Tests

Baseline strain-controlled fatigue tests were conducted on Haynes 188 specimens at 760° under fully reversed ($R = -1$), tensile ($R_\varepsilon = 0$), and compressive ($R_\varepsilon = -\infty$) mean strain conditions. Baseline fatigue data obtained from the near half-life hysteresis loops are listed in Table 1. The average elastic modulus (171 GPa) of Haynes 188 at 760°C was used to compute the elastic strain range from the observed stress range for each test. The inelastic strain range was then obtained for each test by subtracting the elastic strain range from the total strain range. A total strain range versus fatigue life relation (Eq 1) was used to characterize the strain-controlled fatigue data:

TABLE 1—*Strain-controlled fatigue data of Haynes 188 at 760°C.*

Specimen Number	R_ε	$\Delta\varepsilon_t$	$\Delta\sigma$, MPa	σ_m, MPa	$\Delta\varepsilon_{el}$	$\Delta\varepsilon_{in}$	N_f Cycles
HB29	−1	0.01980	1 077	−9	0.00630	0.01350	300
HB28	−1	0.01386	979	−8	0.00573	0.00813	584
HB22	−1	0.00990	852	−3	0.00498	0.00492	1 062
HB23	−1	0.00792	848	−4	0.00496	0.00296	2 043
HB26	−1	0.00692	794	−4	0.00464	0.00228	2 467
HB24	−1	0.00594	808	−3	0.00473	0.00121	6 364
HB25	−1	0.00494	710	−2	0.00415	0.00079	24 364
HB30	−1	0.00460	697	−3	0.00408	0.00052	42 752
HB27[a]	−1	0.00396	674	−1	0.00394	0.00002	105 015
HB34	0	0.01385	1 006	−8	0.00588	0.00797	674
HB38	0	0.00990	909	−4	0.00532	0.00458	1 379
HB36	0	0.00792	846	−6	0.00495	0.00297	2 096
HB37	0	0.00596	780	−4	0.00456	0.00140	5 250
HB54	0	0.00495	793	−3	0.00464	0.00031	25 426
HB35	0	0.00453	734	−10	0.00429	0.00024	57 663
HB39	−∞	0.01385	983	−4	0.00575	0.00810	648
HB42	−∞	0.00991	872	−4	0.00510	0.00481	1 192
HB43	−∞	0.00792	839	−4	0.00491	0.00301	2 282
HB44	−∞	0.00611	781	−4	0.00457	0.00154	4 028
HB56	−∞	0.00513	790	−6	0.00462	0.00051	28 465

[a] Test was a runout.

$$\Delta\varepsilon_t = B(N_f)^b + C(N_f)^c \tag{1}$$

Constants and exponents in the life relation were obtained by performing least square regression fits between logarithms of elastic strain range and fatigue life as well as inelastic strain range and fatigue life for fully reversed ($R_\varepsilon = -1$), tensile ($R_\varepsilon = 0$), and compressive ($R_\varepsilon = -\infty$) mean strain conditions (Table 2). In computing the constants shown in Table 2, any runout data shown in Table 1 was omitted. The elastic, inelastic, and total strain range life relations for the fully reversed condition are shown in Fig. 1. Arrows in this figure identify runout data. Fatigue data from tensile ($R_\varepsilon = 0$) and compressive ($R_\varepsilon = -\infty$) mean strain-controlled tests are plotted together with the total strain range life relationship from the fully reversed ($R_\varepsilon = -1$) tests in Fig. 2.

Fatigue data from tensile and compressive mean strain-controlled tests agree closely with the life relationship obtained from the fully reversed tests. The evolution of stress ranges and mean stresses for two selected total strain ranges ($\Delta\varepsilon_t = 0.02$ and 0.005) are shown for

TABLE 2—*Constants for total strain range—fatigue life relationships.*

R_ε	b	c	B	C
−1	−0.0897	−0.660	0.0100	0.500
0	−0.0735	−0.833	0.00918	1.80
−∞	−0.0796	−0.746	0.00938	0.940
−∞, −1, and 0	−0.0835	−0.751	0.00972	0.980

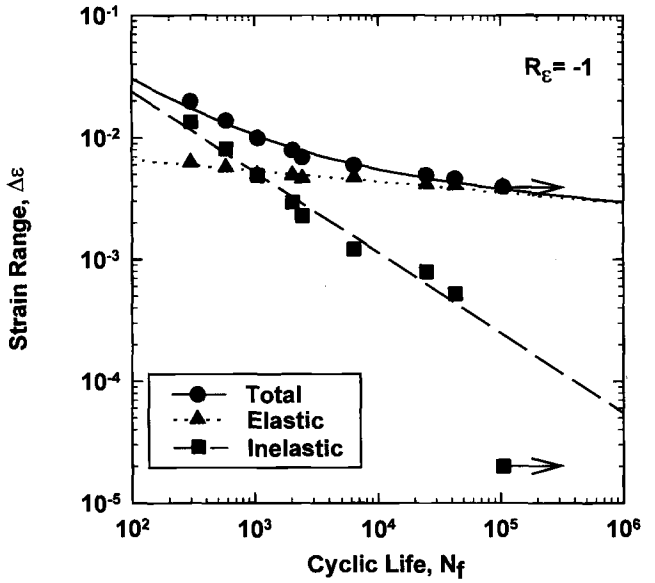


FIG. 1—*Fatigue life relationships for Haynes 188 at 760°C, fully reversed* ($R_\varepsilon = -1$).

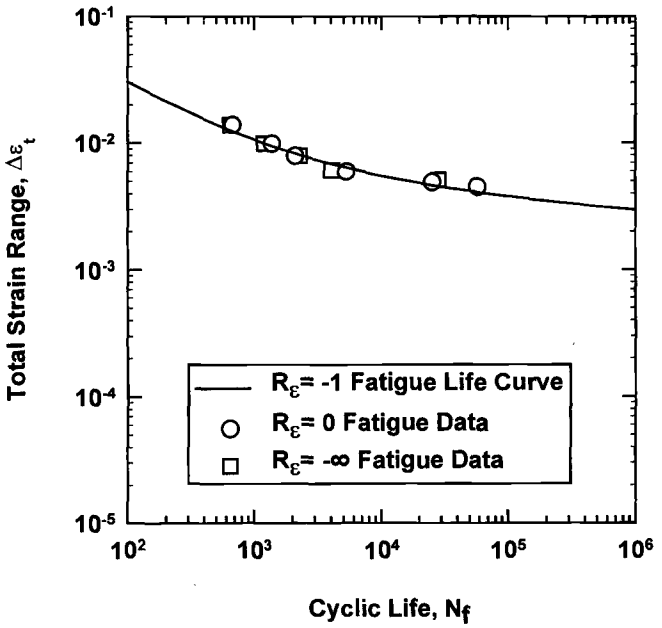


FIG. 2—*Tensile* ($R_\varepsilon = 0$) *and compressive* ($R_\varepsilon = -\infty$) *mean strain-controlled fatigue data and fully reversed* ($R_\varepsilon = -1$) *fatigue life relationship for Haynes 188 at 760°C.*

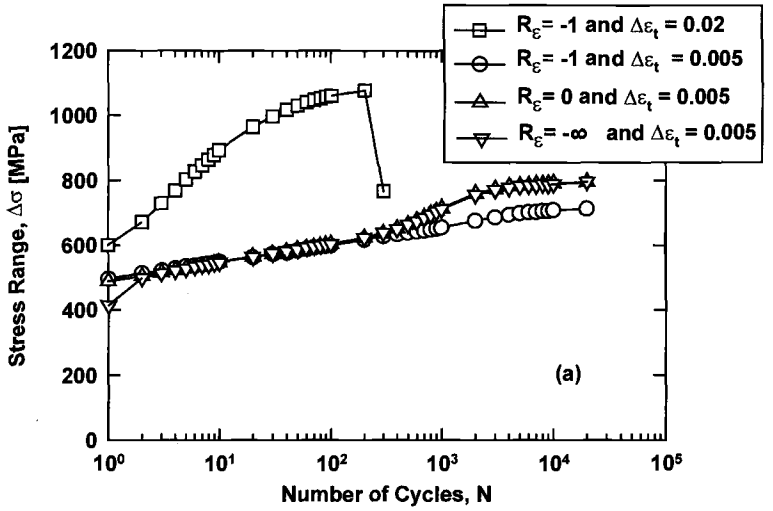


FIG. 3—*Cyclic Stress Evolution in Strain-Controlled Baseline Fatigue Tests:* (a) *stress ranges;* (b) *mean stresses.*

the baseline tests in Fig. 3. Haynes 188 exhibited cyclic hardening at both strain ranges at 760°C (Fig. 3*a*). Moreover, at the strain range of 0.005, mean strain (tensile or compressive) did not significantly influence the cyclic hardening behavior of the superalloy. Under fully reversed conditions, Haynes 188 developed small magnitudes of compressive mean stresses that prevailed through the duration of the fatigue tests (Fig. 3*b* and Table 1). In the specimens tested under tensile and compressive mean strain conditions, during the initial cycles tensile and compressive mean stresses, respectively, were observed (Fig. 3*b*). However, these mean

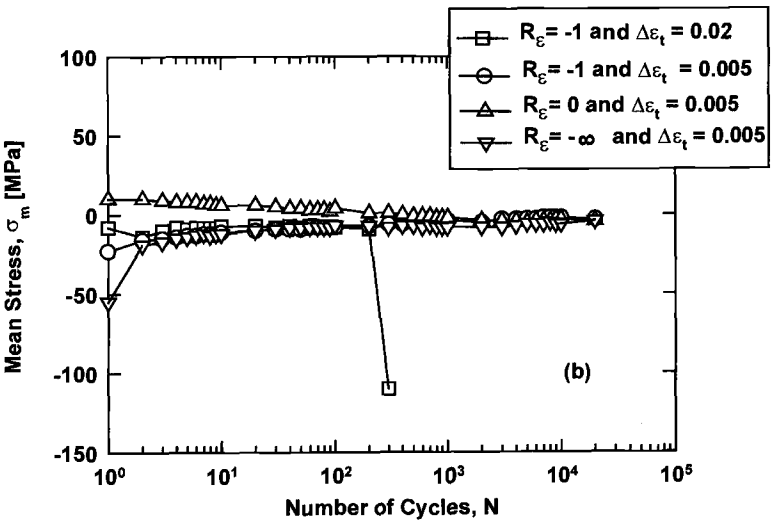


FIG. 3—*Continued.*

stresses relaxed over a few cycles and only small magnitude compressive mean stresses (similar to those observed in fully reversed tests) prevailed near and beyond the half-life durations in these tests (Table 1). Relaxation of the mean stresses in the mean strain-controlled tests is the primary reason for the close agreement observed earlier (Fig. 2) between the fatigue data generated in these tests and the fatigue life relationship obtained from the fully reversed fatigue tests. Since no significant differences in fatigue life were observed in fatigue lives of fully reversed and mean strain-controlled fatigue tests, data from all these tests were combined and a total strain range life relationship (Eq 1) was calculated. This life relationship (constants and exponents listed in Table 2) was subsequently used to estimate fatigue lives in the cumulative fatigue damage tests without mean stress consideration.

In order to estimate fatigue life in the presence of mean stresses, a model that accounts for their influence on fatigue life is necessary.[4] The Smith-Watson-Topper (SWT) parameter [22], (Eq 2a), was selected to estimate the fatigue life of Haynes 188 under mean stress conditions. This parameter was previously used successfully to estimate the fatigue life of another superalloy, Inconel 718, under mean stress conditions [*11*].

$$\text{SWT} = \sigma_{\max}\left(\frac{\Delta\varepsilon_t}{2}\right)E = G(N_f)^g + H(N_f)^h \tag{2a}$$

Fatigue data from the fully reversed and tensile and compressive mean strain-controlled tests were combined to obtain the SWT fatigue life parameter (Eq 2b) for Haynes 188 at 760°C (Fig. 4).

$$\sigma_{\max}\left(\frac{\Delta\varepsilon_t}{2}\right)E = 6.74 \times 10^5\,(N_f)^{-0.165} + 5.86 \times 10^7\,(N_f)^{-0.815} \tag{2b}$$

This parameter was subsequently used to estimate fatigue lives in the cumulative fatigue damage tests with mean stress consideration.

Cumulative Fatigue Tests

Two types of block loading patterns (Fig. 5) were designed to perform the two load-level multi-block fatigue tests on Haynes 188 at 760°C. In both of these block loading patterns, each block consisted of one major cycle with a total strain range of $\Delta\varepsilon_t = 0.02$ and 50 minor cycles with a lower total strain range, $\Delta\varepsilon_a = 0.005$. The major cycle was fully reversed in both of the block loading patterns (B1 and B2). In the case of block loading B1 the minor cycles were applied with $R_\varepsilon = 0.5$ (Fig. 5*a*), whereas in block loading B2 the minor cycles were applied with $R_\varepsilon = 2$ (Fig. 5*b*). Duplicate fatigue tests were conducted with block loading patterns B1 and B2. Hysteresis loops generated during the multi-block fatigue tests are shown in Fig. 6. Block loading B1 lead to a tensile mean stress in the minor cycles (Fig. 6*a*), whereas a compressive mean stress was observed in the minor cycles during block loading B2 (Fig. 6*b*). In both types of block loading patterns, the mean stresses relaxed slightly over the 50 minor cycles within a block of loading (Fig. 7). However, even during the 50th minor cycle, the magnitudes of the mean stresses were significantly large in both cases. Cumulative

[4] The fatigue data generated on Haynes 188 under tensile and compressive mean strain-controlled conditions could not be used for this purpose because of the observed mean stress relaxation in these tests.

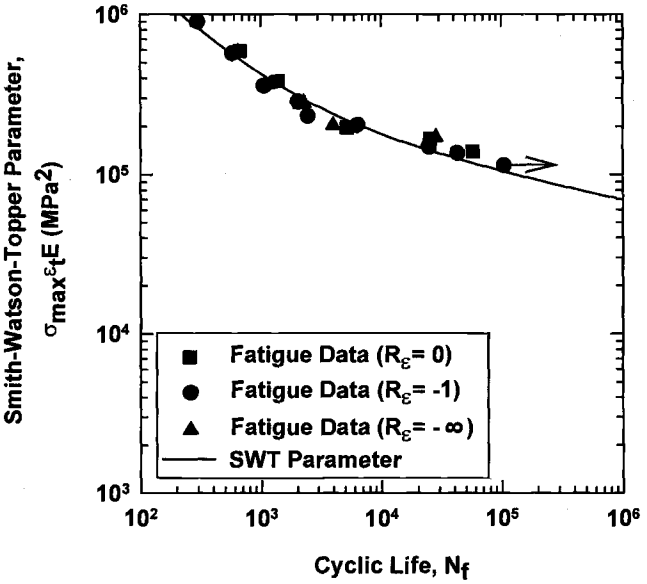


FIG. 4—*Smith-Watson-Topper fatigue life relation for strain-controlled fatigue data* ($R_\varepsilon = -\infty, -1,$ *and 0) of Haynes 188 at 760°C.*

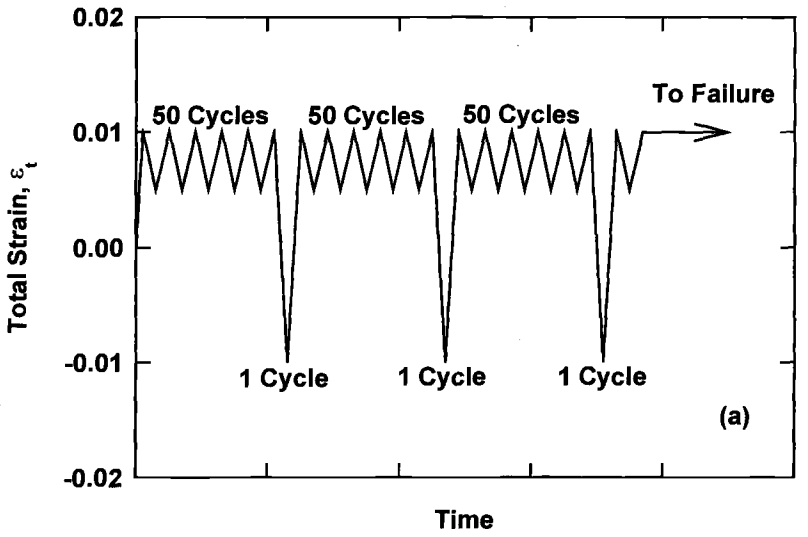


FIG. 5—*Schematics of Block Loading Patterns in Cumulative Fatigue Tests:* (a) *block loading, B1;* (b) *block loading, B2.*

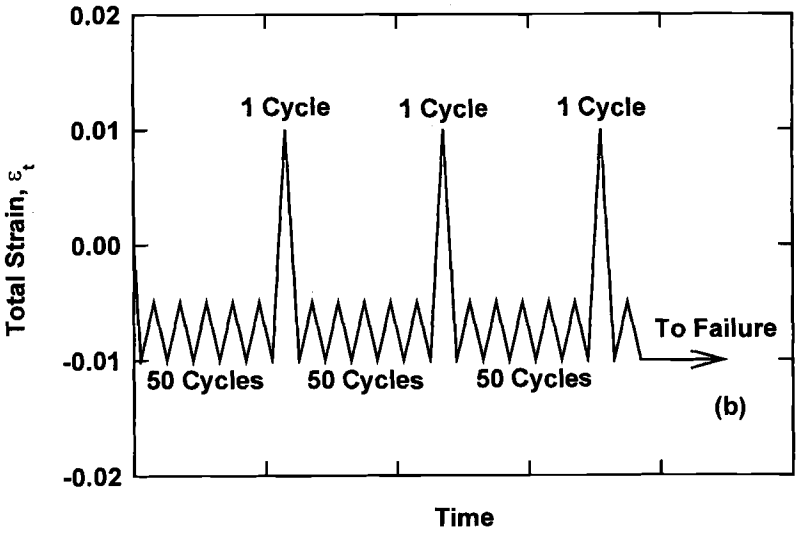


FIG. 5—*Continued.*

fatigue data obtained from the near half-life blocks in the two load-level, multi-block tests are listed in Table 3. Hysteresis loops corresponding to the major cycle and the 25th minor cycle were used to obtain the data shown in Table 3. Even though the cumulative fatigue data are limited, on the average block loading B2, which leads to compressive mean stresses in the minor cycles, exhibited slightly higher fatigue life than block loading B1.

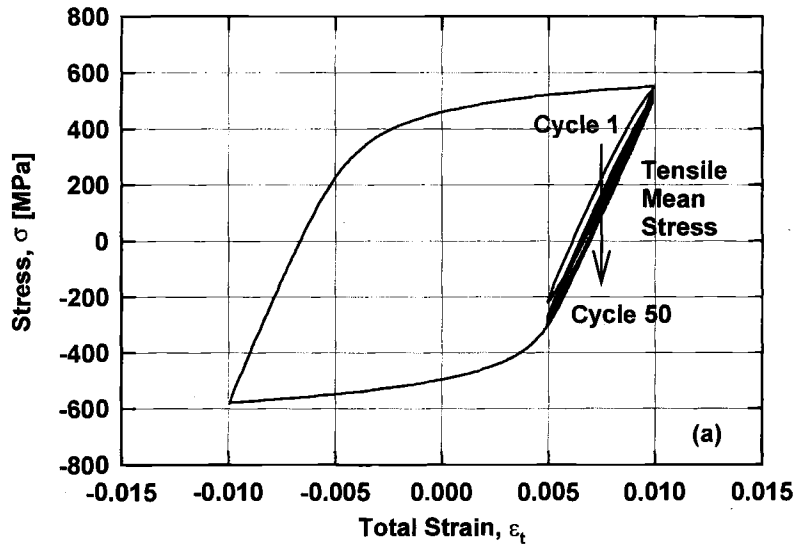


FIG. 6—*Hysteresis loops in cumulative fatigue tests;* (a) *block loading, B1;* (b) *block loading, B2.*

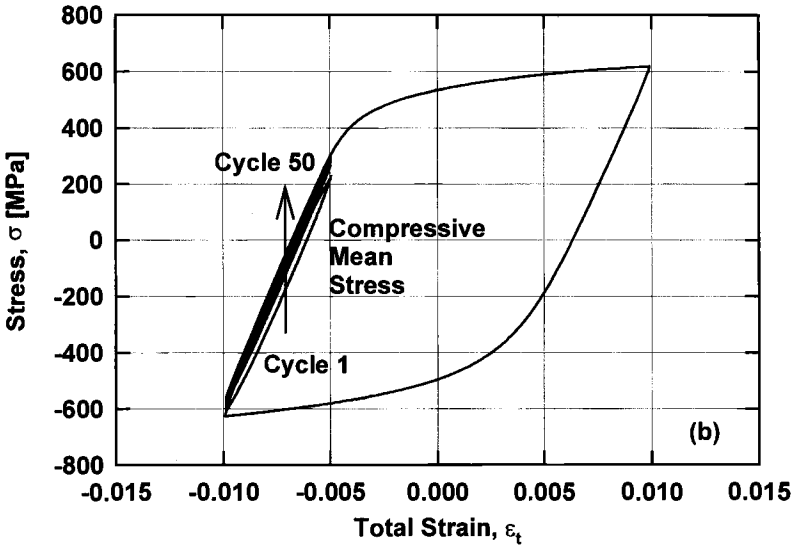


FIG. 6—*Continued.*

Fatigue Life Estimation

Fatigue lives in the cumulative fatigue tests were estimated with LDR (Eq 3) and nonlinear DCA (Eq 4) both with and without the consideration of the tensile and compressive mean stresses generated during the multi-block cyclic loading conditions.

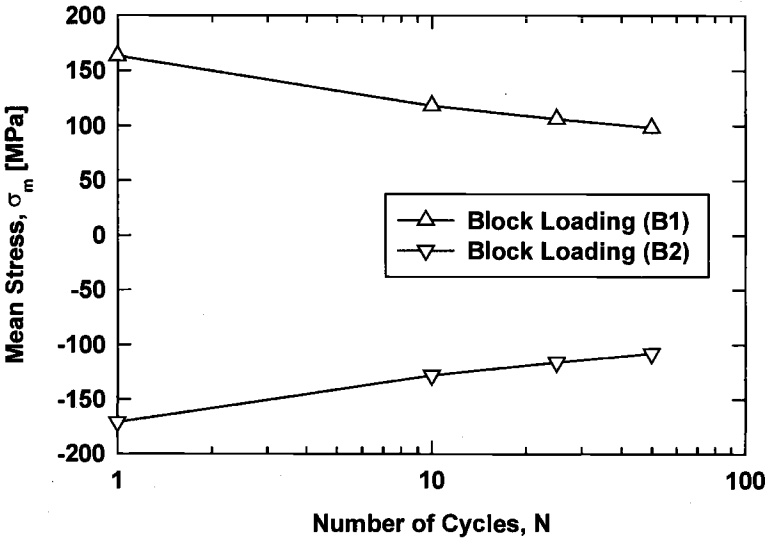


FIG. 7—*Evolution of mean stresses in cumulative fatigue tests.*

TABLE 3—*Cumulative fatigue data of Haynes 188 at 760°C.*

Specimen Number	Block Loading	Major Cycle R_ε	Major Cycle $\Delta\varepsilon_t$	Major Cycle $\Delta\sigma$, MPa	Major Cycle σ_m, MPa	Minor Cycle R_ε	Minor Cycle $\Delta\varepsilon_t$	Minor Cycle $\Delta\sigma$, MPa	Minor Cycle σ_m, MPa	N_B, Blocks
HB49	B1	−1	0.01980	1130	−14	0.5	0.00493	791	106	71
HB45	B1	−1	0.01978	1007	−12	0.5	0.00492	753	73	80
HB57	B2	−1	0.01980	1151	−6	2.0	0.00493	833	−116	76
HB53	B2	−1	0.01978	1245	−4	2.0	0.00493	851	−145	138

$$D(n_1, N_1) = \left(\frac{n_1}{N_1}\right)$$
$$D(n_2, N_2) = \left(\frac{n_2}{N_2}\right) \tag{3}$$

In LDR [*1,18,19*], the damage from the first and second load levels is defined in terms of the life fractions at each of those loads. In the case of nonlinear DCA [*4,8*] damage at the first load level is defined as the life fraction; however, at the second load level it is a nonlinear function of the life fraction and is dependent on the ratio of the baseline fatigue lives at the two load levels.

$$D(n_1, N_1) = \left(\frac{n_1}{N_1}\right)$$
$$D(n_2, N_2) = \left(\frac{n_2}{N_2}\right)^{\left(\frac{N_2}{N_1}\right)^{0.4}} \tag{4}$$

For both models $D = 0$ for the undamaged (or untested) state and $D = 1$ at final failure. For the multi-block tests with two load levels, both models predict failure when the following condition is satisfied.

$$\sum_{i=1}^{k}[D_i(n_1, N_1) + D_i(n_2, N_2)] = 1 \tag{5}$$

where subscript $i = 1$ to k denotes the block number.

The accumulation of fatigue damage in the case of LDR is linear at all life levels and is obtained by an algebraic sum of the life fractions at the two load levels within a block and then by the addition of damage associated with each block of loading. Damage accumulation in the DCA is more complicated and is illustrated in Fig. 8. For every block of loading with the DCA, fatigue damage sustained by the material at each load level must be tracked by the damage curve associated with that load level. For example, during the first block of loading, damage due to the first load level is indicated by point A in Fig. 8. In order to evaluate the damage from the second load level during the first block of loading, initially

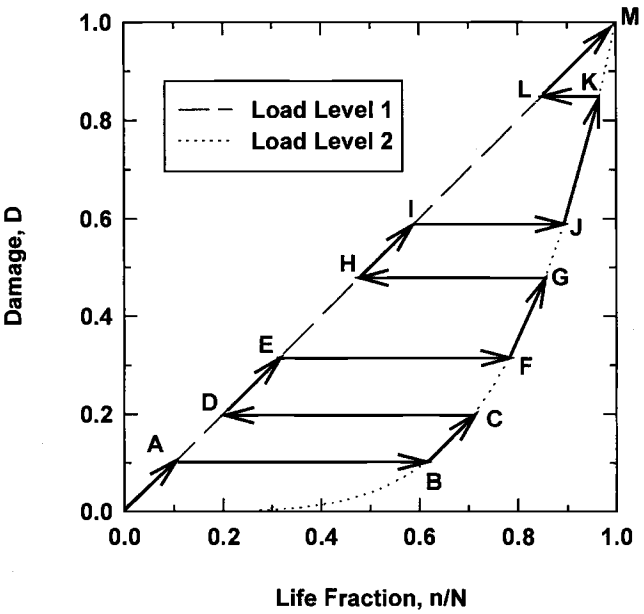


FIG. 8—*Schematic of damage estimation in two load-level multi-block fatigue tests with nonlinear damage curve approach.*

Point A must be translated along a horizontal line to Point B, which is on the damage curve (obtained by using Eq 4) associated with the second load level. The damage from the second load level is represented by BC. At this stage, to assess the damage from the first load level during the second block of loading, Point C must again be translated horizontally to Point D on the damage curve for the first load level. The damage from the two load levels in each succeeding block must be accumulated in a repetitive manner until the criterion for failure (Eq 5) is satisfied. The entire damage calculation process for the two load-level multi-block tests was performed with two computer programs for the LDR and DCA methods.

Fatigue lives of the two load-level, multi-block tests estimated by LDR and DCA without mean stress consideration are shown in Fig. 9*a*. The baseline fatigue lives (N_1 and N_2) for this analysis were obtained with the total strain range life relation (Eq 1 and Table 2) by combining all the strain-controlled fatigue data ($R_\varepsilon = -\infty$, -1, and 0). In general, for both types of block loading patterns (B1 and B2), when mean stresses were not considered, the fatigue life predictions by the LDR were highly nonconservative compared to the life estimations by the DCA. Fatigue life estimations by LDR and DCA for the cumulative fatigue tests with mean stress consideration are shown in Fig. 9*b*. The SWT parameter (Eq 2b) was used to obtain N_1 and N_2 values for the analysis. As in the previous case, the predicted lives by the LDR were higher than those estimated by the DCA for block loading patterns B1 and B2. Both LDR and DCA were able to predict the fatigue lives under block loading B1, which resulted in a tensile mean stress at the second load level, to within approximately 25 blocks of the experimentally observed lives. However, for block loading B2, which resulted in compressive mean stress at the second load level, predictions by both LDR and DCA were worse than when mean stresses were ignored.

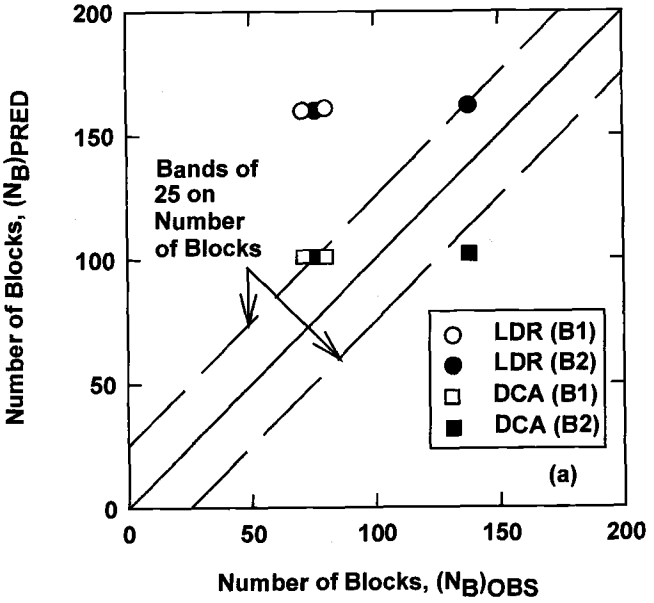


FIG. 9—*Life Prediction of Cumulative Fatigue Tests: Haynes 188 at 760°C:* (a) *without mean stress consideration;* (b) *with mean stress consideration.*

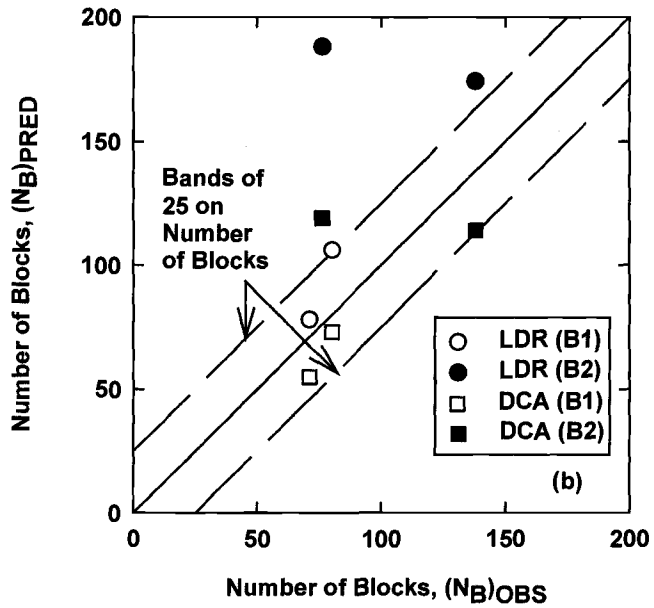


FIG. 9—*Continued.*

Discussion

In this study, no significant differences were observed among the fatigue lives of the baseline fatigue tests conducted under fully reversed ($R_\varepsilon = -1$), tensile ($R_\varepsilon = 0$), and compressive ($R_\varepsilon = -\infty$) mean strain conditions (Figs. 1 and 2 and Table 2). This is due mainly to the relaxation of the mean stresses in the tensile ($R_\varepsilon = 0$) and compressive ($R_\varepsilon = -\infty$) mean strain-controlled tests to the levels observed in the fully reversed strain-controlled tests (Fig. 3 and Table 1). The extent of mean stress relaxation in the mean strain-controlled tests depends upon the ductility of the material, test temperature, and strain range. For Haynes 188 at 760°C, the test conditions in this study facilitated the relaxation of the mean stresses observed during the initial cycles. However, for high-strength materials with low ductility and at moderate temperatures such a mean stress relaxation may not occur in mean strain-controlled tests. Therefore, the influence of mean strain and the associated manifestation of mean stress must be carefully ascertained for each material and test condition.

Under cumulative fatigue loading conditions, regardless of the method used for damage accumulation (LDR or nonlinear DCA), the SWT parameter was able to improve the fatigue life predictions for tensile mean stress conditions (Fig. 9, Block Loading: B1). However, for compressive mean stress conditions (Fig. 9, Block Loading: B2) predictions by the same parameter were worse (higher) than when no mean stress influence was considered. These results indicated that for Haynes 188 at 760°C the SWT parameter accurately represented the detrimental influence of tensile mean stress on the fatigue life. However, this parameter overestimated the beneficial effect of compressive mean stress on the fatigue life of Haynes 188. Note that the SWT parameter (Eq 2a) cannot be used to estimate the fatigue life under complex cumulative fatigue loading conditions that lead to a hysteresis loop with a compressive maximum stress. In such cases, either the effect of mean stress on fatigue life can be ignored or another method should be employed to determine the influence of compressive mean stress on fatigue life.

For the two load-level, multi-block tests (whether the influence of mean stress on fatigue life was considered or ignored) predicted fatigue lives by the nonlinear DCA were much closer to the experimentally observed fatigue lives than those by the LDR. This observation implies that fatigue damage tends to accumulate in the multi-block tests in a nonlinear fashion. The methodology used in this study for cumulative fatigue life estimation with DCA can be extended to a multi-block loading with multiple load levels. Under these circumstances, after selecting a load level for the reference life, the damage curves for all the load levels need to be determined using equations similar to Eqs 4 and 5. Fatigue life calculations can be performed by carefully keeping track of each damage curve and switching among the curves, while computing the damage from each load level within a block of loading, and by adding the damage from all the blocks until the failure criterion is satisfied.

Summary

The cumulative fatigue behavior of a cobalt-base superalloy, Haynes 188 at 760°C, was investigated by conducting baseline fully reversed, tensile, and compressive mean strain-controlled tests and two load-level multi-block fatigue tests. No significant differences were observed among the fatigue lives of the fully reversed, tensile, and compressive mean strain-controlled fatigue tests due mainly to the relaxation of mean stresses in the tensile and compressive mean strain-controlled tests. The fatigue behavior of the baseline tests was adequately characterized by both (1) the total strain range versus fatigue life relation and (2) the Smith-Watson-Topper parameter. Fatigue lives of the two load-level, multi-block tests were estimated by the linear damage rule and the nonlinear damage curve approach both

with and without the consideration of the influence of mean stress on the fatigue life. In general, predictions by the method of nonlinear damage curve were much closer to the experimentally observed fatigue lives. In the presence of tensile mean stresses, the Smith-Watson-Topper parameter improved cumulative fatigue life predictions. However, under compressive mean stress conditions this parameter overestimated the beneficial effect of fatigue life.

Acknowledgment

The assistance provided by Christopher S. Burke (Dynacs Engineering Company, Inc.) for performing all the tests in the High Temperature Fatigue and Structures Laboratory is gratefully acknowledged.

References

[1] Miner, M. A., "Cumulative Damage in Fatigue," *Journal of Applied Mechanics,* Vol. 12, No. 3, September 1945 (*Transactions of the American Society of Mechanical Engineers,* Vol. 67, 1945), pp. A159–A164.

[2] Manson, S. S., Nachtigall, A. J., Ensign, C. R., and Freche, J. C., "Further Investigation of a Relation for Cumulative Fatigue Damage in Bending," *Journal of Engineering for Industry,* Vol. 87, 1965, pp. 25–35.

[3] Wood, W. A. and Reimann, W. H., "Observations on Fatigue Damage Produced by Combinations of Amplitudes in Copper and Brass," *Journal of the Institute of Metals,* Vol. 94, 1966, pp. 66–70.

[4] Manson, S. S. and Halford, G. R., "Practical Implementation of the Double Linear Damage Rule and Damage Curve Approach for Treating Cumulative Fatigue Damage," *International Journal of Fracture,* Vol. 17, No. 2, 1981, pp. 169–192.

[5] Miller, K. J. and Ibrahim, M. F. E., "Damage Accumulation During Initiation and Short Crack Growth Regimes," *Fatigue of Engineering Materials and Structures,* Vol. 4, No. 3, 1981, pp. 263–277.

[6] Bui-Quoc, T., "Cumulative Damage with Interaction Effect due to Fatigue Under Torsion Loading," *Experimental Mechanics,* 1982, pp. 180–187.

[7] Bizon, P. T., Thoma, D. J., and Halford, G. R., "Interaction of High Cycle and Low Cycle Fatigue of Haynes 188 at 1400°F," *Structural Integrity and Durability of Reusable Space Propulsion Systems,* NASA CP-2381, 1985, pp. 139–145.

[8] Manson, S. S. and Halford, G. R., "Re-examination of Cumulative Fatigue Damage Analysis—An Engineering Perspective," *Engineering Fracture Mechanics,* Vol. 25, Nos. 5/6, 1986, pp. 539–571.

[9] Golos, K. and Ellyin, F., "Generalization of Cumulative Damage Criterion to Multilevel Cyclic Loading," *Theoretical and Applied Fracture Mechanics,* Vol. 7, 1987, pp. 169–176.

[10] Chaboche, J. L. and Lesne, P. M., "A Non-Linear Continuous Fatigue Damage Model," *Fatigue and Fracture of Engineering Materials and Structures,* Vol. 11, No. 1, 1988, pp. 1–17.

[11] Kalluri, S., Halford, G. R., and McGaw, M. A., "Prestraining and its Influence on Subsequent Fatigue Life," *Advances in Fatigue Lifetime Predictive Techniques: 3rd Volume, ASTM STP 1292,* M. R. Mitchell and R. W. Landgraf, Eds., American Society for Testing and Materials, 1996, pp. 328–341.

[12] Kalluri, S., and Bonacuse, P. J., "Cumulative Axial and Torsional Fatigue: An Investigation of Load-Type Sequencing Effects," *ASTM STP 1387,* S. Kalluri and P. J. Bonacuse, Eds., American Society for Testing and Materials, West Conshohocken, PA, 2000, pp. 281–301.

[13] Dowling, N. E., "Fatigue Failure Predictions for Complicated Stress-Strain Histories," *Journal of Materials,* JMLSA, Vol. 7, No. 1, March 1972, pp. 71–87.

[14] Walcher, J., Gray, D., and Manson, S. S., "Aspects of Cumulative Fatigue Damage Analysis of Cold End Structures," 79-1190, AIAA/SAE/ASME 15th Joint Propulsion Conference, 18–20 June 1979, Las Vegas, Nevada, pp. 1–13.

[15] Vasek, A. and Polak, J., "Low Cycle Fatigue Damage Accumulation in Armco-Iron," *Fatigue and Fracture of Engineering Materials and Structures,* Vol. 14, Nos. 2/3, 1991, pp. 193–204.

[16] McGaw, M. A., Kalluri, S., Moore, D., and Heine, J., "The Cumulative Fatigue Damage Behavior of Mar-M 247 in Air and High Pressure Hydrogen," *Advances in Fatigue Lifetime Predictive Techniques: Second Volume, ASTM STP 1211,* M. R. Mitchell and R. W. Landgraf, Eds., American Society for Testing and Materials, 1993, pp. 117–131.

[17] "Nickel Base Alloys," International Nickel Company, New York, 1977.

[18] Palmgren, A., "Die Lebensdauer von Kugellagern," *Zeitschrift des Vereinesdeutscher Ingenierure,* Vol. 68, No. 14, April 1924, pp. 339–341 ("The Service Life of Ball Bearings," NASA technical translation of German text, NASA TT 1-13460, 1971).

[19] Langer, B. F., "Fatigue Failure from Stress Cycles of Varying Amplitude," *Journal of Applied Mechanics,* Vol. 4, No. 3, September 1937 (*Transactions of the American Society of Mechanical Engineers,* Vol. 59, 1937), pp. A160–A162.

[20] McGaw, M. A. and Bonacuse, P. J., "Automation Software for a Materials Testing Laboratory," *Applications of Automation Technology to Fatigue and Fracture Testing, ASTM STP 1092,* A. A. Braun, N. E. Ashbaugh, and F. M. Smith, Eds., American Society for Testing and Materials, West Conshohocken, PA, 1990, pp. 211–231.

[21] McGaw, M. A., "Materials Testing Software," LEW-16160, COSMIC, Athens, GA, 1995.

[22] Smith, K. N., Watson, P., and Topper, T. H., "A Stress-Strain Function for the Fatigue of Metals," *Journal of Materials,* JMSLA, Vol. 5, No. 4, 1970, pp. 767–778.

Timothy P. Gabb,[2] *Peter J. Bonacuse,*[2] *Louis J. Ghosn,*[3]
Joseph W. Sweeney,[4] *Amit Chatterjee,*[5] *and Kenneth A. Green*[5]

Assessments of Low Cycle Fatigue Behavior of Powder Metallurgy Alloy U720

REFERENCE: Gabb, T. P., Bonacuse, P. J., Ghosn, L. J., Sweeney, J. W., Chatterjee, A., and Green, K. A., **"Assessments of Low Cycle Fatigue Behavior of Powder Metallurgy Alloy U720,"** *Fatigue and Fracture Mechanics: 31st Volume, ASTM STP 1389,* G. R. Halford and J. P. Gallagher, Eds., American Society for Testing and Materials, West Conshohocken, PA, 2000, pp. 110–127.

ABSTRACT: The fatigue lives of modern powder metallurgy disk alloys are influenced by variabilities in alloy microstructure and mechanical properties. These properties can vary as functions of variables the different steps of materials/component processing: powder atomization, consolidation, extrusion, forging, heat treating, and machining [*1–4*]. It is important to understand the relationship between the statistical variations in life and these variables, as well as the change in life distribution due to changes in fatigue loading conditions. The objective of this study was to investigate these relationships in a nickel-base disk superalloy, U720, produced using powder metallurgy processing. Multiple strain-controlled fatigue tests were performed at 538°C (1000°F) at limited sets of test conditions. Analyses were performed to: (1) assess variations of microstructure, mechanical properties, and LCF failure initiation sites as functions of disk processing and loading conditions; and (2) compare mean and minimum fatigue life predictions using different approaches for modeling the data from assorted test conditions.

Significant variations in life were observed as functions of the disk-processing variables evaluated. However, the lives of all specimens could still be combined and modeled together. The failure initiation sites for tests performed at a strain ratio $R_\varepsilon = \varepsilon_{min}/\varepsilon_{max}$ of 0 were different from those in tests at a strain ratio of −1. An approach could still be applied to account for the differences in mean and maximum stresses and strains. This allowed the data in tests of various conditions to be combined for more robust statistical estimates of mean and minimum lives.

KEYWORDS: superalloy, powder metallurgy, low cycle fatigue, inclusions, facets

The low-cycle fatigue (LCF) lives, life-frequency distributions, and predominant failure modes of power metallurgy disks can be influenced by material-processing details including powder characteristics, consolidation, extrusion, forging, heat treating, and machining processing parameters [*1–4*]. Processing history also introduces dependencies of LCF behavior

[1] Research metallurgist, NASA Glenn Research Center, Mail Stop 49-3, 21000 Brookpark Rd., Cleveland, OH 44135.

[2] Research engineer, U.S. Army Research Laboratory at NASA Glenn Research Center, Mail Stop 49-6, 21000 Brookpark Rd., Cleveland, OH 44135.

[3] Research Engineer, NASA Glenn Research Center, Mail Stop 49-6, 21000 Brookpark Rd., Cleveland, OH 44135. Present affiliation: Eveready Battery Company, Inc., Westlake, OH.

[4] Microscopist, Gilcrest Co., NASA Glenn Research Center, Mail Stop 49-3, 21000 Brookpark Rd., Cleveland, OH 44135.

[5] Research engineers, Allison Engine Co., Indianapolis, IN.

Copyright© 2000 by ASTM International www.astm.org

on location in a disk. These effects on fatigue behavior can change as functions of service/testing conditions: temperatures, times, imposed stresses/strains. It is often not possible to assess these issues with a statistically significant number of fatigue specimen tests in many conditions producing lives $>10^4$ cycles due to testing costs, time, and material constraints. Yet many applications require such design lives. The objective of this work was to study the LCF life behavior of the powder metallurgy (PM) disk alloy U720 in many tests at limited, long life ($>10^4$ cycles) test conditions. The LCF behavior as functions of several processing variables (disk and specimen location) was first assessed. Life distributions and minimum life estimates were then evaluated for each selected test condition when pooling data. Minimum life estimates were also performed when combining data of different test conditions.

Materials and Procedures

Production-scale PM U720 disk material, previously described [*5*], was supplied by Allison Engine Company. The powder for this material was atomized in argon. After screening and blending, the powder was hot isostatic pressed, extruded, and then cluster forged. The disks were separated from the forged clusters and given a subsolvus solution, oil quench, and two-step aging heat treatment. Specimens with uniform gages of 0.635-cm (0.25-in.) diameter were machined from the rims of an outer disk (No. 16) of one cluster and a center disk (No. 43) of another cluster forging (Fig. 1). The specimens were grouped together for each disk in hopes of minimizing location effects. However, tests were designed to allow evaluations of the following variables: disk (*D*), radial location (*R*), and vertical location within disk (*V*). A 2 by 3 by 2 full factorial statistical test matrix with repetitions was used. Two prime test conditions were selected, each estimated to have mean lives of near 200 000 cycles at 538°C (1000°F). A total strain range ($\Delta\varepsilon_t$) of 0.75% was used with a strain ratio

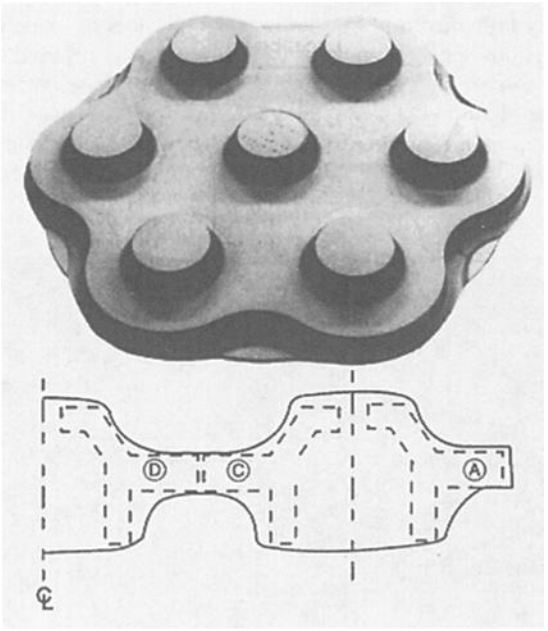


FIG. 1—*Cluster forging [5].*

($R_\epsilon = \epsilon_{min}/\epsilon_{max}$) equal to 0 in one series of 20 tests. A total strain range ($\Delta\epsilon_t$) of 0.90% was used a strain ratio ($R_\epsilon = \epsilon_{min}/\epsilon_{max}$) equal to -1 in the other series of 20 tests. To reduce testing time each experiment was performed in two stages. First, the test was conducted in strain control using a triangular waveform at a frequency of 0.33 Hz. After cycling for 24 h, tests were continued to failure using a triangular waveform in load control at a frequency of 10 Hz. For each test, the load control settings were adjusted to reproduce the stabilized maximum and minimum loads generated during the previous strain cycling at 0.33 Hz. All tests were continued to failure, and fractographic evaluations were performed on all specimens. Metallographic analyses were performed on selected specimens spanning the range of process variables and test conditions. For the fatigue life relationships, least squares multiple linear regressions were performed using forward step-wise inclusion of independent variables, requiring an F-ratio to enter of 2.0. Adjusted correlation coefficients (r_{adj}^2) and root mean square standard deviations were used to compare among the different resulting relationships. The F test for lack of fit and graphical residual analyses were also performed to check the aptness of each model.

Results and Discussion

Overview

The typical microstructure of selected specimens is shown in Fig. 2. The mean grain size ranged from ASTM 12 to 12.5. Primary γ' particles of 1 to 3-μm diameter took up an area fraction of 14 to 18%. Finer cooling γ' precipitates of 0.08 to 0.13-μm diameter and very fine aging γ' were in far greater abundance. The fatigue test results are listed (Tables 1, 2). Twenty fatigue tests were performed at each of the two prime test conditions. Cyclic lives in these tests were from 53 269 to 446 550 cycles. Eight additional screening tests were performed at $R_\epsilon = -1$ with higher $\Delta\epsilon_t$ of 0.92 to 1.0%, giving cyclic lives of 10 017 to 473 868 cycles. The predominant failure initiation sites varied with R_ϵ. Tests performed with $R_\epsilon = 0$ predominantly failed from cracks at elongated clusters of oxide inclusions, as shown in Fig. 3. These inclusions appeared to be of the class generally referred to as Type II reactive inclusions [*1*,*4*]. No surrounding reaction zones containing phases other than the typical γ, γ', and carbides were identified at these Type II inclusions. However, these inclusions were often surrounded by several large grains having less primary γ' apparent. Tests performed with $R_\epsilon = -1$ principally failed from cracks emanating from large, sheared grains ("grain

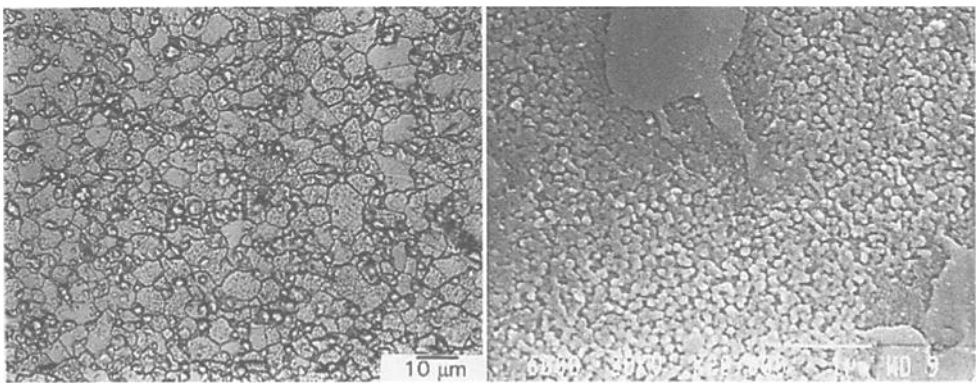


FIG. 2—*Typical microstructure.*

TABLE 1—*LCF tests results at* $R_\epsilon = 0$.

Total Strain Range, $\Delta\epsilon_t$-mm/mm	Inelastic Strain, mm/mm	Elastic Strain, mm/mm	Max Stress, MPa	Min Stress, MPa	Modulus, GPa	Failure Life, N_f	Failure Initiation Site	Max Length, μm	Width, μm	Minimum Depth, μm
0.0075	0	0.0075	1147	−303	193	168 376	Type II: Al-oxide	69.6	31.1	37
0.0075	0.0001	0.0074	1126	−304	194	186 264	Facet, 1 grain	83.8	31.4	3.3
0.0075	0.0001	0.0074	1126	−292	197	172 076	Type II: Al-oxide	47.4	5.2	1763
0.0075	0.0001	0.0074	1134	−290	198	159 414	Type II: Al-oxide	204.3	46.1	487
0.0075	0.0001	0.0074	1143	−271	197	312 603	Pores, clustered	54.5	17.9	37
0.0075	0.0001	0.0074	1103	−314	191	53 269	Type II: Al,Mg,Si-oxide	139	80.8	1409
0.0075	0	0.0075	1149	−330	197	233 639	Type I: Zr-oxide	44.7	39.3	240.8
0.0075	0.0001	0.0074	1107	−343	198	192 204	Type II: Al-oxide	231.1	43.8	1352
0.0075	0.0001	0.0074	1117	−303	192	179 199	Type II: Al,Ti-oxide	93.3	69.4	2040
0.0075	0.0001	0.0074	1089	−316	190	331 636	Type II: Al-oxide	136.5	35.3	891.7
0.0075	0	0.0075	1104	−356	194	446 550	Pores, clustered	36.8	19.1	69.8
0.0075	0.0002	0.0073	1130	−350	203	148 743	Type II: Al-oxide	48.3	11.9	522.4
0.0075	0.0001	0.0074	1086	−387	199	277 463	Type II: Al,Ti-oxide	95.4	15.9	2135.6
0.0075	0.0001	0.0074	1131	−303	194	186 664	Type II: Al,S-oxide	108.5	14.7	92.2
0.0075	0.0001	0.0074	1115	−330	194	194 703	Type II: Al,Si-oxide	231.4	22.7	226
0.0075	0.0002	0.0073	1113	−359	199	149 486	Type II: Al-oxide	237.2	34.8	1560
0.0075	0.0001	0.0074	1127	−303	194	150 470	Type II: Ti,Al-oxide	119.4	52.8	1388
0.0075	0.0001	0.0074	1077	−370	194	167 624	Type II: Al,Ca,Ti-oxide	242	29.4	487.5
0.0075	0.0001	0.0074	1103	−343	197	259 434	Type II: Al-oxide	27.3	4.1	1838
0.0075	0	0.0075	1103	−368	197	345 840	Facet, 1 grain	61.7	34.3	208.7

TABLE 2—*LCF test results at* $R_\varepsilon = -1$.

Total Strain Range, $\Delta\varepsilon_t$-mm/mm	Inelastic Strain, mm/mm	Elastic Strain, mm/mm	Max Stress, MPa	Min Stress, MPa	Modulus, GPa	Failure Life, N_f	Failure Initiation Site	Max Length, μm	Width, μm	Minimum Depth, μm
0.01	0.0004	0.0096	966	−962	199	42 115	Pore	33.7	15.4	4.8
0.0095	0.0001	0.0094	897	−925	194	141 272	Facet, 2 grains	170.1	55.1	2269
0.0092	0.0001	0.0091	868	−898	194	161 486	Type I: Zr-oxide	31.4	18.6	3.9
0.0092	0.0002	0.009	881	−896	196	10 017	Pore	19.6	16.2	1.3
0.0092	0.0002	0.009	924	−900	203	473 868	Pores, cluster	42	10.5	41.2
0.0092	0.0002	0.009	912	−871	197	144 567	Type I, Zr-oxide	33	18.9	4.4
0.0092	0.0002	0.009	899	−901	200	134 510	Facet	51.9	26	28.8
0.0092	0.0001	0.0091	927	−860	194	77 140	Type I: Zr-oxide	80.7	47.7	3.9
0.009	0.0001	0.0089	843	−922	197	309 714	Facet, 1 grain	24.5	19.2	974
0.009	0	0.009	852	−905	196	438 466	Facet, 1 grain	32	20.4	1494
0.009	0.0001	0.0089	881	−840	194	253 263	Pores, clustered	36.6	3.9	1250
0.009	0.0001	0.0089	858	−871	193	446 557	Facet, 1 grain	50.5	18.6	1440
0.009	0	0.009	868	−872	197	324 410	Facets, 3 grains	177.6	47.1	2578.1
0.009	0.0001	0.0089	869	−855	194	325 270	Facet, 1 grain	59.8	38.8	1925.4
0.009	0	0.009	892	−867	194	299 422	Facets, 2 grains	57.7	43	327
0.009	0.0001	0.0089	893	−841	194	340 120	Pores, 2 adjoining	44.2	17.8	31
0.009	0.0001	0.0089	845	−858	192	183 923	Pores, clustered	40.4	14.4	23.1
0.009	0	0.009	865	−895	197	231 456	Facet, 1 grain	39.7	32.5	83.3
0.009	0.0001	0.0089	868	−911	200	255 906	Type II: Al-oxide	31.9	4.8	67.7
0.009	0.0001	0.0089	898	−916	203	199 260	Facet, 1 grain	66.4	44.5	1920
0.009	0	0.009	845	−926	197	217 992	Pores, 2 adjoining	43.3	17.6	11.6
0.009	0	0.009	880	−885	197	345 552	Facets, 2 grains	79.8	20	900.8
0.009	0	0.009	879	−936	203	297 171	Surface mark	21	3.4	0
0.009	0.0002	0.0088	871	−894	202	322 526	Surface mark	77	8.3	0
0.009	0.0001	0.0089	892	−881	197	202 310	Pore	21.6	21	48
0.009	0.0002	0.0088	890	−868	199	182 449	Type II: Al-oxide	107	26.4	18
0.009	0	0.009	872	−879	196	366 996	Facet	63.3	48	2269
0.009	0	0.009	882	−883	196	332 160	Type II: S-rich	23	5	1625

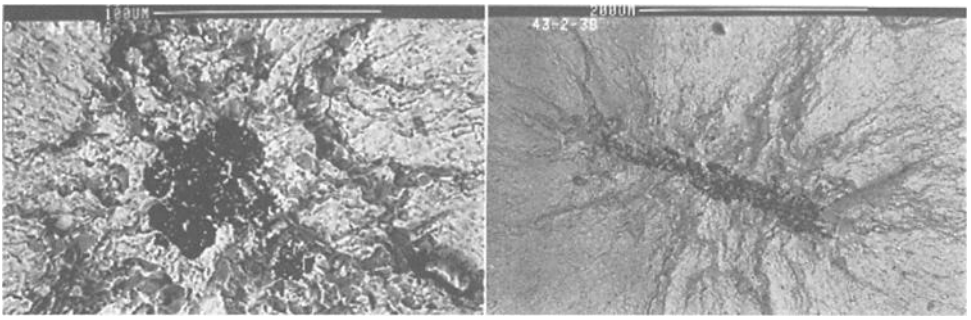


FIG. 3—*Typical failure initiation sites* $\Delta\varepsilon_t = 0.75\%$, $R_\varepsilon = 0$.

facet failures") or at pores, as shown in Fig. 4. The failures initiated internally in about 75% of all tests.

Evaluations of Response Variations Due to Processing/Location Variables

Three processing and location variables were assessed: disk forging and location within the forging cluster (*D*), specimen radial location (*R*), and specimen vertical location (*V*). *D* was treated as a continuous variable at two levels of No. 16 and No. 43, and *R* was treated as a continuous variable at three levels of 6.36, 7.95, and 9.54 cm (2.51, 3.13, and 3.76 in.). *V* was treated as a discrete variable at two levels of 1 (adjacent to the disk top surface) and −1 (adjacent to the bottom). Microstructure, strength, and life responses at each of the two prime test conditions were evaluated. Lives at the two test conditions are plotted versus the three processing/location variables of disk, radial distance in the disk, and vertical position in the disk, Fig. 5. No direct, simple dependencies are evident in these scatter plots. Assessments of the combined effects of the variables were then performed using multiple linear regression analyses, with logarithm of fatigue life, maximum failure defect length, and minimum failure defect length at each prime test condition as the dependent variables. Similar analyses were also performed using mean grain size, standard deviation of grain size, and maximum grain length as the dependent variables, as measured from the metallographic sections of specimens. The resulting derived regression equations that had statistically sig-

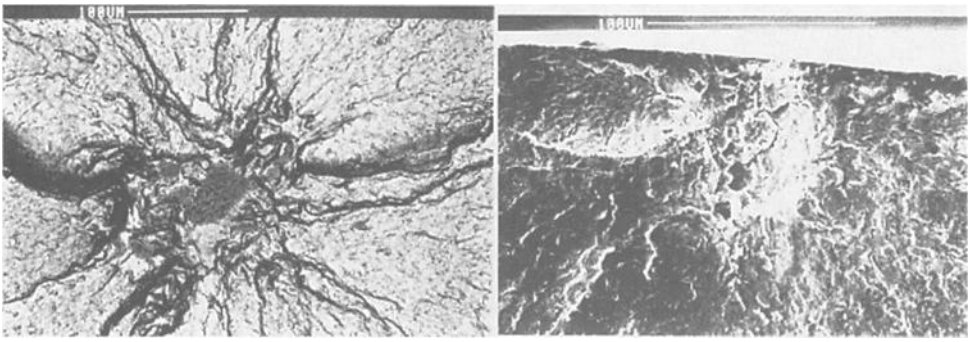


FIG. 4—*Typical failure initiation sites* $\Delta\varepsilon_t = 0.90\%$, $R_\varepsilon = -1$.

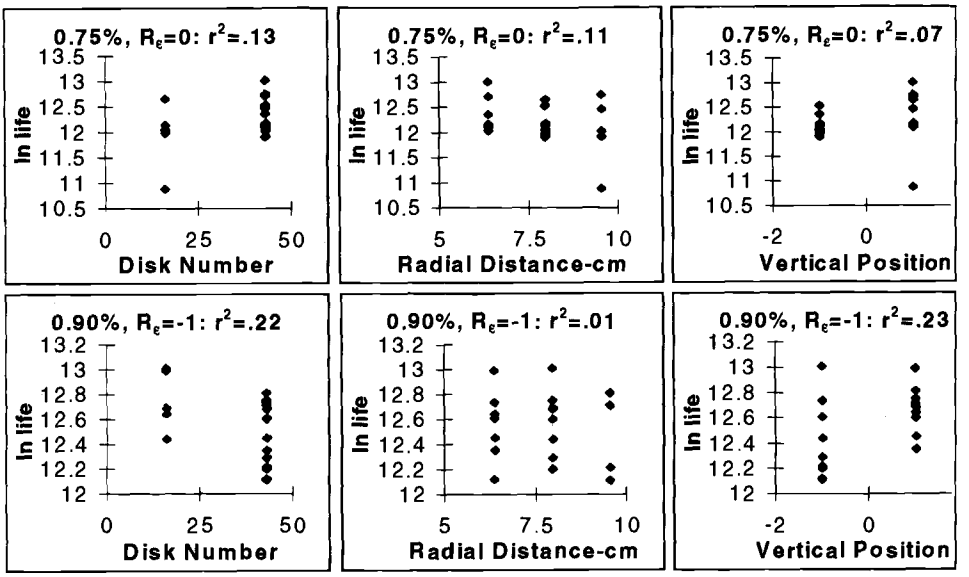


FIG. 5—*Scatter plots of lives versus processing/location variables.*

nificant dependencies ($r^2_{adj} > 0.25$) are summarized in Table 3. Positive and negative signs indicate the signs of the estimated regression constants for each significant independent variable. The dependent variables of ln life at each prime test condition, 0.1% yield strength (measured from the first fatigue cycle in tests at $R_\varepsilon = 0$), and mean grain size had statistically significant relationships with the *D, R, V* variables. In both of the prime test conditions, ln(life) increased with decreasing *R* and increasing $D \cdot R$. This may be somehow related to the finer grain size (increasing ASTM grain size number) observed with decreasing *R*. However, the analyses did not indicate this was due simply to increasing yield strength with finer grain size, as in a traditional Hall-Petch relationship. Instead, yield strength was shown to decrease with decreasing *R*. The physical significance of the $D \cdot R$ term is also unclear.

TABLE 3—*Summarized resulting disk process/location relationships.*

Test	$R_\varepsilon = 0$ $\Delta\varepsilon_t = 0.75\%$	$R_\varepsilon = -1$ $\Delta\varepsilon_t = 0.90\%$	$R_\varepsilon = 0$ $\Delta\varepsilon_t = 0.75\%$	
Response	Log N_f	Log N_f	$\sigma_{y0.1\%}$	Grain size
Data points	20	20	19	15
Model terms	5	6	5	4
Disk (*D*)	+	−		
Radius (*R*)	−	−	+	−
Vertical (*V*)	+		−	
$D \cdot R$	+	+		
$D \cdot V$		+	+	
$R \cdot V$		+		+
R^2			−	−
r^2_{adj}	0.319	0.458	0.534	0.444

The correlation coefficients $r^2 > 0.25$ for these regression equations imply that significant relationships exist between the responses and the processing/location variables. However, the correlation coefficients are relatively low ($r^2 < 0.65$), indicating these relationships have relatively poor predictive capabilities. Therefore, while recognizing that the processing/location variables do account for some of the scatter in the data, the data will be combined to make useful life predictions.

Assessments of Life Relationships and Distributions at Each Prime Test Condition

Plots of estimated cumulative probability versus life are shown in Fig. 6 for each prime test condition. Normally distributed data should lie along a straight line at a constant slope in these probability plots of Fig. 6. Three-parameter Weibull distribution curves were also used to model the probability of life $Pr(N)$ using the equation [7]:

$$Pr(N) = 1 - \exp[-\{(N - a)/b\}^m]$$

where a, b, and m are empirical constants fit by regression. Weibull-distributed data should lie along a straight line when the Weibull function of estimated cumulative probability:

$$\ln(\ln(1 - Pr(N))^{-1})$$

is plotted versus $\ln(N_f)$ as in Fig. 6. An alternative approach is to transform the life data into a more normally distributed parameter using a transformation function. Probability plots of a logarithm transformation of life [6], $\log(N_f)$, are shown in Fig. 7.

Selection among these different approaches of treating life frequency distributions was based in part of the constancy of slope (linearity) of the probability plots. The abilities of each approach in generating robust estimates of mean and minimum lives were also considered. Mean and minimum lives needed to be assessed using a consistent approach that was not overly sensitive to single data points. Estimates of mean and minimum (Pr = 0.00135 = "-3σ") lives were calculated for each prime test condition using each of the

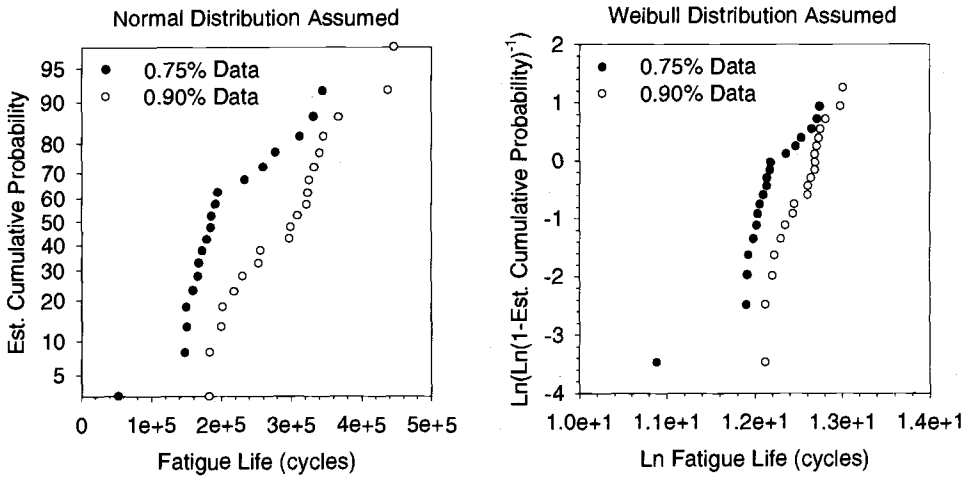


FIG. 6—*Probability plots using normal and Weibull distribution assumptions.*

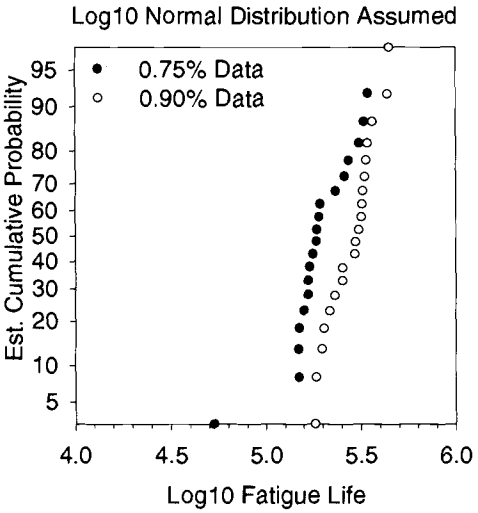


FIG. 7—*Probability plot using log normal distribution assumption.*

frequency distribution assumptions described above. In order to assess the sensitivity of the approach to single data points, mean and minimum lives for each prime condition were calculated using all 20 tests and then using 19 tests, after omitting the lowest life test.

The results are compared in Table 4 and Fig. 8. An assumption of normally distributed lives produced reasonable estimates of mean life. However, the estimates of minimum lives at a probability $Pr = 0.00135$ were negative and invalid. This was a consequence of the non-linear probability curves. Fitting Weibull equations to model the life distributions produced more meaningful estimates of both mean and minimum lives for each prime test condition. However, comparison of Weibull curve minimum life estimates with the lowest life test for each prime condition indicated this approach was highly sensitive to the lowest life test and was not always lower than the observed data. Estimated minimum life tracked unreasonably close to the lowest life test. This response was illustrated by removing the lowest life test for each prime data set.

The log N_f transformation of the life data was selected for subsequent evaluations. This transformation produced more linear cumulative probability curves. The mean and minimum life estimates using the transformed data showed a more reasonable influence of the lowest life test than the other approaches, and the minimum life estimates were always lower than the observed data. For each prime test condition, the estimated mean and minimum lives

TABLE 4—*Comparison of minimum life estimates for different distribution assumptions.*

Prime Test Condition	$\Delta\varepsilon_t = 0.75\%$, $R_\varepsilon = 0$		$\Delta\varepsilon_t = 0.90\%$, $R_\varepsilon = -1$	
Data points	20	19[1]	20	19[1]
Normal	−92 821	−64 671	27 364	40 018
Weibull	64 760	145 076	157 945	160 486
Log normal	42 774	67 738	112 143	119 643
Lowest life	53 269	148 743	182 449	183 923

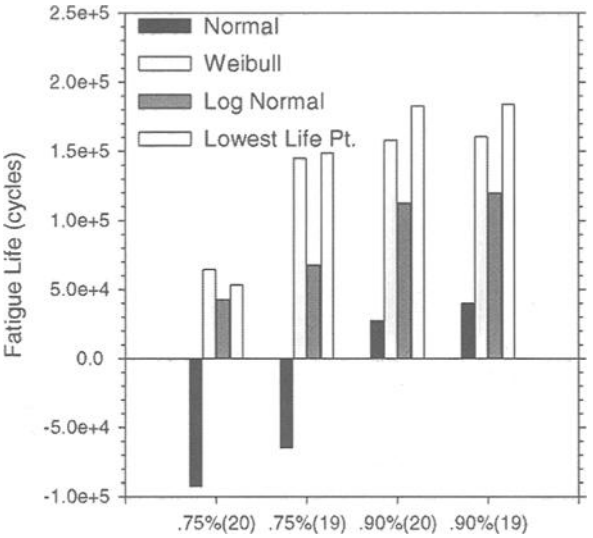


FIG. 8—*Minimum life estimates using the different life distribution assumptions.*

moderately increased after removal of the lowest life test. Based on these findings, the log N_f transformation was selected for further evaluations.

Evaluation of All Available Data in General Stress/Strain-Life Equations

All available test data on this material was now combined for a more general life equation. Allison Engine Company had previously run LCF tests on specimens from the same group of disks at higher strain ranges with $R_\varepsilon = 0$ and -1, and also load-controlled high-cycle fatigue (HCF) tests at $R_\sigma = 0$ and -1. All data were now combined to produce a combined life relationship.

An evaluation was first performed on all available LCF data, where the test variables $\Delta\varepsilon_t$ and R_ε were consistently held constant during testing. A total of 68 LCF tests were analyzed. Stepwise multiple linear regression and residual analyses indicated the equation:

$$\log N_f = C_o + C_1 R_\varepsilon + C_2/\Delta\varepsilon_t^3 + C_3 R_\varepsilon/\Delta\varepsilon_t^3$$

was suitable for fitting the combined LCF data ($r^2_{adj} = 0.847$).

All available LCF and HCF data were now analyzed together. Recall that tests at a given $\Delta\varepsilon_t$ performed with $R_\varepsilon = 0$ had different mean and maximum strains and stresses than those for $R_\varepsilon = -1$ (Tables 1, 2). In a like manner, HCF tests at a given $\Delta\sigma$ performed with $R_\sigma = 0$ had different mean and maximum strains and stresses than those for $R_\sigma = -1$. Stepwise multiple linear regression was performed to find the most significant variables among $\Delta\varepsilon_t$, R_ε, $\Delta\sigma$, R_σ, σ_{max}, and σ_{mean} which influenced log life. In the LCF test cases, $\Delta\varepsilon_t$, R_ε, σ_{max}, and σ_{mean} were taken at half of cyclic life. In the HCF test cases, $\Delta\varepsilon_t$ was approximated as $\Delta\sigma/E$ with $E = 194.1$ GPa (28.15×10^6 psi), as these tests were nominally elastic with strain not monitored. The independent variables $\Delta\varepsilon_t$ and σ_{max} were found to be the most significant parameters influencing log life. Multiple linear regression and residual analyses indicated an equation of the form:

$$\log N_f = C_o + C_1 \log \Delta\varepsilon_t + C_2 \log \sigma_{max} + C_2 \log \Delta\varepsilon_t \log \sigma_{max}$$

was suitable for fitting the combined data ($r^2_{adj} = 0.841$).

Three analytical approaches combining strain and stress effects were then assessed. A simple Smith-Watson-Topper effective stress parameter [*8*] was employed using the equation:

$$\sigma_{SWT} = (\sigma_{max}\, \Delta\varepsilon_t E/2)^{1/2}$$

A Walker equivalent stress parameter [*9*] was also used, with the equation:

$$\sigma_W = \sigma_{max}\, (\Delta\varepsilon_t E/\sigma_{max})^m$$

where m is an additional empirical material constant that must be regressed using the life data. Generalized equations were fit by least squares multiple linear regression combined with residual analyses to the combined data sets using log N_f transformed lives versus σ_{SWT} and σ_W. A value of $m = 0.53$ gave the best fit of σ_W to the life data. Fatigue life has often been related to applied strains and stresses using a power law of the general form, $N_f = C_o$ $(\varepsilon, \sigma)^{C1}$. So logarithms and powers of each of these variables were also assessed using equations of the forms:

$$\log N_f = C_o + C_1 \log \sigma \text{ and } \log N_f = C_o + C_1 \sigma^{C2}$$

For both σ_{SWT} and σ_W, equations of the form:

$$\log N_f = C_o + C_1 \log \sigma$$

were found to be most suitable.

A strain-based Basquin-Coffin-Manson type equation was also applied [*10*] in which the total strain range was separated into elastic and plastic components:

$$\Delta\varepsilon_{corr} = \Delta\varepsilon_{el,corr} + \Delta\varepsilon_{pl} = B(N_f)^b + C(N_f)^c$$

A correction similar to the Walker approach was used to modify the elastic strain range for stress ratio effects:

$$\Delta\varepsilon_{el,corr} = \frac{\Delta\sigma}{E}\,(2 + R_\sigma)^m$$

This equation reduces to $\Delta\sigma/E$ for fully reversed experiments ($R = -1$) and increases the equivalent elastic strain range for larger stress ratios. The resulting strain-life equation was fit using a linear regression approach where the logarithms of the elastic strain range and plastic strain range were each separately fit to log life. As the plastic strain range is a calculated value:

$$\Delta\varepsilon_{pl} = \Delta\varepsilon_t - \frac{\Delta\sigma}{E}$$

and is vanishingly small (at or near the resolution threshold of the strain measurement in-

TABLE 5—*Comparison of life estimates using general life equations.*

Input Data: Gen. Equation Terms	rms Stan. Dev	r^2_{adj}	$\Delta\varepsilon_t$ = 0.75%, R_ε = 0 Mean Life	$\Delta\varepsilon_t$ = 0.75%, R_ε = 0 Min Life	$\Delta\varepsilon_t$ = 0.90%, R_ε = −1 Mean Life	$\Delta\varepsilon_t$ = 0.90%, R_ε = −1 Min Life
n = 20, log normal life	0.193	...	198 099	42 774	...	...
n = 20, log normal life	0.117	...	...	42 774	283 985	112 143
n = 68: $1/\Delta\varepsilon_t^3$, R_ε, $R_\varepsilon/\Delta\varepsilon_t^3$	0.243	0.847	199 883	33 540	256 965	43 451
n = 86: log $\Delta\varepsilon_t$, log σ_{max}, log $\Delta\varepsilon_t$*log σ_{max}	0.3203	0.841	135 981	13 508	203 728	20 211
n = 86: log σ_{SWT}	0.3313	0.829	128 271	11 955	184 963	17 252
n = 86: log σ_{Walker}	0.3298	0.831	139 449	13 142	173 517	16 327
n = 86: log $\Delta\varepsilon_{BCM}$	0.3460	0.816	143 785	13 172	215 524	19 744
n = 67[a]: $1/\Delta\varepsilon_t^3$, R_ε, $R_\varepsilon/\Delta\varepsilon_t^3$	0.19	0.903	199 883	49 342	279 428	69 354
n = 85[a]: log $\Delta\varepsilon_t$, log σ_{max}, log $\Delta\varepsilon_t$*log σ_{max}	0.2912	0.866	136 888	16 762	219 070	26 775
n = 85[a]: log σ_{SWT}	0.3065	0.851	132 602	14 752	191 027	21 267
n = 85[a]: log σ_{Walker}	0.3062	0.852	144 045	16 065	178 738	19 943
n = 85[a]: log $\Delta\varepsilon_{BCM}$	0.3191	0.841	143 301	15 810	215 524	23 778

[a] After removing low life outlier.

strumentation) for many of the experiments, only the highest strain range experiments were used to compute the constants C and c.

The resulting four generalized life equations are compared in Table 5 with the corresponding root mean square standard deviations and correlation coefficients. Actual lives are compared to lives estimated using the log $N_f = f(\log \Delta\varepsilon_t, \log \sigma_{max})$ equation in Fig. 9. These

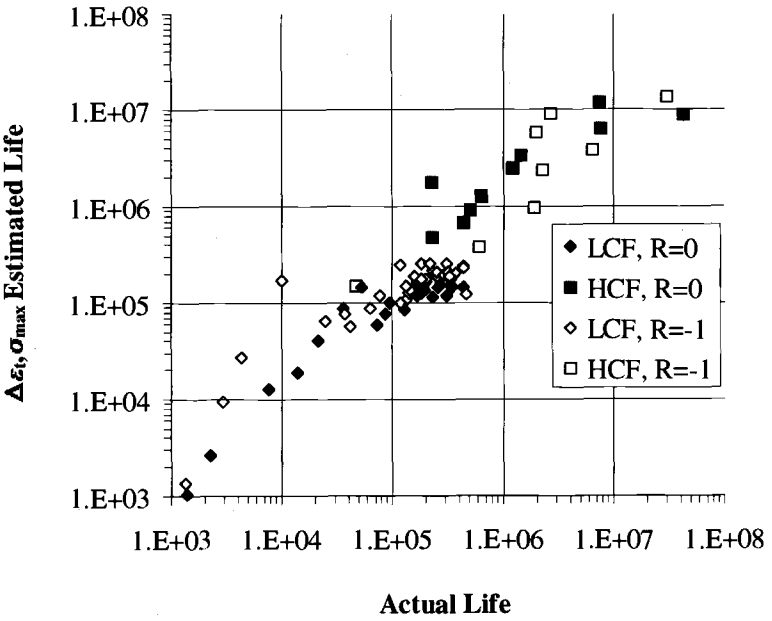


FIG. 9—*Comparison of estimated and actual lives using general equations.*

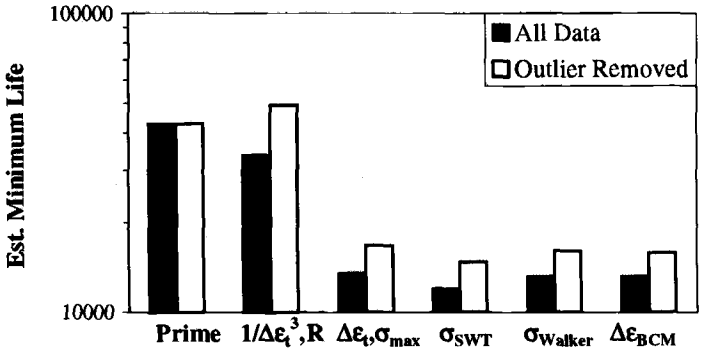


FIG. 10—*Comparison of minimum life estimates using general equations at* $\Delta\varepsilon_t = 0.75\%$, $R_\varepsilon = 0$.

generalized life equations are more versatile for estimating lives at various stress/strain conditions, but they introduced more variability than that previously calculated at each of the prime test conditions. The standard deviations calculated previously using data generated only at each prime test condition with the log N_f life transformation are included for comparison in Table 5. At each condition, the equations' rms standard deviations were 25 to 60% higher than those previously calculated using the prime data sets. The additional HCF data appeared to have more scatter in life, as should be expected, and probably contributed to the increased standard deviations. Another inherent source of this additional variability could be remnant effects on life due to differences in stresses and strains that were not sufficiently compensated with the $\Delta\varepsilon$ and $\Delta\sigma$ variables using the combined approaches selected. Application of other combined stress/strain compensation approaches might reduce such variability. However, a major source of the additional variability of the combined data was provided by a low life outlier LCF test at $\Delta\varepsilon_t = 0.92\%$ having a life of only 10 017 cycles, as will be discussed below.

Minimum life estimates of the generalized life equations were lower and more conservative than those calculated using data generated only at the prime test conditions. Mean and minimum life estimates of the generalized life equations are compared at each of the prime test conditions to those calculated previously using only data generated at these conditions

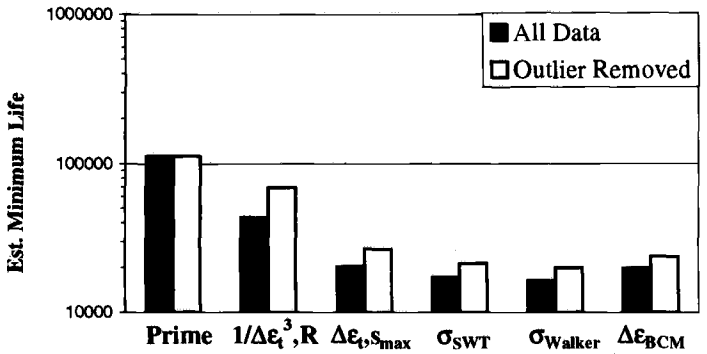


FIG. 11—*Comparison of minimum life estimates using general equations at* $\Delta\varepsilon_t = 0.90\%$, $R_\varepsilon = -1$.

(see Table 5). Mean life estimates of the life equations are similar to those previously calculated using the prime data sets. Minimum life estimates of the generalized life equations were lower than those previously calculated by 38 to 73%.

Additional evaluations were performed to assess the sensitivities of the generalized equations to outlier data points. Regression analyses indicated an LCF test at $\Delta\varepsilon_t = 0.92\%$ having a life of only 10 017 cycles was a low life outlier, with a large influence on the regressions. This data point was removed, and the generalized life equations were again regressed with the combined data set. The resulting life estimates are also included (see Table 5). For both equations, standard deviations of the combined data set decreased substantially. Mean and minimum life estimates consequently increased, with larger increases in the $R_\varepsilon = -1$ life estimates. This indicated that low life outlier data points could influence general life equations and minimum life estimates.

Defect Initiation Sites and Their Influence on Life Estimates

The observed failure initiation sites in this powder material ranked by occurrence were Type II inclusions, faceted grain failures, and pores. While faceted grains can be considered inherent features of the microstructure, the Type II inclusions and pores are clearly undesirable defects that might reduce the fatigue lives by orders of magnitudes. Therefore, further evaluations of failures initiating at these undesirable defects were conducted briefly. The maximum length and minimum depth of these defects initiating failure were measured for every specimen tested in the two prime test conditions. Scatter plots of life versus defect length and depth are shown for each test condition, Fig. 12. No consistent or significant trends were observed using these chosen simple defect parameters. However, other defect parameters incorporating projected area, aspect ratio, and orientation could possibly have more significant relationships to life.

The proportion of cyclic life taken up in initiating cracks at these defects was then estimated for these cases. The number of fatigue cycles necessary to grow cracks initiating from the defects to final fracture was calculated using a fracture mechanics framework. Actual aspect ratios of the inclusions or pores initiating the crack as well as the corresponding distance to the free surface were measured from the fracture surfaces and used in the propagation life calculations. The stress intensity factor solution of an internal elliptical crack near a free surface was employed in the crack propagation code FASTRAN II [*11*], developed at NASA Langley Research Center. But as the crack reached the free surface, the stress intensity factor solution was switched to an elliptical crack in a round specimen, and the analysis was continued until specimen fracture. The applied remote stress ranges assumed in the calculations were the experimentally measured stress ranges at half of the cyclic life. The crack propagation law employed in the analysis used the equation:

$$da/dn = 9.9 \times 10^{-9} (\Delta K_{\text{eff}})^{2.1}$$

based on data generated from compact tension specimens of this material tested at 1000°F.

Since the stress intensity factor ranges (ΔK) incorporate all the major geometric features of the defects as well as locations, the total lives were correlated with the initial ΔK, at a_0 (see Fig. 13). A clear trend of decreasing total cyclic life is observed with increasing ΔK, but with a large scatter in the data. The propagation lives were calculated and plotted in Fig. 14 as a function of the initial ΔK. While the propagation lives were estimated to be between 10 000 to 30 000 cycles in these tests, the total lives were in the range of 10^5 to 10^6 cycles. As a refinement, only the initiation lives (total life − propagation life) were plotted as a

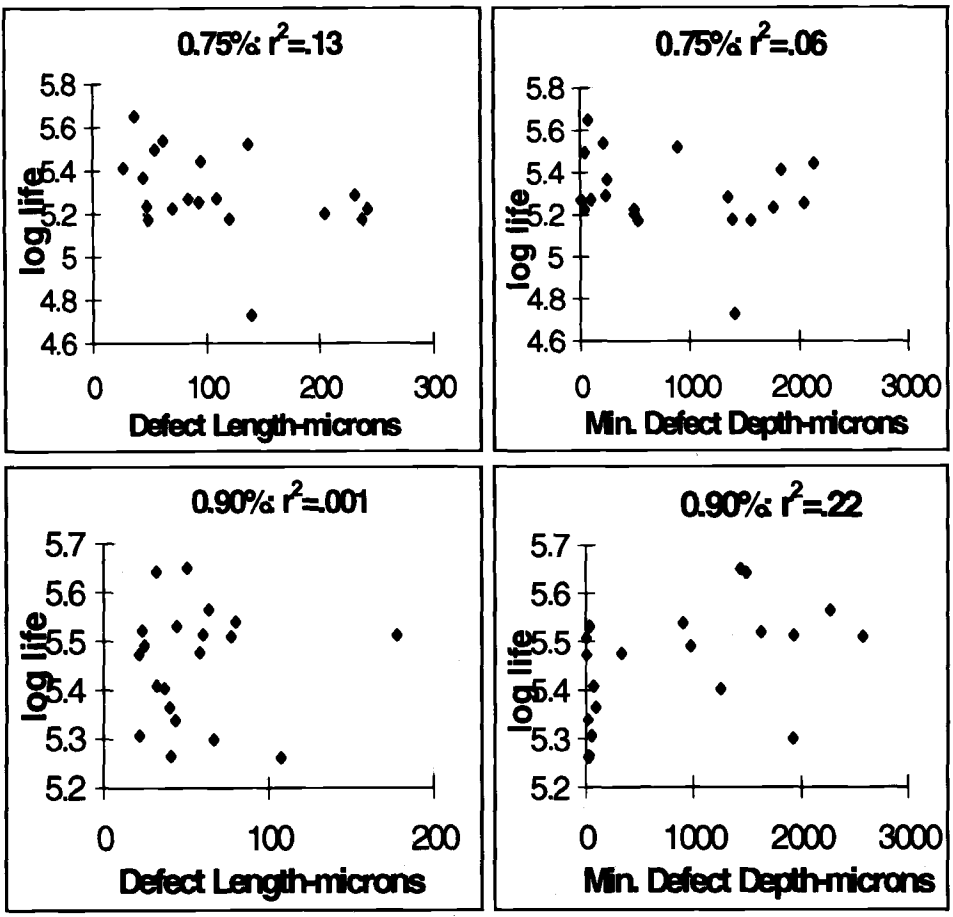


FIG. 12—*Scatter plots of life versus failure defect size and depth.*

function of the initial ΔK (see Fig. 15), with still no great improvement in the scatter. The percent of the calculated propagation lives was only 5 to 10% of the total lives (see Fig. 16), except for the two outliers where the propagation lives are 20 and 40% for an inclusion and a pore, respectively. Hence, no pronounced reduction in the scatter was observed with only the initiation lives. Refinements using actual crack growth data generated on this material in vacuum for the internal crack propagation phase and in air for the subsequent surface-connected crack growth could change the crack propagation life estimates. Furthermore, using crack propagation laws generated from highly constrained specimens such as the K_b specimen [*12*] simulating the actual condition that the defects are subjected to might also improve the estimated propagation lives. However, it is clear that these defects can withstand a large number of cycles before initiating cracks in the prime, long-life test conditions evaluated. Predictions of overall life in this material could benefit from determining the initiation lives associated with these defects, as functions of defect size, location, and test conditions.

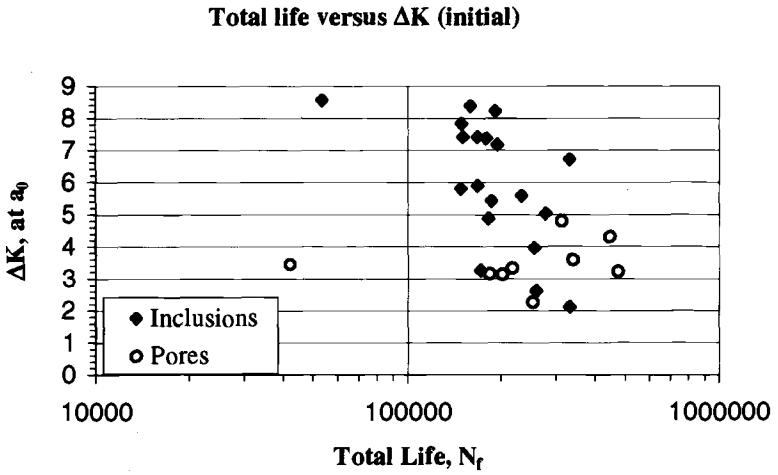


FIG. 13—*Comparison of life and initial stress intensity at failure initiation points.*

Summary of Results and Conclusions

Summary of Results

Fatigue tests of powder metallurgy U720 were performed at 538°C (1000°F) principally using two prime test conditions with multiple replicates. Statistical, microstructural, and failure analyses were performed to assess life response and relationships.

1. Several significant property correlations as functions of processing/location variables were identified; however, the correlations had poor predictive capabilities.
2. Data were successfully combined at each of the two prime test conditions for life distribution assessments in spite of the processing/location dependencies.

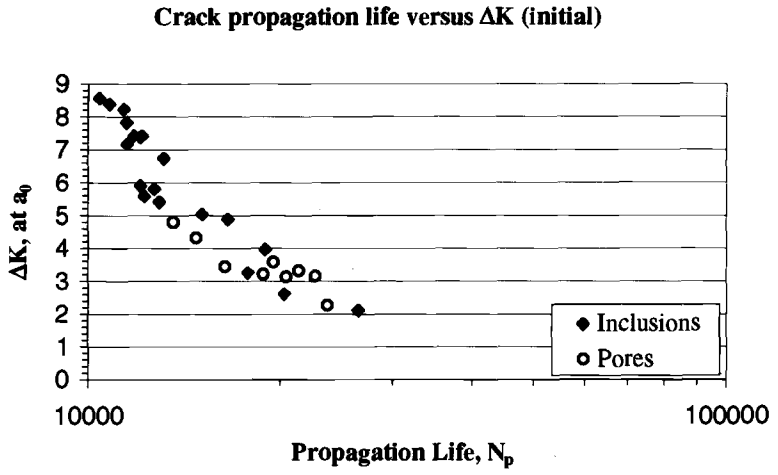


FIG. 14—*Calculated crack propagation life versus initial stress intensity at failure initiation points.*

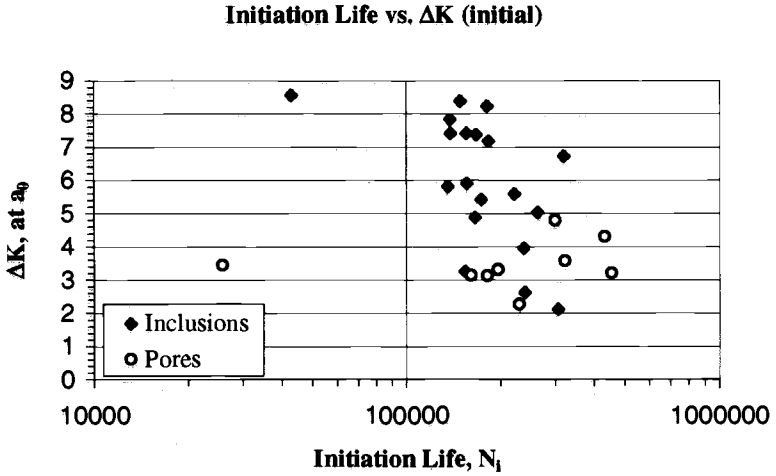


FIG. 15—*Calculated crack initiation life versus initial stress intensity at failure initiation points.*

3. Predominant failure initiation sites varied between the two prime test conditions; however, the data were combined after using a logarithmic life transformation to produce generalized life equations including both LCF and HCF test results.

4. The generalized equations fitted to the combined data gave lower, more conservative minimum life estimates than those generated only from data at the prime test conditions.

5. Crack propagation life calculations using fractographic measurements indicated near 90% of cyclic life were required to initiate cracks at inclusions or pores in the prime test conditions.

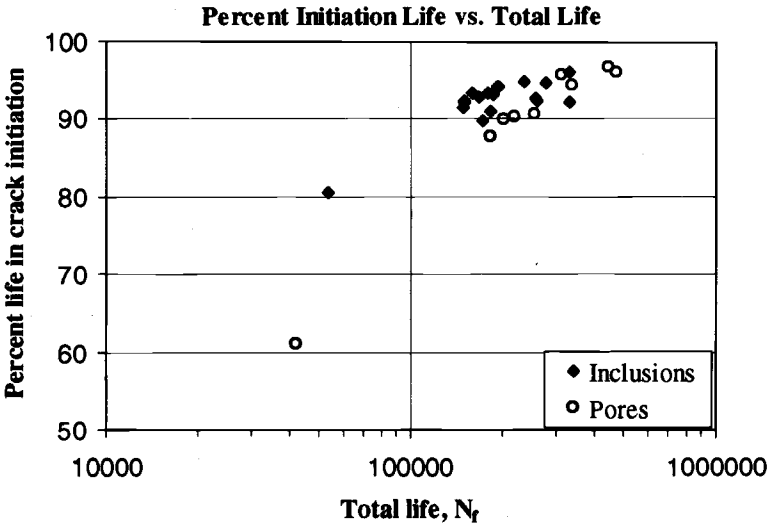


FIG. 16—*Calculated percent crack initiation life versus total life.*

Conclusions

1. Disk alloy processing/location variables can influence fatigue lives in certain conditions, and their influences can account for some of the statistical scatter observed in life.

2. Fatigue life for these conditions can be treated as normally distributed, after appropriate transformations such as log life.

3. Data generated for these conditions at different R ratios and test control modes can be combined using a generalized approach employing total strain range and maximum stress, using either direct multiple linear regression equations or combined stress-strain parameters that account for different strain ranges and maximum stresses.

4. Generalized life equations using the logarithm of life can be generated to allow life estimation in other stress and strain conditions, which give reasonable, conservative mean and minimum life estimates.

5. General improvements in the fatigue life of this material for these conditions would require improvements in the control of Type II inclusions, pores, and grain-size variability. An understanding of the crack initiation characteristics of these defects could also allow more accurate life predictions of the current material.

Acknowledgments

The authors wish to acknowledge the extensive statistical assistance provided by Dennis Keller of RealWorld Quality Systems.

References

[1] Chang, D. R., Kruger, D. D., and Sprague, R. A. in *Superalloys 1984,* TMS-AIME, Warrendale, PA, 1984, pp. 245–252.

[2] Kissinger, R. D. in *Superalloys 1996.* TMS-AIME, Warrendale, PA, 1996, pp. 687–696.

[3] Domas, P. A., "Elevated Temperature Component Fatigue Robustness—An Holistic Approach," *AGARD-CP-569,* AGARD, March 1996.

[4] Huron, E. S. and Roth, P. G. in *Superalloys 1996.* TMS-AIME, Warrendale, PA, 1996, pp. 359–368.

[5] Green, K. A., Lemsky, J. A., and Gasior, R. M. in *Superalloys 1996,* TMS-AIME, Warrendale, PA, 1996, pp. 697–704.

[6] Sinclair, G. M. and Dolan, T. J., "Effect of Stress Amplitude on Statistical Variability in Fatigue Life of 75S-T6 Aluminum Alloy," *Transactions of the ASME,* Vol. 19, July 1953, pp. 867–872.

[7] Weibull, W., "A Statistical Distribution Function of Wide Applicability," *Journal of Applied Mechanics,* 1951.

[8] Smith, K. N., Watson, P., and Topper, T. H., "A Stress-Strain Function for the Fatigue of Metals," *Journal of Materials,* Vol. 5, No. 4, December 1970, pp. 767–778.

[9] Walker, K., "The Effect of Stress Ratio During Crack Propagation and Fatigue for 2024-T3 and 7075-T6 Aluminum," *Effects of Environment and Complex Load History on Fatigue Life, ASTM STP 642,* American Society for Testing and Materials, West Conshohocken, PA, 1970, pp. 1–14.

[10] Manson, S. S., *Thermal Stress and Low-cycle Fatigue,* McGraw-Hill, New York, 1966, p. 141.

[11] Newman, J. C., *FASTRAN-II—A Fatigue Crack Growth Structural Analysis Program, NASA TM-104159,* February 1992.

[12] Vanstone, R. H. and Richardson, T. L., "Potential-Drop Monitoring of Cracks in Surface-Flawed Specimens," *Automated Test Methods for Fracture and Fatigue Crack Growth, ASTM STP 877,* American Society for Testing and Materials, West Conshohocken, PA, 1985, pp. 148–166.

Katsuhiko Kumagai,[1] *Haruo Nakamura,*[2] *and Hideo Kobayashi*[3]

Computer Aided Nondestructive Evaluation Method of Welding Residual Stresses by Removing Reinforcement of Weld (Proposal of a New Concept and Its Verification)

REFERENCE: Kumagai, K., Nakamura, H., and Kobayashi, H., **"Computer Aided Nondestructive Evaluation Method of Welding Residual Stresses by Removing Reinforcement of Weld (Proposal of a New Concept and Its Verification),"** *Fatigue and Fracture Mechanics: 31st Volume, ASTM STP 1389,* G. R. Halford and J. P. Gallagher, Eds., American Society for Testing and Materials, West Conshohocken, PA, 2000, pp. 128–142.

ABSTRACT: A new method (the bead flush method) is proposed to estimate welding residual stresses non-destructively. First, the reinforcement of the weld is removed. Then from released strains on the surface due to removal, eigenstrain distributions are estimated by an inverse analysis. Finally, residual stresses are determined by the finite element method (FEM) using estimated eigenstrains as boundary conditions.

Numerical simulations were conducted to develop a sophisticated procedure. It is shown by numerical simulations that the proposed method gives reasonably good predictions of residual stress. Also, the validity of the proposed method was evaluated experimentally for a butt-welded plate joint. Based on this work, future problems to overcome are discussed.

KEYWORDS: welding residual stresses, eigenstrain, reinforcement of weld, non-destructive evaluation, inverse problem

In order to assess the structural integrity of aged-welded structures under long-term service, non-destructive evaluation of welding residual stresses is required. During the welding process, non-uniform eigenstrains [*1*] (or inherent strains) defined as inelastic strains such as thermal and plastic strains, are left near the weld bead and cause the residual stresses. In this situation, eigenstrains are the cause and residual stresses are the result. Thus, experimental evaluation methods can be classified as forward and inverse (or backward) methods. The forward methods measure the residual stresses directly like the X-ray diffraction methods, the ultrasonic techniques, the hole-drilling strain-gage method (ASTM Standard Test Method for Determining Residual Stresses by the Hole-Drilling Strain-Gage Method, E 837-95), the dissection methods, and the layer-removal methods. In these methods, only one value or values at a specific location concerned can be evaluated. Accordingly, multiple measurements are required to infer the values at critical locations where a maximum stress

[1] Graduate student, Department of Mechanical Sciences and Engineering, Tokyo Institute of Technology, 2-12-1, Ookayama, Meguro-ku, Tokyo 152-8552, Japan.

[2] Professor, Department of Mechanical Sciences and Engineering, Tokyo Institute of Technology, 2-12-1, Ookayama, Meguro-ku, Tokyo 152-8552, Japan.

[3] Professor, Department of Mechanical Sciences and Engineering, Tokyo Institute of Technology, 2-12-1, Ookayama, Meguro-ku, Tokyo 152-8552, Japan.

Copyright© 2000 by ASTM International www.astm.org

exists or undesirable initiation and/or propagation of a crack may be anticipated due to fatigue or stress corrosion cracking.

On the other hand, the inverse method measures eigenstrains as a source of residual stresses by the dissection method [*2*]. Its analytical process determining eigenstrains from released strains after dissection is called the inverse problem where many applications to strength evaluation have been attempted in recent years [Ref *3*]. Three-dimensional residual stresses in the whole area are evaluated by this method using any commercial finite element method (FEM) software. The method uses eigenstrains as mechanical boundary conditions.

However, its dissection process has prevented us from applying that method to aged structures where destructive techniques are not allowed. To overcome this disadvantage, authors have developed a new method (the bead flush method) where only the reinforcement of the weld is removed instead of dissection of the whole body. The method developed has been studied by using a two-dimensional simulation [*4*]. The toe of weld is regarded as the critical or harmful location because it tends to become a crack starter. However, it is usually left untreated mainly for economic reasons. So, removal of reinforcement or elimination of the toe should rather be regarded as preferable from a viewpoint of the structural integrity. In this sense, this method can be regarded as "the non-destructive method" intrinsically.

Recently, further development has been attempted and a new concept has been proposed to evaluate three-dimensional welding residual stresses non-destructively [*5*]. The proposed method has the following characteristics:

1. It is almost nondestructive.
2. Stresses in the whole body may be evaluated (although under restricted conditions).
3. As residual stress is estimated based on experimentally measured strain data, it has a verification characteristic that is often required in the assessment of structural integrity. So, it would be superior to the genuine thermo-elastic-plastic simulations of welding.
4. The residual stress data are produced in the form readily applicable to the structural designs and the assessment of structural integrity by the FEM because they are calculated by using the same FEM program in the final stage.

In this study, its numerical background is reviewed and its applicability is examined by three-dimensional numerical simulations. Then, its utility is shown based on experiments for a butt-welded plate. Based on this, future problems to be overcome are discussed.

Analytical Background

During the welding process, non-uniform eigenstrains are left near the weld bead. When non-uniform eigenstrains are imposed on a structural component, it will deform elastically until an equilibrium condition is attained during which welding residual stresses are generated. In some guidebooks concerning the FEM analysis, eigenstrains are called "initial strains" that don't generate stresses solely. In this sense, if an eigenstrain distribution is known, a possible equilibrium condition, that is, the residual stresses in any location, can be determined easily by a simple elastic FEM analysis by imposing eigenstrains as boundary conditions.

A concept of a proposed method (the bead flush method) is shown in Fig. 1 [*5*]. As can be seen, the reinforcement of weld is removed on one side surface first. From release strains during removal, eigenstrain distributions are determined by the inverse analysis. Then, residual stresses are estimated by a commercial FEM code by distributing determined eigenstrains as initial strains. Throughout these analyses, the material properties required are the elastic constants at room temperature. No further information such as temperature depend-

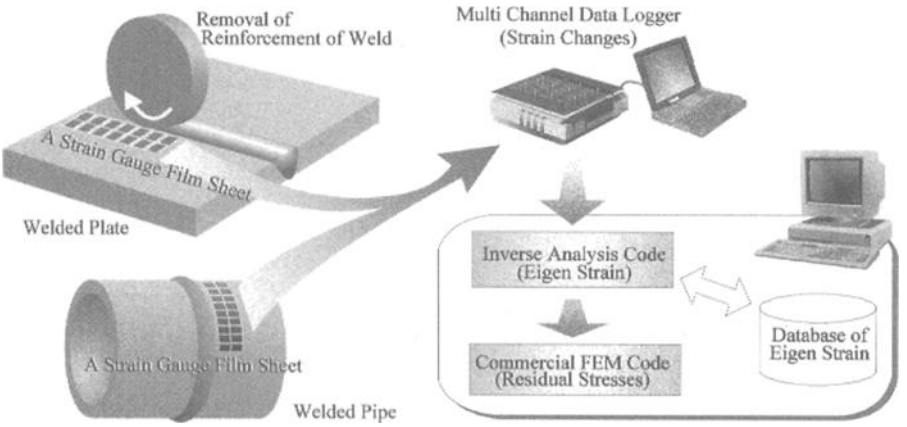


FIG. 1—*Concept of the bead flush method.*

ence of the constitutive equations for both base and deposited metals, the thermal expansion coefficients, or the transformation temperature as a function of cooling rate is necessary in contrast with the complicated metallo-thermo-elasto-plastic simulation of welding processes.

The three-dimensional eigenstrain distributions within specific regions are approximated by an eigenstrain vector $\{\varepsilon^*\}$ with q unknown parameters. Then, the relation between $\{\varepsilon^*\}$ and an elastic strain vector $\{\varepsilon\}$ within concerned elements induced by $\{\varepsilon^*\}$ is given as follows [*4*]

$$\{\varepsilon\} = [H]\ \{\varepsilon^*\} \tag{1}$$

where $[H]$ = the so-called elastic response matrix derived using the elastic FEM analysis.

The j-th column of $[H]$ is defined as the released strain due to removal under the existence of unit eigenstrain at the j-th component alone in $\{\varepsilon^*\}$ shown below.

$$\{{}_u\varepsilon^*\}_j = \{0, \cdots, \varepsilon^* = 1, 0, \cdots, 0\}^T \tag{2}$$

From Eq 1, elastic strain before and after removal of the reinforcement of the weld can be given as follows

$$\{\varepsilon_b\} = [H_b]\ \{\varepsilon_b^*\} \tag{3}$$

$$\{\varepsilon_a\} = [H_a]\ \{\varepsilon_a^*\} \tag{4}$$

where subscripts of b and a denote before and after removal, respectively.

Since the eigenstrain distribution is unchanged ($\{\varepsilon_b^*\} = \{\varepsilon_a^*\} = \{\varepsilon^*\}$) unless additional plastic or thermal strains are generated throughout the removal process, a released strain vector $\{\Delta\varepsilon\}$ within concerned elements is given as follows

$$\{\Delta\varepsilon\} = \{\varepsilon_a\} - \{\varepsilon_b\} = [H_a]\{\varepsilon_a^*\} - [H_b]\{\varepsilon_b^*\}$$

$$= ([H_a] - [H_b])\{\varepsilon^*\} = [H_{ab}]\{\varepsilon^*\} \quad (5)$$

$$[H_{ab}] = [H_a] - [H_b]$$

If k components ($k > q$) of released strain $\{\Delta\varepsilon\}$, $\{{}_m\Delta\varepsilon\}$, are measured experimentally, the most probable value of the eigenstrain vector $\{{}_p\varepsilon^*\}$ can be given as

$$\{{}_p\varepsilon^*\} = [H_{ab}]^-\{{}_m\Delta\varepsilon\} \quad (6)$$

where $[H_{ab}]^-$ = the generalized inverse matrix of $[H_{ab}]$.

By imposing the determined eigenstrains as initial strains to an FEM model either before or after removal, residual stresses at any location can be obtained easily by the elastic analysis.

Numerical Simulation

Numerical simulations were conducted to develop a sophisticated procedure to satisfy the following points:

1. Firstly, accurate residual stresses can be evaluated if there are no experimental errors.
2. Under existence of possible experimental errors, a reasonably accurate solution can be evaluated.

Analytical Model

Numerical simulations by FEM were conducted for a butt-welded plate. Generally speaking, the different order of welding passes in multi-pass welding can bring a different residual stress distribution because eigenstrain distribution in the thickness direction differs in each case. For simplicity of analysis, however, the eigenstrains were assumed to be constant in the thickness direction as is the case with single pass welding of a relatively thin plate. The FEM model used is shown in Fig. 2. A total of 1764 elements with eight nodes was used. The minimum element size in the y direction of 2 mm was determined so as to fit the size of strain gages used in experiments. A Young's modulus of $2.00 \times 10.^5$ MPa and a Poisson's ratio of 0.265 was used. It is noted that no further properties are necessary throughout this analysis as mentioned earlier. Possible small differences in elastic constants between the base metal and HAZ (heat-affected zone) were neglected.

At present, only limited information is available regarding eigenstrain distributions of welded plate. One of the major reasons should be attributed to the fact that eigenstrain data have in the past been regarded as not useful in contrast with residual stress data for the structural design. So, eigenstrain distributions were assumed in this study as shown in Fig. 3 based on Refs *6* and *7*. It indicates that the distribution in bead direction is regarded as constant as in automatic welding.

As will be shown later, an eigenstrain component in x direction, ε^*_x, plays an important role on residual stresses and the contributions of other components, ε^*_y and ε^*_z, are neglected. So, relatively higher magnitudes of eigenstrains are imposed regarding ε^*_y and ε^*_z in contrast

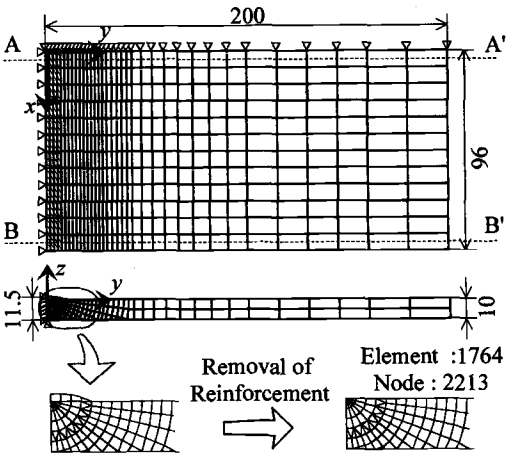


FIG. 2—*Finite element model of butt-welded joint.*

with the published data [*6,7*] to show their less contribution to estimation results even under their exaggerated values.

Simulation Procedure

Firstly, eigenstrains in Fig. 3 were imposed as mechanical boundary conditions in the FEM analysis. Then the removal process was simulated by deactivating concerned mesh elements corresponding to reinforcement to determine exact released strains, $\Delta\varepsilon_x$ and $\Delta\varepsilon_y$ on the surface. The results of $\Delta\varepsilon_x$ and $\Delta\varepsilon_y$ at y = 9 mm are shown in Fig. 4 by open symbols. To account for measuring error in experiments, random values of strain with standard deviation $N(0, 20\mu)$ were added to the exact solution (see solid symbols in Fig. 4).

The estimation of three-dimensional eigenstrain distributions from information regarding two-dimensional released strain becomes a so-called ill-posed problem. To capture solution sets in enough accuracy, it is necessary to introduce some regularization methods in the inverse problem.

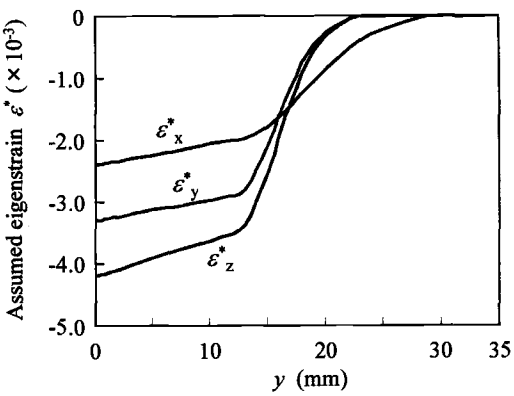


FIG. 3—*Eigenstrain distributions adopted in this simulation.*

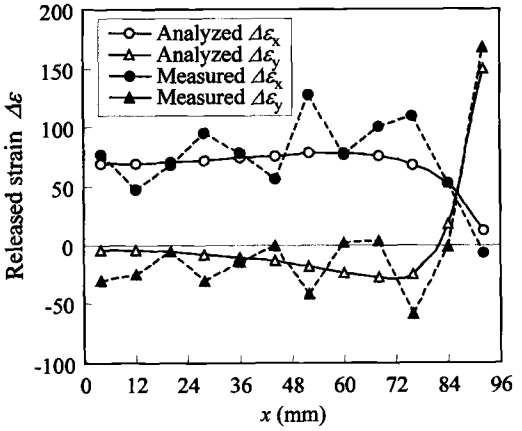


FIG. 4—*Effect of measuring error on surface-released strain due to removal of reinforcement of weld* (y = *9 mm*).

Reduction of Unknown Parameter

In order to reduce the number of unknown parameters, the component(s) of eigenstrain that play a major role in producing residual stresses were identified. Since the determination of residual stresses or released strain under given eigenstrains is an elastic problem, residual stresses $\sigma_s(s = x \text{ or } y \text{ or } z)$ are given as the sum of those due to a single eigenstrain component based on the principle of superposition.

$$\sigma_s(\varepsilon^*_x, \varepsilon^*_y, \varepsilon^*_z) = \sigma_s(\varepsilon^*_x, 0, 0) + \sigma_s(0, \varepsilon^*_y, 0) + \sigma_s(0, 0, \varepsilon^*_z) \tag{7}$$

Each right side term can be calculated by imposing one corresponding component in Fig. 3. The results are shown in Fig. 5 by solid symbols where the whole distribution of residual stresses (the left hand side of term of Eq 7) is also shown by open symbols for comparison. As shown by Fig. 5*a*, stresses produced by ε^*_x, $\sigma_s(\varepsilon^*_x, 0, 0)$ roughly agree with whole distribution. Besides, as shown in Figs. 5*b* and 5*c*, $\sigma_s(0, \varepsilon^*_y, 0)$ and $\sigma_s(0, 0, \varepsilon^*_z)$ are considerably smaller than $\sigma_s(\varepsilon^*_x, 0, 0)$. This observation enables us to focus on only ε^*_x in the inverse analysis, which results in the reduction of unknown parameters.

The further technique introduced is that eigenstrain distributions were approximated by a polynomial expression of logistic function forms expressed as

$$\varepsilon^*_x = \sum_{i=1}^{4} \frac{A_i}{1 + \exp(p + q_i y)} \tag{8}$$

where

$A_i(i = 1 \sim 4)$ = unknown parameters, and
$\{p, q_1, q_2, q_3, q_4\}$ = constant values which are given as $\{-5, 0.6, 0.4, 0.3, 0.25\}$.

Above $\{p, q_1, q_2, q_3, q_4\}$ were determined considering the fact that the eigenstrains exist within about 40 mm from the bead line [*7*], which of course depends on the welding method used. The distributions of each term in Eq 8 are shown in Fig. 6.

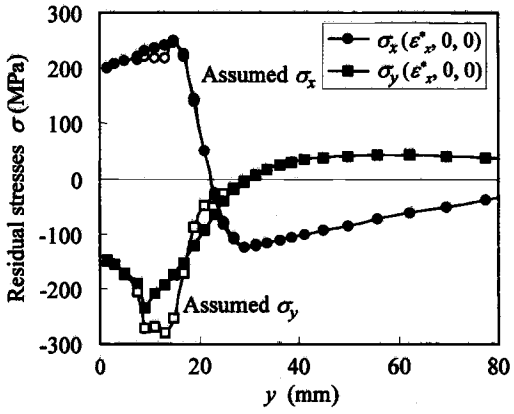


FIG. 5—*Residual stresses produced by a single component of eigenstrain (solid symbols: whole values)*: (a) *distribution of* $\sigma_s(\varepsilon^*_x, 0, 0)$ *on plate surface;* (b) *distribution of* $\sigma_s(0, \varepsilon^*_y, 0)$ *on plate surface;* (c) *distribution of* $\sigma_s(0, 0, \varepsilon^*_z)$ *on plate surface.*

Optimization of Strain-Measuring Locations

In determining eigenstrains, $\{_p\varepsilon^*\}$, in Eq 3 based on the least squares method, the more the measuring points, the higher the accuracy becomes. For simplicity of the proposed method, on the other hand, less measuring points may be desirable. Ueda et al. have proposed to apply the A-optimality criterion [*8*], widely used in the experimental design theory to obtain a consistent solution. As four components of eigenstrains in Eq 8 are not independent of each other when they are expressed by nonlinear polynomial terms, the A-optimality criterion cannot be applied in this analysis. So, a new optimizing method determining locations where strains are measured is proposed based on the D-optimality criterion [*9*]. The *k*-th row of [*H*] in Eq 1 represents the released strain at the specific mesh element (or

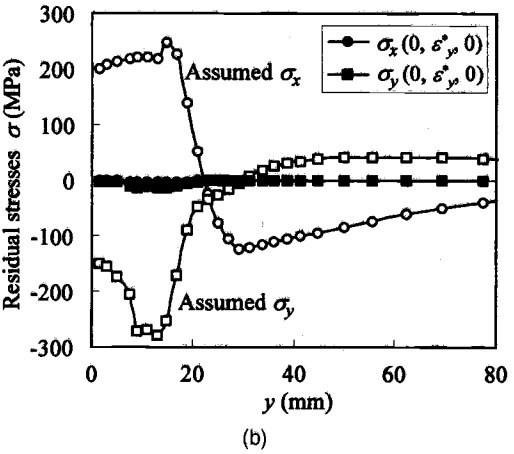
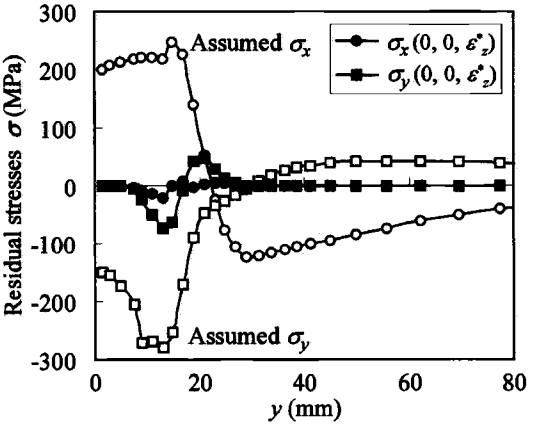


FIG. 5—*Continued.*



(c)

FIG. 5—*Continued.*

location) concerned. In the D-optimality criterion, the set of optimal measuring locations for a given total number of measuring points, N_{tot}, is selected so as to maximize $\det([H_o]^T[H_o])$, where $[H_o]$ is the submatrix of $[H]$ consisting of the candidate elements to be selected. Maximizing $\det([H_o]^T[H_o])$ based on the D-optimality criterion is mathematically equivalent to minimizing a generalized variance of the solution vector $\{_p\varepsilon^*\}$.

Figure 7 shows the selected locations based on the proposed method for $N_{tot} = 30$, where the darker the color, the more important becomes the eigenstrain estimation. The right and left blocks of each mesh element denote that $\Delta\varepsilon_x$ and $\Delta\varepsilon_y$ should be measured, respectively.

Of course, N_{tot} to be measured depends on accuracy required for assessment of the structural integrity, as well as on the anticipated damage types (fatigue, fatigue crack growth, corrosion fatigue, stress corrosion cracking, etc.). In the present simulation, 30 strain data ($N_{tot} = 30$) shown in Fig. 7 were used, because it was confirmed that an increasing rate of $\det([H_o]^T[H_o])$ due to increase of N_{tot} levels off when N_{tot} exceeds about 30.

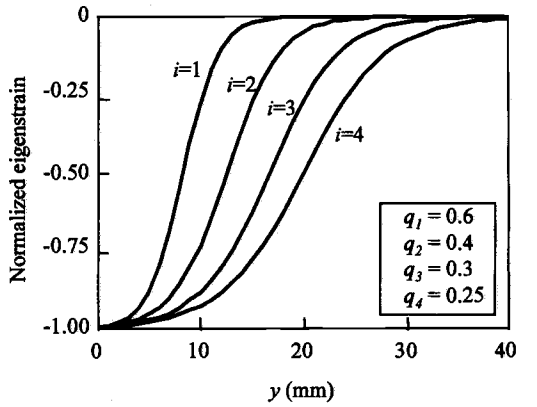


FIG. 6—*Normalized distribution of each logistic function.*

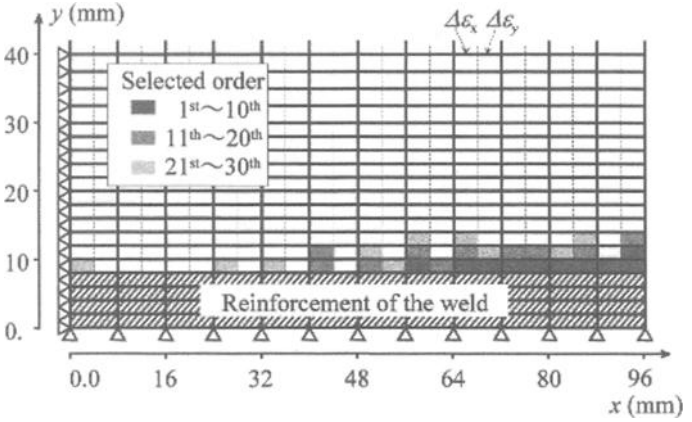


FIG. 7—*Optimized locations of strain change measurement.*

Results of the Simulation

When an inverse analysis was conducted for the exact value of released strains shown by open symbols in Fig. 4, an estimated eigenstrain distribution shows good agreement with an exact one as shown by a bold-broken line in Fig. 8, where a simple regularization method alone was introduced as already shown by Eq 8 by focusing the solution on ε^*_x.

On the other hand, when estimation was attempted for the values containing possible experimental errors shown by solid symbols in Fig. 4, solutions of the eigenstrain distribution became unstable as shown by fine lines in Fig. 8 due to ill-posedness of the problem, where variations in 15 distributions are due to difference of the seed in determining random numbers of errors. Under existence of errors in measurements, it is clear an estimation error becomes beyond allowable ranges.

Regularization by SVD Method

To overcome above ill-posedness, the singular value decomposition (SVD) method, one of most popular regularization methods in the inverse analysis, was incorporated. In this

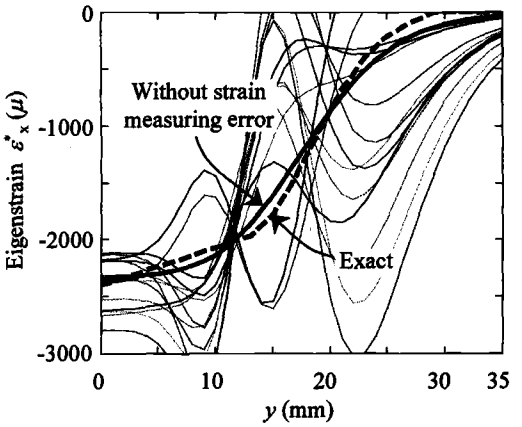


FIG. 8—*Estimated eigenstrain distribution* (s_{err} = *20* μ, *without regularization*).

technique, determination of an optimum rank number of $[H_o]$, R_{opt} is essential and there are many sophisticated approaches to it. In this study, however, we determined R_{opt} by a relatively simple method shown below [*9*].

After expressing the eigenstrain distribution by Eq 8, the number of unknown parameters, which agrees with that of columns of $[H_o]$, has been reduced to only 4. So, R_{opt} may take the value of 1, 2, or 3 because $R_{opt} = 4$ was obviously inadequate as already shown in Fig. 8. Thus, an inverse analysis was conducted for each $R(= 1, 2, 3)$ to determine R_{opt} giving highest accuracy. It is noted that R_{opt} depends not on the solution of $\{\varepsilon^*\}$ but only on $[H]$, which is a function of unknown parameters in expressing eigenstrain in Eq 8. So, R_{opt} can be evaluated by a single elastic FEM analysis and a simple matrix calculation by assuming any $\{\varepsilon^*\}$. After the above calculation, $R = 2$ was proved to be optimum.

Incorporation of Regularization

Figure 9 shows estimated ε^*_x distributions by 15 times the inverse analyses for different seeds of the random number by using the regularized matrix $[H_{opt}]^-$ with the rank $R_{opt} = 2$. By comparing the results in Figs. 8 and 9, where the seeds of the random number are the same in both figures, it is clear that stability and accuracy of the solutions are greatly improved in the latter.

Based on the results in Fig. 9, residual stresses produced by each estimated eigenstrain were determined. The ones on the *backside surface* (opposite to that where reinforcement was removed) are shown in Fig. 10. Strictly speaking, estimation errors in σ_y are larger than those in σ_x because ε^*_z, which has been neglected in the inverse analysis, has a slight effect on σ_y (see Fig. 5*c*). From an engineering point of view, however, both results show a good agreement with exact distribution.

Experiments

Experimental Procedure

A proposed method was applied to a butt-welded plate of a high-yield-strength steel HT780 (the yield stress = 782 MPa, the tensile strength = 867 MPa). Its size is shown in Fig. 11, which was cut down from the center of a larger plate with the size of 500 × 500

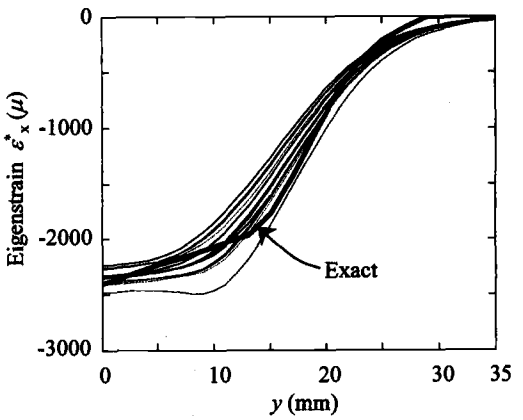
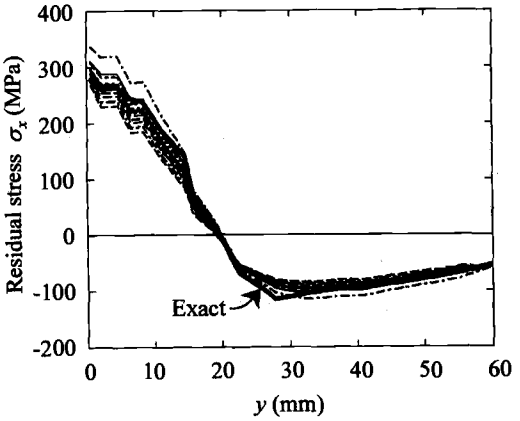


FIG. 9—*Estimated eigenstrain distribution* (s_{err} = *20* μ, *with regularization*).



(a)

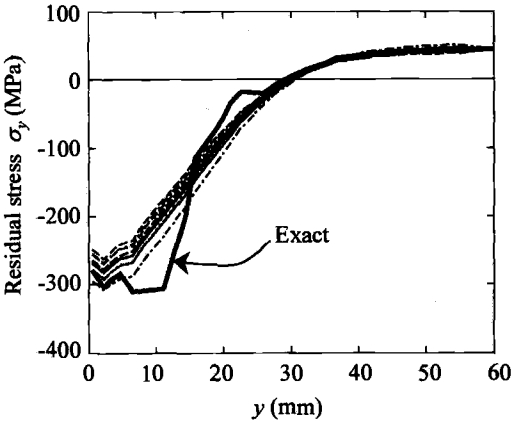
FIG. 10—*Estimated residual stress distributions on the backside surface* (s_{err} = *20* μ): (a) *distribution of* σ_x *(Line A-A')*; (b) *distribution of* σ_y *(Line B-B')*.

× 15 mm. The three welding passes on the front side were followed by the last three passes on the opposite side after back-chipping. All the passes were by TIG arc welding at 0.968 ~ 1.44 kJ/mm.

Reinforcement of the weld only on the front side was removed by milling. The depth of cut in each time was set as 0.3 ~ 0.1 mm to reduce the effects of possible temperature rise and plastic strain produced during milling. Released strains were measured by 33 strain gages put on the surface near the reinforcement. The locations were determined according to the procedure shown in Fig. 7.

Results

Figure 12 shows measured released strain due to removal of reinforcement of the weld. Using this measured data, the ε^*_x distribution in the *y*-direction was estimated by Eq 6,



(b)

FIG. 10—*Continued.*

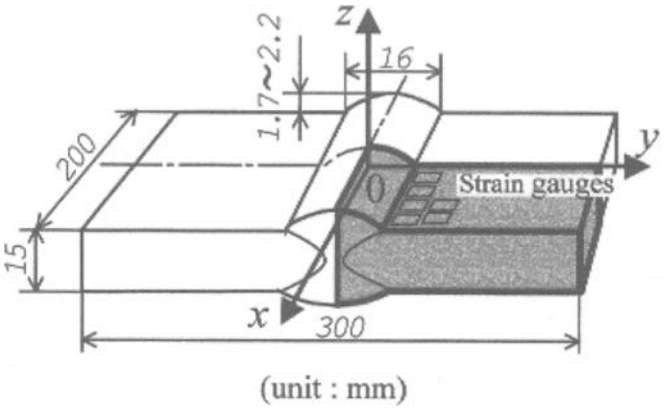


FIG. 11—*Configuration of butt-welded plate.*

where the distribution in thickness direction was assumed to be constant. Then residual stresses were determined by the FEM analysis by using estimated eigenstrain as boundary conditions.

To evaluate the accuracy of estimated residual stresses, stress measurements by the X-ray method were carried out after the removal of reinforcement. In Fig. 13, the estimations shown by lines are compared with the measurements shown by solid symbols.

Discussion

Roughly speaking, estimated results show good agreement with measurements by the X-ray method as shown by Fig. 13. However, close examination of the results suggests that

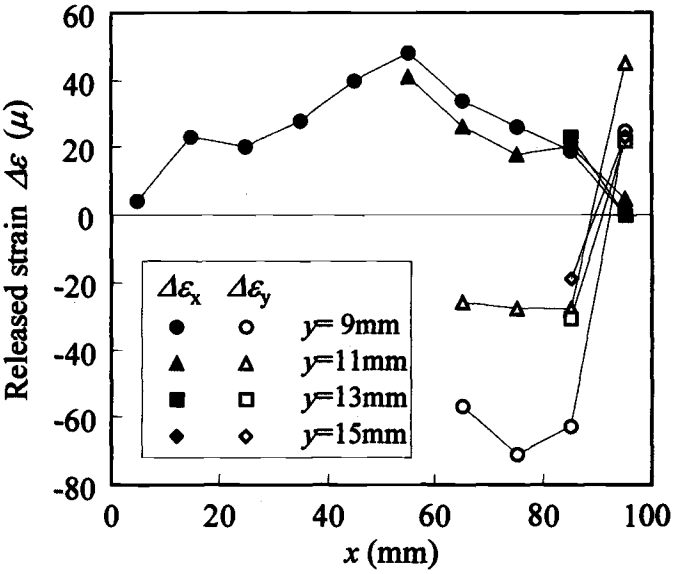
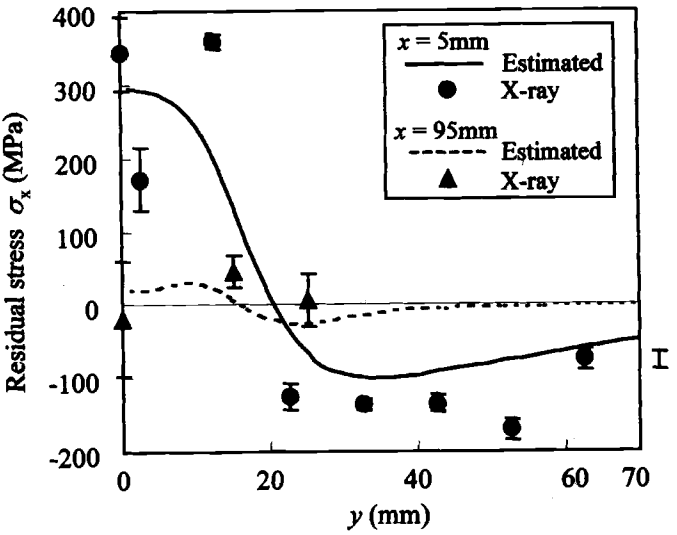
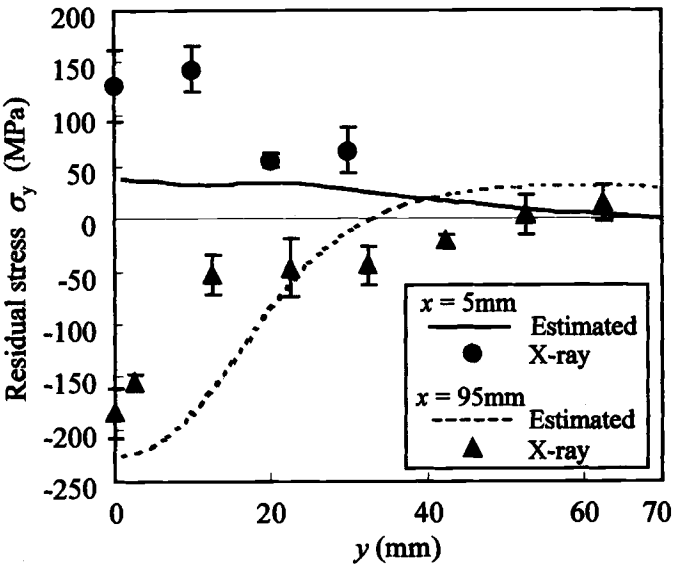


FIG. 12—*Measured strain changes on plate surface.*



(a)

FIG. 13—*Comparison between estimated and measured (by X-ray) residual stresses on plate surface:* (a) *distribution of* σ_x; (b) *distribution of* σ_y.



(b)

FIG. 13—*Continued.*

the estimated σ_y near the bead line ($0 \leq y \leq 15$ mm) are lower than X-ray measurements (see Fig. 13*b*).

The main reason for relatively poor agreement may be due to the effect of ε^*_y on σ_y, which has been neglected in this analysis. As shown by Fig. 5*b*, ε^*_y has little effect in producing any residual stresses under the assumption that its variation in thickness direction is small. However, when its variation in thickness direction is drastic, it was confirmed that ε^*_y generates additional residual stresses, especially regarding σ_y. In the multi-pass welding joints as used in this experiment, the welding process of final pass may have a relatively important role on eigenstrain distribution near the surface that would bring drastic variation of ε^*_y in the thickness distribution. To improve accuracy of σ_y in such a case, a thickness distribution of ε^*_y should be estimated correctly, which is the future work to be solved.

Toward Future Improvement

In contrast with eigenstrain data, residual stress data may have been accumulated by now because the latter can be directly used in the safety design. However, this study has critically proved that the information on eigenstrains may also contain valuable suggestions about determining residual stresses. At present, the utility of the proposed method is limited. In the future, this procedure may be much more improved if such data are accumulated or a proposed method is used in combination with the thermo plastic-elastic welding simulation where an approximate eigenstrain distribution can be determined. Examination of three-dimensional distributions of eigenstrain and their effects on the estimation procedure may be major future problems.

Conclusions

A new method (the bead flush method) was proposed to estimate welding residual stresses nondestructively. From the released strain due to removal of reinforcement of the weld, eigenstrain distribution can be estimated by incorporating proper regularization methods. Based on estimated eigenstrains, it is shown by numerical simulations that the proposed method gives reasonably good predictions of residual stresses.

Experiments for a relatively thin, simple-shaped, butt-welded plate proves that results from this method may show agreement with those obtained by the conventional X-ray method, especially regarding a stress component in bead direction under some restrictions. To improve accuracy for a rest of stress components, distribution of a specific eigenstrain component in thickness direction that has been neglected in this work must be estimated.

References

[*1*] Mura, T., "The Continuum Theory of Dislocations," *Advances in Material Research, Interscience Publication,* Vol. 3, 1968, pp. 1–107.

[*2*] Ueda, Y. and Fukuda, K., "New Measuring Method of Three-Dimensional Residual Stresses in Long Welded Joints Using Inherent Strains as Parameters, L_z Method," *Transactions of the American Society of Mechanical Engineers, Journal of Engineering Materials and Technology,* Vol. 111, 1989, pp. 1–8.

[*3*] Bui, H. D., *Inverse Problems in the Mechanics of Materials: An Introduction,* CRC Press, 1993.

[*4*] Nakamura, H., Naka, Y., Park, W., and Kobayashi, H., "Computer Aided Non-Destructive Evaluation Method of Welding Residual Stresses by Removing Reinforcement of Weld," *Current Topics in Computational Mechanics, ASME Pressure Vessel and Piping,* Vol. 305, 1995, pp. 49–56.

[5] Kumagai, K., Nakamura, H., and Kobayashi, H., "Computer Aided Nondestructive Evaluation Method of Welding Residual Stresses by Removing Reinforcement of Weld (A Proposal of New Concept and Its Application to Butt Welded Plate)," *Transactions of the Japan Society of Mechanical Engineers, Series A,* Vol. 65, No. 629, 1999, pp. 133–140 (in Japanese).

[6] Ueda, Y., Ma, N., and Koki, R., "TL_yL_z Method and T Method for Measurement of 3 Dimensional Residual Stresses in Bead-on-Plate Welds," *Quarterly Journal of the Japan Welding Society,* Vol. 11, No. 4, 1993, pp. 555–562 (in Japanese).

[7] Ueda, Y. and Ma, N., "Function Expression for Inherent Strains in Fillet Welds and Its Accuracy," *Quarterly Journal of the Japan Welding Society,* Vol. 12, No. 4, 1994, pp. 554–560 (in Japanese).

[8] Myers, R. H. and Montgomery, D. C., *Response Surface Methodology,* Wiley International Science, 1995.

[9] Kumagai, K., Nakamura, H., and Kobayashi, H., "Computer Aided Nondestructive Evaluation Method of Welding Residual Stresses by Removing Reinforcement of Weld (Introduction of Regularization Method and Optimization of Strain Measuring Location)," *Transactions of the Japan Society of Mechanical Engineers, Series A,* Vol. 65, No. 634, 1999, in press (in Japanese), pp. 1397–1404.

Ed F. Rejda,[1] *Darrell F. Socie,*[2] *and Brian P. Nuel*[3]

Bulk Property Evaluation of a Thick Thermal Barrier Coating

REFERENCE: Rejda, E. F., Socie, D. F., and Nuel, B. P., **"Bulk Property Evaluation of a Thick Thermal Barrier Coating,"** *Fatigue and Fracture Mechanics: 31st Volume, ASTM STP 1389,* G. R. Halford and J. P. Gallagher, Eds., American Society for Testing and Materials, West Conshohocken, PA, 2000, pp. 143–161.

ABSTRACT: Thick thermal barrier coatings (TTBCs) for diesel engine applications are being developed to improve engine performance through increased operating temperatures and lower emissions. To more completely assess the bulk properties of coating materials, a miniature test stand for the mechanical testing of coating materials independent of the substrate was developed. Using a piezoelectric translator as an actuator and a miniature load cell, it was possible to conduct uniaxial testing in both compression and tension of very small samples. In this study, room temperature deformation experiments were conducted on an air plasma-sprayed 24% CeO_2-ZrO_2 coating material. Mechanical properties in both the in-plane and transverse coating directions were evaluated in both compression and tension. From simple monotonic tests, the anisotropy of the material could be quantified. A key finding was that both the loading modulus and tensile strength were about two to three times higher in the in-plane direction. This anisotropy is believed to be due to the directionality of microcracking in the material. Cyclic loading experiments showed that the coating material also exhibits considerable irreversible strain behavior in both the transverse and in-plane directions. A model describing the irreversible strain behavior based on the combined sliding and closing of pre-existing microcracks is proposed and compared with experimental results. It is shown that the model describes the qualitative and quantitative aspects of the material behavior quite well, especially in compression.

KEYWORDS: zirconia, plasma-sprayed coatings, constitutive behavior, cyclic hysteresis

For more than 30 years, ceramic coatings have received increasing attention because of their effectiveness in insulating components during high-temperature service. Most of the development during this time has been on thin coatings (0.01 to 0.1 mm) for the gas turbine industry and is well documented [*1–3*]. Recently, however, emphasis has been placed on the development of even thicker coatings with thicknesses on the order of a millimeter for the diesel engine industry [*4–5*]. Typically, these ceramic coatings are plasma sprayed onto a metallic substrate in a bi-layer structure consisting of a thin NiCrAlY intermediate bond coat and a thicker ZrO_2-based top coat.

The plasma spray process produces a microstructure with a considerable amount of porosity and microcracking. While these pores and microcracks can reduce the thermal con-

[1] Research assistant, University of Illinois at Urbana-Champaign, Department of Mechanical Engineering, 1206 West Green Street, Urbana, IL 61801.

[2] Professor, University of Illinois at Urbana-Champaign, Department of Mechanical Engineering, 1206 West Green Street, Urbana, IL 61801.

[3] Research and development engineer, Medtronic AneuRx, 1312 Crossman Avenue, Sunnyvale, CA 94089.

Copyright© 2000 by ASTM International www.astm.org

ductivity by as much as a factor of three compared to that of the fully dense ceramic, they also significantly lower the internal cohesiveness of the coating material. As a result, failures of thick thermal barrier coatings (TTBCs) are often accompanied by the formation of in-plane and transverse tensile cracks from within the coating layer [*6–7*]. Allowed to grow, these cracks can eventually link up and lead to delamination and/or spallation failures. The proper durability assessment of TTBCs therefore relies on adequate knowledge of the properties of the bulk coating material.

The purpose of the current investigation was to isolate a plasma-sprayed ceramic deposit from the substrate in order to determine its constitutive behavior. Since coatings will be exposed to both in-plane and transverse stresses during service, room temperature mechanical properties in both directions were determined to help assess their durability. In addition, a constitutive model was developed and compared to experimental results. It is hoped that this study can provide a meaningful contribution to the proper characterization and durability assessment of TTBCs at elevated temperatures.

Experimental Methods

Material

In this study, uniaxial specimens were designed and constructed for the mechanical property evaluation of a plasma-sprayed ceramic coating independent of a substrate. The ceramic coating investigated was prepared from a 24%CeO_2-ZrO_2 powder with an average particle size of 60 μm and was air plasma-sprayed with a bulk porosity level of about 17%. In order to obtain bulk coating material for testing, ceramic powder was first sprayed onto a mild steel disk to a thickness of about 5 mm. The disk was then etched away in a nitric acid bath, leaving only the freestanding coating. The remaining specimen preparation process outlined in Fig. 1 was then followed. First, the disk of bulk coating material was sectioned into long strips using a low-speed diamond saw and epoxied to grooved copper blocks as shown in Fig. 1*a*. The resulting assembly was then cut into sections of the desired thickness to provide the intermediate samples shown in Fig. 1*b*. After drilling mounting holes for specimen gripping, each sample was then ground using low-speed diamond grinders to the final specimen shape shown in Fig. 1*c*. Using this specimen preparation method, the directionality of testing could be well controlled.

Mechanical Testing

The test stand used for the deformation experiments is shown schematically in Fig. 2 with its main features highlighted. The first of these is the piezoelectric translator (PZT) that was used as an actuator. The PZT used had a maximum displacement of 180 μm and allowed

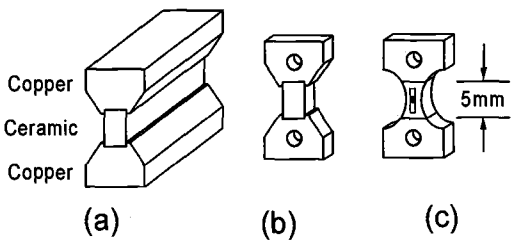


FIG. 1—*Specimen preparation process.*

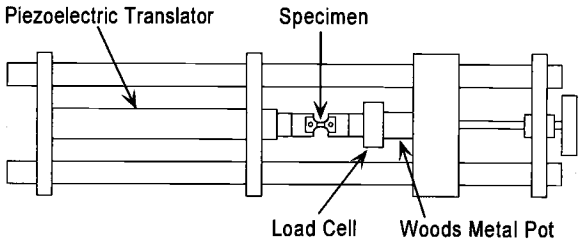


FIG. 2—*Miniature test stand used for uniaxial loading experiments.*

for very fine and precise control of the load and strain. Next, small loads on the sample were measured using a precision miniature load cell with a capacity of ±250 lb (±1110 N). Corresponding strains were measured by instrumenting the specimen on the front and back (see Fig. 1) with miniature strain gages with a gage length of 0.38 mm. Finally, a woods metal pot was implemented to help minimize bending stresses during testing.

In the current investigation, uniaxial experiments were conducted in tension and compression for both the in-plane and transverse material directions. All of the experiments were conducted at room temperature in stress control at a loading rate of about 10 MPa/s. In order to verify the performance of the experimental setup, modulus measurements were conducted on specimens of a more conventional material, 7075 Aluminum, and compared with a published value ($E_{7075\ Al} \sim 72$ GPa). From 15 separate tests, the average modulus was found to be 69.4 GPa and the average bending strain was found to be 1.6% of the measured axial strains. These performance characteristics helped confirm that the test stand was operating as expected.

Results and Discussion

The densely cracked microstructure of plasma-sprayed coating materials plays a dominant role in their deformation behavior. Figure 3 shows a typical cross-sectional SEM micrograph of the 24%CeO_2-ZrO_2 coating material with the in-plane and transverse directions as indicated. From the figure, it is readily seen that the microstructure contains a very high density of microcracks. In addition, these cracks can be seen to have complex features such as irregular shapes and a large amount of interconnectedness. In the following sections, the impact of this microcracked structure on monotonic and cyclic deformation behavior is discussed through the results of room temperature deformation experiments. Afterward, a simple model is proposed to quantitatively describe the observed mechanical behavior.

Monotonic Behavior

The combined results from four separate monotonic loading experiments conducted on the 24%CeO_2-ZrO_2 coating material are shown in Fig. 4. These four experiments—transverse tension, transverse compression, in-plane tension, and in-plane compression—were all conducted on individual samples and show the typical monotonic deformation characteristics commonly seen in plasma-sprayed materials [*8,9*]. The tension tests shown were conducted to specimen failure, while the compressive tests were conducted until the maximum displacement of the PZT actuator was reached and did not result in specimen failure.

Immediately apparent in the figure is the considerable non-linear behavior exhibited in both material directions and throughout the entire stress range tested. This non-linear be-

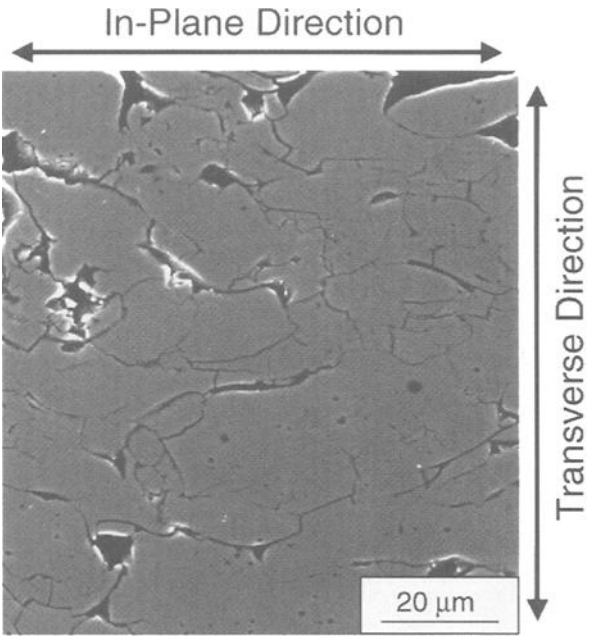


FIG. 3—*SEM micrograph of plasma-sprayed 24%CeO_2-ZrO_2 material used in this study.*

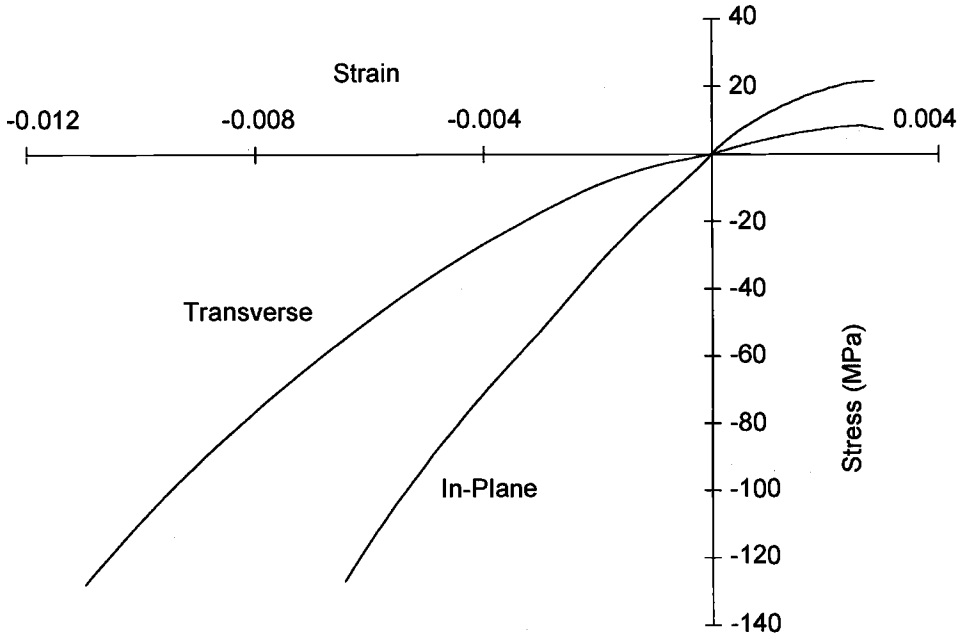


FIG 4—*Monotonic deformation curves for in-plane and transverse material directions.*

havior can be attributed partly to compaction processes that occur during deformation of microcracked structures like those typically seen in plasma-sprayed materials [*8*]. In compression, compaction may occur as cracks that are initially open at zero stress gradually close as the stress is increased. This results in an increase in load-bearing area and a corresponding increase in overall material stiffness. The opposite may occur in tension. Cracks that are initially closed at zero stress may open as the tensile stress is increased and cause a reduction in the material stiffness. Non-linearity during monotonic loading can also be caused by additional microcracking of the plasma-sprayed microstructure. This will have the effect of producing a decreasing stiffness with stress and is expected to become an important factor as the failure strength of the material is approached. Therefore, for the tension tests shown in Fig. 4, the deformation curve also includes a microcracking contribution. The compression tests, on the other hand, do not show a decreasing stiffness for the stress range tested and probably have little influence from additional microcracking that may occur during compressive loading.

Also seen in Fig. 4 is the large difference in stiffness between the in-plane and transverse material directions. Table 1 gives a numerical comparison of the loading moduli for the four tests. It can be seen that the in-plane loading moduli were about twice that of the transverse direction. This measured anisotropy can be related directly to the microstructure. As seen in Fig. 3, plasma-sprayed materials have an anisotropically cracked structure with cracks having more of a tendency to be parallel to the in-plane than the transverse directions. Therefore, the average load-bearing area in the transverse direction will be smaller, leading to a lower relative stiffness.

The final aspect worth noting from the monotonic behavior concerns the tensile strengths in the two material directions, given in Table 1. It can be seen that the tensile strengths in both directions are quite low. This means that a small amount of tension in either the in-plane or transverse material directions is very damaging and will greatly effect the overall durability of the coating material. It is also seen that there is a significant difference in tensile strengths between the two material directions, with the in-plane direction being about three times as strong. This difference can be attributed once again to the directionality of pre-existing microcracks in the virgin material. Since cracks have a general bias to be perpendicular to the transverse direction, they will have a more significant effect on lowering that direction's strength.

Cyclic Behavior

The typical room temperature cyclic deformation behavior for the 24%CeO_2-ZrO_2 coating material is shown in Figs. 5 and 6 for the in-plane and transverse directions, respectively. These tests were similar to the monotonic tests in Fig. 4, but instead involved unloading and reloading steps as shown.

TABLE 1—*Monotonic test results.*

Monotonic Test	Secant Modulus,[a] GPa	Failure Strength,[b] MPa
In-Plane Tension	7.6	22
In-Plane Compression	19.7	...
Transverse Tension	3.2	8
Transverse Compression	11.6	...

[a] Calculated at the maximum stress of the test.
[b] Compressive strengths were not evaluated in the current study.

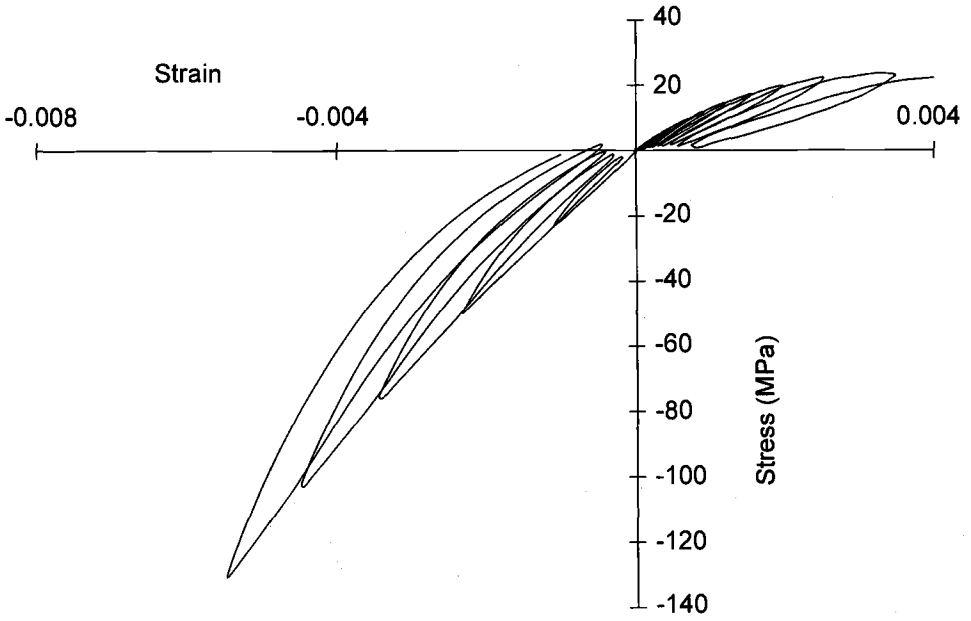


FIG. 5—*Cyclic deformation behavior for in-plane material direction.*

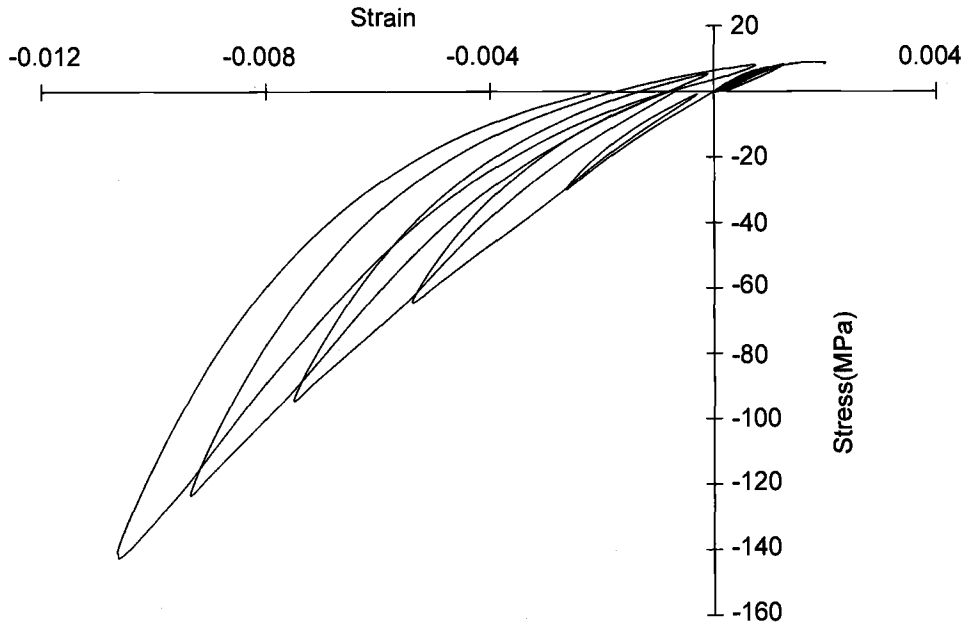


FIG. 6—*Cyclic deformation behavior for transverse material direction.*

Several aspects of the cyclic deformation behavior are noteworthy. The first of these is the presence of material memory to prior deformation. It can be seen that when the material is reloaded past a previous maximum stress, it deforms as if all previous deformation never occurred. So, if the monotonic curves in Fig. 4 were superimposed onto the curves shown in Figs. 5 and 6, it would be seen that the monotonic curves effectively provide an envelope to the cyclic stress-strain behavior. The second interesting aspect in the cyclic deformation is the considerable hysteresis that occurs during a cycle and the resulting irreversible strain. Figures 7 and 8 show the amount of irreversible strain as a function of the maximum stress of the cycle for the compressive and tensile cyclic tests, respectively. It can be seen that for compressive cycling, the irreversible strain increases linearly with the maximum stress of the cycle and that this linearity holds for the entire stress range tested. For the case of tensile cycling, a similar increase of irreversible strain with maximum stress is observed. A departure from linearity, however, is seen as the maximum stress of the tensile cycle approaches the failure strength of the material. This sudden increase in non-linear strain is most likely the result of severe microcracking occurring in the material.

Generally speaking, the observed cyclic deformation behavior can be explained by frictional processes that occur during deformation. Considering the high density of microcracks that exist in the coating, it is reasonable to postulate that the observed hysteresis is the result of frictional processes in which microcracks slide back and forth during stress cycling [*9*]. Such frictional processes dissipate energy and will generate hysteretic behavior similar to that observed in the coating material.

Modeling—Theory

In view of the dominant effect of microcracks on the deformation behavior of the 24%CeO_2-ZrO_2 coating material, a model incorporating the basic physics of microcrack

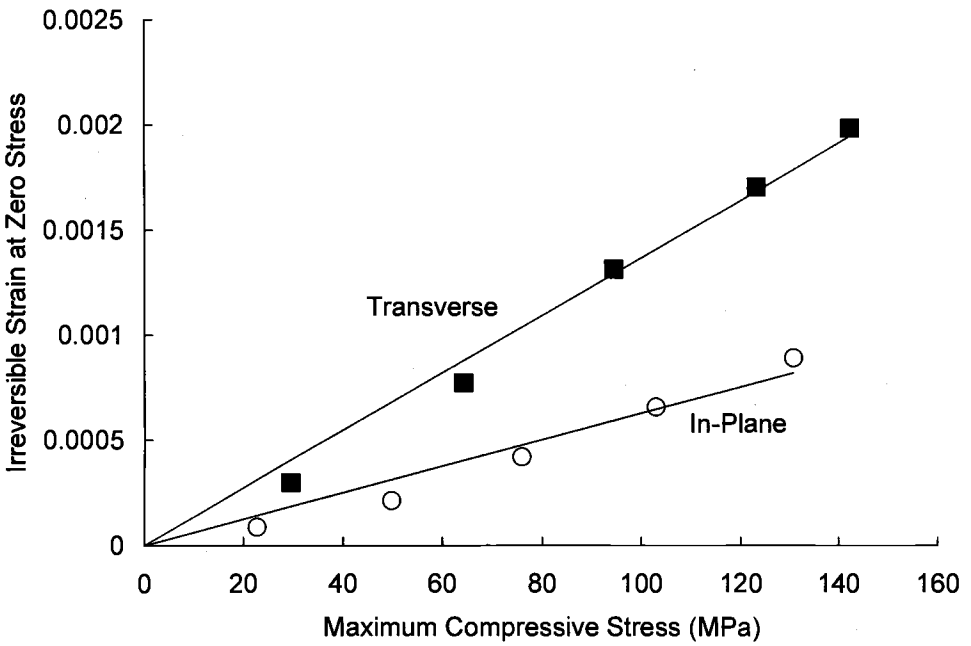


FIG. 7—*Irreversible strain for in-plane and transverse cyclic compression.*

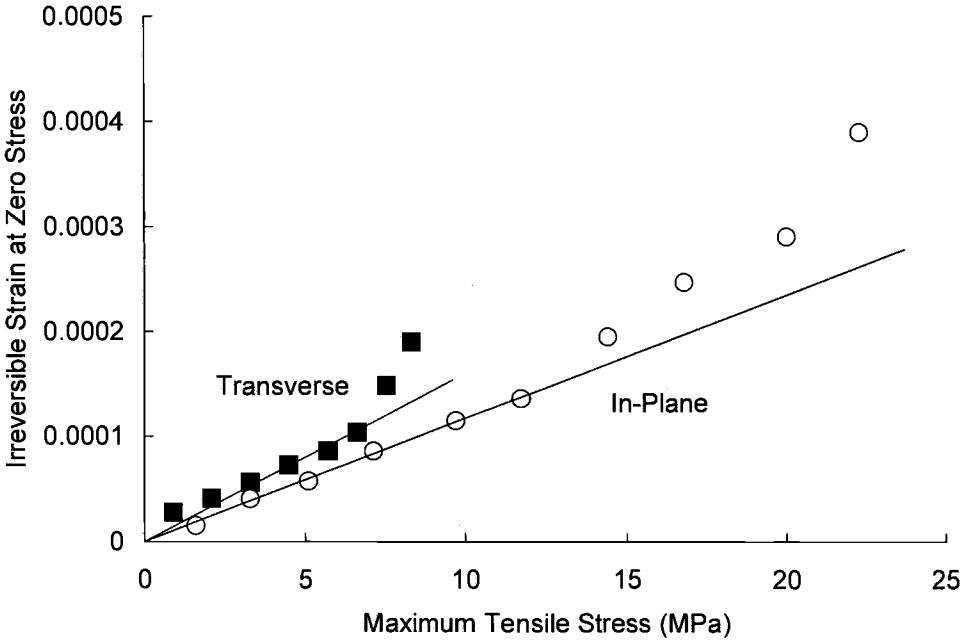


FIG. 8—*Irreversible strain for in-plane and transverse cyclic tension.*

behavior was developed. For the current model, three basic mechanisms were considered to drive the deformation behavior: elasticity, microcrack closure, and sliding along microcrack surfaces. Since the complex features of the plasma-sprayed microstructure make their deformation behavior very difficult to predict analytically, a phenomenological approach is used to characterize the effects of each of these mechanisms.

The effect of open cracks on the deformation behavior is considered first. In the idealized case of a random distribution of circular cracks in an elastic body, the effective modulus, E_{open}, is reduced relative to the intrinsic modulus of the material, E_o, by the following relation [*10*]:

$$\frac{1}{E_{\text{open}}} = \frac{1}{E_o}\left(1 + \frac{4\pi N_{\text{open}}\,\bar{c}^3_{\text{open}}}{3V}\right) \tag{1}$$

where $\bar{c}_{\text{open}}$ is the average length of an open crack and the ratio N_{open}/V is the number of open cracks per unit volume. During compressive loading of the coating material, microcrack closure will occur and can cause a decrease in both the total number of open cracks, N_{open}, and the average effective crack length, $\bar{c}_{\text{open}}$. The effect is the same in each case: an increasing modulus with increasing compressive stress. In tension, the opposite will occur. Initially closed cracks will open, causing an increase in the number of open cracks, and partially open cracks will continue to open, causing an increase in the effective crack length. Therefore, the modulus E_{open} will decrease with increasing tensile stress. In the present model, the effects of changing values of N_{open} and $\bar{c}_{\text{open}}$ are captured by lumping them into a single parameter, V_{open}, defined as

$$V_{\text{open}} = \frac{4\pi N_{\text{open}} \bar{c}^3_{\text{open}}}{3V} \tag{2}$$

Combining Eqs 1 and 2 then leads to a simpler relation describing the effects of open cracks:

$$\frac{1}{E_{\text{open}}} = \frac{1}{E_o}(1 + V_{\text{open}}) \tag{3}$$

Physically, the parameter V_{open} provides a measure of the strain energy interaction volume of all open cracks in the coating material and its value can be determined readily from experimental results. This procedure is discussed in the *Modeling—Application* section.

Now, the effects of sliding cracks on the deformation behavior of the coating material are considered. Once again, an idealized case is first used to help understand the physics of the problem. Consider the initially closed crack shown in Fig. 9 that is subjected to a local compressive stress, σ_{local}, during far-field loading. Assume that the crack has no residual stresses on its surface from the result of any previous loading. For a crack oriented at an angle β, the local stress can be decomposed into a normal and shear stress, σ_n and τ, on the crack plane by

$$\tau = \sigma_{\text{local}} \sin \beta \cos \beta \tag{4}$$

$$\sigma_n = \sigma_{\text{local}} \sin^2 \beta \tag{5}$$

where σ_{local} and σ_n are taken to be positive in compression to simplify signs. As the local compressive stress is increased, sliding can occur at the crack surface if the shear stress, τ, on the plane of the crack is greater than the resistance due to friction. In the present model, the frictional resistance stress, τ_f, is assumed to be governed by a simple coefficient of friction, μ, such that

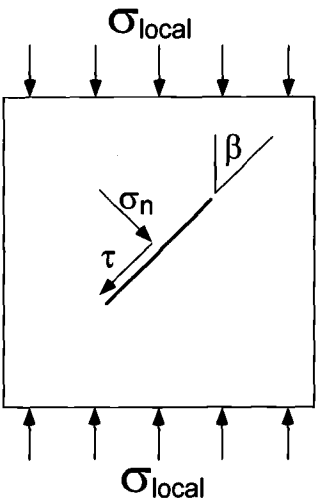


FIG. 9—*Concept of a local compressive stress on a crack.*

$$\tau_f = \mu\sigma_n \tag{6}$$

where μ is considered to be constant throughout loading. By combining Eqs 4 through 6, the initial sliding criteria $\tau > \tau_f$ will be satisfied for the following range of crack orientation angles:

$$0 < \beta < \tan^{-1}(1/\mu) \tag{7}$$

It can be seen that the angular range of cracks involved in initial forward sliding is therefore a sole function of the coefficient of friction and not of stress level. A further analysis of the problem [*10*] shows that since the angular range of forward sliding cracks is fixed during initial loading, the average crack-sliding displacements (and subsequently the average strains) will be a linear function of stress. For a body of randomly oriented forward-sliding circular cracks, the effective modulus, E_{forward}, for initial loading is then given by

$$\frac{1}{E_{\text{forward}}} = \frac{1}{E_o}\left[1 + \frac{4\pi N_{\text{forward}}\,\bar{c}^3_{\text{forward}}}{3V} f_{\text{forward}}(\mu, \beta_{\max})\right] \tag{8}$$

where $\bar{c}_{\text{forward}}$ is the average length of a forward sliding crack, the ratio N_{forward}/V is the number of forward sliding cracks per unit volume, and

$$f_{\text{forward}}(\mu, \beta_{\max}) = \frac{1}{80}[30\sin\beta_{\max} - 5\sin 3\beta_{\max} - 3\sin 5\beta_{\max} + 30\mu\cos\beta_{\max} + 5\mu\cos 3\beta_{\max} - 3\mu\cos 5\beta_{\max} - 32\mu] \tag{9}$$

where $\beta_{\max}$ is as defined in Eq 7. It can now be seen from Eq 8 that if it is assumed that cracks do not grow, the initial forward sliding modulus will maintain a constant value during the entire initial stage of loading.

When the crack in Fig. 9 is unloaded, the direction of the frictional stress, τ_f, changes to resist the reverse sliding of the crack. Therefore, in order for reverse sliding to occur, a minimal reduction in applied stress, $\Delta\sigma$, is necessary and is given by [*10*]:

$$\Delta\sigma > \frac{2\sigma'_{\text{local}}\,\mu\tan\beta}{1 + \mu\tan\beta} \tag{10}$$

where σ'_{local} is the maximum local stress reached during loading. It can be seen from Eq 10 that the reverse sliding of a crack is dependent on three factors: the maximum stress of the cycle, the angular orientation of the crack, and the coefficient of friction. Therefore, cracks at different angles will begin to reverse slide at different reversed stresses and the entire effect will be scaled by the maximum stress reached during loading. Rearranging Eq 10 and solving for the angular range of reverse sliding cracks yields the following for local compressive unloading:

$$0 < \beta < \tan^{-1}[(\sigma'_{\text{local}} - \sigma_{\text{local}})/\mu(\sigma'_{\text{local}} + \sigma_{\text{local}})] \tag{11}$$

Note that the angular range of reverse sliding cracks is zero upon initial unloading and gradually increases with the reverse stress until being equal to that during initial loading when the stress is fully reversed ($\sigma_{\text{local}} = 0$). Since the angular range of reverse sliding cracks

changes, the average crack displacements will be non-linear with stress. For a body with randomly oriented reversed-sliding circular cracks, the effective modulus, $E_{reverse}$, is given by [*11*]:

$$\frac{1}{E_{reverse}} = \frac{1}{E_o}\left[1 + \frac{4\pi N_{reverse}\bar{c}^3_{reverse}}{3V} f_{reverse}(\mu, \beta_{max})\right] \tag{12}$$

where $\bar{c}_{reverse}$ is the average length of a forward-sliding crack, the ratio $N_{reverse}/V$ is the number of reverse sliding cracks per unit volume, and

$$f_{reverse}(\mu, \beta_{max}) = \frac{1}{80}[30 \sin \beta_{max} - 5 \sin 3\beta_{max} - 3 \sin 5\beta_{max} - 30\mu \cos \beta_{max} - 5\mu \cos 3\beta_{max} + 3\mu \cos 5\beta_{max} + 32\mu] \tag{13}$$

where β_{max} is as defined in Eq 11. Upon evaluation of Eq 12, it is found that since all reverse crack sliding activity is impeded, the modulus during initial unloading is equal to the intrinsic modulus of the material. Then, as unloading continues, the value of the reversed-sliding modulus decreases as more and more cracks start reverse sliding.

Figure 10 illustrates the effect of a single-sliding crack on the local deformation behavior for a single stress cycle. During initial compressive loading, deformation occurs with a reduced modulus due to forward sliding of the crack. When the load is decreased, reverse sliding does not occur until the reversed stress, $\Delta\sigma$, is reached. Before reversed sliding initiates, the local deformation behavior is the same as that for an uncracked material. Once reverse sliding does begin, the local modulus decreases significantly, attaining a value even lower than that during initial loading. The reason for the considerable difference in the forward- and reverse-sliding moduli comes from the fact that forward sliding occurs against an increasing frictional stress, while reverse sliding occurs against a decreasing frictional

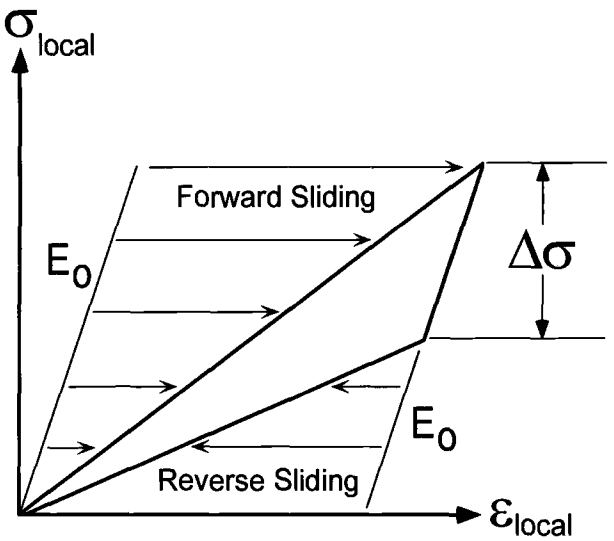


FIG. 10—*Local hysteresis generated during a compressive stress cycle of the crack in Fig. 9.*

stress. This happens in such a way that for a complete local stress cycle, crack sliding generates hysteresis in the materials local deformation response but not an irreversible strain. It can be seen that the state of the crack is equivalent at the beginning and end of the cycle. Since the state of the crack does not change, further cycling between the same two local stress levels will produce a repeating hysteresis loop.

To incorporate the physics of sliding cracks into the model for the coating material, a few assumptions need to be made. It will first be assumed that the cracks that undergo forward sliding are the same ones that undergo reverse sliding and that crack extension does not occur during the sliding process. Therefore,

$$\bar{c}_{\text{forward}} \approx \bar{c}_{\text{reverse}} \approx \text{constant} \tag{14}$$

Next, it will be assumed that the number of reverse-sliding cracks is only a fraction of the forward-sliding cracks such that the nature of sliding is not truly reversible. Since microcrack surfaces could become locked due to asperities or the presence of debris, their return to their initial state will be impeded upon unloading. These same cracks are then assumed to remain "locked" in place until the local stress exceeds the previously established maximum stress. Once this occurs, they are then allowed to once again forward slide as they did during initial loading. For simplicity, the current model assumes that the ratio of locked to initially forward-sliding cracks is constant whenever the stress is lower than any previous maximum stress. The introduction of a sliding irreversibility factor, α, is hereby made to account for this effect and is defined as

$$\alpha = \frac{N_{\text{locked}}}{N_{\text{forward}}} \tag{15}$$

where N_{locked} is the number of cracks that are locked during any subcycle of a larger loading sequence. The parameter α will have a value between zero and one, depending on the amount of irreversibility that occurs from sliding cracks. It will also have an identical value during the unloading and reloading portions of a subcycle, since it is assumed that locked cracks can not become free until the previous maximum stress is exceeded. The sliding irreversibility factor, α, allows the material model to account for permanent strain during stress cycling since the effective number of sliding cracks is reduced during the unloading portion of a stress cycle. It also provides memory in the material model by vanishing above the previous maximum stress.

Now that the assumptions to the model are established, the crack configurational parameters in Eqs 8 and 12 can be lumped together in a similar manner as was done for the open crack case such that

$$V_{\text{forward}} = \frac{4\pi N_{\text{forward}}\,\bar{c}^3_{\text{forward}}}{3V} \tag{16a}$$

and

$$V_{\text{reverse}} = \frac{4\pi N_{\text{reverse}}\,\bar{c}^3_{\text{reverse}}}{3V} \tag{16b}$$

where V_{forward} and V_{reverse} provide a measure of the strain energy interaction volume of forward- and reverse-sliding cracks, respectively. Combining Eqs 14 through 16 then gives

$$V_{\text{reverse}} = V_{\text{forward}} (1 - \alpha) \tag{17}$$

Now, by combining Eqs 8, 12, 16, and 17, the relations that describe the crack-sliding portion of the behavior in the coating material can be determined and are summarized as follows:

$$\frac{1}{E_{\text{forward}}} = \frac{1}{E_o} [1 + V_{\text{forward}} (1 - \alpha) f_{\text{forward}} (\mu, \beta_{\max})] \tag{18a}$$

$$\frac{1}{E_{\text{reverse}}} = \frac{1}{E_o} [1 + V_{\text{forward}} (1 - \alpha) f_{\text{reverse}} (\mu, \beta_{\max})] \tag{18b}$$

where α is used in the forward-sliding equation (Eq 18a) to distinguish between forward sliding that occurs during initial loading ($\alpha = 0$) and that occurring during a reloading segment up to a previous maximum stress ($0 < \alpha < 1$). The final assembly of the model can now take place. By combining Eqs 3 and 18, the total deformation behavior of the coating material is given as:

$$\frac{1}{E_{\text{loading}}} = \frac{1}{E_o} [1 + V_{\text{open}} + V_{\text{forward}} (1 - \alpha) f_{\text{forward}} (\mu, \beta_{\max})] \tag{19a}$$

$$\frac{1}{E_{\text{unloading}}} = \frac{1}{E_o} [1 + V_{\text{open}} + V_{\text{forward}} (1 - \alpha) f_{\text{reverse}} (\mu, \beta_{\max})] \tag{19b}$$

where α is again used as it was in Eq 18.

Modeling—Application

In order for the model to sufficiently describe the deformation behavior of the coating material, the values of five parameters—E_o, μ, V_{open}, V_{forward}, and α—need to be known. For the current model, a constant coefficient of friction of $\mu = 0.4$ was assumed for the microcrack surfaces and an intrinsic modulus $E_o = 210$ GPa was used for 24%CeO_2-ZrO_2. The remaining three parameters can be determined by the experimental results.

The parameter V_{open} is determined first by measuring the initial unloading modulus, $E^o_{\text{unloading}}$, as a function of stress. As previously discussed, the effect of sliding cracks on the overall modulus of the material is negligible during the initial stages of unloading because they are locked in friction. Therefore, the last term in Eq 19b is approximately zero. Equation 19b then becomes

$$\frac{1}{E^o_{\text{unloading}}} = \frac{1}{E_o} (1 + V_{\text{open}}) \tag{20}$$

from which V_{open} can be readily determined.

Figure 11 shows the measurements of the initial unloading moduli from the cyclic tests (Figs. 5 and 6) conducted in both the in-plane and transverse material directions. It is seen from the figure that the initial unloading modulus is linear with stress. After calculating the initial unloading moduli and inserting the result into Eq 20, values for V_{open} were calculated to range from about 2 to 13 for the in-plane direction and from about 4 to 21 for the transverse direction for the stress ranges tested. Such high values for V_{open} indicate that there

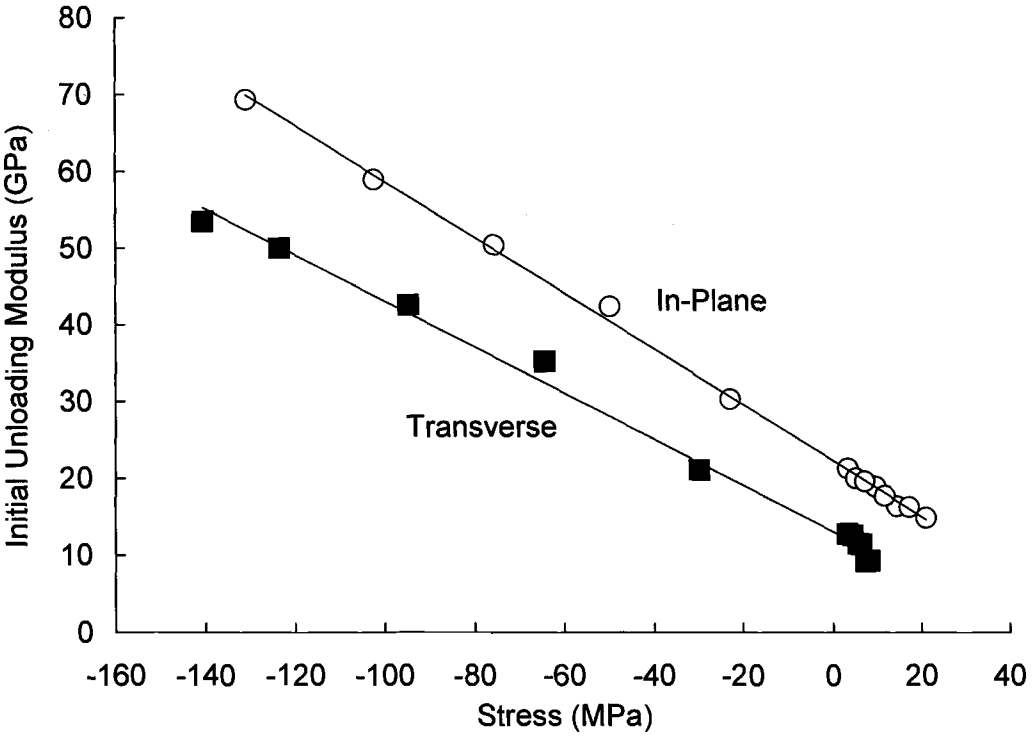


FIG. 11—*Initial unloading modulus measurements for the in-plane and transverse directions as taken from Figs. 5 and 6.*

is either a considerable amount of long cracks in the microstructure, that the density of microcracks is quite large, or both. Recalling the definition of V_{open} in Eq 2, the effect of cracks increases by the cube of their length and is proportional to their number. Therefore, a microstructure with many long, interconnected cracks will have a very large impact on the deformation behavior of the material. As seen in Fig. 3, such features dominate the microstructure of plasma-sprayed coating materials. In addition to having a large value, the range of values for V_{open} also indicates that microcrack closure is a very active mechanism during deformation.

With adequate knowledge of V_{open} obtained, the value of $V_{forward}$ can now be determined by the use of Eq 19a. By setting α in Eq 19a to zero for initial loading, the value of $V_{forward}$ was evaluated for both the in-plane and transverse directions by using the cyclic compressive results shown in Figs. 5 and 6. It was found that the value of $V_{forward}$ for both the in-plane and transverse directions was approximately constant, indicating that the overall effect of sliding cracks was not varying significantly during the stress ranges of the tests. Therefore, the value of $V_{forward}$ was assigned a constant value that was determined by matching the model's results to the secant moduli at the maximum compressive stress measured by experiment. In doing so, the values for $V_{forward}$ for the in-plane and transverse directions were found to be about 15 and 35, respectively. These high values indicate that the effect of sliding cracks on the deformation behavior of the coating material is indeed quite significant. By comparing the values of $V_{forward}$ with those of V_{open} previously determined, it is seen that both open and sliding cracks have effects that are of the same order of magnitude. This

means that both mechanisms have to be considered equally in order to accurately describe the deformation behavior of the coating material.

The final parameter for the compressive deformation model to be obtained is α, the sliding irreversibility factor. This was done in such a way so that the model produced an irreversible strain that approximately matched that seen in Fig. 7. It was found that both the in-plane and transverse coating material directions had an α value of about 0.35. The physical significance of this in terms of the model is that, on average, 35% of the sliding crack activity is halted during unloading and reloading to a previous maximum stress.

Results of the model for compression are compared to the cyclic loading curves in Figs. 12 and 13 for the in-plane and transverse coating material directions, respectively. For the sake of clarity, the cyclic data for only a few of the cycles shown in Figs. 5 and 6 were used for comparison. It can be seen that the model captures both the quantitative and qualitative aspects of the cyclic deformation behavior quite well. The model accounts for the non-linear initial loading behavior, exhibits an appropriate amount of hysteresis during unloading, and follows reasonably well the increase in permanent strain as a function of maximum stress.

Though seemingly biased toward compressive loading, the present model also accounts for similar sliding mechanisms operating in tension. Consider the schematic shown in Fig. 14, which depicts an irregular crack surface. Upon far-field loading, a local stress will occur in the region of the material and may cause sliding. It can be seen that sliding may occur during local tension as well as local compression. In either case, hysteresis will be generated from local stress cycles that occur at the crack. Due to the inhomogeneous and densely microcracked structure of plasma-sprayed coating materials, these local sliding events will occur from any far-field loading that is applied, be it tension or compression. This is evi-

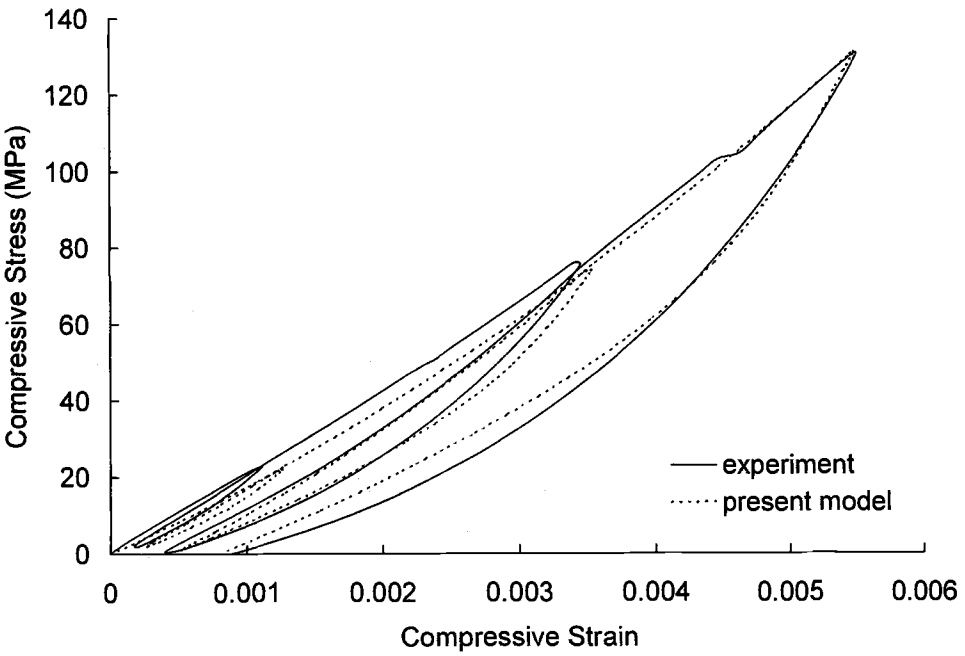


FIG. 12—*In-plane cyclic compression: model versus experiment.*

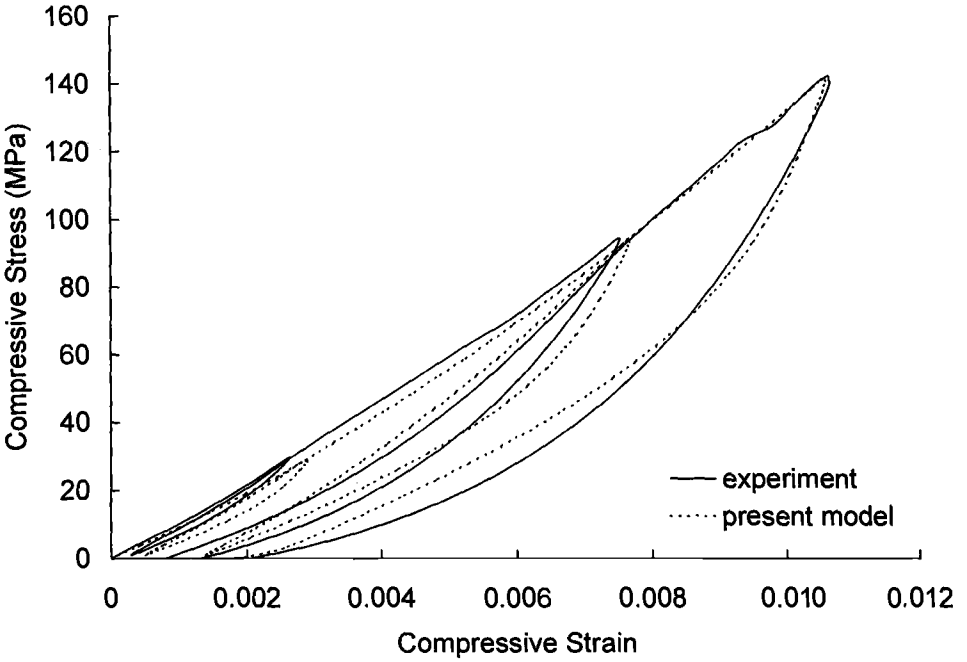


FIG. 13—*Transverse cyclic compression: model versus experiment.*

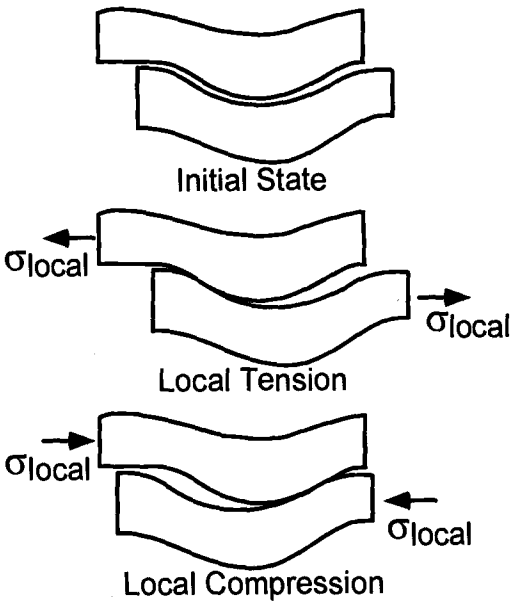


FIG. 14—*Schematic of irregular crack surface sliding due to either a local tensile or compressive stress.*

denced by the fact that hysteresis is seen in the deformation behavior in both tension and compression.

For the current study it was assumed that local sliding mechanisms were as equally active in far-field tension as they were in far-field compression and that local compressive stresses caused by far-field tension were similar to those caused by far-field compression. As an approximation, it was therefore assumed that the values of $V_{forward}$ for the in-plane and transverse coating material directions were the same in tension as they were in compression. Furthermore, Eq 19 was still assumed to hold.

The results of the model in tension are shown in Figs. 15 and 16. For comparison purposes, only the outermost tensile loading cycle from Figs. 5 and 6 were used. It can be seen that although the quantitative aspects are not as good as they were for compression, the model does allow both hysteresis and permanent strains to occur. The fact that the magnitude of these features is underestimated indicates that additional microcracking probably has a significant effect on tensile behavior. It also indicates that the magnitude of crack-sliding activity may be different for tension and compression.

Summary and Conclusions

In this study, the room temperature in-plane and transverse deformation behavior of a 24%CeO_2-ZrO_2 plasma-sprayed coating material was investigated independent of a substrate. It was observed experimentally that the coating material exhibits non-linear behavior during monotonic loading and both hysteretic and irreversible behavior during cyclic tensile and

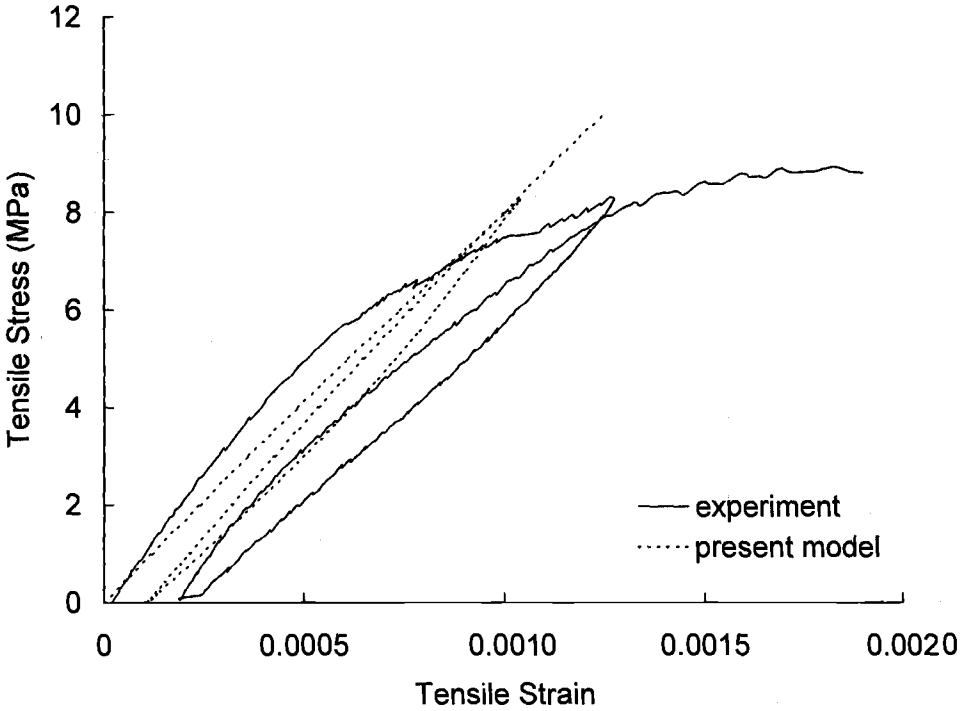


FIG.15—*In-plane cyclic tension: model versus experiment.*

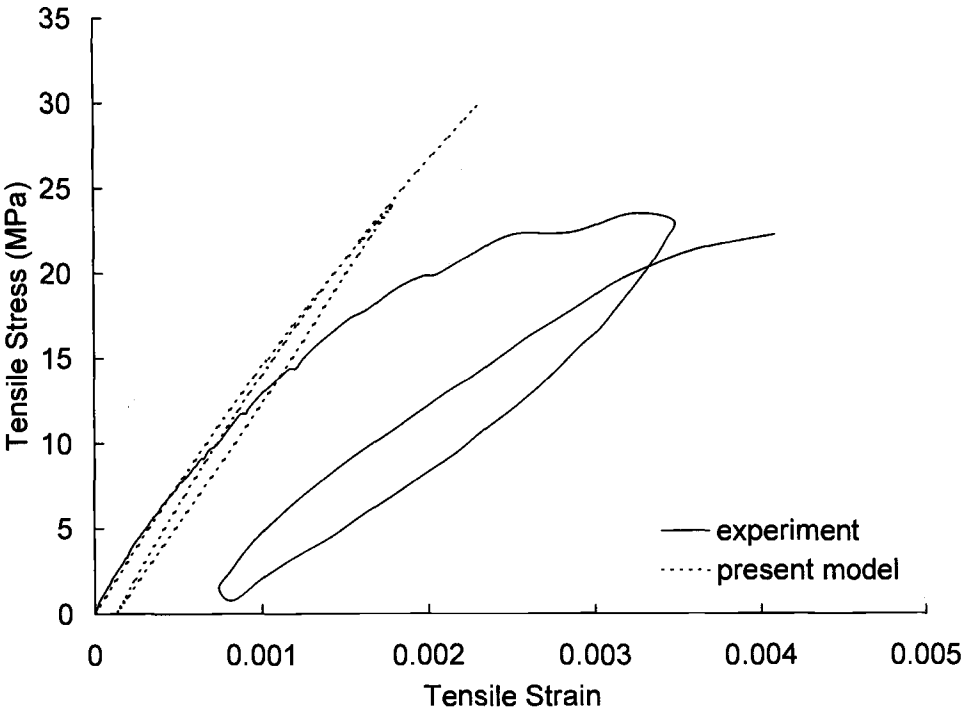


FIG. 16—*Transverse cyclic tension: model versus experiment.*

compressive loading. Based on the fact that the coating microstructure has a considerable density of microcracking in the as-sprayed condition, a phenomenological model was proposed to account for three fundamental mechanisms that were believed to occur during deformation: elasticity, microcrack sliding, and the microcrack closure. The constants of the model were shown to be readily obtainable from the experimental results and described the qualitative and quantitative features of the material quite well, especially in compression. Deficiencies of the model in tension were believed to be due to the lack of any account for additional microcracking, which may be important in the tensile regime.

Acknowledgments

The authors gratefully acknowledge the U.S. Department of Energy for supporting this work under Contract No. DE-FG02-96ER-45439 and DE-FG02-91ER-45439.

References

[*1*] Miller, R. A., "Current Status of Thermal Barrier Coatings—An Overview," *Surface & Coatings Technology*, Vol. 30, 1987, pp. 1–11.

[*2*] Liebert, C. H. and Stepka, F. S., "Ceramic Thermal-Barrier Coatings for Cooled Turbines," *AIAA Journal of Aircraft*, Vol. 14, No. 5, May 1977, pp. 487–493.

[*3*] Levine, S. R., Miller, R. A., and Hodge, P. E., "Thermal Barrier Coatings for Heat Engine Components," *Sample Quarterly*, Vol. 12, October 1980, pp. 20–26.

[4] Larson, H. J., "Thick Thermal Barrier Coatings," *Proceedings of the Twenty-Fourth Automotive Technology Development Contractors Coordination Meeting, Society of Automotive Engineers,* SAE SP-179, 1986, pp. 73–82.

[5] Brink, R. C., "Material Property Evaluation of Thick Thermal Barrier Coating Systems," *ASME Journal of Engineering for Gas Turbines and Power,* Vol. 111, 1989, pp. 570–577.

[6] Takeuchi, Y. R. and Kokini, K., "Thermal Fracture of Ceramic Thermal Barrier Coatings," *ASME Journal of Engineering for Gas Turbines and Power,* Vol. 116, 1996, pp. 266–271.

[7] Zhu, D. and Miller, R. A., "Thermal Fatigue Testing of ZrO_2-Y_2O_3 Thermal Barrier Coating Systems Using a High Power CO_2 Laser," *NASA Technical Memorandum 107439, Army Research Laboratory Technical Report ARL-TR-1354,* April 1997.

[8] Rejda, E. F., Socie, D. F., and Itoh, T., "Deformation Behavior of Plasma-Sprayed Thick Thermal Barrier Coatings," *Surface & Coatings Technology,* Vol. 113, 1999, pp. 218–226.

[9] DeMasi-Marcin, J. T., Sheffler, K. D., and Bose, S., "Mechanisms of Degradation and Failure in a Plasma-Sprayed Thermal Barrier Coating," *ASME Journal of Engineering for Gas Turbines and Power,* Vol. 112, 1990, pp. 521–526.

[10] Walsh, J. B., "The Effects of Cracks on the Uniaxial Elastic Compression of Rocks," *Journal of Geophysical Research,* Vol. 70, No. 2, 1965, pp. 399–411.

[11] Lawn, B. R. and Marshall, D. B., "Nonlinear Stress-Strain Curves for Solids Containing Closed Cracks with Friction," *Journal of the Mechanics and Physics of Solids,* Vol. 46, No. 1, 1998, pp. 85–113.

Elastic-Plastic Fracture Mechanics

Y. J. Chao,[1] *X. K. Zhu,*[1] *P.-S. Lam,*[2] *M. R. Louthan,*[2] *and N. C. Iyer*[2]

Application of the Two-Parameter J-A_2 Description to Ductile Crack Growth

REFERENCE: Chao, Y. J., Zhu, X. K., Lam, P.-S., Louthan, M. R., and Iyer, N. C., **"Application of the Two-Parameter J-A_2 Description to Ductile Crack Growth,"** *Fatigue and Fracture Mechanics: 31st Volume, ASTM STP 1389*, G. R. Halford and J. P. Gallagher, Eds., American Society for Testing and Materials, West Conshohocken, PA, 2000, pp. 165–182.

ABSTRACT: Typical ASTM fracture testing determines the J-integral resistance (J-R) curve or fracture toughness (J_{IC}) based on specimens with high-constraint geometry such as those specified in ASTM E 1737-96. A three-term asymptotic solution with two parameters, J and A_2 (a constraint parameter), has been developed for characterizing the constraint effect of various geometries. The present paper extends the J-A_2 characterization of a stationary crack tip to the regime of stable crack growth. Similar to the concept of J-controlled crack growth, the J-A_2 description can be approximately used to characterize ductile crack growth under certain amount of crack extension. The region of J-A_2 controlled crack growth is much larger than that controlled by the J-integral alone. From the relationships between A_2 and the test data, J_{IC}, and tearing modulus, T_R, the coefficients used to define a J-R curve can be determined. For non-standard specimens or actual structures, once the constraint parameter A_2 is determined, the J-R curves appropriate for these geometries can then be obtained. A procedure of transferring J-R curves determined from the standard ASTM procedure to non-standard specimens or flawed structures is outlined in the paper.

KEYWORDS: constraint effect, fracture toughness, tearing modulus, J-R curve, J-A_2, asymptotic solution, J-controlled crack growth

Introduction

The ductile failure of engineering materials is characterized by the fracture initiation toughness J_{IC} and the subsequent fracture resistance (J-R) curve. The standard J-R curve shows that the J-integral is a function of crack extension and is size-independent within a J-controlled growth region. However, for non-standard, low-constraint specimens or flawed structures, the J-R curve may be size and geometry dependent when J-dominance is lost.

The American Society for Testing and Materials (ASTM) standardized the specimen geometries for measuring J_{IC} and J-R curves. These specimens are typically high crack-tip constrained, such as the deeply cracked three-point bend (3PB) and the compact tension (CT) specimens that are specified in ASTM Standard Test Method for J-Integral Characterization of Fracture Toughness (E 1737).

Using the ASTM 710 Grade A steel, Hancock et al. [*1*] measured the fracture toughness J_{IC} and J-R curves for specimens of 3PB, 1CT, center-cracked panel (CCP), and surface-cracked panel (SCP). Joyce and Link [*2,3*] presented the experimental data of ductile crack

[1] Department of Mechanical Engineering, University of South Carolina, Columbia, SC 29208.
[2] Savannah River Technology Center, Materials Technology Section, Westinghouse Savannah River Company, Aiken, SC 29808.

Copyright© 2000 by ASTM International www.astm.org

extension in A533B, HY-100, and HY-80 steels with specimens of 3PB, 1CT, single edge-notched bend (SENB), single edge-notched tensile (SENT), and double edge-cracked plate (DECP). A variety of crack tip constraints were achieved by using these specimens with different crack depths. The results did not show noticeable constraint effects on the crack growth initiation J_{IC}, but a significant difference in the slopes of the *J-R* curves was observed after some amount of crack growth. Similar results were obtained from ductile crack extension experiments of large-size fracture specimens by Marschall et al. [*4*], Eisele et al. [*5*] and Roos et al. [*6,7*], Kordisch et al. [*8*], Klemm et al. [*9*], Henry et al. [*10*], and Haynes and Gangloff [*11*].

Roos et al. [*6*] showed the dependence of the *J-R* curve on specimen geometry and specimen thickness for KS01 (22NiMoCr37) that is typically used in the German nuclear industry. Their results indicated that a thicker specimen tends to lower the *J-R* curve. Of particular interest is the *J-R* curve from the SENT specimen. It is substantially lower than that from the standard CT that is used widely in fracture testing. This implies that the standard ASTM CT specimen may not always form the lower bound *J-R* curve among various specimen geometries. Therefore, the fracture properties determined from the standard CT specimens might not safely represent the tearing resistance of an actual structural component. They also showed that in the case of DENT specimens, deep cracks result in lower *J-R* curves. The trend of all their test data is consistent with a general rule in the constraint effect of fracture, that is, specimens with higher constraint result in lower *J-R* curves.

In some nuclear applications such as the fracture testing for irradiated materials, the specimen size is limited due to the test facility or the material availability. Miniature or subsized disk compact tension (DCT) specimens are often used (Alexander [*12*]). Similar sub-sized fracture specimens were also used, for instance, by Elliot et al. [*13*] and Yoon et al. [*14*] and in ceramics materials used by Zhang and Ardell [*15*] and Gilbert et al. [*16*]. The *J-R* curves for these specimen geometries differed significantly from those of standard specimens because of the effect of crack-tip constraints, while the values of initiation toughness J_{IC} remained similar [*12*].

For a stationary crack in elastic-plastic materials, the effect of constraint on crack-tip fields has been investigated extensively by Betegon and Hancock [*17*], O'Dowd and Shih [*18,19*], Yang et al. [*20,21*], and Chao et al. [*22*], etc. A review can be found in Chao and Zhu [*23*]. This paper is focused on the J-A_2 approach [*20–22*], which was derived from a rigorous asymptotic solution and has been developed for two-parameter characterization of a crack tip field for application to fracture toughness testing. With J being the driving force and A_2 the constraint parameter, this approach has been used successfully to quantify the constraints of crack-tip fields for various geometry and loading configurations [*22–26*]. Note that the parameter A_2 is almost independent of its position near the crack tip (Nikishkov et al. [*27*]).

Similar to the concept of J-controlled crack growth, it is expected that the J-A_2 description can approximately characterize the effect of crack-tip constraints on ductile crack growth, at least for a certain amount of crack extension. As shown in Fig. 1, the amount of J-A_2 controlled crack growth, Δa, should be much larger than that controlled by J alone [*23*].

The objective of this paper is to extend the J-A_2 characterization of crack tip fields to the stable crack growth regime. A procedure is outlined for transferring the *J-R* curves determined from ASTM standard specimens to non-standard specimens or to flawed structures. Based on a set of test data, a constraint modified *J-R* curve can be developed. Using literature data [*3*], the predicted *J-R* curve is demonstrated and is compared to the experimental *J-R* curve.

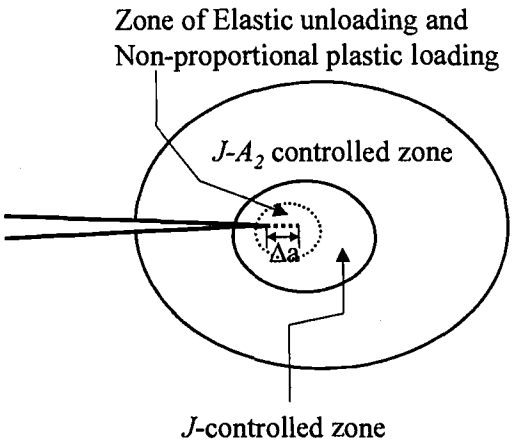


FIG. 1—*Schematic regimes for* J *and* J-A_2 *controlled crack growth.*

Theoretical Background

A Mode I crack under plane strain condition is considered. The elastic-plastic material behavior is described by the Ramberg-Osgood power-law strain-hardening curve where the uniaxial strain ε is related to the uniaxial stress σ in simple tension by

$$\frac{\varepsilon}{\varepsilon_0} = \frac{\sigma}{\sigma_0} + \alpha \left(\frac{\sigma}{\sigma_0}\right)^n \tag{1}$$

where σ_0 is a reference stress, $\varepsilon_0 = \sigma_0/E$ is a reference strain with E as the Young's modulus (for actual elastic-plastic solids, σ_0 and ε_0 may be taken as the yield stress and the yield strain of the material, respectively), α is a material constant, and n is a strain-hardening exponent. By using the J_2 deformation theory of plasticity, the uniaxial stress-strain relation (1) can be generalized to

$$\frac{\varepsilon_{ij}}{\varepsilon_0} = (1 + \upsilon)\frac{\sigma_{ij}}{\sigma_0} - \nu \frac{\sigma_{kk}}{\sigma_0}\delta_{ij} + \frac{3}{2}\alpha \left(\frac{\sigma_e}{\sigma_0}\right)^{n-1} \frac{s_{ij}}{\sigma_0} \tag{2}$$

where υ is the Poisson's ratio, δ_{ij} is the Kronecker delta, s_{ij} is the deviatoric stress, and σ_e is the von Mises effective stress defined as $\sigma_e = \sqrt{3s_{ij}s_{ij}/2}$. The tensor summation convention has been used.

J-A_2 *Three-Term Asymptotic Solution*

Equation 2 is rewritten with respect to a polar coordinate system (r,θ) with its origin at the crack tip. The $\theta = 0$ is along the uncracked ligament. Yang [*28*], Yang et al. [*20,21*], and Chao et al. [*22*] developed a three-term asymptotic crack-tip solution with only two parameters J and A_2, in which the J-integral can be used to quantify the magnitude of applied loading and A_2 describes the crack tip constraints. The asymptotic fields of stress (σ_{ij}), strain (ε_{ij}), and displacement (u_i) can be expressed as

$$\frac{\sigma_{ij}}{\sigma_0} = A_1 \left[\left(\frac{r}{L}\right)^{s_1} \tilde{\sigma}_{ij}^{(1)}(\theta,n) + A_2 \left(\frac{r}{L}\right)^{s_2} \tilde{\sigma}_{ij}^{(2)}(\theta,n) + A_2^2 \left(\frac{r}{L}\right)^{s_3} \tilde{\sigma}_{ij}^{(3)}(\theta,n) \right] \tag{3}$$

$$\frac{\varepsilon_{ij}}{\alpha\varepsilon_0} = A_1^n \left[\left(\frac{r}{L}\right)^{ns_1} \tilde{\varepsilon}_{ij}^{(1)}(\theta,n) + A_2 \left(\frac{r}{L}\right)^{(n-1)s_1+s_2} \tilde{\varepsilon}_{ij}^{(2)}(\theta,n) + A_2^2 \left(\frac{r}{L}\right)^{(n-1)s_1+s_3} \tilde{\varepsilon}^{*(3)}_{ij}(\theta,n) \right] \tag{4}$$

$$\frac{u_i}{\alpha\varepsilon_0 L} = A_1^n \left[\left(\frac{r}{L}\right)^{ns_1+1} \tilde{u}_i^{(1)}(\theta,n) + A_2 \left(\frac{r}{L}\right)^{(n-1)s_1+s_2+1} \tilde{u}_i^{(2)}(\theta,n) + A_2^2 \left(\frac{r}{L}\right)^{(n-1)s^1+s_3+1} \tilde{u}_i^{(3)}(\theta,n) \right] \tag{5}$$

where the angular functions $\tilde{\sigma}_{ij}^{(k)}$, $\tilde{\varepsilon}_{ij}^{(k)}$, and $\tilde{u}_i^{(k)}$, the stress power exponents s_k, and the dimensionless integration constant I_n are dependent only of the hardening exponent n and independent of the other material constants (i.e., α, ε_0, σ_0) and applied load. The characteristic length, L, can be the crack length a, the specimen width W, the thickness B, or a unity 1 cm. The parameters A_1 and s_1 are given by the Hutchinson-Rice-Rosengren (HRR) field [*29–31*],

$$A_1 = \left(\frac{J}{\alpha\varepsilon_0\sigma_0 I_n L}\right)^{-s_1}, \qquad s_1 = -\frac{1}{n+1} \tag{6}$$

and $s_3 = 2s_2 - s_1$ for $n \geq 3$. The values of s_2 can be determined numerically and are shown in Table 1 [*22,25*]. The parameter A_2 is undetermined and is related to the loading and geometry of the specimen. The Mode I plane strain dimensionless functions $\tilde{\sigma}_{ij}^{(k)}$, $\tilde{\varepsilon}_{ij}^{(k)}$, $\tilde{u}_i^{(k)}$, s_k, and I_n have been calculated and tabulated by Chao and Zhang [*32*]. When $A_2 = 0$, the three-term asymptotic solutions Eqs 3 to 5 coincide with the HRR singular field.

Yang et al. [*20*] showed that the above three-term asymptotic solutions are the fully plastic or the pure power-law solutions when the material is moderate or low strain hardening, $n \geq 3$. Comparing them with the finite element results, it can be shown that the three-term solution can be used to characterize the crack tip region well beyond $r/(J/\sigma_0) = 5$ [*20,21,23,26*]. This solution is valid under both small-scale yielding and large-scale yielding conditions and is independent of the crack tip constraint in any strain-hardening materials.

TABLE 1—*Stress exponents in higher order terms (Mode I plane strain solution).*

n	$s_1 = -1/(n+1)^a$	s_2	s_3
3	−0.25	−0.01284	0.2243
4	−0.2	0.03282	0.2656
5	−0.16667	0.05456	0.2758
10	−0.09091	0.06977	0.2304
13	−0.07143	0.06468	0.2008

[a] HRR solution.

Relationship Between J *and* A_2 *under Fully Plastic Conditions*

For a pure power-law or fully plastic material, Ilyushin [*33*] showed that under monotonically increasing load a solution to the boundary value problem has a simple form, that is, the stress is linearly related to the applied load P, and the strain and the displacement are proportional to P^n. Therefore,

$$\frac{\sigma_{ij}}{\sigma_0} = \left[\frac{P}{P_0}\right] \hat{\sigma}_{ij}(x_i,n) \tag{7}$$

$$\frac{\varepsilon_{ij}}{\alpha\varepsilon_0} = \left[\frac{P}{P_0}\right]^n \hat{\varepsilon}_{ij}(x_i,n) \tag{8}$$

$$\frac{u_j}{\alpha\varepsilon_0 L} = \left[\frac{P}{P_0}\right]^n \hat{u}_i(x_i,n) \tag{9}$$

where the dimensionless $\hat{\sigma}_{ij}$, $\hat{\varepsilon}_{ij}$, and $\hat{u}_i$ are functions of spatial coordinates x_i and strain-hardening exponent n, and are independent of the applied load P. The reference load, P_0, can be the limit load. These expressions are the direct result of the homogenous nature of the equations of equilibrium, compatibility, and the constitutive relation (Eq 2).

Since the integrand of the J-integral involves products of stress and displacement gradients, from Eqs 7 to 9, Goldman and Hutchinson [*34*] showed that the fully plastic J-integral is proportional to P^{n+1}:

$$\frac{J}{\alpha\varepsilon_0\sigma_0 a} = \left[\frac{P}{P_0}\right]^{n+1} \hat{J}(a/W,n) \tag{10}$$

where a is a crack length and W is a specimen width. The dimensionless function $\hat{J}$ depends only on the geometry size ratio a/W and strain-hardening exponent n.

Substituting Eq 10 into Eqs 7 to 9 and eliminating load term P/P_0, one can obtain the relationship between the field quantities and J-integral

$$\frac{\sigma_{ij}}{\sigma_0} = \left[\frac{J}{\alpha\varepsilon_0\sigma_0 a\hat{J}(a/W,n)}\right]^{1/n+1} \hat{\sigma}_{ij}(x_i,n) \tag{11}$$

$$\frac{\varepsilon_{ij}}{\alpha\varepsilon_0} = \left[\frac{J}{\alpha\varepsilon_0\sigma_0 a\hat{J}(a/W,n)}\right]^{n/n+1} \hat{\varepsilon}_{ij}(x_i,n) \tag{12}$$

$$\frac{u_j}{\alpha\varepsilon_0 L} = \left[\frac{J}{\alpha\varepsilon_0\sigma_0 a\hat{J}(a/W,n)}\right]^{n/n+1} \hat{u}_i(x_i,n) \tag{13}$$

The above expressions are the unique forms of solutions for plane crack problems under fully plastic deformation. Therefore, the three-term asymptotic solutions (Eqs 3 to 5) must meet the functional forms (Eqs 11 to 13), or

$$\left(\frac{r}{L}\right)^{s_1} \tilde{\sigma}_{ij}^{(1)}(\theta) + A_2 \left(\frac{r}{L}\right)^{s_2} \tilde{\sigma}_{ij}^{(2)}(\theta) + A_2^2 \left(\frac{r}{L}\right)^{s_3} \tilde{\sigma}_{ij}^{(3)}(\theta) = \left[\frac{I_n L}{a\hat{J}(a/W,n)}\right]^{1/n+1} \hat{\sigma}_{ij}(r,\theta,n) \quad (14)$$

$$\left(\frac{r}{L}\right)^{ns_1} \tilde{\varepsilon}_{ij}^{(1)}(\theta) + A_2 \left(\frac{r}{L}\right)^{(n-1)s_1+s_2} \tilde{\varepsilon}_{ij}^{(2)}(\theta) + A_2^2 \left(\frac{r}{L}\right)^{(n-1)s_1+s_3} \tilde{\varepsilon}^{*(3)}_{ij}(\theta) = \left[\frac{I_n L}{a\hat{J}(a/W,n)}\right]^{n/n+1} \hat{\varepsilon}_{ij}(r,\theta,n) \quad (15)$$

$$\left(\frac{r}{L}\right)^{ns_1+1} \tilde{u}_i^{(1)}(\theta) + A_2 \left(\frac{r}{L}\right)^{(n-1)s_1+s_2+1} \tilde{u}_i^{(2)}(\theta) + A_2^2 \left(\frac{r}{L}\right)^{(n-1)s_1+s_3+1} \tilde{u}_i^{(3)}(\theta) = \left[\frac{I_n L}{a\hat{J}(a/W,n)}\right]^{n/n+1} \hat{u}_i(r,\theta,n) \quad (16)$$

In Eqs 14 to 16, the exponents s_k and the constant I_n are dependent only on the hardening exponent n. The angular functions $\tilde{\sigma}_{ij}^{(k)}(\theta)$, $\tilde{\varepsilon}_{ij}^{(k)}(\theta)$, and $\tilde{u}_i^{(k)}(\theta)$ and the dimensionless quantities $\hat{\sigma}_{ij}$, $\hat{\varepsilon}_{ij}$, and $\hat{u}_i$ are the functions of polar coordinates (r,θ) and hardening exponent n. The dimensionless function $\hat{J}$ depends upon geometry size ratio a/W and hardening exponent n. Moreover, all these quantities are independent of the other material properties (α, ε_0, σ_0) and the level of the applied load or J-integral. If the characteristic length L is independent of J, for instance, $L = a,W,B$, or 1 cm, one can conclude immediately from Eqs 14 to 16 that A_2 is only the function of the strain-hardening exponent n and the geometry dimension (a,W, a/W), namely,

$$A_2|_{\text{fully plastic}} = f(n, \text{geometry}) \quad (17)$$

As a result, under fully plastic deformation conditions the constraint parameter A_2 in the three-term solutions (Eqs 3 to 5) is independent of the applied J for a given specimen and material.

Using a 3PB and SEN specimens, the finite element results [*22,28*] showed that A_2 becomes a constant value as the applied load (characterized by J) increases beyond about 1.2 times the limit load with the hardening exponent $n = 4$, 7, and 12. Therefore, for a specimen fracturing at large-scale yielding or near fully plastic condition, the value of A_2 determined at $J = J_{IC}$ can be used for loads $J \geq J_{IC}$, as long as the growing crack tip is still within the J-A_2 field and the elastic unloading behind the crack tip does not significantly alter the crack tip field.

Determination of the Constraint Parameter A_2

A *point matching technique* was used by Yang et al. [*20,21*] and Chao et al. [*22*] to determined the value of A_2. The stress obtained by finite element analysis at a point (r,θ) near the crack tip is set equal to the three-term analytical solution (Eq 3) to solve for A_2. In particular, these authors used σ_{rr} and $\sigma_{\theta\theta}$ at $r = 2(J/\sigma_0)$, $\theta = 0°$ or 45°. Chao and Zhu [*23*] also used this approach to determine A_2, but r is chosen from J/σ_0 to $5(J/\sigma_0)$.

To reduce the finite element mesh size sensitivity on the value of A_2, Nikishkov et al. [*27*] developed another technique, the *least square procedure,* for fitting the finite element data

in the region $1 < r/(J/\sigma_0) < 5$. They found that A_2 is almost independent of its location within the region of interest.

A *simple weight average technique* is developed for the determination of A_2. It is assumed that the resultant force due to the crack opening stress $\sigma_{\theta\theta}(r,\theta)$ on the remaining ligament in the region of $1 < r/(J/\sigma_0) < 5$ has the same magnitude from a finite element result and from the three-term solution (Eq 3). Mathematically, it is expressed as

$$\int_1^5 \frac{\sigma_{\theta\theta}^{FEA}(\bar{r},0)}{\sigma_0}\, d\bar{r} = \left(\frac{J}{\alpha\varepsilon_0\sigma_0 I_n L}\right)^{-s_1} \int_1^5 \left[\left(\frac{J\bar{r}}{\sigma_0 L}\right)^{s_1} \tilde{\sigma}_{ij}^{(1)}(0) + A_2\left(\frac{J\bar{r}}{\sigma_0 L}\right)^{s_2} \tilde{\sigma}_{ij}^{(2)}(0) + A_2^2\left(\frac{J\bar{r}}{\sigma_0 L}\right)^{s_3} \tilde{\sigma}_{ij}^{(3)}(0)\right] d\bar{r}$$

where $\bar{r} = r/J/\sigma_0)$ and $\sigma_{\theta\theta}^{FEA}$ is the crack opening stress for points on the $(r,\theta) = (r,0)$ line determined from finite element calculations. Upon integrating the above expression, the value of A_2 can be determined simply by solving the following second-order algebraic equation:

$$aA_2^2 + bA_2 + c = 0 \tag{18}$$

where

$$a = \frac{5^{s_3+1} - 1}{(s_3 + 1)(L\sigma_0/J)^{s_3}} \tilde{\sigma}_{\theta\theta}^{(3)}(0) \tag{19a}$$

$$b = \frac{5^{s_2+1} - 1}{(s_2 + 1)(L\sigma_0/J)^{s_2}} \tilde{\sigma}_{\theta\theta}^{(2)}(0) \tag{19b}$$

$$c = \frac{5^{s_1+1} - 1}{(s_1 + 1)(L\sigma_0/J)^{s_1}} \tilde{\sigma}_{\theta\theta}^{(1)}(0) - \left(\frac{J}{\sigma\varepsilon_0\sigma_0 I_n L}\right)^{s_1} \int_1^5 \frac{\sigma_{\theta\theta}^{FEA}(\bar{r},0)}{\sigma_0}\, d\bar{r} \tag{19c}$$

Table 2 gives the values of $\tilde{\sigma}_{\theta\theta}^{(k)}(0)$ for Mode I plane strain cracks [22,25]. The integration in Eq 19c can be determined approximately by numerical summation of $\sigma_{\theta\theta}^{FEA}(\bar{r},0)$ values at the finite element nodes in $1 < \bar{r} < 5$. Note that the weight averaging in Eq 18 and Eq 19 determines the averaged value for A_2 within the range $1 < \bar{r} < 5$ along the $(r,0)$ line. Other ranges of $\bar{r}$ for averaging A_2 may be used.

TABLE 2—*Opening stress* $\tilde{\sigma}_{\theta\theta}^{(k)}(0)$ *in higher order terms (Mode I plane strain solution).*

n	$k = 1^a$	$k = 2$	$k = 3$
3	1.9407	0.2834	−1.2764
4	2.1042	0.3092	−2.1506
5	2.2171	0.3184	−3.2224
10	2.4969	0.3130	−6.4128
13	2.5775	0.3036	−7.2798

[a] HRR solution.

J-A_2 Description of Ductile Crack Growth

The two-parameter, J-A_2 three-term solution has been successfully used to quantify the effect of constraint for stationary crack-tip fields with various geometries and loading configurations [*20–22,26*]. For a growing crack, similar to the concept of J-controlled crack growth, it is assumed that that, within a certain amount of crack extension, the J-A_2 description can approximately characterize the effect of geometry constraint on ductile crack growth with J being the driving force and A_2 the constraint parameter. It is expected that the amount of J-A_2 controlled crack growth is much larger than that of the J-controlled since the crack tip zone dominated by the J-A_2 is much larger than that controlled by J alone [*23*].

A procedure for transferring the J-R curve determined from a standard ASTM procedure to that for a non-standard specimen or to a flawed structure is described in the following. It is then illustrated by using the test data (J_{IC} and T_R) of Joyce and Link [*3*]. A constraint based J-R curve is established for the case of stable crack growth which is characterized by the parameter A_2.

General Framework for Constructing Constraint-Modified J-R *Curves*

The ASTM E 1737 specifies test procedures for the determination of fracture toughness as characterized by the J-integral under plane strain conditions. Based on the amount of crack extension, three toughness properties are identified as: (a) instability without significant prior crack extension (J_C); (b) onset of stable crack extension (J_{IC}); and (c) stable crack growth resistance curve (J-R) in the region of J-controlled growth. The present investigation is focused on the last two fracture properties, (b) and (c).

It is specified in ASTM E 1737 that the fracture toughness J_{IC} is defined as the value of J at crack extension $\Delta a = \Delta a_Q = J_{IC}/2\sigma_F + 0.2$ (mm) or

$$J_{IC} = J(\Delta a_Q)|_{\Delta a_Q = J_{IC}/2\sigma_F + 0.2(\text{mm})} \tag{20}$$

where σ_F is the flow stress or effective yield stress. In addition, the J-resistance curve can be approximated by a best-fit power-law relationship,

$$J(\Delta a) = C_1 \left(\frac{\Delta a}{k}\right)^{C_2} \tag{21}$$

where the coefficients C_1 and C_2 are constants, and $k = 1$ mm or 1 in. depending on the unit of Δa. Note that Eq 21 assumes $J = 0$ at $\Delta a = 0$.

Since J_{IC} corresponds to crack initiation, the constraint parameter A_2 can be solved from Eq 18 by matching the three-term solution (Eq 3) to the finite element results at load level J_{IC}. If the specimens are nonstandard, the corresponding value of A_2 can be obtained in a similar manner, as long as the J_{IC} value is measured.

As described earlier, under large-scale yielding or near fully plastic deformation, the constraint parameter A_2 determined at $J = J_{IC}$ remains constant for $J \geq J_{IC}$. If the crack extension occurs and the location of the current crack tip is within the J-A_2 dominant region, the value of A_2 is approximately invariant for the specific specimen. Incorporating the constraint effect into the J-R curve, a curve of J versus crack extension Δa under J-A_2 controlled growth can be expressed as

$$J(\Delta a, A_2) = C_0(A_2) + C_1(A_2)\left(\frac{\Delta a}{k}\right)^{C_2(A_2)} \tag{22}$$

The coefficients $C_0(A_2)$, $C_1(A_2)$, $C_2(A_2)$ are unknown constants and depend upon the constraint A_2 at the crack tip for a specific material and specimen. The coefficient $C_0(A_2)$ is added to include the fact that J is nonzero at zero crack extension (Δa). That is, if the J value is known prior to crack initiation, then

$$C_0(A_2) = J(\Delta a = 0, A_2) \equiv J_0(A_2) \tag{23}$$

It should be noted that Eq 22 extends the current ASTM J-resistance curve concept of $J(\Delta a)$ to a constraint modified J-resistance curve $J(\Delta a, A_2)$. Once the functional forms of $C_0(A_2)$, $C_1(A_2)$, and $C_2(A_2)$ are known, the constraint modified J-resistance curve (or function), Eq 22 is completely determined. The determination of $C_0(A_2)$, $C_1(A_2)$, and $C_2(A_2)$ is described in the following steps:

Step 1: J-R curves are determined experimentally based on ASTM procedures, but for different crack sizes or specimen types, as shown in Fig. 2*a*. The specimens should be chosen to include several low-constraint to high-constraint specimens. As shown in Fig. 2*a*, each *J-R* curve corresponds to a constant A_2 value, which is determined at the crack initiation load by using finite element results and Eq 18.

Step 2: With three points on each *J-R* curve as shown in Fig. 2*a*, the three coefficients $C_0(A_2)$, $C_1(A_2)$, and $C_2(A_2)$ can be determined for each *J-R* curve or A_2. That is

$$C_1(A_2)\left(\frac{\Delta a_i}{k}\right)^{C_2(A_2)} = J_i(\Delta a_i, A_2) - C_0(A_2); \quad i = 1, 2, 3 \tag{24}$$

Of course, more than three data points on each *J-R* curve can be selected to have a best fit for these three coefficients.

If $\Delta a = \Delta a_Q = J_{IC}/2\delta_F + 0.2$ (mm), $k = 1$ mm and the International System of Units (SI) are used, one has

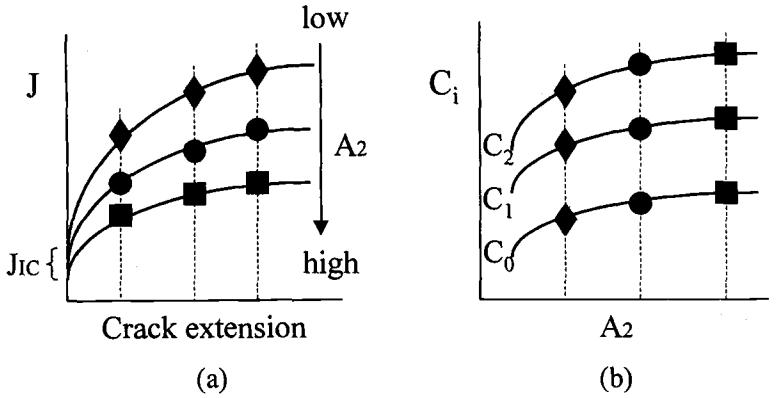


FIG. 2—*Analysis procedure for constructing the constraint-modified* J-R *curves, Eq 24:* (a) *experimental* J-R *curves from various specimens;* (b) *determination of the functional relationship* $C_0(A_2)$, $C_1(A_2)$, $C_2(A_2)$.

$$C_1(A_2)\left(\frac{J_{IC}}{2\sigma_F} + 0.2\right)^{C_2(A_2)} = J_{IC}(A_2) - C_0(A_2) \tag{25}$$

Step 3: Step 2 is repeated for several *J-R* curves, as illustrated in Fig. 2*a*. Through curve fitting, the functional forms of $C_0(A_2)$, $C_1(A_2)$, and $C_2(A_2)$ are determined as shown in Fig. 2*b*.

Alternatively, these coefficients can be determined by the values of the initiation fracture toughness J_{IC} and the corresponding tearing modulus T_R. Note that ASTM E 1737 specifies detailed procedures for the determination of J_{IC} (J at $\Delta a = \Delta a_Q = J_{IC}/2\sigma_F + 0.2$ mm) and $T_R = E/\sigma_0^2\ dJ/da$ at $\Delta a = 1$ mm [*3*]. The fracture toughness at $\Delta a = 0$ is often close to zero, as assumed in Eq 21. The constraint modified *J-R* curve, Eq 22, has therefore only two coefficients $C_1(A_2)$ and $C_2(A_2)$ for each curve or A_2, which can then be determined by J_{IC} and T_R. Using Eq 22 and Eq 25 with SI units, one obtains the following two equations to determine the unknown coefficients C_1 and C_2:

$$\begin{aligned} C_1(A_2)\left(\frac{J_{IC}}{2\sigma_F} + 0.2\right)^{C_2(A_2)} &= J_{IC}(A_2) \\ C_1(A_2)C_2(A_2) = \left.\frac{\partial J(\Delta a, A_2)}{\partial a}\right|_{\Delta a = 1\text{ mm}} &= T_R(A_2)\frac{\sigma_0^2}{E} \end{aligned} \tag{26}$$

Note that both the initiation fracture toughness J_{IC} and the tearing modulus $T_R = E/\sigma_0^2\ dJ/da$ are now functions of the constraint parameter A_2. Using the *J-R* curves obtained for several specimens of various constraint levels, the functional relationship on the right hand sides of Eq 26 can be established as shown in Figs. 3*a* and 3*b*. For a given A_2 value (e.g., A_2 from -1.0 to 0), solving Eq 26 gives the solutions for C_1 and C_2. Consequently, the functional forms of $C_1(A_2)$ and $C_2(A_2)$ are obtained by curve fitting as shown in Fig. 3*c*.

Once the constraint modified *J-R* curve, Eq 22, is completely determined for a material of interest, the *J-R* curves appropriate for any specimen or for any structural component can then be obtained provided that the value of the constraint parameter A_2 is known.

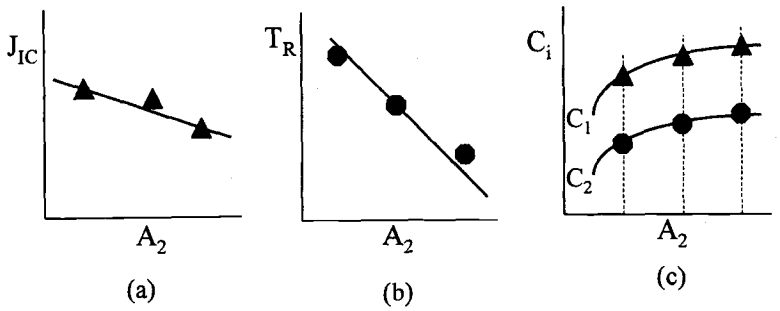


FIG. 3—*Analysis procedure for constructing the constraint-modified* J-R *curves, Eq 26:* (a) *determination of the functional relationship between* J_{IC} *and* A_2; (b) *determination of the functional relationship between* T_R *and* A_2; (c) *determination of the functional relationship* $C_1(A_2)$, $C_2(A_2)$.

Overview of Procedure for Obtaining a Structural J-R *Curve*

A five-step procedure is required to determine the *J-R* curve for a cracked structure:

1. Prepare at least three specimens (from the structure's material) with different constraint levels.
2. Experimentally determine the J_{IC} values and the *J-R* curves for each specimen based on the ASTM fracture test procedures.
3. Determine the value of A_2 for each specimen at load level $J = J_{IC}$ using finite element results and Eq 18.
4. Determine the functional relationship of the three coefficients, C_0, C_1, and C_2 with the constraint parameter A_2. Then obtain the resulting constraint-modified *J-R* curve, (Eq 22), for the material.
5. Determine the value of A_2 for the cracked structure at load level $J = J_{IC}$ by performing finite element analysis of the cracked structure and using Eq 18. Substitute this value of A_2 into Eq 22 obtained in the previous step and obtain the geometry specific *J-R* curve.

Experimental Results of Joyce and Link (1997)

Following ASTM E 1737, Joyce and Link [*3*] tested a series of SENB specimens with a/W ratios ranging from 0.13 to 0.83 for the HY80 steel. The material properties[3] are: 0.2% yield strength $\sigma_0 = 610$ MPa, ultimate strength $\sigma_{us} = 726$ MPa, Young's modulus $E = 199$ GPa, Poisson's ratio $v = 0.29$, and the strain hardening exponent $n = 10$.

The initiation fracture toughness J_{IC} and the material tearing resistance T_R at $\Delta a = 1$ mm, obtained with ASTM E 1737, were presented by Joyce and Link [*3*]. Their results are reproduced in Table 3. Because there is a simple relation between the Q-stress [*18*] and the A_2 parameter, the A_2 parameter used in the current analysis was obtained by converting the Q-stress reported by Joyce and Link [*3*].

Comparing Eq 3 to the definition of Q, that is, $Q\sigma_0 = \sigma_{\theta\theta} - \sigma_{\theta\theta}^{HRR}$ at $\theta = 0$ and $r = 2J/\sigma_0$, the relationship between Q and A_2 is

$$A_2 \left(\frac{2J}{\sigma_0 L}\right)^{s_2} \tilde{\sigma}_{\theta\theta}^{(2)}(0) + A_2^2 \left(\frac{2J}{\sigma_0 L}\right)^{s_2} \tilde{\sigma}_{\theta\theta}^{(2)}(0) = Q \left(\frac{J}{\alpha\varepsilon_0\sigma_0 I_n L}\right)^{s_1} \tag{27a}$$

For strain-hardening exponent $n = 10$, the following constants were determined: $s_1 = 0.09091$, $s_2 = 0.06977$, $s_3 = 0.23044$, $I_n = 4.53985$, $\hat{\sigma}_{\theta\theta}^{(2)} = 0.3130$, and $\tilde{\sigma}_{\theta\theta}^{(3)}(0) = -6.4127$. Letting $\alpha = 1$ and $L = 10$ mm, Eq 27a becomes

$$0.313 \left(\frac{J}{3050}\right)^{0.06977} A_2 - 6.4127 \left(\frac{J}{3050}\right)^{0.23044} A_2^2 = \left(\frac{84.882}{J}\right)^{0.09091} Q \tag{27b}$$

Using Eq 27 and the Q-stresses reported by Joyce and Link [*3*], the A_2 values were determined and are listed in Table 3.

[3] Joyce, J. A., private communication, 1998.

TABLE 3—*Fracture toughness and constraint quantities for SENB specimens [3].*

Specimen I.D.	a/W	a/b, mm	J_{IC}, kJ/m^2	T_R, Δa = 1 mm	Q	A_2
94A	0.29	14.5/35.5	211.8	95.8	−0.36	−0.274
94B	0.26	13.0/37.0	225.6	99.1	−0.43	−0.299
94D	0.19	9.5/40.5	217.2	104.0	−0.60	−0.362
94E	0.39	19.5/30.5	216.0	77.9	−0.24	−0.217
94G	0.55	27.5/22.5	195.2	72.1	−0.15	−0.168
94H	0.55	27.5/22.5	169.2	71.1	−0.10	−0.134
94J	0.13	6.5/43.5	219.3	109.4	−0.70	−0.393
94K	0.14	7.0/43.0	215.1	117.4	−0.70	−0.394
94E	0.14	7.0/43.0	183.0	100.0	−0.67	−0.395
94J	0.13	6.5/43.5	196.5	108.7	−0.68	−0.394
FYB507	0.61	30.5/19.5	189.5	55.0	−0.10	−0.132
95H	0.83	41.5/8.5	162.9	73.7	−0.25	−0.232
95G	0.78	39.0/11.0	145.6	78.7	−0.22	−0.220
95X	0.70	35.0/15.0	172.6	56.1	−0.15	−0.171

NOTE: Specimen length l = 203 mm, width W = 50 mm, thickness B = 25 mm, l/W = 4, B/W = 0.5, side groove 20%, and b is the uncracked ligament.

Prediction of J-R *Curves Using the J-A_2 Description*

With the data given in Table 3 and following the procedures described earlier, a constraint-modified *J-R* curve can be constructed. Figure 4*a* shows that the relationship of J_{IC}, and A_2 can be linearly fitted by

$$J_{IC} = 119.79A_2 + 161.86 \quad (\text{kJ/m}^2) \tag{28}$$

It can be seen that J_{IC} may also be approximated by

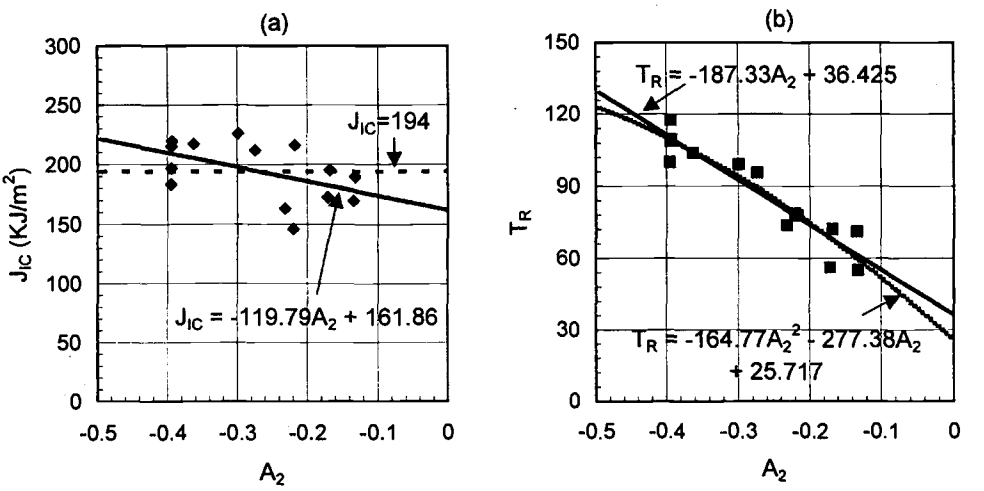


FIG. 4—*Experimental data and fitted curves for SENB specimens. Data points are from Joyce and Link (1997), and the lines are the best-fit curves:* (a) *initiation toughness* J_{IC} *versus* A_2; (b) *tearing toughness* T_R *versus* A_2.

$$J_{IC} = 194 \quad (\text{kJ/m}^2) \tag{29}$$

In Fig. 4*b*, the relationship of T_R and A_2 is fitted by a straight line

$$T_R = -187.33A_2 + 36.425 \tag{30}$$

or by a quadratic equation

$$T_R = -164.77A_2^2 - 277.38A_2 + 25.717 \tag{31}$$

Figure 4*b* shows that Eqs 30 and 31 are almost indistinguishable. Therefore, the linear equation (Eq 30) is used in this analysis.

Based on Eq 30 and the definition of material tearing modulus $T_R = E/\sigma_0^2\ (\partial J/\partial a)|_{\Delta a=1\ \text{mm}}$, substitution of material properties (E and σ_0) yields the slope of the *J-R* curve at Δa = 1 mm:

$$\left.\frac{\partial J}{\partial a}\right|_{\Delta a=1\ \text{mm}} = -350.31A_2 + 68.109 \quad (\text{N/mm}^2) \tag{32}$$

J-R *Curves with J_{IC} Independent of Constraint*—The material flow stress of HY80 is 668 MPa and is defined as $\sigma_F = \frac{1}{2}(\sigma_0 + \sigma_{us})$. Substituting Eq 29 and Eq 32 into Eq 26 gives

$$\begin{cases} C_1(0.3452)^{C_2} = 194 \\ C_1C_2 = -350.31A_2 + 68.109 \end{cases} \tag{33}$$

For a specific value of A_2, the coefficients C_1 and C_2 can be solved from Eq 33 with a non-linear Newton iteration method. Within the range $-1.0 \le A_2 \le 0$, the values of C_1 and C_2 are plotted in Figs. 5*a* and 5*b*, respectively. They are expressed as

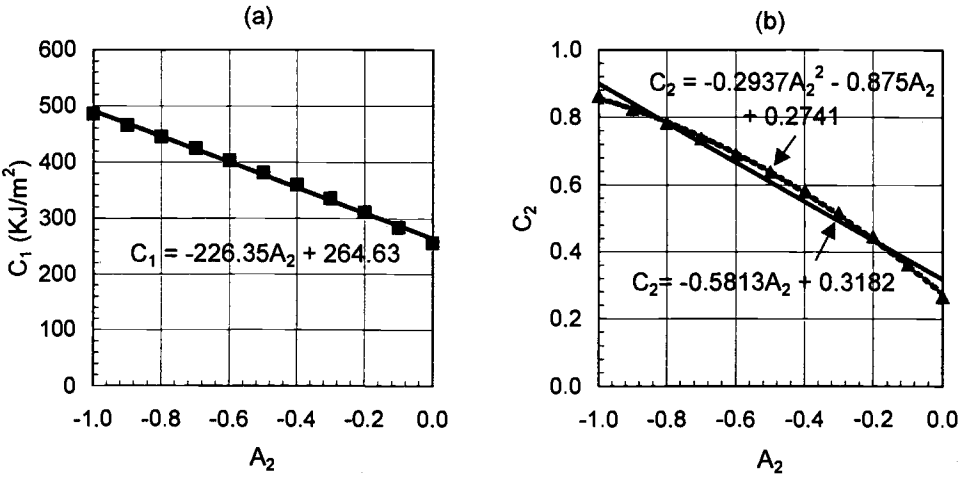


FIG. 5—*Fitted curves for parameters in constraint-modified* J-R *curves with* J_{IC} = *194 KJ/m*^{2}. (*The dots are calculated from Eq 33; the lines are the best-fit curves.*) (a) *Variation of* C_1 *versus* A_2; (b) *variation of* C_2 *versus* A_2.

$$C_1(A_2) = -226.35A_2 + 264.63$$
$$C_2(A_2) = -0.5813A_2 + 0.3182 \tag{34}$$

By substituting Eq 34 into Eq 22, the constraint modified *J-R* curve for HY-80 steel is found to be

$$J(\Delta a, A_2) = (-226.35A_2 + 264.63)\left(\frac{\Delta a}{1\text{ mm}}\right)^{(-0.5813A_2+0.3182)} \tag{35}$$

J-R *Curves with* J_{IC} *Linearly Related to Constraint* A_2—It is not uncommon that the fracture toughness J_{IC} is weakly dependent of the specimen geometry. Therefore, Eq 28 is used to investigate the effect of the J_{IC}-A_2 relationship on the *J-R* curves. Following the same procedure and by substituting Eq 28 and Eq 32 into Eq 26, it can be shown that

$$\begin{cases} C_1(0.3212 - 0.0897A_2)^{C_2} = -119.79\,A_2 + 161.86 \\ C_1C_2 = -350.31A_2 + 68.109 \end{cases} \tag{36}$$

Solving Eq 36 for a given value of A_2, the coefficients C_1 and C_2 are obtained and are plotted in Figs. 6*a* and 6*b*, respectively. For $-1.0 \leq A_2 \leq 0$, the expressions for C_1 and C_2 are:

$$C_1(A_2) = -323.15A_2 + 237.78$$
$$C_2(A_2) = -0.4365A_2 + 0.3551 \tag{37}$$

Substituting Eq 37 into Eq 22, the constraint modified *J-R* curve for HY-80 steel is obtained:

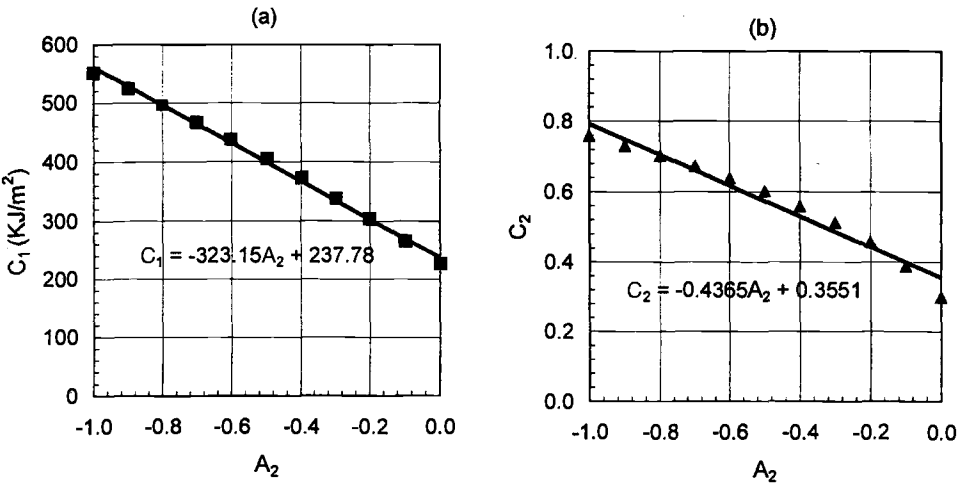


FIG. 6—*Fitted curves for parameters in constraint-modified* J-R *curves with* $J_{IC} = -119.79\ A_2 + 161.86$ *(KJ/m²). (The dots are calculated from Eq 36; the lines are the best-fit curves.)* (a) *Variation of* C_1 *versus* A_2; (b) *variation of* C_2 *versus* A_2.

$$J(\Delta a, A_2) = (-323.15A_2 + 237.78)\left(\frac{\Delta a}{1\ \text{mm}}\right)^{(-0.4365A_2+0.3551)} \tag{38}$$

Figure 7 shows the J-R curves predicted by Eq 35, solid curves, and by Eq 38, dashed curves, for several A_2 values (0.0, −0.168, −0.2, −0.3, and −0.4). It indicates that the predicted J-R curves are insensitive to the functional forms of J_{IC} (28 or 29). Therefore, J_{IC} can be approximately considered as a material constant and is independent of the level of constraint. This agrees with the experimental observations of Hancock et al. [*1*] and Joyce and Link [*3*].

Some experimental data of Joyce and Link [*3*] are also included in Fig. 7. The predicted J-R curves ($A_2 = -0.168$ and -0.393) are compared with the test data of a shallow crack specimen ($a/W = 0.13$) and a deep crack specimen ($a/W = 0.55$). Note that the present analysis used only two data points from each specimen of Joyce and Link, namely, J_{IC} at $\Delta a \cong 0.35$ mm and T_R at $\Delta a = 1$ mm, and yet the predicted J-R curves match very well with the experimental data up to $\Delta a = 7$ mm. Therefore, the J-A_2 description can successfully predict the J-resistance curves even though considerable amount of crack growth has occurred.

Conclusions

To quantity the crack tip constraint effect on J-R curves in ductile crack growth, this paper extends the concept of J-controlled crack growth to J-A_2 controlled crack growth, in which

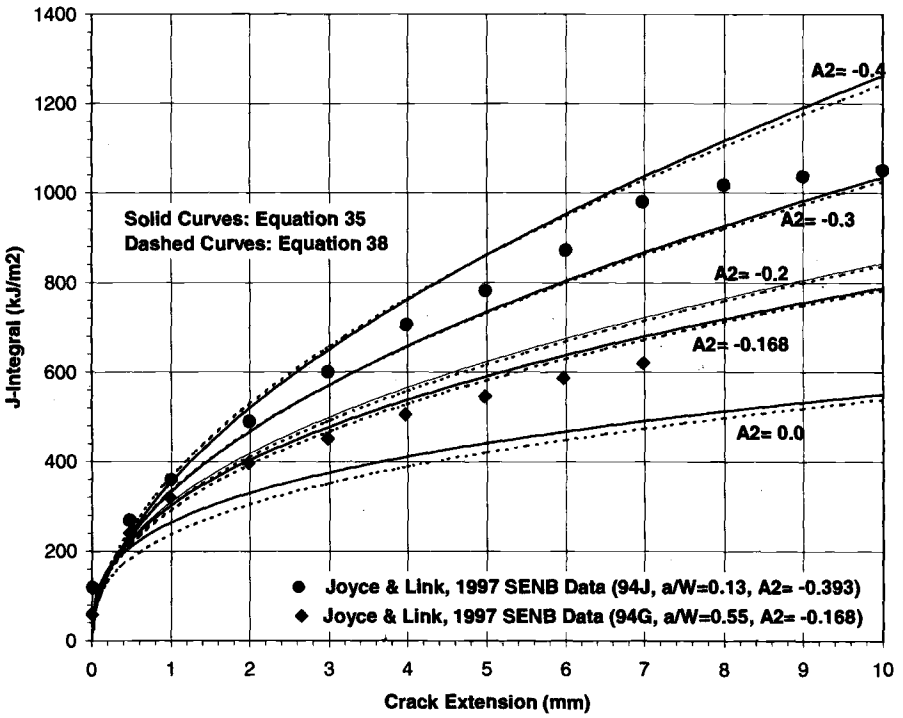


FIG. 7—*Comparisons of predicted* J-R *curves (Eqs 35 and 38)* and SENB J-R *curves of Joyce and Link (1997).*

the J-integral represents the load level and the A_2 parameter indicates the level of constraint. The main results are summarized as follows:

1. Under a fully plastic condition, it is proved by the deformation theory of plasticity (Ilyushin [*33*]) that the constraint parameter A_2 is independent of the applied load. As a result, the constraint parameter A_2, determined at the crack initiation (J_{IC}), remains invariant as long as the growing crack tip is still within a J-A_2 controlled regime.
2. A simple weight average technique is developed to evaluate the value of A_2 by matching the finite element result with the three-term asymptotic solution [*20–22*]. The value of A_2 determined in this manner is almost independent of the distance from the crack tip within $1 \leq r/(J/\sigma_0) \leq 5$, where the fracture event normally takes place.
3. Using A_2 as a constraint parameter, the concept of a constraint modified J-R curve is proposed. A procedure is outlined for transferring the J-R curves determined from the ASTM standards to non-standard specimens or to structures with flaws. Once the constraint parameter A_2 is determined, the J-R curve for any specimen can be readily predicted.
4. The methodology of the constraint modified J-R curve has been applied to a set of SENB test data obtained by Joyce and Link [*3*]. Using the initiation fracture toughness J_{IC} and the tearing modulus T_R, the constraint modified J-R curves are constructed for the test material. The predicted J-R curves agree very well with the experimental data up to a crack extension of 7 mm. Note that only two test data points (J_{IC} and T_R measured at $\Delta a < 1$ mm) were needed to successfully construct the constraint modified J-R curve. These results also indicate that (a) a nearly linear relationship exists between the slope of the material J-resistance curve at 1 mm of crack extension and the constraint parameter A_2; and (b) the predicted J-R curves are insensitive to the value of J_{IC} which may be weakly dependent of the crack tip constraint. Therefore, it can be concluded that the initiation fracture toughness J_{IC} may be regarded as a constant and is independent of the crack tip constraint. This was proposed earlier by Hancock et al. [*1*] and Joyce and Link [*3*].

References

[*1*] Hancock, J. W., Reuter, W. G., and Parks, D. M., "Constraint and Toughness Parameterized by *T*, *Constraint Effects in Fracture, ASTM STP 1171,* American Society of Testing and Materials, West Conshohocken, PA, 1993, pp. 21–40.

[*2*] Joyce, J. A. and Link, R. E., "Effects of Constraint on Upper Shelf Fracture Toughness," *Fracture Mechanics: 26th Volume, ASTM STP 1256,* American Society for Testing and Materials, West Conshohocken, PA, 1995, pp. 142–177.

[*3*] Joyce, J. A. and Link, R. E., "Application of Two Parameter Elastic-Plastic Fracture Mechanics to Analysis of Structures," *Engineering Fracture Mechanics,* Vol. 57, 1997, pp. 431–446.

[*4*] Marschall, C. W., Papaspyropoulos, V., and Landow, M. P., "Evaluation of Attempts to Predict Large-Crack Growth *J-R* Curves from Small Specimen Tests," *Nonlinear Fracture Mechanics: Volume II—Elastic-Plastic Fracture, ASTM STP 995,* American Society of Testing and Materials, West Conshohocken, PA, 1989, pp. 123–143.

[*5*] Eisele, U., Roos, E., Seidenfuss, M., and Silcher, "Determination of *J*-Integral-Based Crack Resistance Curve and Initiation Values for the Assessment of Cracked Large-Scale Specimens," *Fracture Mechanics: Twenty-Second Symposium (Volume I),* ASTM STP 1133, American Society for Testing and Materials, West Conshohocken, PA, 1992, pp. 37–59.

[*6*] Roos, E., Eisele, U., and Silcher, H., "Effect of Stress State on the Ductile Fracture Behavior of Large Scale Specimens," *Constraint Effects in Fracture, ASTM STP 1171,* American Society for Testing and Materials, West Conshohocken, PA, 1993, pp. 41–63.

[*7*] Roos, E., Eisels, U., Silcher, H., and Eckert, W., "Impact of the Stress State on the Fracture Mechanics of Heavy Section Steel Component Failure Mechanics," *Fracture Mechanics Verification by Large-Scale Testing,* EGF/ESIS8, K. Kussmaul, Ed., 1991, pp. 65–85.

[8] Kordisch, H., Sommer, E., and Schmitt, W., "The Influence of Triaxiality on Stable Crack Growth," *Nuclear Engineering and Design,* Vol. 112, 1989, pp. 27–35.

[9] Klemm, W., Memhard, D., and Schmitt, W., "Experimental and Numerical Investigation of Surface Cracks in Plates and Pipes," *Fracture Mechanics Verification by Large-Scale Testing,* EGF/ESIS8, K. Kussmaul, Ed., 1991, pp. 139–150.

[10] Henry, B. S., Luxmoore, A. R., and Sumpter, J. D. G., "Elastic-Plastic Fracture Mechanics Assessment of Low Constraint Aluminium Test Specimens," *International Journal of Fracture,* Vol. 81, 1996, pp. 217–234.

[11] Haynes, M. J. and Gangloff, R. P., "High Resolution *R*-Curve Characterization of the Fracture Toughness of Thin Sheet Aluminum Alloys," *Journal of Testing and Evaluation,* Vol. 25, 1997, pp. 82–98.

[12] Alexander, D. J., "Fracture Toughness Measurements with Subsize Disk Compact Specimens," *Small Specimens Test Techniques Applied to Nuclear Vessel Thermal Annealing and Plant Life Extension, ASTM STP 1204,* American Society of Testing and Materials, West Conshohocken, PA, 1993, pp. 130–142.

[13] Elliot, C., Emark, M., Lucas, G. E., et al., "Development of Disk Compact Tension Specimens and Test Techniques for HFIR Irradiation," *Journal of Nuclear Materials,* Vol. 179, Part A, 1991, pp. 434–437.

[14] Yoon, K. K., Gross, L. B., Wade, C. S., and VanDerSluys, W. A., "Evaluation of Disk-Shaped Compact Specimen for Determining *J-R* Curves," *Fracture Mechanics: 26th Volume, ASTM STP 1256,* American Society of Testing and Materials, West Conshohocken, PA, 1995, pp. 272–283.

[15] Zhang, J. M. and Ardell, A. J., "Measurement of the Fracture-Toughness of CVD-GROWN ZNS Using a Miniaturized Disk-Bend Test," *Journal of Materials Research,* Vol. 6, 1991, pp. 1950–1957.

[16] Gilbert, C. J., Cao, J. J., De Jonghe, L. C., and Ritchie, R. O., "Crack-Growth Resistance-Curve Behavior in Silicon Carbide: Small Versus Long Cracks," *Journal of American Ceramics Society,* Vol. 80, 1997, pp. 2253–2261.

[17] Betegon, C. and Hancock, J. W., "Two-Parameter Characterization of Elastic-Plastic Crack-Tip Fields," *Journal of Applied Mechanics,* Vol. 58, 1991, pp. 104–110.

[18] O'Dowd, N. P. and Shih, C. F., "Family of Crack-Tip Fields Characterized by a Triaxiality Parameter—I. Structure of Fields," *Journal of the Mechanics and Physics of Solids,* Vol. 39, 1991, pp. 989–1015.

[19] O'Dowd, N. P. and Shih, C. F., "Family of Crack-Tip Fields Characterized by a Triaxiality Parameter—II. Fracture Applications," *Journal of the Mechanics and Physics of Solids,* Vol. 40, 1992, pp. 939–963.

[20] Yang, S., Chao, Y. J., and Sutton, M. A., "Higher Order Asymptotic Crack Tip Fields in a Power-Law Hardening Material," *Engineering Fracture Mechanics,* Vol. 45, 1993a, pp. 1–20.

[21] Yang, S., Chao, Y. J., and Sutton, M. A., "Complete Theoretical Analysis for Higher Order Asymptotic Terms and the HRR Zone at a Crack Tip for Mode I and Mode II Loading of a Hardening Material," *Acta Mechanica,* Vol. 98, 1993b, pp. 79–98.

[22] Chao, Y. J., Yang, S., and Sutton, M. A., "On the Fracture of Solids Characterized by One or Two Parameters: Theory and Practice," *Journal of the Mechanics and Physics of Solids,* Vol. 42, 1994, pp. 629–647.

[23] Chao, Y. J. and Zhu, X. K., "J-A_2 Characterization of Crack-Tip Fields: Extent of J-A_2 Dominance and Size Requirements," *International Journal of Fracture,* Vol. 89, 1998, pp. 285–307.

[24] Chao, Y. J. and Ji, W., "Cleavage Fracture Quantified by J and A_2," *Constraint Effects in Fracture Theory and Applications: Second Volume, ASTM STP 1244,* American Society of Testing and Materials, West Conshohocken, PA, 1995, pp. 3–20.

[25] Chao, Y. J. and Lam, P. S., "Effects of Crack Depth, Specimen Size, and Out-of-Plane Stress on the Fracture Toughness of Reactor Vessel Steels," *ASME Journal of Pressure and Vessel Technology,* Vol. 118, 1996, pp. 415–423.

[26] Zhu, X. K. and Chao, Y. J., "Characterization of Constraint of Fully Plastic Crack-Tip Fields in Non-Hardening Materials by the Three-Term Solution," *International Journal of Solids and Structures,* Vol. 36, 1999, pp. 4497–4517.

[27] Nikishkov, G. P., Bruckner-Foit, A., and Munz, D., "Calculation of the Second Fracture Parameter for Finite Cracked Bodies Using a Three-Term Elastic-Plastic Asymptotic Expansion," *Engineering Fracture Mechanics,* Vol. 52, 1995, pp. 685–701.

[28] Yang, S., *Higher Order Asymptotic Crack Tip Fields in a Power-Law Hardening Material,* Ph.D. dissertation, University of South Carolina, 1993.

[29] Rice, J. R. and Rosengren, G. F., "Plane Strain Deformation near a Crack Tip in a Power Law Hardening Material," *Journal of the Mechanics and Physics of Solids,* Vol. 16, 1968, pp. 1–12.

[30] Hutchinson, J. W., "Singular Behavior at the End of a Tensile Crack in a Hardening Material," *Journal of the Mechanics and Physics of Solids,* Vol. 16, 1968, pp. 13–31.
[31] Hutchinson, J. W., "Plastic Stress and Strain Fields at a Crack Tip," *Journal of the Mechanics and Physics of Solids,* Vol. 16, 1968, pp. 337–347.
[32] Chao, Y. J. and Zhang, L., "Tables of Plane Strain Crack Tip Fields: HRR and Higher Order Terms," ME-Report, 97-1, Department of Mechanical Engineering, University of South Carolina, 1997.
[33] Ilyushin, A. A., "The Theory of Small Elastic-Plastic Deformations," *Prikadnaia Matematika i Mekhanika, P.M.M.,* Vol. 10, 1946, pp. 347–356.
[34] Goldman, N. J. and Hutchinson, J. W., "Fully Plastic Crack Problems: The Center-Cracked Strip under Plane Strain," *International Journal of Solids and Structures,* Vol. 11, 1975, pp. 575–591.

Mark T. Kirk[1] *and Randy G. Lott*[2]

The Technical Basis for ASTM E 1820-98 Deformation Limits on J_c

REFERENCE: Kirk, M. T. and Lott, R. G., **"The Technical Basis for ASTM E 1820-98 Deformation Limits on J_c,"** *Fatigue and Fracture Mechanics: 31st Volume, ASTM STP 1389,* G. R. Halford and J. P. Gallagher, Eds., American Society for Testing and Materials, West Conshohocken, PA, 2000, pp. 183–205.

ABSTRACT: ASTM Standard Test Method E 1820-96, "Measurement of Fracture Toughness," was recently revised (E 1820-98). This revision includes a relaxation of the deformation limits/size requirements that must be satisfied to report a valid value of fracture toughness at instability prior to significant stable crack extension (J_c). E 1820-96 required that valid J_c values satisfy the following inequality (with an M value of 200).

$$B, b_o \geq M \frac{J_c}{\sigma_{\text{flow}}}$$

E 1820-98 relaxes this requirement to $M = 100$ for all metals and to $M = 50$ for ferritic steels. In this paper we present results from both finite element analysis and from fracture toughness testing that supports these changes. This evidence demonstrates that J_c values meeting the deformation limits of E 1820-98 are specimen-size invariant. Consequently, these values can be applied with confidence in fracture integrity assessments of much larger structures.

KEYWORDS: fracture toughness testing, cleavage fracture toughness, deformation limits, size requirements, J_c, constraint, ferritic steels

All ASTM fracture toughness test methods include requirements on the minimum specimen size, or, equivalently, on the measuring capacity of the specimens used to measure fracture toughness values. These requirements limit the deformation before fracture to ensure that specimen size does not influence significantly the measured fracture toughness. Deformation limits thereby ensure that all fracture toughness values measured in accordance with prescribed procedures will apply to fracture integrity assessments of much larger structures. The deformation limits imposed by ASTM fracture test methods place a bound on the permissible violation of the mathematical and physical assumptions that underlie the standard. Due to its basis on linear elastic fracture mechanics (LEFM), ASTM Standard Test Method E 399 has the most restrictive limits. By comparison, test methods based on elastic-plastic fracture mechanics (EPFM) theory (i.e., E 813, E 1152, E 1737, E 1820, E 1921) have less restrictive limits because the underlying mathematical description (elastic-plastic fracture mechanics, or EPFM) accurately models a much larger range of deformation.

[1] Senior materials engineer, Office of Nuclear Regulatory Research, United States Nuclear Regulatory Commission, Washington, DC 20277-2904. Formerly, senior engineer, Westinghouse Electric Co.
[2] Advisory engineer, Westinghouse Electric Co., LLC (Science and Technology Division), 1310 Beulah Rd., Pittsburgh, PA 15235.

Copyright© 2000 by ASTM International www.astm.org

ASTM Standard Test Method E 1820-96, "Measurement of Fracture Toughness," was the first elastic-plastic fracture testing standard to permit measurement of fracture toughness using the *J*-integral when the specimen fractures by instability before substantial stable tearing (i.e., either a ductile or a cleavage instability). In E 1820-96, this value, termed J_c, is considered to be invariant relative to the in-plane dimensions of the specimen provided the following requirement is satisfied:

$$B, b_o \geq M \frac{J_c}{\sigma_{flow}} \tag{1}$$

where B is the specimen thickness, b_o is the length of the uncracked ligament, σ_{flow} is the flow strength, and $M = 200$. A recent revision to E 1820-96 (E 1820-98) relaxed this deformation limit as follows:

1. $M = 100$ for all materials, irrespective of fracture mode.
2. $M = 50$ for ferritic steels failing by transgranular cleavage and having room temperature tensile properties falling within the box illustrated in Fig. 1.

This change of E 1820 is particularly significant, for it marks the first occasion that ASTM Subcommittee E08.08 has recommended deformation limits that depend on material type and/or fracture mode.

In this paper, we present the technical basis for these changes to the E 1820 deformation limits, beginning with a short review of the basis for the E 1820-96 $M = 200$ limit. We then summarize the published information considered by Subcommittee E08.08 to support these recent changes. Finally, we detail experimental evidence supporting the $M = 50$ limit for ferritic steels considered when Subcommittee E08.08 drafted E 1820-98 but not available previously in the open literature.

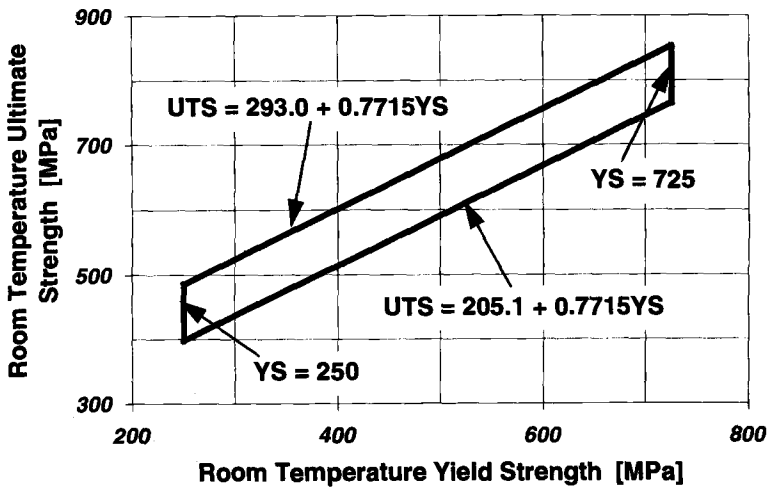


FIG. 1—*Region of tensile properties for ferritic steels where the E 1820-98* M = *50 deformation limit on* J_c *applies.*

Existing E 1820-96 Requirements (M = 200)

ASTM Test Method E 1820-96 uses a coefficient of M = 200 in Eq 1. The 200 coefficient is motivated by plane-strain finite element analysis that couples a global failure parameter (J_c) with a micro-continuum mechanics failure model [*1*]. This failure model applies to ferritic materials in the ductile to brittle transition, thereby limiting the fracture mechanism to transgranular cleavage. Several recently proposed models for this failure mechanism all assume that a favorably oriented particle initiates cleavage fracture [*2–4*]. Failure of this particle generates a micro-crack, which then triggers global fracture though a local Griffith instability. The sampling effects for a favorably oriented particle to create the initial micro-crack suggest that the highly stressed volume of material ahead of the crack tip plays a dominant role in controlling cleavage fracture. This feature of the models leads to adoption of the volume of material ahead of the crack over which the normalized maximum principal stress exceeds a critical value as an appropriate local fracture parameter for failure by transgranular cleavage.

Dodds et al. use nonlinear finite element analysis of plane strain models to calculate areas within principal stress contours ahead of a crack tip [*1*]. These analyses reveal that as the deformation applied to a specimen increases, the area within a principal stress contour ahead of the crack tip increases, but at a lower rate (due to constraint loss) than the small-scale yielding (or infinite body) reference solution. These analyses define deformation limits beyond which specimen dimensions influence the relationship between the applied J and the area within a principal stress contour that drives cleavage fracture. When failure occurs at deformations exceeding these limits, measured J_c values become a function of specimen dimensions. Figure 2 illustrates the result from the finite element analyses used to establish the M = 200 limit.

In later work, Koppenhoefer et al. compare the proposed deformation limit of Eq 1 to experimental data sets [*5*]. The data sets include both low- and medium-strength steels (i.e., A36 and A533B C1. 1) where failure was by transgranular cleavage. This evaluation also includes higher-strength steels (i.e., an 18Ni maraging steel, and SAE 4340 with a 399°C

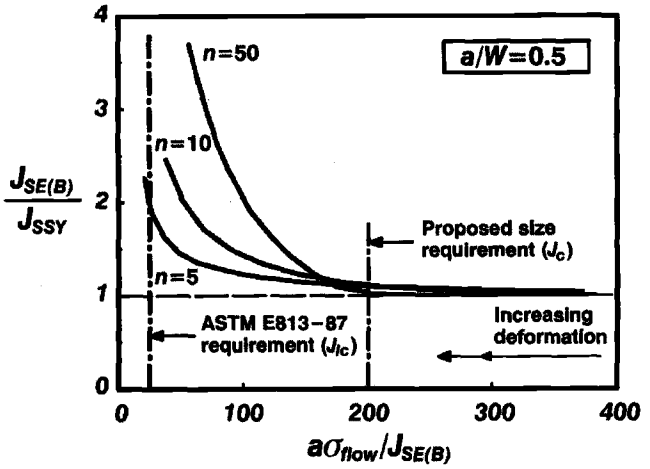


FIG. 2—*Plane strain finite element results from Dodds et al. [1] used to justify the E 1820-96* M = *200 deformation limit.*

temper) and a high-strength titanium alloy (Ti 6Al-6Vn-2Sn). These higher-strength alloys all failed by mechanisms other than transgranular cleavage. These fracture toughness data support the use of $M = 200$ in Eq 1 even for non-cleavage failures, and prompted ASTM Subcommittee E08.08 to adopt a $M = 200$ limit for all metals, irrespective of failure mode.

New E 1820-98 Requirements

General

As stated earlier, the deformation limits imposed on J_c by E 1820-98 differ from E 1820-96 limits in the following ways:

1. $M = 100$ for all materials, irrespective of fracture mode.
2. $M = 50$ for ferritic steels failing by transgranular cleavage and having room temperature tensile properties falling within the box illustrated in Fig. 1.

The following sections detail the evidence supporting these changes to the test method.

M = *100 for all Materials*

Prior to adopting these new deformation limits, ASTM Subcommittee E08.08 reviewed the results of three-dimensional finite element analysis of both single edge notch bend, SE(B), and compact tension, C(T), specimens published by Nevalainen and Dodds [*6*] and by Ruggieri et al. [*7*]. Table 1 summarizes the results of these analyses. The values in the M coefficient column represent the value of M in Eq 1 when the applied J value for a particular geometry/material combination differs by 20% from the small-scale yielding reference value (J_{SSY}). The Subcommittee considered this 20% difference between the applied J reported at failure (J_c) and the J representing the true driving force for cleavage fracture (J_{SSY}) acceptably small in view of the considerable scatter inherent to cleavage fracture data, as illustrated in Fig. 3.

The Ramberg-Osgood work-hardening coefficients (n) and modulus to yield strength ratios (E/σ_{ys}) summarized in Table 1 cover a wide range of materials. Furthermore, information available from these finite element analyses also address the influence of specimen type, and the sensitivity of the J error to M limits about 100. ASTM Subcommittee E08.08 felt that this information supports adoption of a coefficient of $M = 100$ for use with all metals in Eq 1. Thus, a J_c value that satisfies Eq 1 (with a coefficient of $M = 100$) is not expected to differ by more than 20% from a J_c value determined using a specimen of considerably larger in-plane dimensions. For a high work-hardening material ($n = 5$) failing at the $M = 100$ limit, this expected difference is substantially below 20%.

M = *50 for Ferritic Steels*

The information presented in Table 1 suggests that it may be possible to ensure 20% accuracy in J_c values using deformation limits less restrictive than $M = 100$, particularly for moderate to high work-hardening materials ($n = 10$ and 5, respectively). Here we assess this possibility using a database of fracture toughness values for ferritic steels, particularly nuclear reactor pressure vessel (RPV) steels. This evaluation considers all data sets having multiple measurements of cleavage fracture toughness made at a single temperature using more than one size specimen. Table 2 summarizes the tensile properties of data sets that meet these criteria. Figure 4 compares the room temperature tensile properties of these materials to

TABLE 1—*Coefficients for the* J_c *qualification equation, Eq 1.*

Ref.	Specimen Type	Side Grooves	*a/W*	*W/B*	*n*	E/σ_{ys}	*M*-coefficient at 20% deviation from *SSY*	*J* deviation from *SSY* at *M*=100
[6]	SE(B)	0%	0.5	1	5	500	25	
[6]	SE(B)	0%	0.5	2	5	500	25	
[6]	C(T)	0%	0.6	2	5	500	20	
[7]	SE(B)	0%	0.5	1	5	800	29	6%
[7]	SE(B)	0%	0.5	1	10	500	66-125	6%-21%
[7]	SE(B)	20%	0.5	1	10	500	76-143	11%-23%
[6]	SE(B)	0%	0.5	1	10	500	60	
[6]	SE(B)	0%	0.5	2	10	500	55	
[6]	SE(B)	20%	0.5	2	10	500	65	
[6]	C(T)	0%	0.6	2	10	500	45	
[6]	C(T)	20%	0.6	2	10	500	55	
[7]	SE(B)	0%	0.5	1	20	300	87-117	14%-24%
[7]	SE(B)	20%	0.5	1	20	300	97-105	15%-23%
[6]	SE(B)	0%	0.5	1	20	500	115	
[6]	SE(B)	0%	0.5	2	20	500	115	
[6]	C(T)	0%	0.6	2	20	500	90	

Note: If more than one value appears in the last two columns, these values reflect conservative assumptions regarding either the principal stress contour or the Weibull modulus that controls failure [6-7].
The material properties from the analyses in the shaded rows are plotted in Figure 5.

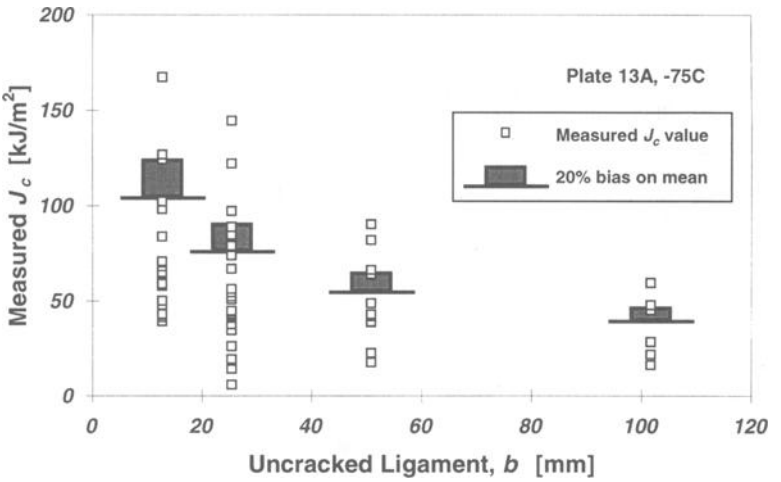


FIG. 3—*Comparison of the 20% over-prediction of* J_c *permitted by E 1820-98 deformation limits with scatter typical of cleavage fracture toughness data [13].*

those from a much larger database for RPV steels [*8*]. The data in Table 2 both represent and bound the tensile properties of this larger population. Furthermore, Fig. 5 demonstrates that the Ramberg-Osgood work-hardening coefficient (n) and elastic modulus to yield ratio (E/σ_{ys}) of these data cover the range of conditions modeled in the finite element analysis [*6–7*]. These observations suggest that the data sets assembled in Table 2 apply to a wide range of conditions of practical interest and provide an appropriate basis for an empirical assessment of deformation limits established based on finite element computations [*6–7*].

We evaluate these fracture toughness data sets as follows (see also Fig. 6):

Step 1: Identify a data set that includes J_c values determined using multiple specimen sizes tested at a single temperature in fracture mode transition.

Step 2: Remove the statistical effect of crack front length on toughness by normalizing all of the toughness values to a reference 1 T (25.4-mm thick) specimen thickness according to the following equation [*9*]:

$$J_{c|1T} = \frac{1}{E}\left\{20 + (K_{Jc}|_{\text{Measured}} - 20)\cdot\left[\frac{B_{\text{Measured}}}{1}\right]^{1/4}\right\}^2 \tag{2}$$

where E is in MPa, K is in MPa$\sqrt{\text{m}}$, and B is in inches.

If the fracture toughness values have not experienced constraint loss, this normalization should produce J_c values that do not vary with ligament dimension, as illustrated in Fig. 7. Conversely, if loss of constraint does occur, then the data should exhibit an upward sweeping tail at small ligament dimensions (see Fig. 6, Step 2).

Step 3: Plot candidate deformation limits through the data from Step 2. Calculate these limits using Eq 1, flow strength data from Table 2, and candidate M values of 200, 100, 50, and 30. Establish an appropriate deformation limit as the M value that satisfies both of the following criteria:

1. Removes any upper tail in the data set produced by loss of constraint at small ligament sizes, but

TABLE 2—*Tensile properties of the fracture toughness database.*

Ref.	Author	Material		Strength at Ambient (*Note 1*)		Properties at Fracture Test Temperature					
		ASTM Spec. or Flux Lot	HSST Program Designation	σ_{ys} [MPa]	σ_{uts} [MPa]	Temp. [°C]	σ_{ys} [MPa]	σ_{uts} [MPa]	E/σ_{ys} (*Note 2*)	*n* (*Note 3*)	Tensile Data Source (*Note 4*)
Un-Irradiated RPV Steels											
[10]	Marston	A533B Cl. 1	Plate 02	467	622	-18	508	664	410	10.6	Measured
[11]	Nanstad	Linde 0124	Weld 72W	498	606	-50	543	681	387	12.0	Measured
[11]	Nanstad	Linde 0124	Weld 72W	498	606	-30	524	659	399	11.8	Measured
[11]	Nanstad	Linde 0124	Weld 72W	498	606	-15	513	644	405	11.9	Measured
[11]	Nanstad	Linde 0124	Weld 72W	498	606	10	503	621	411	12.5	Measured
[11]	Nanstad	Linde 0124	Weld 73W	490	599	-50	540	674	389	12.1	Measured
[11]	Nanstad	Linde 0124	Weld 73W	490	599	-30	521	653	401	12.0	Measured
[11]	Nanstad	Linde 0124	Weld 73W	490	599	-15	510	638	408	12.0	Measured
[11]	Nanstad	Linde 0124	Weld 73W	490	599	-5	504	629	411	12.2	Measured
[12]	Alexander	A508 Cl. 2		545	696	-18	547	699	381	11.3	Measured
[13]	McCabe	A533B Cl. 1	Plate 13A	441	600	-75	525	697	403	10.2	Ambient
[13]	McCabe	A533B Cl. 1	Plate 13A	441	600	-150	614	801	351	10.7	Ambient
[14]	Ingham	A533B Cl. 1		469	621	-71	541	717	390	10.2	Measured
[14]	Ingham	A533B Cl. 1		469	621	-50	522	694	402	10.2	Measured
[14]	Ingham	A533B Cl. 1		469	621	-10	491	651	424	10.2	Measured
[14]	Ingham	A533B Cl. 1		469	621	10	477	631	434	10.3	Measured
[15]	McCabe	Linde 80	Midland WF70 Beltline	407	586	-50	469	676	448	8.6	Measured
[15]	McCabe	Linde 80	Midland WF70 Beltline	407	586	-25	441	642	473	8.5	Measured
[15]	McCabe	Linde 80	Midland WF70 Beltline	407	586	0	418	612	495	8.4	Measured
[15]	McCabe	Linde 80	Midland WF70 Nozzle	545	655	-50	594	733	354	12.6	Measured
[16]	Lidbury	A508 Cl. 3		469	621	-45	527	687	398	10.7	Generic
[16]	Lidbury	A508 Cl. 3		469	621	-15	500	656	416	10.5	Generic
[17]	Iwadate	A508 Cl. 3		483	634	-100	605	771	352	11.4	Ambient
[17]	Iwadate	A508 Cl. 3		483	634	-60	558	719	378	11.0	Ambient
[17]	Iwadate	A508 Cl. 3		483	634	-20	519	676	402	10.7	Ambient

TABLE 2—*Continued*

Ref.	Author	Material		Strengths at Ambient (*Note 1*)		Properties at Fracture Test Temperature					
		ASTM Spec. or Flux Lot	HSST Program Designation	σ_{ys} [MPa]	σ_{uts} [MPa]	Temp. [°C]	σ_{ys} [MPa]	σ_{uts} [MPa]	E/σ_{ys} (*Note 2*)	n (*Note 3*)	Tensile Data Source (*Note 4*)
Non-RPV Steels											
[18]	Sorem	A36		248	462	-196	382	675	571	6.5	Ambient
[18]	Sorem	A36		248	462	-112	319	574	670	6.3	Ambient
[18]	Sorem	A36		248	462	-76	296	538	714	6.2	Ambient
[18]	Sorem	A36		248	462	-43	278	509	754	6.1	Ambient
[18]	Sorem	A36		248	462	-18	266	490	783	6.1	Ambient
[17]	Iwadate	A470		765	869	-100	958	1055	222	22.2	Ambient
[17]	Iwadate	A470		765	869	-75	911	1010	232	21.2	Ambient
[17]	Iwadate	A470		765	869	-60	885	985	238	20.7	Ambient
Irradiated RPV Steels											
[11]	Nanstad	Linde 0124	72W, 1.5×10^{-19} n/cm^2	613	714	50	607	702	337	16.5	Measured
[11]	Nanstad	Linde 0124	72W, 1.5×10^{-19} n/cm^2	613	714	75	597	689	340	16.6	Measured
[11]	Nanstad	Linde 0124	72W, 1.5×10^{-19} n/cm^2	613	714	85	594	685	341	16.7	Measured
[11]	Nanstad	Linde 0124	72W, 1.5×10^{-19} n/cm^2	613	714	95	591	681	341	16.9	Measured
[11]	Nanstad	Linde 0124	73W, 1.5×10^{-19} n/cm^2	655	743	50	637	730	321	17.3	Measured
[11]	Nanstad	Linde 0124	73W, 1.5×10^{-19} n/cm^2	655	743	85	622	713	325	17.3	Measured
Note 5	Nanstad	Linde 80	Midland WF-70 Beltline, 1×10^{19} n/cm^2	646	747	21	650	752	317	16.4	Ambient

Notes:

1. All strength values given in this table are average values.
2. Modulus (E) calculated from temperature: $E = 207200 - 57.1 \cdot T$ (E in MPa, T in °C)
3. Ramberg-Osgood work hardening coefficient (n) is calculated from the σ_{uts}/σ_{ys} ($\equiv R$) ratio [19]: $R = \left[1/(0.002n)\right]^{1/n} / \exp(1/n)$
4. In the column "Tensile Data Source":
   - **Measured** means that the reference reported measured tensile data as a function of temperature.
   - **Ambient** means that the reference reported measured tensile data at room temperature only.
   - **Generic** means no strength data were reported. Specification values are assumed at room temperature.
   - For both **Ambient** and **Generic**, strength properties at the test temperature were determined by forcing a general fit for RPV steels to go through the room temperature data.
5. Nanstad, Personal communication, 1997.

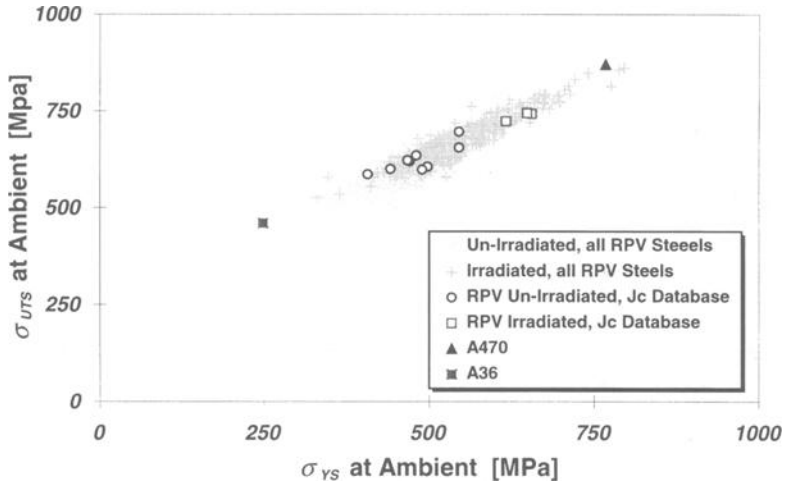


FIG. 4—*Tensile properties for a large population of RPV steels (crosses and pluses) [8] compared to those of the fracture toughness data sets considered herein.*

2. Does not disqualify any toughness values measured using small ligament specimens that lie within the same range as toughness values measured using large ligament specimens.

Table 3 summarizes the result of this evaluation for all of the data sets listed in Table 2. Table 3 includes a ranking of each of the four candidate deformation limits according to the criteria illustrated in Fig. 6, Step 3. Unfortunately, data sets containing only low J_c values are not useful for assessing the appropriateness of the $M = 50$ and $M = 30$ deformation limits. Table 4 is a reduced version of Table 3; it includes only data sets that have high

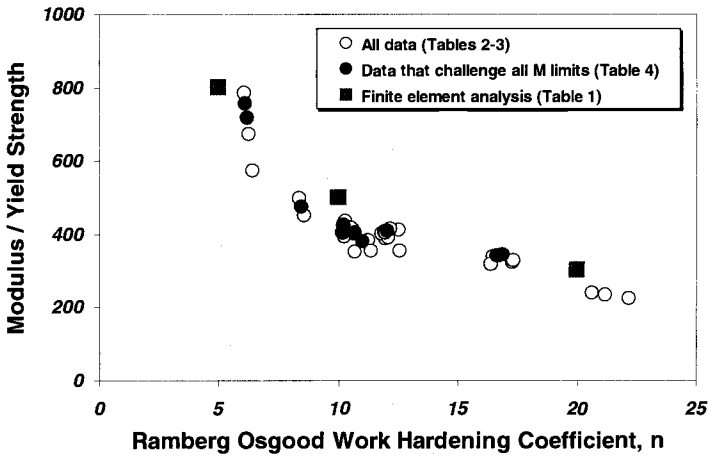


FIG. 5—*Tensile properties for the fracture toughness data sets considered herein compared to tensile properties used for the finite element models [6–7].*

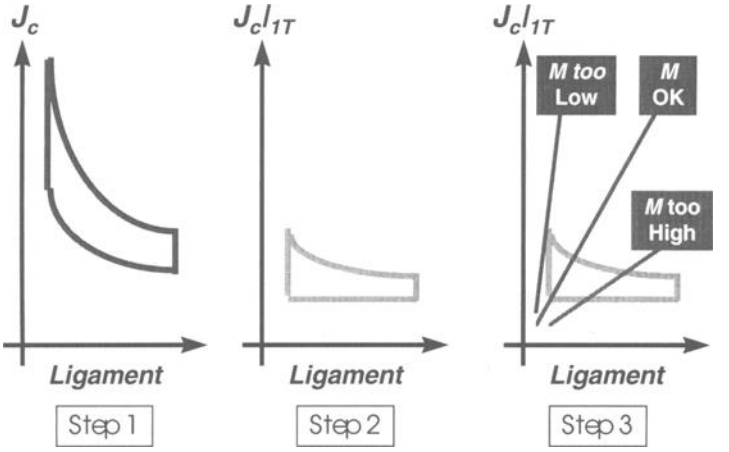


FIG. 6—*Procedure for assessment of appropriate deformation limit* (M) *using fracture toughness data.*

enough J_c values to challenge all of the candidate deformation limits. These data sets are compared with the candidate deformation limits in Figs. 8 to 19.[3] Inspection of these figures reveals that the $M = 50$ deformation limit eliminates geometry-dependent toughness values from all twelve of the data sets that challenge all of the candidate deformation limits. Thus,

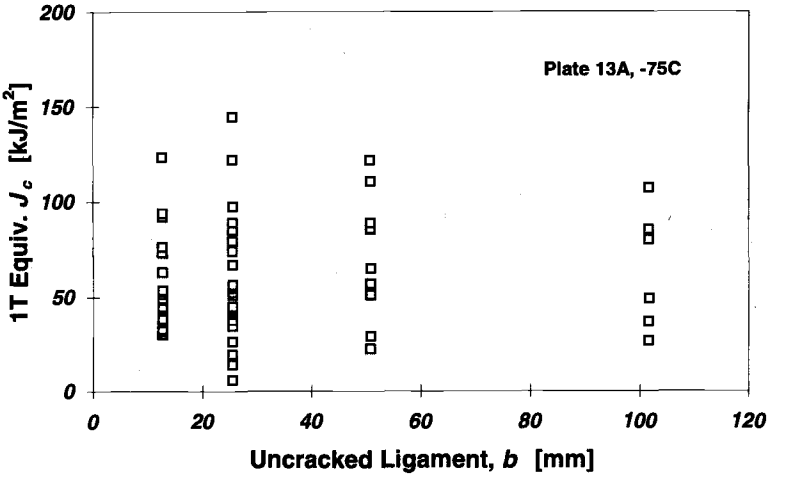


FIG. 7—*Example data showing the effect of normalization to remove the statistical crack front length effect. This same data are plotted as measured in Fig. 3 [13].*

[3] In these figures, toughness data having ductile crack growth exceeding the E 1820-98 limit of {0.2 mm + $J_c/(2\ \sigma_{flow})$} are denoted by a "X" symbol. In some cases with deformation limit curves appear discontinuous because specimens having different width to thickness (W/B) ratios are plotted together. Actual a/W and W/B ratios from the specimens tested were used to calculate points on the deformation limit curves.

TABLE 3—*Assessment of* M*-limits for all data sets.*

Ref.	Author	Material		Temp. [°C]	n	J_c Specimen Thicknesses		# of J_c Data	Assessment of M Limits (*Note 1*)				
		ASTM Spec. or Flux Lot	HSST Program Designation			Min. [mm]	Max. [mm]		200	100	50	30	Comment
Un-Irradiated RPV Steels													
[10]	Marston	A533B Cl. 1	Plate 02	-18	10.6	50.8	254.0	7					Jc all too low
[11]	Nanstad	Linde 0124	Weld 72W	-50	12.0	25.4	101.6	13	HI	OK			
[11]	Nanstad	Linde 0124	Weld 72W	-30	11.8	25.4	101.6	9	HI	HI	OK		
[11]	Nanstad	Linde 0124	Weld 72W	-15	11.9	25.4	101.6	9	HI	HI	OK		
[11]	Nanstad	Linde 0124	Weld 72W	10	12.5	50.8	203.2	11	HI	HI	OK		
[11]	Nanstad	Linde 0124	Weld 73W	-50	12.1	25.4	101.6	13	HI	OK			
[11]	Nanstad	Linde 0124	Weld 73W	-30	12.0	25.4	101.6	11	HI	HI	OK		
[11]	Nanstad	Linde 0124	Weld 73W	-15	12.0	25.4	101.6	15	HI	HI	OK	LOW	
[11]	Nanstad	Linde 0124	Weld 73W	-5	12.2	50.8	203.2	10	HI	HI	OK		
[12]	Alexander	A508 Cl. 2		-18	11.3	25.4	101.6	19	HI	OK			
[13]	McCabe	A533B Cl. 1	Plate 13A	-75	10.2	12.7	101.6	64	HI	HI	HI	OK	
[13]	McCabe	A533B Cl. 1	Plate 13A	-150	10.7	12.7	50.8	46					Jc all too low
[14]	Ingham	A533B Cl. 1		-71	10.2	10.0	25.4	10	HI	HI	HI	HI	Only 2 sizes
[14]	Ingham	A533B Cl. 1		-50	10.2	25.4	101.6	20	HI	HI	HI	HI	
[14]	Ingham	A533B Cl. 1		-10	10.2	25.4	228.6	13	HI	HI	HI	OK	
[14]	Ingham	A533B Cl. 1		10	10.3	76.2	203.2	6					All lost constraint
[15]	McCabe	Linde 80	Midland WF70 Beltline	-50	8.6	12.7	50.8	17	HI	HI	OK		
[15]	McCabe	Linde 80	Midland WF70 Beltline	-25	8.5	12.7	101.6	17	HI	HI	OK	LOW	
[15]	McCabe	Linde 80	Midland WF70 Beltline	0	8.4	25.4	50.8	5	HI	HI	HI	HI	Only 2 sizes
[15]	McCabe	Linde 80	Midland WF70 Nozzle	-50	12.6	12.7	25.4	13	HI	OK			
[16]	Lidbury	A508 Cl. 3		-45	10.7	76.2	203.2	15	HI	OK			
[16]	Lidbury	A508 Cl. 3		-15	10.5	76.2	203.2	24	HI	HI	OK	LOW	Only 2 sizes
[17]	Iwadate	A508 Cl. 3		-100	11.4	12.7	25.4	12	HI				
[17]	Iwadate	A508 Cl. 3		-60	11.0	12.7	101.6	39	HI	HI	LOW		
[17]	Iwadate	A508 Cl. 3		-20	10.7	19.1	101.6	36	HI	HI	HI	LOW	

TABLE 3—*Continued*

Ref.	Author	Material		Temp. [°C]	n	J_c Specimen Thicknesses		# of J_c Data	Assessment of M-Limits (*Note 1*)				
		ASTM Spec. or Flux Lot	HSST Program Designation			Min. [mm]	Max. [mm]		200	100	50	30	Comment
Non-RPV Steels													
[18]	Sorem	A36		-196	6.5	12.7	31.8	14					Jc all too low
[18]	Sorem	A36		-112	6.3	12.7	31.8	20	HI	OK			
[18]	Sorem	A36		-76	6.2	12.7	31.8	44	HI	HI	LOW		
[18]	Sorem	A36		-43	6.1	12.7	31.8	26	HI	HI	HI	OK	
[18]	Sorem	A36		-18	6.1	12.7	31.8	9					Data too limited
[17]	Iwadate	A470		-100	22.2	12.7	76.2	39	HI	OK			
[17]	Iwadate	A470		-75	21.2	25.4	101.6	7					Jc all too low
[17]	Iwadate	A470		-60	20.7	9.5	101.6	61	HI	HI	OK		
Irradiated RPV Steels													
[11]	Nanstad	Linde 0124	72W, 1.5×10^{-19} n/cm^2	50	16.5	25.4	101.6	12	HI	OK			
[11]	Nanstad	Linde 0124	72W, 1.5×10^{-19} n/cm^2	75	16.6	25.4	101.6	10	HI	HI	OK	LOW	
[11]	Nanstad	Linde 0124	72W, 1.5×10^{-19} n/cm^2	85	16.7	25.4	101.6	19	HI	HI	HI	LOW	
[11]	Nanstad	Linde 0124	72W, 1.5×10^{-19} n/cm^2	95	16.9	25.4	101.6	18	HI	HI	HI	OK	
[11]	Nanstad	Linde 0124	73W, 1.5×10^{-19} n/cm^2	50	17.3	25.4	101.6	9	HI	OK			
[11]	Nanstad	Linde 0124	73W, 1.5×10^{-19} n/cm^2	85	17.3	25.4	101.6	18	HI	HI	OK		
Note 2	Nanstad	Linde 80	Midland WF-70 Beltline, 1×10^{19} n/cm^2	21	16.4	10.0	12.7	16	HI	HI	OK	LOW	Only 2 sizes

Notes:

1. In the "Assessment of M-Limits" column:
   - "HI" means that the candidate M-limit disqualifies J_c values from small ligament specimens that are within the range of J_c values measured using larger ligament specimens.
   - "LOW" means that the candidate M-limit does not disqualify J_c values from small ligament specimens that are above the range of J_c values measured using larger ligament specimens.
   - "OK" means that the candidate M-limit partitions the data set appropriately, as illustrated in Fig. 6, Step 3.
   - A blank cell means that the data set does not include J_c values that are high enough to qualify the candidate M-limit.
2. Nanstad, Personal communication, 1997.

TABLE 4—*Assessment of data sets that challenge all candidate deformation limits.*

Ref.	Author	Material		Temp. [°C]	n	J_c Specimen Thicknesses		# of J_c Data	Assessment of M-Limits (*Note 1*)			
		ASTM Spec. or Flux Lot	HSST Program Designation			Min. [mm]	Max. [mm]		200	100	50	30
Un-Irradiated RPV Steels												
[11]	Nanstad	Linde 0124	Weld 73W	-15	12.0	25.4	101.6	15	HI	HI	OK	LOW
[13]	McCabe	A533B Cl. 1	Plate 13A	-75	10.2	12.7	101.6	64	HI	HI	HI	OK
[14]	Ingham	A533B Cl. 1		-50	10.2	25.4	101.6	20	HI	HI	HI	HI
[14]	Ingham	A533B Cl. 1		-10	10.2	25.4	228.6	13	HI	HI	HI	OK
[15]	McCabe	Linde 80	Midland WF70 Beltline	-25	8.5	12.7	101.6	17	HI	HI	OK	LOW
[17]	Iwadate	A508 Cl. 3		-60	11.0	12.7	101.6	39	HI	HI	LOW	
[17]	Iwadate	A508 Cl. 3		-20	10.7	19.1	101.6	36	HI	HI	HI	LOW
Non-RPV Steels												
[18]	Sorem	A36		-76	6.2	12.7	31.8	44	HI	HI	LOW	
[18]	Sorem	A36		-43	6.1	12.7	31.8	26	HI	HI	HI	OK
Irradiated RPV Steels												
[11]	Nanstad	Linde 0124	72W, 1.5×10^{-19} n/cm^2	75	16.6	25.4	101.6	10	HI	HI	OK	LOW
[11]	Nanstad	Linde 0124	72W, 1.5×10^{-19} n/cm^2	85	16.7	25.4	101.6	19	HI	HI	HI	LOW
[11]	Nanstad	Linde 0124	72W, 1.5×10^{-19} n/cm^2	95	16.9	25.4	101.6	18	HI	HI	HI	OK

Notes:

1. In the "Assessment of M-Limits" column:
   - "HI" means that the candidate M-limit disqualifies J_c values from small ligament specimens that are within the range of J_c values measured using larger ligament specimens.
   - "LOW" means that the candidate M-limit does not disqualify J_c values from small ligament specimens that are above the range of J_c values measured using larger ligament specimens.
   - "OK" means that the candidate M-limit partitions the data set appropriately, as illustrated in Fig. 6, Step 3.
   - A blank cell means that the data set does not include J_c values that are high enough to qualify the candidate M-limit.

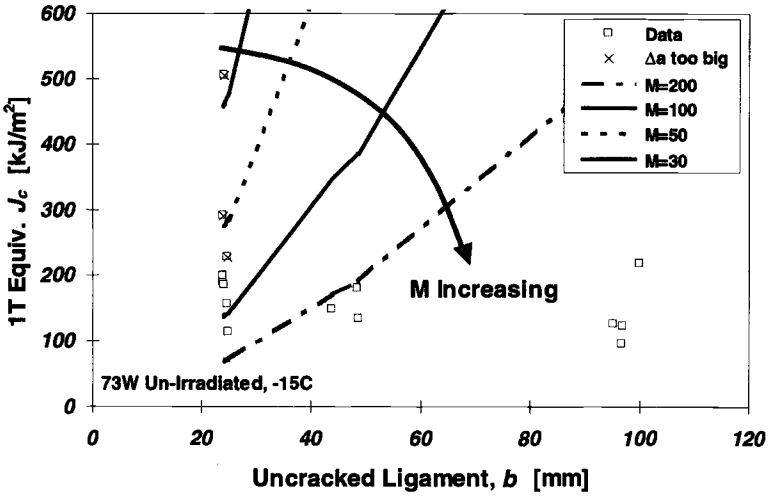


FIG. 8—*Comparison of candidate deformation limits* (M) *with 1*T *normalized fracture toughness data from Ref* 11. *The legend also applies to Figs. 9 through 19.*

E 1820-98 adopts $M = 50$ as an appropriate deformation limit for ferritic steels providing that their ambient temperature tensile properties fall within the box illustrated by Fig. 1. This box represents $\pm 2\sigma$ confidence bounds on the best fit line to the data in Fig. 4. Figure 20 compares the E 1820-98 qualification box with the data.

Comparison of E 1820-98 and E 1921-97 Size Requirements

ASTM E 1921-97, "Test Method for the Determination of Reference Temperature, T_o, for Ferritic Steels in the Transition Range," also addresses fracture toughness testing of ferritic

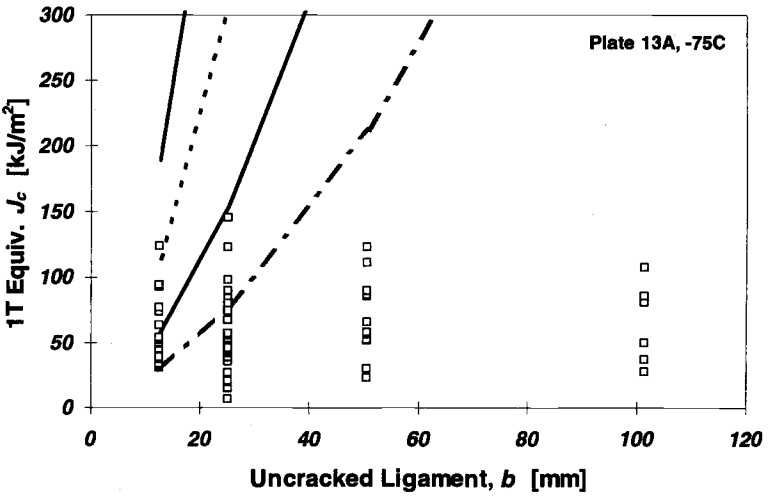


FIG. 9—*Comparison of candidate deformation limits* (M) *with 1*T *normalized fracture toughness data from Ref* 13.

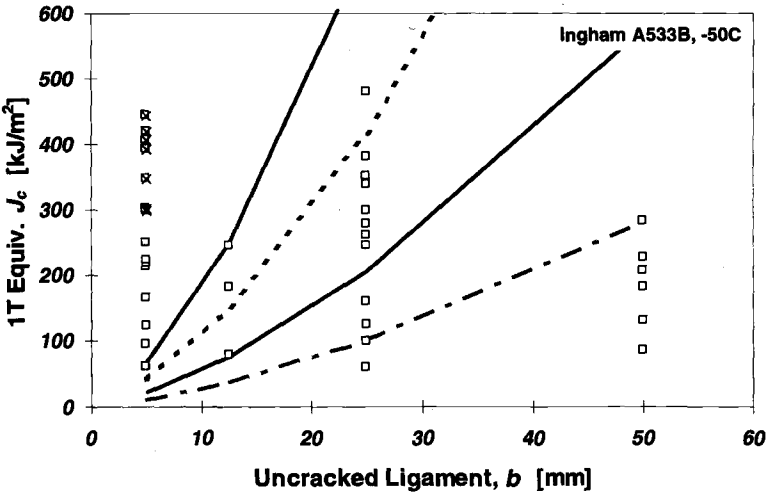


FIG. 10—*Comparison of candidate deformation limits* (M) *with 1T normalized fracture toughness data from Ref* 14.

steels. We therefore compare the deformation limits adopted by these two test methods. E 1921-97 includes the following specimen size requirement for data validity:

$$b_o \geq 30 \frac{K_{Jc}^2}{E \cdot \sigma_{ys}} \tag{3}$$

where σ_{ys} is the yield strength. Converting K_{Jc} to J_c assuming plane strain (as per E 1921-97) produces the following relationship:

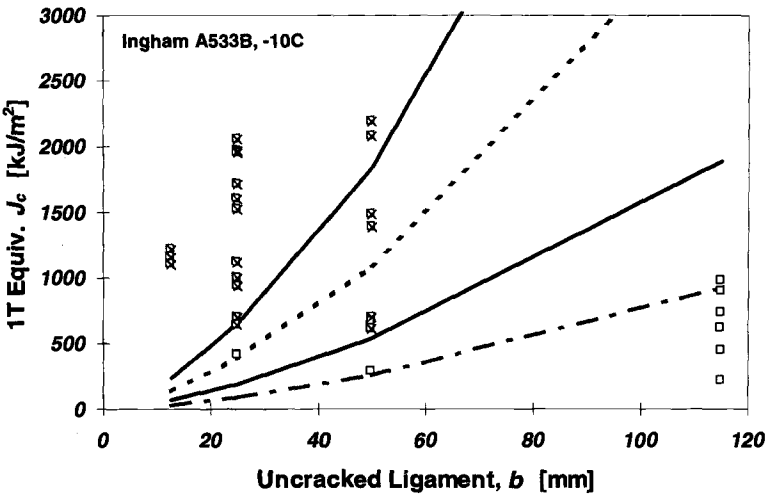


FIG. 11—*Comparison of candidate deformation limits* (M) *with 1T normalized fracture toughness data from Ref* 14.

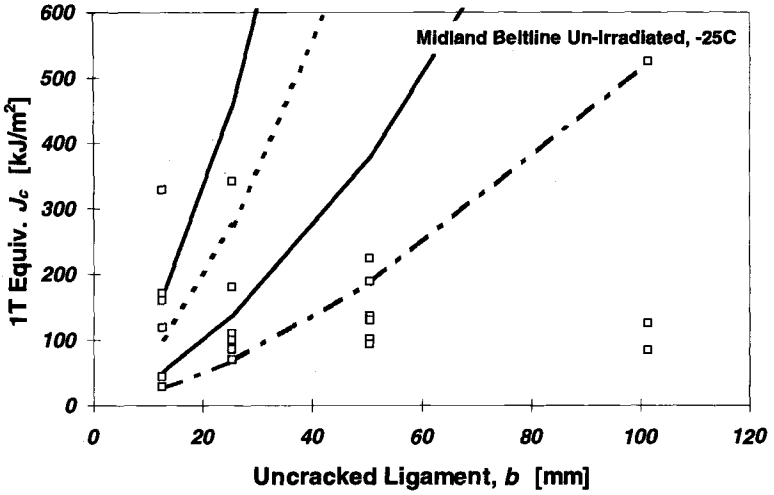


FIG. 12—*Comparison of candidate deformation limits* (M) *with 1T normalized fracture toughness data from Ref* 15.

$$b_o \geq 30 \frac{J_c}{\sigma_{ys}} \tag{4}$$

This requirement is somewhat less restrictive than the requirement of E 1820-98 for ferritic steels (Eq 1), which uses a numerical coefficient of 50 rather than 30. The two size requirements also differ in the strength value used (flow strength in E 1820-98 versus yield strength in E 1921-97). The specimen size requirements of E 1820-98 are compared to E 1921-97

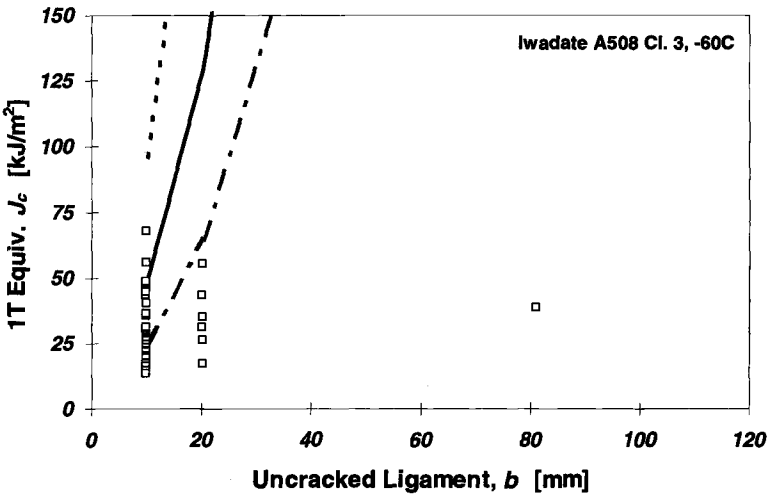


FIG. 13—*Comparison of candidate deformation limits* (M) *with 1T normalized fracture toughness data from Ref* 17.

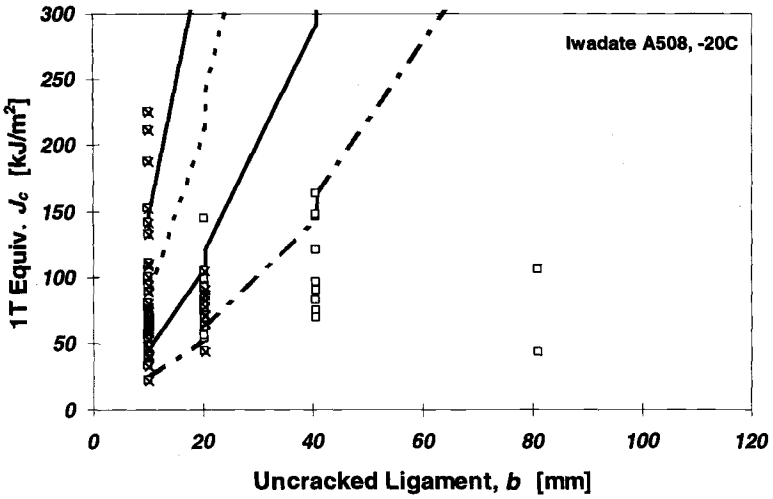


FIG. 14—*Comparison of candidate deformation limits* (M) *with 1*T *normalized fracture toughness data from Ref* 17.

size requirements by taking a ratio of Eq 1 to Eq 4. After some simplification, the result is as follows:

$$\frac{b_{E1820}}{b_{E1921}} = \frac{333}{1 + \frac{\sigma_{uts}}{\sigma_{ys}}} \text{ (for } M = 50 \text{ in Eq 1)} \tag{5}$$

This ratio is presented in Fig. 21 as a function of both σ_{uts}/σ_{ys} and of n (n was calculated

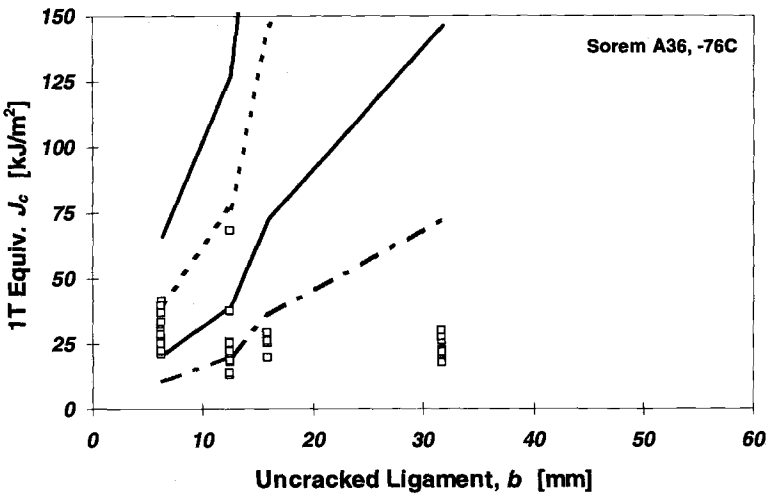


FIG. 15—*Comparison of candidate deformation limits* (M) *with 1*T *normalized fracture toughness data from Ref* 18.

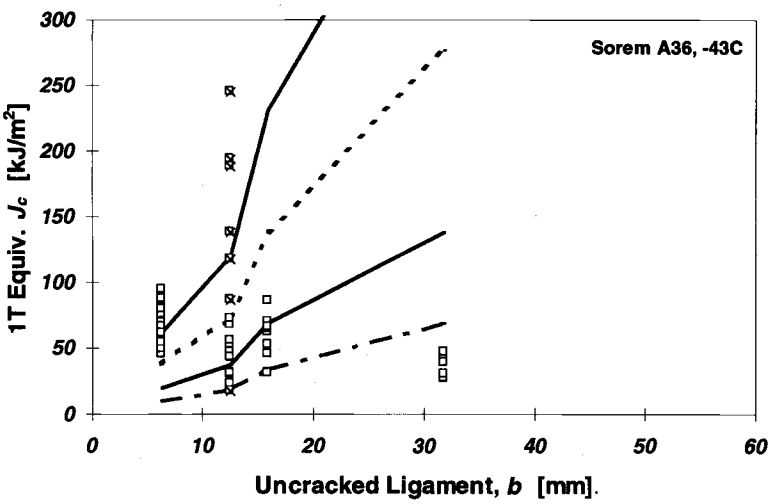


FIG. 16—*Comparison of candidate deformation limits* (M) *with 1T normalized fracture toughness data from Ref* 18.

from σ_{uts}/σ_{ys} using the formula found after Table 2). The E 1820-98 size requirement for ferritic steels approaches a limit value of 167% (=50/30) of the E 1921-97 size requirement only for a non-hardening material (i.e. $\sigma_{uts}/\sigma_{ys} = 1$, or $1/n = 0$). The size requirements of E 1820-98 and E 1921-97 become equal for $\sigma_{uts}/\sigma_{ys} > 2.33$, or $n < 4.4$. For higher work-hardening materials (i.e., lower n values) E 1820-98 requires smaller specimens than E 1921-97 to obtain a value toughness value.

Even though E 1820-98 and E 1921-97 both address testing of ferritic steels, their deformation limits need not be identical due to differences in the intent of the two test methods.

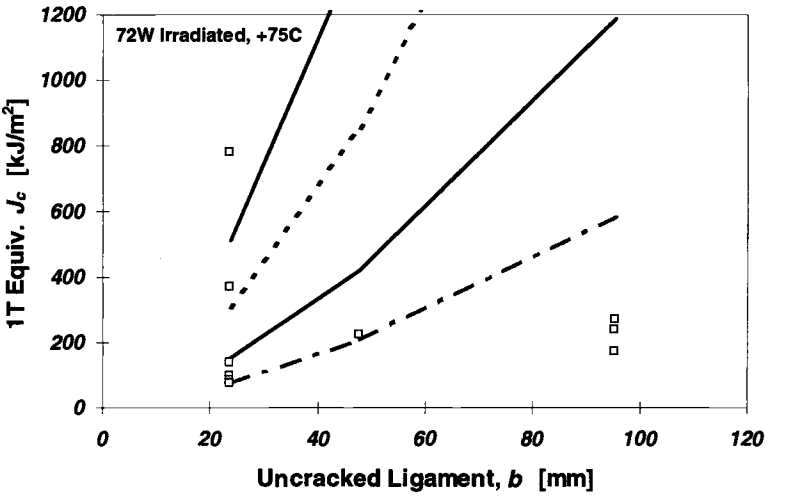


FIG. 17—*Comparison of candidate deformation limits* (M) *with 1T normalized fracture toughness data from Ref* 11.

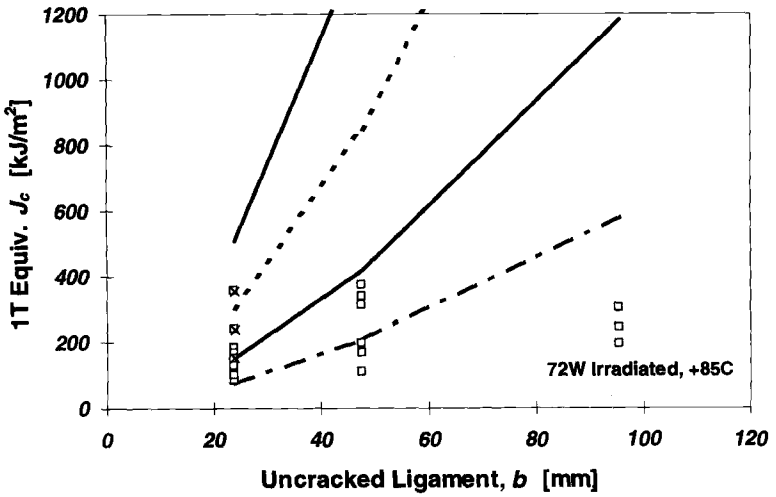


FIG. 18—*Comparison of candidate deformation limits* (M) *with 1T normalized fracture toughness data from Ref* 11.

Individual J_c values result from E 1820-98 testing. Also, E 1820-98 recommends, but places no requirements on, replicate testing. As such, E 1820-98 must have deformation limits that restrict the error possible in individual J_c values. While J_c values are measured as part of E 1921-97 testing, these values are not the result of the testing. Measured J_c values are used to calculate a median toughness value, which is converted to a reference temperature that positions the fracture mode transition curve (T_o). It is therefore the accuracy of T_o, not J_c, that E 1921-97 must control. While T_o accuracy is influenced by the accuracy of individual

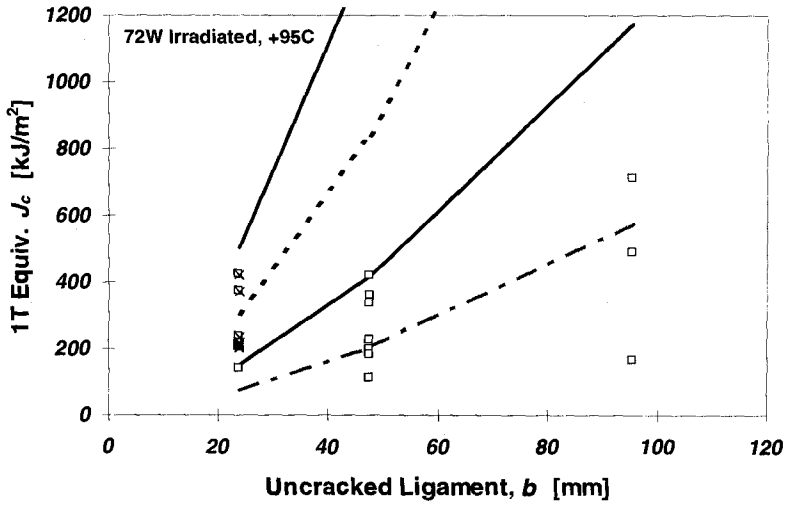


FIG. 19—*Comparison of candidate deformation limits* (M) *with 1T normalized fracture toughness data from Ref* 11.

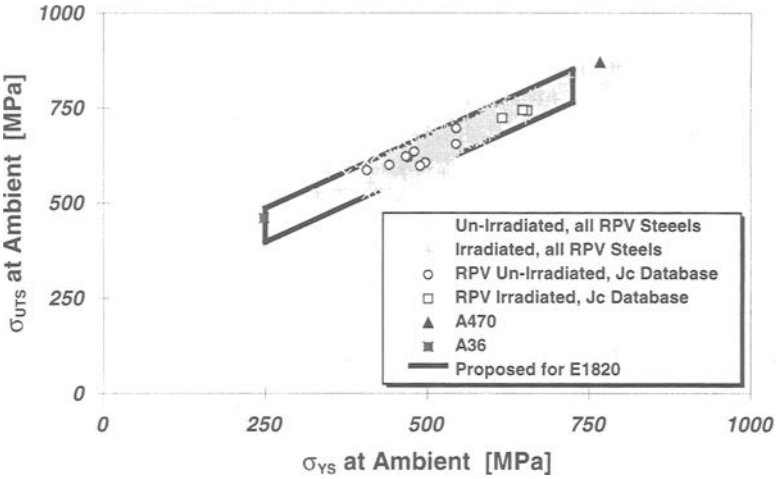


FIG. 20—*Comparison of tensile data for ferritic steels with the region of tensile properties where the E 1820-98* M = *50 deformation limit on* J_c *applies.*

J_c values, these two accuracies cannot be identical. The following factors mitigate the influence that inaccuracy in individual J_c values have on T_o.

1. E 1921-97 includes requirements on J_c data replication (six to ten specimens depending upon test temperature). These replicate data are used to estimate a median toughness value ($K_{Jc(median)}$), and $K_{Jc(median)}$ is used to estimate T_o. The replication requirements and use of median values ensures that individual J_c values, which may have experienced some constraint loss, are not considered alone in the estimation of T_o.
2. The Master Curve defines the non-linear relationship between T_o and $K_{Jc(median)}$ Fig. 22 shows the Master Curve, and also shows its differential ($dT_o/dK_{Jc(median)}$. The differential quantifies how changes in $K_{Jc(median)}$ produce changes in T_o. Because the differential is so small (below 2°C/MPa $\sqrt{m}$ over the range of permissible test temperatures), loss of constraint would have to elevate $K_{Jc(median)}$ substantially to increase T_o in any significant way.

Quantification of these effects lies beyond the scope of this investigation. Nevertheless, these observations suggest that the differences in M limits between E 1820-98 (M = 50) and E 1921-97 (M = 30) do not necessarily represent an inconsistency between the two test methods, but rather a need to control the accuracy of different reported values (J_c in E 1820-98, T_o in E 1921-97).

Summary and Conclusions

ASTM Standard Test Method E 1820-96, "Measurement of Fracture Toughness," was recently revised (E 1820-98). This revision includes a relaxation of the deformation limits/size requirements that must be satisfied to report a valid value of fracture toughness at instability prior to significant stable crack extension (J_c). E 1820-96 required that valid J_c values satisfy the following inequality (with a M value of 200).

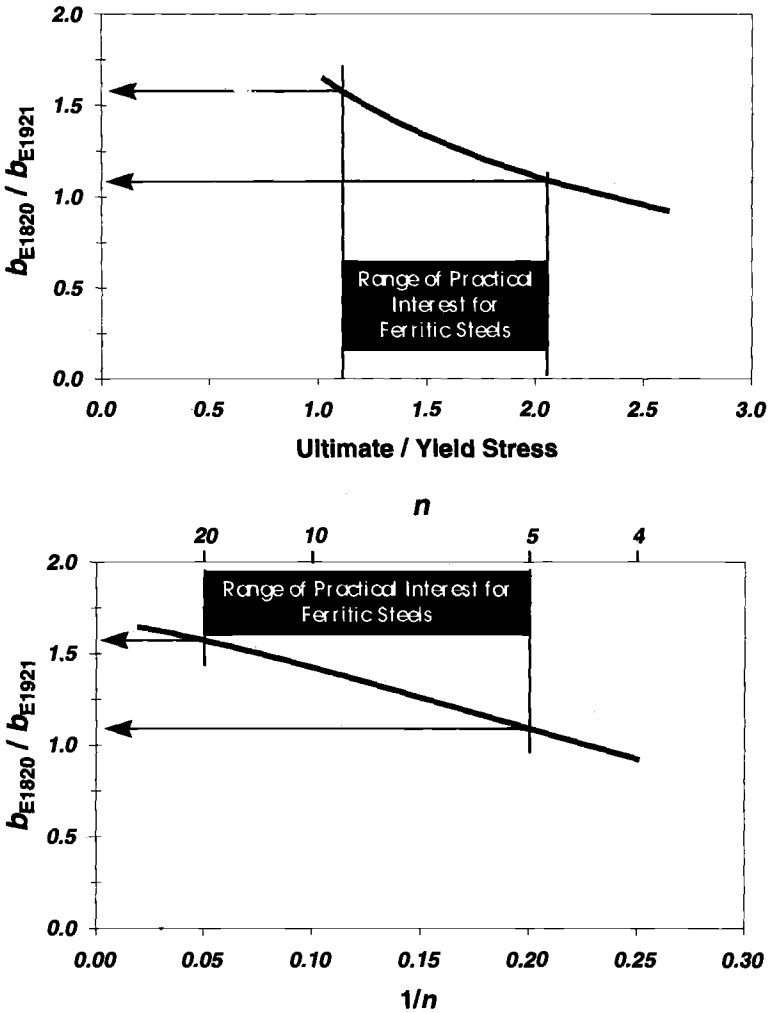


FIG. 21—*Comparison of E 1820-98 and E 1921-97 specimen size requirements for ferritic steels.*

$$B, b_o \geq M \frac{J_c}{\sigma_{\text{flow}}}$$

E 1820-98 relaxes this requirement to $M = 100$ for all metals and to $M = 50$ for ferritic steels. In this paper we review the basis for the original $M = 200$ limit and present results from both finite element analysis and from fracture toughness testing that supports the new, less restrictive limits. Finite elements results for a wide range of material tensile properties, presented previously by Dodds and co-workers, supports the applicability of the $M = 100$ limit to all metals. Here we present fracture toughness data for a number of different ferritic steels in support of the $M = 50$ limit for those materials. No available fracture toughness data suggest that ferritic steels require more restrictive limits than $M = 50$ to ensure the specimen size invariance of J_c values measured in accordance with E 1820-98 procedures.

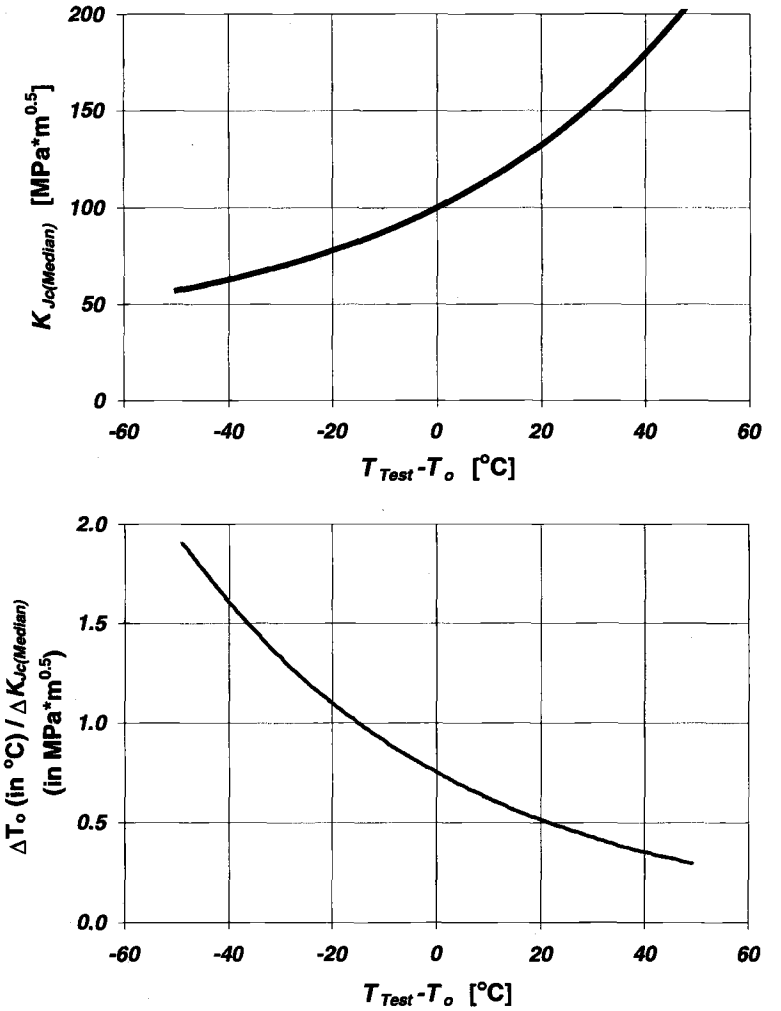


FIG. 22—*The Master Curve (top) and sensitivity of changes in* T_o *to changes in experimental measurements of* $K_{Jc(Median)}$ *(bottom).*

References

[1] Dodds, R. H., Anderson, T. L., and Kirk, M. T., "A Framework to Correlate a/W Ratio Effects on Elastic-Plastic Fracture Toughness (J_c)," *International Journal of Fracture,* Vol. 48, 1991, pp. 1–22.

[2] Anderson, T. L. and Stienstra, D., "A Model to Predict the Sources and Magnitude of Scatter in Toughness Data in the Transition Region," *Journal of Testing and Evaluation,* JTEVA, Vol. 17, 1989, pp. 46–53.

[3] Lin, T., Evans, A. G., and Ritchie, R. O., "Statistical Model for Carbide Induced Brittle Fracture in Steel," *Journal of the Mechanics and Physics of Solids,* Vol. 34, 1986, pp. 477–496.

[4] Beremin, F. M., "A Local Criterion for Cleavage Fracture of a Nuclear Pressure Vessel Steel," *Metallurgical Transactions A,* Vol. 14A, 1983, pp. 2277–2287.

[5] Koppenhoefer, K. C., Kirk, M. T., and Dodds, R. H., "Requirements for Determining Small Scale Yielding Fracture Toughness Values from Bend Specimens," *Constraint Effects in Fracture, Theory*

and Applications: Second Volume, ASTM STP 1244, M. Kirk and A. Bakker, Eds., American Society for Testing and Materials, West Conshohocken, PA, 1995, pp. 445–460.

[6] Nevalainen, M. and Dodds, R. H., "Numerical Investigation of 3-D Constraint Effects on Brittle Fracture in SE(B) and C(T) Specimens," *International Journal of Fracture,* Vol. 74, 1995, pp. 131–161.

[7] Ruggieri, C., Dodds, R. H., and Wallin, K., "Constraint Effects on Reference Temperature T_o, for Ferritic Steels in the Transition Region," *Engineering Fracture Mechanics,* Vol. 60, 1998, pp. 19–36.

[8] WCAP-14616, Greisbach, T. J., and Williams, J. F., "User's Guide to RPVDATA, Reactor Vessel Materials Database," Westinghouse Energy Systems Business Unit, 1996.

[9] Wallin, K., "The Size Effect in K_{Ic} Results," *Engineering Fracture Mechanics,* Vol. 22, 1985, pp. 149–163.

[10] Marston, T. U., "Flaw Evaluation Procedures, Background and Application of ASME Section XI Appendix A," EPRI Report NP-719-SR, Electric Power Research Institute, Palo Alto, CA, 1978.

[11] Nanstad, R. K. et al., "Irradiation Effects on Fracture Toughness of Two High-Copper Submerged-Arc Welds," HSSI Series 5, NUREG/CR-5913, U.S. Nuclear Regulatory Commission, 1992.

[12] Alexander, D. J. and Cheverton, R. D., "Fracture Properties of Specially Heat Treated ASTM A508 Cl. 2 Pressure Vessel Steel," *Fracture Mechanics 23rd Symposium, ASTM STP 1189,* R. Chona, Ed., American Society for Testing and Materials, West Conshohocken, PA, 1993, pp. 365–380.

[13] McCabe, D. E., "A Comparison of Weibull and β_{Ic} Analysis of Transition Range Data," *Fracture Mechanics, 23rd Symposium, ASTM STP 1189,* R. Chona, Ed., American Society for Testing and Materials, West Conshohocken, PA, 1984, pp. 80–94.

[14] Ingham, T. et al., "Fracture Toughness in the Transition Regime for A533B Steel: Prediction of Large Specimen Results from Small Specimen Tests," *Fracture Mechanics: Perspectives and Directions, 20th Symposium, ASTM STP 1020,* R. P. Wei and R. P. Gangloff, Eds., American Society for Testing and Materials, West Conshohocken, PA, 1989, pp. 369–389.

[15] McCabe, D. E. et al., "Unirradiated Material Properties of Midland Weld WF-70," NUREG/CR-6249, U.S. Nuclear Regulatory Commission, 1994.

[16] Lidbury, D. and Moskovic, R., "Assessment of the Ductile-to-Brittle Transition Toughness Behavior of an A508 Cl. 3 PWR Pressure Vessel Steel by a Statistical Approach," *American Society of Mechanical Engineers Pressure Vessel and Piping Conference Proceedings,* Vol. 250: *Pressure Vessel Integrity,* 1993, pp. 283–294.

[17] Iwadate, T., Tanaka, Y., Ono, S., and Watanabe, J., "An Analysis of Elastic Plastic Fracture Toughness Behavior for J_{IC} Measurement in the Transition Region," *Elastic-Plastic Fracture: Second Symposium, Volume II—Fracture Resistance Curves and Engineering Applications, ASTM STP 803,* C. F. Shih and J. P. Gudas, Eds., American Society for Testing and Materials, West Conshohocken, PA, 1983, pp. II-531–II-561.

[18] Sorem, W. A., "The Effect of Specimen Size and Crack Depth on the Elastic-Plastic Fracture Toughness of a Low-Strength High-Strain Hardening Steel," Ph.D. dissertation, University of Kansas, 1989.

[19] Kirk, M. T. and Dodds, R. H., "*J* and CTOD Estimation Equations for Shallow Cracks in Single Edge Notch Bend Specimens," *Journal of Testing and Evaluation, JTEVA,* Vol. 21, No. 4, American Society for Testing and Materials, West Conshohocken, PA, 1983, pp. 228–238.

C. R. Aveline, Jr.[1] *and S. R. Daniewicz*[2]

Variations of Constraint and Plastic Zone Size in Surface-Cracked Plates Under Tension or Bending Loads

REFERENCE: Aveline, C. R., Jr. and Daniewicz, S. R., **"Variations of Constraint and Plastic Zone Size in Surface-Cracked Plates Under Tension or Bending Loads,"** *Fatigue and Fracture Mechanics: 31st Volume, ASTM STP 1389,* G. R. Halford and J. P. Gallagher, Eds., American Society for Testing and Materials, West Conshohocken, PA, 2000, pp. 206–220.

ABSTRACT: Elastic-plastic finite element analyses of surface-cracked plates are performed using the commercial finite element code ANSYS. Various crack geometries are analyzed under tension and bending loads. A constraint factor dependent on the location along the perimeter of the surface crack, similar to the global constraint factor defined by Newman, is presented. This newly defined constraint factor is the averaged normal stress to flow stress ratio acting on a line originating on and perpendicular to the crack front at a prescribed location and terminating at the perimeter of the plastic zone on the crack plane.

The plastic zone shape and size around the three-dimensional crack front determined from the finite element analyses are also presented. The analyses indicate that the maximum plastic zone size occurs beneath the free surface ($2° < \phi < 5°$). Geometry and applied loading parameters are considered in equations relating them to constraint along the crack front.

KEYWORDS: surface cracks, part-through cracks, constraint, plastic zone, elastic-plastic finite element analysis

Nomenclature

a	Surface-crack depth, mm
b	Focus distance for elliptic curvilinear conversions
c	Surface-crack half-length, mm
d	Smallest finite element size in the direction perpendicular to the crack front, mm
E	Modulus of elasticity, MPa
h	Height of finite element model, mm
k	Ramberg-Osgood hardening coefficient, MPa
n	Ramberg-Osgood hardening exponent
S	Arc length at ϕ over which $\alpha(\phi)$ is calculated
t	Thickness of finite element model, mm
T	Applied tensile load, MPa
w	Width of finite element model, mm
x,y,z	Cartesian coordinates

[1] Project engineer, Manta Corporation, 1000 Ford Circle, Suite A, Milford, OH 45150.
[2] Associate professor, Department of Mechanical Engineering, P.O. Box ME, Mississippi State, MS 39762.

Copyright© 2000 by ASTM International www.astm.org

α Constraint factor
α_g Global constraint factor
α_h Hyper-local constraint factor
α_l Local constraint factor
ε_o Flow strain
ε_{VMe} Equivalent elastic strain
ε_{VMp} Equivalent plastic strain
η,ξ,y Elliptic curvilinear coordinates
ν Poisson's ratio
ρ Plastic zone radius, mm
ρ_{max} Maximum plastic zone radius, mm
σ_{ij} Stress tensor, MPa
σ_o Flow stress (average of yield and ultimate strengths), MPa
α_u Ultimate strength, MPa
σ_{ys} Yield strength, MPa
ϕ Parametric angle for semi-elliptical crack, degree
ϕ_{max} Parametric angle where maximum plastic zone is located, degree

Introduction

Constraint has been recognized as an important factor in developing criteria to predict and characterize crack propagation growth under monotonic and cyclic loading. Numerous investigations have used three-dimensional elastic-plastic finite element analyses to relate constraint to fatigue crack growth, ductile tearing, and fracture [*1–11*]. Although versatile, 3D elastic-plastic FEA is time consuming, especially for large models typical of those with sufficient refinement to capture the stress variations and plastic zone sizes that enable accurate prediction of crack growth and fracture. The global constraint factor, α_g, which is the averaged normal stress to flow stress ratio acting on the plastic zone across the plate thickness, has been calculated from FEA of planar geometries and has been used with good success in predicting fatigue crack growth (FCG) and ductile tearing through the use of strip-yield models [*5*].

Three-dimensional elastic-plastic FEA of non-planar crack geometries, such as the semi-elliptical part-through or surface crack, poses a more difficult problem when predicting crack growth in terms of modeling and sufficient refinement, leading to its impracticality for engineering applications. Investigations of the refinement issue have determined that very small element sizes in the direction perpendicular to the crack front are needed for accurate prediction of FCG [*12*] and constraint calculation [*11*]. Other studies have observed rapid changes in various fatigue and fracture criteria as the level of stress triaxiality degrades rapidly near the free surface, further emphasizing the need for adequate mesh refinement [*1–2,4–8,10,13*].

Dugdale-type strip yield models, such as that in development by Daniewicz [*14*], are designed to predict crack growth in arbitrary crack geometries and circumvent the need for time-consuming finite element analyses. These models require closed-form solutions of constraint variation along the crack front to incorporate closure effects. The current study provides a numerical basis for verification of such models by supplying constraint variation and plastic zone sizes.

A constraint factor based on the concept of a global constraint factor is defined here for the surface crack and is inherently dependent on the shape of the plastic zone ahead of the crack front. It has long been widely accepted that the plastic zone radius at a crack tip is

largest for the plane stress approximation and is smallest for locations where the plane strain approximation is appropriate. This has also been observed in 2D FEA and assumed to be applicable for 3D bodies. To date, only one study by Newman et al. [*8*] has presented results to contradict this premise of plastic zone variation in solid crack models.

This paper presents a closed-form equation for constraint variation along the surface crack front as a function of geometry and loading. Plastic zone shape as determined prior to constraint evaluation is also discussed.

Finite Element Analyses

Elastic-plastic finite element stress analyses of surface-flawed plates were made with ANSYS 5.4 [*15*] and used to obtain constraint factors along the crack front. The surface crack configuration is shown in Fig. 1. The range of crack geometries analyzed was chosen using the preferred propagation paths specified by ASTM E 740 [*16*] as a model: $0.10 \leq a/t \leq 0.42$ and $0.742 \leq a/c \leq 0.998$ for tension; $0.10 \leq a/t \leq 0.40$ and $0.462 \leq a/c \leq 0.900$ for bending.

Modeling

The finite element meshes were generated using the code, *mesh3d_scpcell,* from J. Faleskog (Royal Institute of Technology, Stockholm, Sweden). The meshes generated with this program assume two planes of symmetry exist in terms of configuration and loading; therefore, only one quarter of the complete physical model is created. The Faleskog code provides

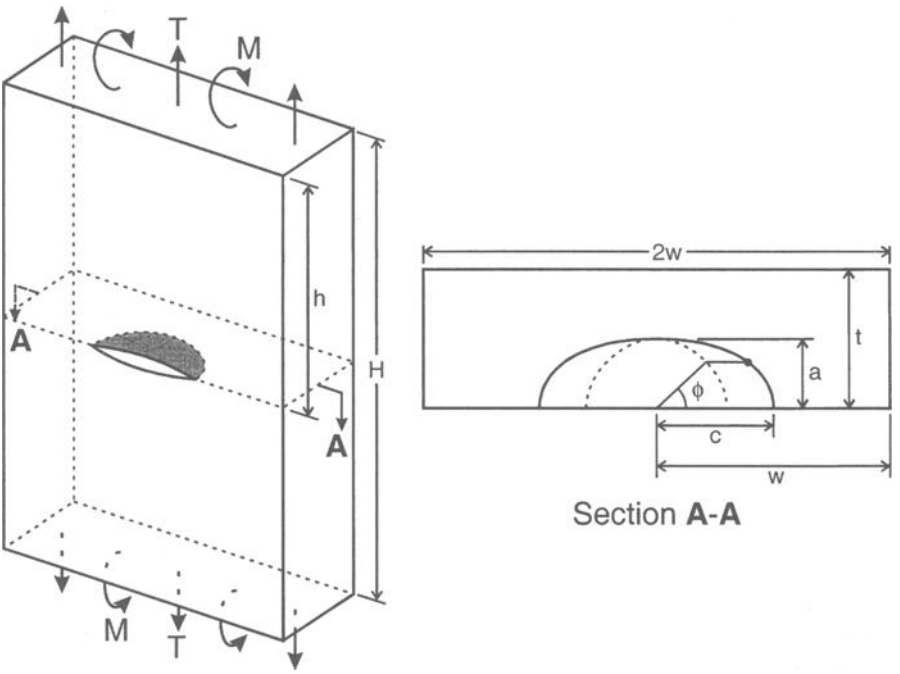


FIG. 1—*Surface crack configuration analyzed.*

for several levels of refinement necessary to capture the relatively small plastic zone sizes ahead of the crack front and the abrupt change in constraint near the free surface with good resolution using a user-specified number of nearly uniform elements. When compared to the work by Newman et al. [*11*], the smaller crack sizes combined with lower loads in the present study were expected to produce smaller plastic zone sizes; therefore, the smallest element size was chosen to be 0.0005 times the plate thickness. Since the remainder of the resulting meshes are essentially built around these critical cell elements, model sizes were quite large, ranging from about 26 400 to 112 000 nodes and from 23 300 to 102 000 eight-noded hexahedral elements. A typical model is shown in Fig. 2.

The plate geometry in all of the surface-crack models analyzed was constant with equal thickness and half-width, $t = w = 12.7$ mm (see Fig. 1). The model half-height, h, was also chosen to be $h = 2w$ to ensure that the applied traction did not affect the stress distribution near the crack front. Equations specified in ASTM E 740 for propagating surface crack paths were used as a basis for choosing crack geometries (a/t, a/c) based on load type as given below.

$$\text{tension} \qquad \frac{a}{c} = 1 - 0.2\left(\frac{a}{t}\right)^2 \tag{1}$$

$$\text{bending} \qquad \frac{a}{c} = 1 - \frac{a}{t} \tag{2}$$

In addition to each unique a/c-a/t combination, two more models of greater crack length were analyzed for completeness and were determined by increasing c by both 15 and 30%. The resulting matrix of analyzed crack geometries allowed for 15 tension models and 18 bending models [*17*]. Table 1 presents a matrix of loading conditions for the analyzed geometries.

Subsequent constraint evaluations were based on an elastic-perfectly plastic material with a flow stress $\sigma_o = 516.5$ MPa, modulus of elasticity $E = 70$ GPa, and Poisson's ratio $v = 0.33$. A single analysis was conducted on a tension model ($a/t = 0.18$, $a/c = 0.764$) with a Ramberg-Osgood stress-strain curve ($k = 595$ MPa, $n = 30$)

$$\varepsilon = \frac{\sigma}{E} + \left(\frac{\sigma}{k}\right)^n \tag{3}$$

to determine the effects of hardening on constraint and plastic zone variation. Representations of both material response curves are shown in Fig. 3.

Solution

Finite element analyses were conducted using ANSYS 5.4 with the iterative Jacobi Conjugate Gradient Out-Of-Core (JCG-Out) solver on one of four separate computers (a-d); dual 400-MHz processor 32-bit PC w/(a) 1024 MB RAM, (b, c) 512 MB RAM, or (d) 8 100-MHz processor 64-bit UNIX server w/2048 MB RAM. Parallel processing for this solver in the ANSYS 5.4 version was available only for the 64-bit machine, which was restricted to only two processors for time-sharing purposes. Even with this limitation, the PCs outperformed the UNIX server by requiring less than half the computing time on similarly sized models. The larger models resulted in long solution times that ranged from about 7 to 196 h, suggesting the impracticality of FEA for engineering applications. The von Mises yield

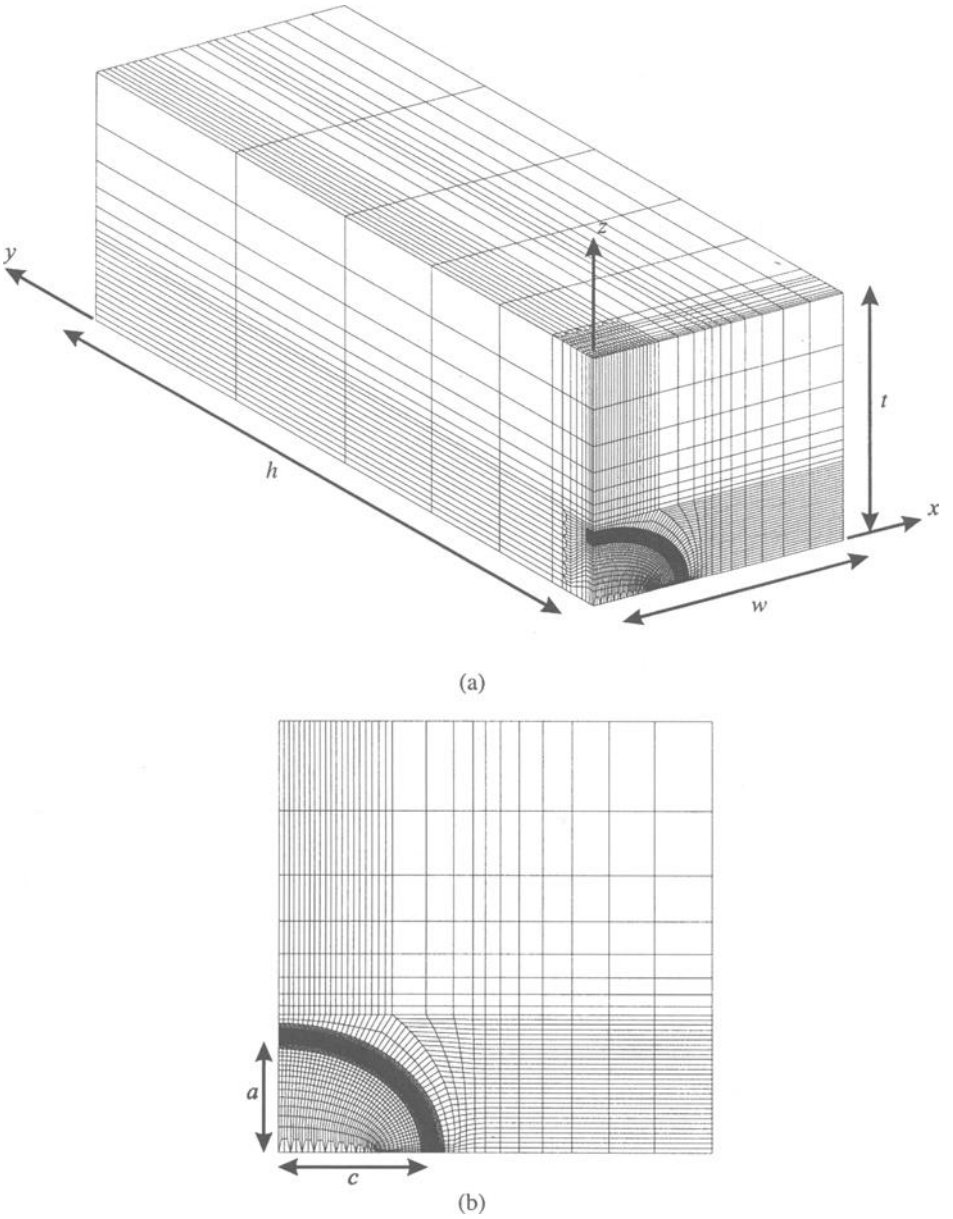


FIG. 2—*Typical finite element model of surface crack configuration.*

criterion, no strain hardening, small-deformation theory, and the associated flow rule were used in the nonlinear analyses.

Displacements of nodes lying on the $x = 0$ symmetry plane were fixed in the x-direction. Nodes lying on the crack plane, $y = 0$, and outside of the quarter-ellipse defined by the crack parameters, $(x/c)^2 + (z/a)^2 = 1$, were fixed in the y-direction. In order to prevent

TABLE 1—*Matrix of analyzed geometries.*

Tension				Bending			
a/t	*a/c*	*a*, in.	*x*, in.	*a/t*	*a/c*	*a*, in.	*c*, in.
0.10	0.998	0.05	0.05010	0.10	0.900	0.05	0.05556
0.10	0.868	0.05	0.05762	0.10	0.783	0.05	0.06389
0.10	0.768	0.05	0.06513	0.10	0.692	0.05	0.07222
0.18	0.993	0.09	0.09059	0.16	0.840	0.08	0.09524
0.18	0.864	0.09	0.10418	0.16	0.730	0.08	0.10952
0.18	0.764	0.09	0.11776	0.16	0.646	0.08	0.12381
0.26	0.986	0.13	0.13178	0.22	0.780	0.11	0.14103
0.26	0.858	0.13	0.15155	0.22	0.678	0.11	0.16218
0.26	0.759	0.13	0.17132	0.22	0.600	0.11	0.18333
0.34	0.977	0.17	0.17402	0.28	0.720	0.14	0.19444
0.34	0.849	0.17	0.20013	0.28	0.626	0.14	0.22361
0.34	0.751	0.17	0.22623	0.28	0.554	0.14	0.25278
0.42	0.965	0.21	0.21768	0.34	0.660	0.17	0.25758
0.42	0.839	0.21	0.25033	0.34	0.574	0.17	0.29621
0.42	0.742	0.21	0.28298	0.34	0.508	0.17	0.33485
				0.40	0.600	0.20	0.33333
				0.40	0.522	0.20	0.38333
				0.40	0.462	0.20	0.43333

gross model translation, the node located on the crack plane farthest from the origin at $\{x = w, y = 0, z = t\}$ was fixed in the z-direction.

The models were loaded monotonically in either tension or pure bending by applying pressure to the nodes lying on the $y = h$ plane. Tension was applied as a constant pressure, T or σ_T, and bending was applied as a moment M, simulated as a pressure varying linearly in the z-direction from σ_B to $-\sigma_B$. Three successive loads with maximum applied stress to flow stress ratios (σ_{max}/σ_o) of 0.3, 0.4, and 0.5 were applied to each of the tension and bending models, with the minimum chosen to produce sufficient plasticity to yield credible results.

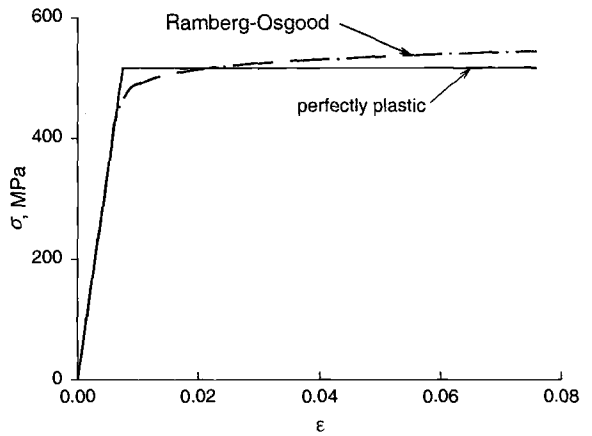


FIG. 3—*Stress-strain curves used in analyses.*

Each solution was completed in a three-step process. First, an elastic solution was performed with a maximum unit load, $\sigma_{max} = 1$, and the resulting maximum equivalent stress extracted from the nodal results. This resulting stress was used to calculate an applied load at which yielding first occurs, the "elastic-limit" load. Next, the initial elastic-plastic solution was performed using this elastic-limit to speed convergence. Lastly, the successive loads of interest were applied with a sufficient number of substeps to minimize the number of equilibrium iterations. Storage of nodal data needed for subsequent post-processing was kept to a minimum by specifying only the locations of interest for output (addressed below).

Numerical Results and Discussion

The constraint factor α is defined at discreet locations ϕ along the crack front as the average normal stress to flow stress ratio acting on a line lying on the crack plane inside the plastic zone. Using the FEA results, the plastic zone region was determined and the constraint variation fit to a generic equation with parameters dependent on geometry and loading.

Constraint Definition

The constraint factor α investigated in the current study is a modified version of the hyper-local normal-stress constraint factor α_h [*11*], which is an evolution of the global constraint factor α_g [*5*]. The hyper-local normal-stress constraint factor is the average normal stress to flow stress ratio acting along a row of yielded elements perpendicular to the crack front and evaluated at the centroid of the individual elements. Due to the unavoidable inclusion of the projected areas of partially yielded elements along the perimeter of the plastic zone, constraint results tend to exhibit noise, especially at lower loads. The need for calculation of individual element areas was eliminated entirely by defining constraint as the normal stress to flow stress ratio acting along a line or path as shown in Fig. 4. This new constraint factor is defined as

$$\alpha(\phi) = \frac{1}{S(\phi)} \int_0^{S(\phi)} \left(\frac{\sigma_{yy}}{\sigma_o} \right) ds \tag{4}$$

where $S(\phi)$ defines the arc length of a hyperbolic path originating and perpendicular to the crack front at ϕ and terminating at the perimeter of the plastic zone (see Fig. A1), and

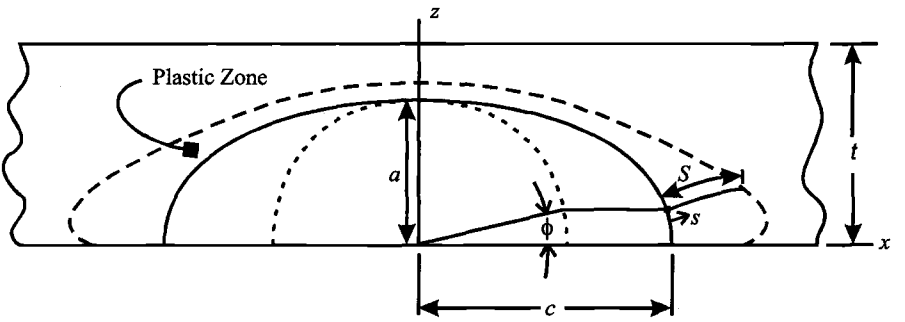


FIG. 4—*Normal stress constraint factor for shallow surface crack under remote tension.*

(σ_{yy}/σ_o) is the normalized stress component interpolated onto the defined path at Location s.

Plastic Zone Location

A simple but effective extrapolation method was developed in the current study to locate the assumed continuous boundary of the plastic zone on the crack plane using elastic and plastic strain data stored for each nodal location. This method is depicted in Fig. 5 where the hatched areas represent the plastic zone. The method involves moving along a line or ray of elements emanating from the crack front until at least one of the element's four nodes on the crack plane has a zero value of equivalent plastic strain, ε_{VMp} (Node 1 in Fig. 5). From this representation, it is obvious that the edge of the plastic zone must occur within that element and between two adjacent nodes of zero and non-zero ε_{VMp}. Next, it is assumed that the boundary of the plastic zone is defined at the location where the equivalent elastic strain, ε_{VMe}, is equal to the flow strain ε_o. Finally, Location x, the location at which the plastic zone boundary intersects the line joining adjacent elastic and plastic nodes, is found by extrapolating the ε_{VMe} of the first two adjacent elastic nodes (1 and 2 of Fig. 5) outside of the yielded region to ε_o and extracting the corresponding Cartesian coordinates.

The importance of using this method was most readily observed at the lowest loads where yielding is often limited to four elements or fewer ahead of the crack front. Constraint variation at these loads remained smooth where they would otherwise, without the use of this method, have exhibited erratic variations along the crack front.

Constraint Evaluations

Constraint factors were calculated by first defining a series of points in Cartesian coordinates converted from equally spaced locations on a curve of constant η (see Appendix 1) extending from a nodal point on the crack front to the edge of the plastic zone. The number of equally spaced points was arbitrarily chosen as five times the maximum number of yielded elements in the plastic zone. Once a given path was defined, the normalized stress component, (σ_{yy}/σ_o), was mapped onto it and averaged over the arc length S using a line integral. Path operations included in the ANSYS postprocessor greatly simplified this task.

Typical variations in constraint along the crack front ϕ are shown in Fig. 6 for cracks of similar size under tension and bending loads. For the tension cases, α increases from values ranging from 1.1 to 1.2 near the free surface ($0 < \phi < 15°$) to an asymptotic value nearly independent of load at the deepest point ($\phi = 90°$). Bending cases, however, exhibit a more load dependent variation of α for deeper locations ($15° < \phi \leq 90°$) leading to a slightly larger range of magnitudes at the deep point. It is important to note here the slightly larger value of the constraint factor at the free surface ($\phi = 0$) compared to those located just beneath the surface ($0 < \phi < 2°$). This was observed in both tension and bending analyses and is shown in greater detail in Fig. 7 for the tensile loading case only. It has generally been assumed that constraint is always a minimum at the free surface due to a loss of stress triaxiality. Since constraint data in earlier work [*11*] was extracted from element centroids, it was impossible to analyze the condition at the actual free surface. It is suspected that this increased value of constraint at the free surface is due to the observed smaller plastic zone size at this location and may also be influenced by the loss of the $1/\sqrt{r}$ singularity here [*18*]. The magnitude of this anomaly was observed to diminish with increasing load and crack size and was ignored in the following constraint equation.

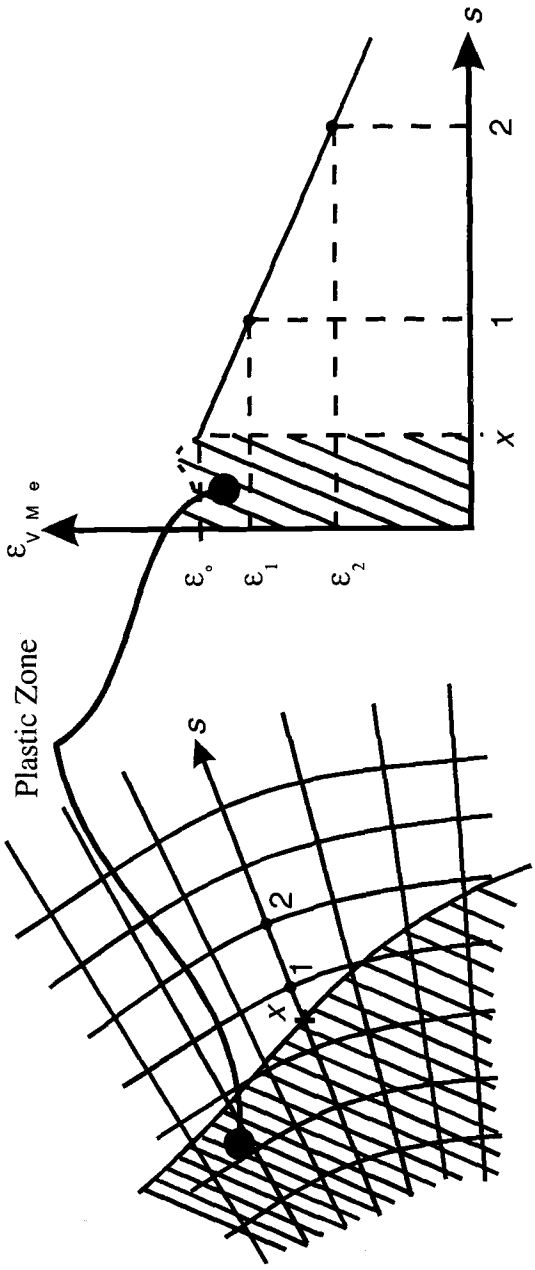


FIG. 5—*Extrapolation to locate plastic zone boundary.*

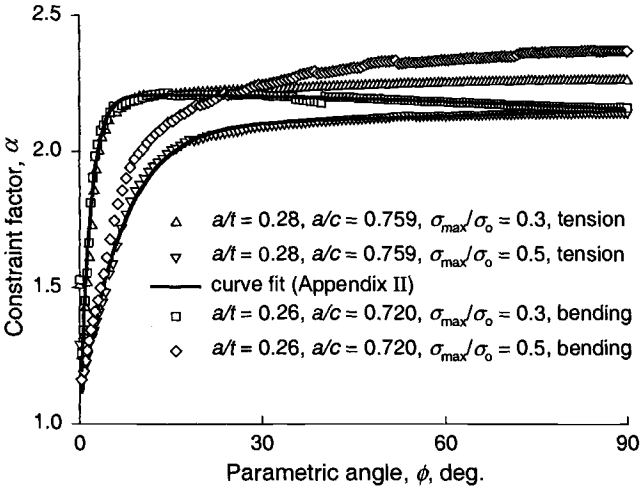


FIG. 6—*Typical variations of constraint factor for tension and bending loads.*

Each set of constraint data for given geometry and loading (a/t, a/c, σ_{max}/σ_o) was fitted to an equation of the form:

$$\alpha(\phi) = A + B\left(1 - \frac{2\phi}{\pi}\right)^p + C\left(\frac{2\phi}{\pi}\right)^q \tag{5}$$

The first term, A, represents a rough average of the constraint variation along the crack front; the second term, B, accounts for the loss of constraint near the free surface ($\phi \rightarrow 0$); and the third term, C, accounts for slight differences in constraint at the maximum depth location.

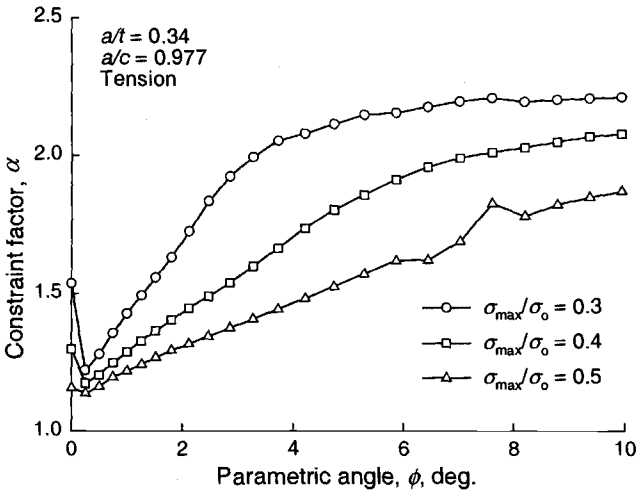


FIG. 7—*Increase of constraint factor at the free surface.*

The first exponent, p, governs the rate of constraint increase below the free surface, while q was observed to have only minor effects in curvature. Each of the five parameters (A, B, C, p, and q) is dependent on crack geometry (a/t, a/c), applied stress level (σ_{max}/σ_o), and loading type (tension or bending). Separate equations for tension and bending are given in Appendix 2.

Plastic Zone Shape

Accurate calculation of constraint variation according to Eq 4 depends on knowing the location of the plastic boundary along the crack front. This necessary determination of the shape of the plastic zone shape revealed a discrepancy at variance with conventional wisdom. Plastic zone size was observed to be relatively constant for locations of $\phi > 20°$ but to increase sharply to a maximum just below the free surface ($2° < \phi < 5°$) for both loading types. Plastic zone size at the free surface ($\phi = 0$) was frequently seen to be smaller than that observed at the mid-plane ($\phi = 90°$). These observations seemingly contradict the plastic zone sizes predicted by the familiar plane stress and plane strain approximations. Only one mention of this subsurface plastic zone size phenomenon was found in the literature [*8*] and was shown to shift as deep as the quarter point in thin through-cracked plates subject to high loading. Experimental fracture results for surface cracks in D6AC steel plates presented by Reuter et al. [*19*] identified fracture initiation locations well below the free surface with fracture surfaces shaped similarly to that depicted in Fig. 4. The development of the plastic zone shape to deeper locations with increasing load predicted by FEA presented here and by Newman et al. [*8*], combined with the fracture results mentioned above, suggests that accurate prediction of the plastic zone shape may be essential in characterizing crack growth under monotonic loading. Typical variations of plastic zone radius in the crack plane are shown in Fig. 8 with the relation to crack front curvature and in Fig. 9 plotted against the parametric.

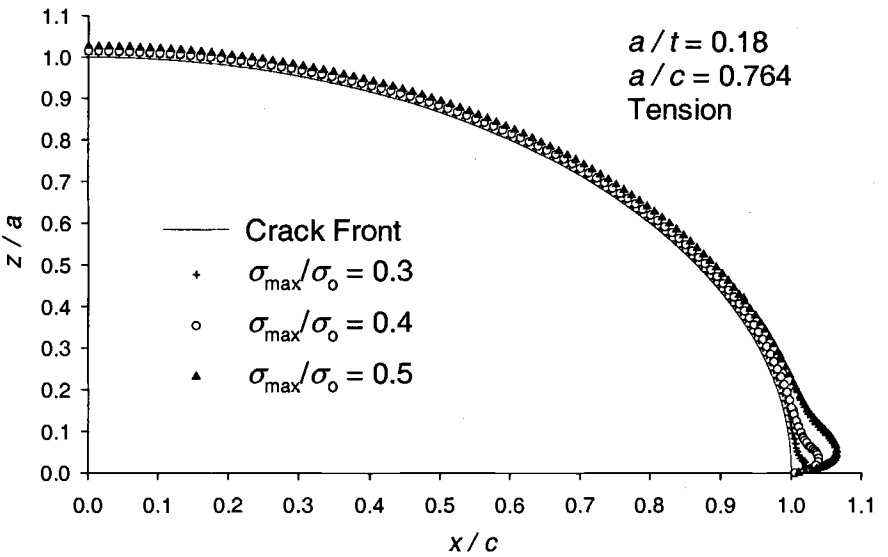


FIG. 8—*Typical plastic zone shape along the crack front.*

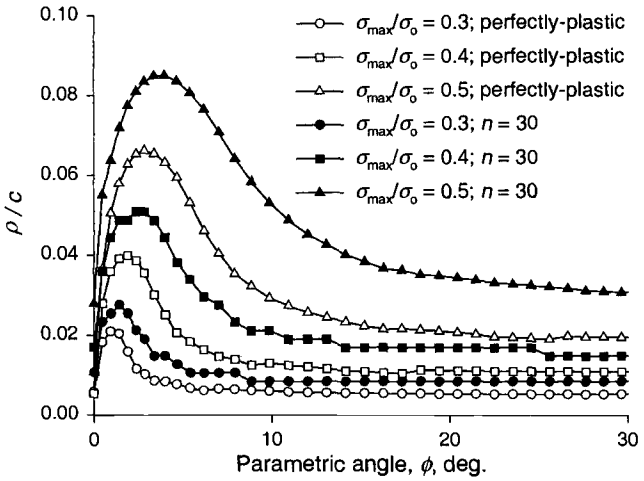


FIG. 9—*Hardening effects on plastic zone radius* (a/t = *0.18*, a/c = *0.764*).

Hardening Effects

One analysis was run for the tension case, $a/t = 0.18$ and $a/c = 0.764$, to explore the effects of hardening on both constraint and plastic zone size. As is shown in Figs. 9 and 10, the incorporation of strain hardening elicits a significant increase in plastic zone size while constraint variation decreases. The increase in plastic zone size when including hardening effects is due to the lower stress value at which plasticity is initiated, as shown in Fig. 3. It should be emphasized here that an elastic–perfectly plastic stress-strain curve based on flow stress is a simple approximation of actual material response. Although constraint shows an

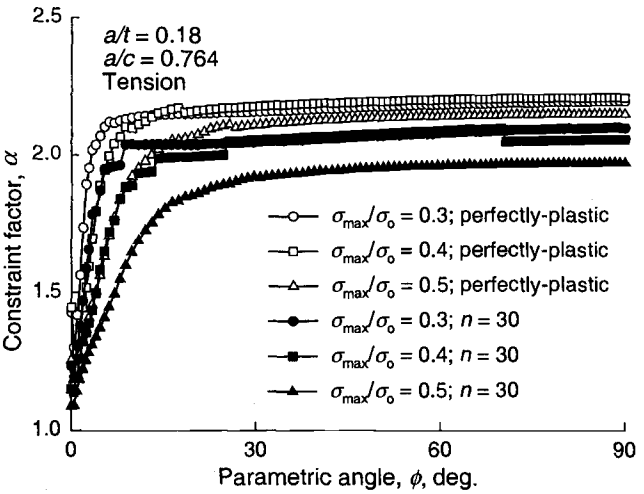


FIG. 10—*Hardening effects on constraint variation.*

obvious dependence on hardening effects, this was not taken into account in the development of the constraint variation equation and should be investigated further.

Concluding Remarks

Elastic-plastic finite element analyses were performed on 33 different surface crack geometries to determine constraint variation along the crack front. Plastic zone size was also calculated as a preliminary step to evaluating constraint. The results of the analyses support the following conclusions:

1. Plastic zone shape as calculated using well-defined meshes contradicts conventional thinking regarding the plastic zone sizes predicted by the familiar plane stress and plane strain approximations.
2. Material hardening had a greater effect on constraint variation and plastic zone size than anticipated.

Acknowledgment

Gratitude is extended to R. H. Dodds of the University of Illinois for making available software written by J. Faleskog for generation of surface crack finite element meshes.

APPENDIX 1

Cartesian-Elliptic Curvilinear Coordinate Transformation

For a family of ellipses and hyperbolas with a focal point, b, centered about a Cartesian origin ($x = 0$, $z = 0$) as shown in Fig. A1, every unique set of Cartesian coordinates has a corresponding elliptic curvilinear set (ξ, η) defined as

$$x + iz = b \cosh(\xi, +i\eta) \tag{A.1}$$

where the focus distance b is determined by the minor and major axes of any ellipse, a and c, respectively. Each ellipse is defined by constant ξ, which is defined here for the known crack front dimensions as ξ_o and calculated by the following:

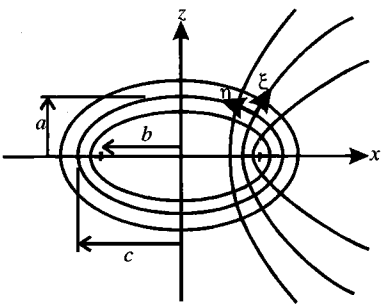


FIG. A1—*Family of confocal ellipses and hyperbolas.*

$$\xi_o = \tanh^{-1}\left(\frac{a}{c}\right) = \frac{1}{2}\ln\left(\frac{c+a}{c-a}\right) \tag{A.2}$$

Using this value, the focus distance is then

$$b = \frac{a}{\sinh(\xi_o)} = \frac{c}{\cosh(\xi_o)} \tag{A.3}$$

Combining the Cartesian coordinates into a single complex variable Ψ and applying Eq A.1, the corresponding elliptic curvilinear coordinates can be extracted from Eq A.6.

$$\Psi = x + iz \tag{A.4}$$

$$\zeta = \cosh^{-1}\left(\frac{\Psi}{b}\right) = \ln\left(\frac{\Psi + \sqrt{\Psi^2 - b^2}}{b}\right) \tag{A.5}$$

$$\zeta = \xi + i\eta \tag{A.6}$$

APPENDIX II

Normal Stress Constraint Factor Equations

The constraint factor along the surface crack front, calculated from elastic–perfectly-plastic finite element stress analyses, was fit to an equation of the form

$$\alpha(\phi) = A + B\left(1 - \frac{2\phi}{\pi}\right)^p + C\left(\frac{2\phi}{\pi}\right)^q \tag{A.7}$$

In the finite element analyses, the plate dimensions (see Fig. 1) in all of the surface crack models were constant with thickness and half-width, $t = w = 12.7$ mm. The surface crack geometries analyzed were in the ranges $0.10 \le a/t \le 0.42$ and $0.742 \le a/c \le 0.998$ for tension and $0.10 \le a/t \le 0.40$ and $0.462 \le a/c \le 0.900$ for bending. These analyses were also conducted for maximum applied stress to flow stress ratios (σ_{max}/σ_o) of 0.3, 0.4, and 0.5. Further study is needed on hardening effects on constraint variation. No secondary analyses were performed with geometry and loading outside the specified range to verify the applicability of Eq A.7 to deeper cracks and higher loads; therefore, the following equation parameters apply only to the geometry and loading range specified above.

For remote tension: $A = 2.25 - (1 - a/c)^2 - 0.43\,(\sigma_{max}/\sigma_o)^{1.65} + (a/t)^{4.25}$; $B = -1.5 + \sigma_{max}/\sigma_o$; $C = 0.05$; $p = 750\,[1 - \sqrt{(a/t)}]\exp(-7\sigma_{max}/\sigma_o)$ and $q = 0.5$.

For remote bending: $A = 3.05 - (1 - a/c)^{0.53} - \sigma_{max}/\sigma_o - (a/t)^4$; $B = -1.5 + \sigma_{max}/\sigma_o + 0.3\,a/t$; $C = 0.25$; $p = 750\,[1 - \sqrt{(a/t)}]\exp(-6.85\sigma_{max}/\sigma_o)$ and $q = 0.5$.

The above relations were found to have the best fit across the range of specified crack geometry and loading with a relative error at the 0 and 90° locations of roughly 10 to 20%.

References

[1] Levy, N., Marcal, P. V., and Rice, J. R., "Progress in Three-Dimensional Elastic-Plastic Stress Analysis for Fracture Mechanics," *Nuclear Engineering and Design*, Vol. 17, 1971, pp. 64–75.

[2] Trantina, G. G., deLorenzi, H. G., and Wilkening, W. W., "Three-Dimensional Elastic-Plastic Finite Element Analysis of Small Surface Cracks," *Engineering Fracture Mechanics,* Vol. 18, 1983, pp. 925–938.

[3] Chermahini, R. G., Shivakumar, K. N., and Newman, J. C., Jr., "Three-Dimensional Finite-Element Simulation of Fatigue Crack Growth and Closure," *Mechanics of Fatigue Crack Closure, ASTM STP 982,* J. C. Newman, Jr. and W. Elber, Eds., American Society for Testing and Materials, Philadelphia, 1988, pp. 398–413.

[4] Siegele, D., "3D-Crack Propagation Using ADINA," *Computers & Structures,* Vol. 32, No. 3/4, 1989, pp. 639–645.

[5] Newman, J. C., Jr., Bigelow, C. A., and Shivakumar, K. N., "Three-Dimensional Elastic-Plastic Finite-Element Analyses of Constraint Variations in Cracked Bodies," *Engineering Fracture Mechanics,* Vol. 46, No. 1, 1993, pp. 1–13.

[6] Wang, Y.-Y., "On the Two-Parameter Characterization of Elastic-Plastic Crack-Front Fields in Surface-Cracked Plates," *Constraint Effects in Fracture, ASTM STP 1171,* E. M. Hackett, K.-H. Schwalbe, and R. H. Dodds, Eds., American Society for Testing and Materials, 1993, pp. 120–138.

[7] Faleskog, J., "Effects of Local Constraint Along Three-Dimensional Crack Fronts—A Numerical and Experimental Investigation," *Journal of the Mechanics of Physics of Solids,* Vol. 43, No. 3, 1995, pp. 447–493.

[8] Newman, J. C., Jr., Crews, J. H., Jr., Bigelow, C. A., and Dawicke, D. S., "Variations of a Global Constraint Factor in Cracked Bodies Under Tension and Bending Loads," *Constraint Effects in Fracture Theory and Applications: Second Volume, ASTM STP 1244,* M. Kirk and A. Bakker, Eds., American Society for Testing and Materials, Philadelphia, 1995.

[9] Zhang, J. Z. and Bowen, P., "On the Finite Element Simulation of Three-Dimensional Semi-Circular Fatigue Crack Growth and Closure," *Engineering Fracture Mechanics,* Vol. 60, No. 3, 1998, pp. 341–360.

[10] Gao, X., Faleskog, J., Shih, C. F., and Dodds, R. H., "Ductile Tearing in Part-Through Cracks: Experiments and Cell-Model Predictions," *Engineering Fracture Mechanics,* Vol. 59, No. 6, 1998, pp. 761–777.

[11] Newman, J. C., Jr., Reuter, W. G., and Aveline, C. R., Jr., "Stress and Fracture Analyses of the Surface Crack," *Fatigue and Fracture Mechanics: 30th Volume, ASTM STP 1360,* K. L. Jerina and P. C. Paris, Eds., American Society for Testing and Materials, Philadelphia, PA, 1999.

[12] McClung, R. C. and Sehitoglu, H., "On the Finite Element Analysis of Fatigue Crack Closure—1. Basic Modeling Issues," *Engineering Fracture Mechanics,* Vol. 33, 1989, pp. 237–252.

[13] Fujikubo, M., Berge, S., and Moan, T., "CTOD Estimates of Surface Cracked Wide Plates in Bending—I. Finite Element Analysis," *Engineering Fracture Mechanics,* Vol. 40, No. 3, 1991, pp. 627–639.

[14] Daniewicz, S. R., "A Modified Strip-Yield Model for Prediction of Plasticity-Induced Closure in Surface Flaws," *Fatigue and Fracture of Engineering Materials and Structures,* Vol. 21, 1998, pp. 885–901.

[15] *ANSYS User's Manuals,* Revision 5.4, Swanson Analysis Systems, Inc., 1998.

[16] ASTM, "ASTM E740, Standard Practice for Fracture Testing with Surface-Crack Tension Specimens," *1998 Annual Book of ASTM Standards,* ASTM, p. 609.

[17] Aveline, C. R., Jr., *Analysis of Constraint and Plastic Zone Size in Surface Cracked Geometries,* M.S. thesis, Mississippi State University, 1999.

[18] Parks, D. M., "A Surface Crack Review: Elastic and Elastic-Plastic Behavior," *Surface-Crack Growth: Models, Experiments, and Structures, ASTM STP 1060,* W. G. Reuter, J. H. Underwood, and J. C. Newman, Jr., Eds., American Society for Testing and Materials, Philadelphia, PA, 1990, pp. 9–33.

[19] Reuter, W. G., Elfer, N., C., Hull, A., Newman, J. C., Jr., Munz, D., and Panontin, T. L., "Fracture Toughness Results and Preliminary Analysis for International Cooperative Test Program on Specimens Containing Surface Cracks," *Fatigue and Fracture Mechanics: 28th Volume, ASTM STP 1321,* J. H. Underwood, B. D. Macdonald, and M. R. Mitchell, Eds., American Society for Testing and Materials, 1997, pp. 147–166.

S. R. Daniewicz[1] *and C. R. Aveline*[2]

A Strip-Yield Model for Part-Through Surface Flaws Under Monotonic Loading

REFERENCE: Daniewicz, S. R. and Aveline, C. R., **"A Strip-Yield Model for Part-Through Surface Flaws Under Monotonic Loading,"** *Fatigue and Fracture Mechanics: 31st Volume, ASTM STP 1389,* G. R. Halford and J. P. Gallagher, Eds., American Society for Testing and Materials, West Conshohocken, PA, 2000, pp. 221–241.

ABSTRACT: A slice synthesis methodology was developed and used to construct a weight function based strip-yield model for a semi-elliptical part-through surface flaw in an elastic–perfectly plastic material under monotonic loading. The model enables rapid approximate computation of crack surface displacements and the crack front plastic zone size. A mathematical description of the model is presented. A model verification is discussed in which results from the strip-yield model were compared with results from finite element analyses. Crack surface displacements and crack mouth opening displacements from the model are shown to compare well with results from detailed three-dimensional elastic-plastic finite element analyses. Plastic zone sizes from the model were found to be significantly larger than those determined from the finite element model.

KEYWORDS: surface cracks, part-through cracks, strip-yield model, plastic zone, weight functions

The part-through semi-elliptical surface flaw is commonly encountered in engineering practice. Models enabling the computation of crack surface displacement and the extent of the plastically deformed region along the crack front are needed for assessing ligament yielding under monotonic loading, for development of compliance expressions, and for the modeling of plasticity-induced closure in surface flaws under cyclic loading. The author's primary interest is the modeling of plasticity-induced crack closure, with the research reported here representing a necessary but intermediate activity.

Monotonic analyses of the semi-elliptical surface flaw have been performed using three dimensional elastic-plastic finite element analysis [*1–5*]. However, from an engineering perspective, this approach is impractical because the finite element models required are prohibitively large and complex. An alternate approach is the use of strip-yield models. Strip-yield models have been used for computation of crack surface displacements and the extent of the crack tip plastic zone in planar geometries with through-cracks [*6–13*]. While approximate in nature, strip-yield models require less computational resources when compared to more rigorous and computationally intensive finite element analyses.

This paper discusses the development and validation of a strip-yield model for surface flaws under monotonic loading. An elastic–perfectly plastic plate containing a semi-elliptical surface flaw was considered as shown in Fig. 1*a*. The flaw is opened with an arbitrary

[1] Associate professor, Department of Mechanical Engineering, Mississippi State University, P.O. Box ME, Mississippi State, MS 39762.

[2] Project engineer, Manta Corporation, 1000 Ford Circle, Suite A, Milford, OH 45150.

Copyright© 2000 by ASTM International www.astm.org

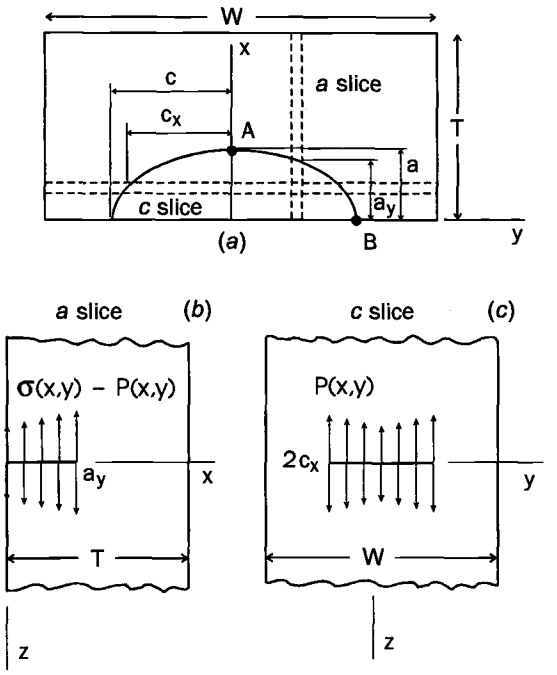


FIG. 1—*Slice synthesis model.*

symmetrical applied stress $\sigma_{zz}(x,y)$. Using the model, the crack plane plastic zone may be computed at the deepest point of penetration and the free surface (Points A and B). Crack surface displacements may also be determined along both the x and y axes.

In the model development process, a slice synthesis methodology [*14–20*] previously limited to stress intensity factor and crack surface displacement computation in elastic bodies was employed. The slice synthesis methodology was extended to allow consideration of elastic–perfectly plastic materials. To date, strip-yield modeling of surface flaws under monotonic loading has been limited to the prediction of limit loads and plastic zone size [*21,22*].

Strip-Yield Model

First consider the slice synthesis methodology as applied to elastic bodies. A weight function based slice synthesis methodology presented by Zhao et al. [*14–20*] may be used to approximate surface flaw stress intensity factors and crack surface displacements using through-crack weight functions for two-dimensional elastic bodies. The slice synthesis methodology was first introduced by Grandt and Sinclair [*23*], Fujimoto [*24*], and Saff et al. [*25*] for stress intensity factor computation. Zhao et al. [*14–20*] have used the methodology to compute surface crack and corner crack stress intensity factors and crack opening displacements.

As illustrated in Fig. 1*b* and 1*c*, the behavior of the surface flaw is synthesized using two groups of through-crack slices. The surface flaw is characterized using a crack depth a and length $2c$. The slices situated parallel with the x axis are denoted as primary slices or a slices, while those aligned parallel with the y axis are termed spring slices or c slices. Each

primary slice constitutes an edge-cracked strip and is assumed to be in a plane stress condition. A primary slice exhibits a modulus of elasticity E, Poisson's ratio ν, and a crack length a_y as defined by the elliptical shape

$$a_y = a\sqrt{1 - (y/c)^2} \tag{1}$$

Surface flaw stress intensity factors and crack surface displacements may be estimated using these two-dimensional slices if an unknown shear traction $\sigma_{yz} = P(x,y)$ acting between adjacent primary slices and in a direction opposed to the applied stress $\sigma(x,y) = \sigma_{zz}(x,y)$ is introduced. The crack surface displacement $w_a(x,y)$ for an arbitrarily located primary slice resulting from the applied stress $\sigma(x,y)$ is given by

$$w_a(x,y) = \frac{1}{E}\int_x^{a_y}\int_o^{\alpha}[\sigma(\xi,y) - P(\xi,y)]m_a(\xi,\alpha)m_a(x,\alpha)d\xi d\alpha \tag{2}$$

where the primary slice weight function for an edge crack of length a_y is denoted as $m_a(\sigma, a_y)$.

Using an exact solution for an embedded elliptical flaw under uniform tension as well as results from finite element analyses, it may be shown [*14,17,24*] that an estimate of the surface flaw stress intensity factor at Point A is given by

$$K_A = \frac{1}{1 - \nu^2}\int_o^a [\sigma(\xi,0) - P(\xi,0)]m_a(\xi,a)d\xi \tag{3}$$

The spring slices or c slices enable the computation of the unknown shear traction through enforcement of compatibility with $w_a = w_c$ where w_c is the spring slice displacement. As shown in Fig. 1*c*, each spring slice constitutes a center-cracked panel and is assumed to be under a plane stress condition. These slices exhibit a modulus of elasticity E_s and a crack length $2c_x$, with c_x defined from the elliptical shape

$$c_x = c\sqrt{1 - (x/a)^2} \tag{4}$$

E_s is a fictitious quantity defining the level of mechanical coupling between adjacent primary slices. It may be demonstrated [*14,24,25*] that for $a/c \leq 1$

$$\frac{E_s}{E} = \left(\frac{\Phi}{1 - \nu^2} - 1\right)\frac{c}{a} \tag{5}$$

Where Φ represents a complete elliptic integral of the second kind. The spring slice crack surface displacement $w_c(c,y)$ resulting from the applied stress $\sigma(x,y)$ is given by

$$w_c(x,y) = \frac{1}{E_s}\int_y^{c_x}\int_0^{\gamma} P(x,\psi)m_c(\psi,\gamma)m_c(y,\gamma)d\psi d\gamma \tag{6}$$

where the spring slice weight function for a center-crack with length $2c_x$ under symmetrical loading with $P(x,y) = P(x, -y)$ is denoted as $m_c(\psi,c_x)$. This symmetrical shear traction is a consequence of the symmetrical applied stress. It may also be shown [*14,17,24*] that an estimate of the surface flaw stress intensity factor at Point B may be written as

$$K_B = \frac{E}{E_s}\int_o^c P(0,\eta)m_c(\eta,c)d\eta \tag{7}$$

Next consider extending the elastic slice synthesis such that plastic deformation along the crack front may occur as illustrated in Fig. 2. The primary slice was assumed to exhibit a uniform cohesive stress Y, while the spring slice has a value Y_s. Using a strip-yield modeling approach, the surface flaw and subsequent plastic zone were treated as an effective crack in an elastic body. The effective surface crack was characterized using a crack depth a, crack length $2c$, and plastic zones ρ_A and ρ_B. The effective and actual surface flaws were assumed to form concentric semi-ellipses. Note that from a rigorous perspective, the actual shape of the effective crack will be a function of the stress intensity factor and the degree of constraint along the crack front. Given the approximate nature of the strip-yield modeling approach, the assumed shape of the effective flaw was considered adequate.

As suggested by Dugdale [*26*], the extent of the plastic zone may be determined if the material flow stress is assumed to act as a compressive cohesive stress applied within the plastic zone. At the effective crack front the stress is assumed finite with the net stress intensity factor equal to zero. The slice plastic zone sizes $\rho_A = \rho_y$ and $\rho_B = \rho_x$ for slices passing through Points A and B may be found using the following relationships that enforce a zero net stress intensity factor at A and B, respectively

$$\int_o^{a+\rho_A} [\sigma(\xi,0) - P(\xi,0)]m_a(\xi, a + \rho_A)d\xi - \int_a^{a+\rho_A} \alpha_A Y m_a(\xi, a + \rho_A)d\xi = 0 \tag{8}$$

$$\int_o^{c+\rho_B} P(0,\eta)m_c(\eta,c + \rho_B)d\eta - \int_c^{c+\rho_B} \alpha_B Y_s m_c(\eta,c + \rho_B)d\eta = 0 \tag{9}$$

In Eqs 8 and 9, α_A and α_B are constraint factors that describe the ratio of average stress to flow stress in the plastic zone at Points A and B. These factors are required inputs for the strip-yield model. Equations 8 and 9 constitute a system of nonlinear equations for the two unknowns ρ_A and ρ_B, which was solved iteratively. Note that the unknown shear traction $P(x,y)$ couples Eqs 8 and 9.

Next consider the computation of the unknown shear traction $P(x,y)$. The shear traction plays a role similar to that of an applied stress. Given that strip-yield models utilize the

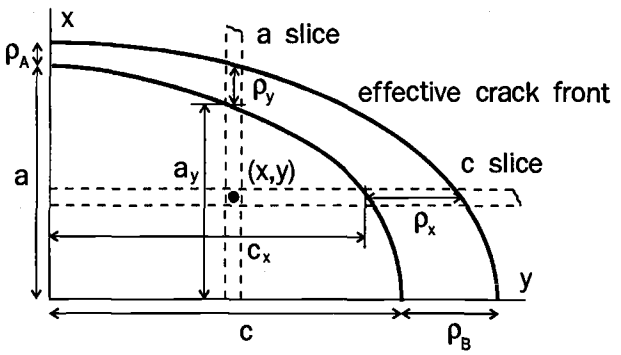


FIG. 2—*Crack front localized plastic deformation.*

applied stress acting on an effective crack in an elastic body, the shear traction was determined considering the surface flaw and subsequent plastic zone as an effective crack in an elastic body.

For equilibrium, at arbitrary points (x,y) on the crack surface where the primary and spring slices intersect, the total applied stress must be $\sigma(x,y)$. Equilibrium then dictates that each spring slice be subject to an applied stress $P(x,y)$ as shown in Fig. 1*c*. In addition, compatibility dictates the displacement for the intersecting slices must be equal at the point of intersection with $w_a = w_c$, where these displacements consider an effective crack in an elastic body with no plastic zone loading. The effective crack is assumed to have a semi-elliptical shape with a depth $a + \rho_A$ and length $c + \rho_B$. Consequently, these displacements are obtained from Eqs 2 and 6 with a_y and c_x replaced by

$$a_y^* = (a + \rho_A)\sqrt{1 - [y/(c + \rho_B)]^2} \tag{10}$$

$$c_x^* = (c + \rho_B)\sqrt{1 - [x/(a + \rho_A)]^2} \tag{11}$$

As shown in the Appendix, if $P(x,y)$ is assumed to be a linear combination of prescribed basis functions $p_i(x,y)$, compatibility enables the computation of 18 coefficients, λ_i such that the shear traction is defined as follows [*18*]

$$P(x,y) = \sum_{i=1}^{18} \lambda_i p_i(x,y) \tag{12}$$

In expanded form this expression may be written as

$$\begin{aligned} P(x,y) = {} & \lambda_1 + \lambda_2(\xi)^{1/3} + \lambda_3(\eta)^{1/3} + \lambda_4(\xi)^{1/3}(\eta)^{1/3} + \lambda_5(\xi)^{1/3}(\eta) + \lambda_6(\xi)(\eta)^{1/3} \\ & + \lambda_7(\xi) + \lambda_8(\eta) + \lambda_9(\xi)(\eta) + \lambda_{10}(\xi)^2 + \lambda_{11}(\eta)^2 + \lambda_{12}(\xi)(\eta)^2 + \lambda_{13}(\xi)^2(\eta) \\ & + \lambda_{14}(\xi)^3 + \lambda_{15}(\eta)^3 + \lambda_{16}(\xi)^2(\eta)^2 + \lambda_{17}(\xi)^4 + \lambda_{18}(\eta)^4 \end{aligned} \tag{13}$$

where $\xi = x/(a + \rho_A)$ and $\eta = y/(c + \rho_B)$. Note that in an earlier paper prepared by one of the authors [*27*], the displacements used when computing $P(x,y)$ erroneously incorporated plastic zone loading. This resulted in a difficulty for points of interest (x,y) located within the plastic zone as a net cohesive stress $[-(Y + Y_s)]$ occurred.

The shear traction and the plastic zones were determined iteratively. An initial estimate of $P(x,y)$ was obtained (see Appendix) assuming no plastic deformation. With this $P(x,y)$ plastic zone sizes ρ_A and ρ_B were computed using Eqs 8 and 9 and with these a new $P(x,y)$ was found. This process was continued until ρ_A and ρ_B converged.

Having determined the plastic zone sizes and the shear traction, the crack surface displacements for the two slices passing through Points A and B, respectively, resulting from both the applied stress and the plastic zone loading may be derived [*27*]

$$w_a(x,0) = \frac{1}{E}\int_x^a \left\{\int_o^\alpha [\sigma(\xi,0) - P(\xi,0)]m_a(\xi,\alpha)d\xi\right\} m_a(x,\alpha)d\alpha \tag{14}$$

$$+ \frac{1}{E}\int_a^{a+\rho_A} \left\{\int_o^\alpha [\sigma(\xi,0) - P(\xi,0)]m_a(\xi,\alpha)d\xi - \int_a^\alpha \alpha_A Y m_a(\xi,\alpha)d\xi\right\} m_a(x,\alpha)d\alpha$$

$$w_c(0,y) = \frac{1}{E_s}\int_y^c \left\{\int_o^\gamma P(0,\psi)m_c(\psi,\gamma)d\psi\right\} m_c(y,\gamma)d\gamma \tag{15}$$

$$+ \frac{1}{E_s}\int_c^{c+\rho_B} \left\{\int_o^\gamma P(0,\psi)m_c(\psi,\gamma)d\psi - \int_c^\gamma \alpha_B Y_s m_c(\psi,\gamma)d\psi\right\} m_c(y,\gamma)d\gamma$$

The elastic slice synthesis required a calibration process using an exact solution for an embedded elliptical flaw. This process allowed the derivation of Eqs 3, 5, and 7. A calibration process was also necessary to define the uniform cohesive stresses Y and Y_s for the primary and spring slices, respectively. As derived in the Appendix, the cohesive stress Y is a function of the maximum applied stress level S and the material flow stress σ_o with

$$Y/\sigma_o = 0.31603 - 0.06565(S/\sigma_o) + 0.11712(S/\sigma_o)^2 - 0.13332(S/\sigma_o)^3 \tag{16}$$

For the primary slice, the calibration process consisted of determining a nonuniform cohesive stress acting on a two-dimensional center-crack primary slice such that the crack surface displacement for the slice was identical to that for an embedded circular flaw in an elastic-perfectly plastic infinite body. This nonuniform cohesive stress was then averaged to obtain an approximate uniform cohesive stress Y. In addition, as shown in the Appendix, the spring slice cohesive stress Y_s is defined by

$$\frac{Y_s}{Y} = \frac{E_s}{E} = \left(\frac{\Phi}{1-\nu^2} - 1\right)\frac{c}{a} \tag{17}$$

The calibration process employed a crack surface displacement matching scheme. This displacement matching was performed along the entire effective crack length of the embedded flaw, both along the crack surface and in the plastic zone. Consequently, the plastic zone size for the slices was forced to be the same as that for the embedded flaw. The work presented here differs from that documented in Ref *27* in that the earlier effort did not include any comparisons with finite element analysis results. In addition, the model discussed in Ref *27* employed the assumption $Y/\sigma_o = 1$ as opposed to that given Eq 16.

Finite Element Analyses

To verify the strip-yield model, a three-dimensional finite element model of a surface cracked plate was generated and loaded monotonically, allowing determination of crack surface displacements and the plastic zone along the crack front in the crack plane. These displacements and plastic zones were then compared with computations from the strip-yield model. The commercial finite element analysis program ANSYS Rev. 5.4 was used.

The surface-cracked plate exhibits two planes of symmetry, and consequently only one quarter of the geometry was modeled using eight-noded hexahedral elements as illustrated in Fig. 3. A thickness T = 12.7 mm (0.50 in.) and width W = 25.4 mm (1.0 in.) was used. The material was assumed to be an elastic–perfectly plastic aluminum alloy with modulus E = 69.93 GPa (10.15 E6 psi), flow stress σ_o = 516 MPa (74.9 ksi), and Poisson's ratio ν = 0.33. The von Mises yield criterion and the associated flow rule were used. Small deformation theory was employed. A relatively small crack with a/T = 0.050 and a/c = 0.50 was modeled. The model was loaded in either uniform tension or pure bending with maximum stresses S equal to 30, 40, and 50% of the flow stress. The local constraint factor α along the crack front was also computed as the ratio of the average stress in the plastic zone $\bar{\sigma}_{zz}$ to the flow stress with $\alpha = \bar{\sigma}_{zz}/\sigma_o$.

Results and Discussion

Crack surface displacements from the strip-yield model and the finite element analyses are compared in Figs. 4–7. Using Eqs 16 and 17, uniform cohesive stresses Y and Y_s were computed from the finite element model flow stress σ_o with these cohesive stresses utilized for the strip-yield model calculations. Displacements are plotted along the x axis and along the y axis for stress levels of S/σ_o = 0.30 and S/σ_o = 0.50. Various constraint factor combinations were considered to demonstrate the impact of constraint on displacement with α_A = 2.0 and 3.0 and α_B = 1.0 and 2.0. As determined from the finite element analyses, constraint factors at the deepest point of penetration varied from 1.7 to 2.4, while at the free surface the computed constraint factors varied from 1.1 to 1.5. Thus, the assumed factors corresponded closely with those observed from the finite element analyses.

The crack surface displacements along both the x and y axes were seen to correlate well with the finite element analysis results. At either stress level the best correlations occurred for α_A = 3 and α_B = 2. Analyses with α_B = 3 were not performed as these were considered physically unrealistic. For the lower applied stress of S/σ_o = 0.30, the constraint factors employed when using the strip-yield model were observed to have a relatively small effect on the subsequent crack surface displacement. For the larger applied stress of S/σ_o = 0.50, the constraint factors used produced a larger effect. This was expected as a larger applied stress will result in a larger plastic zone size, with a larger region over which the cohesive stress is applied. This larger region allows the magnitude of the cohesive stress applied to produce a larger influence on the total crack surface displacement.

Crack plane plastic zone sizes from the strip-yield model and the finite element analyses are compared in Figs. 8 and 9. The crack plane plastic zones at the free surface and the deepest point of penetration are plotted for stress levels S/σ_o ranging from 0.10 to 0.50. From the strip-yield model, plastic zone sizes were determined using various constraint factor combinations.

The plastic zone size was observed to be a strong function of the specified constraint factors. The plastic zone sizes at both the free surface and the deepest point of penetration were seen to be considerably larger than those from the finite element analyses. This may

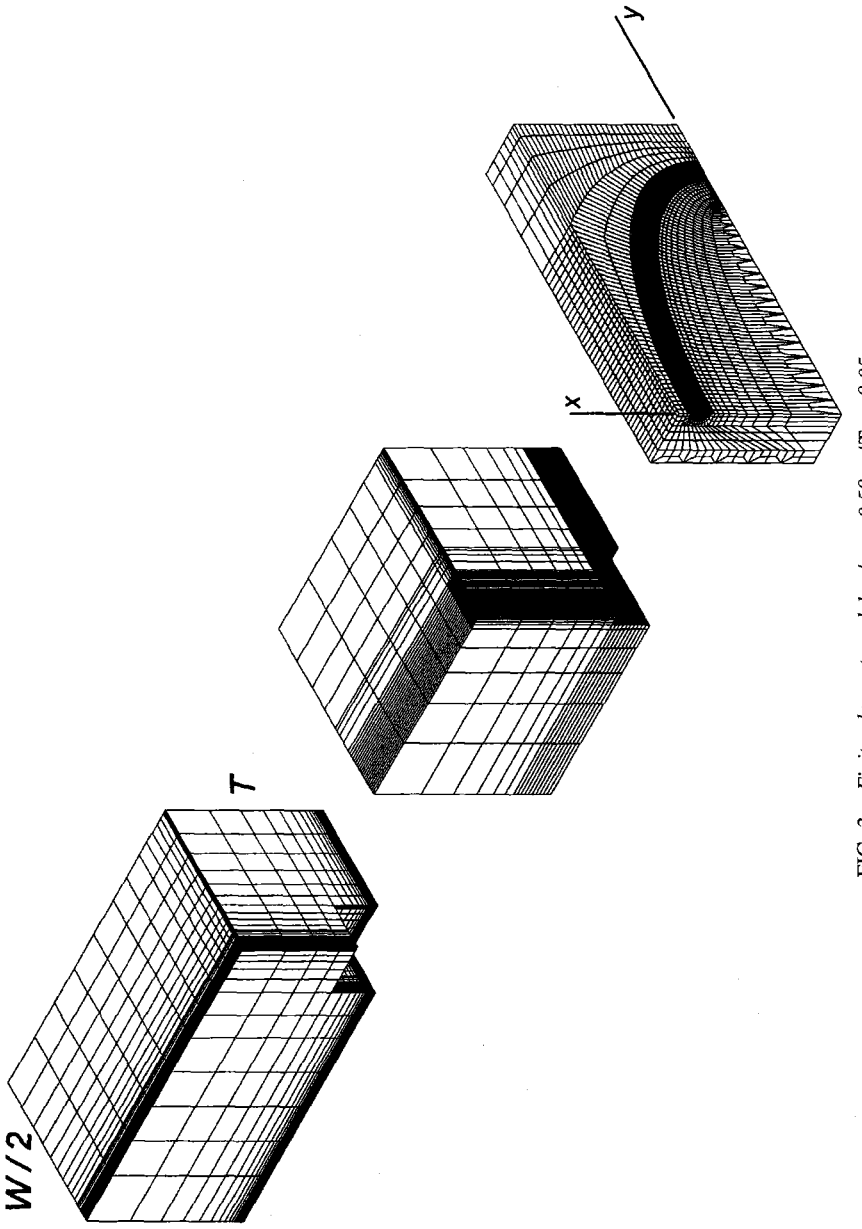


FIG. 3—*Finite element model,* a/c = *0.50,* a/T = *0.05.*

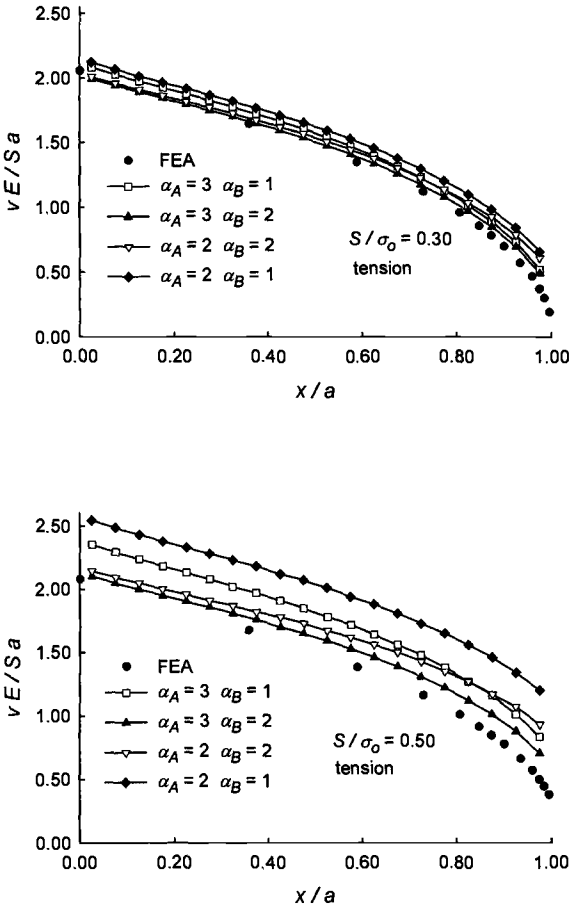


FIG. 4—*Crack surface displacements on the x axis under uniform tension.*

be a result of a limitation of the surface crack strip-yield model. The accuracy of the finite element analysis results are also suspect, as the number of elements in the crack plane plastic zone was relatively small with two to four elements yielding at the deepest point of penetration and three to four elements yielding at the free surface. In the authors' opinion, perhaps ten elements within the crack plane plastic zone would be sufficient to accurately discretize this region. In particular, it appears that increases in the finite element plastic zone size observed under increases in applied stress were relatively small. With the first author's focus on the eventual modeling of plasticity-induced crack closure, only the displacements were considered to be of primary interest, and this issue was not investigated further.

While the crack mouth opening displacements (CMOD) $\delta = 2\ v\ (0,0)$ determined at the origin of the x-y axes may be found from Figs. 4–7 for both the finite element analyses and the strip-yield model, a more detailed presentation is given in Fig. 10 for uniform tension. With the level of crack front plasticity increasing with applied stress, the CMOD are a function of the applied stress. Also shown in this figure is a CMOD value as determined from an independent elastic finite element analysis [*28*] conducted by Raju et al. The elastic CMOD value represents, as anticipated, a lower bound.

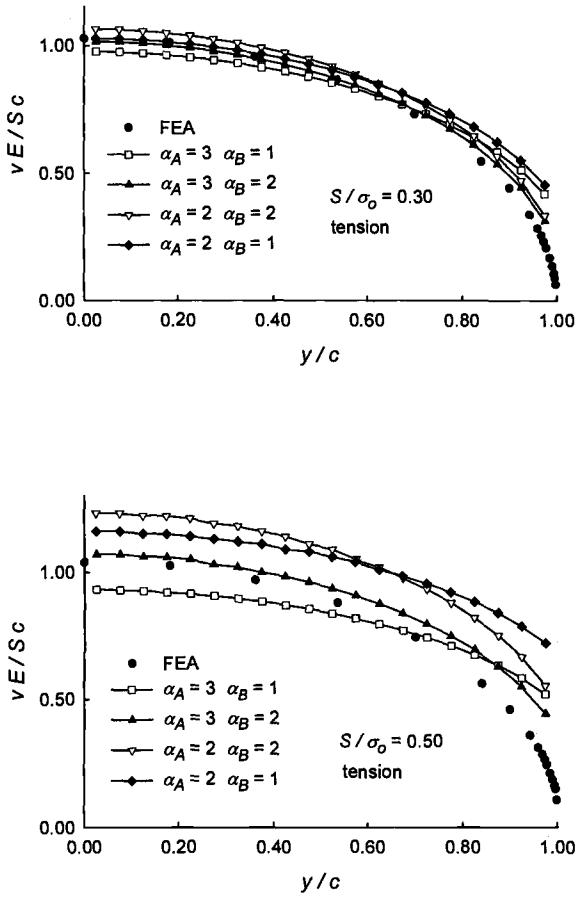


FIG. 5—*Crack surface displacement on the y axis under uniform tension.*

The strip-yield model CMOD compares best with the elastic-plastic finite element results when low stresses are applied and relatively large constraint factors are used. At an applied stress level of $S/\sigma_o = 0.30$, results from the two models compared well. For larger applied stresses, the strip-yield model results were consistently larger, with the finite element results again showing little variation with applied stress. This lack of sensitivity to stress level might suggest that the finite element results be viewed with some skepticism.

While the results presented in Fig. 10 serve as a limited validation or calibration if relatively low applied stresses are of interest, given the uncertainty associated with the finite element results, it would be desirable to compare the strip-yield model CMOD with experimental measurements in a future effort.

Summary and Conclusions

A slice synthesis methodology was developed and used to construct a strip-yield model for the semi-elliptical surface flaw under monotonic loading, enabling approximate computation of crack surface displacements and the plastic zone size. Displacements were computed

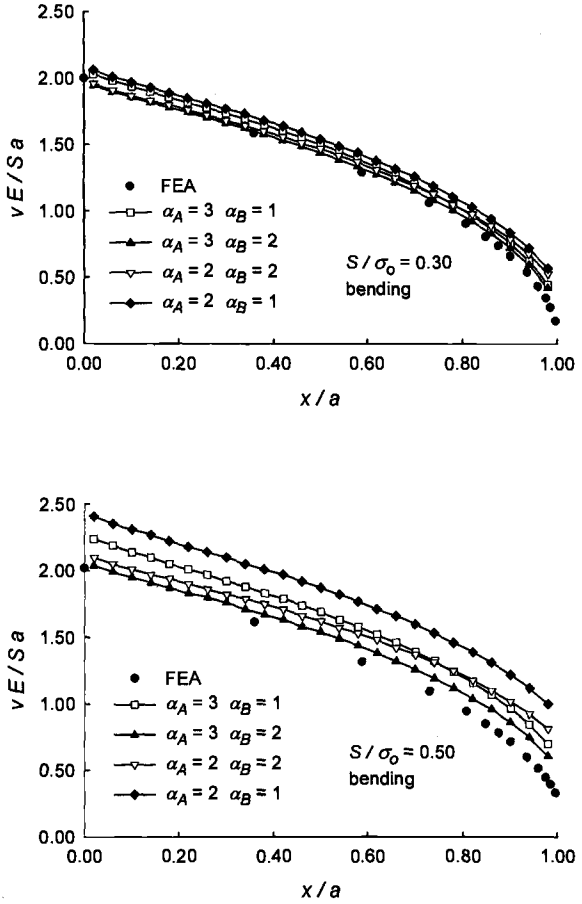


FIG. 6—*Crack surface displacements on the x axis under bending.*

along the free surface and along a line connecting the free surface with the deepest point of flaw penetration. The crack front plastic zone size in the crack plane was computed at the free surface and at the deepest point of penetration. To use the model, the surface flaw depth a, length $2c$, material flow stress, and the applied stress distribution must be prescribed. An additional model input is the crack front constraint factor $\alpha(1 \leq \alpha \leq 3)$ at both the free surface and the deepest point of penetration.

The crack front plastic zone size in the crack plane was observed to be a strong function of the specified constraint factor. The plastic zone size at both the free surface and the deepest point of penetration was seen to be much larger than those determined from the finite element analyses, suggesting there may be some difficulties with the strip-yield model. However, as the accuracy of the finite element analysis results could be questioned as well due to a limited number of elements within the crack plane plastic zone, the only conclusion that can be drawn with regard to the plastic zone size discrepancy is that additional comparisons with more refined finite element meshes are needed.

Crack surface displacements from the model were shown to compare well with results from three-dimensional elastic-plastic finite element analyses. For an applied stress of

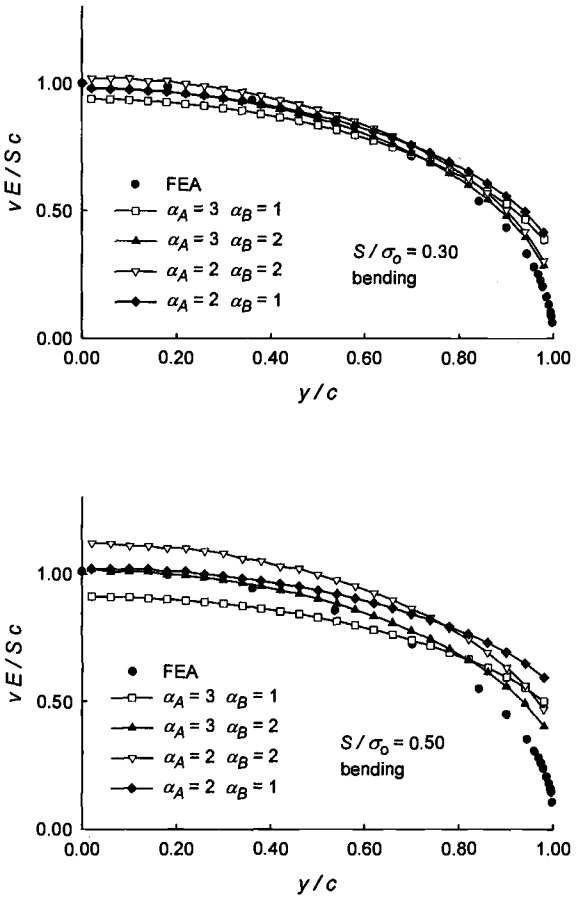


FIG. 7—*Crack surface displacements on the y axis under bending.*

$S/\sigma_o = 0.30$, the constraint factors employed when using the strip-yield model were observed to have only a modest effect on the subsequent crack surface displacement. If stress levels were to be reduced further, the constraint level effect would become negligible. For an applied stress of $S/\sigma_o = 0.50$, the constraint factors used produced a larger effect, with larger values of constraint giving more accurate results. Due to the approximate nature of strip-yield models in general, the authors would be skeptical of results generated with $S/\sigma_o > 0.50$.

Unlike elastic normalized CMOD ($\delta E/Sa$), elastic-plastic normalized CMOD from the strip-yield model was seen to be a function of the applied stress level due to crack front plasticity effects. A limited validation of the strip-yield model CMOD was achieved as an independently computed elastic CMOD result served as a lower bound to the strip-yield elastic-plastic CMOD. Experimental measurements of CMOD under various applied stress levels and a subsequent comparison to the strip-yield model results would be a welcome additional validation.

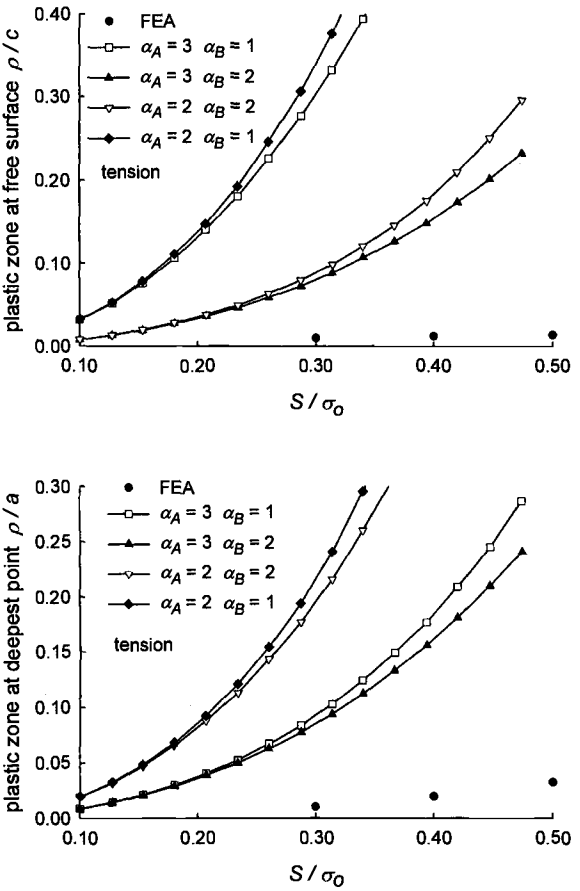


FIG. 8—*Plastic zone size under tension.*

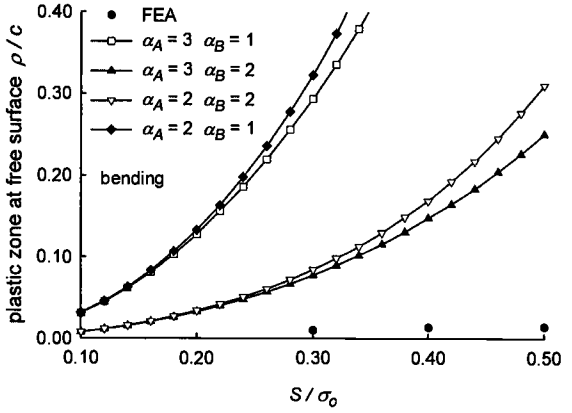
Acknowledgment

Gratitude is extended to R. H. Dodds of the University of Illinois for making available software written by J. Faleskog for generation of surface crack finite element meshes.

APPENDIX

Weight Functions

Both the primary slices and spring slices were modeled using an elastic boundary condition as shown in Fig. A1. This type of boundary condition approximately simulates the restraint associated with the uncracked portion of the plate as discussed by Zhao et al. [*14,15*]. Use of the elastic boundary conditions allows approximate consideration of the effects of finite thickness T and finite width W.



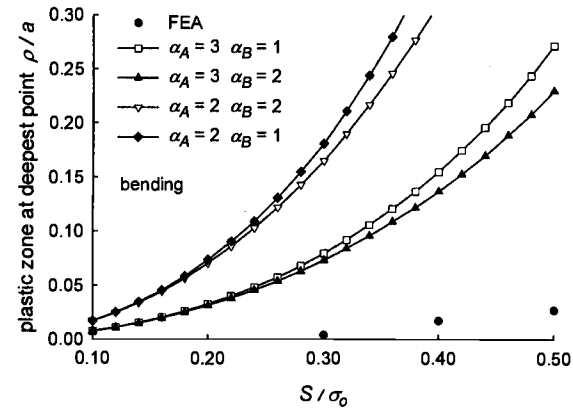


FIG. 9—*Plastic zone size under bending.*

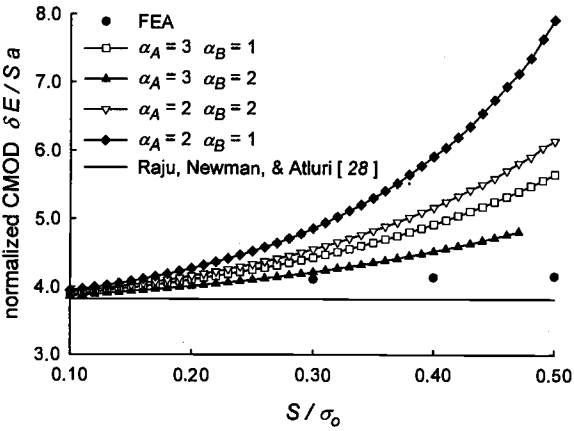


FIG. 10—CMOD *for uniform tension.*

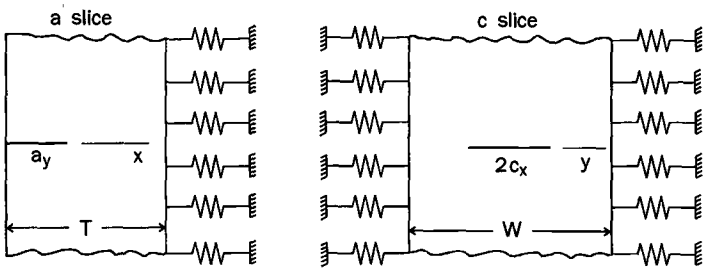


FIG. A1—*Primary and spring slices.*

The weight functions associated with the slices shown in Fig. A1 are approximated as an interpolation between a fixed condition with no displacement where the spring stiffness $k \to \infty$ and a free condition with $k \to 0$. To achieve the required interpolation, weight functions for both the free and fixed conditions were needed. Details of the interpolation may be found in Ref *14*.

For the edge-crack with $k \to \infty$, the stress intensity factor solution for a double edge-crack under a symmetrical concentrated load on the crack surface [*29*] was used to derive

$$m_a(x,a_y) \cong \frac{2}{\sqrt{2T}} \{1 + 0.15[1 - (x/a_y)^{5/4}][1 - \sin(\pi a_y/T)][2 + \sin(\pi a_y/T)]\} * \frac{\sqrt{\tan(\pi a_y/2T)}}{\sqrt{1 - \left[\frac{\cos(\pi a_y/2T)}{\cos(\pi x/2T)}\right]^2}} \tag{A.1}$$

For the edge-crack with a free surface ($k \to 0$), from Wu and Carlsson [*30*]

$$m_a(x,a_y) \cong \frac{1}{\sqrt{2\pi(a_y/T)}} \sum_{i=1}^{5} \beta_i(a_y/T) \left[1 - \frac{x}{a_y}\right]^{i-3/2} \tag{A.2}$$

where the β_i values have been tabulated [*30*]. This weight function is valid for $a_y/T < 0.90$.

For the center-crack with $k \to \infty$, an exact weight function is given by Wu and Carlsson

$$m_c(y,c_x) = \frac{2}{\sqrt{\pi c_x}} \cos(\pi y/W) \left[\frac{\frac{\pi c_x}{W}\tan(\pi c_x/W)}{\sin^2(\pi c_x/W) - \sin^2(\pi y/W)}\right]^{1/2} \tag{A.3}$$

For the center-crack with a free surface ($k \to 0$) Wu and Carlsson give

$$m_c(y,c_x) \cong \sqrt{\frac{W}{2\pi c_x}} \sum_{i=1}^{3} \beta_i(2c_x/W) \left[1 - \left(\frac{y}{c_x}\right)^2\right]^{i-3/2} \tag{A.4}$$

where the β_i are tabulated values. This weight function is valid for $2c_x/W < 0.90$.

Calibration of Surface Flaw Strip-Yield Model

Consider an embedded circular crack with radius b in an infinite body under a uniform tension S as shown in Fig. A2. An elastic–perfectly plastic material is assumed with modulus E, Poisson's ratio ν, and flow stress σ_o. Defining $\lambda = S/\sigma_o$, $\xi = x/(b + \rho)$, $m = b/(b + \rho)$, and assuming a cohesive stress equal to $-\sigma_o$ acts to close the crack over the plastic zone ρ, the crack surface displacement $w(\xi)$ may be written as [*31*]

$$0 \leq \xi \leq m \tag{A.5}$$

$$w(\xi) = \frac{4(1 - \nu^2)(b + \rho)\sigma_o}{\pi E}\left[\lambda\sqrt{1 - \xi^2} - \sqrt{\frac{1 - m^2}{1 - \xi^2}} + mE(\mu_1,\xi/m)\right]$$

$$1 \geq \xi > m \tag{A.6}$$

$$w(\xi) = \frac{4(1 - \nu^2)(b + \rho)\sigma_o}{\pi E}\left[\sqrt{1 - \xi^2}\left(\lambda - \frac{1}{\sqrt{1 - m^2}}\right) + \frac{m^2 - \xi^2}{\xi}F(\mu_2,m/\xi) + \xi E(\mu_2,m/\xi)\right]$$

where $F(\phi,k)$ and $E(\phi,k)$ are elliptical integrals of the first kind and second kind, respectively,

$$b/(b + \rho) = \sqrt{1 - \lambda^2},\ \mu_1 = \sin^{-1}\sqrt{(1 - m^2)/(1 - \xi^2)},\ \text{and}$$

$$\mu_2 = \sin^{-1}\sqrt{(1 - \xi^2)/(1 - m^2)}.$$

Next consider modeling this crack using a slice synthesis methodology. Primary and spring slices (a and c slices) passing through the origin constitute center-cracked panels with a crack length of $2b$. If the primary slice is to exhibit the same crack surface displacement as that for the embedded flaw, the primary slice must exhibit a nonuniform cohesive stress σ_c within the plastic zone. The calibration problem is thus reduced to an inverse problem in

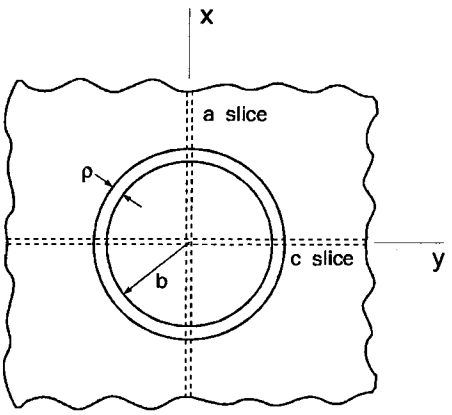


FIG. A2—*Embedded circular crack.*

which an unknown cohesive stress is to be determined such that a prescribed displacement distribution is induced. An analytical solution to this inverse problem has been presented by Smith [*32*]. This solution involves an integration with a singular integrand comprised in part by the derivative of the crack surface displacement. Given the complexity of Eqs A.5 and A.6, a numerical approach was pursued.

Defining $z = (x - b)/\rho$, the cohesive stress within the plastic zone was assumed given by

$$\sigma_c(z) = C_1 + C_2 z + C_3 z^2 + C_4 z^3 \tag{A.7}$$

The coefficients C_j were determined such that the resulting displacement for the center-crack slice $v(x,C_j)$ was equal to that for the embedded flaw for n points along the effective crack length $b + \rho$. This required a minimization of the following function

$$f(S,C_j) = \sum_{i=1}^{n} |w(x_i) - v(x_i,C_j)| \tag{A.8}$$

Using a downhill simplex method [*33*], the C_j values were determined numerically such that the function was a minimum, thus resulting in a set of coefficients which produced crack surface displacements equal to that for the embedded flaw. To define $f(S,C_j)$, the crack surface displacement $v(x,C_j)$ for a center-crack under arbitrary plastic zone loading was needed. This displacement may be written as follows:

for $x \leq b$

$$v(x,C_j) = \frac{1}{E}\int_x^b \left\{\int_o^\alpha S_1 m_a(\xi,\alpha)d\xi\right\} m_a(x,\alpha)d\alpha \tag{A.9}$$

$$+ \frac{1}{E}\int_b^{b+\rho} \left\{\int_o^b S_1 m_a(\xi,\alpha)d\xi + \int_b^\alpha S_2 m_a(\xi,\alpha)d\xi\right\} m_a(x,\alpha)d\alpha$$

for $x \geq b$

$$v(x,C_j) = \frac{1}{E}\int_x^{b+\rho} \left\{\int_o^b S_1 m_a(\xi,\alpha)d\xi\right\} m_a(x,\alpha)d\alpha \tag{A.10}$$

$$+ \frac{1}{E}\int_x^{b+\rho} \left\{\int_b^\alpha S_2 m_a(\xi,\alpha)d\xi\right\} m_a(x,\alpha)d\alpha$$

Where S_1 and S_2 are the net applied stresses for $x < b$ and $x > b$, respectively. Because of the uniform applied stress S, the shear traction P is a constant [*14*] such that the stresses on the primary slice are

$$S_1 = S - P = \frac{2(1 - \nu^2)}{\pi} S \qquad 0 < x < b \tag{A.11}$$

$$S_2 = S_1 - \sigma_c(x) \qquad b < x < b + \rho \tag{A.12}$$

The nonuniform cohesive stress obtained from the minimization of Eq A.8 is shown in Fig.

A3. For simplicity, a uniform cohesive stress is desirable when considering strip-yield models. Having determined the nonuniform cohesive stress σ_c for the primary slice, a uniform cohesive stress Y was defined as the average cohesive stress in the plastic zone

$$Y = \frac{1}{\rho} \int_b^{b+\rho} \sigma_c(x)dx \tag{A.13}$$

Because the cohesive stress is a function of the applied curve level, the uniform cohesive stress is a function of the normalized applied stress S/σ_o also. Equation A.13 was utilized to determine Y values for a sequence of normalized applied stresses ranging from 0.10 to 0.90. These values were fit to a third-order polynomial giving

$$Y/\sigma_o = 0.31603 - 0.06565(S/\sigma_o) + 0.11712(S/\sigma_o)^2 - 0.13332(S/\sigma_o)^3 \tag{A.14}$$

Use of the uniform cohesive stress Y will give a primary slice crack surface displacement which approximately equals that of an embedded flaw. Given the approximate nature of strip-yield models in general, this was considered acceptable. From Fig. A4, the error introduced through use of the uniform cohesive stress was seen to be small.

Next consider the spring slice with a modulus E_s and a uniform cohesive stress Y_s. The spring slice crack surface displacement may be written as [*34*]

$$v_c(y) = \frac{Y_s}{E_s} g(y,b) \tag{A.15}$$

For the primary slice we have

$$v_a(x) = \frac{Y}{E} g(x,b) \tag{A.16}$$

From Eqs A.15 and A.16, with $v_a(x) = v_c(y)$

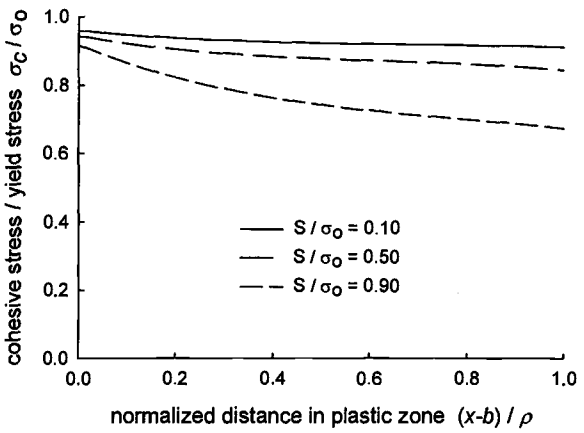


FIG. A3—*Nonuniform cohesive stress.*

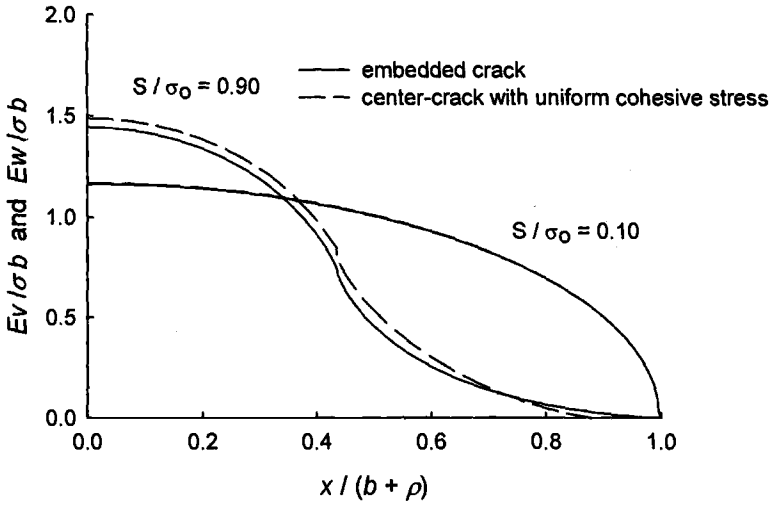


FIG. A4—*Crack surface displacements.*

$$\frac{Y_s}{Y} = \frac{E_s}{E} \tag{A.17}$$

Equation A. 17 defines the spring slice uniform cohesive stress.

Determination of Shear Traction

The slice crack surface displacements for an effective flaw in an elastic body were given as Eqs 2 and 6 with a_y and c_x replaced by a_y^* and C_x^* from Eqs 10 and 11. For compatibility at a given point (x,y) these displacements must be equal. Using the compatibility requirement in conjunction with Eq 12

$$Y(x,y) = \sum_{i=1}^{18} \lambda_i X_i(x,y) \tag{A.18}$$

$$Y(x,y) = \int_x^{\alpha^*_y} \int_o^{\alpha} \sigma(\xi,y) m_a(\xi,\alpha) m_a(x,\alpha) d\xi d\alpha \tag{A.19}$$

$$\begin{aligned} X_i(x,y) = &\int_x^{\alpha^*_y} \int_o^{\alpha} p_i(\xi,y) m_a(\xi,\alpha) m_a(x,\alpha) d\xi d\alpha \\ &+ \frac{E}{E_s} \int_y^{C^*_x} \int_o^{\gamma} p_i(x,\psi) m_c(\psi,\gamma) m_c(y,\gamma) d\psi d\gamma \end{aligned} \tag{A.20}$$

Equations A.19 and A.20 are identical to that given by Zhao et al. [*14*] with a_y and c_x replaced with a_y^* and c_x^*, respectively.

Consider m arbitrary but evenly distributed points within the semi-elliptical flaw boundary.

If Eq A.18 is written for each of these points, then a system of m equations for the 18 unknown λ_i results. This system may be written as

$$\{Y\} = [X]\{\lambda\} \tag{A.21}$$

where $\{Y\}$ is a $m \times 1$ vector, $\{\lambda\}$ is a 18×1 vector, and $[X]$ is a $m \times 18$ matrix. As discussed by Zhao et al. [*14*], for a prescribed m with $m > 18$, Eq A.21 represents an overdetermined system of equations. This system was solved for the unknown vector $\{\lambda\}$ using singular value decomposition. A value $m = 43$ was used. A value of 34 was used by Zhao et al. [*14*].

References

[*1*] Trantina, G. G., deLorenzi, H. G., and Wilkening, W. W., "Three-Dimensional Elastic-Plastic Finite Element Analysis of Small Surface Cracks," *Engineering Fracture Mechanics,* Vol. 18, 1983, pp. 925–938.

[*2*] Fujikubo, M., "CTOD Estimates of Surface Cracked Wide Plates in Bending—I. Finite Element Analysis," *Engineering Fracture Mechanics,* Vol. 40, 1991, pp. 627–639.

[*3*] Wang, Y.-Y., "On the Two-Parameter Characterization of Elastic-Plastic Crack-Front Fields in Surface-Cracked Plates," *Constraint Effects in Fracture, ASTM STP 1171,* American Society for Testing and Materials, 1993, pp. 120–138.

[*4*] Faleskog, J., "Effects of Local Constraint Along Three-Dimensional Crack Fronts—A Numerical and Experimental Investigation," *Journal of Mechanics and Physics of Solids,* Vol. 43, 1995, pp. 447–493.

[*5*] Gao, X., Faleskog, J., Shih, C. F., and Dodds, R. H., "Ductile Tearing in Part-Through Cracks: Experiments and Cell-Model Predictions," *Engineering Fracture Mechanics,* Vol. 59, 1998, pp. 761–777.

[*6*] Newman, J. C., "Fracture of Cracked Plates Under Plane Stress," *Engineering Fracture Mechanics,* Vol. 1, 1968, pp. 137–154.

[*7*] Hayes, D. J. and Williams, J. G., "A Practical Method for Determining Dugdale Model Solutions for Cracked Bodies of Arbitrary Shape," *International Journal of Fracture Mechanics,* Vol. 8, 1972, pp. 239–256.

[*8*] Smith, E., "The Size of the Cohesive Zone at a Crack Tip," *Engineering Fracture Mechanics,* Vol. 7, 1975, pp. 285–289.

[*9*] Chell, G. G., "Bilby, Cottrell and Swinden Model Solutions for Centre and Edge Cracked Plates Subject to Arbitrary Mode I Loading," *International Journal of Fracture,* Vol. 12, 1976, pp. 135–147.

[*10*] Petroski, H. J., "Dugdale Plastic Zone Sizes for Edge Cracks," *International Journal of Fracture,* Vol. 15, 1979, pp. 217–230.

[*11*] Lardner, T. J., "A Note on the Length and Displacements of a Dugdale or Craze Zone," *Journal of Applied Mechanics,* Vol. 49, 1982, pp. 925–926.

[*12*] Mall, S. and Newman, J. C., "The Dugdale Model for a Compact Specimen," *Fracture Mechanics, 16th Symposium, ASTM STP 868,* American Society for Testing and Materials, 1985, pp. 113–128.

[*13*] Huang, N. C., "On the Size of the Cohesive Zone at the Crack Tip," *Journal of Applied Mechanics,* Vol. 52, 1985, pp. 490–492.

[*14*] Zhao, W., Wu, X. R., and Yan, M. G., "Weight Function Method for Three Dimensional Crack Problems—I. Basic Formulation and Application to an Embedded Elliptical Crack in Finite Plates," *Engineering Fracture Mechanics,* Vol. 34, 1989, pp. 593–607.

[*15*] Zhao, W., Wu, X. R., and Yan, M. G., "Weight Function Method for Three Dimensional Crack Problems—II. Application to Surface Cracks at a Hole in Finite Thickness Plates Under Stress Gradients," *Engineering Fracture Mechanics,* Vol. 34, 1989, pp. 609–624.

[*16*] Zhao, W., "Analysis of Infinite Pairs of Surface Cracks in Elastic Plates," *International Journal of Fracture,* Vol. 55, 1992, pp. 143–152.

[*17*] Zhao, W., Newman, J. C., Sutton, M. A., Shivakumar, K. N., and Wu, X. R., *Analysis of Surface Cracks at Hole by a 3-D Weight Function Method with Stresses from Finite Element Method,* NASA TM 110145, NASA Langley Research Center, 1995.

[18] Zhao, W. and Sutton, M. A., "Elastic Solutions for Corner Cracks Undergoing Uniform Displacement-Controlled Loading," *International Journal of Fracture,* Vol. 70, 1995, pp. 335–346.
[19] Zhao, W., Newman, J. C., Sutton, M. A., Wu, X. R., and Shivakumar, K. N., "Stress Intensity Factors for Corner Cracks at a Hole by A 3-D Weight Function Method with Stresses from the Finite Element Method," *Fatigue and Fracture of Engineering Materials and Structures,* Vol. 20, 1997, pp. 1255–1267.
[20] Zhao, W., Newman, J. C., and Sutton, M. A., "A Three-Dimensional Weight Function Method-Evaluation and Applications," *Fatigue and Fracture Mechanics, 27th Volume, ASTM STP 1296,* American Society for Testing and Materials, 1997, pp. 563–579.
[21] Mattheck, C. and Görner, F., "Leak Prediction by Use of a Generalized Dugdale Model for Semi-Elliptical Surface Flaws in Plates Under Tension Loading," *Proceedings of the 5th European Conference on Fracture,* Portugal, 1984.
[22] Mattheck, C., Morawietz, P., Munz, D., and Wolf, B., "Ligament Yielding of a Plate with Semi-Elliptical Surface Cracks under Uniform Tension," *International Journal of Pressures Vessels and Piping,* Vol. 16, 1984, pp. 131–143.
[23] Grandt, A. F., Jr. and Sinclair, G. M., "Stress Intensity Factors for Surface Cracks in Bending," *Stress Analysis and Growth of Cracks, ASTM STP 513,* American Society for Testing and Materials, 1972, pp. 37–58.
[24] Fujimoto, W. T., "Determination of Crack Growth and Fracture Toughness Parameters for Surface Flaws Emanating from Fastener Holes," *Proceedings of the AIAA/ASME/SAE 17th Structures, Structural Dynamics, and Material Conference,* King of Prussia, PA, 1976, pp. 522–531.
[25] Saff, C. R. and Sanger, K. B., "Part-Through Flaw Stress Intensity Factors Developed by a Slice Synthesis Technique," *Fracture Mechanics: 15th Symposium, ASTM STP 833,* American Society for Testing and Materials, 1984, pp. 24–43.
[26] Dugdale, D. S., "Yielding of Steel Sheets Containing Slits," *Journal of Mechanics and Physics of Solids,* Vol. 8, 1960, pp. 100–104.
[27] Daniewicz, S. R., "A Modified Strip-Yield Model for Prediction of Plasticity-Induced Closure in Surface Flaws," *Fatigue and Fracture of Engineering Materials and Structures,* Vol. 21, 1998, pp. 885–901.
[28] Raju, I. S., Newman, J. C., and Atluri, S. N., "Crack Mouth Displacements for Semi-Elliptical Surface Cracks Subjected to Remote Tension and Bending Loads," *Fracture Mechanics: 22nd Symposium, ASTM STP 1131,* American Society for Testing and Materials, 1992, pp. 19–28.
[29] Tada, H., Paris, P. C., and Irwin, G. R., *The Stress Analysis of Cracks Handbook,* Paris Production Inc. and Del Research Corp., 1985, p. 2.31.
[30] Wu, X. R. and Carlsson, A. J., *Weight Functions and Stress Intensity Factor Solutions,* Pergamon Press, 1991, p. 128.
[31] Olesiak, Z. and Wnuk, M., "Plastic Energy Dissipation Due to a Penny-Shaped Crack," *The International Journal of Fracture Mechanics,* Vol. 4, 1968, pp. 383–396.
[32] Smith, E., "The Structure in the Vicinity of a Crack Tip: A General Theory Based on the Cohesive Zone Model," *Engineering Fracture Mechanics,* Vol. 6, 1974, pp. 213–222.
[33] Press, W. H., Vetterling, W. T., Teukolsky, S. A., and Flannery, B. P., *Numerical Recipes in Fortran,* Cambridge University Press, 1992, pp. 402–406.
[34] Parker, A. P., *The Mechanics of Fracture and Fatigue,* E.&F.N. Spon Ltd., 1981, p. 106.

Paul T. Williams,[1] *B. Richard Bass,*[1] *and Wallace J. McAfee*[1]

Application of the Weibull Methodology to a Shallow-Flaw Cruciform Bend Specimen Tested Under Biaxial Loading Conditions

REFERENCE: Williams, P. T., Bass, B. R., and McAfee, W. J., **"Application of the Weibull Methodology to a Shallow-Flaw Cruciform Bend Specimen Tested Under Biaxial Loading Conditions,"** *Fatigue and Fracture Mechanics: 31st Volume, ASTM STP 1389,* G. R. Halford and J. P. Gallagher, Eds., American Society for Testing and Materials, West Conshohocken, PA, 2000, pp. 242–270.

ABSTRACT: This paper describes the application of the Weibull methodology to the analysis of a shallow-flaw cruciform bend specimen tested under biaxial loading conditions. The cruciform bend fracture mechanics specimen was developed at Oak Ridge National Laboratory (ORNL) to introduce a far-field, out-of-plane biaxial bending stress component in the test section that approximates the nonlinear stresses resulting from pressurized-thermal-shock or pressure-temperature loading of a nuclear reactor pressure vessel (RPV). Tests with the cruciform specimen demonstrated that biaxial loading can have a pronounced effect on shallow-flaw fracture toughness in the lower transition temperature region for an RPV material. High-constraint deep-flaw compact tension C(T) and low-constraint shallow-flaw cruciform fracture toughness data were used to assess the ability of the Weibull methodology to predict the observed effects of biaxial loading on shallow-flaw fracture toughness. A new hydrostatic stress criterion along with five equivalent-stress criteria from the literature were selected to serve as candidate kernels in the integral formulation of the Weibull stress. Among these candidates, the hydrostatic stress criterion, derived from the first invariant of the Cauchy stress tensor, was determined to have the required sensitivity to multiaxial-loading states. In addition, a new calibration technique developed by researchers at the University of Illinois for determining the necessary Weibull parameters is applied to the C(T) and cruciform data. A three-parameter Weibull model based on the hydrostatic stress criterion is shown to predict the experimentally observed biaxial effect on cleavage fracture toughness by providing a scaling mechanism between uniaxial and biaxial loading states. In summary, the conclusions that can be drawn from this study are as follows: (1) With respect to its effect on fracture toughness, the biaxial effect is a constraint effect. (2) A Weibull statistical fracture model has been successfully calibrated with uniaxial toughness data obtained from a conventional high-constraint C(T) specimen and a uniaxially loaded shallow-flaw cruciform that is effectively equivalent to a conventional shallow-flaw SE(B) specimen. (3) The calibrated fracture model was able to successfully predict the intermediate constraint-loss effects associated with two levels of biaxial loading. (4) These preliminary results at a single test temperature offer encouragement that complex multiaxial loading effects on transition region fracture toughness can be predicted with statistical fracture models developed using data obtained from conventional specimens. (5) Future work is required to investigate these effects at other temperatures within the transition region.

KEYWORDS: Weibull stress, local approach, cleavage fracture, biaxial loading, pressure vessels

[1] Senior research engineer, Oak Ridge National Laboratory, P.O. Box 2009, MS-8056, Oak Ridge, TN 37831-8056.

Copyright© 2000 by ASTM International www.astm.org

The Heavy-Section Steel Technology (HSST) Program at Oak Ridge National Laboratory (ORNL) has been engaged in an experimental and analytical study of the effects of constraint loss associated with shallow flaws and constraint increase associated with biaxial far-field stresses for application to the safety assessment of reactor pressure vessel (RPV) steels. In the lower transition temperature region, shallow-flaw fracture toughness data [*1*] for RPV materials exhibit mean values and scatter that are greater than those measured for deep flaws. This increase in fracture toughness has been attributed to a loss of crack-dip constraint due to the close proximity of the crack tip to a free surface of the specimen [*2*]. Any increase in crack-tip constraint due to out-of-plane near-surface biaxial stresses could partially offset this observed trend of shallow-flaw fracture toughness enhancement.

The service life of commercial nuclear RPVs can be limited by safety requirements related to postulated pressurized-thermal-shock (PTS) accident conditions [*3*]. Occurring under PTS upset conditions as well as normal pressure-temperature (P-T) operational transients, the thermal, pressure, and residual stresses in an RPV wall are all biaxial (Fig. 1) and combine to form a complex nonlinear biaxial state of stress that consists of significant tensile out-of-plane stresses aligned parallel to possible surface cracks oriented in either the longitudinal or circumferential directions. These far-field out-of-plane stresses are not produced by uniaxial compact tension, C(T), or single-edge bend, SE(B), specimens used in standard fracture toughness testing.

A special cruciform bend specimen [*4–8*] has been developed at ORNL to introduce a linear, far-field, out-of-plane biaxial bending stress component in the test section that approximates the nonlinear stresses of PTS or P-T loading (Fig. 2). The cruciform specimen permits the application of biaxial loading ratios resulting in controlled variations of crack-tip constraint for shallow surface flaws. The biaxial load ratio is defined as P_T/P_L, where P_T

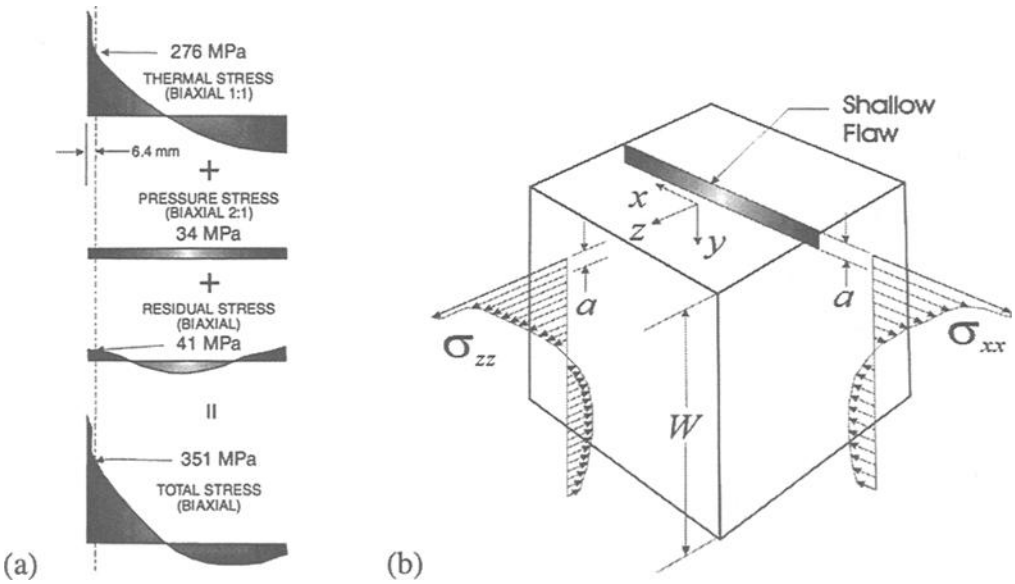


FIG. 1—*Pressurized thermal shock loading produces nonlinear biaxial stress state in pressure vessel wall:* (a) *contributions of thermal, pressure, and residual stresses and* (b) *total complex state of stress applied to a shallow surface flaw.*

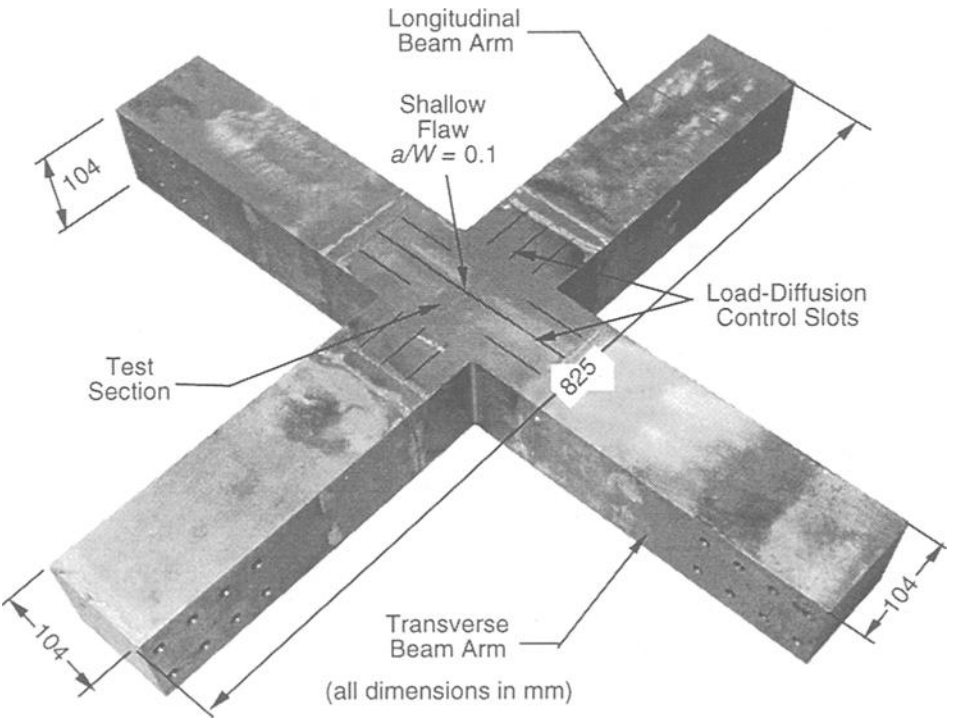


FIG. 2—*Shallow flaw cruciform specimen.*

is the load applied to the transverse beam arms, and P_L is the load applied to the longitudinal arms. A special test fixture was also designed and fabricated, permitting testing under a uniaxial (4-point bending) loading, P_T/P_L ratio of (0:1), and two biaxial (8-point bending) loading ratios, P_T/P_L ratios of (0.6:1) and (1:1). The specimen and test fixture have been described extensively in earlier HSST publications [*4–6*].

Stress-based *local approach* methodologies adopt the Weibull stress [*9*] as a fracture parameter (reflecting local damage near the crack tip) that reaches a critical value at material failure due to transgranular cleavage. Conventional applications of the Weibull methodology utilize the maximum principal stress as the equivalent tensile stress in the kernel of the integral representation of the Weibull stress. The maximum principal stress has been shown to be insensitive to biaxial loading states [*10–12*]; however, in contrast to the maximum principal stress, the hydrostatic stress criterion, derived from the first invariant of the Cauchy stress tensor, has been shown to be sensitive to variations in crack-tip constraint induced by the biaxial loading of the cruciform specimen [*10–12*]. The local approach using this hydrostatic stress criterion has been investigated with a three-parameter Weibull model to develop a scaling mechanism between low-constraint uniaxial and high-constraint biaxial loading states. This paper presents results from that investigation.

Material Characterization

HSST Plate 14 was the source material (with chemical analysis C(0.22%), P(0.05%), S(0.003%), Mo(0.36%), and Ni(0.62%) conforming to SA533, Grade B material specification

requirements) for the cruciform bend specimens. This plate was selected primarily for its relatively high carbon content, which made it more responsive to increasing the yield strength by heat treatment and retaining relatively uniform properties through the thickness of the plate after tempering. The base material underwent heat treatment to achieve an elevated yield strength approximating that of a typical radiation-sensitive RPV steel irradiated to a fluence of 1.5×10^{19} n/cm^2 (energy > 1 MeV). The heat treatment was performed successfully, providing a room-temperature yield stress in the desired range (Fig. 3). The elastic modulus, E, of 182.7 GPa shown in Fig. 3 is the value used in the finite-element models (to be discussed) of the cruciform and C(T) specimens. This value is lower than the elastic modulus of 217.5 GPa measured with tension specimens for Plate 14 at −5°C. As discussed in Ref *4*, early analyses indicated that the measured value for Plate 14 produced a finite-element model that was too "stiff" relative to the measured deformation response of the cruciform specimens. The lower value of 182.7 GPa produced a close match between the model and the specimen.

Fracture Toughness Test Data

The results of 21 cruciform tests (6 at a test temperature of −30°C and 15 at −5°C) have been reported previously [*10–12*] and are plotted in Figs. 4*a* and 4*b* for three biaxial ratios (P_T/P_L): uniaxial (0:1), biaxial (0.6:1), and equibiaxial (1:1). In addition, a series of compact tension C(T)-½T specimens, taken from the parent Plate 14, were tested over the range from −130°C to room temperature. Eight C(T) toughness data points at −30°C and twelve C(T) data points at a nominal temperature of −5°C have been positioned in Figs. 4*a* and 4*b*, respectively, at a P_T/P_L = (2:1). The rationale for locating these high-constraint data at this biaxial ratio will be presented in a following section. To be consistent with the thickness of

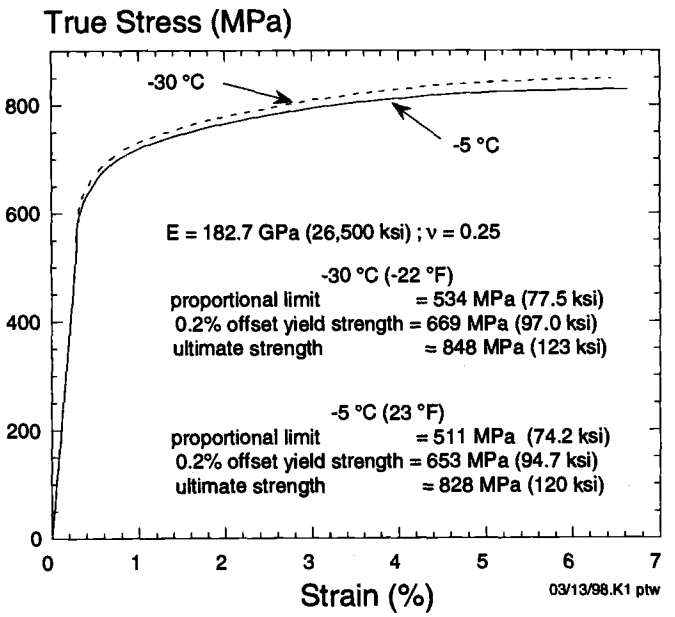


FIG. 3—*Stress versus strain curve for HSST Plate 14 (SA 533 B) steel at test temperatures of −5 and −30°C.*

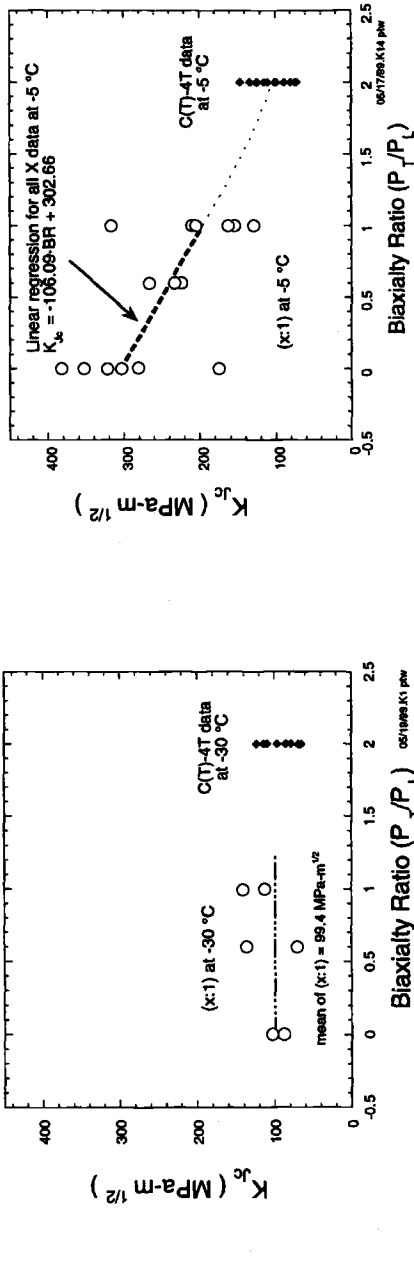


FIG. 4—*Plate 14 cruciform and C(T) ½T (converted to 4T) toughness data at test temperatures of* (a) *−30°C and* (b) *−5°C.*

the cruciform specimen, these C(T)-½T data have been adjusted to a 4T crack-front length using a size correction (based on weakest link statistics) given in the ASTM Test Method for the Determination of Reference Temperature, T_0, for Ferritic Steels in the Transition Range (E 1921).

The six cruciform specimens tested at −30°C provided data for: (a) three biaxial load ratios and (b) two duplicate tests at each condition. The specimens exhibited very little plastic deformation as measured by both crack-mouth-opening displacement (CMOD) and load-line displacement (LLD), regardless of the applied biaxial load. At this test temperature, biaxial loading showed no effect on failure loads or deformation at failure.

A second set of 15 cruciform specimens was tested at a nominal test temperature of —5°C. This higher temperature was expected to provide a better balance between cleavage behavior and accumulated plasticity at failure for evaluation of biaxial effects on toughness. Six specimens each were tested under uniaxial (0:1) and equibiaxial (1:1) loadings and three specimens under biaxial loading (0.6:1). For the tests performed at −5°C, the test data demonstrate a significant effect of biaxial loading on shallow-flaw fracture toughness as shown in Fig. 4*b*. The mean value of the biaxial (1:1) toughness resulted in approximately a 35% decrease from the mean uniaxial toughness ($\bar{K}_{Jc(1:1)}/\bar{K}_{Jc(0:1)} = 0.65$). In terms of the median of the data sets, the decrease was 41% ($K_{med-Jc(1:1)}/K_{med-Jc(0:1)} = 0.59$). The statistical significance of the observed difference in sample means ($\bar{K}_{Jc(0:1)} - \bar{K}_{Jc(1:1)} = 106.3$ MPa$\sqrt{\text{m}}$) can be estimated with a two-sample comparison of the means. The critical and fundamental assumption of statistical independence of the sample data is made. The application of the t statistic also requires the assumption of normal parent populations; however, the procedure is robust in the presence of non-normalcy due to the *central limit theorem* and the use of linear statistics. A one-sided test based on the difference of the means asserts a *null hypothesis* that states that the two samples represent random drawings from the same parent population, $H0$-$\mu_{(0:1)} - \mu_{(1:1)} = 0$, against the alternative hypothesis, $H1$-$\mu_{(0:1)} - \mu_{(1:1)} > 0$. For 10 degrees of freedom ($\nu = n_{(0:1)} + n_{(1:1)} - 2$), the resulting heteroscedastic t-statistic ($t_{10} = 2.656$) produces a p-value of 0.0121, i.e., the probability that the null hypothesis is true is only 1.21%, and the null hypothesis is rejected. The test data therefore support the contention that the biaxial effect indicated by the trends of the means of the uniaxial (0:1) and biaxial (1:1) toughness data in Fig. 4*b* is statistically significant.

Finite-Element Models

Three-dimensional finite-element models were developed for local crack-tip field analyses of the cruciform bend and compact tension C(T) specimens. The ¼-symmetric models of the cruciform bend and C(T) specimens are shown in Figs. 5 and 6, respectively. Two models of each specimen were used in the analyses: (1) sharp-tip small-strain elastic-plastic models to obtain accurate determinations of the J-integrals as a function of loading, and (2) blunt-tip (finite-root-tip radius) nonlinear finite-strain elastic-plastic models to calculate displacement and stress fields near the crack tip as input for the Weibull stress calculations. The ABAQUS code [*13*] carried out all displacement, stress, strain, and J-integral calculations. Employing a nonlinear elastic-plastic constitutive formulation based on J_2 flow theory and Mises plasticity, incremental static loading was applied to the specimen models. The analyses of the cruciform specimen neglected the potential impact of ductile tearing observed in two of the uniaxially loaded cruciform specimens, tested at —5°C at the two highest (0:1) toughness values plotted in Fig. 4*b*.

A new Weibull parameter calibration scheme, proposed by researchers at the University of Illinois, requires stress and displacement solutions to the plane-strain, modified boundary layer (MBL) problem [*14,15*] as representative of the asymptotic crack-tip stress fields as-

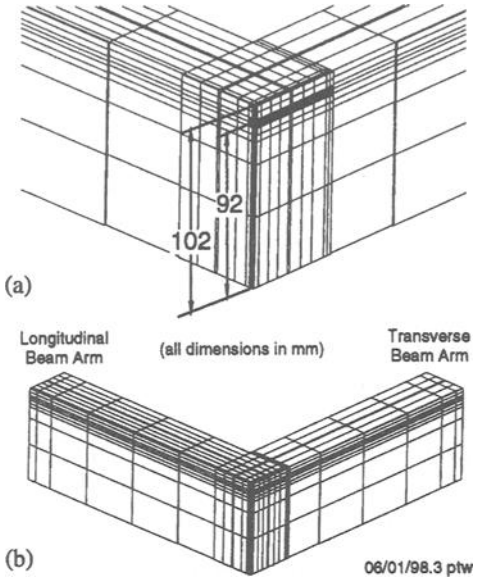


FIG. 5—*Finite-element model of cruciform specimen.*

sociated with the small scale yielding (SSY) limit. The MBL model used in this study is shown in Fig. 7.

Characterization of Cruciform Crack-Tip Stress and Strain Fields

Profiles of maximum principal stress σ_1, normalized by the yield stress σ_0 and plotted in the crack-extension plane as a function of distance r ahead of the stationary crack tip, are shown in Fig. 8*a* evolving under increased uniaxial loading as quantified by the J-integral.

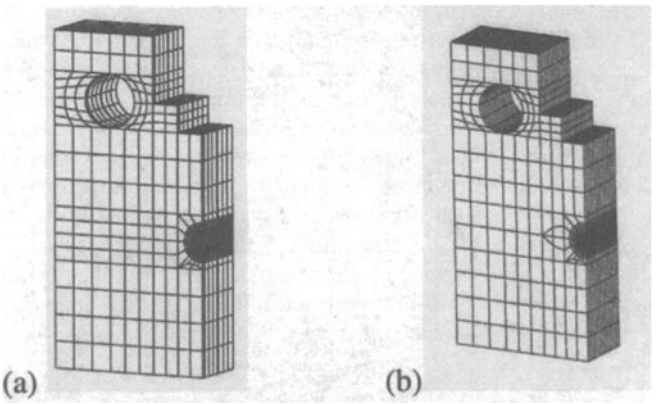


FIG. 6—*Finite-element mesh of C(T) specimen* (a) *sharp-tip small-strain model and* (b) *blunt-tip finite-strain model.*

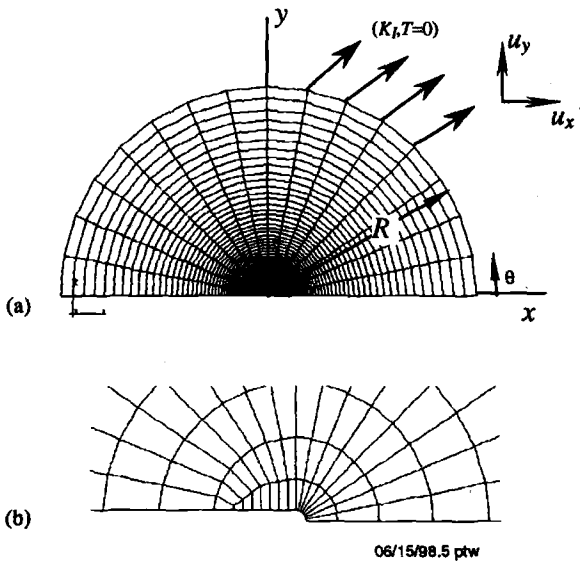


FIG. 7—*Finite-element plane-strain model of small-scale-yielding (SSY) modified boundary layer (MBL) problem:* (a) *global mesh with 16 fans, 2671 elements, and 5708 nodes;* (b) *close up of finite root tip with* $\rho_0 = 2.54$ *μm,* $\rho_0/R = 10^{-7}$.

In this paper, an ordering of the principal stresses of $\sigma_1 > \sigma_2 > \sigma_3$ is assumed. These profiles are plotted in Fig. 8*b* versus a normalized distance, $r/(J/\sigma_0)$, and compared to the self-similar plane-strain SSY profile. The hydrostatic stress (σ_H) profiles, under the same loading conditions, are plotted in Figs. 8*c* and 8*d*. For both the maximum principal and hydrostatic stresses, their stress peaks can be seen to shift to the right (i.e., farther away from the crack tip) and broaden out under increased loadings in Figs. 8*a* and 8*c*. In terms of the normalized distance, however, this shift with increasing load is to the left with an apparent sharpening of the stress peak. The sensitivities of the maximum principal and hydrostatic stresses to variations in biaxial loading are shown in Figs. 9*a* and 9*b*, respectively. Over a fracture process zone defined as material with a maximum principal stress greater than twice the yield stress, Fig. 9*a* demonstrates that the maximum principal stress is effectively insensitive to the effects of biaxial loading in the cruciform specimen. At a position to the right of the hydrostatic stress peak, at $r/(J/\sigma_0) \approx 1.2$ and extending to the outer boundary of the fracture process zone for $J \approx 100$ kJ/m^2, the equibiaxial (1:1) loading condition produces a hydrostatic stress greater than the hydrostatic stress of uniaxial (0:1) loading. Other biaxial loadings show a consistent elevation of the hydrostatic stress that increases with increasing biaxial ratio.

Profiles of effective plastic strain, ε_{pl}, and a triaxiality parameter, defined as the ratio of the hydrostatic to the von Mises effective stress, σ_H/σ_{eff}, are plotted in Figs. 10*a* and 10*b*, respectively. In the finite-strain blunting region to the left of the stress peak, the high effective plastic strains show little sensitivity to biaxial loading. To the right of the stress peak, the small uniaxial (0:1) plastic strains are slightly higher than the strains produced by biaxial loading. As a measure of constraint, the triaxiality parameter profiles in Fig. 10*b* demonstrate that, to the right of the stress peak, crack-tip constraint in the cruciform specimen is a controllable and monotonically increasing function of the biaxial load ratio.

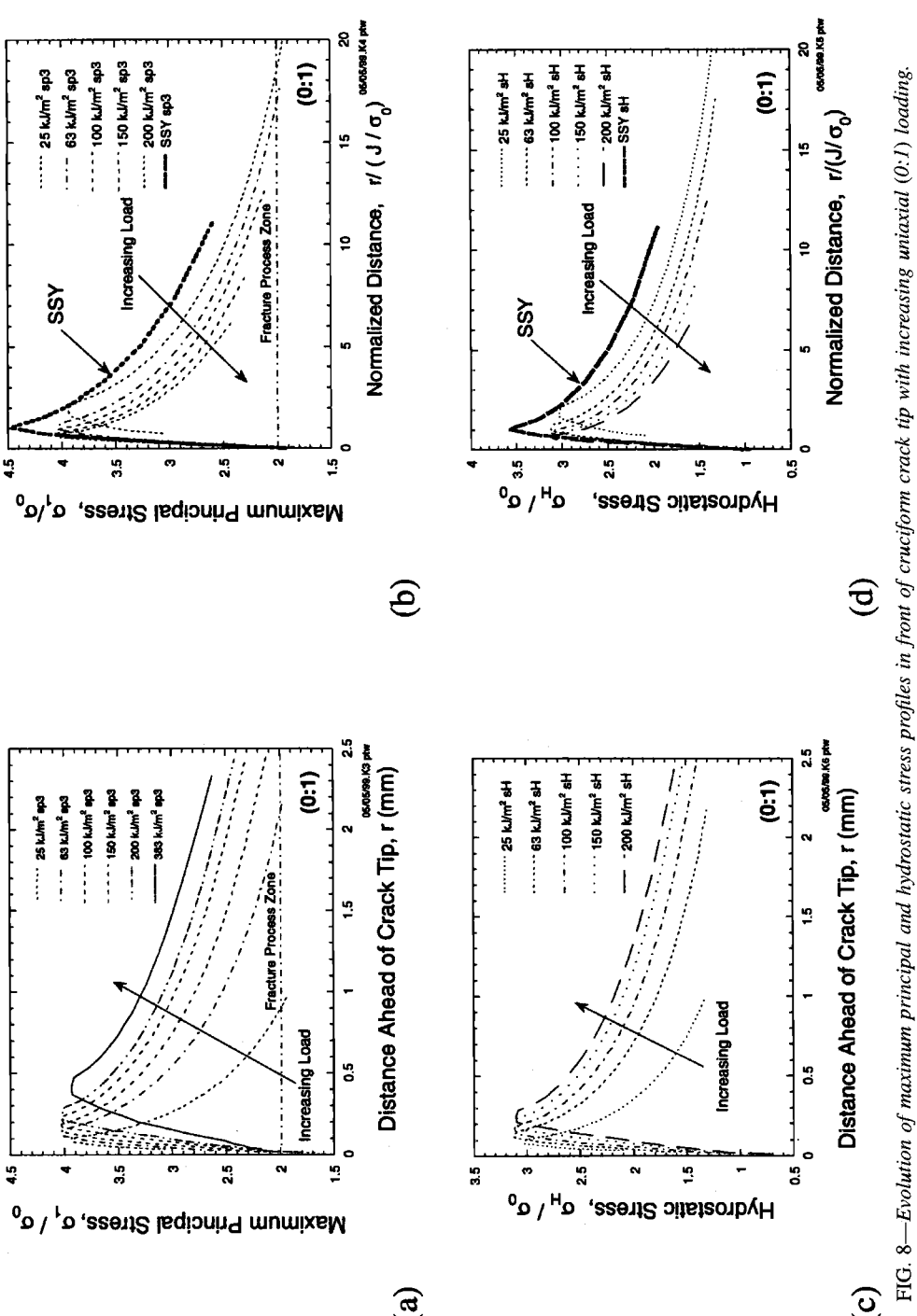


FIG. 8—*Evolution of maximum principal and hydrostatic stress profiles in front of cruciform crack tip with increasing uniaxial (0:1) loading.*

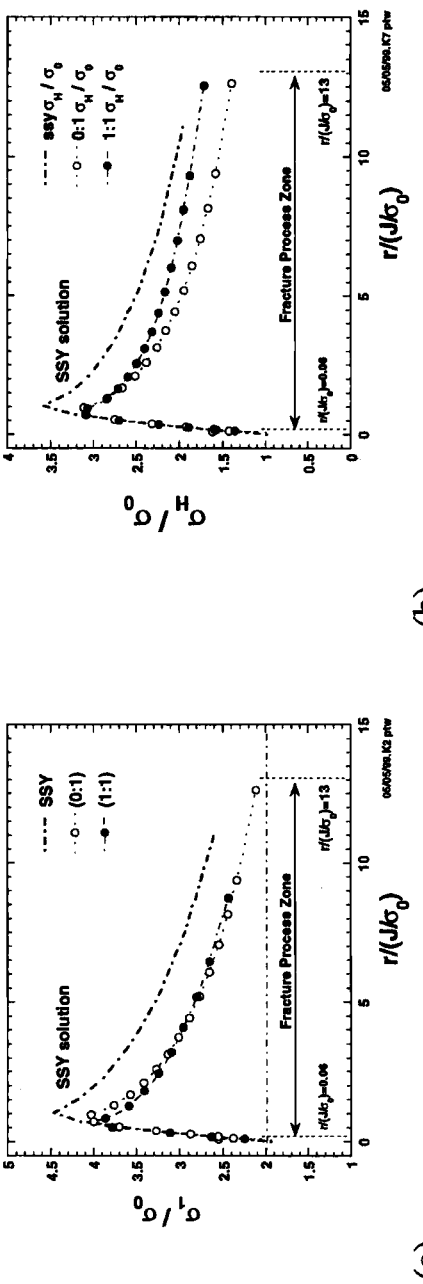


FIG. 9—*Sensitivity of* (a) *maximum principal and* (b) *hydrostatic stress profiles (plotted along the length of the fracture process zone defined by* $\sigma_1 \geq -2\sigma_0$ *for* J $\approx$*100 kJ/m*^{2}*) to biaxial loading in the cruciform specimen.*

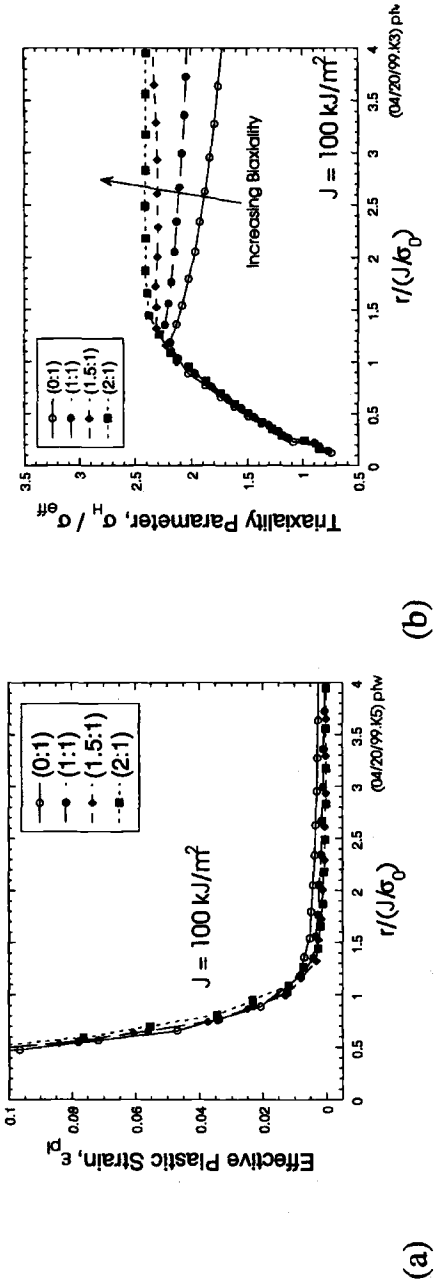


FIG 10.—*Profiles of* (a) *effective plastic strain, and* (b) *triaxiality parameter ahead of cruciform crack tip at* J = *100 kJ/m*^{2}.

Weibull Methodology

The methodology implemented in the WSTRESS (Version 2.0) computer code [*16*] was used to study the effects of biaxial loading on Weibull analyses of shallow-flow fracture toughness data in the lower transition temperature region. The WSTRESS code employs a multiaxial form of the *weakest link* model applicable for a 3-D cracked solid; the Weibull stress, σ_w, is characterized as a fracture parameter reflecting the local damage of the material near the crack tip. The Weibull stress, σ_w, defined by the expression

$$\sigma_w = \left[\frac{1}{4\pi V_0}\int_\Omega \int_0^{2\pi}\int_0^{\pi} \sigma_q^m \sin\varphi d\varphi \quad d\theta \quad d\Omega\right]^{1/m} \tag{1}$$

is evaluated by integration of the equivalent stress, σ_q, over the process zone. In Eq 1, V_0 is a reference volume, m is the Weibull modulus, θ and φ are curvilinear coordinates for integration of the tensile stress, and Ω denotes the volume of the near-tip fracture process zone, conventionally defined as the contiguous volume within the contour surface $\sigma_1 \geq 2\sigma_0$. Other definitions for Ω are possible, including material volumes defined by contour surfaces of von Mises effective stress or hydrostatic stress. Preliminary calculations indicated that the calculated Weibull stress was essentially insensitive to the final definition of Ω as long as the resulting volume was not too restricted (i.e., not too small) by the definition. The conventional definition for Ω was therefore applied for all of the analyses.

Fracture Criteria

A fracture criterion must be specified to determine the equivalent (tensile) stress, σ_q, acting on a microcrack embedded in the fracture process zone. Three options for fracture criteria are implemented in the distributed version of WSTRESS [*16*] to evaluate the critical stress at which the crack becomes unstable: maximum principal stress (MPS), coplanar energy release rate (CER), and normal stress averaging (NSA). Three additional fracture criteria were added to WSTRESS: the principal of independent action (PIA) [*17*] as proposed by Dortmans et al. [*18*], the noncoplanar energy release (NCER) rate [*19,20*], and the hydrostatic stress (HYDRO) criterion, developed during the present study. These criteria are implemented using the following definitions for the equivalent tensile stress, σ_q, in Eq 1:

$$\begin{aligned}
&(1)\ \text{MPS} \quad \sigma_q = \sigma_1 && (2)\ \text{NSA} \quad \sigma_q = \sigma_n \\
&(3)\ \text{PIA} \quad \sigma_q = (\langle\sigma_1\rangle^m + \langle\sigma_2\rangle^m + \langle\sigma_3\rangle^m)^{1/m} && (4)\ \text{CER} \quad \sigma_q = \left(\sigma_n^2 + \frac{4\tau^2}{(2-\nu)^2}\right)^{1/2} \\
&(5)\ \text{NCER} \quad \sigma_q = (\sigma_n^4 + 6\alpha_n^2\tau^2 + \tau^4)^{1/4} && (6)\ \text{HYDRO} \quad \sigma_q = \frac{I_1}{3} = \sigma_H
\end{aligned} \tag{2}$$

where I_1 is the first invariant of the Cauchy stress tensor, the state of stress is defined by the principal stresses ($\sigma_1 \geq \sigma_2 \geq \sigma_3$), and the operator $\langle\ \rangle$ and normal σ_n and shear τ stresses are defined by

$$\langle\sigma\rangle \equiv \begin{cases}\sigma & \text{if} \quad \sigma > 0 \\ 0 & \text{if} \quad \sigma \leq 0\end{cases} \tag{3}$$

Normal stress $\sigma_n = \sigma_1 \sin^2 \varphi \cos^2 \theta + \sigma_2 \sin^2 \varphi \sin^2 \theta + \sigma_3 \cos^2 \varphi$

Shear stress $\tau^2 = \sigma_1^2 \sin^2 \varphi \cos^2 \theta + \sigma_2^2 \sin^2 \varphi \sin^2 \theta + \sigma_3^2 \cos^2 \varphi - \sigma_n^2$

Applying the maximum principal stress criterion with the uniaxial (0:1) cruciform model, the resulting Weibull stresses are plotted in Figs. 11*a* and 11*b* for a range of *J*- and *m*-levels. For all of the *J*-levels shown in Fig. 11*a*, as *m* increases the Weibull stress rapidly decreases until it reaches a point where large changes in *m* produce small changes in the Weibull stress. In Fig. 11*b*, *m*-values above 20 produce a closely grouped family of Weibull stresses that gradually separate with increasing *J*. The Weibull stress trajectory for $m = 10$ follows a distinctly different path than those trajectories exhibited by the higher moduli. Due to the effect of raising the equivalent stress to the power *m* in the calculation of the Weibull stress (see Eq 1), increasing *m*-values place a heavier weighting on the contributions of material volumes with stresses near the peak. For high *m* values, the peak stress regions essentially dominate the resulting Weibull stress. The Weibull stresses continue to grow in magnitude with increasing *J*-integral due to the broadening of the stress peak as observed in Fig. 8*a* with a consequent increased volume weighting by the additional material associated with the highest stresses.

Of the six fracture criteria studied, the first five followed essentially the same trends; therefore, a comparison between the maximum principal and hydrostatic stress criteria is indicative of the general results.

Figure 12 compares the MPS criterion to the HYDRO criterion by calculating Weibull stresses at a fixed *J*-integral of 100 kJ/m^2 for a range of *m*-values. This *J*-integral corresponds to an applied stress-intensity factor of approximately 140 MPa-$\sqrt{\text{m}}$, which is within the range of toughness values obtained for the cruciform under equibiaxial (1:1) loading. The maximum principal stress criterion is effectively insensitive to variations in biaxiality (see Fig. 12*a*); however, the hydrostatic stress criterion produces a consistently different set of Weibull stress curves for $m < 20$. For $m > 20$, the Weibull stresses begin to converge to a common value. This convergence is due to the dominance of the hydrostatic stress peak at high *m*-values. Figure 9*b* shows that near and to the left of the peak the uniaxial (0:1) and equibiaxial (1:1) hydrostatic stress profiles converge. At $m = 10.5$, Fig. 13 compares the MPS and HYDRO criteria by plotting Weibull stress trajectories over a range of *J*-integrals for the SSY reference condition, the high-constraint deep-flaw ($a/W = 0.5$) C(T) specimen, and the shallow-flaw ($a/W = 0.1$) cruciform under four loading states, uniaxial (0:1), and three biaxial (1:1), (1.5:1), and (2:1). The MPS criterion is able to distinguish between the SSY reference, the C(T) specimen, and the cruciform specimen in Fig. 13*a*; however, the four cruciform loading states collapse into a single curve, thereby completely missing the variation in constraint due to biaxial loading as quantified by the triaxiality parameter in Fig. 10*b*. The HYDRO criterion in Fig. 13*b* presents Weibull trajectories that manifest a continuous and consistent variation in constraint levels from the upper limit of the SSY solution to the lowest constraint level of the shallow-flaw uniaxial (0:1) cruciform. The trajectory of the high-constraint deep-flaw C(T) specimen follows very closely the trajectory of the shallow-flaw (2:1) cruciform. As viewed by the Weibull methodology with the hydrostatic stress criterion, the C(T) specimen, therefore, exhibits a constraint level that is comparable to a biaxial loading state of (2:1). For this reason, the C(T) toughness data in Figs. 4*a* and 4*b* have been placed at a biaxial ratio of 2.

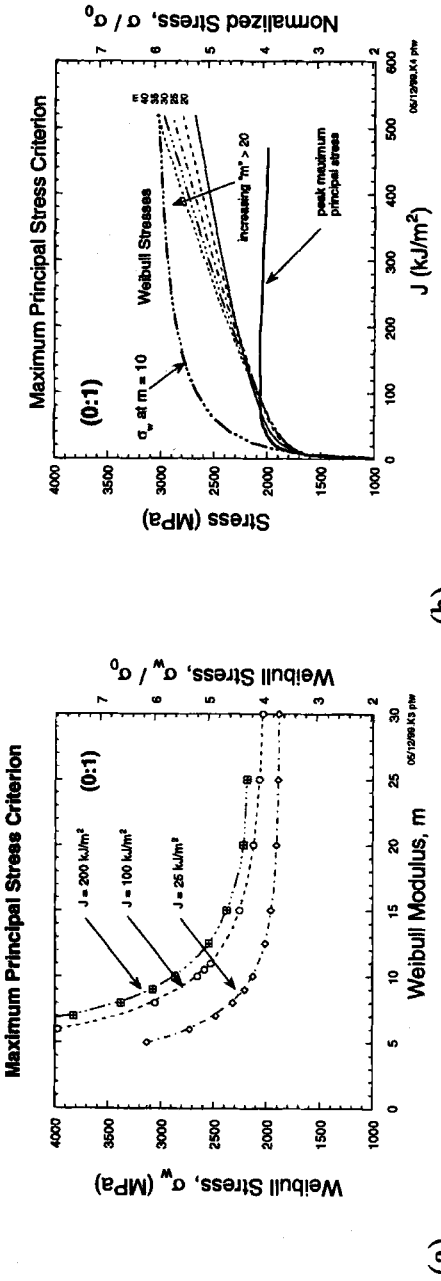


FIG. 11—*Effects of increasing magnitude of Weibull modulus on computed Weibull stress for uniaxial (0:1) loading with maximum principal stress criterion.*

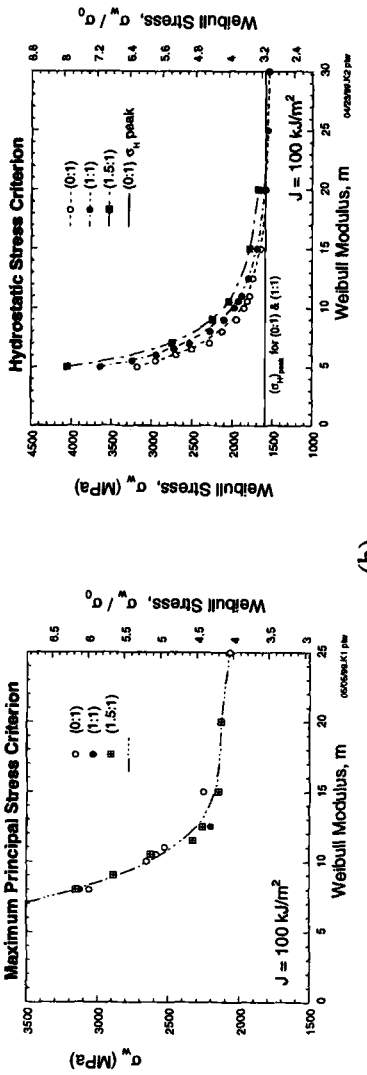


FIG. 12—*Sensitivity of Weibull stress to Weibull modulus and biaxiality for* (a) *maximum principal stress criterion and* (b) *hydrostatic stress criterion at* J = *100 kJ/m*^{2}.

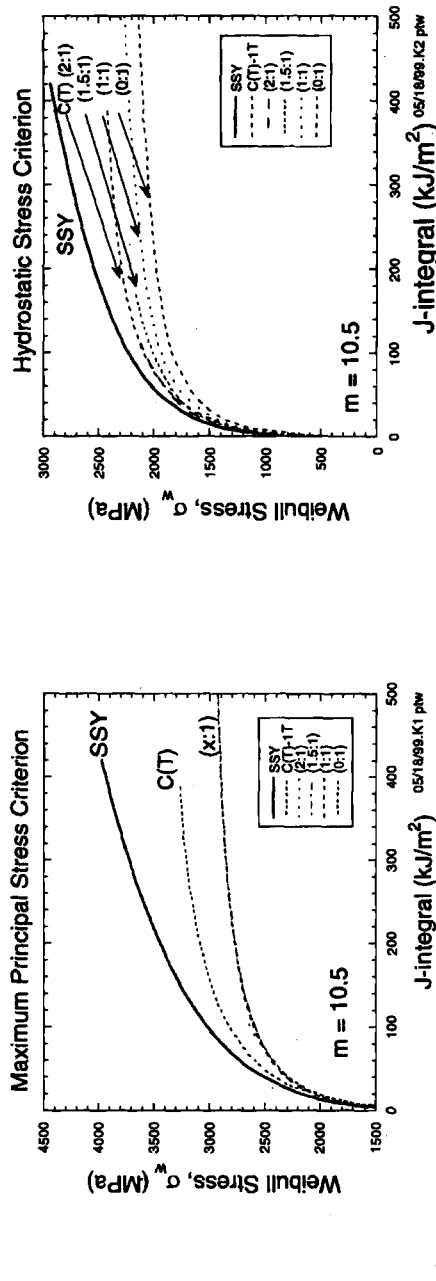


FIG. 13—*Sensitivity of Weibull stress to variations in constraint levels for* (a) *maximum principal stress criterion and* (b) *hydrostatic stress criterion at* m = *10.5.*

Cleavage Fracture Statistical Models

The cumulative probability of failure (P_f) by transgranular cleavage can be described in terms of a statistical fracture model (with the Weibull stress as the fracture parameter) based on either a two-parameter Weibull distribution of the form

$$P_f(\sigma_w) = 1 - \exp\left[-\left(\frac{\sigma_w}{\sigma_u}\right)^m\right] \tag{4}$$

or a three-parameter Weibull distribution

$$P_f(\sigma_w) = 1 - \exp\left[-\left(\frac{\sigma_w - \sigma_{w-\min}}{\sigma_u - \sigma_{w-\min}}\right)^m\right] \tag{5}$$

where the parameters of the distribution are the Weibull modulus m; the scaling stress (scaling factor) σ_u, and the minimum Weibull stress for cleavage fracture σ_{w-min}. Fracture toughness in terms of J_c may also serve as a fracture parameter with a two-parameter (α,β) Weibull distribution given by

$$P_f(J_c) = 1 - \exp\left[-\left(\frac{J_c}{\beta}\right)^\alpha\right] \tag{6}$$

ASTM E 1921 adopts a three-parameter Weibull distribution with K_{Jc} as the fracture parameter,

$$P_f(K_{Jc} = 1 - \exp\left(-\left[\frac{K_{Jc} - K_{\min}}{K_0 - K_{\min}}\right]^\alpha\right) \tag{7}$$

where K_{Jc} and K_0 are in MPa-$\sqrt{m}$, $\alpha = 4$, and $K_{\min} = 20$ MPa-$\sqrt{m}$. Strictly speaking, Eq 7, as applied in ASTM E 1921, is a one-parameter Weibull model with the shape, α, and location, K_{min}, parameters fixed. In this study the conversion between J and K_J is accomplished with the plane-strain formulation

$$K_J = \sqrt{\frac{E\ J}{(1 - \nu^2)}} \tag{8}$$

where E is Young's modulus and ν is Poisson's ratio.

Calibration Procedures

As evident by the sensitivity of the Weibull stress to the Weibull modulus m shown in Figs. 11 and 12, a valid calibration of the cleavage fracture model is a critical step in the application of the methodology. The open literature reports values of m for common structural and pressure vessel steels ranging from 10 to 50 [*21*], suggesting a significant uncertainty regarding an acceptable calibration procedure.

Procedure 1: Calibration with High-Constraint Toughness Data—Minami et al. [*22*] developed an iterative process (implemented in WSTRESS) involving maximum likelihood (ML) estimates for (m,σ_u) in Eq 4 that enforce equal probabilities for the maximum likelihood estimates of (α,β) in Eq 6. For a large number of toughness data available from

specimens tested under high-constraint conditions in the transition temperature region, it was postulated that the shape parameter α in Eq 6 would approach a value of 2, derived from a theoretical treatment of cleavage initiation based on weakest link and SSY assumptions. With α fixed at 2, an ML estimate for β can then be calculated. The WSTRESS code uses a Monte Carlo simulation with inverse transformation to generate a large statistical sample from a distribution described by Eq 6. This Monte Carlo simulation has the form

$$J_{c(\text{gen})} = \beta[-\ln(1 - U)]^{1/\alpha} \tag{9}$$

where U is a random variate uniformly distributed between [0,1]. Applying the 12 C(T) toughness data taken at a test temperature of −5°C and α set to 2, a dataset of 10 000 J_c values was generated and used in the iterative process by WSTRESS to calculate ML estimates for a two-parameter Weibull model. Using the maximum principal stress criterion, values for (m,σ_u) = (25.6, 2166 MPa) were estimated. Figure 14 plots the resulting failure probabilities for the C(T), (1:1) cruciform, and (0:1) cruciform models. The median rank probabilities assigned to the toughness data were calculated using the following estimate [*23*] for the *i*th data point in a sample dataset of n data points

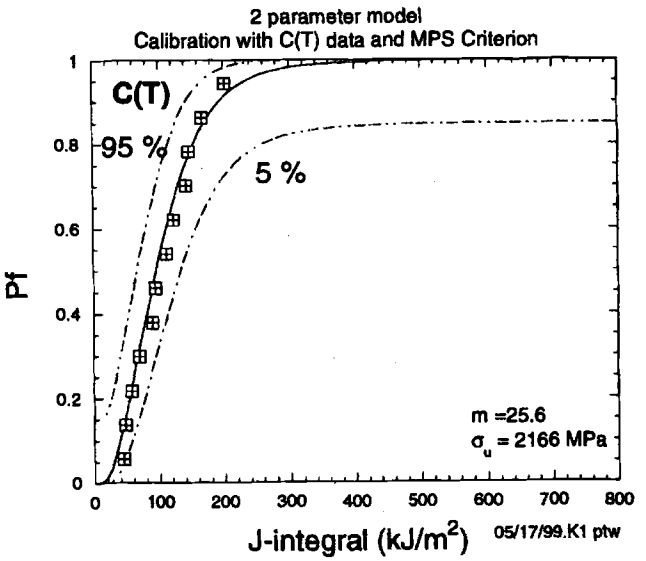
$$P_{i-\text{rank}} = \frac{i - 0.3}{n + 0.4} \tag{10}$$

where the toughness data are ranked according to increasing magnitude. The 90% confidence limits on the median rank probability estimates were determined with an algorithm presented in Ref *23*. The spread of these confidence limits is a function of n only.

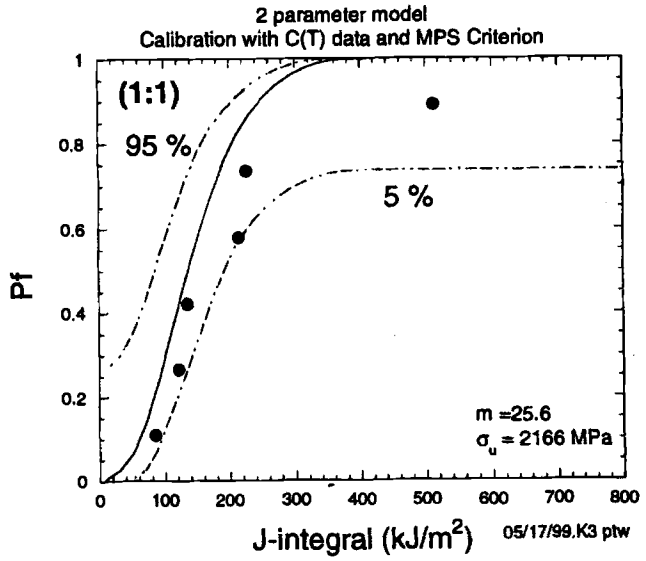
The calibration process with high-constraint C(T) toughness data only is shown in Fig. 14*a* to produce a good correlation of the data used to calibrate the model. However, when this model is extended to data from lower constraint specimens, specifically the equibiaxial (1:1) cruciform data in Fig. 14*b* and the uniaxial (0:1) cruciform data in Fig. 14*c*, the correlation progressively breaks down. Gao et al. [*21*,*23*] show that fixing α in the calibration process using high-constraint fracture toughness data leads to nonunique values of (m,σ_u), whereas fitting α to the high-constraint data using ML estimates as in Ref *22* can introduce large uncertainties in the resulting m value.

Procedure 2: Calibration with High- and Low-Constraint Toughness Data—A new calibration scheme has been proposed by Gao et al. [*21*] to determine unique values of the Weibull parameters (m,σ_u) by applying toughness data measured under high- and low-constraint conditions at the crack front. The new calibration scheme eliminates the nonuniqueness associated with Procedure 1 by mapping the two sets of toughness data to an SSY Weibull stress space where α takes on the theoretical values of 2 or 4 for Weibull distributions expressed in terms of J_c or K_{Jc}, respectively. The mapping to SSY Weibull stress space, therefore, converts the problem from an ill-posed two-parameter (m,σ_u) procedure to a well-posed, one-parameter (β_{SSY}) point-estimation procedure. Upon convergence, the necessary parameters for the Weibull stress model (m,σ_u) can be extracted from the solution as discussed below.

In the SSY Weibull stress space, the scheme requires iterations with the Weibull modulus m to determine a unique value of β_{SSY} and thereby a unique m-value. The calibration process employs large-scale yielding (LSY) toughness data from two fracture specimens (tested in the transition temperature region) that exhibit distinctly different levels of crack-tip constraint. The procedure then seeks the unique m-value that, upon mapping the two LSY sample datasets back to the corresponding SSY Weibull stress space, results in constraint-

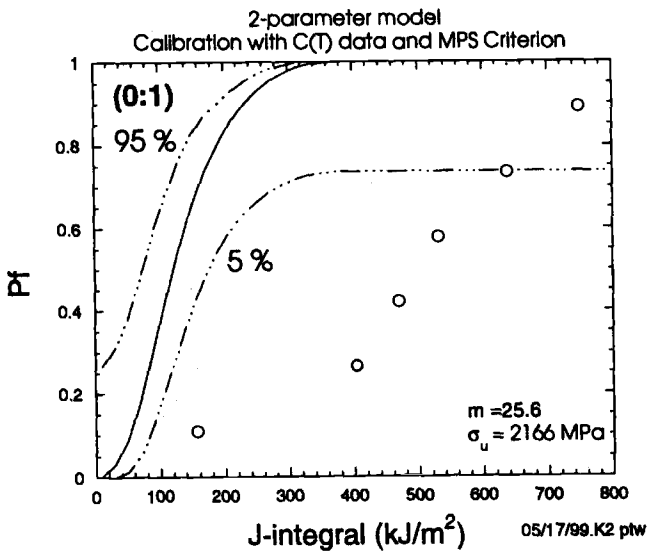


(a)



(b)

FIG. 14—*Failure probabilities resulting from calibration using maximum principal stress criterion with C(T) toughness data, two-parameter Weibull model:* m = *25.6,* σ_u = *2166 MPa:* (a) *C(T) correlation,* (b) *equibiaxial (1:1) correlation, and* (c) *uniaxial (0:1) correlation.*



(c)

FIG. 14—*Continued.*

corrected toughness distributions that have the same statistical properties, specifically the same SSY Weibull distributions as described by the (α,β) parameters in Eq 6.

In summary, the new method (designated as the G-R-D scheme) proceeds by the following steps:

Step 1: Test two sets of specimens (both tested under LSY conditions) with different levels of crack-tip constraint. In the terminology of Ref *21*, the C(T) data would be designated as Configuration A (high constraint), and the shallow-flaw uniaxial (0:1) data would be designated as Configuration B (low constraint).

Step 2: Perform detailed 3-D finite-element analyses for Configurations A and B and for a plane-strain SSY model with a reference thickness adjusted to be consistent with the specimens in Configurations A or B.

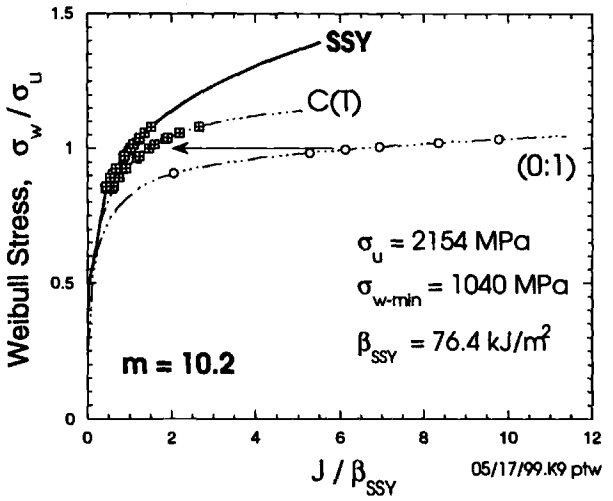
Step 3: Assume a trial m-value and calculate the σ_w versus J histories for Configurations A and B and the SSY model. Constraint-correct the Configurations A and B toughness data by mapping the data points on the σ_w versus J curves back to the SSY curve as shown in Fig. 15*a* such that $J_{c-(i)} \rightarrow J_{(i)-SSY}$ for $\sigma_{w(c:1)} = \sigma_{w-SSY}$.

Step 4: Estimate β_A and β_B in SSY Weibull stress space for the two configurations by the maximum likelihood point estimation relation (without small-sample bias)

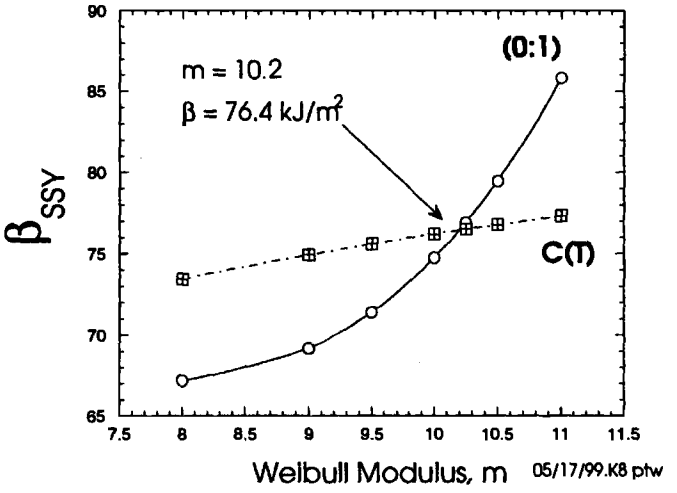
$$\beta = \sqrt{\frac{1}{n}\sum_{i=1}^{n}(J_{(i)-SSY})^2} \tag{11}$$

and calculate a relative error $R(m)$ with the error function

$$R(m) = \frac{\beta_B - \beta_A}{\beta_A} \tag{12}$$



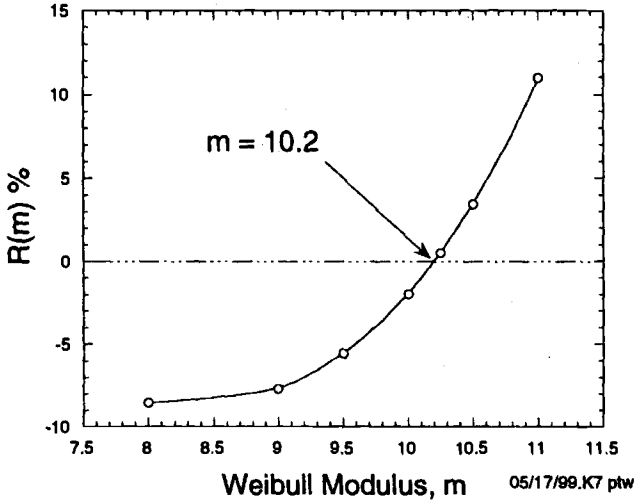
(a)



(b)

FIG. 15—*Calibration results using (high-constraint) C(T) and (low-constraint) uniaxial (0:1) cruciform toughness data:* (a) *constraint correction to SSY,* (b) β_{SSY} *versus* m, *and* (c) *error function* R(m) *versus* m.

Step 5: Repeat Steps 3 and 4 for a range of trial *m*-values and determine the *m*-value that produces an acceptably small relative error *R*(*m*) (see Figs. 15*b* and 15*c*). The scaling stress, σ_u, can then be calculated from the converged SSY-(σ_{w-SSY} versus *J*) curve by



(c)

FIG. 15—*Continued.*

$$\sigma_u = \sigma_{w-ssy} \text{ @ } J_{SSY} = \beta_{SSY} = \beta_A = \beta_B \tag{13}$$

For the 3-parameter Weibull distribution, the third parameter, σ_{w-min}, is calculated from the intercept of the SSY-(σ_{w-SSY} versus J) curve at J_{min} = 2.05 kJ/m^2 corresponding to a K_{min} = 20 MPa-$\sqrt{m}$.

Results and Discussion

Calibration

Several calibration exercises were carried out using the two procedures described in the previous section. For Procedure 1, all six candidate fracture criteria were applied with the high-constraint deep-flaw C(T) data. The resulting Weibull parameters (m,σ_u) ranged in value from a low of (21.0, 1706 MPa) for the HYDRO criterion to a high of (26.9, 2156 MPa) for the PIA criterion. Intermediate values included NSA (24.9, 1982 MPa), CER (25.2, 1996 MPa), MPS (25.6, 2166 MPa), and NCER (26.9, 2011 MPa). All of these parameter pairs demonstrated an ability to correlate the data used in the calibration (see Fig. 14*a*) with a similar inability to correlate data from low-constraint specimens (see Figs. 14*b* and 14*c*).

Of the six fracture criteria under study, the first five exhibited an insensitivity to biaxial loading of the cruciform; therefore, the MPS criterion was selected as representative of this group and also as the more commonly applied criterion in conventional Weibull stress calculations. An attempt was made to apply Procedure 2 using MPS with the C(T) specimen serving as Configuration A (high constraint) and the uniaxial (0:1) cruciform specimen (analogous to a shallow-flaw bend bar) serving as Configuration B (low constraint). No solution was obtained, however, because the β_A and β_B curves failed to cross for any m-value. The error function $R(m)$ at first decreased with increasing m until it passed through a minimum and then continued to increase.

Procedure 2 was then applied with the HYDRO criterion for several combinations of Configurations A and B. Employing the equibiaxial (1:1) cruciform (6 data points) as Configuration A and the uniaxial (0:1) cruciform (6 data points) as Configuration B resulted in the lowest Weibull modulus and highest scaling stress, (m,σ_u) = (8.5, 2401 MPa), calculated in the current study. With the C(T) specimen (6 data points) as Configuration A and the uniaxial (0:1) specimen (6 data points) as Configuration B, the resulting Weibull parameters were (m,α_u) = (10.4, 2140 MPa). Increasing the number of C(T) specimen data points to 12 produced the final calibration results of (m,σ_u) = (10.2, 2154 MPa). These Weibull parameters were selected for additional study, because they were based on a calibration that used data spanning the full range of constraint conditions to be addressed by the scaling model. For the three-parameter Weibull model, the third parameter $\sigma_{w-\min}$ was determined to be 1040 MPa from the $\sigma_{w,SSY}$ versus J curve at $J_{\min}$ = 2.05 kJ/m^2 ($K_{\min}$ = 20 MPa-$\sqrt{\text{m}}$). Figure 16 presents plots of the resulting failure probabilities calculated by Eq 5 for the two data sets used to calibrate the model (Fig. 16*a* for C(T) and Fig. 16*c* for uniaxial (0:1)). Failure probabilities for the equibiaxial (1:1) condition, representing an intermediate constraint level not employed in the calibration, are shown in Fig. 16*b*. Comparing Figs. 14*b* and 14*c* with Figs. 16*b* and 16*c*, respectively, clearly shows the ability of the HYDRO criterion calibrated with the G-R-D scheme to correlate low-constraint conditions.

Biaxial Scaling Model

With the Weibull statistical fracture model calibrated, a toughness biaxial scaling model can now be constructed and expressed in several graphical forms as shown in Figs. 17 and 18. In Fig. 17*a*, the ordinate is the J-integral normalized by the value of β_{SSY} obtained from the converged solution in the G-R-D calibration scheme. Curves of $J_{(x:1)}/\beta_{SSY}$ for the different biaxial ratios (i.e., constraint levels) are plotted as a function of the normalized Weibull stress serving as the fracture parameter. For a given probability of failure, P_f, Eq 5 can be inverted to calculate the corresponding critical Weibull stress

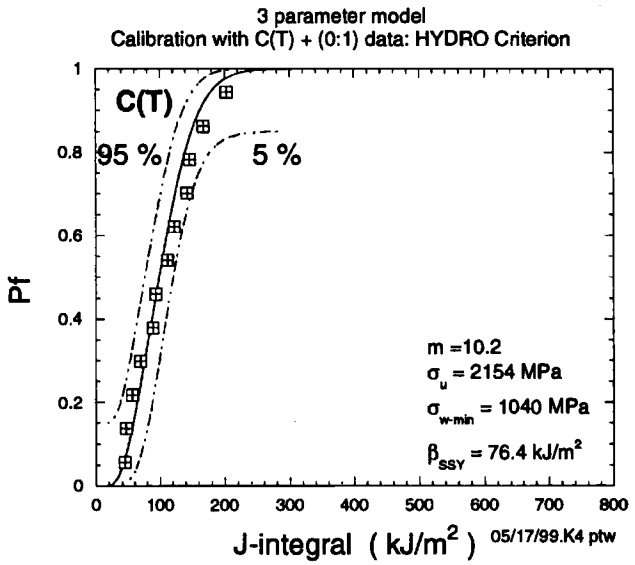
$$\frac{\sigma_w^*}{\sigma_u^*} = \frac{\sigma_w - \sigma_{w-\min}}{\sigma_u - \sigma_{w-\min}} = [-\ln(1 - P_f)]^{1/m} \tag{14}$$

As shown in Fig. 17*a* for a P_f = 0.5, the intersection of the vertical line of constant Weibull stress with the $J_{(x:1)}/\beta_{SSY}$ curves gives the scaling of the various constraint levels for the same probability of failure. Traversing a range of failure probabilities allows the construction of Fig. 17*b* where the abscissa is the normalized uniaxial $J_{(0:1)}/\beta_{SSY}$.

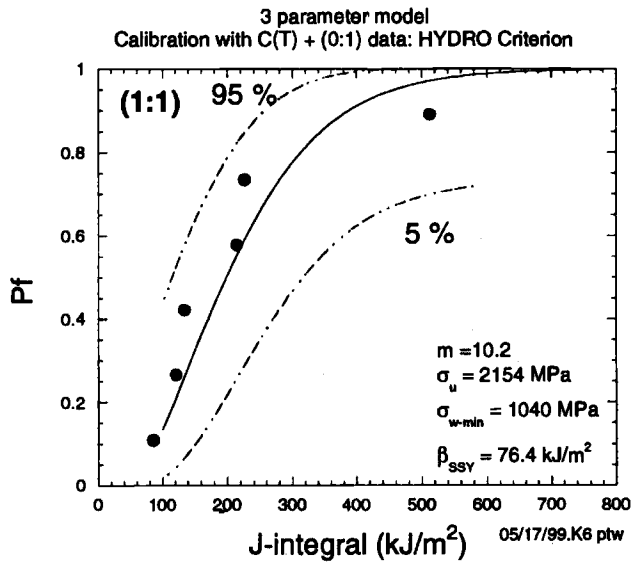
The scaling model may also be expressed in terms of toughness ratios as in Figs. 18*a* and 18*b*. By Eq 8, ratios of stress intensity factors can be calculated from J-integral ratios by

$$\frac{K_{Jc(x:1)}}{K_{Jc(0:1)}} = \sqrt{\frac{J_{c(x:1)}}{J_{c(0:1)}}} \tag{15}$$

In Fig. 18*a*, the ratio $K_{Jc(x:1)}/K_{Jc(0:1)}$ is plotted as a function of $K_{Jc(0:1)}$. As discussed in a previous section, the C(T) curve can be seen to follow very closely the biaxial (2:1) cruciform curve in Fig. 18*a*. The ratio of the median toughness $K_{Jc\text{-med}(x:1)}/K_{Jc\text{-med}(0:1)}$ at the failure probability P_f = 0.5 can be plotted as a function of the biaxial ratio. In Fig. 18*b*, the predicted biaxial scaling model curve for the median failure probability of P_f = 0.5 is compared to the medians of the cruciform data sets normalized by the median toughness of the uniaxial (0:1) specimen predicted by the scaling model. Good agreement at P_T/P_L = 0 is to be

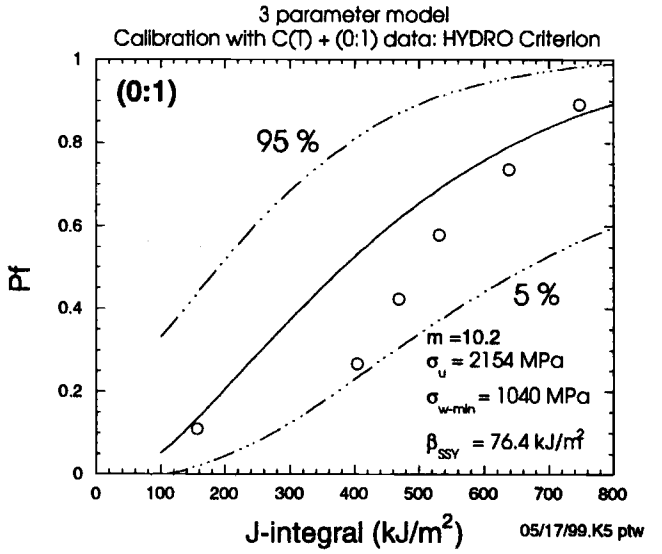


(a)



(b)

FIG. 16—*Failure probabilities resulting from calibration using hydrostatic stress criterion with (high-constraint) C(T) and (low-constraint) uniaxial (0:1) cruciform toughness data, three-parameter Weibull model:* m = *10.2,* σ_u = *2154, and* $\sigma_{w\text{-}min}$ = *1040 MPa:* (a) *C(T) correlation,* (b) *equibiaxial (1:1) correlation, and* (c) *uniaxial (0:1) correlation.*



(c)

FIG. 16—*Continued.*

expected since the uniaxial (0:1) data were used in the calibration of the model. The fact that the data points at $P_T/P_L = 0.6$ and $P_T/P_L = 1.0$ also show good agreement with the biaxial scaling model, however, provides encouraging evidence of the validity of the analysis, since these data were not used in the model calibration.

Conclusions

The Weibull methodology has been applied to the analysis of a shallow-flaw cruciform bend specimen tested under biaxial loading conditions. Tests were conducted under biaxial load ratios ranging from uniaxial (0:1) to equibiaxial (1:1). These tests demonstrated that biaxial loading can have a pronounced effect on shallow-flaw fractures toughness in the lower transition temperature region for a RPV material. High-constraint deep-flaw uniaxial compact tension C(T) and low-constraint shallow-flaw uniaxial and biaxial cruciform fracture toughness data were used to assess the ability of the Weibull methodology to predict the observed effects of biaxial loading on shallow-flaw fracture toughness. A new hydrostatic stress criterion (developed during this study) and a set of five equivalent-stress criteria selected from the literature were applied as candidate kernels in the integral formulation of the Weibull stress. Among these candidates, the hydrostatic stress criterion, derived from the first invariant of the Cauchy stress tensor, was determined to have the required sensitivity to multiaxial-loading states. In addition, the G-R-D scheme, recently developed by researchers at the University of Illinois, was used to calibrate a statistical fracture model with uniaxial C(T) and uniaxial cruciform data.

In summary, the conclusions that can be drawn from this study are as follows:

1. With respect to its effect on fracture toughness, the biaxial effect is a constraint effect.
2. A Weibull statistical fracture model has been successfully calibrated with uniaxial toughness data, obtained from a conventional high-constraint C(T) specimen and a

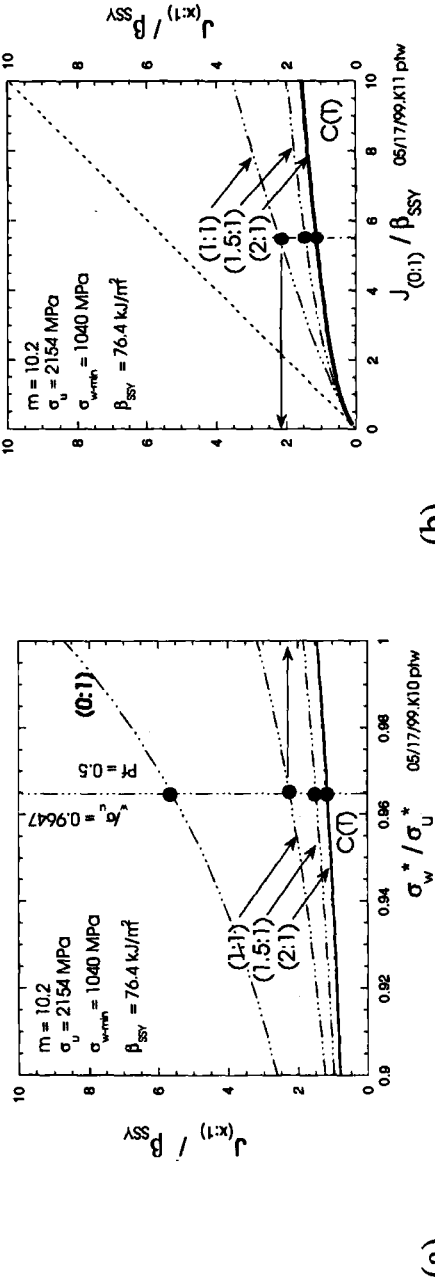
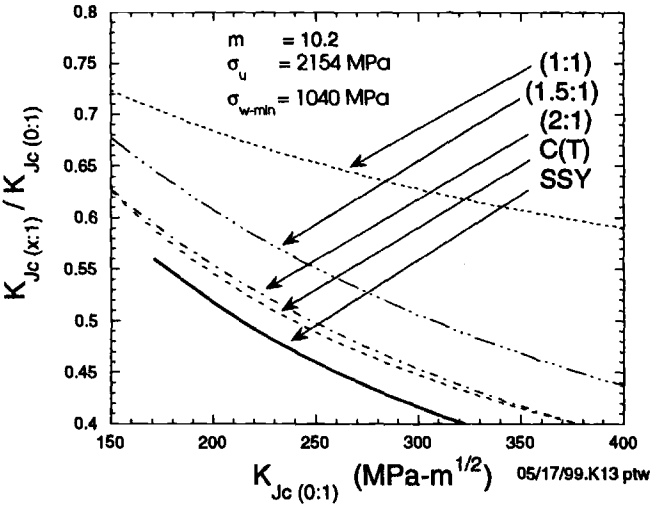
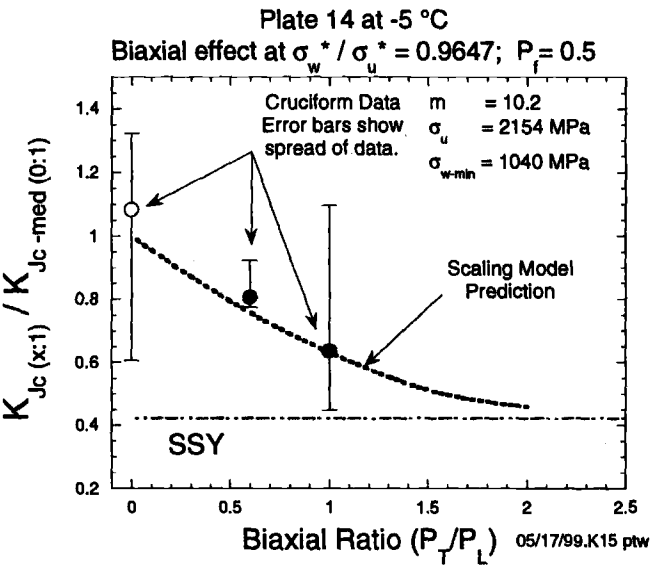


FIG. 17—*Biaxial scaling model for variations in biaxiality in terms of* J*-integral.*



(a)



(b)

FIG. 18—*Biaxial scaling model for variations in biaxiality in terms of toughness ratios:* (a) *variation with uniaxial (0:1) toughness and* (b) *variation with biaxiality ratio for* P_f = *0.5. Experimental points are the medians of the test data normalized by the predicted median of the uniaxial (0:1) cruciform.*

uniaxially loaded shallow-flaw cruciform that is effectively equivalent to a conventional shallow-flaw SE(B) specimen.

3. The calibrated fracture model was able to successfully predict the intermediate constraint-loss effects associated with two levels of biaxial loading.

4. These preliminary results at a single test temperature offer encouragement that complex multiaxial loading effects on transition region fracture toughness can be predicted with statistical fracture models developed using data obtained from conventional specimens.
5. Future work is required to investigate these effects at other temperatures, within the transition region.

Acknowledgments

The authors wish to thank Professor Robert H. Dodds, Jr., University of Illinois, for his many helpful contributions to the constraint applications described in this paper. The finite-element models of the cruciform specimen were developed by J. W. Bryson, Jr.

References

[1] Theiss, T. J. and Shum, D. K. M., "Experimental and Analytical Investigation of the Shallow-Flaw Effect in Reactor Pressure Vessels," USNRC Report NUREG/CR-5886 (ORNL/TM-12115), Oak Ridge National Laboratory, July 1992.

[2] Theiss, T. J., Bass, B. R., Bryson, Jr., J. W., McAfee, W. J., Nanstad, R. K., Pennell, W. E., and Rao, M. C., "Initial Results of the Influence of Biaxial Loading on Fracture Toughness," USNRC Report NUREG/CR-6036 (ORNL/TM-12349), Oak Ridge National Laboratory, June 1993.

[3] *Code of Federal Regulations,* Title 10, Part 50, Section 50.61 and Appendix G.

[4] McAfee, W. J., Bass, B. R., and Bryson, Jr., J. W., "Development of a Methodology for the Assessment of Shallow-Flaw Fracture in Nuclear Reactor Pressure Vessels," *ASME Pressure Vessel and Piping Conference,* Orlando, FL, 27–31 July 1997, PVP-Vol. 346, pp. 85–94.

[5] Pennell, W. E., Bass, B. R., Bryson, Jr., J. W., Dickson, T. L., and Merkle, J. G., "Preliminary Assessment of the Effects of Biaxial Loading on Reactor Pressure Vessel Structural-Integrity-Assessment Technology," *Proceedings of 4th ASME/JSME International Conference in Nuclear Engineering,* New Orleans, LA, 10–14 March 1996.

[6] McAfee, W. J., Bass, B. R., Bryson, Jr., J. W., and Pennell, W. E., "Biaxial Loading Effects on Fracture Toughness of Reactor Pressure Vessel Steel," USNRC Report NUREG/CR-6273 (ORNL/TM-12866), Oak Ridge National Laboratory, March 1995.

[7] Bass, B. R., Bryson, Jr., J. W., Theiss, T. J., and Rao, M. C., "Biaxial Loading and Shallow-Flaw Effects on Crack-Tip Constraint and Fracture Toughness," USNRC Report NUREG/CR-6132 (ORNL/TM-12498), Oak Ridge National Laboratory, January 1994.

[8] Bass, B. R., McAfee, W. J., Bryson, Jr., J. W., and Pennell, W. E., "Determination of Cladding Effects on Shallow-Flaw Fracture Toughness of Reactor Pressure Vessel Steel under Prototypic Biaxial Loading," *5th International Conference on Nuclear Engineering,* Nice, France, 26–30 May 1997.

[9] Ruggieri, C. and Dodds, Jr., R. H., "Probabilistic Modeling of Brittle Fracture Including 3-D Effects on Constraint Loss and Ductile Tearing," *International Conference on Local Approach to Fracture (MECAMAT 96),* Fontainebleau, France, 1996.

[10] Bass, B. R., McAfee, W. J., Williams, P. T., and Pennell, W. E., "Evaluation of Constraint Methodologies Applied to a Shallow-Flaw Cruciform Bend Specimen Tested under Biaxial Loading Conditions," *Fatigue, Fracture, and High Temperature Design Methods in Pressure Vessels and Piping, ASME/JSME Joint Pressure Vessels and Piping Conference,* San Diego, CA, 26–30 July 1998, PVP-Vol. 365, pp. 11–25.

[11] Bass, B. R., McAfee, W. J., Williams, P. T., and Pennell, W. E., "Fracture Assessment of Shallow-Flaw Cruciform Beams Tested under Uniaxial and Biaxial Loading Conditions," *Nuclear Engineering and Design,* Vol. 188, No. 3, 1999, pp. 259–288.

[12] Williams, P. T., Bass, B. R., and McAfee, W. J., "Shallow Flaws under Biaxial Loading Conditions—Part II: Application of a Weibull Stress Analysis of the Cruciform Bend Specimen using a Hydrostatic Stress Criterion," *Advances in Life Prediction Methodology, ASME 1999 Pressure Vessels and Piping Conference,* Boston, MA, 1–5 Aug. 1999, PVP-Vol. 391, pp. 75–85.

[13] *ABAQUS Theory Manual, Version 5.8,* Hibbit, Karlson and Sorensen, Inc., Providence, RI, 1998.

[14] Larsson, S. G. and Carlson, A. J., "Influence of Non-Singular Stress Terms and Specimen Geometry on Small Scale Yielding of Crack-Tips in Elastic-Plastic Materials," *Journal of the Mechanics and Physics of Solids,* Vol. 21, 1973, pp. 447–473.

[15] Rice, J. R., "Limitations to the Small Scale Yielding Approximation for Crack-Tip Plasticity," *Journal of the Mechanics and Physics of Solids,* Vol. 22, 1974, pp. 17–26.

[16] Ruggieri, C. and Dodds, Jr., R. H., "Numerical Evaluation of Probabilistic Fracture Parameters with WSTRESS," *Engineering and Computers,* Vol. 15, No. 1, 1998, pp. 49–73.

[17] Freudenthal, A. M., "Statistical Approach to Brittle Fracture," *Fracture: An Advanced Treatise, Vol. 2, Mathematical Fundamentals,* H. Liebowitz, Ed., Academic Press, New York, 1968, pp. 591–619.

[18] Dortmans, L., Thiemeier, T., Brückner-Foit, A., and Smart, J., "WELFEP: A Round Robin for Weakest-Link Finite Element Postprocessors," *Journal of the European Ceramic Society,* 0955-2219/93/S6.00, Elsevier Science Publishers Ltd, England, 1993.

[19] Hellen, T. K. and Blackburn, W. S., "The Calculation of Stress Intensity Factors for Combined Tension and Shear Loading," *International Journal of Fracture,* Vol. 11, 1975, pp. 605–617.

[20] Lamon, J. and Evans, A. G., "Statistical Analysis of Bending Strengths for Brittle Solids: A Multiaxial Fracture Problem," *Journal of the American Ceramic Society,* Vol. 66, 1983, pp. 177–182.

[21] Gao, X., Ruggieri, C. and Dodds, R., "Calibration of Weibull Stress Models Using Fracture Toughness Data," *International Journal of Fracture,* Vol. 92, 1998, pp. 175–200.

[22] Minami, F., Brückner-Foit, A., Munz, D., and Trolldenier, B., "Estimation Procedure for the Weibull Parameters used in the Local Approach," *International Journal of Fracture,* Vol. 54, 1992, pp. 197–210.

[23] Gao, X., Dodds, Jr., R. H., Tregoning, R. L., Link, R. E., and Joyce, J. A., "A Weibull Stress Model to Predict Cleavage Fracture in Plates Containing Surface Cracks," *Fatigue and Fracture of Engineering Materials and Structures,* Vol. 22, 1999, pp. 481–493.

Fumiyoshi Minami,[1] *Takao Ochiai,*[2] *Tomoyuki Hashida,*[2]
Kazushige Arimochi,[3] *and Noboru Konda*[3]

Local Approach to Dynamic Fracture Toughness Evaluation

REFERENCE: Minami, F., Ochiai, T., Hashida, T., Arimochi, K., and Konda, N., **"Local Approach to Dynamic Fracture Toughness Evaluation,"** *Fatigue and Fracture Mechanics: 31st Volume, ASTM STP 1389,* G. R. Halford and J. P. Gallagher, Eds., American Society for Testing and Materials, West Conshohocken, PA, 2000, pp. 271–304.

ABSTRACT: Fracture toughness properties of structural steels of 490-MPa strength class and weld metals under dynamic loading are studied in the light of the near crack tip stress fields. The loading rate in toughness tests range from 0.1 to 500 mm/s. The near-tip stress fields are analyzed by 3D-FEM considering the strain rate effect on the flow properties of materials. Temperature rise caused by high-speed plastic deformation is also included in the FE analysis. The critical CTOD at brittle fracture initiation decreases when increasing the loading rate. This is due to the elevation of a local stress near the crack tip. The local approach is applied to the dynamic fracture toughness evaluation. It is shown that the brittle fracture resistance evaluated in terms of the Weibull stress, an integrated stress over a highly stressed region near the crack tip, is a material property independent of the loading rate. Based on the Weibull stress fracture criterion, the dynamic fracture toughness can be predicted from static toughness results. An engineering procedure to estimate the loading rate effect on the fracture toughness is also presented.

KEYWORDS: dynamic fracture toughness, CTOD, brittle fracture, structural steels, weld metals, Local Approach, Weibull stress, rate-temperature parameter, 3D dynamic FEM

It is known that the mechanical properties and fracture toughness of structural steels are affected by the strain rate of loading. Generally, the yield stress and tensile strength increase and the fracture toughness decreases when increasing the strain rate. Such material response to the strain rate may facilitate unstable fracture of structural components under the dynamic loading condition. In fact, two recent earthquakes, the Northridge and the Kobe great earthquakes, provoked serious incidents of brittle fracture of steel-framed structures, in particular, at beam-to-column connections. Some were attributed to unsatisfactory fabrication of the connections. However, the importance of material property evaluations considering the strain rate effect was pointed out.

For the characterization of the mechanical properties of bcc materials under dynamic loading, the rate-temperature parameter R proposed by Bennet and Sinclair [*1*] is useful. It has been shown [*2–5*] that the dependence of the yield stress on the strain rate $\dot{\varepsilon}$ and tem-

[1] Associate professor and graduate student, respectively, Department of Manufacturing Science, Graduate School of Engineering, Osaka University, 2-1 Yamada-Oka, Suita, Osaka 565-0871, Japan.
[2] Structural department manager, Katayama Stratech Corporation, 6-2-21 Minami-Okajima, Taisho-ku, Osaka 551-0021 Osaka, Japan.
[3] Principal researcher and senior research engineer, respectively, Corporate Research and Development Laboratories, Sumitomo Metal Industries Ltd., 1-8 Fuso-cho, Amagasaki 660-0891, Japan.

Copyright© 2000 by ASTM International www.astm.org

perature T is uniquely determined by the parameter $R = T \ln (A/\dot{\varepsilon})$, where A is a material constant. Another aspect of the dynamic loading is the generation of heat [*6*]. High-speed plastic deformation does not allow sufficient time for heat conduction, which leads to a temperature rise from the service temperature. In the dynamic fracture toughness evaluation, attention must be paid to the temperature rise effect as well as the strain rate effect on the material properties.

Attempts were made by Toyosada et al. [*4,7*] to analyze the dynamic fracture toughness of structural steels with the rate-temperature parameter R. A local strain rate and a temperature rise near the crack tip were used for the calculation of the parameter R. According to the results, the dynamic fracture toughness seems to be controlled by the parameter R near the crack tip. However, the fracture criterion is not made clear, which should be incorporated with the dynamic stress field. In addition, the constraint effect was not taken into account in the evaluation of the near-tip strain rate of the fracture toughness specimen, which was converted from the remote strain rate of a notched wide plate subjected to tension.

This paper applies the Local Approach [*8,9*] to the dynamic fracture toughness evaluation. The Weibull stress, an integrated stress over a highly stressed region near the crack tip, is used as a fracture-driving force. The near-tip stress field is analyzed by 3D dynamic FEM, where the mechanical properties of materials are incorporated as a function of the rate-temperature parameter R. The dynamic fracture toughness is predicted from static toughness results under the assertion that the critical Weibull stress at brittle fracture initiation is a material property independent of the strain rate.

Material Properties of Structural Steels and Weld Metals Under Dynamic Loading

Experiments

Firstly, the strain rate effect on the mechanical properties and fracture toughness of recent structural steels and weld metals was examined. High-strength steels of 490-MPa strength class, SN490B-I and SN490B-II steels, with a plate thickness of 25 mm were used. SN490B-I steel was of a conventional type and SN490B-II a developed steel for large heat input welding of column-to-beam connections. Tensile properties of these steels were similar, but SN490B-II had a superior fracture toughness than SN490B-I. Electrogas arc welding was conducted for these two steels with a heat input of 17.2 MJ/m with a half-K groove preparation [*10*]. The shield gas used was 100% CO_2. Table 1 gives the chemical composition and mechanical properties of the base and weld metals. The mechanical properties of the weld metals differed slightly, although the welding wire and heat input conditions were the same between the two welds.

From these steels and welded joints, the round-bar tension specimen and compact specimen were extracted. Figure 1 shows the configuration of the specimens. The round-bar specimen had a gage length of 32 mm with a diameter of 6 mm. The specimen taken from the welds consisted of all the weld metals. The compact specimen was of a standard type specified in the fracture toughness test. The notch for the weld metal was located at the center of the welds.

The round-bar tension test was conducted in the temperature range -150 to 40°C at the crosshead speed of 0.025 to 1000 mm/s. A longer specimen was used for medium- to high-speed loading (crosshead speed: 12, 300 and 1000 mm/s). The load was calibrated using a strain gage attached on the specimen surface to reduce a dynamic noise during loading. An optical extensometer was employed to measure the displacement over a reduced gage length of 24 mm marked within the test section. Another specimen was used for the static tests at crosshead speeds of 0.025 and 0.1 mm/s. The load was measured with a load cell, and the

TABLE 1—*Chemical composition and mechanical properties of structural steels of 490-MPa strength class and weld metals used.*

	Chemical Composition, Mass %						
	C	Si	Mn	P	S	Ti	C_{eq}
SN490B-I	0.17	0.36	1.36	0.011	0.002	—	0.42
SN490B-II	0.14	0.36	1.29	0.010	0.003	0.01	0.37
Weld metal (SN490B-I welds)	0.077	0.45	1.70	0.012	0.010	0.04	0.40
Weld metal (SN490B-II welds)	0.062	0.36	1.67	0.012	0.011	0.03	0.38

C_{eq} = C + Mn/6 + (Cr + Mo + V)/5 + (Cu + Ni)/15.

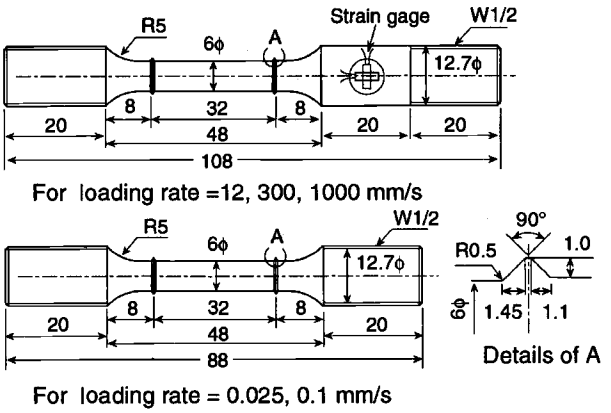
	Mechanical Properties							
	σ_Y, MPa	σ_T, MPa	YR, %	ε_T, %	El., %	RA, %	vE_0, J	vTrs, °C
SN490B-I	334	518	64.5	15.6	29.4	80.8	154	−19
SN490B-II	352	481	73.0	12.9	27.2	81.9	294	−70
Weld metal (SN490B-I welds)	391	566	69.1	13.8	24.1	68.8	95	7
Weld metal (SN490B-II welds)	358	500	71.6	13.4	25.7	72.9	113	−16

NOTES:
σ_Y = lower yield stress, σ_T = tensile strength.
YR = yield-to-tensile ratio (σ_Y/σ_T), *RA* = reduction in area.
ε_T = uniform elongation, El. = elongation (G.L. = 32 mm, Dia. = 6 mm).
vE_0 ;= Charpy energy at 0°C, vTrs = fracture transition temperature.

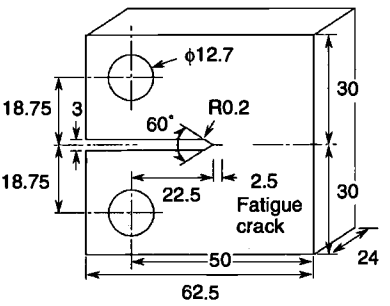
displacement over the original gage length of 32 mm was measured with an inductive transducer. The contraction of the diameter was also measured with a micrometer during the test at a room temperature with the crosshead speed of 0.025 mm. The compact specimen was loaded at a crosshead speed of 0.1 to 500 mm/s in the temperature range −130 to 45°C. The crack mouth displacement was measured using a low compliance clip gage of a double cantilever type. The crack tip opening displacement (CTOD) was calculated from the crack mouth displacement according to the procedure specified in the British Standard of Fracture Mechanics Toughness Tests—Part 1, Method for Determination of K_{Ic}, Critical CTOD and Critical *J* Values of Metallic Materials (BS7448-Part 1).

Strain Rate Effect on Mechanical Properties

Figure 2 shows the change in the nominal stress and strain with the loading time at crosshead speeds of 0.1 and 12 mm/s for SN490B-I steel. After yielding, an almost linear relationship is found between the nominal strain and time. In this paper, an average of the plastic strain rate up to the maximum load was defined as the strain rate of loading. The strain rate ranged from 0.001/s to 30/s depending on the crosshead speed. Figure 3 exhibits the strain rate effect on the yield stress and tensile strength of SN490B-I and SN490B-II steels. The yield stress σ_Y depends to a larger extent on the strain rate than the tensile strength σ_T. As a result, the yield ratio, $YR = \sigma_Y/\sigma_T$, increases when increasing the strain rate. In Fig. 4, the uniform elongation is given, which is the nominal strain at the attainment of a



(a) Round-bar tension specimens



(b) Compact specimen

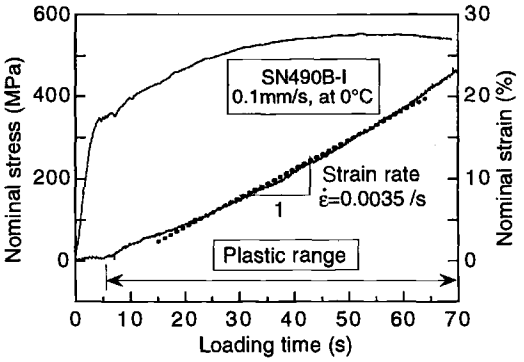
FIG. 1—*Test specimens used.*

maximum load. The uniform elongation seems to be independent of the strain rate. These tensile properties under dynamic loading are consistent with the published reports [*11–13*]. A similar tendency was observed in the round-bar tension test of the weld metals.

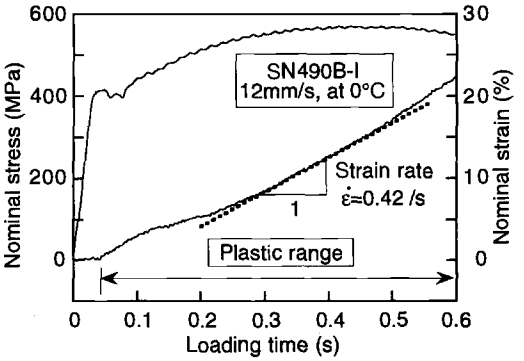
The rate-temperature parameter R proposed by Bennet and Sinclair [*1*] was applied for the evaluation of the strain rate effect on the tensile properties. The R-parameter considering the temperature rise during loading is expressed as

$$R = (T + \Delta T) \cdot \ln(A/\dot{\varepsilon}) \tag{1}$$

where $\dot{\varepsilon}$ is the strain rate, T and ΔT are the test temperature and temperature rise, respectively,



(a) Crosshead speed of 0.1 mm/s



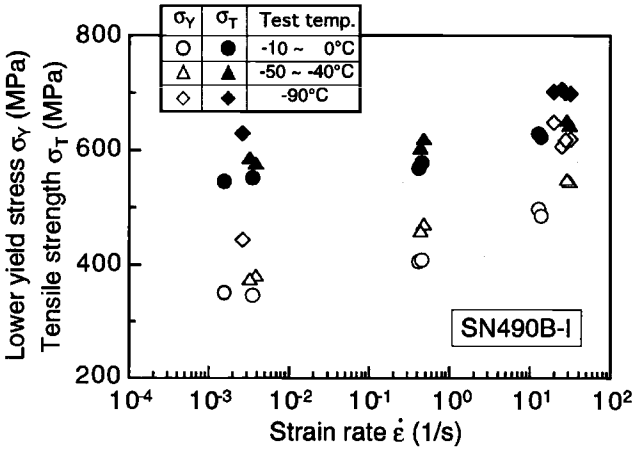
(b) Crosshead speed of 12 mm/s

FIG. 2—*Change in nominal stress and nominal strain with time during round-bar tension test.*

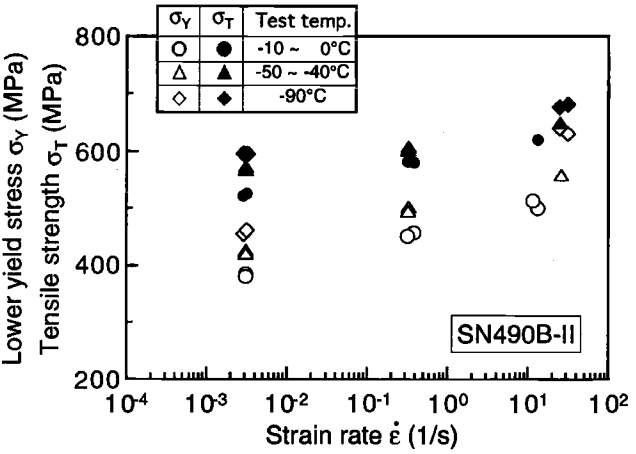
and A is a material constant. The temperature rise ΔT was computed by a dynamic FE analysis described later. It is known that the yield stress σ_Y shows the Arrehenius-type dependence on the temperature [*14*]. Accordingly, the yield stress σ_Y would be given in the form

$$\sigma_Y = B \cdot \exp\,(C/R) \tag{2}$$

as a function of the parameter R, where B and C are material constants [*3,15*]. Figure 5 shows the relationship between the parameter R and the yield stress σ_Y. The tensile strength

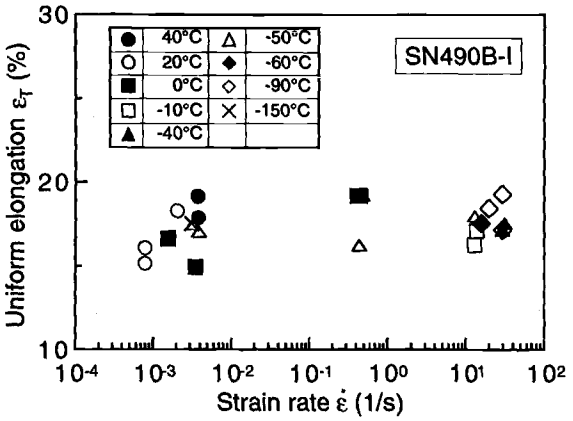


(a) SN490B-I steel

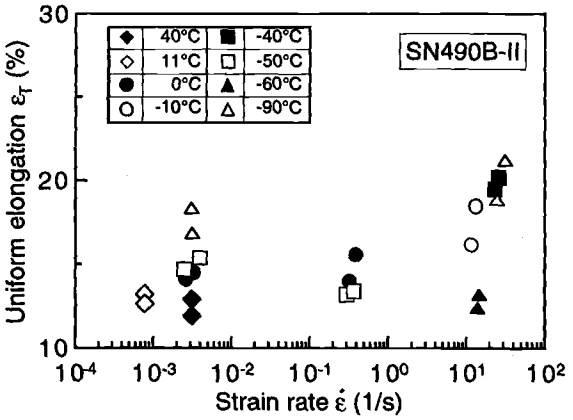


(b) SN490B-II steel

FIG. 3—*Effect of strain rate on yield stress* σ_Y *and tensile strength* σ_T

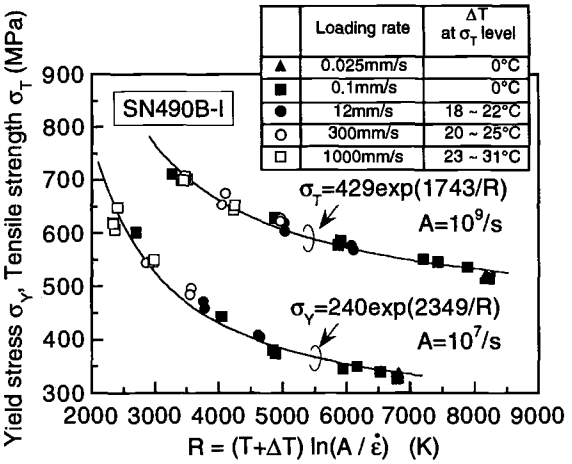


(a) SN490B-I steel

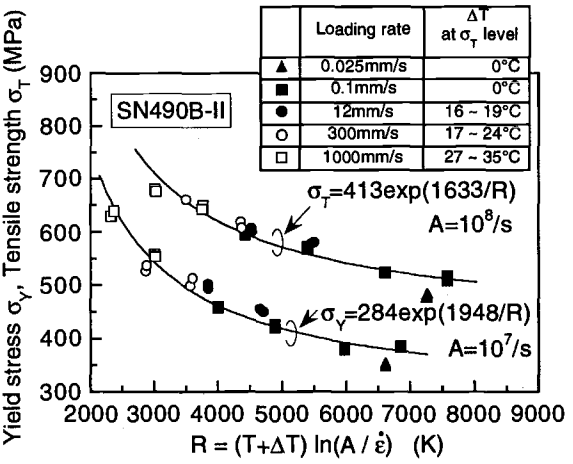


(b) SN490B-II steel

FIG. 4—*Effect of strain rate on uniform elongation* ε_T.

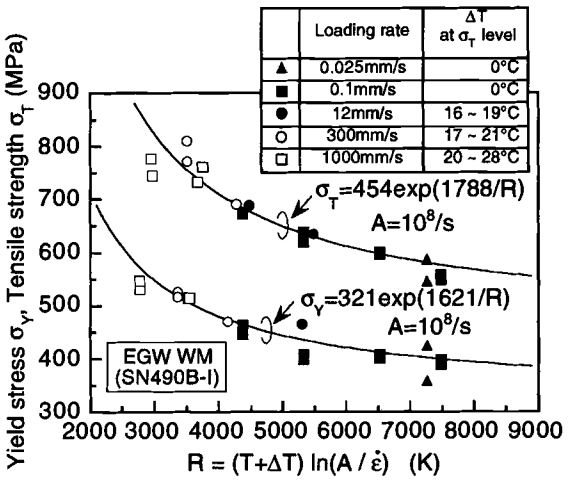


(a) SN490B-I steel

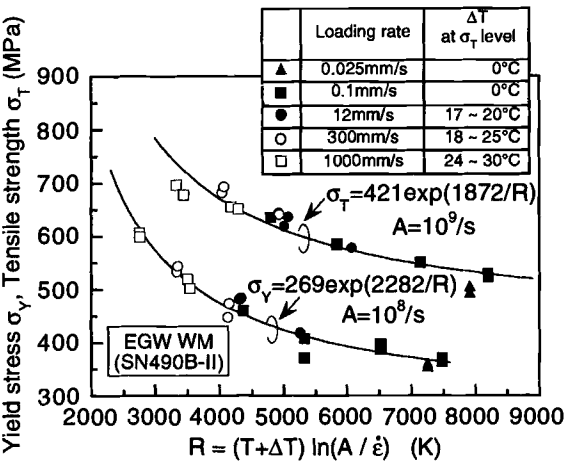


(b) SN490B-II steel

FIG. 5—*Characterization of yield stress and tensile strength with rate-temperature parameter* R.



(c) Weld metal in SN490B-I welds



(d) Weld metal in SN490B-II welds

FIG. 5—*Continued.*

σ_T was also arranged with the parameter R. It is found that behaviors of the yield stress and tensile strength at different test conditions are controlled by the parameter R [2–5]. The A-values determined by a regression analysis were 10^7 to 10^8/s and 10^8 to 10^9/s for the yield stress and tensile strength, respectively, which were compatible with $A = 10^8$/s reported by Bennet and Sinclair [1].

Strain Rate Effect on Fracture Toughness

Figure 6 shows the fracture toughness results for the base and weld metals. The critical CTOD was classified into three categories according to the British Standard BS7448-Part 1: (1) δ_c – critical CTOD at the onset of brittle fracture with stable crack growth less than 0.2 mm, (2) δ_u – one with stable crack growth equal to or greater than 0.2 mm, and (3) δ_m – CTOD value at the first attainment of the maximum load plateau for a fully ductile fracture. The maximum crack growth in δ_u mode fracture was 1.2 mm for the materials tested. The effect of the loading rate on the yield stress, which may decrease the elastic component of CTOD in the case of high-speed loading, was not considered in the calculation of the CTOD value, because a careful discussion is necessary for the definition of the strain rate of the compact specimen. Nevertheless, the high-speed loading results in a lower critical CTOD and raises the fracture transition temperature.

Dynamic Stress Fields Near Crack Tip Region

FE Analysis

Stress fields near the crack tip play an important role in the fracture toughness properties under dynamic loading. Near-tip stress fields of the compact specimen were analyzed by 3-dimensional FEM using the FE code, ABAQUS ver. 5.7, which included the procedure to solve the temperature and stress/displacement fields simultaneously.

Figure 7 shows the FE models used. Because of symmetry, one quarter of the compact specimen was modeled. The width of the weld metal was 10 mm in the weld metal notched specimen, which was based on the measurement. In thickness direction, the models had six layers. Elements used were 8-node isoparametric elements with 8 Gaussian points. The mesh division near the crack tip was common between the base steel specimen and weld metal notched specimen. Fine and coarse meshes were employed for the crack tip element depending on the CTOD level: 0.01 by 0.01 by 0.5 mm for CTOD $\leq$ 0.1 mm and 0.1 by 0.1 by 0.5 mm for CTOD $>$ 0.1 mm. AT CTOD = 0.1 mm, the fine and coarse meshes presented almost the same stresses/strains near the crack tip.

The flow properties of materials in the FEM follow the strain hardening in the form

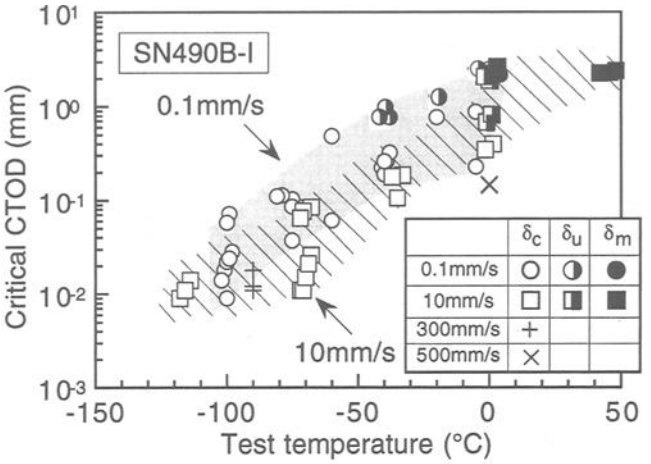
$$\bar{\sigma} = \sigma_Y \cdot (1 + \bar{\varepsilon}_p/\alpha)^n \tag{3}$$

where $\bar{\sigma}$ and $\bar{\varepsilon}_p$ are the equivalent stress and equivalent plastic strain, respectively, σ_Y is the yield stress, n is the strain-hardening exponent, and α is a material constant. According to Eq 3, the tensile strength σ_T and the uniform elongation ε_T are given by

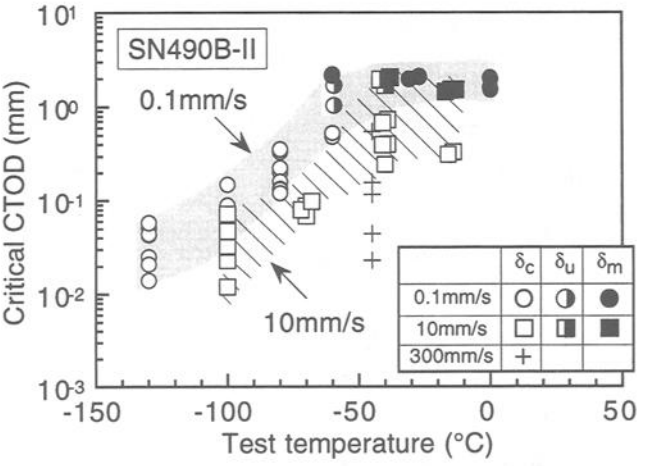
$$\sigma_T = \sigma_Y \cdot (n/\alpha)^n \cdot \exp(\alpha - n) \tag{4}$$

$$\varepsilon_T = \exp(n - \alpha) - 1 \tag{5}$$

The dependence of σ_T on the strain rate $\dot{\varepsilon}$ was simulated using the Cowper-Symonds model

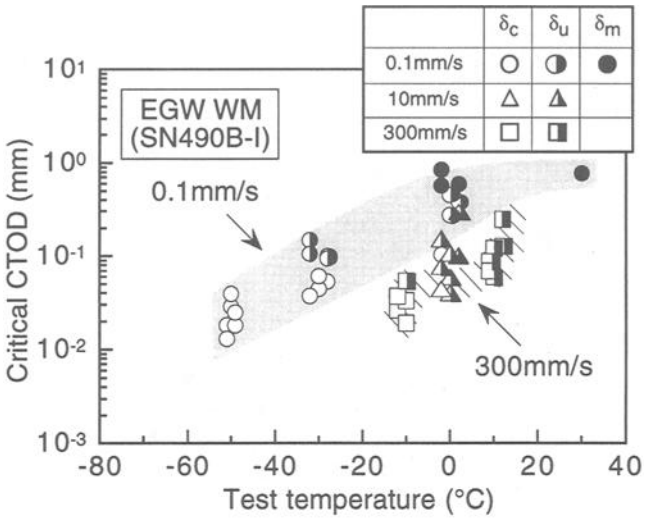


(a) SN490B-I steel



(b) SN490B-II steel

FIG. 6—*Temperature dependence of critical CTOD at different loading rates.*



(c) Weld metal in SN490B-I welds

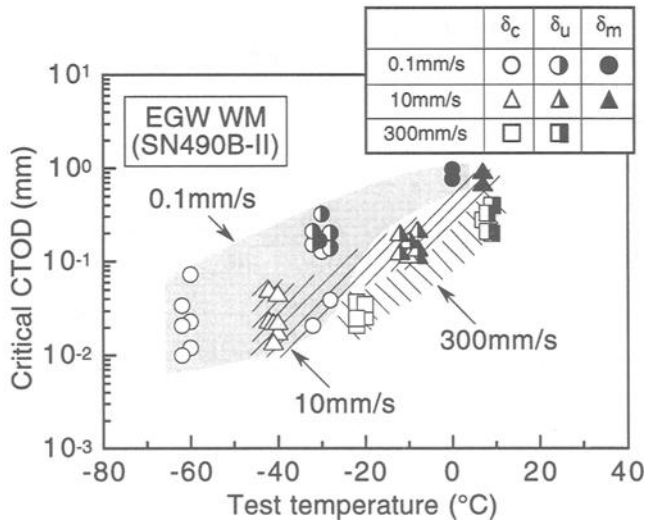
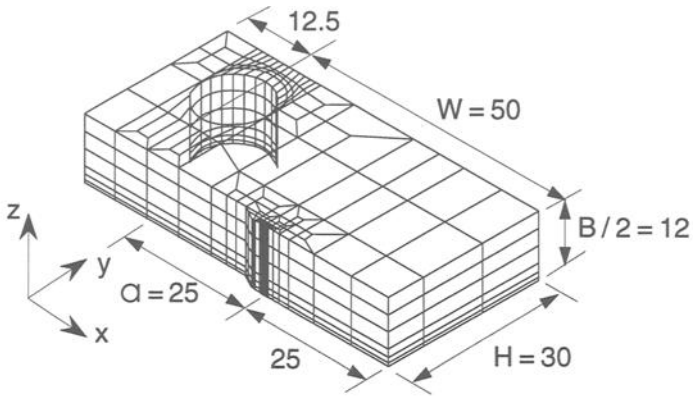
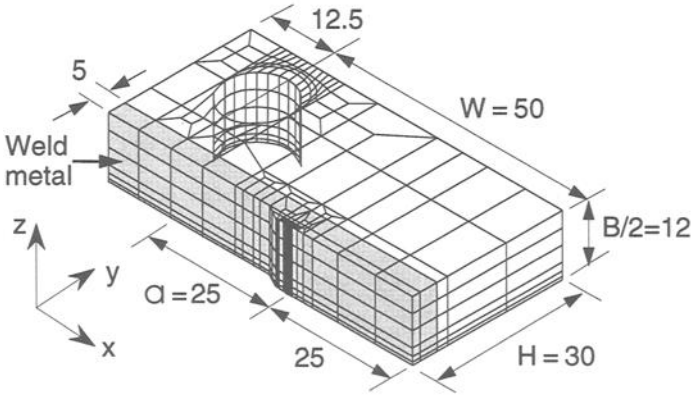


FIG. 6—*Continued.*



(a) Base steel specimen



(b) Weld metal notched specimen

FIG. 7—*Models of compact specimen used for FE analysis.*

$$\sigma_T(\dot{\varepsilon}) = \sigma_{T0} \cdot [1 + (\dot{\varepsilon}/p)^{1/q}] \tag{6}$$

where σ_{T0} is the static tensile strength. The σ_T-value at the strain rate of $\dot{\varepsilon} = 10^{-4}$/s was adopted as σ_{T0}. Parameters p and q were determined in a manner that the tensile strength σ_T given by Eq 6 consisted with the results characterized by the R-parameter (see Fig. 5). The σ_{T0}, p, and q values used for the FE analysis are listed in Table 2. Since the uniform elongation ε_T was not affected by the strain rate (Fig. 4), the exponent $(n - \alpha)$ was assigned to be independent of the strain rate. The n and α were determined in the light of round-bar tension results with attention to the strain rate effect on the yield ratio, YR. The n and α in the FE analysis ranged from 0.14 to 0.22 and 0.004 to 0.06, respectively, depending on the material and test conditions.

Dynamic loading will give rise to heat generation. In the FE analysis, the temperature rise ΔT was calculated under the assumption that 90% of the plastic work, $0.9 \int \bar{\sigma}\, d\bar{\varepsilon}_p$, is transferred to heat [*16*]. Table 3 gives the thermal constants used for the analysis. Heat conduction during loading was also considered, while its effect was expected to be marginal under a high-speed loading. The temperature rise exerts an influence on the flow properties of the material. The FE code, ABAQUS ver. 5.7, provides a fully coupled, simultaneous heat transfer and stress analysis.

Analysis of Round-Bar Specimen

In order to check the reliability of material parameters adopted in the FEM, the round-bar tension specimen was also analyzed. Figure 8 compares the tension results for SN490-I steel at the loading rate of 12 mm/s obtained by the experiment and FE analysis. The nominal stress-strain relationship and the variation of the strain rate at each instance are shown. The computed results are almost consistent with the experimental measurements. It can be seen that the temperature rise ΔT at the onset of yielding is negligibly small and that a substantial temperature rise occurs after yielding. The ΔT value computed at the maximum load is tabulated in Fig. 5. It was at most 35°C even if the highest loading rate of 1000 mm/s was applied.

A 9% Ni steel was tested additionally at a room temperature with the crosshead speed of 300 mm/s to examine the temperature rise during loading. The dimensions of the 9% Ni specimen were 10 mm in gage length and 8 mm in diameter at the test section. The temperature was measured on a mid-surface of the specimen with a Cu-Constantan thermocouple of diameter 0.072 mm. Figure 9 shows the change in the specimen temperature, machine stroke, and the load with the time. The temperature rise ΔT at the attainment of a maximum load was about 30°C, although a significant amount of ΔT was observed after the maximum load. The FE results are also given in Fig. 9. Material parameters for the analysis were determined in the same manner as described before. It is found that the temperature rise ΔT during loading is properly simulated by the FEM.

Stress/Strain and Temperature Fields of Compact Specimen Under Dynamic Loading

Stress/strain fields and a temperature rise near the crack tip of the compact specimen under dynamic loading are discussed. Figure 10*a* shows the distributions of the maximum principal stress near the crack tip at mid-thickness of the specimen for SN490B-I steel in a small-scale yielding (CTOD = 0.06 mm) and large-scale yielding (CTOD = 0.4 mm) conditions. Yielding states are determined in the light of the plastic zone size r_p ahead of the crack tip; for instance, at a loading rate of 10 mm/s, r_p at CTOD = 0.06 mm is 0.4 mm $\ll$ a (crack length) = 25 mm, and r_p at CTOD = 0.4 mm is 7 mm, which does not meet the

TABLE 2—*Material parameters p, q and static tensile strength* σ_{T0} *in Cowper-Symonds model for dynamic FE analysis.*

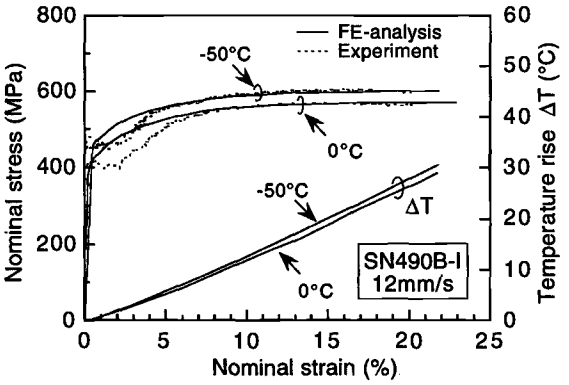
Temp., °C	SN490B-I			SN490B-II			Weld Metal (SN490B-I welds)			Weld Metal (SN490B-II welds)		
	σ_{T0}, MPa	$p(/s)$	q	σ_{T0}, MPa	$p(/s)$	q	σ_{T0}, MPa	$p(/s)$	q	σ_{T0}, MPa	$p(/s)$	q
20	523	1.42×10^5	4.84	505	4.98×10^4	4.68	566	9.38×10^4	5.21	521	3.63×10^5	5.42
0	531	9.64×10^4	4.82	513	3.41×10^4	4.67	575	6.10×10^4	5.19	529	2.33×10^5	5.41
−20	540	6.35×10^4	4.81	522	2.27×10^4	4.66	586	3.84×10^4	5.17	539	1.45×10^5	5.39
−40	551	4.04×10^4	4.80	532	1.45×10^4	4.64	599	2.31×10^4	5.15	550	8.65×10^4	5.37
−60	564	2.46×10^4	4.78	546	8.94×10^3	4.62	615	1.33×10^4	5.12	565	4.91×10^4	4.91
−80	581	1.42×10^4	4.76	561	5.22×10^3	4.60	635	7.23×10^3	5.08	582	2.63×10^4	5.31
−100	601	7.72×10^3	4.73	581	2.87×10^3	4.57						

σ_{T0} = Tensile strength at strain rate of 10^{-4}/s; p and q = parameters in Cowper-Symonds model.

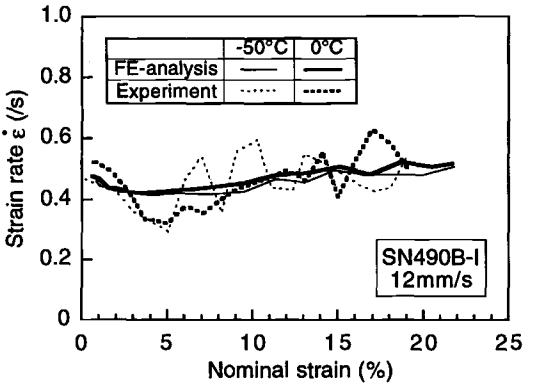
TABLE 3—*Thermal constants used for FE-analysis.*

c (J/(kg · K))	ρ (kg/mm^3)	κ (m^2/s)	β (1/K)
4.8×10^2	8.0×10^{-6}	2.17×10^{-5}	1.2×10^{-5}

NOTE: c = specific heat, ρ = density, κ = heat conductivity, β = coefficient of heat.



(a) Nominal stress versus nominal strain curve



(b) Variation of strain rate during loading

FIG. 8—*Round-bar tension results obtained by experiment and FE analysis.*

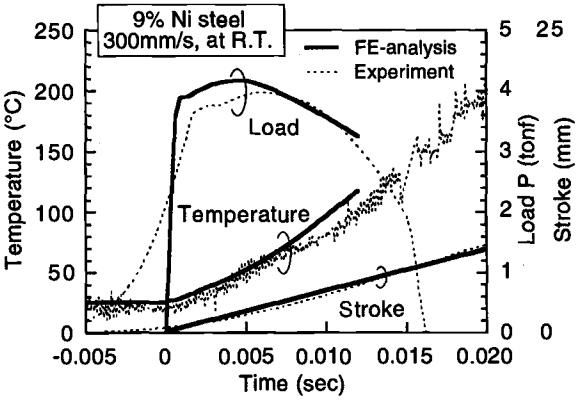
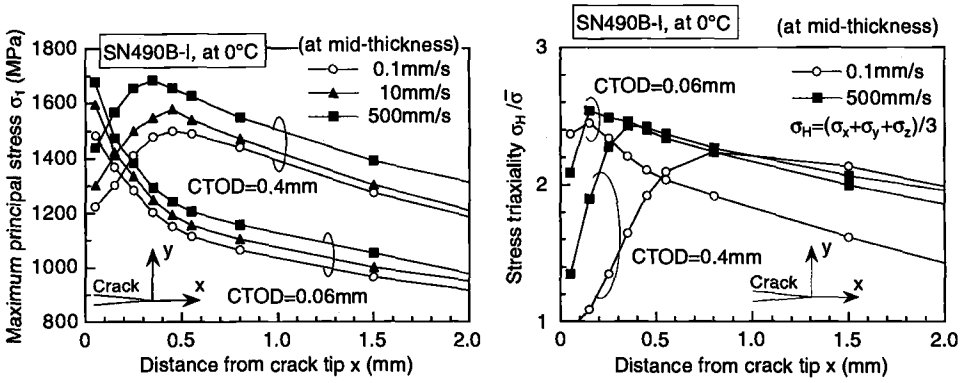


FIG. 9—*Temperature rise during round-bar tension test of 9% Ni steel at crosshead speed of 300 mm/s.*

SSY condition specified in ASTM Standard Test Method for Plane-Strain Fracture Toughness of Metallic Materials (ASTM E 399). In both SSY and LSY conditions, high-speed loading elevates the near-tip stress to a large extent. This is due to the strain rate effect on the flow properties of the material. Figure 10*b* shows the near-tip stress triaxiality $\sigma_H/\bar{\sigma}$, where σ_H is the hydrostatic stress and $\bar{\sigma}$ is the equivalent stress (von Mises stress). The stress triaxiality is also elevated by increasing the loading rate. It is noted that the maximum triaxiality at CTOD = 0.06 mm is higher than one at CTOD = 0.4 mm, although the peak stresses at these CTOD levels were almost the same (Fig. 10*a*).

Figure 11 shows the distributions of the strain rate near the crack tip. The strain rate was calculated at each element from the increment of the equivalent plastic strain with time. The near-tip strain rate depends significantly on the loading rate. It is noted that the strain rate distributions are almost parallel to each other and scaled with the loading rate. Figure 12



(a) Maximum principal stress (b) Stress triaxiality

FIG. 10—*Effect of loading rate on stress fields near crack tip of compact specimen.*

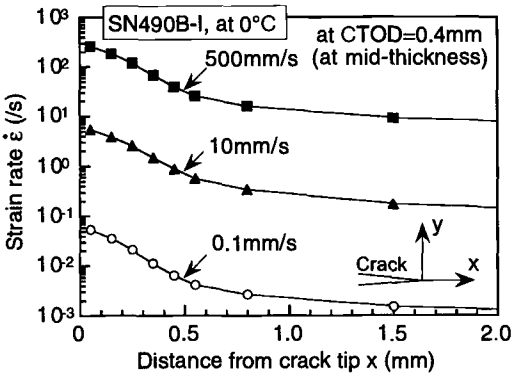


FIG. 11—*Distribution of strain rate near crack tip of compact specimen at different loading rates.*

draws the change in the near-tip strain rate with the CTOD, where a local strain rate at the location of a peak stress is focused. Except for an initial stage, the near-tip strain rate $\dot{\varepsilon}$ maintains a certain level approximated by $\dot{\varepsilon} = v/10$, where v is the loading rate in mm/s.

The dynamic compact test will generate heat near the crack tip. Figure 13 shows the temperature rise ahead of the crack tip computed by FEM at the CTOD level of 0.4 mm. In Fig. 14, a local temperature rise at the location of the peak stress is plotted versus CTOD. High-speed loading produces a marked temperature rise in the vicinity of the crack tip. However, the amount of temperature rise is not large enough to change the flow properties of the material dramatically; for instance, a 30°C temperature rise leads to only 6% change in the yield strength. This would be related to a steep gradient of stresses and strains near the crack tip; intensive plastic deformation is localized at the crack tip region. In the case of low and medium loading rates, the temperature rise was at most 6°C at a CTOD level less than 1.0 mm.

The rate-temperature parameter $R = (T + \Delta T) \ln (A/\dot{\varepsilon})$ was calculated on the basis of FE results with $A = 10^9$/s for SN490B-I steel. Figure 15 shows the distributions of the parameter R near the crack tip at CTOD levels of 0.06 and 0.4 mm. The maximum principal stress

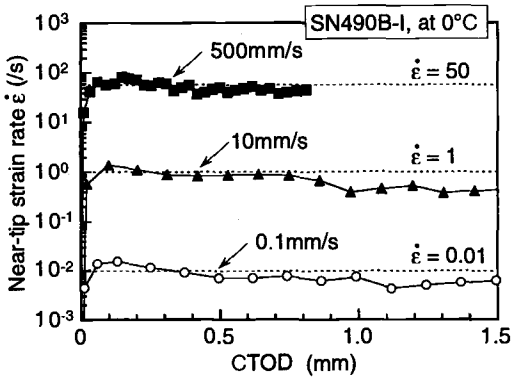


FIG. 12—*Change in near-tip strain rate with CTOD for compact specimen, where strain rate was evaluated at a region including peak value of maximum principal stress.*

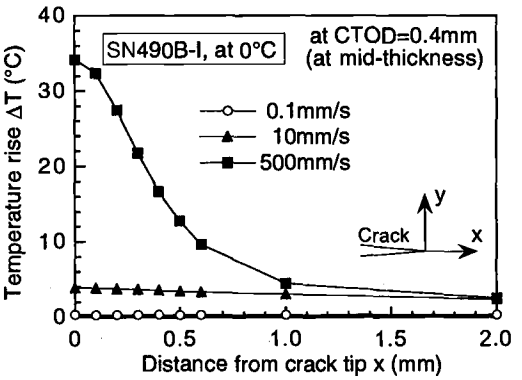


FIG. 13—*Temperature rise near crack tip of compact specimen at different loading rates.*

described in Fig. 10 is also given. The parameter R increases monotonically with the distance from the crack tip, approaching to a threshold value. This implies that the R-parameter in the vicinity of the crack tip is controlled mainly by the strain rate and that the contribution of the temperature rise ΔT is rather weak. At CTOD = 0.06 mm in the small-scale yielding (SSY), the near-tip peak stress is linked with the lowest R-value. In the case of large-scale yielding (LSY), however, such a feature is not observed. The location of the peak stress in LSY would be related to the stress triaxiality ahead of the crack tip. The stress/strain fields for the specimen with a notch in the weld metal were very similar to those for the base steel specimen.

Local Approach to Dynamic Fracture Toughness Evaluation

Fracture Resistance Evaluation by the Weibull Stress

With the properties of near crack tip stress fields in mind, this paper applies the Local Approach [*8,9*] to the dynamic fracture toughness evaluation. The Local Approach is based

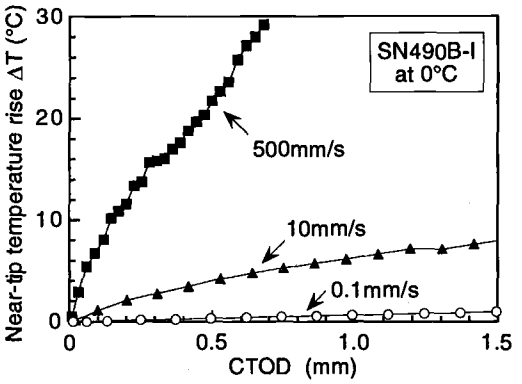
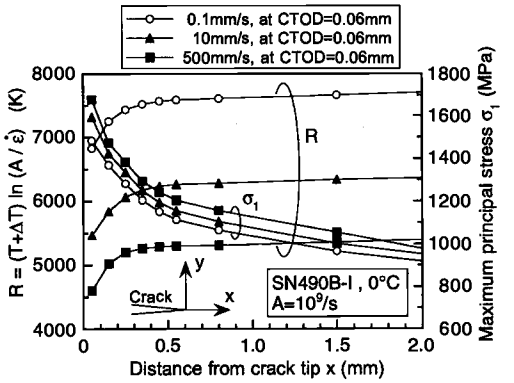
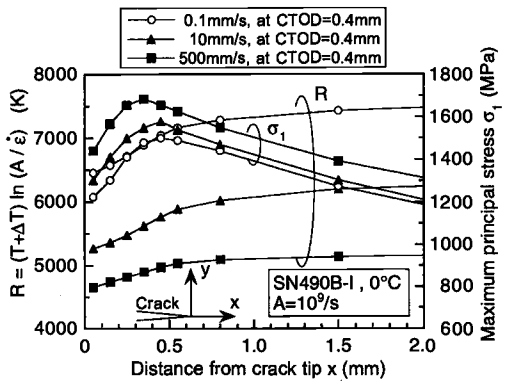


FIG. 14—*Change in near-tip temperature rise* ΔT *with CTOD for compact specimen, where* ΔT *was evaluated at a region including peak value of maximum principal stress.*



(a) at CTOD = 0.06 mm in small scale yielding condition



(b) at CTOD = 0.4 mm in large scale yielding condition

FIG. 15—*Distributions of parameter* R *and maximum principal stress near crack tip at different loading rates.*

on a local instability of microcracks near the crack tip and assumes that the weakest microcrack controls the unstable fracture of materials. Such characterization led to a new parameter of fracture driving force, the so-called Weibull stress. The Weibull stress is given by

$$\sigma_W = \left[\frac{1}{V_0}\int_{V_f} [\sigma_{\text{eff}}]^m \, dV_f\right]^{1/m} \tag{7}$$

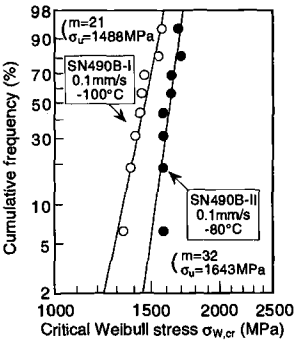
where σ_{eff} is an effective stress in a small volume dV_f in the fracture process zone, m is a shape parameter for the material, and V_0 and V_f are a reference volume defined in the Local Approach and the volume of the fracture process zone, respectively. The m-value reflects

the distribution of microcracks for the material and generally is in the range 10 to 40 [*8,17–23*]. The critical Weibull stress $\sigma_{W,cr}$ at brittle fracture initiation obeys the Weibull distribution with two parameters

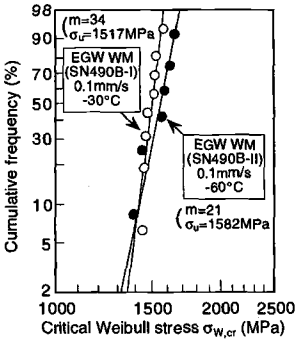
$$F(\sigma_{W,cr}) = 1 - \exp\left[-\left(\frac{\sigma_{W,cr}}{\sigma_u}\right)^m\right] \tag{8}$$

where m (shape parameter) and σ_u (scale parameter) are assumed to be a material property independent of the specimen geometry. The scale parameter σ_u is associated with the toughness level of the material, the microcrack distribution, and the reference volume V_0.

This paper aims at predicting the dynamic fracture toughness from static toughness results based on the Weibull stress fracture criterion. Since the m-value does not depend on V_0, a unit volume for V_0 is convenient for calculating the Weibull stress [*20*]. The selection of V_0 does not affect the prediction of the dynamic fracture toughness, although the absolute value of the Weibull stress depends on V_0. An iteration procedure [*20*] was employed for the

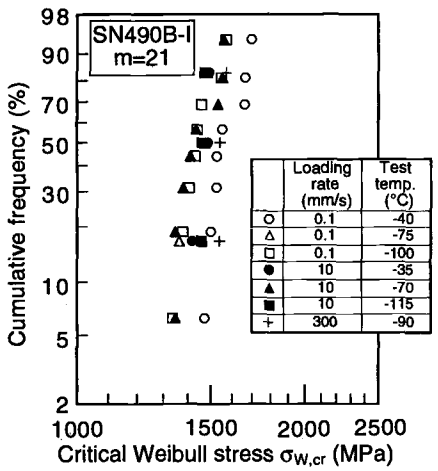


(a) SN490B-I and SN490B-II steels

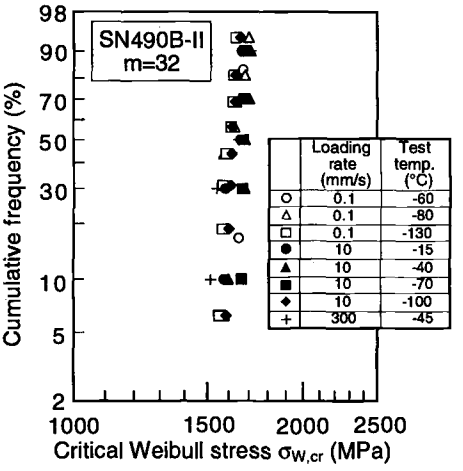


(b) Weld metals in SN490B-I and SN490B-II welds

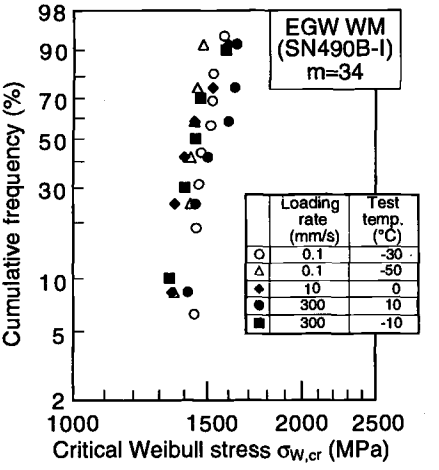
FIG. 16—*Cumulative distributions of critical Weibull stress at brittle fracture initiation at static test.*



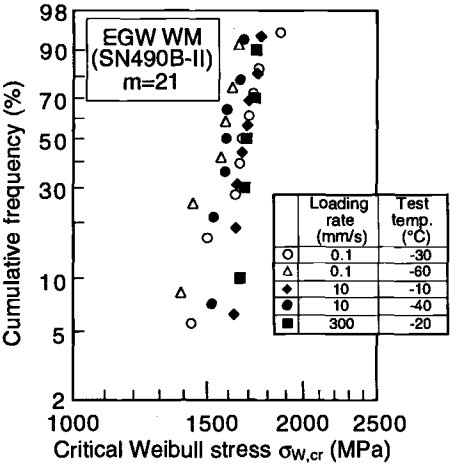
(a) SN490B-I steel



(b) SN490B-II steel

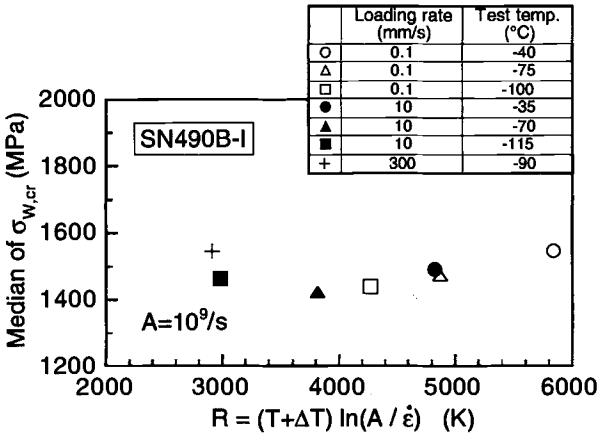


(c) Weld metal in SN490B-I welds

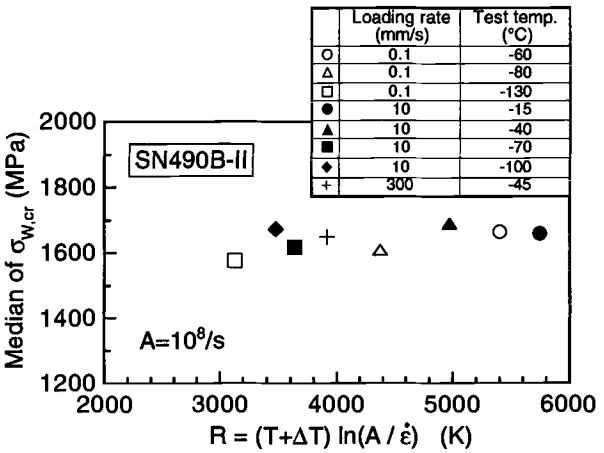


(d) Weld metal in SN490B-II welds

FIG. 17—*Distributions of critical Weibull stress at different loading rates calculated with* m*-value obtained by a static toughness test.*

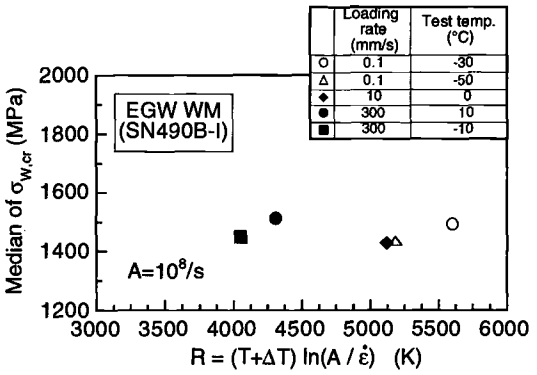


(a) SN490B-I steel

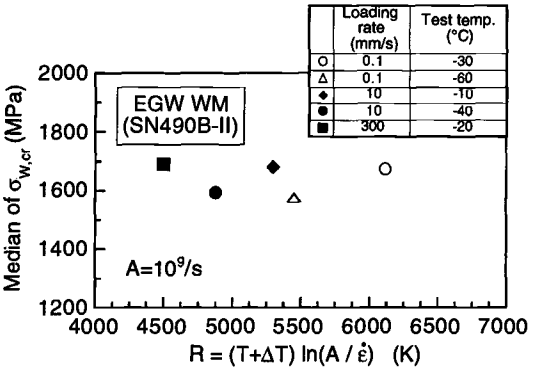


(b) SN490B-II steel

FIG. 18—*Median of critical Weibull stress at different test conditions.*



(c) Weld metal in SN490B-I welds



(d) Weld metal in SN490B-II welds

FIG. 18—*Continued.*

determination of the parameters m and σ_u, where the statistical toughness data are analyzed in conjunction with the near-tip stress fields.

Using the Weibull stress σ_W, the fracture resistance of SN490B-I and SN490B-II steels and weld metals was evaluated. Figure 16 shows the cumulative distributions of the critical Weibull stress $\sigma_{W,cr}$ at brittle fracture initiation under static tests of loading rate 0.1 mm/s. A set of test data, which showed δ_c mode fracture dominantly, was analyzed. The effective stress σ_{eff} in Eq 7 was evaluated considering the multiaxial stress state near the crack tip and

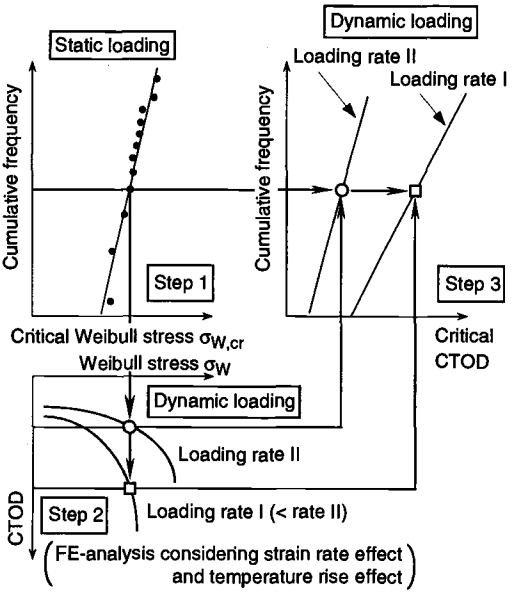


FIG. 19—*Procedure for prediction of dynamic fracture toughness based on the Local Approach.*

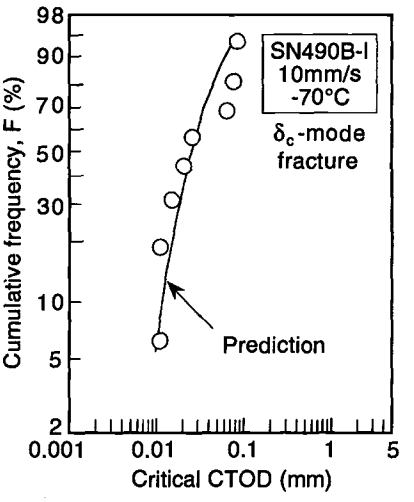
a random spatial distribution of microcracks [*20*]. The *m*-values determined for the materials were in the range 21 to 34.

With the *m*-value obtained from the static toughness results, the critical Weibull stress $\sigma_{W,cr}$ in the dynamic loading condition was calculated. Near-tip stress fields necessary for the calculation of the Weibull stress were addressed from the FE analysis. Figure 17 exhibits the calculated results of the cumulative distributions of $\sigma_{W,cr}$ in different test conditions. Marked effects of the loading rate and test temperature are not observed on the distribution of $\sigma_{W,cr}$. A specific variation in $\sigma_{W,cr}$ from a material aspect is also not found.

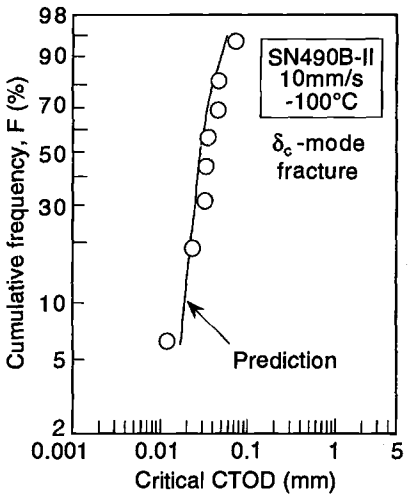
In Fig. 18, the median of $\sigma_{W,cr}$ obtained from Fig. 17 is arranged with the rate-temperature parameter *R*. Since the brittle fracture is of stress-controlled type, the parameter *R* in Fig. 18 was evaluated in a near-tip region including the peak stress at the fracture load level. With respect to the *A*-values, $A = 10^8$ or 10^9/s determined for the tensile strength σ_T was used (see Fig. 5). It can be seen that the median of $\sigma_{W,cr}$ does not depend on the parameter *R*. Namely, the brittle fracture resistance evaluated by the Weibull stress has shown to be a material property independent of the loading rate and test temperature, where the brittle fracture includes δ_c-mode (amount of crack growth, $\Delta a < 0.2$ mm) and δ_u-mode ($\Delta a \geq 0.2$ mm) fractures.

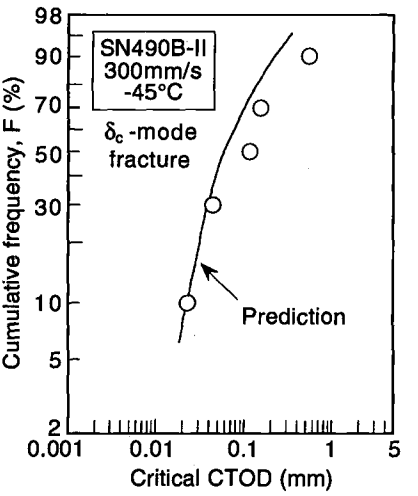
Prediction of Dynamic Fracture Toughness

The strain rate effect on the fracture toughness is predicted in this study based on the Local Approach. Figure 19 shows the procedure for prediction. It was assumed that the critical Weibull stress $\sigma_{W,cr}$ at the onset of brittle fracture is independent of the loading rate and test temperature. In this paper, the statistical distribution of $\sigma_{W,cr}$ determined in Fig. 16 was used as a material property. With the *m*-value obtained in Fig. 16, we calculate the



(a) SN490B-I steel (at 10 mm/s, -70 °C)

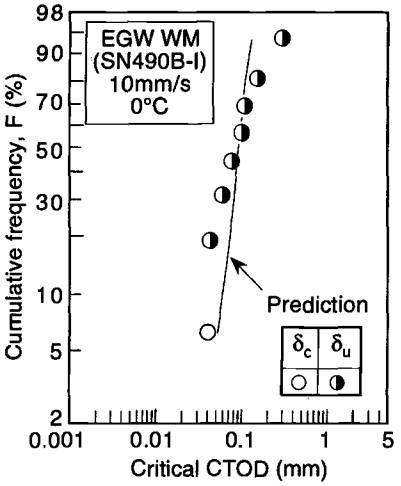




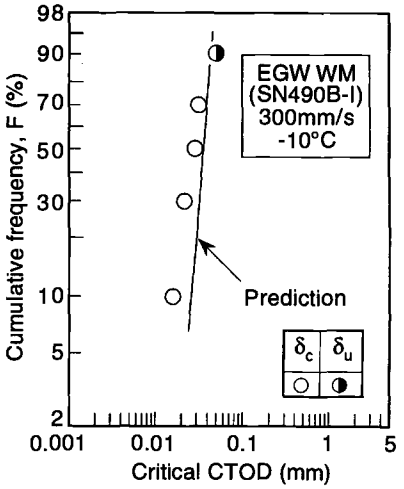
(b-1) at 10 mm/s, -100 °C (b-2) at 300 mm/s, -45 °C

(b) SN490B-II steel

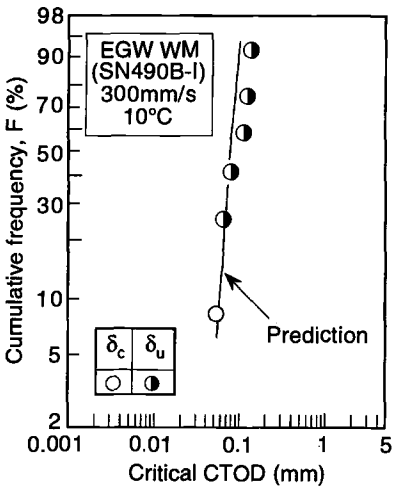
FIG. 20—*Cumulative distributions of critical CTOD at high loading rates predicted by the Local Approach.*



(c-1) at 10 mm/s, 0 °C



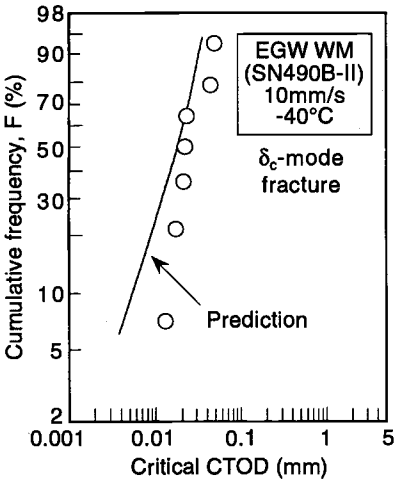
(c-2) at 300 mm/s, -10 °C



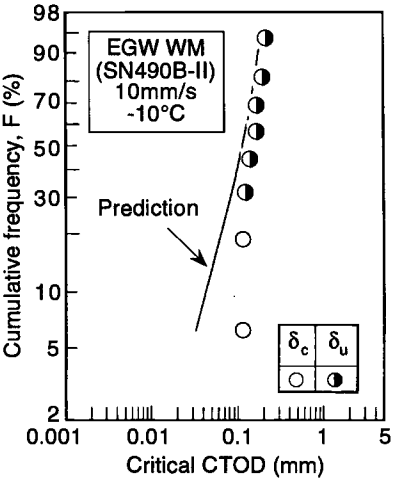
(c-3) at 300 mm/s, 10 °C
(c) Weld metal in SN490B-I welds

FIG. 20—*Continued.*

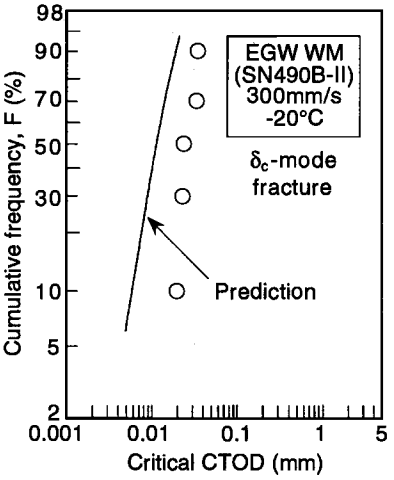
relationship between the Weibull stress σ_W and the CTOD in a dynamic condition of interest. This calculation is performed with the aid of the FE analysis, where the dependence of the flow properties of materials on the strain rate and temperature is considered. Combining the fracture probability with the CTOD by way of the Weibull stress σ_W, the cumulative distribution of the critical CTOD in the target test condition is drawn up.



(d-1) at 10 mm/s, -40 °C



(d-2) at 10 mm/s, -10 °C

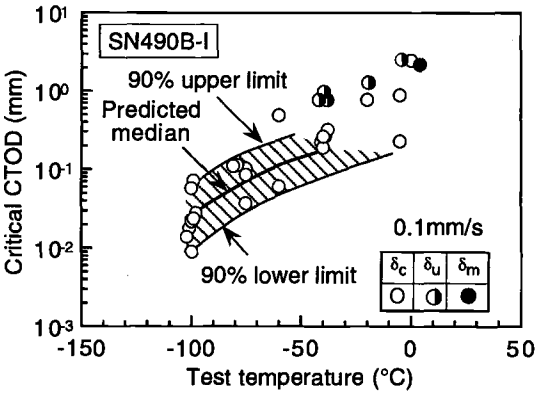


(d-3) at 300 mm/s, -20 °C

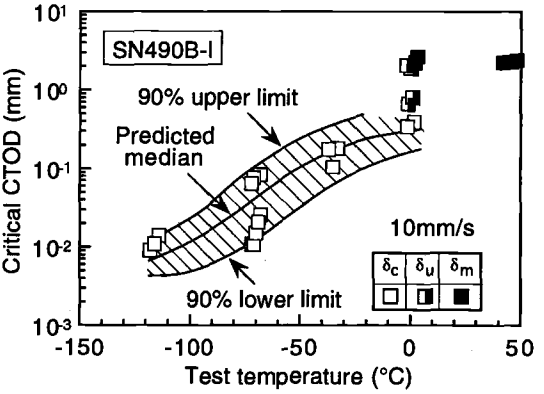
(d) Weld metal in SN490B-II welds

FIG. 20—*Continued.*

Figure 20 displays the predicted distributions of the critical CTOD at loading rates of 10 and 300 mm/s. The predicted distributions are close to those obtained by the experiment, although a slight conservative deviation is found in some cases. It is noted that the results in Fig. 20 give the most likelihood of prediction, and the statistical scatter arising from small sets of fracture toughness data is not taken into account. In Fig. 21, the temperature dependence of the critical CTOD is predicted. The median, 90% upper and lower confidence limits of the critical CTOD correspond to those fractiles of the critical Weibull stress $\sigma_{W,cr}$.



(a) Loading rate of 0.1 mm/s (SN490B-I steel)

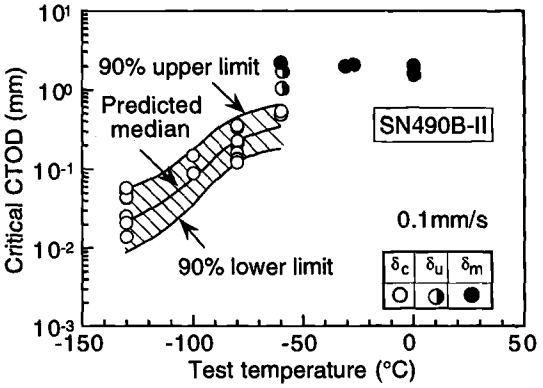


(b) Loading rate of 10 mm/s (SN490B-I steel)

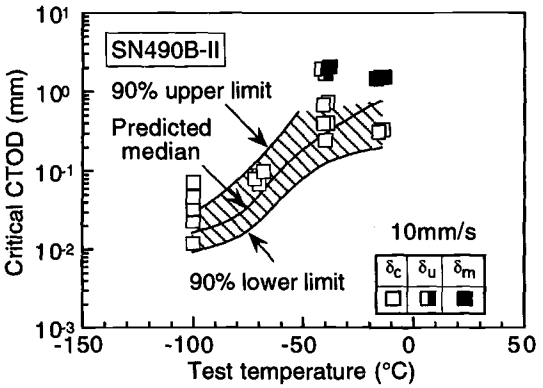
FIG. 21—*Temperature dependence of critical CTOD predicted by the Local Approach.*

The temperature dependence of the critical CTOD predicted is consistent with the experimental results.

The methodology employed in this paper for the dynamic fracture toughness prediction relies on the Weibull stress fracture criterion, where the evolution of the Weibull stress at dynamic conditions is calculated using the shape parameter m determined by the iteration method [*20*]. Recent work [*24*] has pointed out that the m-value determined by this procedure



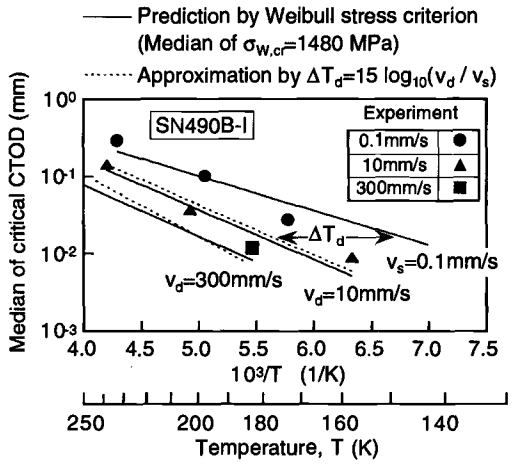
(c) Loading rate of 0.1 mm/s (SN490B-II steel)



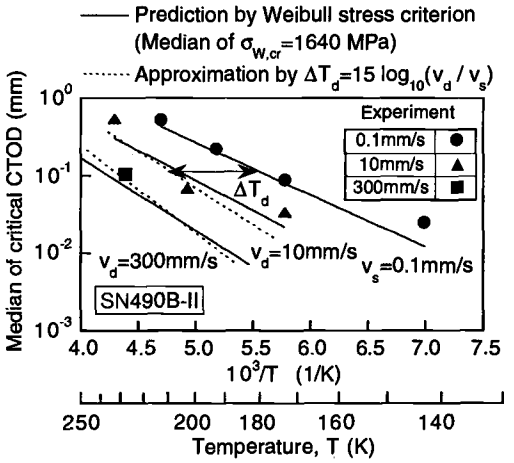
(d) Loading rate of 10 mm/s (SN490B-II steel)

FIG. 21—*Continued.*

is sensitive to FE meshing details, namely non-uniqueness of m-values. A numerical examination was performed on this issue. As a matter of fact, the absolute value of the Weibull stress depends on the m-value used. However, a bias in the m-value determination does not contribute to the toughness prediction significantly. For instances, the use of $m = \hat{m}/2$ and $2\hat{m}$ instead of $m = \hat{m}$ (m-value in Fig. 16 determined by the iteration procedure) hardly affected the predicted results of the dynamic fracture toughness. A similar result was ob-



(a) SN490B-I steel



(b) SN490B-II steel

FIG. 22—*Temperature shift of fracture toughness caused by high-speed loading.*

served in the authors' recent paper [*25*] describing the CTOD ratio $\beta = \delta_{3P.Euiv.}/\delta_{WP}$ between the 3-point bend fracture toughness specimen and a surface-cracked wide plate subjected to tension, where $\delta_{3P.Euiv.}$ was the 3-point bend CTOD equivalent to the wide plate CTOD δ_{WP} in terms of the Weibull stress. The only exception was a case of a small m-value combined with a long surface crack. The Weibull stress σ_W consists of a stress component and a volume component. The stress component is given by $(\sigma_{eff}^m)^{1/m}$ and almost independent of m. On the other hand, the volume component includes the shape parameter m in the form $V_f^{1/m}$.

This term becomes significant when a large process zone V_f is combined with a small m-value.

Nevertheless, as demonstrated in Figs. 20 and 21, the Weibull stress fracture criterion is useful to predict the loading rate effect on the fracture toughness. Figure 22 shows the temperature shift of the fracture toughness caused by dynamic loading, where the median of the critical CTOD is focused. The solid line presents the strict evaluation of the temperature shift ΔT_d according to the Weibull stress fracture criterion, and the dotted line gives an approximation by

$$\Delta T_d = 15 \log_{10} (\nu_d/\nu_s) \tag{9}$$

where ν_d and ν_s are the dynamic and static loading rates (ν_s = 0.1 mm/s in this paper), respectively. Equation 9 may be used as an engineering estimation of the loading rate effect on the critical CTOD for structural steels of the 490-MPa strength class; the critical CTOD at a dynamic loading rate ν_d at test temperature T is almost equivalent to the critical CTOD at the static test at test temperature $T - \Delta T_d$. In this paper, the critical CTOD analyzed was in the range 0.01 to 0.5 mm.

Conclusions

The loading rate effect on the fracture toughness was investigated by the Local Approach for high-strength structural steels of the 490-MPa class and weld metals. The critical CTOD is affected by the loading rate to a large extent, which decreases when increasing the loading rate. By contrast, the brittle fracture resistance evaluated in terms of the Weibull stress can be considered as a material property independent of the loading rate. Using the Weibull stress fracture criterion, the loading rate effect on the critical CTOD can be predicted from static roughness results. The prediction is made by finding the CTOD level at which the Weibull stress in a dynamic condition reaches the critical Weibull stress at the static test. The Weibull stress criterion led to an engineering procedure to estimate the temperature shift of the dynamic fracture toughness from static toughness results. The critical CTOD shifts by approximately +15°C with an increase of loading rate by a factor by 10 for structural steels of the 490-MPa strength class.

Acknowledgments

Tension test and fracture toughness tests of SN490B-I steel were conducted as a sub-task of the APD II Committee in the Japan Welding Engineering Society. Technical discussions and cordial arrangements by the Committee members are highly acknowledged.

References

[1] Bennett, P. E. and Sinclair, G. M., "Parameter Representation of Low-Temperature Yield Behavior of Body-Centered Cubic Transition Metals," *ASME Publication 65-MET-11*, 1965.

[2] Nakano, Y., Sakai, Y., Yagawa, G., Ando, K., and Ando, Y., "Dynamic Fracture Toughness of LWR Pressure Vessel Steel A508 Cl.3: A Japanese Round-Robin Study," *International Journal of Pressure Vessel and Piping*, Vol. 31, 1988, pp. 255–270.

[3] Fujii, E., Ohkuma, I., Kawaguchi, Y., and Tsukamoto, M., "Effects of Temperature and Strain Rate on Dynamic Fracture Toughness of Steel," *Journal of the Society of Naval Architects of Japan,* Vol. 158, 1985, pp. 619–629 (in Japanese).

[4] Toyosada, M., Fujii, E., Nohara, K., Kawaguchi, Y., Arimochi, K., and Isaka, K., "The Effect of Strain Rate on Critical CTOD and J Integral," *Journal of the Society of Naval Architects of Japan,* Vol. 161, 1987, pp. 343–356 (in Japanese).

[5] Toyosada, M. and Gotoh, K., "The Estimating Method of Critical CTOD and J Integral at Arbitrary Crosshead Speed," *Journal of the Society of Naval Architects of Japan,* Vol. 172, 1992, pp. 663–674 (in Japanese).

[6] Sano, K., "Effects of Local Temperature Rise at a Crack Tip on the Fracture Toughness of 9% Ni Steels," *Tetsu-to-Hagané,* Vol. 73, 1987, pp. 380–386 (in Japanese).

[7] Gotoh, K., Hirasawa, H., and Toyosada, M., "A Simple Method for Estimating the Effect of Loading Rate on Fracture Toughness," *Journal of the Society of Naval Architects of Japan,* Vol. 176, 1994, pp. 491–500 (in Japanese).

[8] Beremin, F. M., "A Local Criterion for Cleavage Fracture of a Nuclear Pressure Vessel Steel," *Metallurgical Transactions A,* Vol. 14A, 1983, pp. 2277–2287.

[9] Mudry, F., "A Local Approach to Cleavage Fracture," *Nuclear Engineering Design,* Vol. 105, 1987, pp. 65–76.

[10] Hashida, T., Fujihira, S., Arimochi, K., Ohnishi, K., Minami, F., and Toyoda, M., "Large Heat Input Automatic Welding Process to Beam-to-Column Connection of Steel Framed Structures (Report 1)," *Quarterly Journal of the Japan Welding Society,* Vol. 16, 1998, pp. 405–415 (in Japanese).

[11] Nuclear Research Committee, Annual Report, The Japan Welding Engineering Society, 1987 (in Japanese).

[12] Kuwamura, H. and Maeda, K., "Strain-Rate Effects on the Mechanical Properties of Low-Yield-Ratio High-Strength Steel," *Journal of Structural Engineering,* Vol. 36B, 1990, pp. 89–101 (in Japanese).

[13] Ushijima, M., Kitamura, S., Kobayashi, T., and Fujii, E., "Influence of High-Speed Straining on Strength Properties of Structural Steels," Reports of Ship Research Institute, Ministry of Transport, 1991 (in Japanese).

[14] TM Committee, "Qualification of Steel Properties in Terms of Resistance to Brittle Fracture Initiation," The Japan Welding Engineering Society, 1975 (in Japanese).

[15] Gotoh, K., Hirasawa, H., and Toyosada, M., "A Simple Estimating Method of Constitutive Equation for Structural Steel as a Function of Strain Rate and Temperature," *Journal of the Society of Naval Architects of Japan,* Vol. 176, 1994, pp. 501–507 (in Japanese).

[16] Toyosada, M., Gotoh, K., and Sagara, K., "Temperature Rise Distribution Near a Crack Tip Due to Plastic Work Under-High Loading Rate," *Journal of the Society of Naval Architects of Japan,* Vol. 170, 1991, pp. 651–663 (in Japanese).

[17] Miyata, T., Otsuka, A., Otake, T., and Suzuki, Y., "Correlation Between Fracture Toughness and Tensile Strength Properties of Steels," *Journal of the Society of Materials Science Japan,* Vol. 39, 1990, pp. 1549–1555 (in Japanese).

[18] Bakker, A. and Koers, R. W. J., "Prediction of Cleavage Fracture Events in the Brittle-Ductile Transition Region of a Ferritic Steel," *ESIS/EGF 9,* Mechanical Engineering Publications, 1991, pp. 613–632.

[19] Ruggieri, C., Minami, F., Toyoda, M., Hagiwara, Y., and Inoue, T., "Local Approach to Notch Depth Dependence of CTOD Results," *Journal of the Society of Naval Architects of Japan,* Vol. 171, 1992, pp. 493–499.

[20] Minami, F., Brückner-Foit, A., Munz, D., and Trolldenier, B., "Estimation Procedure for the Weibull Parameter Used in the Local Approach," *International Journal of Fracture,* Vol. 54, 1992, pp. 197–210.

[21] Minami, F., Ohata, M., Toyoda, M., Tanaka, T., Arimochi, K., Glover, A. G., and North, T. H., "Fracture Toughness Requirement for Fracture Performance Evaluation of Welded Joints Based on the Local Approach," *Mis-Matching of Interfaces and Welds,* K.-H. Schwalbe and M. Koçak, Eds., GKSS Research Center Publications, 1997, pp. 269–280.

[22] Minami, F., Ohata, M., Toyoda, M., Arimochi, K., Suzuki, S., Bessyo, K., Thaulow, C., and Hauge, M., "Prediction of Specimen Geometry Effect on Fracture Resistance of HAZ-Notched Welds by the Local Approach," *Mis-Matching of Interfaces and Welds,* K.-H. Schwalbe and M. Koçak, Eds., GKSS Research Center Publications, 1997, pp. 319–330.

[23] Euromech-Mecamat 1996, 1st European Mechanics of Materials Conference on Local Approach to Fracture 86–96, Fontainebleau, *Journal de Physique IV,* Vol. 6, N. Cardinal et al., pp. 185–194; O.

Cleizergues et al.; pp. 195–204; I. Dlouhy et al., pp. 205–214; D. Moinereau et al., pp. 243–257, M. Ohata et al., pp. 269–278; A. Rossoll et al., pp. 279–286; C. S. Wiesner and M. R. Goldthorpe, pp. 295–304; S. Renevey et al., pp. 343–352.

[24] Gao, X., Ruggieri, C., and Dodds, Jr., R. H., "Calibration of Weibull Stress Parameters Using Fracture Toughness Data," *International Journal of Fracture,* Vol. 92, 1998, pp. 175–200.

[25] Minami, F., Katou, T., Nakamura, T., and Arimochi, K., "Equivalent CTOD Concept for Fracture Toughness Requirement of Materials for Steel Structures," *Proceedings of 18th International Conference on Offshore Mechanics and Arctic Engineering,* St. John's, Newfoundland, Canada, OMAE99/MAT-2130, 1999, pp. 1–12.

Christopher D. Wilson[1] *and John D. Landes*[2]

Transition Fracture Toughness Testing with Notched Round Bars (NRB)

REFERENCE: Wilson, C. D. and Landes, J. D., **"Transition Fracture Toughness Testing with Notched Round Bars (NRB),"** *Fatigue and Fracture Mechanics: 31st Volume, ASTM STP 1389*, G. R. Halford and J. P. Gallagher, Eds., American Society for Testing and Materials, West Conshohocken, PA, 2000, pp. 305–317.

ABSTRACT: The notched round bar (NRB) geometry was assessed for use with ASTM E 1921-97 Standard for Test Method for the Determination of Reference Temperature, T_0, for Ferritic Steels in the Transition Range. Instead of precracking the NRB specimens, apparent fracture toughness using three different notch root radii was extrapolated to a zero radius to infer sharp crack fracture toughness. The reference temperature using A302B NRB specimens was determined to be −89°C, while A302B C(T) specimens yield T_0 of −87.3°C. In applying ASTM E 1921 to the NRB geometry, a simple scheme to remove notch root radius bias from apparent fracture toughness was developed. In addition, a size correction for converting NRB results to comparable 1T-C(T) results was investigated.

KEYWORDS: notched round bars (NRB), A302B steel, transition fracture toughness

The two most commonly used specimens for fracture toughness testing are the compact tension C(T) specimen and the single edge bend SE(B) specimen. These standard specimens have planar geometries. For thin planar specimens, a plane stress condition exists and the constraint is nearly uniform through the thickness. For thick planar specimens, a plane stress condition exists on the lateral surfaces of the specimen and transitions toward a plane strain condition in the middle of the specimen. If the planar specimen is thick enough, a state of plane strain will exist in the middle. Thus, the constraint will always vary from plane stress to plane strain (or nearly plane strain) in planar specimens. Very stringent requirements are placed on the machining of the notches in both specimen geometries. The specimens must be fatigue precracked, and the reproducibility of symmetric fatigue crack fronts depends, in part, on the machining of the notch.

The round bar geometry is an alternative to the planar C(T) and SE(B) specimens. The round bar was rejected as a specimen geometry by The Committee on Rapid Inexpensive Tests for Determining Fracture Toughness [*1*] in the 1970s because of high load capacity requirements for linear elastic conditions and difficulty in fatigue precracking. First, a round bar with a very large diameter, 130 mm (5.0 in.), would be necessary to maintain the constraint level of a 25 mm (1.0 in.) thick planar specimen for linear elastic conditions. Second, asymmetric crack growth occurred when there was a small load misalignment. However, if smaller-diameter (much less than 25 mm) specimens are used and if the precracking requirement can be removed, then the round bar seems likely to be a reasonable alternative to current planar geometries.

[1] Assistant professor, Tennessee Technological University, P.O. Box 5014, Cookeville, TN 38505-0001.
[2] Professor, The University of Tennessee, 314 Perkins Hall, Knoxville, TN 37996-2030.

Copyright© 2000 by ASTM International www.astm.org

The use of notched, then fatigue precracked specimens for fracture toughness testing dates back to the inception of Griffith-Irwin fracture mechanics. However, Brown [*2*] noted that only a small amount of K_{Ic} data had been generated by 1975 from fatigue precracked round bars because of the difficulty with maintaining concentric crack growth during fatigue cycling. Precracking was often done in reverse bending on a lathe. A second difficulty came in trying to determine when the crack had grown to be desired length for the toughness test.

In the late 1980s, Stark and Ibrahim [*3–5*] performed fracture toughness tests on small fatigue precracked round bars with a bar radius R of 4.2 mm and a notch radius r of approximately 2 mm so that $r/R \approx 0.5$. Using the maximum load in the test to calculate K_{Ic}, their results were within 3% of 1T-C(T) data for a high-strength aluminum alloy. They used finite element analyses to determine two size requirements for a valid K_{Ic} test. First, the fatigue crack must be at least twice r_y in depth. Second, the average axial stress across the final ligament at fracture must not exceed 2.5 times the yield strength so that general yielding does not precede fracture. Stark and Ibrahim did report that a significant number of their specimens had eccentric final ligaments. They analyzed the specimens in question to determine a bending correction to the stress intensity factor.

In 1995, Giovanola et al. [*6*] used small precracked round bars to measure the fracture toughness of Ti-10V-2Fe-3Al, HY-130 steel, and A508 class 2A steel. These materials were selected because they have a wide range of fracture toughness to yield strength ratios and were previously well-characterized. The specimens had diameter of 16 mm and initial ligament (notch diameter before precracking) of 8 mm. Precracking was done on a lathe until the ratio of crack depth a to nominal specimen radius R varied from 0.56 to 0.78. Eccentricity increased with increasing crack size, varying from 0.10 to 0.75 mm. In an arrangement similar to a standard tension test, the crack opening was measured using a 25.4 mm gage length. The maximum load was used to calculating fracture toughness based on fractographic evidence and analysis of the load-displacement records.

For the Ti-10V-2Fe-3Al, K_{Ic} values obtained using cracked round bars were about 15% lower than determined using a conventional specimen. For the embrittled HY-130, fractographic analysis revealed that initiation and propagation of the crack were cleavage driven. For the ductile HY-130, fractographic evidence revealed that crack initiation occurred at maximum load, followed by a rapid "quasi-stable" growth for a certain distance before complete instability. For the A508 material, the cracked round bars gave similar toughness values as conventional specimens. Crack eccentricity occurred in specimens of all three materials.

The use of notched, but not fatigue precracked, specimens for fracture toughness testing also dates back to the inception of Griffith-Irwin fracture mechanics. In 1964, Irwin [*7*] used the middle crack tension M(T) geometry to investigate the fracture toughness of H-11 steel. Irwin's results (Fig. 1) led many researchers to postulate that a critical notch root radius existed, below which the fracture toughness was invariant. For geometries with a notch root radius greater than this critical value, the fracture toughness was linearly dependent on notch root radius.

In 1973, Clark and Logsdon [*8*] used a notch in place of a fatigue precrack for the fracture toughness evaluation of a porcelain ceramic. They performed fracture toughness tests on notched single edge bend specimens using various notch radii. In addition, they performed fracture toughness tests using fatigue precracked single edge bend and compact tension specimens—achieving the same value for fracture toughness.

In 1977, Begley, Logsdon, and Landes [*9*] applied a similar procedure to determine J_{Ic} for ASTM A 471 NiCrMoV rotor steel and 6061-T651 aluminum alloy using M(T) and C(T) specimens. In addition, they performed fracture toughness tests using fatigue precracked

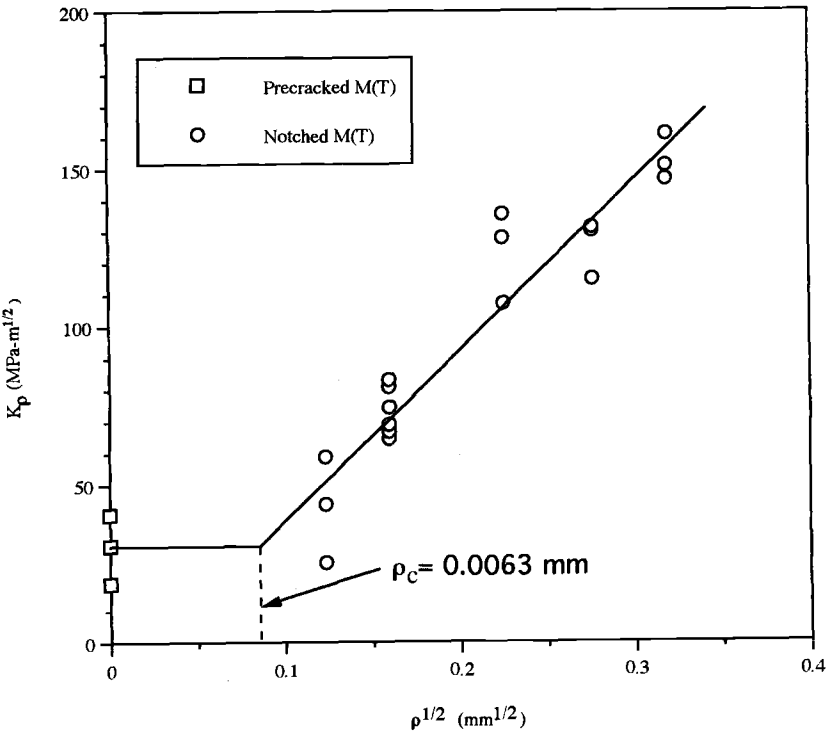


FIG. 1—*Apparent fracture toughness versus square root of notch root radius for H-11 steel [7].*

specimens and found excellent agreement with the extrapolated value of fracture toughness for a zero notch radius (Fig. 2) from the notched (no fatigue precrack) specimens. The *J-R* curve slopes of the notched specimen results were identical to the fatigue precracked specimen results.

More recently in 1996, Reiff and Ernst [*10*] determined that initiation values of CTOD could be calculated by extrapolating apparent CTOD values from notched Charpy specimens to a zero notch root radius. They used four different sizes of notch root radii and observed a linear increase in CTOD. By extrapolating to a zero notch root radius, they obtained CTOD values that equaled those obtained from fatigue precracked Charpy specimens.

The purpose of this paper is to explore the use of notched round bars (NRB) in the application of the fracture toughness testing of steels in the ductile to brittle transition. ASTM E 1921-97 Standard for Test Method for the Determination of Reference Temperature, T_0, for Ferritic Steels in the Transition Range will be assessed for use with notched round bars.

Technical Background

ASTM E 1921-97 quantifies fracture toughness of ferritic steels, in the 275 to 825 MPa (40 to 120 ksi) range of yield strength, that experience cleavage cracking in the ductile to brittle transition. In the draft test method, fracture toughness is expressed in terms of an elastic-plastic stress intensity factor, K_{Jc}, that is determined from J_c at the onset of cleavage fracture

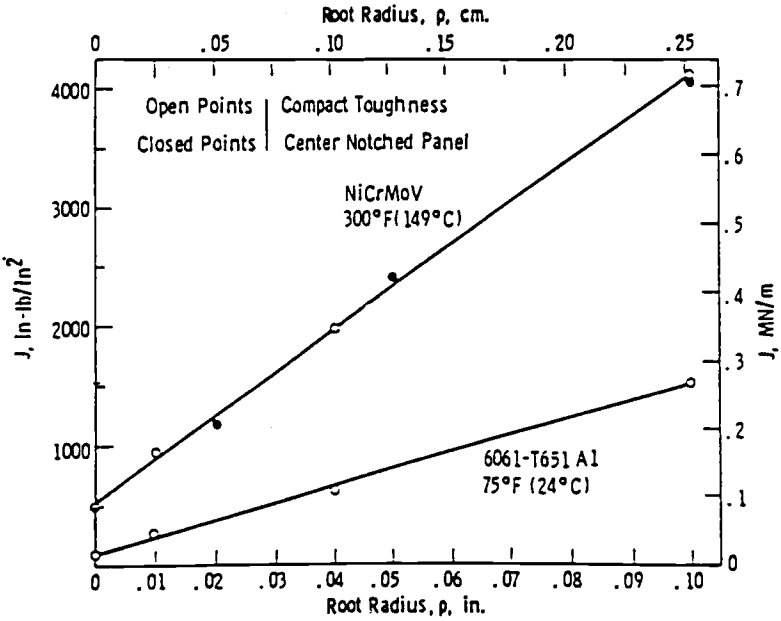


FIG. 2—*Critical* J *versus Notch Root Radius [9].*

$$K_{Jc} = \sqrt{J_c E}, \tag{1}$$

where J_c is calculated using a procedure similar to the one described in the ASTM E 813 Test Method for J_{Ic}, A Measure of Fracture Toughness.

ASTM E 1921-97 uses specimen geometries, fatigue precracking, and crack length measurement procedures that are similar to previous ASTM fracture toughness test methods. The major difference between ASTM E 1921 and previous ASTM fracture toughness test methods is the use of Weibull statistics to predict the transition fracture toughness curve. The statistical effect of specimen size on K_{Jc} in the transition range is modeled using a weakest-link theory embodied in a three parameter Weibull distribution of fracture toughness values.

The *J*-Integral at crack instability is denoted as J_c and is converted to a *K*-based fracture toughness value using Eq 1. A valid K_{Jc} is obtained if $K_{Jc} < K_{Jc(\text{limit})}$ where $K_{Jc(\text{limit})}$ is given by

$$K_{Jc(\text{limit})} = \sqrt{\frac{E\, b_0\, \sigma_{ys}}{30}} \tag{2}$$

where b_0 is the remaining ligament of the specimen.

A median K_{Jc} value can be determined if at least six valid K_{Jc} results are determined at a single temperature. A three-parameter Weibull model relates K_{Jc} and the cumulative probability for failure at or before K_{Jc}, p_f

$$p_f = 1 - \exp\left\{-\left[\frac{K_{Jc} - K_{\min}}{K_0 - K_{\min}}\right]^c\right\}, \tag{3}$$

where K_0 is the Weibull scale parameter to be determined, c is the Weibull exponent, assumed

to be 4, and K_{min} is a lowerbound fracture toughness for ferritic steels, taken as 20 MPa$\sqrt{m}$ (18.2 ksi$\sqrt{in.}$). The actual Weibull exponent c can be determined by calculating the slope of a graph of $\ln[-\ln(1 - p_f)]$ versus $\ln(K_{Jc} - K_{min})$.

The probability values p_f are assigned to K_{Jc} values after the K_{Jc} values are ranked in order of increasing magnitude. Cumulative probability values for failure are assigned to each ranked $K_{Jc(i)}$ using

$$p_{f(i)} = \frac{i - 0.3}{N + 0.4} \tag{4}$$

where $i = 1$ is the lowest ranked K_{Jc} value, $i = 2$ is the next ranked K_{Jc} value, and $i = N$ is the highest ranked K_{Jc} value.

Using the method of maximum likelihood, the Weibull parameter K_0 can be calculated, for $c = 4$, from

$$K_0 = \left[\sum_{i=1}^{N} \frac{K_{Jc(i)} - K_{min}}{N - 0.3068}\right]^{1/4} + K_{min} \tag{5}$$

where N is the number of specimens. The estimated median K_{Jc} of the test population is

$$K_{Jc(med)} = (K_0 - K_{min})(\ln 2)^{1/4} + K_{min} \tag{6}$$

ASTM E 1921-97 utilizes of a fracture toughness versus temperature curve (sometimes referred to as a master curve). The curve for 1T (1 in. thick) compact specimens is given by

$$K_{Jc(med)} = 30 + 70 \exp [0.019(T - T_0)] \tag{7}$$

where T is the test temperature (°C), T_0 is the reference temperature (°C) and $K_{Jc(med)}$ is given in MPa$\sqrt{m}$. T_0 is determined by rearranging Eq 7, giving

$$T_0 = T - \frac{1}{0.019} \ln \left[\frac{K_{Jc(med)} - 30}{70}\right] \tag{8}$$

The preceding discussion focused on the development of a master curve using 1T (1 in. thick) specimens. When a specimen size other than a 1T is used, a size adjustment must be made to adjust the K_{Jc} data to its 1T equivalent using

$$K_{Jc(1T)} = 20 + [K_{Jc(x)} - 20] \left(\frac{B_x}{B_{1T}}\right)^{1/4} \tag{9}$$

where $K_{Jc(x)}$ and $K_{Jc(1T)}$ have the units of MPa$\sqrt{m}$. The thickness B_x is the nominal thickness of the test specimen and B_{1T} is the thickness of a $1T$ (1 in. or 50 mm). After the size adjustment is made, Eq 5 is used to determine K_0, Eq 6 is used to determine $K_{Jc(med)}$, and Eq 8 is used to determine T_0.

The reference temperature T_0 is the temperature where the median K_{Jc} for $1T$ size compact specimens is 100 MPa$\sqrt{m}$ (90.9 ksi$\sqrt{in.}$). The value of T_0 should be relatively independent of the test temperature chosen. However, the selection of a test temperature that would lead

to a median K_{Jc} close to 100 MPa$\sqrt{m}$ is recommended, and a means of estimating this temperature is provided in ASTM E 1921.

Experimental Program

A combined experimental and analytical research program was designed to study the suitability of the notched round bar (NRB) for fracture toughness testing. A modified ferritic A302 Grade B pressure vessel steel was tested at room temperature and at −67°C (−88.6 °F). The room temperature properties were E = 203 GPa (29.5 × 10^6 psi), ν = 0.3, S_y = 630 MPa (91 ksi), S_{ut} = 760 MPa (110 ksi), and the Ramberg-Osgood hardening exponent n = 8.

The NRB specimen details are shown in Fig. 3. The specimens had a nominal radius R of 6.35 mm (0.25 in.) and a neck radius r of 3.175 mm (0.125 in.); thus r/R = 0.5. All specimens had a notch flank angle of 45°. The notch root radii ρ chosen were 0.127, 0.254, and 0.508 mm (0.005, 0.010, and 0.020 in.). All notch root radii ρ had a tolerance of ±0.025 mm (±0.001 in.). Three specimens of each notch root radii were tested.

To maintain proper alignment, buttonhead specimen ends were used in place of threaded ends. A mechanical gripping apparatus used in low-cycle fatigue testing was used with the buttonhead ends with a percent bending stress PBS in an unnotched specimen of less than 5% up to 207 MPa (30 ksi), where PBS is defined as

$$\text{PBS} = \frac{\Delta\sigma_{\max}}{\sigma_{\text{nom}}} \times 100 \tag{10}$$

where $\Delta\sigma_{\max}$ is the difference between the maximum outer fiber stress and the nominal stress

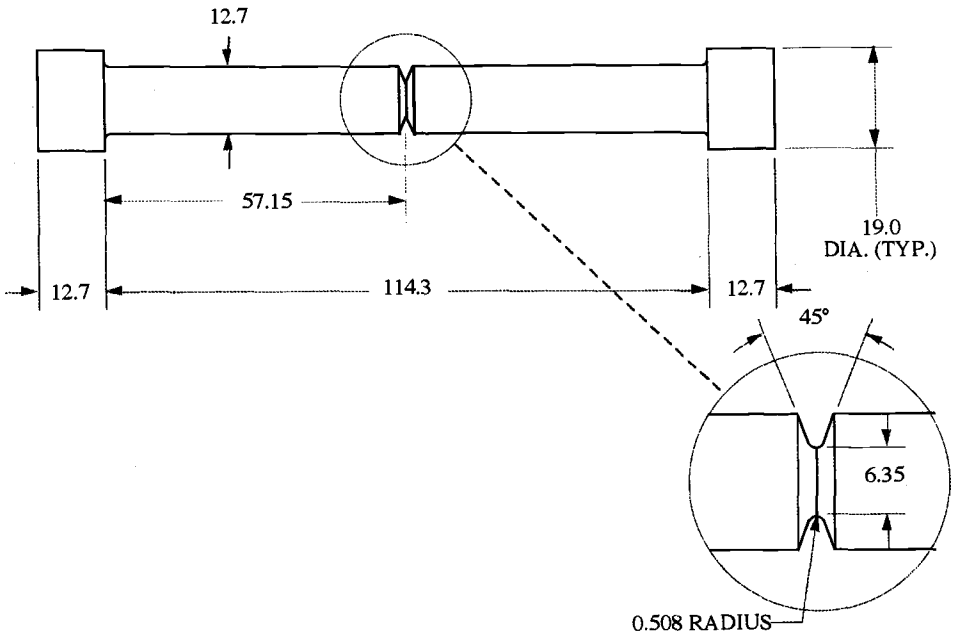


FIG. 3—*Engineering drawing of the notched round bar specimen.*

σ_{nom} in the specimen. An alignment straight (unnotched) specimen with a set of four strain gages was used to determine the PBS according to the method prescribed by ASTM E 602-74 Standard Method for Notch Tension Testing with Cylindrical Specimens. ASTM E 602 allows no more than 10% bending stress for a nominal tensile stress of 207 MPa.

All tests were conducted on screw-driven universal testing machines with constant crosshead motion. An extensometer with a gage length of 10.2 mm (0.4 in.) and a 10% extension range was used in all tests. Load and gage displacement data were recorded with a *X-Y* plotter and digitized afterward. The NRB tests were performed using a testing machine at the Oak Ridge National Laboratory (ORNL). In addition, McCabe and Swain [*12*] at ORNL performed *J-R* curve testing on the A302B steel using 1T-C(T) specimens.

ASTM E 1921-97 does not provide equations for calculating *J* for a notched round bar. However, *J* at the onset of fracture can be calculated for the notched round bar in the same manner as for planar specimens. *J* is calculated as the sum of elastic and plastic components.

$$J = J_e + J_p$$

The elastic component of *J* is calculated from the stress intensity factor K_e using

$$J_e = \frac{K_e^2}{E}$$

where K_e for a round bar is given by Tada, Paris, and Irwin [*13*] as

$$K_e = \frac{P}{\pi r^2}\sqrt{\pi(R - r)}\, f\left(\frac{r}{R}\right)$$

with

$$f\left(\frac{r}{R}\right) = \frac{1}{2}\sqrt{\frac{r}{R}}\left[1 + \frac{1}{2}\frac{r}{R} + \frac{3}{8}\left(\frac{r}{R}\right)^2 - 0.363\left(\frac{r}{R}\right)^3 + 0.731\left(\frac{r}{R}\right)^4\right].$$

The plastic component of *J* for a deeply cracked round bar is given by Rice, Paris, and Merkle [*14*] as

$$J_p = \frac{1}{2\pi r^2}\left(3\int_0^{v_p} P dv_p - Pv_p\right),$$

where *P* is the applied load and v_p is the displacement at the loading point due to the presence of the crack.

Results and Discussion

The load-displacement *P-v* curves for ρ = 0.127 mm (0.005 in.) are shown in Fig. 4. The test specimens exhibited significant plastic displacements. The maximum load in the NRB tests was approximately 44.5 kN (10 000 lb). Similar *P-v* curves for the other notch root radii are reported in Ref *11*. No visible surface crack growth was observed. Limited fractographic analysis revealed a combination of ductile tearing and cleavage fracture.

Calculations for K_{Jc} were performed using the methodology of ASTM E 1921. Since the K_{Jc} values were not generated using precracked specimens, the values are referred to as

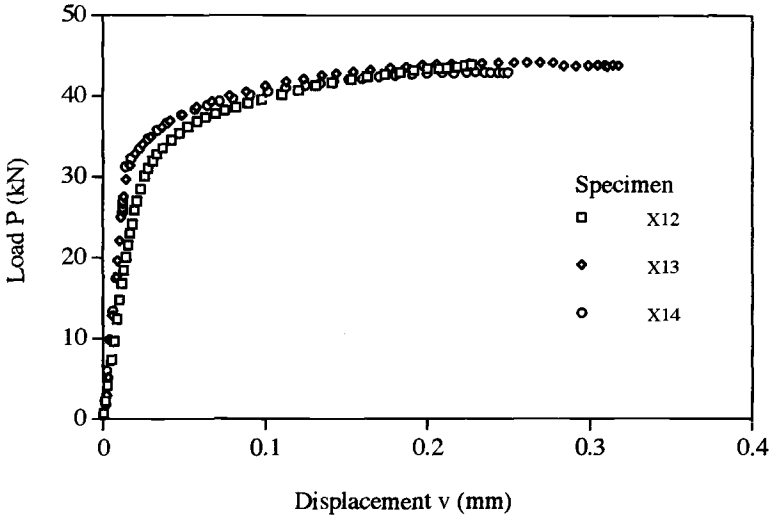


FIG. 4—*Load-displacement* P-ν *curves for modified A302B,* ρ = *0.127 mm (0.005 in.).*

apparent K_{Jc} values. A plot of apparent K_{Jc} versus $\sqrt{\rho}$ is shown in Fig. 5. A value of K_{Jc} = 177 MPa$\sqrt{m}$ (161 ksi$\sqrt{in.}$) was found by extrapolating a linear curve fit to $\rho = 0$. Clearly, the apparent K_{Jc} values are biased by their respective notch root radii.

To use ASTM E 1921, the data must be treated as a single group—not three separate groups. It was necessary to develop a scheme to remove the notch root radius bias from the data and essentially create a single data set from the three notch root radii groups. A simple

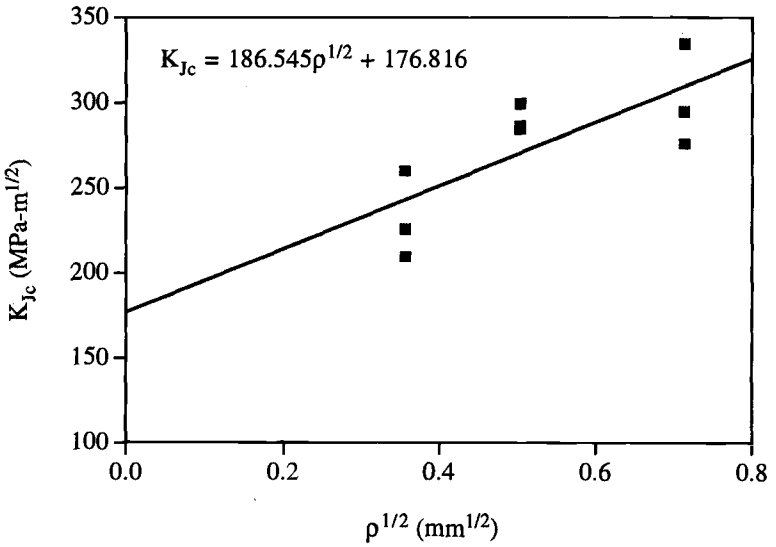


FIG. 5—K_{Jc} *versus* $\sqrt{\rho}$ *for Modified A302B NRB specimens.*

scheme to adjust for bias is shown in Fig. 6. The mean apparent K_{Jc} values were determined from the linear curve fit for each notch root radius. Then the individual data points were projected onto the K_{Jc} axis using lines that were drawn parallel to the linear curve fit in Fig. 6. All data points were adjusted in this manner.

After the adjustment for notch root radius bias was made, the procedure ASTM E 1921 for the Weibull analysis of the data was performed. The results are shown in Fig. 7. The Weibull slope of 4 and a K_{min} = 20 MPa$\sqrt{m}$ were used to determine a reference temperature T_0 = 100°C. For comparison, McCabe and Swain [*12*] determined T_0 to be −87.3°C using 1T-C(T) specimens. The resulting master curves for both the NRB tests and the test using 1T-C(T) specimens are shown in Fig. 8.

The $K_{Jc(limit)}$ was calculated using Eq 2 to be 116 MPa$\sqrt{m}$ (106 ksi$\sqrt{in.}$). The remaining ligament b_0 in Eq 2 was assumed to be equal to the ligament radius of the NRB, 3.175 mm. None of the data in Fig. 8 has a K value less than 116 MPa$\sqrt{m}$—implying that none of the data are valid using ASTM E 1921. The main cause for this failure to meet the validity requirement is the excessive plasticity in the load-displacement records (see Fig. 4).

The validity limit in ASTM E 1921 is based on planar specimens. Ibrahim and Stark [*4*] studied the validity limit for K_{Ic} testing of precracked round bars. They found that the average axial stress across the final ligament of a cracked round bar should not exceed 2.5 times the yield strength so that general yielding does not precede fracture. The results presented in this paper do not violate this criterion.

The size adjustment in ASTM E 1921 is based on the length of crack front in a planar specimen. For the NRB specimens used in this test series, the length of crack front (notch front) is the circumference $2\pi r \approx 20$ mm (0.8 in.). The size adjustment ratio $\theta^{1/4}$ is

$$\theta^{1/4} = \left(\frac{B_x}{B_{1T}}\right)^{1/4}. \tag{11}$$

where the circumference of the NRB is treated as an equivalent planar specimen thickness.

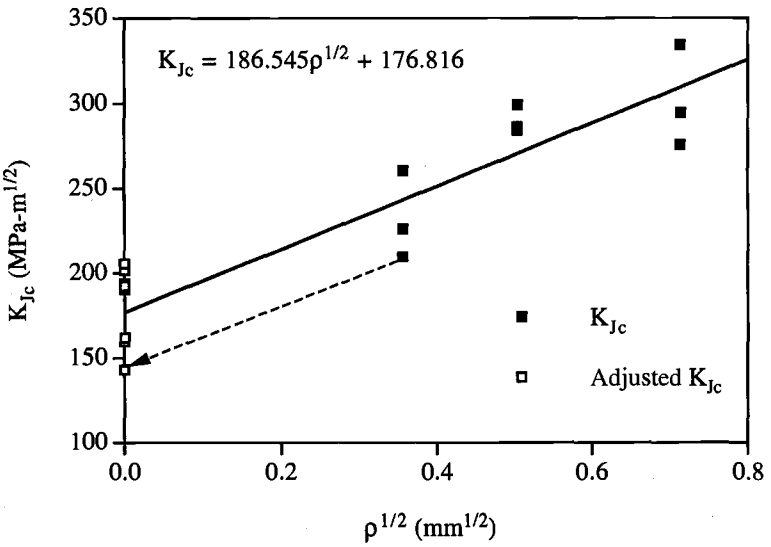


FIG. 6—*Bias adjustment for* K_{Jc} *versus* $\sqrt{\rho}$ *for modified A302B NRB specimens.*

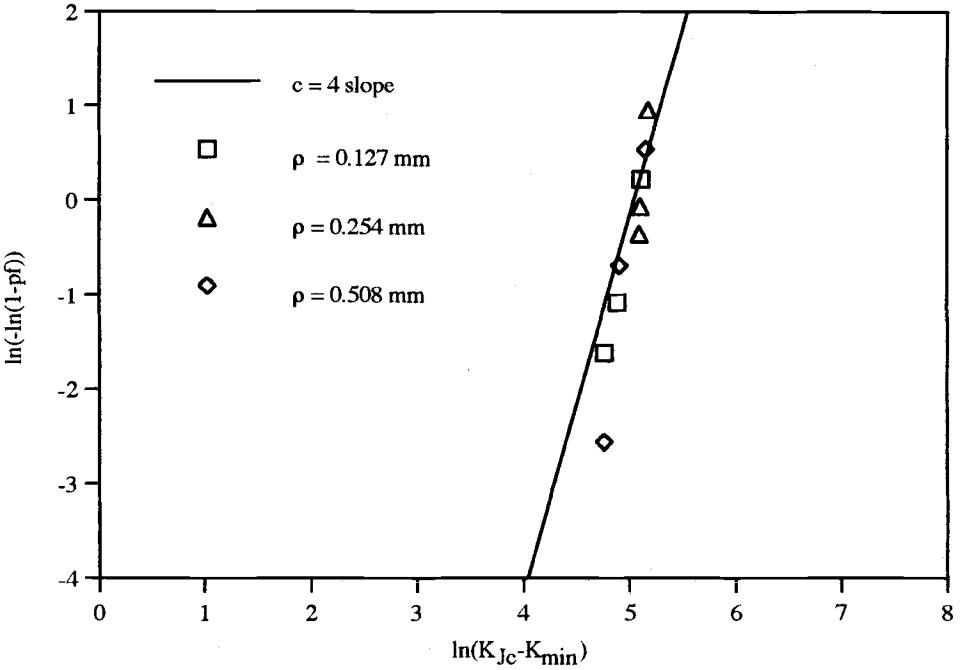


FIG. 7—*Weibull plot for modified A302B NRB specimens.*

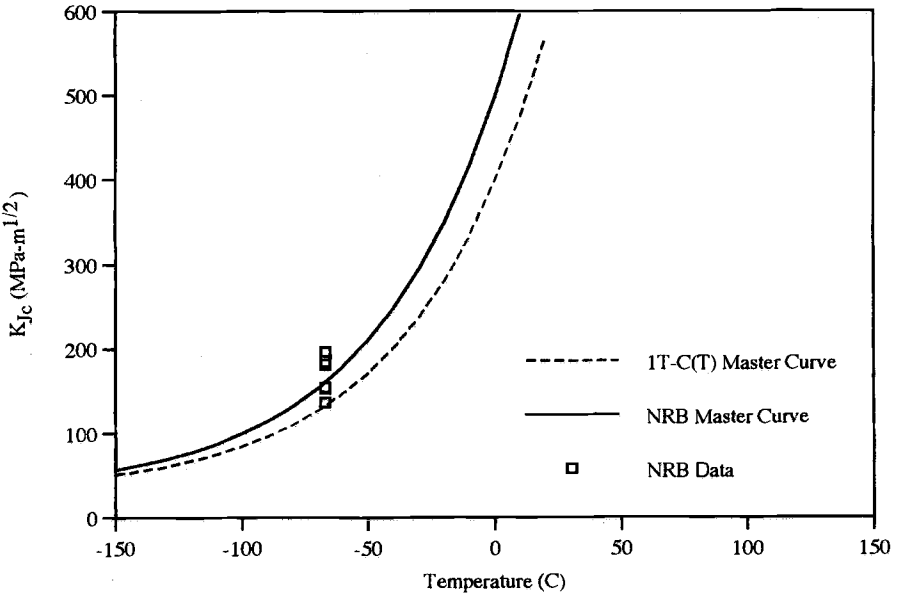


FIG. 8—*Modified A302B master curves for* K_{Jc} *from NRB and C(T) specimens.*

For B_x = 20 mm, the size adjustment ratio $\theta^{1/4}$ = 0.95. This size adjustment may not be applicable for a NRB.

If the size adjustment is generalized to an area in the crack (notch) front region, then the result is equivalent to a length of crack front adjustment for a planar specimen. However, the result is very different for the notched round bar. In Fig. 9, the area $dA = B\ r_c$ for a planar specimen is shown. The distance r_c can be interpreted as the distance from the crack (notch) tip to the cleavage initiation site by Heerens, Read, Cornec, and Schwalbe [*15*]. They studied the scatter in fracture toughness data in the ductile to brittle transition using C(T) specimens and found $r_c \approx$ 1.5 to 2.0 mm (0.06 to 0.08 in.).

A similar area approach (Fig. 9) for a notched round bar would give

$$dA = \pi r^2 - \pi(r - r_c)^2 \tag{12}$$

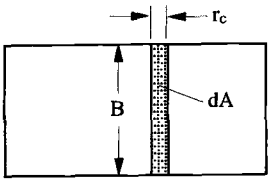
Using an area approach for a size adjustment for planar specimens yields

$$\theta^{1/4} = \left(\frac{B_x r_c}{B_{1T} r_c}\right)^{1/4}, \tag{13}$$

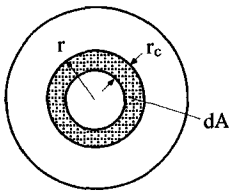
which is nothing more than the current size adjustment. However, the size adjustment between a NRB specimen and a 1T planar specimen is

$$\theta^{1/4} = \left(\frac{\pi r^2 - \pi(r - r_c)^2}{B_{1T} r_c}\right)^{1/4} \tag{14}$$

For example, if r_c = 1.5 mm is used to adjust the NRB K_{Jc} data, size adjustment is $\theta^{1/4}$ = 0.82. The resulting expression for $K_{Jc(1T)}$ is



Planar Crack Front



Circular Crack Front

FIG. 9—*Areas used for* K_{Jc} *size adjustments.*

$$K_{Jc(1T)} = 20 + [K_{Jc(x)} - 20]\theta^{1/4}. \quad (15)$$

If $K_{Jc(\text{med})} = 161.6$ MPa$\sqrt{\text{m}}$ is used, then $K_{Jc(1T\text{-med})} = 136$ MPa$\sqrt{\text{m}}$. The resulting T_0 is -89°C. The use of $r_c = 1.5$ mm as an example has not been verified by fractographic results.

Conclusions and Recommendations

For the modified A302B steel, the NRB geometry produced a master curve that was very similar to the master curve generated using precracked C(T) specimens. Two specific violations of ASTM E 1921 occurred in this set of experiments: the requirement for precracking to obtain a sharp crack and the requirement that the limiting K_{Jc} value not be exceeded. In addition, the size adjustment procedure in ASTM E 1921 may not be appropriate for NRB specimens. Overall, the NRB geometry performed very favorably when compared to the more traditional C(T) geometry.

The first violation of ASTM E 1921 results from the use of notched, but not precracked specimens. The effects of notch root radius on apparent fracture toughness was treated very simply. Since, no notched, nonprecracked C(T) specimens were used, no observation concerning the invariance of the apparent fracture toughness versus notch root radius slope was made. This paper proposes a simple method to remove the bias of notch root radius by "sliding" the apparent fracture toughness data along a line parallel to the linear fit of all data. This construction has no physical basis and should be critically examined in light of existing experimental results which indicate that scatter in the transition region is affected by the degree of constraint (see references in ASTM E 1921).

The second violation of ASTM E 1921 also results from using notched instead of precracked specimens. Using notched specimens led to increased plasticity in the load-displacement records. The appropriateness of the limit requirement for $K_{Jc(\text{limit})}$ when testing notched round bars needs to further studied. The use of alternate criteria, such as the stress calculation of Ibrahim and Stark [*4*], should also be studied.

This paper proposes a size adjustment for NRB results that is based on the area of the ligament. This size adjustment depends on the determination of a fractographic quantity r_c. Future experiments must be made to determine the validity and use of the proposed size adjustment model.

References

[*1*] "Rapid Inexpensive Tests for Determining Fracture Toughness," Report of The Committee on Rapid Inexpensive Tests for Determining Fracture Toughness, National Materials Advisory Board, National Academy of Science, Washington, 1976.

[*2*] Brown, W. F., Jr., "The Circumferentially Notched Cylindrical Bar as a Fracture Toughness Test Specimen," *Linear Fracture Mechanics,* Envo Publishing, 1975, pp. 175–187.

[*3*] Stark, H. L. and Ibrahim, R. N., "Estimating Fracture Toughness from Small Specimens," *Engineering Fracture Mechanics,* Vol. 25, No. 4, 1986, pp. 395–401.

[*4*] Ibrahim, R. N. and Stark, H. L., "Validity Requirements for Fracture Toughness Measurements Obtained from Small Circumferentially Notched Cylindrical Specimens," *Engineering Fracture Mechanics,* Vol. 28, No. 4, 1987, pp. 455–460.

[*5*] Ibrahim, R. N. and Stark, H. L., "Establishing K_{Ic} from Eccentrically Fatigue Cracked Small Circumferentially Grooved Cylindrical Specimens," *International Journal of Fracture,* Vol. 44, 1990, pp. 179–188.

[*6*] Giovanola, J. H., Homma, H., Lichtenberger, M., Crocker, J. E., and Klop, R. W., "Fracture Toughness Measurements Using Small Cracked Round Bars," *Constraint Effects in Fracture Theory and Applications: Second Volume, ASTM STP 1244,* Philadelphia, 1995, pp. 255–285.

[7] Irwin, G. R., "Structural Aspects of Brittle Fracture," *Applied Materials Research,* Vol. 3, No. 2, April 1964, pp. 65–81.

[8] Clark, W. G., Jr. and Logsdon, W. A., "The Applicability of Fracture Mechanics Technology to Porcelain Ceramics," Westinghouse Research Laboratories Report 73-1E7-CPNAL-P1, 10 May 1973.

[9] Begley, J. A., Logsdon, W. A., and Landes, J. D., "Ductile Rupture Blunt-Notch Fracture Criterion," *Flaw Growth and Fracture, ASTM STP 631,* Philadelphia, 1977.

[10] Reiff, K. and Ernst, P., "CTODi Measured by Means of a Modified Charpy-V Specimen," *Fatigue and Fracture of Engineering Materials and Structures,* Vol. 20, No. 1, 1997, pp. 29–39.

[11] Wilson, C. D., *Fracture Toughness Testing with Notched Round Bars,* Ph.D. dissertation, The University of Tennessee, Knoxville, TN, August 1997.

[12] McCabe, D. E. and Swain, R. L., unpublished data, Fracture Mechanics Group, Metals and Ceramics Division, Oak Ridge National Laboratory, 1997.

[13] Tada, H., Paris, P., and Irwin, G. R., *The Stress Analysis of Cracks Handbook,* Paris Productions, St. Louis, 1985.

[14] Rice, J. R., Paris, P. C., and Merkle, J. G., "Some Further Results of J-Integral Analysis and Estimates," *Progress in Flaw Growth and Fracture Toughness Testing, ASTM STP 536,* 1973, pp. 231–245.

[15] Heerens, J., Read, D. T., Cornec, A., and Schwalbe, K. H., "Interpretation of Fracture Toughness in the Ductile-to-Brittle Transition Region by Fractographical Observations," *Defect Assessment in Components—Fundamentals and Applications,* ESIS/EGF9, Mechanical Engineering Publications, London, 1991, pp. 659–678.

MarjorieAnn E. Natishan,[1] *Matthew Wagenhofer,*[1] *and Mark T. Kirk*[2]

Dislocation Mechanics Basis and Stress State Dependency of the Master Curve

REFERENCE: Natishan, M. E., Wagenhofer, M., and Kirk, M. T., **"Dislocation Mechanics Basis and Stress State Dependency of the Master Curve,"** *Fatigue and Fracture Mechanics: 31st Volume, ASTM STP 1389,* G. R. Halford and J. P. Gallagher, Eds., American Society for Testing and Materials, West Conshohocken, PA, 2000, pp. 318–327.

ABSTRACT: The Master Curve approach to characterizing fracture toughness transition behavior of pressure vessel steels is based on statistical analysis of empirical data and not on a physics-based understanding of the fracture behavior of these steels. While there is an overabundance of empirical data that supports the idea of a single curve shape for all pressure vessel steels, this cannot replace the need for solid physical modeling. The lack of fracture toughness data for a considerable proportion of the nuclear fleet suggests that a purely empirical argument cannot validate the Master Curve for all conditions of interest. In order to validate the Master Curve approach research has been undertaken to provide a physical understanding of the fracture behavior of pressure vessel steels. This will provide the basis for defining the limits of the Master Curve as well as for enabling extrapolation of the Master Curve model to other material conditions with only limited testing. A previous paper [*1*] detailed a dislocation mechanics-based constitutive model approach to describe the link between microstructure and temperature dependence of flow and fracture toughness behavior. In this paper, the strain to fracture under the appropriate stress state will be discussed in terms of the dislocation mechanics-based constitutive models and the effect on the shape of the Master Curve.

KEYWORDS: master curve, fracture toughness transition behavior, T_o, steel

In 1980, Landes and Schaffer reported a statistical "size" effect for specimens failing by transgranular cleavage [*2*]. They found that larger specimens exhibit lower mean fracture toughness than smaller specimens, even when the severe specimen size requirements of linear elastic fracture mechanics are satisfied. In 1984, Wallin published two papers concerning the fracture toughness of ferritic steels in fracture mode transition that built on the Landes and Schaffer's "weakest link" effect [*3,4*]. Using a weakest-link failure model, Wallin statistically described the dispersion of toughness values at a fixed temperature in fracture mode transition, and developed a formula to account for the effect of crack front length on fracture toughness. In a 1903 paper on reactor pressure vessel (RPV) steels, Wallin observed that the increase of fracture toughness with increasing temperature is not sensitive to steel alloying, heat treatment, or irradiation [*5*]. This observation led to the concept of a universal transition curve shape, or "Master Curve," applicable to all ferritic steels.

Today the term Master Curve refers to a technology that incorporates both the weakest link failure model and the universal curve shape. ASTM recently adopted Standard Test

[1] Assistant professor and graduate student, respectively, Mechanical Engineering Department, University of Maryland, College Park, MD 20742.
[2] Senior mechanical engineer, Westinghouse Electric Company, Pittsburgh, PA 15235.

Copyright© 2000 by ASTM International www.astm.org

Method E 1921-97, "Test Method for the Determination of Reference Temperature, T_o, for Ferritic Steels in the Transition Range" [6] E 1921-97 which uses these features of the Master Curve to estimate the index temperature (T_o) based on replicate testing of between six and ten fracture toughness specimens at a single test temperature. T_o positions the median Master Curve, given by Eq 1 for a 1T specimen, on the temperature axis:

$$K_{Jc(\text{median})} = 30 + 70 \cdot \exp[0.019(T - T_o)] \quad (1)$$

By reference to empirical studies that demonstrate a universal curve shape, E 1921-97 defines the variation of fracture toughness with temperature even though testing is only conducted at a single temperature [7,8]. Use of the weakest link failure model [3,4] permits definition of statistical confidence bounds on this median curve, and scaling of the curve to account for the effect of crack front length, or specimen size, on fracture toughness. In addition to embracing Master Curve technology, E 1921-97 also incorporates a modern understanding of elastic-plastic fracture mechanics, thereby permitting determination of T_o using specimens as small as precracked Charpys.

Application of Master Curve Technology to Nuclear Reactor Pressure Vessels

Recently, ASME Section XI passed Code Case N-629 that uses T_o from E 1921-97 to define a Master Curve-based index temperature ($RT_{To} \equiv T_o + 35°F$) [9]. N-629 permits use of RT_{To} as an alternative to traditional (RT_{NDT}-based) methods of positioning the ASME K_{Jc} and K_{IR} curves. Acceptance of Code Case N-629, and the existence of specimens of an appropriate size for E 1921-97 testing in on-going nuclear surveillance programs, paves the way for use of Master Curve technology in RPV assessment. The K_{IC} and K_{IR} curves are used to assess defects found during in-service inspections, and to establish safe allowable pressure/temperature windows for heat-up and cool down operations. RT_{To} indexed K_{IC} and K_{IR} curves should provide more accurate and realistic representations of lower bound fracture toughness in these applications. Furthermore, a value of RT_{NDT} adjusted for the effects of neutron irradiation (an adjusted reference temperature, or *ART*) serves as a screening criteria to assess RPV integrity during postulated severe accident scenarios, such as pressurized thermal shock (PTS) [10]. RT_{NDT} has long been recognized as a poor indicator of the transition temperature exhibited by fracture toughness data [11]. Thus, use of an index temperature based on direct measurement of toughness (i.e., RT_{To}) as an alternative to RT_{NDT} signifies a fundamental advance in nuclear RPV assessment technology.

Physical Basis for a Single Master Curve

The existence of a single "master" curve describing fracture mode transition relies upon two physical assumptions: that deformation prior to fracture occurs by dislocation glide, and that fracture occurs by cleavage, or a local, critical stress-controlled fracture. These assumptions limit the use of the Master Curve method to the transition region since lower shelf is twinning-dominated and upper shelf is hole-growth dominated. E 1921-97 excludes lower shelf from consideration by the following requirement:

$$K_{Jc(\text{median})} \geq 50 \text{ MPa}\sqrt{\text{m}} \quad (2)$$

Consideration of upper shelf behavior is precluded by both limiting the amount of ductile crack growth permitted, i.e.,

$$\Delta a_{max} \leq 0.05b, \tag{3}$$

and by establishing an upper limit on K_{Jc} related to material flow properties and specimen size, i.e.,

$$K_{Jc} \leq \sqrt{\frac{MIN(a,b,B) \cdot \sigma_{ys} \cdot E}{30}} \tag{4}$$

Here b is the specimen ligament, a is the crack length, B is the specimen thickness, σ_{ys} is the yield strength and E is Young's modulus.

Validation of this method has, to date, involved testing of a wide range of pressure vessel steels and product forms. Most of this data "fits" the predicted "Master Curve," but empirical validation does not provide a basis for extrapolation to new product forms, load conditions or compositions. Each new composition or load condition requires additional testing to ensure conformity with the Master Curve model. To confidently identify the limits of applicability of this method it is necessary to understand the physical basis for this methodology.

The physical process assumed to control cleavage fracture in the transition region is dislocation accumulation-induced cracking or decohesion of 2nd phase particles upon loading followed by propagation of one of these cracks upon attainment of a critical, local stress. Dislocation motion or the plastic deformation that occurs prior to fracture controls the energy absorbed to fracture in this process. Wallin, Saario, and Törrönen (WST) [*12*] suggest a link between the micro-mechanics of cleavage fracture and the empirical observation of a single "master" curve shape through the temperature dependence of the plastic deformation process as described by the plastic work term, w_p. Using the Griffith equation as the basis for their model, they suggest that the temperature dependence of fracture toughness enters through the plastic work term, w_p, shown in the modified Griffith equation below:

$$K_{ssy} = \sqrt{\frac{E(\gamma + w_p)}{2(1 - \nu^2)}} \tag{5}$$

where K_{ssy} is the fracture toughness in small scale yield conditions, γ is the surface energy, and ν is Poisson's ratio. The proposed form of the plastic work term has been given as:

$$w_p = A + B \cdot \exp(C \cdot T) \tag{6}$$

In this equation T is the temperature of interest and A, B, and C are material parameters.

WST attribute the temperature-dependence of the plastic work to the temperature-dependence of the Peierls-Nabarro (P-N) stress (that which resists dislocation motion through the crystal), but provide little detail documenting the derivation of their plastic work equation from the P-N stress. We can define the basis for the WST form of the plastic work equation and thus the temperature dependence of the fracture toughness transition curve through understanding the parameters that effect dislocation motion in steels. The objective of this study is to provide a physics-based understanding for the Master Curve model, which will permit its confident use, and identify its limitations.

Dislocation Mechanics

To understand the physical basis for a single curve shape for fracture toughness transition with temperature for all ferritic steels we need to connect the Master Curve equation back

through the equation for plastic work-dependence on temperature to the constitutive equations that have been developed to describe the plastic deformation behavior of metals. These take into account the various strengthening mechanisms present in the alloy, the crystal structure, and the dependence of the deformation mechanisms on temperature and strain rate. Dislocation mechanics-based deformation models describe how various aspects of the microstructure of a material control dislocation motion and how these vary with temperature and strain rate. The microstructural characteristics of interest include short and long-range barriers to dislocation motion. Short-range barriers are provided by the lattice structure itself, which affects the atom-to-atom movement required for a dislocation to change position within the lattice. Long range barriers are defined by an inner-barrier spacing that is typically several orders of magnitude greater than the lattice spacing or short range barriers. These include point defects (solute and vacancies), precipitates (semicoherent to noncoherent), boundaries (twin, grain, etc), and other dislocations.

As a stress is applied to a metal, dislocations begin to move, resulting in plastic deformation. For a dislocation to move it must change position from one equilibrium position in the lattice to another, overcoming an energy barrier to do so as shown in Fig. 1. The dislocation requires application of a force to overcome this activation barrier and the magnitude of this force is the Peierls-Nabarro stress, τ_{PN}. The wavelength of these barriers is equal to the periodicity of the lattice. The moving dislocation will also encounter other barriers such as solute atoms, vacancies, precipitates, inclusions, boundaries, and other dislocations. These additional periodic barriers are described by different spacings and size scales.

At temperatures other than absolute zero, atoms vibrate about their lattice sites at an amplitude that is temperature-dependent. Additions of thermal energy act to increase the amplitude of atom vibration. The effect of this thermal energy is to decrease the height of lattice barriers (short range) to dislocation motion at any instant in time, thereby decreasing the force required to move the dislocation from one equilibrium position to the next. The effect of strain rate (dislocation velocity) has a similar but opposite effect to that of tem-

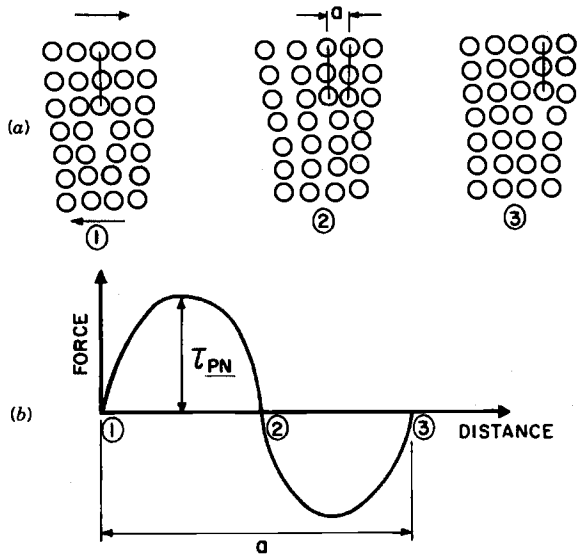


FIG. 1—*Schematic showing the movement of a dislocation from one equilibrium position to the next, and* (b) *the applied stress versus distance for this movement.*

perature. As strain rate, and thus dislocation velocity, is increased, there is less time available for the dislocation to overcome the short-range barriers and the effect of thermal energy is decreased, resulting in an increased force required for dislocation motion.

Long-range obstacles cannot be overcome by thermal energy because atomic vibration amplitude has little effect on the size of the long-range energy barrier presented to the dislocation, which is on the order of the interparticle spacing. So no matter how large the amplitude of atomic vibration, the amount of energy required to move the dislocation past these large obstacles is orders of magnitude larger than that provided by increased lattice vibration. This is why obstacles are separated into short-range barriers to dislocation motion (thermally activated) and long range barriers (non-thermally activated). The flow stress of a material can then be expressed as having an athermal and a thermal component:

$$\sigma = \sigma_G(\text{microstructure}) + \sigma^*(T, \dot{\varepsilon}, \text{microstructure}) \tag{7}$$

The first term is due to the athermal or long-range barriers to dislocation motion while the second term is due to the thermally activated barriers, short-range barriers. The short-range barriers include the Peierls-Nabarro stress and dislocation forests. Peierls-Nabarro stresses (lattice friction stresses) are the controlling short range barriers in BCC metals while dislocation forest structures are the controlling short range barriers in FCC and HCP metals. This difference is responsible for the difference in strain are sensitivity between BCC and FCC metals.

The temperature dependence of the probability that a dislocation will overcome a short range obstacle is given by:

$$P_B = \exp\left(\frac{\Delta G}{\kappa T}\right) \tag{8}$$

where κ is Boltzmans constant, T is temperature of interest and ΔG is the activation energy of a given barrier [*13*]. The strain rate effect can be shown to have a similar form:

$$\dot{\varepsilon} = \dot{\varepsilon}_o \exp\left(\frac{\Delta G}{\kappa T}\right) \tag{9}$$

Solving this equation for ΔG gives

$$\Delta G = \kappa T \cdot \ln\left(\frac{\dot{\varepsilon}}{\dot{\varepsilon}_o}\right) \tag{10}$$

This equation clearly shows that activation energy for dislocation motion decreases with decreasing temperature and decreasing strain rate.

Using these equations as the basis for their model, Zerilli and Armstrong found that overcoming P-N barriers was the principal thermally activated mechanism in BCC metals [*14*]. The spacing of these obstacles is equal to the lattice spacing and thus is not affected by prior plastic strain as are the forest dislocation barriers in FCC metals. Using this information, Zerilli and Armstrong developed an expression for the thermal portion of the stress (assuming a constant obstacle spacing for BCC) as:

$$\sigma^* = C_1 \exp(-\beta T) \tag{11}$$

where β is a parameter that is dependent on strain and strain rate given by:

$$\beta = -C_2 + C_3 \ln \dot{\varepsilon} \tag{12}$$

Combining this with commonly accepted terms describing Orowan-type strengthening due to athermal barriers results in a reasonably complete description of the flow behavior of BCC metals given by:

$$\sigma_f = \sigma_G + C_4 \varepsilon^n + kd^{-1/2} + C_1 \cdot \exp[-C_2 T + C_3 T \cdot \ln(\dot{\varepsilon})] \tag{13}$$

where ε is the strain, $\dot{\varepsilon}$ is the strain rate, T is the absolute temperature, d is the average grain diameter and σ_G is the contribution to the flow stress from solutes and the initial dislocation density. The values C_4, n, k, C_1, C_2, and C_3 are material specific constants. The form of this equation is consistent with constitutive equations developed by many other researchers accounting for the action of short range and long range barriers on the activation energy for dislocation motion [*15,16*]. This equation does not account for dynamic strain aging, solute drag, climb, and other interactions between diffusional processes and dislocation velocity. Programs are ongoing to modify constitutive equations to account for these affects [*17*].

The nature of the long-range barriers and their effects on dislocation motion are controlled by alloy composition, heat treatment, and prior strain history. Test temperature and strain rate do not alter the effects of these barriers on dislocation motion (as long as we assume that dynamic strain aging is not occurring at the temperatures and strain rates of interest). However, temperature and strain rate can significantly alter the stress required for dislocation motion through short-range barriers as discussed above.

Empirical Validation of Z-A for a Variety of Steels

The theoretically derived, Zerilli-Armstrong constitutive equation for BCC materials was used as the basis for predicting the temperature-dependence of the plastic work term in the Master Curve. The Zerilli-Armstrong (Z-A) equation for BCC metals (Eq 13) describes the strain rate and temperature dependence of flow curve behavior based on dislocation-mechanics. Athermal terms account for the effects of long-range dislocation barriers such as precipitates, grain boundaries, solute atoms, and other dislocations (strain hardening) on flow curve behavior while the thermal term is only affected by the lattice structure, accounting for the effects of short-range barriers on dislocation motion. This equation has been well validated for BCC and FCC materials [*14*].

In order to confirm that the lattice structure common to all ferritic steels is the physical basis for the universality of the Master Curve, a comparison is made between the Armco iron based Z-A predictions of yield versus temperature behavior and yield versus temperature data for a wide variety of ferritic steels. Based on the argument above, these coefficients should predict the temperature dependency of yield strength for all steels having a BCC lattice structure. Figure 2 shows σ_y versus T for a variety of reactor pressure vessel (RPV) steels both in the unirradiated and irradiated conditions. These are typical pressure vessel steels such as ASTM A508, A533, and A302. All of these steels have the same BCC lattice structure with very similar lattice constants. Only their long-range barriers to dislocation motion vary. If the yield strength is offset by the ambient value so as to account for the different flow curve shapes (controlled by the athermal terms in the Z-A equation), then it

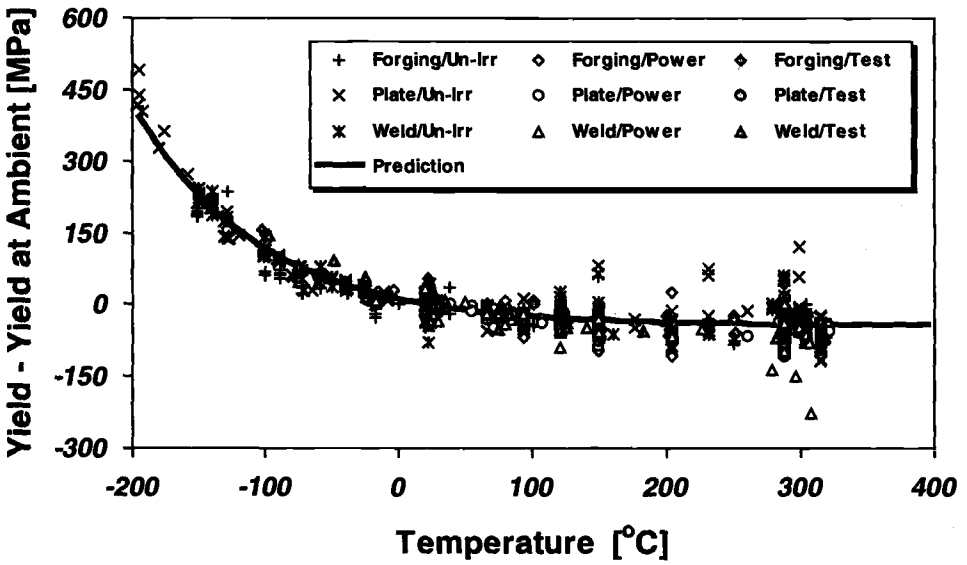


FIG. 2—*Tensile yield strength offset by yield at room temperatures versus test temperature compared to a plot of the Z-A equation using ARMCO iron coefficients.*

is apparent that all of the data falls on a single curve as predicted by Z-A using the coefficients for Armco iron. This validates the supposition that only the lattice structure controls the temperature dependency of flow curve behavior and provides confidence in use of the Z-A equation to predict temperature dependence of plastic deformation.

Flow Curves to Predict K versus T Behavior

Now that we have demonstrated confidence in Z-A for accurately predicting temperature dependence of flow behavior in RPV steels, we can use it to model the plastic work absorbed to fracture. Plastic work, or energy per unit area of crack surface created, can be taken as the area under the true stress strain curve and thus integration of the Z-A equation should provide a measure of this energy. Since only the lattice structure affects the thermal portion of the Z-A equation, increasing temperature only shifts the flow curve down without causing a change in shape of the curve. This predicts a decreasing plastic work with increasing temperature in opposition to the WST Master Curve equation. This basic result suggests that more information is required to detail the link between dislocation mechanics and the empirically derived Master Curve. First, an appropriate limit of integration must be applied that is based on the strain to fracture under an appropriate stress state. Then the equation must be modified by considering the volume over which the work is performed. The form of this equation is shown below:

$$w_p = \int_0^{\varepsilon_f} \sigma d\varepsilon * X \tag{14}$$

where X is taken as the {process zone volume/crack area}. In Eqs 5 and 6 the plastic work term is given in units of work per unit area of crack extension, not work per unit volume

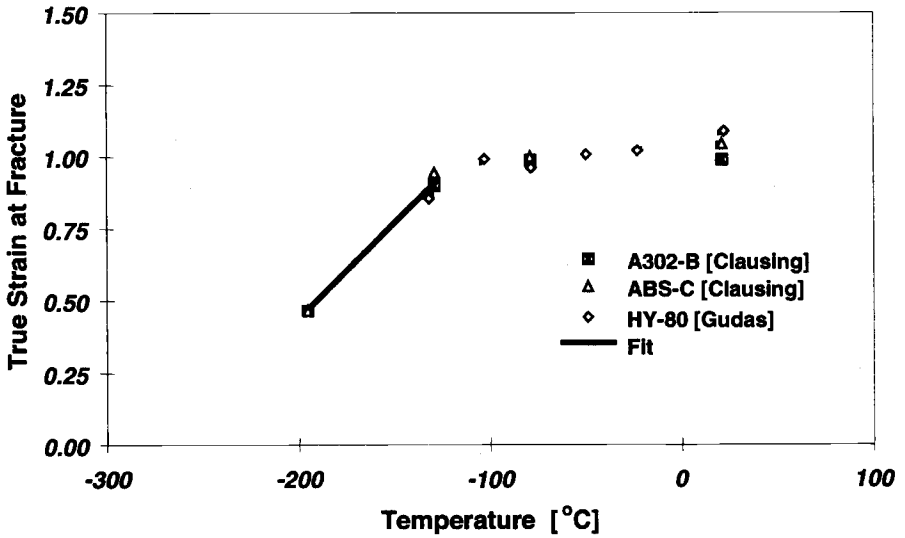


FIG. 3—*Strain to fracture versus test temperature for several RPV and low-alloy steels. The solid line shows the best fit to the data in the fracture mode transition region.*

as determined by integrating the Z-A equation. Thus, the volume of plasticity at the crack tip involved in the fracture process and the crack extension area must be considered and used to modify the equation.

The temperature dependent terms in Eq 14 include the flow stress, the strain at fracture, and the characteristic distance (process volume/crack area). The flow curve dependence on temperature has already been discussed. The temperature dependence of the other two terms, ε_f and X, have been empirically demonstrated and are shown in Figs. 3, [*18,19*] and 4 [*20*], respectively. In Fig. 3, the data from −125°C to −200°C suggest some form of strong

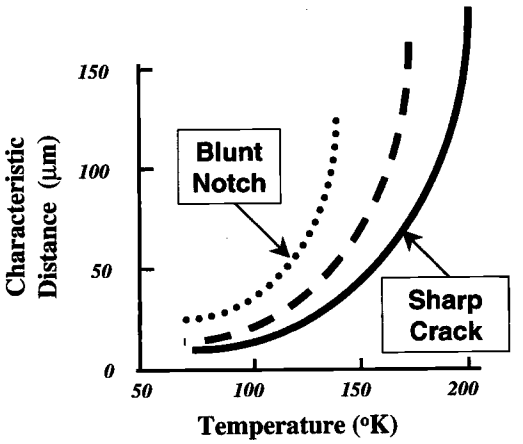


FIG. 4—*Calculations of characteristic distance versus temperature for several steels following the work of Kotilainen.*

temperature dependence corresponding to the transition region. However, there is insufficient data to determine whether this is truly linear or more exponential. Barsom [*21*] performed detailed plane-strain tensile tests to determine the temperature dependence of the strain to fracture. His results suggests a more linear trend for HY-80 steel while A517-F and HY-130 exhibit a more exponential trend. Stress state also affects these two terms with increasing triaxiality decreasing both the strain to fracture and the volume of material involved in the fracture process as shown in Fig. 4. It is imperative that the strain to fracture and X for the appropriate stress state be used in determining the plastic energy absorbed to fracture. Physically based, theoretical models for strain to fracture and X are being developed. However, the data provides encouragement that the proposed model for w_p, based on the physical process of fracture, will have the same form as that suggested by WST. More work, though, on defining the theoretical relationship of strain to fracture and the volume of material involved in the fracture process with temperature is necessary to complete the model.

Conclusions

1. The Zerilli-Armstrong equation, using coefficients derived for Armco Iron, describes the temperature-dependence of the yield stress for a wide variety of steels and provides the basis for physics-based modeling of the fracture toughness transition behavior of RPV steels.
2. The thermal portion of the Z-A equation is controlled only by the lattice structure and so is similar for all ferritic steels.
3. The plastic work term can be defined by integrating the Z-A equation, using the strain to fracture under the appropriate stress state as the limit of integration, and modifying this result by a characteristic distance term given by the fracture process zone volume divided by the crack extension area.
4. More work is needed to fully define the physical basis for strain to fracture and characteristic distance dependence on temperature.

References

[*1*] Natishan, M. E. and Kirk, M. T., "A Micromechanical Evaluation of the Master Curve," *Fatigue and Fracture Mechanics, Vol. 30, ASTM STP 1360,* American Society for Testing and Materials, West Conshohocken, PA, 2000, pp. 51–60.

[*2*] Landes, J. D. and Shaffer, D. H., "Statistical Characterization of Fracture in the Transition Region," *Fracture Mechanics, 12th Conference, ASTM STP 700,* American Society for Testing and Materials, West Conshohocken, PA, 1980, pp. 368–382.

[*3*] Wallin, K., "The Scatter in K_{Ic} Results," *Engineering Fracture Mechanics,* Vol. 19, No. 6, 1989, pp. 1085–1093.

[*4*] Wallin, K., "The Size Effect in K_{Ic} Results," *Engineering Fracture Mechanics,* Vol. 22, 1985, pp. 149–163.

[*5*] Wallin, K., "Irradiation Damage Effects on the Fracture Toughness Transition Curve Shape for Reactor Vessel Steels," *Int. J. Pres. Ves. & Piping,* Vol. 55, 1993, pp. 61–79.

[*6*] ASTM E 1921-97, "Standard Test Method for Determination of Reference Temperature, T_0, for Ferritic Steels in the Transition Range," American Society for Testing and Materials, West Conshohocken, PA, 1999.

[*7*] Sokolov, M. A. and Nanstad, R. K., "Comparison of Irradiation Induced Shifts of K_{Jc} and Charpy Impact Toughness for Reactor Pressure Vessel Steels," *ASTM STP 1325,* American Society for Testing and Materials, 1996.

[8] Kirk, M., Lott, R., Kim, C., and Server, W., "Empirical Validation of the Master Curve for Irradiated and Unirradiated Reactor Pressure Vessel Steels," presented at the 1998 ASME/JSME Pressure Vessel and Piping Symposium, 26–30 July 1998, San Diego, California, USA.

[9] ASME Code Case N-629, "Use of Fracture Toughness Test Data to Establish Reference Temperature for Pressure Retaining Materials for Section XI."

[10] SECY-82-465, Enclosure A, "NRC Staff Evaluation of Pressurized Thermal Shock," November 1982.

[11] Kirk, M., Lott, R., Server, B., Hardies, B., and Rosinski, S., "Bias and Precision of T_o Values Determined Using ASTM Standard E 1921-97 for Reactor Pressure Vessel Steels," *Effects of Radiation on Materials, 19th International Symposium, ASTM STP 1366,* M. L. Hamilton, A. S. Kumar, S. T. Rosinski, and M. L. Grossbeck, Eds., American Society for Testing and Materials, West Conshohocken, PA, 1999.

[12] Wallin, K., Saario, T., and Törrönen, K., "Statistical Model for Carbide Induced Brittle Fracture in Steel," *Metal Science,* Vol. 18, 1984, pp. 13–16.

[13] Kocks, U. F., Argon, A. S., and Ashby, M. F., "Thermodynamics and Kinetics of Slip," *Progr. Mater. Sci.,* Vol. 19, 1975, p. 1.

[14] Zerilli, F. J. and R. W. Armstrong, "Dislocation-Mechanics-Based Constitutive Relations for Material Dynamics Calculations," *Journal of Applied Physics,* Vol. 61, No. 5, 1 March 1987.

[15] Johnson, G. R., "Dynamic Analysis of a Torsion Test Specimen Including Heat Conduction and Plastic Flow," *ASME J. Eng. Mater. Tech.,* Vol. 103, 1981, p. 201.

[16] Follansbee, P. S. and Kocks, U. F., "A Constitutive Description of the Deformation of Copper Based on the Use of the Mechanical Threshold Stress as an Internal State Variable," *Acta Metallurgica,* Vol. 36, 1988, p. 81.

[17] Wagenhofer, M., Natishan, M. E., Armstrong, R. W., and Zerilli, F. J., "Influence of Strain Rate and Grain Size on Yield and Serrated Flow in Commercial Al-Mg Alloy 5086," *Scripta Metallurgica,* September 1999.

[18] Clausing, D. P., "Tensile Properties of Eight Constructional Steels Between 70 and −320°F," *Journal of Materials,* JMLSA, Vol. 4, No. 2, July 1969, pp. 473–492.

[19] Gudas, J. P., "Micromechanisms of Crack Arrest in Two High Strength Steels," David Taylor Naval Ship Research and Development Center, DTNSRDC/SME-87-20, December 1987.

[20] Kotilainen, H., "The Micromechanisms of Cleavage Fracture and Their Relationship to Fracture Toughness in a Bainitic, Low Alloy, Steel," Publication 23, Technical Research Centre of Finland, Materials and Processing Technology, 1980.

[21] Barsom, J. M., "Relationship Between Plane-Strain Ductility and K_{Ic} for Various Steels," *Journal of Engineering for Industry-Transactions of the ASME,* November 1971, pp. 1209–1215.

Crack Analyses and Application to Structural Integrity

Stephanie C. TerMaath[1] *and S. Leigh Phoenix*[2]

Investigation of a New Analytical Method for Treating Kinked Cracks in a Plate

REFERENCE: TerMaath, S. C. and Phoenix, S. L., **"Investigation of a New Analytical Method for Treating Kinked Cracks in a Plate,"** *Fatigue and Fracture Mechanics: 31st Volume, ASTM STP 1389*, G. R. Halford and J. P. Gallagher, Eds., American Society for Testing and Materials, West Conshohocken, PA, 2000, pp. 331–347.

ABSTRACT: A new analytical method for treating kinked and branched cracks is investigated to understand its subtleties and their effects on accuracy and efficiency. Based on a weighted superposition approach, this method uses analytical functions built from opening displacement profiles to determine full stress and displacement fields in a linearly elastic two-dimensional infinite plate containing interacting kinked and branched cracks under far field loading. In addition, results include stress intensity factors at tip and kink locations. Rapid convergence is achieved for few degrees of freedom yielding crack face tractions consistent with those prescribed. Moreover, this method involves no numerical integration, eliminating unnecessary computational errors. The features of this method are demonstrated by the solution of a V-shaped crack. The method yields stress intensity factor results that are in agreement with a particular case found in a well-known handbook.

KEYWORDS: dislocation density distribution, stress intensity factor, basis function, crack-face tractions, superposition, wedge

Introduction

To study the growth of multiple straight, kinked, and branched cracks in brittle materials, it is necessary to evaluate the material stress state at all locations where crack growth is possible. These locations include crack tips, material wedges formed by kinks, and small-scale material flaws. Burton and Phoenix [*1*] have developed an analytical weighted superposition method to study this problem. Their method can be used to calculate the stress intensity factors at crack tips and kinks. In addition, since small-scale flaws justifiably ignored in initial modeling may grow and become sizably important if located in an area with a high stress state, the Burton and Phoenix method can be used to determine the full stress and displacement fields in all areas of the material. Moreover, their method involves no numerical integration when evaluating the Cauchy singular integrals necessary to the solution of this problem, thus overcoming many of the difficulties experienced by other researchers who have studied the behavior of kinked cracks. The purpose of this follow-up research is to improve upon and to gain a greater understanding of the many important, yet subtle, issues in multiple kinked crack behavior raised by the Burton and Phoenix research.

[1] Graduate research associate, Civil and Environmental Engineering, Cornell University, 354 Hollister Hall, Ithaca, NY 14853.

[2] Professor, Theoretical and Applied Mechanics, Cornell University, 321 Thurston Hall, Ithaca, NY 14853.

Copyright© 2000 by ASTM International www.astm.org

Approaches in the Literature

Numerous researchers have studied the behavior of kinked and branched cracks and the interactions of multiple cracks of this type. Some authors have utilized traction-based procedures [*2–3*], and Kachanov [*4*] gives a comprehensive literature review of previous work in this area. Meanwhile, others have approached the problem in terms of dislocations [*5–12*], and Hills et al. [*13*] detailed such methods in their book. Chang and Mear [*14*] applied the boundary element method to this problem, and Dwyer and Pan [*15*] investigated such problems using special edge functions. The finite element method has been applied to the problem [*16*] as has an element-free Galerkin method [*17*] and perturbation methods [*18*]. Finally, Chen and Nisitani [*19*] studied the wedge problem. An extensive review of current literature can be found in TerMaath [*20*].

Overview of Method

Burton and Phoenix have developed a weighted superposition method based on opening displacement profiles for the analysis of kinked and branched cracks in an infinite two-dimensional linearly elastic isotropic solid under general far field loading. The integral equation formulation is based on the well-known dislocation method. However, their innovative approach to building the dislocation profiles is a potential improvement over current analysis methods in that it accounts for singularities at branch and kink locations, and it also yields full stress and displacement fields in the cracked material. In addition, it converges rapidly for very few degrees of freedom. Moreover, this method involves no numerical integration, eliminating unnecessary computational errors.

To solve the kinked crack problem, the crack is first modeled as straight crack segments, spanning from kink to kink or kink to tip. Opening displacement profiles are then computed for each segment by imposing the condition of traction-free crack faces. These opening displacements are determined by choosing a set of basis functions, representing dislocation densities (a measure of the crack opening displacement), for each type of fundamental crack and wedge behavior (such as singularities at kinks, branches, and tips). These basis functions are then multiplied by a calculated weight, and then all are summed to yield the opening shape.

A crucial aspect of this analytical technique is matching singular features of adjoining crack segments at wedges so as not to create non-physical singular tractions. This requires careful determination of physically based constraints at the kinks. This deceptively difficult but essential mathematical exercise is detailed in Burton and Phoenix.

Physical conditions dictate that the crack faces are traction-free in the full problem (or constant in the auxiliary problem as induced by the boundary conditions). Therefore, the weights for each basis function are determined by setting the calculated tractions on each crack face in the auxiliary problem (caused by the opening displacements) equal to the tractions induced by the boundary conditions (or far field loading). These equations contain singular integrals of the first kind that must be evaluated as Cauchy Principal Values. Most researchers have solved these integrals numerically using Gauss-Chebychev Quadrature, but, in the current work, these integrals are evaluated analytically.

Satisfying the traction-free condition along the crack faces results in a system of equations. These equations are functions of the unknown weights of each basis function, where each basis function is a degree of freedom. To calculate the weights a large matrix must be inverted; therefore, the use of efficient and physically realistic basis functions is imperative to reduce the number of degrees of freedom to the smallest number realistically possible. It will be shown that in addition to effective choices of basis functions, allocation of points

(where the traction conditions are enforced) along the crack segments can also be optimized for computational efficiency. It should be emphasized that the location of these points is arbitrary and not dictated by a numerical scheme, thus allowing for maximum efficiency in convergence.

Objective

While the Burton and Phoenix method contains many desirable features, the original implementation still leaves several unanswered questions. First is a determination of the cause of certain numerical problems they encountered in their analysis of a crack with two kinks. Second, it is necessary to address certain minor convergence problems they experienced in the wedge stress intensity factor that appeared even in a single kink crack. In addition, refinement of their traction plots shows many subtle features including mildly erratic behavior at the crack tips and kinks. And lastly, their basis functions appear to be somewhat arbitrary, and it is necessary to understand the effects of each term to efficiently utilize the features of each.

The goal of the current work is to understand the sources of their numerical convergence difficulties when calculating stress intensity factors and to study the effects of basis functions on wedge and tip behavior. Revised basis functions are developed and evaluated for efficiency and accuracy improvement. The developed method will be presented in the context of an equal arm length V-shaped crack in an infinite linearly elastic isotropic plate under far field loading. Results with the new basis functions will be compared to the Burton and Phoenix scheme in an effort to distinguish certain characteristics inherent in each set of basis functions. Results are also generated for comparison to those for a special case found in a stress intensity factors handbook.

Superposition Approach

The developed analytical method to study the behavior of kinked cracks utilizes superposition on two levels, global and local. On the global level, the cracked plate is modeled as two separate problems, the trivial problem and the auxiliary problem (Fig. 1). The trivial problem consists of merely determining the stress and displacement fields in an uncracked plate under the specified far field loading conditions. Meanwhile, the auxiliary problem is comprised of solving for stress and displacement fields in the given cracked plate with no far field loading but with crack face tractions determined by the loading conditions. These crack face tractions are calculated to be equal and opposite to the stresses induced in the uncracked material at the location of crack faces, thus insuring that the crack faces are traction-free when the solutions to the trivial and auxiliary problems are added together.

Auxiliary Problem

The solution of the auxiliary problem constitutes the bulk of the computational effort. To solve for the stress and displacement fields in the auxiliary problem, an opening displacement profile for the crack due to the applied tractions must be determined. According to Bueckner's Principle [*21*] this solution can also be used to determine the stress intensity factors at the crack tips and kink. To solve for the opening displacement profiles, superposition is now applied at the local level to the auxiliary problem by sectioning the kinked crack into a series of straight crack segments (spanning from kink to kink or kink to tip). For the V-shaped crack (Fig. 2*a*), each arm of the crack represents one crack segment of length a (Fig. 2*b*), and the effects on the displacement field caused by each segment are evaluated separately

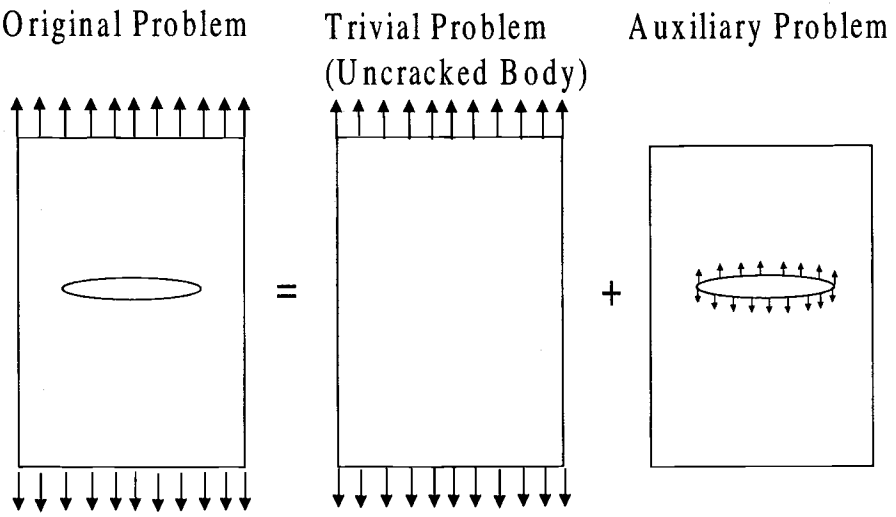


FIG. 1—*Global superposition method.*

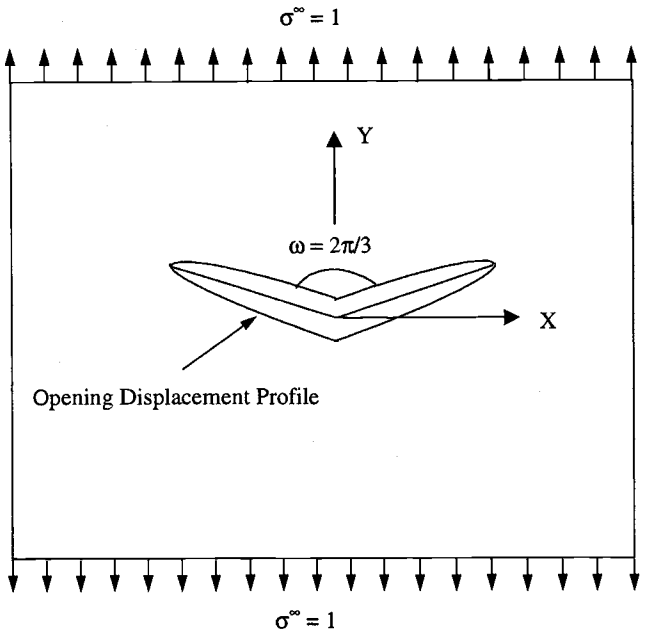


FIG. 2*a*—*V-shaped crack in an infinite plate loaded in far field unit tension.*

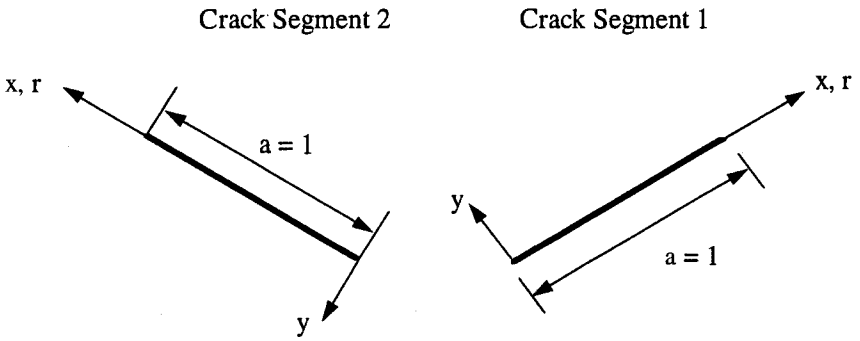


FIG. 2*b*—*Local and polar coordinate systems for individual crack segments.*

and then summed with those from the trivial solution to yield the displacement field of the full problem.

Satisfying the Traction-Free Condition

To ensure that the crack faces are traction-free in the full problem, the opening displacement profiles for each crack must be exactly those caused by the applied tractions (in the auxiliary problem). Therefore, a series of equations to enforce traction-free crack faces in the normal and shear directions must be enforced simultaneously at a given number of points along each crack segment.

These equations take the following form

$$\begin{aligned} \sigma^{\infty}_{xy} n_y + \sigma^{\infty}_{xx} n_x &= -n_y \sum_{i=1}^{c} s^{(i)}_{xy} - n_x \sum_{i=1}^{c} s^{(i)}_{xx} \\ \sigma^{\infty}_{yy} n_y + \sigma^{\infty}_{xy} n_x &= -n_y \sum_{i=1}^{c} s^{(i)}_{yy} - n_x \sum_{i=1}^{c} s^{(i)}_{xy} \end{aligned} \tag{1}$$

The left-hand side of Eq 1 represents the tractions induced at the crack faces by the loading conditions, while the right-hand side represents the tractions caused by the opening displacements of the crack segments. Also, n_x and n_y are the normals to the bottom crack faces in the x and y directions, respectively. The σ^{∞} are the far field loads in the directions denoted by their subscripts. The number of crack segments is c, and the $s^{(i)}$ are the tractions along crack segment i due to the opening displacement profile of the crack segment. It should be noted that there is no need for kinked cracks to be continuous. Crack segments do not need to be connected. Thus, the method is applicable to multiple kinked cracks although only a single kinked crack is used as the current example.

A set of Eq 1 is formed for each point along a given crack segment in the local coordinate system for that crack segment. Definitions of global (X,Y) and local (x,y) coordinate systems are shown in Fig. 2. The $s^{(i)}$ are the tractions at a particular point due to the opening displacement of crack segment i and are calculated using Eq 2. These terms will be referred to as monotractions.

$$s_{xy}^{(i)} = -\frac{2G}{\pi(1+\kappa)}\{y\,\mathrm{Re}(Z_2^2) + \mathrm{Re}(Z_1^1) + y\,\mathrm{Im}(Z_2^1)\}$$

$$s_{yy}^{(i)} = -\frac{2G}{\pi(1+\kappa)}\{\mathrm{Re}(Z_1^2) - y\,\mathrm{Im}(Z_2^2) + y\,\mathrm{Re}(Z_2^1)\} \tag{2}$$

$$s_{xx}^{(i)} = -\frac{2G}{\pi(1+\kappa)}\{\mathrm{Re}(Z_1^2) + y\,\mathrm{Im}(Z_2^2) + 2\,\mathrm{Im}(Z_1^1) - y\,\mathrm{Re}(Z_2^1)\}$$

where G is the shear modulus of the material, κ is Kosolov's constant ($3 - 4\nu$ for plane strain and $(3 - \nu)/(1 + \nu)$ for plane stress), and ν is Poisson's ratio. The Z are Cauchy singular integrals that are solved in terms of the dislocation densities μ, where $\eta = 1, 2$ stands for the tangential and normal directions, respectively (Eq 3).

$$Z_1^\eta = \int_0^a \frac{\mu_\eta(t)dt}{z - t}$$

$$Z_2^\eta = \int_0^a \frac{\mu_\eta(t)dt}{(z - t)^2} = -\frac{d}{dz} Z_1^\eta \tag{3}$$

These integrals are evaluated in closed form where $z = x + iy$ is a complex variable, and x and y are local coordinates for each crack segment (Fig. 2*b*).

At this stage, the traction-free condition is developed in terms of an unknown set of dislocation densities. These dislocation densities will be approximated by building together a set of basis functions that capture the physical properties of crack behavior.

Basic Functions

Sets of basis functions are developed to build dislocation density profiles. When enforcing the traction-free conditions, a weighting coefficient will be calculated for each basis function. Each weighting coefficient represents a degree of freedom. These weighted basis functions are then summed to determine the opening displacement profile. Once the crack opening displacements are known, the stress intensity factors at tips and kinks and the stress and displacement fields in the plate can be determined.

Each basis function is used independently in both the tangential and normal modes of deformation. Furthermore, the basis functions represent opening behavior of a single crack segment, or, more succinctly, a separate set of basis functions must be included for each crack segment.

The basis functions used by Burton and Phoenix appear somewhat arbitrary, so emphasis was placed on creating efficient basis functions to capture all necessary physical behavior while minimizing the number of degrees of freedom in the analysis. Attention in the current study was placed on understanding the individual effects of each term in the analysis.

Semi-Ellipse Basis Functions

The first basis function to be included in the dislocation density profile (used in both the normal and tangential opening profiles) is the shape of a semi-ellipse multiplied by the unknown weighting function c_{se} to be determined, $E(r) = [(1/a)(a^2 - r^2)^{1/2}\,(H(r) - H(r - a))]c_{se}$. Use of the Heaviside unit step function, $H(r)$, allows this basis function to be

turned on and off at the beginning and end of each crack segment. In particular, it allows for the jump opening displacement at the kink. This term also captures the singular behavior at the crack tip. Such a term will allow accurate evaluation of crack tip stress intensity factors in addition to modeling a jump dislocation at the kink end of the crack segment. This term has been found to dominate the overall crack shape. The corresponding dislocation density profile for this shape necessary to solve the integral equations (Eq 3) is

$$\mu(t) = \frac{d}{dt}\left[\frac{1}{a}\sqrt{a^2 - t^2}\,(H(t) - H(t-a))\right]$$

$$= \frac{-t}{a\sqrt{a^2 - t^2}}\,(H(t) - H(t-a)) + \delta(t) \tag{4}$$

where $\delta(t)$ is the Dirac Delta function arising from the jump opening at the kink end of the crack segment.

To solve for the monotractions (Eq 2) caused by this term, integrals of the form of Eq 3 need to be evaluated yielding

$$Z_1 = \frac{\pi}{2a} - \frac{\pi z}{2a\sqrt{z^2 - a^2}} + \frac{z}{2a\sqrt{a^2 - z^2}} \ln\left(\frac{a + \sqrt{a^2 - z^2}}{\sqrt{a^2 - z^2} - a}\right) + \frac{1}{z}$$

$$Z_2 = \frac{1}{a^2 - z^2} - \frac{\pi a}{2(z^2 - a^2)^{3/2}} - \frac{a}{2(a^2 - z^2)^{3/2}} \ln\left(\frac{a + \sqrt{a^2 - z^2}}{\sqrt{a^2 - z^2} - a}\right) + \frac{1}{z^2} \tag{5}$$

These solutions are variations of those given in Burton and Phoenix. To eliminate the $1/r$ singularity in the tractions induced by the jump opening at the kink end, it is necessary to add a natural constraint equation to ensure that the jump opening between adjoining crack segments is continuous.

Wedge Basis Functions

From Williams [22] it is well-established that the opening displacement, *OD*, at a traction-free kink can be written as the summation

$$OD \approx \sum_{\rho} c_\rho(\theta) r^\rho \tag{6}$$

where ρ satisfies the conditions

$$\sin(\rho\omega) = \pm\rho \sin(\omega)$$

$$\sin(\rho(2\pi - \omega)) = \pm\rho \sin(\omega) \tag{7}$$

for the upper and lower wedges, respectively. Figures 2*a* and 2*b* define r (a polar coordinate system), ω, and the lower and upper wedges. Solving Eq 7 for real values of ρ that cause singular monotractions and considering continuity and boundedness results in either three or four eigenvalues depending on the wedge angle. These eigenvalues are 0, 1, and one or two values $0 < \rho < 1$. Eigenvalues, real or complex, which do not cause singular monotractions or singularities in the material are not included in the current analysis, and their effects are

approximated by a power series. There seem to be no effects of neglecting higher order eigenvalues. The traction errors appear to be uniformly convergent.

The values $\rho = 0, 1$ largely model translation and rotation of one kink wedge relative to its mate. These eigenvalues are accounted for in the polynomial basis functions and will be detailed in the next section. However, the one or two values $0 < \rho_1 \leq \rho_2 < 1$ that cause singular behavior in the lower wedge are considered wedge terms and must be included in the wedge basis functions. ρ_1 is dominant and represents symmetric deformation of the lower wedge, and, when it exists, ρ_2 accounts for anti-symmetric singular deformation. When two eigenvalues less than 1 exist, each will have its own series as described below. For the V-shaped example problem, the wedge angle is 120° and produces only one eigenvalue less than 1, ρ_1, equal to 0.61573. For the purpose of solving the necessary integrals, irrational eigenvalues are approximated as a rational fraction, $\rho = \alpha/\beta$. In the example, ρ_1 is approximated as 8/13, resulting in a relative error of only 0.06%.

In order to include material singularities in the lower wedge while retaining constant tractions in the auxiliary problem, a power series of the form

$$W(r) = c_{j\rho}\left(\frac{r}{a}\right)^{\rho} + c_{2\rho}\left(\frac{r}{a}\right)^{2\rho} + c_{3\rho}\left(\frac{r}{a}\right)^{3\rho} + \ldots + c_{n\rho}\left(\frac{r}{a}\right)^{n\rho} \tag{8}$$

was used where $c_{j\rho}$ are the weighting coefficients. This series must be subjected to constraints that prohibit a displacement jump and slope of the opening profile at the crack tip end. Applying these constraints reduces the number of weighting coefficients by two, resulting in the following wedge basis function

$$W(r) = \sum_{j=1}^{n-2} c_{j\rho}\left(\left(\frac{r}{a}\right)^{j\rho} - (n-j)\left(\frac{r}{a}\right)^{(n-1)\rho} + (n-j-1)\left(\frac{r}{a}\right)^{n\rho}\right) \tag{9}$$

The value of ρ is known from Eq 7, and when two eigenvalues less than 1 exist (ρ_1, ρ_2), separate wedge basis functions, Eq 9, must be included for each. To solve for the monotractions (Eq 2) that occur due to the individual terms in this function, the profile for each is of the form

$$\begin{aligned} \mu(t) &= \frac{d}{dt}\left[t^{\rho}(H(t) - H(t-a))\right] \\ &= \rho t^{\rho-1}(H(t) - H(t-a)) - a^{\rho}\delta(t-a) \end{aligned} \tag{10}$$

The corresponding integral results, from Eq 3, for $0 < \rho < 1$ are

$$\begin{aligned} Z_1 &= -\frac{\rho}{z}\sum_{k=0}^{\beta-1} z_k^{\alpha} \ln\left(1 - \frac{a^{1/\beta}}{z_k}\right) - \frac{a^{\rho}}{z-a} \\ z_k &= z^{1/\beta} e^{2\pi i k/\beta} \\ Z_2 &= -\frac{\rho(1-\rho)}{z^2}\sum_{k=0}^{\beta-1} z_k^{\alpha} \ln\left(1 - \frac{a^{1/\beta}}{z_k}\right) + \frac{\rho a^{\rho}}{z(z-a)} - \frac{a^{\rho}}{(z-a)^2} \end{aligned} \tag{11}$$

where $\rho = \alpha/\beta$ is the rational approximation for the eigenvalue. When $n\rho > 1$ a recursive

procedure based on the identity $t^{n\rho-1} = -(z - t)t^{n\rho-2} + z\,t^{n\rho-2}$ must be performed. Constraints relating the $c_{1\rho}$ coefficients between adjoining crack segments are also necessary to eliminate unwanted singularities in the tractions at the kink.

Polynomial Basis Functions

To include the effects of the $\rho = 0$ and 1 eigenvalues, a polynomial series basis function is included in the analysis. In addition to accounting for these eigenvalues, the polynomial series also performs the task of manipulating the overall shape of the opening displacement profile by allowing greater flexibility in the possible midspan deformations. Similar to the kink power series, the polynomial series is written as

$$P(r) = \sum_{j=0}^{n-2} c_{jp}\left(\left(\frac{r}{a}\right)^{j} - (n-j)\left(\frac{r}{a}\right)^{(n-1)} + (n-j-1)\left(\frac{r}{a}\right)^{n}\right) \tag{12}$$

after the constraints of zero slope and zero displacement jump on the opening profile at the crack tip have been applied.

To solve for the monotractions that occur due to this function, the profile for an individual term is

$$\begin{aligned}\mu(t) &= \frac{d}{dt}\left[t^{n}(H(t) - H(t-a))\right] \\ &= \rho t^{n-1}(H(t) - H(t-a)) - a^{n}\delta(t-a)\end{aligned} \tag{13}$$

and the corresponding integral results are, for $n = 0$

$$\begin{aligned}Z_1 &= \frac{1}{z} - \frac{1}{z-a} \\ Z_2 &= \frac{1}{z^2} - \frac{1}{(z-a)^2}\end{aligned} \tag{14}$$

for $n = 1$

$$\begin{aligned}Z_1 &= \ln(-z) - \ln(a-z) - \frac{a}{z-a} \\ Z_2 &= \frac{a}{z(z-a)} - \frac{a}{(z-a)^2}\end{aligned} \tag{15}$$

and for integer $n > 1$ where $m = n - 1$

$$Z_1 = -n\left(\sum_{k=1}^{m}\frac{a^k}{k}z^{m-k} + z^m(\ln(a-z) - \ln(-z))\right) - \frac{a^n}{z-a}$$

$$Z_2 = n\left(\sum_{k=1}^{m}\frac{(m-k)a^k}{k}z^{m-k-1} + mz^{m-1}(\ln(a-z) - \ln(-z)) + z^m\left(\frac{1}{z-a} - \frac{1}{z}\right)\right) - \frac{a^n}{(z-a)^2} \quad (16)$$

As before with the wedge basis functions, additional constraints must be implemented at the kink on the coefficients of the adjoining crack segments due to the jump discontinuity caused by the r^0 term and due to the slope discontinuity caused by the r^1 term.

Tip Basis Functions

Lastly, basis functions to represent higher order behavior at the crack tips are introduced [*23*]. These basis functions are constructed as a series of powers incremented by ½ and are subject to the constraints of zero slope and displacement at the crack tip.

$$T(r) = \sum_{j=1}^{n-2} c_{jt}\left(\left(\frac{r}{a}\right)^{(j+2)/2} - (n-j)\left(\frac{r}{a}\right)^{(n+1)/2} + (n-j-1)\left(\frac{r}{a}\right)^{(n+2)/2}\right) \quad (17)$$

The integrals resulting from this basis function can be evaluated using the expressions previously presented. Furthermore, no additional constraints are required since no traction singularities are induced at the kink.

Solving for the Unknown Coefficients

Once the basis function as detailed above are included the analysis, the result is a system of equations that must be solved simultaneously. This requires the inversion of a large matrix; therefore, it is evident that adding points along the crack segments where the tractions are enforced is computationally more efficient than adding basis functions resulting in the solution of additional coefficients. So, a scheme for optimizing computational efficiency through effective choices of point allocation and inclusion of an appropriate number of basis functions warrants further study. An over-determined matrix is produced that is solved by a least squares fit. This allows for an error estimate of the tractions (which is calculated by dividing the least squares error of the fit by the sum of the squared applied tractions and then taking the square root of the quantity). This error is called the relative root mean squares (RRMS) error. Results of this convergence study are presented for the V-shaped crack example.

Calculation of Stress Intensity Factors

Equations for computing the SIFs from the weighting coefficients are as follows. At the crack tips

$$\begin{pmatrix} K_{II} \\ K_I \end{pmatrix} = \frac{2G}{1+\kappa}\sqrt{\frac{\pi}{a}}\begin{pmatrix} c^1_{se} \\ c^2_{se} \end{pmatrix} \tag{18}$$

and at the kink

$$K_I^{(\rho_1)} = -\frac{2G}{1+\kappa}(2\pi)^{(1-\rho_1)}\rho_1(\rho_1+1)\left(1 - \frac{(\rho_1-1)\sin[(\rho_1-1)\omega'/2]}{(\rho_1+1)\sin[(\rho_1+1)\omega'/2]}\right)\frac{c^2_{1\rho_1}}{\sin[(\rho_1-1)\omega'/2]}$$

$$K_{II}^{(\rho_2)} = -\frac{2G}{1+\kappa}(2\pi)^{(1-\rho_2)}\rho_2(\rho_2+1)\left(\frac{\sin[(\rho_2-1)\omega'/2]}{\sin[(\rho_2+1)\omega'/2]} - \frac{\rho_2-1}{\rho_2+1}\right)\frac{c^1_{1\rho_2}}{\sin[(\rho_2-1)\omega'/2]} \tag{19}$$

where $\omega' = 2\pi - \omega$ and $a = 1$. The superscript notation on the constants (1,2) represents the tangential and normal directions, respectively. (A set of each type of basis functions is included independently in both the normal and tangential directions.) When $\rho_2 < 1$ does not exist for certain wedge angles, K_{II} at the kink is not relevant.

Equation 19 is derived from the expressions

$$K_I = \sigma_\theta(2\pi r)^{1-\rho 1}$$

$$K_{II} = \tau_{r\theta}(2\pi r)^{1-\rho 2} \tag{20}$$

where θ is evaluated at the bisector of the wedge. Note that these equations explicitly preserve the $(2\pi r)^{1-\rho}$ component. In addition, when $\omega = 0$ and $\rho = \frac{1}{2}$, Eq 19 is equivalent to twice those for a crack tip. (This factor of 2 discrepancy occurs because the lower wedge is assumed to absorb all of the displacment.)

V-Shaped Crack Example

To demonstrate the method, results for a V-shaped crack in an infinite plate loaded in far field unit tension will be discussed (Fig. 2). The crack consists of one kink and has equal length arms of unit value. The upper wedge angle is 120°.

Point Allocation

One benefit of this method is the ability to arbitrarily choose the locations of points along the crack segments. Two allocation schemes were studied, one where the points were evenly spaced and one where the spacing varied with increasing density as tips and kinks were approached. The method with varying point density followed the rule where the crack segment was divided in half. Points were then spaced towards each end of the crack segment according to

$$\frac{x_j}{a} = \sin\left(\frac{j\pi}{N+2}\right) \tag{21}$$

where N is the number of points per crack segment.

TABLE 1—*Results using varying density method.*

Number of Points	K_I	K_{II}	$K_{I,kink}$	RRMS Error	
				Normal	Shear
30	1.2548	0.8455	−0.4505	2.67×10^{-5}	5.58×10^{-5}
50	1.2548	0.8455	−0.4505	3.51×10^{-5}	8.52×10^{-5}
80	1.2548	0.8455	−0.4501	4.26×10^{-5}	1.14×10^{-4}
100	1.2548	0.8455	−0.4500	4.63×10^{-5}	1.29×10^{-4}

The point allocation methods were studied using 48 degrees of freedom (basis functions) as it was observed in preliminary studies that convergence with respect to basis functions had been reached by this number of terms. The results (Tables 1 and 2) imply several key points. One, it is clear that increasing the density of points near the tips and kinks results in much faster convergence of all three stress intensity factors. This occurs since points are able to be placed much closer to the kink and tip than is allowed with equally spaced points. Thus, behavior at these locations is captured to a much greater degree. Two, convergence can be achieved using the varying density method with only 30 points. And, finally, the RRMS error slightly increases with increasing numbers of points. Again, this is due to the fact that constant tractions are harder to enforce at kinks and tips than in the middle of the crack segment. For a small number of points, points are located relatively far from the ends, and this effect is neglected. Therefore, as an increasing number of points are added in these regions, the traction error increases.

Convergence of SIFs and Tractions with Respect to Degrees of Freedom

Table 3 shows the effects of varying the degrees of freedom on the SIFs while Figs. 3*a* and 3*b* show convergence of the crack face tractions in the normal direction (results in the shear direction are similar and are not shown). The constant target traction was 0.7500. The first basis function, or degree of freedom, included was the semi-ellipse function, followed by the kink term r^p, representing the singular material behavior at the wedge. Basis functions of the other types were added in a rotating manner.

When only the semi-ellipse term was included, 2 degrees of freedom (dof) were available. Adding the kink term increased this value to 3 (after constraints were applied, but not accounting for symmetry). Twelve dof were obtained by including all terms up to order

TABLE 2—*Results using equal spacing.*

Number of Points	K_I	K_{II}	$K_{I,kink}$	RRMS Error	
				Normal	Shear
30	1.2511	0.8473	−0.4269	3.22×10^{-6}	2.65×10^{-6}
50	1.2531	0.8467	−0.4375	7.12×10^{-6}	8.65×10^{-6}
80	1.2540	0.8461	−0.4447	1.16×10^{-5}	1.70×10^{-5}
100	1.2542	0.8459	−0.4470	1.37×10^{-5}	2.13×10^{-5}
150	1.2545	0.8457	−0.4496	1.69×10^{-5}	2.89×10^{-5}
200	1.2547	0.8456	−0.4505	1.88×10^{-5}	3.38×10^{-5}
300	1.2547	0.8455	−0.4510	2.10×10^{-5}	3.99×10^{-5}

TABLE 3—*Results for varying degrees of freedom.*

Degrees of Freedom	K_I	K_{II}	$K_{I,kink}$	RRMS Error	
				Normal	Shear
2	1.2437	0.7180	...	1.08	2.09
3	1.2715	0.7341	−0.3612	1.11	2.06
12	1.2528	0.8339	−0.4298	0.0388	0.129
24	1.2546	0.8462	−0.4396	0.0023	0.0093
36	1.2550	0.8457	−0.4484	4.68×10^{-4}	7.25×10^{-4}
48	1.2548	0.8455	−0.4500	4.63×10^{-5}	1.29×10^{-4}

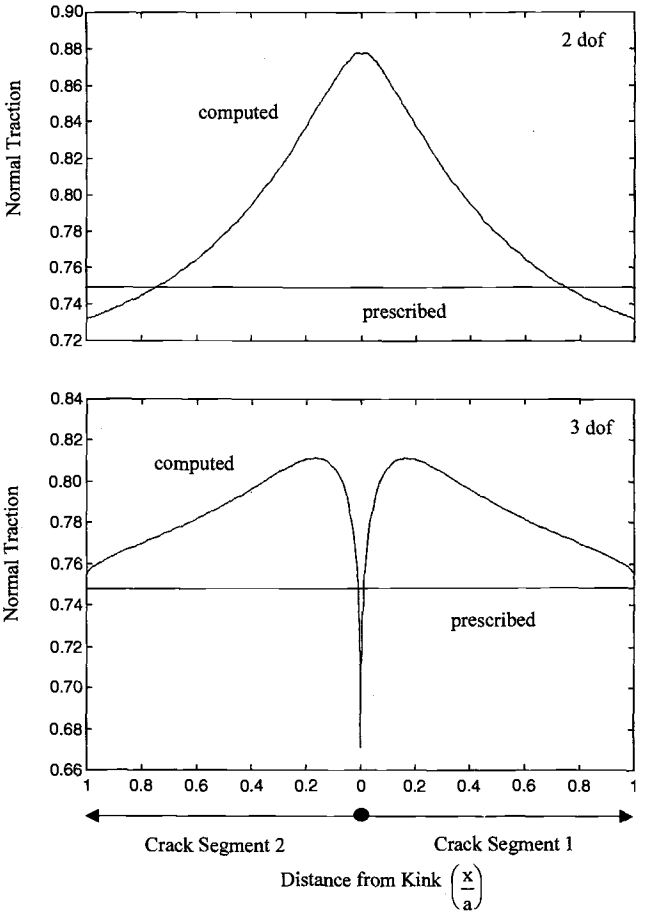


FIG. 3*a*—*Normal traction plots for 2 and 3 degrees of freedom.*

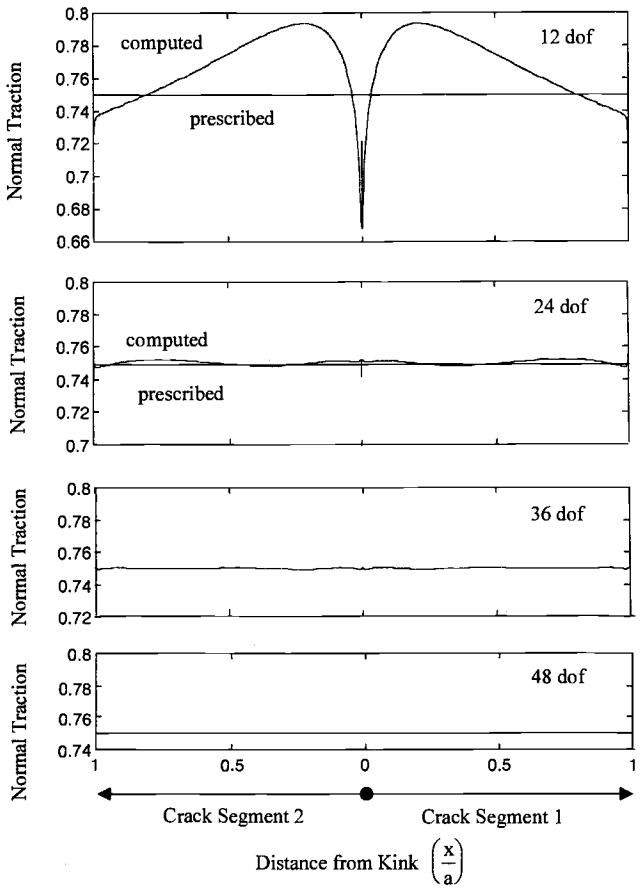


FIG. 3*b*—*Normal traction plots for 12, 24, 36, and 48 degrees of freedom.*

$n = 3$. Similarly, including all terms up to orders $n = 4, 5, 6$ results in 24, 36, and 48 dof, respectively.

While the semi-ellipse term alone (2 dof) does capture the opening displacement shape, the corresponding tractions do not match the prescribed tractions as noted in the RRMS error and Fig. 3. At this stage, no attempt is made to capture the singular behavior at the wedge. However, once the kink term is added to account for this behavior, a drastic change takes place in the traction behavior near the kink. Additional calculations show that the traction at the kink is bounded and does not approach infinity within the accuracy of the eigenvalue. SIF convergence is achieved by 48 dof as shown in Table 3 and Figs. 3*a* and 3*b*. If symmetry were taken into consideration, only 24 dof would be necessary. However, under general loading the full 48 dof would be necessary. One last item of note is that although the tractions for 48 dof look smooth on a large scale, it can be seen that they do oscillate albeit on an extremely refined scale (Fig. 4*a*).

Comparison with the Burton and Phoenix Results

To compare the two methods, traction results were calculated for each method with comparable degrees of freedom (44 dof with the Burton and Phoenix method and 48 dof with

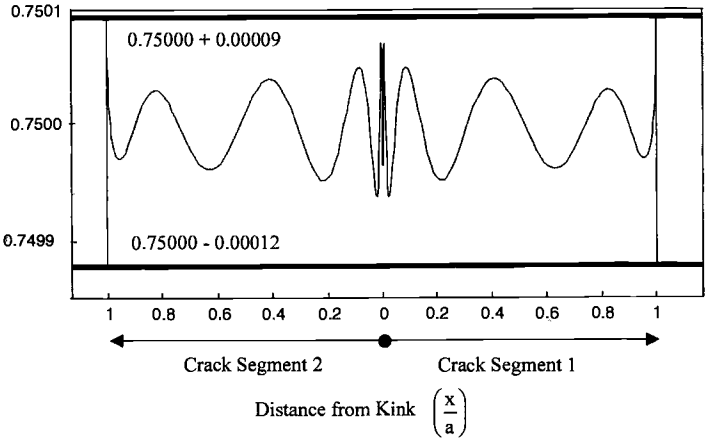


FIG. 4*a*—*Normal traction plot for 48 degrees of freedom on a refined scale.*

the revised method) and the same point allocation scheme (100 points per crack segment with the varying density method). While both methods yield the correct and converged SIFs, the new basis functions perform slightly better with respect to the tractions (see Fig. 4). As seen in the figure, the Burton and Phoenix method has slightly larger fluctuations at the tip and kink. The thick lines on the figures indicate the maximum and minimum values of the fluctuations at the tip. One reason for the increased values in the Burton and Phoenix method appears to be an r^0 wedge basis function that is included in their analysis. This function does not approach a zero slope at the kink until infinitesimally close to the kink. Therefore, although there is no actual singularity, the rapid slope change does cause numerical problems.

Comparison with a Result in a Stress Intensity Factors Handbook

Results for a special case of the 120° V-shaped crack are compared with those found in the Stress Intensity Factors Handbook [*24*]. Results in the handbook are available only for

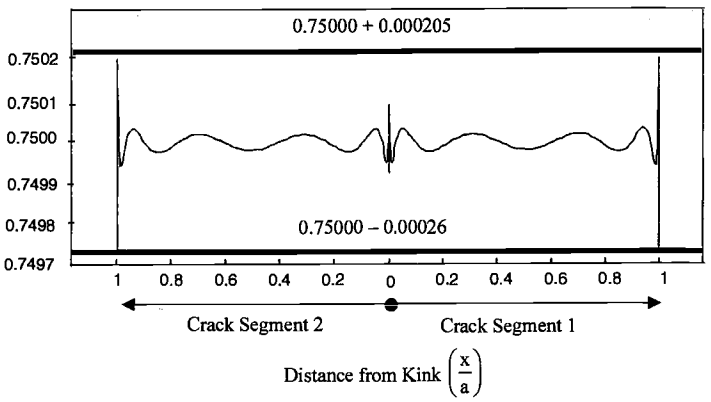


FIG. 4*b*—*Normal traction plot using the Burton and Phoenix Method with 44 degrees of freedom.*

the stress intensity factor at the crack tip of crack segment 2 (in our notation), and the far field loading must be uniform tension that is at 0, 45, or 90° to crack segment 1. For loading perpendicular to crack segment 1, the handbook method (a conformal mapping technique [*25,26*]) yields stress intensity factors at the crack tip of crack segment 2 that are K_I = 0.4867 and K_{II} = −1.040. This method, using 48 dof, yields K_I = 0.4866 and K_{II} = −1.039. For this particular case, the results are in agreement. No results are given in the handbook for the generalized stress intensity factor at the wedge. This method yields a converged value of 0.0093.

Conclusions

While the new method produces only slight improvement over the Burton and Phoenix approach, new insight and understanding of the problem has been accomplished. A key area for future study is evident. Computational efficiency can be optimized by an effective point allocation scheme. Further development is warranted to place points such that tip and kink behavior is captured using the minimum number of points.

Future applications of this method include studying the V-crack problem with different angles and under skew loading. Also, this approach will be applied to multiple crack cases.

Acknowledgment

This work was supported by a National Science Foundation Fellowship.

References

[*1*] Burton, J. K. and Phoenix, S. L., "Superposition Method for Calculating Singular Stress Fields at Kinks, Branches and Tips in Multiple Crack Arrays," *International Journal of Fracture,* Vol. 102, 2000, pp. 99–139.

[*2*] Benveniste, V., Dvorak, G. J., Zarzour, J., and Wung, E. C. J., "On Interacting Cracks and Complex Crack Configurations in Linear Elastic Media," *International Journal of Solids and Structures,* Vol. 25, 1989, pp. 1279–1293.

[*3*] Atluri, S. N., *Structural Integrity and Durability,* Tech Science Press, Forsyth, GA, 1997.

[*4*] Kachanov, M., "Elastic Solids with Many Cracks and Related Problems," *Advances in Applied Mechanics,* Vol. 30, J. W. Hutchinson and T. Y. Wu, Eds., Academic Press, New York, 1994.

[*5*] Chen, Y. Z. and Hasebe, N., "New Integration Schemes for the Branch Crack Problem," *Engineering Fracture Mechanics,* Vol. 52, 1995, pp. 791–801.

[*6*] He, M.-Y. and Hutchinson, J. W., "Kinking of a Crack Out of an Interface," *Journal of Applied Mechanics,* Vol. 56, 1989, pp. 270–278.

[*7*] Lo, K. K., "Analysis of Branched Cracks," *Journal of Applied Mechanics,* Vol. 45, 1978, pp. 797–802.

[*8*] Hayashi, K. and Nemat-Nasser, S., "Energy Release Rate and Crack Kinking under Combined Loading," *Journal of Applied Mechanics,* Vol. 48, 1981, pp. 520–524.

[*9*] Hu, K. X. and Chandra, A., "Interactions among General Systems of Cracks and Anticracks: An Integral Equation Approach," *Journal of Applied Mechanics,* Vol. 60, 1993, pp. 920–928.

[*10*] Han, X. and Wang, T., "A General Method for Solving the Problem of Both Open and Closed Multiple Cracks," *International Journal of Fracture,* Vol. 79, 1996, pp. R69–R72.

[*11*] Zang, W. L. and Gudmundson, P., "A Boundary Integral Method for Internal Piece-Wise Smooth Crack Problems," *International Journal of Fracture,* Vol. 38, 1988, pp. 275–294.

[*12*] Niu, J. and Wu, M. S., "Strong Interactions of Morphologically Complex Cracks," *Engineering Fracture Mechanics,* Vol. 57, 1997, pp. 665–687.

[*13*] Hills, D. A., Kelly, P. A., Dai, D. N., and Korsunsky, A. M., *Solution of Crack Problems: The Distributed Dislocation Technique,* Kluwer Academic Publishers, Dordrecht, The Netherlands, 1996.

[14] Chang, C. and Mear, M. E., "A Boundary Element Method for Two Dimensional Linear Elastic Fracture Analysis," *International Journal of Fracture,* Vol. 74, 1995, pp. 219–251.
[15] Dwyer, J. F. and Pan, E., "Edge Function Analysis of Stress Intensity Factors in Cracked Anisotropic Plates," *International Journal of Fracture,* Vol. 72, 1995, pp. 327–342.
[16] Gray, L. J. and Paulino, H., "Crack Tip Interpolation Revisited," *SIAM Journal of Applied Mechanics,* Vol. 58, 1998, pp. 428–455.
[17] Fleming, M., Chu, Y. A., Moran, G., and Belytschko, T., "Enriched Element-free Galerkin Methods for Crack Tip Fields," *International Journal of Numerical Methods in Engineering,* Vol. 40, 1996, pp. 1483–1504.
[18] Cotterell, B. and Rice, J. R., "Slightly Curved or Kinked Cracks," *International Journal of Fracture,* Vol. 16, 1980, pp. 155–169.
[19] Chen, D.-H. and Nisitani, H., "Singular Stress Field Near the Corner of Jointed Dissimilar Materials," *Journal of Applied Mechanics,* Vol. 60, 1993, pp. 607–613.
[20] TerMaath, S. C., "A Two-Dimensional Analytical Technique for Studying Fracture in Brittle Materials Containing Interacting Kinked and Branched Cracks," Ph.D. dissertation, Cornell University, New York, 2000.
[21] Cartwright, D. J. and Rooke, D. P., "Green's Functions in Fracture Mechanics," *Fracture Mechanics: Current Status, Future Prospects,* R. A. Smith, Ed., Pergamon, Oxford, 1979, pp. 91–123.
[22] Williams, M. L., "Stress Singularities Resulting from Various Boundary Conditions in Angular Corners of Plates in Extension," *Journal of Applied Mechanics,* Vol. 19, 1952, pp. 526–528.
[23] Hui, C. Y. and Ruina, A., "Why K? High Order Singularities and Small Scale Yielding," *International Journal of Fracture,* Vol. 72, 1995, pp. 97–120.
[24] *Stress Intensity Factors Handbook,* 1st ed., Vol. 1, Y. Murakami, Ed., Pergamon, New York, 1987, pp. 352–353.
[25] Kitagawa, H., Yuuki, R., and Ohira, T., "Crack-Morphological Aspects in Fracture Mechanics," *Engineering Fracture Mechanics,* Vol. 7, 1975, pp. 515–529.
[26] Kitagawa, H. and Yuuki, R., "Stress Intensity Factors for Branched Cracks in a Two-Dimensional Stress State," *Transactions of the Japan Society of Mechanical Engineers,* Vol. 41, No. 346, 1975, pp. 1641–1649.

G. Glinka[1] *and Wolf Reinhardt*[2]

Calculation of Stress Intensity Factors for Cracks of Complex Geometry and Subjected to Arbitrary Nonlinear Stress Fields

REFERENCE: Glinka, G. and Reinhardt, W., **"Calculation of Stress Intensity Factors for Cracks of Complex Geometry and Subjected to Arbitrary Nonlinear Stress Fields,"** *Fatigue and Fracture Mechanics: 31st Volume, ASTM STP 1389,* G. R. Halford and J. P. Gallagher, Eds., American Society for Testing and Materials, West Conshohocken, PA, 2000, pp. 348–370.

ABSTRACT: Fatigue cracks in shot-peened and case-hardened notched machine components are subjected to stress fields induced by the external load and residual stresses resulting from the surface treatment. Both stress fields are characterized by nonuniform distributions, and handbook stress intensity factor solutions are in such cases unavailable, especially in the case of planar nonelliptical cracks. The method presented here is based on the generalized weight function technique enabling the stress intensity factors to be calculated for any Mode I loading applied to arbitrary planar convex and embedded crack. The stress intensity factor can be determined at any point on the crack contour by using one general weight function discussed in the paper. The weight function, m_A, can be sufficiently well described by two quantities, i.e., the distance, ρ, from the load point, $P(x, y)$, on the crack surface to the point, A, on the crack front where the stress intensity is to be calculated and the length, Γ_c, of the inverted crack contour. The stress intensity factors are calculated by integrating the product of the stress field and the weight function over the entire crack area.

The general weight function and calculated stress intensity factors are validated against various numerical and analytical data. The numerical procedure for calculating stress intensity factors for arbitrary nonlinear stress distributions is briefly discussed as well. Several examples of typical input data and stress intensity factor results are presented including embedded and edge cracks subjected to two-dimensional stress fields. The method is particularly suitable for modeling fatigue crack growth in the presence of complex stress fields.

KEYWORDS: stress intensity factor, weight function, nonlinear stress field

Nomenclature

a	Depth of an edge crack or half width of an elliptical crack (minor semi-axis)
A	Point on the crack contour where the stress intensity factor is to be calculated
c	Half length of an elliptical crack (major semi-axis)
G_c	Crack contour
G_b	External free boundary contour
K_I	Mode I stress intensity factor (general)

[1] Department of Mechanical Engineering, University of Waterloo, Waterloo, Ontario N2L 3G1, Canada.

[2] Babcock & Wilcox, 581 Coronation Blvd., Cambridge, Ontario N1R 5V3, Canada.

Copyright© 2000 by ASTM International www.astm.org

K_{IA}	Mode I stress intensity factor at the point A on the crack contour
l	Contour coordinate for the embedded square crack
M_i	Coefficients of the 1-D line load weight functions (i = 1, 2, 3)
$m(x, a)$	Weight function (general)
$m_A(x, y, F)$	Weight function for point A on the crack contour
F	Point load (force) applied to the crack surface at point $P(x, y)$
$P(x, y)$	Point on the crack surface where the load F is applied
Q	Elliptical crack shape factor
S	External (applied) load
SIF	Stress intensity factor
s	Shortest distance between the load point and the crack contour
t	Thickness
Γ_c	Inverted crack contour
Γ_b	Inverted external free boundary contour
Φ	Angle coordinate for parametric representation of an ellipse
Ω	Crack area
$\Delta\Omega_j$	Segment of crack area
ρ	Distance between the load point and any point A on the crack front
$\sigma(x, y)$	Stress distribution over the crack surface, Ω
σ_0	Nominal or reference stress (usually the maximum value of $\sigma(x, y)$)
x	Local, through the thickness coordinate
Y, Y_{wf}	Geometric stress intensity correction factors (Y_{wf}—obtained from weight function)

Fatigue durability, damage tolerance, and strength evaluations of cracked structural components require calculation of stress intensity factors for cracks subjected to complex stress fields. This is particularly true for cracks emanating from notches or other stress concentration regions that are frequently found in engineering practice. Such components require the fatigue analysis of cracks propagating through a variety of interacting stress fields. Moreover, these are often planar two-dimensional surface-breaking or buried cracks with irregular shapes. The existing handbook stress intensity factor solutions are not sufficient in such cases due to the fact that most of them have been derived for simple geometry and load configurations. The variety of crack configurations and the complexity of stress fields occurring in engineering components require more versatile tools for calculating stress intensity factors than the available solutions, obtained for a range of specific geometry and load combinations.

Therefore, a method for calculating stress intensity factors for one- and two-dimensional cracks subjected to two-dimensional stress fields is discussed below. The method is based on the use of the weight function technique.

Stress Intensity Factors and Weight Functions

Most of the existing methods of calculating stress intensity factors require separate analysis of each load and geometry configuration. Fortunately, the weight function method developed by Bueckner [*1*] and Rice [*2*] simplifies considerably the determination of stress intensity factors. The important feature of the weight function is that it depends only on the geometry of the cracked body. If the weight function is known for a given cracked body, the stress intensity factor due to any load system applied to the body can be determined by using the same weight function. The success of the weight function technique for calculating stress intensity factors lies in the possibility of using superposition. It can be shown [*3*] that the stress intensity factor for a cracked body (Fig. 1*a*) subjected to the external loading, S, is

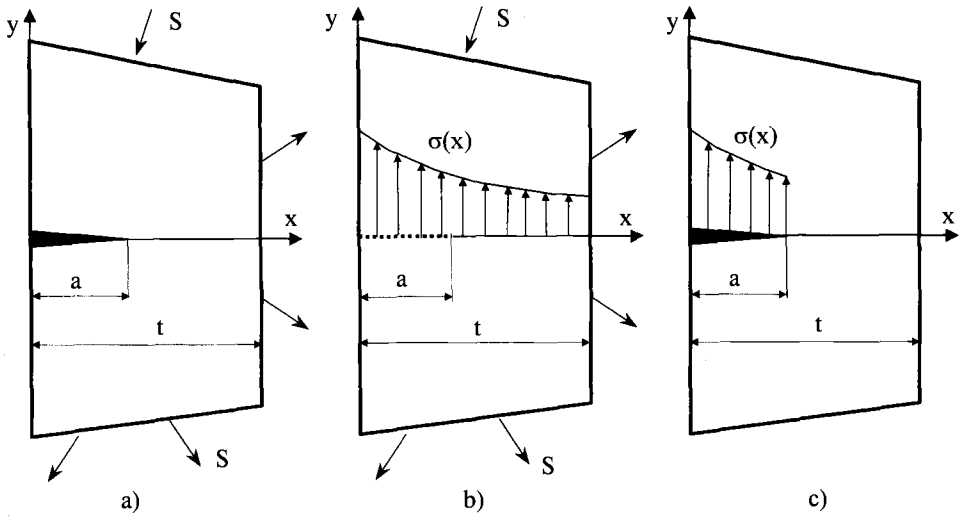


FIG. 1—*Nomenclature and the concept of superposition:* (a) *cracked body subjected to the load system S,* (b) *geometrically identical uncracked body with the stress field* σ(x) *in the crack plane, induced by the loading system S,* (c) *geometrically identical cracked body with the crack subjected to the stress field* σ(x).

the same as the stress intensity factor in a geometrically identical body (Fig. 1*c*) with the local stress field $\sigma(x)$ applied to the crack faces. The local stress field, $\sigma(x)$, induced in the prospective crack plane by preload *S*, is determined for an *uncracked* body (Fig. 1*b*) that makes the stress analysis relatively simple. Therefore, if the weight function is known, for given geometrical configuration, there is no need to derive ready-made stress intensity factor expressions for each load system and associated internal stress distribution induced in the cracked body. The stress intensity factor for a one-dimensional crack can be obtained by multiplying the weight function, $m(x, a)$, and the internal stress distribution, $\sigma(x)$, in the prospective crack plane, and integrating the product over the crack length *a*.

$$K = \int_0^a \sigma(x)m(x, a)dx \tag{1}$$

The weight function, $m(x, a)$, can be interpreted (Fig. 2*a*) as the stress intensity factor that results from a pair of splitting forces, $F = 1$, applied to the crack face at position x. The unit force F shown in Fig. 2*a* represents actually a uniformly distributed pressure along a line normal to the plane xz (Fig. 2*b*). Such configurations are customarily treated as plane stress or plane strain boundary problems because the stress field is independent of coordinate z.

Since the stress intensity factor is linearly dependent on the applied load, the contributions from multiple splitting forces applied over the crack surface can be superposed and the resultant stress intensity factor can be calculated as the sum of all individual load contributions. This results in the integral, Eq 1, of the product of the weight function, $m(x, a)$, and the stress function, $\sigma(x)$, for a continuously distributed one-dimensional stress field being a function of coordinate x only. A variety of one-dimensional (line-load) weight functions can be found in Refs *4–6*. However, their mathematical forms vary from case to case and

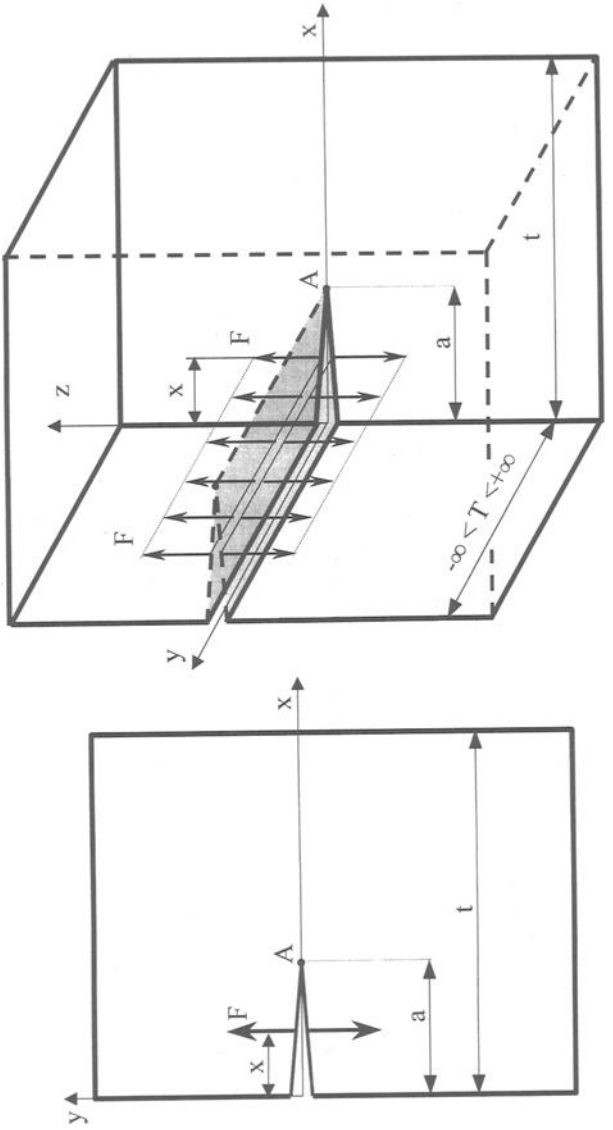


FIG. 2—(a) *Weight function nomenclature for one-dimensional crack in a two-dimensional body;* (b) *three dimensional representation of the same configuration.*

therefore they are not easy to use. Therefore, Glinka and Shen [*7*] have proposed one general weight function expression, which can be used for a wide variety of one-dimensional Mode I cracks.

$$m(x, a) = \frac{2F}{\sqrt{2\pi(a - x)}}\left[1 + M_1\left(1 - \frac{x}{a}\right)^{1/2} + M_2\left(1 - \frac{x}{a}\right)^{1} + M_3\left(1 - \frac{x}{a}\right)^{3/2}\right] \quad (2)$$

The system of coordinates and the notation for an edge crack are given in Fig. 2 as an example. In order to determine the weight function, $m(x, a)$, for a particular cracked body, it is sufficient to determine [*8*] the three parameters M_1, M_2, and M_3 in Eq 2. Because the mathematical form of the weight function, Eq 2, is the same for all cracks, the same method can be used for the determination of parameters M_1, M_2, and M_3 and calculation of stress intensity factors from Eq 1. The method of finding the M_i parameters was discussed in Ref *8*.

A variety of line load weight functions [*7–13*] have been derived and published already. In order to calculate stress intensity factors using the weight function technique the following tasks need to be carried out:

- Determine stress distribution, $\sigma(x)$, in the prospective crack plane using the linear elastic analysis of uncracked body (Fig. 1*b*), i.e., perform the stress analysis ignoring the crack and determine the stress distribution $\sigma(x) = \sigma_0 f(S, x)$.
- Apply the "uncracked" stress distribution, $\sigma(x)$, to the crack surfaces (Fig. 1*c*) as tractions.
- Choose an appropriate generic weight function.
- Integrate the product of the stress function $\sigma(x)$ and the weight function, $m(x, a)$, over the entire crack length or crack surface, Eq 1.

Point Load Weight Functions for Planar Cracks Subjected to Two-Dimensional Stress Fields

In spite of the high efficiency and usefulness of line load weight functions, they cannot be used if the stress field is of a two-dimensional nature, i.e., when the stress field, $\sigma(x, y)$, in the crack plane depends on both the x and y coordinates. Therefore, in order to calculate stress intensity factors for planar cracks subjected to two-dimensional stress field a weight function for a point load (Fig. 3) is needed. The two-dimensional point-load weight function, $m_A(x, y)$, represents the stress intensity factor at point A on the crack front (Fig. 3), induced by a pair of unit force, F, attached to the crack surface at point $P(x, y)$. If the weight function is known, it is possible to calculate the stress intensity factor at any point on the crack front.

In order to determine the stress intensity factor induced by a two-dimensional stress field, $\sigma(x, y)$, at a point A on the crack front, the product of the stress field, $\sigma(x, y)$, and the weight function, $m_A(x, y)$, needs to be integrated over the entire crack surface area Ω.

$$K_A = \iint_{\Omega} \sigma(x, y) m_A(x, y; F) dx dy \quad (5)$$

Rice has shown [*14*] that the 2-D point load weight function for an arbitrary planar crack in an infinite body can be generally written as:

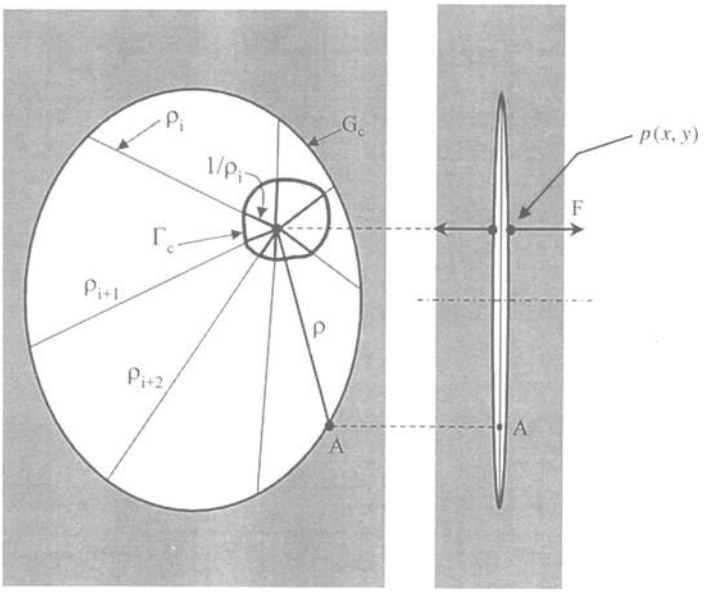


FIG. 3—*Notation for the 2-D weight function.*

$$K_A = m_A(x, y, F) = \frac{F\sqrt{2s}}{\pi^{3/2}\rho^2} w(x, y; F) \tag{6}$$

The function $w(x, y; F)$ accounting for the effect of the crack geometry is usually unknown and has to be determined for each particular crack geometry.

Oore and Burns [*15*] proposed an approximate 2-D point-load weight function, Eq 7, from which the function $w(x, y; F)$ can be derived for a several crack configurations.

$$K_A = m_A(x, y; F) = \frac{F\sqrt{2}}{\pi\rho^2 \sqrt{\oint_{G_c} \frac{dG_c}{\rho_i^2}}} \tag{7}$$

The notation for the weight function, Eq 7, is given in Fig. 3. Oore and Burns [*15*] have shown that after deriving closed form expressions for the line integral in Eq 7 several exact weight functions could be derived for straight and circular cracks in infinite bodies. Unfortunately, some difficulties were encountered while integrating the weight function, Eq 7, and when it was used for cracks with variable front curvature. In its original form, the weight function, Eq 7, was also unable to account for finite boundaries of a cracked body. However, it was found later that the integration procedure could be significantly simplified if one uses a geometrical interpretation of the line integral in Eq 7. Namely, it can be proved that the line integral $\oint_{G_c} (dG_c/\rho_i^2)$ represents the arc length, Γ_c, of the crack contour inverted (Fig. 3) with respect to the point, $P(x, y)$, where the load F is applied. As a consequence the weight function, Eq 7, can be written in a simpler and easier form for integration.

$$K_A = m_A(x, y, F) = \frac{F\sqrt{2}}{\pi\rho^2\sqrt{\Gamma_c}} \tag{8}$$

The inverted contour, Γ_c can also be looked at (Fig. 3) as the locus of inverted radii $1/\rho_i$. The area enclosed by the inverted contour, Γ_c, represents the inverted area of the uncracked cross section area surrounding the crack. Subsequently, it can be proved that the inverted contours form circles in the case of straight line and circular crack contours. In other words the inverted contour is a circle in the case of cracks with constant curvature. Subsequently, the general weight function, Eq 8, makes it possible to derive closed form weight functions for a variety of straight and circular crack configurations.

Point Load Weight Functions for Planar Cracks in Infinite Bodies

Cracks in infinite bodies are the easiest for the mathematical treatment and therefore a few closed form weight functions for such cases can be found in the literature [*4*]. It can be shown that all of them can be derived from the general weight function, Eq 8.

Infinite Edge Crack in an Infinite Body

In order to illustrate the use of the proposed weight function and to check its accuracy, several closed form weight functions for straight and circular cracks were derived from Eq 8. The first one was the weight function for an infinite edge crack in an infinite body (Fig. 4).

It can be shown that the locus of inverted radii, $1/\rho_i$, representing the inverted (with respect to the point $P((x, y))$ edge crack contour, Γ_c, forms a circle of diameter $D = 1/s$. Therefore the arc length of the inverted contour, Γ_c, is:

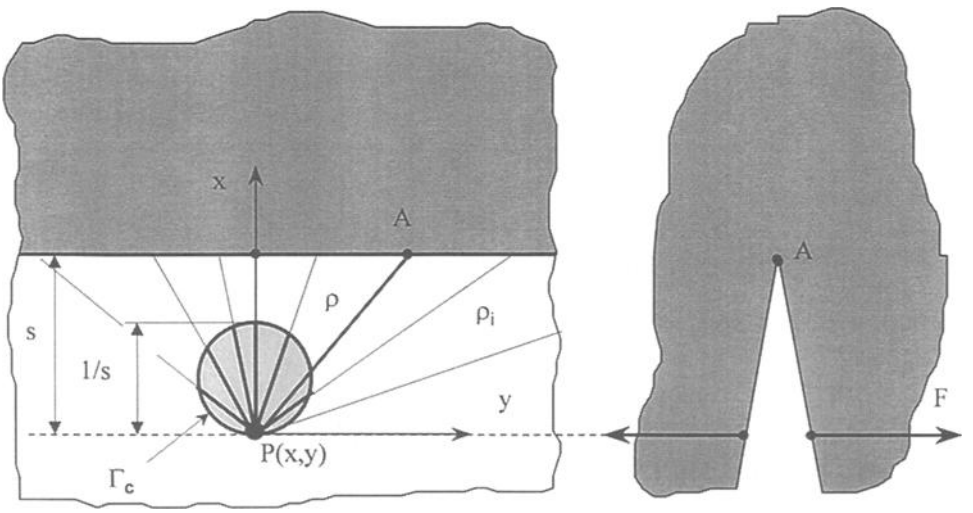


FIG. 4—*An infinite edge crack in an infinite body.*

$$\Gamma_c = \pi D = \frac{\pi}{s} \tag{9}$$

After substituting the arc length, Eq 9, into Eq 8, the 2-D point load weight function for an infinite edge crack in an infinite body is derived.

$$m_A(x, y; F) = \frac{F\sqrt{s}}{\pi^{3/2}\,\rho^2}\sqrt{2} \tag{10}$$

The weight function, Eq 10 is the exact form of the weight function for an infinite edge crack in an infinite body as shown in Ref *4*.

Infinite Tunnel Crack in Infinite Body Subjected to a Line Load

The point load (2-D) weight function for a tunnel crack (Fig. 5) is not known. However, it can be derived from the general weight function, Eq 8. Because there are two parallel straight-line crack contours, there also are two inverted circular contours, Γ_{c1} and Γ_{c2}. One

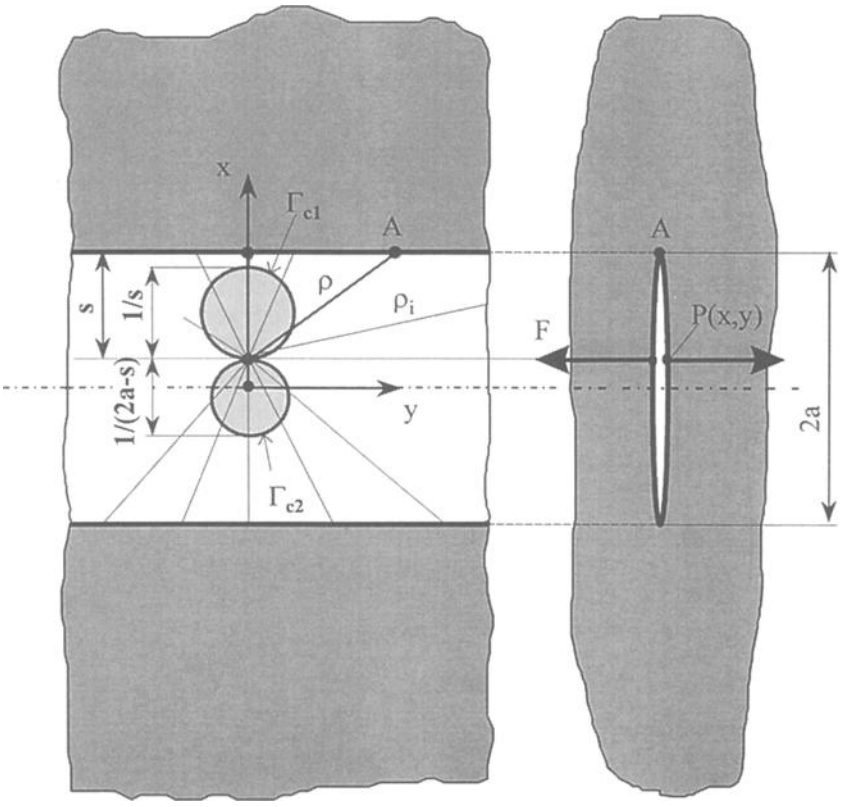


FIG. 5—*Infinite tunnel crack in an infinite body subjected to uniformly distributed line load.*

is a circle with diameter $D_1 = 1/s$ and the other also a circle but with diameter $D_2 = 1/(2a - s)$. Thus, the total arc length, Γ_c, of the inverted crack contour can be calculated as:

$$\Gamma_c = \pi D_1 + \pi D_2 = \frac{\pi}{s} + \frac{\pi}{2a - s} = \frac{2\pi a}{s(2a - s)} \tag{11}$$

Substitution of the inverted arc length, Eq 11, into Eq 8 leads to the derivation of the 2-D point load weight function for an infinite tunnel crack (Fig. 5) of constant width $2a$.

$$m_A(x, y; F) = \frac{F\sqrt{s}}{\pi^{3/2}\rho^2}\sqrt{2 - \frac{s}{a}} \tag{12}$$

The weight function, Eq 12, was subsequently integrated along the load line $x = a - s$ resulting in Eq 13.

$$m_A(x; F) = \oint_{x=a-s} \frac{F\sqrt{s}}{\pi^{3/2}\rho^2}\sqrt{2 - \frac{s}{a}}\,dy = \frac{F\sqrt{2}}{\sqrt{\pi s}}\sqrt{\frac{2a - s}{2a}} \tag{13}$$

The final form of Eq 13 is the well-known line load weight function for a through crack in an infinite plate derived by Sih [*16*]. Because the exact weight function, Eq 13, was derived from the general weight function, it indicates that Eq 8 correctly accounts for all important effects of geometry and loading. The weight function for a penny-shaped crack in an infinite body can also be derived from the same weight function, Eq 8.

Planar Cracks with Variable Crack Front Curvature—The Local Curvature Effect

It was also found that the accuracy of weight functions and subsequently accuracy of stress intensity factors for elliptical and other cracks with variable contour curvature was decreasing as the ellipses became more slender, i.e., when they departed significantly from the ideal constant curvature contour. It was concluded that the inverted crack contour, Γ_c, in Eq 8 is only an average measure of the crack geometry effect. The weight function and the stress intensity factor depend also on the immediate curvature surrounding (Fig. 6) the load point P and point A on the crack front. Therefore the local curvature effect was introduced in terms of the ratio, r_A/r_F, of radii shown in Fig. 6. The correction for the local curvature effect is empirical in nature and was based on the stress intensity data for a variety of elliptical cracks in embedded bodies and some general properties of weight functions.

$$m_A(x, y; F) = \frac{F\sqrt{2}}{\pi\rho^2\sqrt{\Gamma_c\left(\frac{r_A}{r_F}\right)^2}} \tag{14}$$

The parameter, r_F, is the radius of the largest circle drawn inside the crack and being tangent to the crack contour at the point closest to the load point $P(x, y)$. The parameter, r_A, is the radius of the largest circle which can be drawn inside the crack and being tangent to the crack contour at point A. In the case of cracks with parallel and straight front lines (tunnel cracks) or circular cracks radii, r_A, and, r_F, are the same and the weight function, Eq 14, reduces to the previous form of Eq 8.

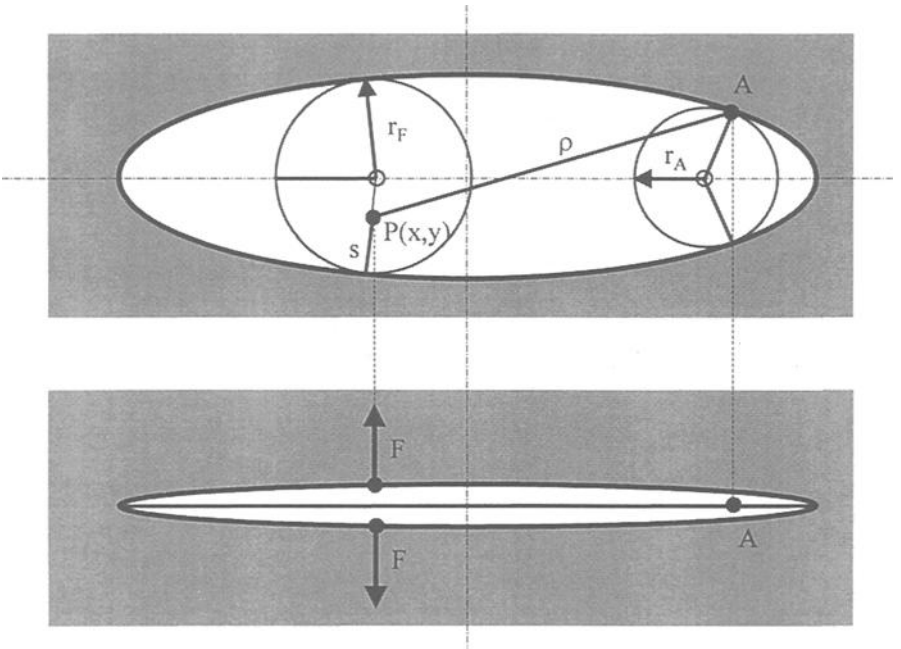


FIG. 6—*The circles* r_A *and* r_F *representing the effect of the local crack curvature on the effective length of the inverted arc.*

An Elliptical Crack in Infinite Body Subjected to a Nonlinear Mode I Stress Field

In order to verify the 3-D capability of the weight function, Eq 14, several stress intensity factors were calculated for an elliptical crack in an infinite body subjected to 2-D stress field, Eq 15, shown in Fig. 7.

$$\sigma(x, y) = \sigma_0 \frac{xy}{ac} \tag{15}$$

The stress intensity factor was calculated by integrating numerically the product of the stress function, Eq 15, and the weight function, Eq 14, over the entire crack surface area.

$$K_A = \iint_{\Omega} \sigma(x, y) m_A(x, y; F) dxdy = \iint_{\Omega} \sigma_0 \frac{xy}{ac} * \frac{\sqrt{2}}{\pi\rho^2 \sqrt{\Gamma_c \left(\frac{r_A}{r_F}\right)^2}} dxdy \tag{16}$$

The analytical integration of Eq 16 is rather difficult in the case of complex geometrical crack contours, and a special numerical integration technique was developed and is described in the Appendix.

The stress intensity factors were determined for several points along the crack front defined by the parametric angle Φ as shown in Fig. 8. A slender elliptical crack with the aspect ratio $a/c = 0.2$ was chosen for the analysis. The calculated stress intensity factors were compared

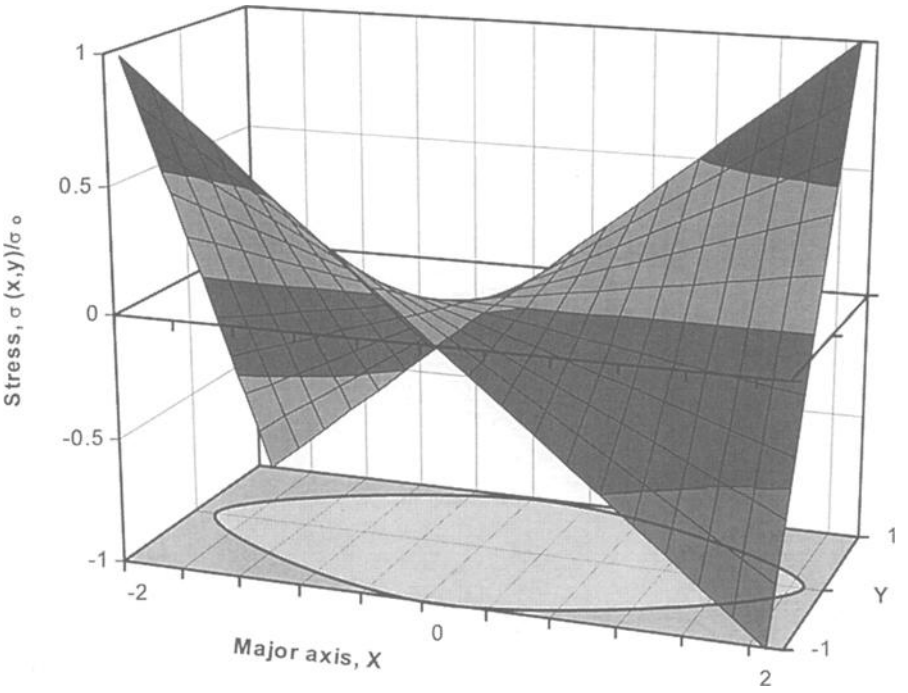


FIG. 7—*Two-dimensional nonlinear stress field applied to the elliptical crack.*

(Fig. 9) with the data of Shah and Kobayashi [*17*] obtained analytically. The comparison is given in terms of the geometrical stress intensity correction factor Y defined in the figure. Good agreement between the weight function based SIF and Kobayashi's [*17*] data indicates that both the shape of the crack and the stress distribution were adequately accounted for.

Embedded Square Crack in an Infinite Body Subjected to Uniform Tension

The embedded square crack was chosen in order to check the validity of weight function, Eq 14, in the case of cracks with severe change of curvature due to the presence of sharp corners. The crack shape and its coordinates are shown in Fig. 10. The stress intensity factor was calculated at several points along the crack front specified by the coordinate "*l*." The comparison of the weight function, Eq 16, based stress intensity factors with the finite-element data of Murakami [*18*] is shown in Fig. 11. It can be noted that the agreement is good over the entire crack contour and the weight function, Eq 16, seems to be capable of accounting for very extreme changes in the crack geometry.

Embedded Cracks in Finite Bodies—The External Boundary Effect

The examples presented above indicate that the general point load weight function, Eq 14, supplies accurate SIF results for cracks in infinite bodies. However, in the case of finite bodies both the crack contour and the free boundary contour have to be accounted for. The influence of these two boundaries on the stress intensity factor is not the same. The increase

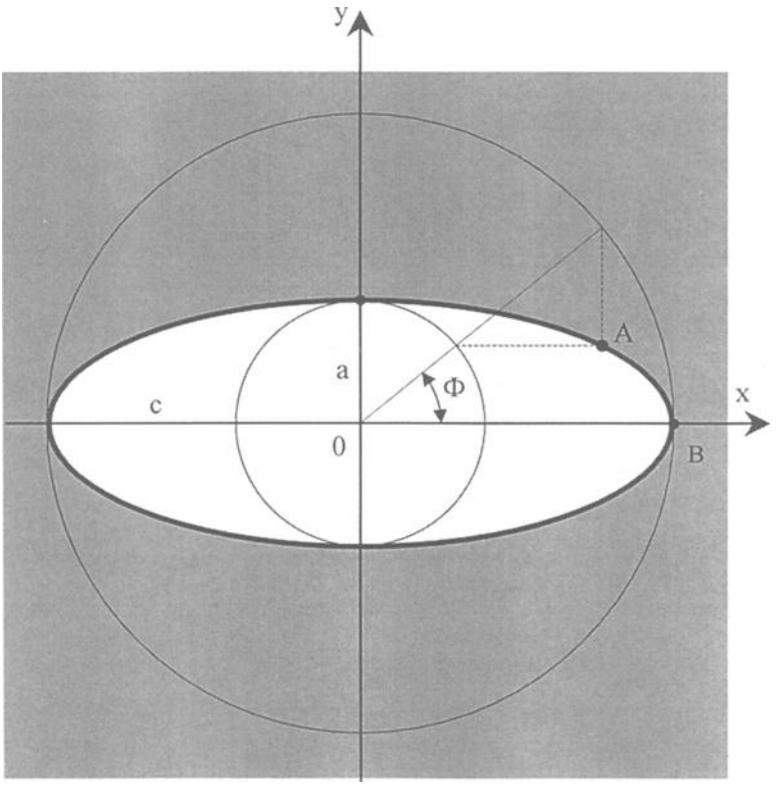


FIG. 8—*Elliptical crack in an infinite body; basic dimensions and the parametric angle Φ.*

(expansion) of the crack boundary increases the stress intensity factor while the increase of the free boundary decreases the SIF.

An analysis of the existing weight functions in finite bodies [*4*] led to the conclusion that the effect of the free boundary depends on the location of the point on the crack contour with respect to the external free boundary contour. This effect can be expressed in terms of an analogous inverted arc as in the case of the inverted crack contour. However, the free boundary contour has to be inverted with respect to the point on the crack front, where the SIF is going to be determined. The general 2-D weight function accounting for the local curvature and the free boundary effect was found by qualitative analysis of existing weight functions such as the infinite edge crack approaching free boundary and two infinite edge cracks separated by a ligament [*4*].

$$K_A = m_A(x, y; F) = \frac{F\sqrt{2}}{\pi\rho^2} \times \frac{\sqrt{\Gamma_c \left(\frac{r_A}{r_F}\right)^2 + \Gamma_b}}{\Gamma_c \left(\frac{r_A}{r_F}\right)^2} \tag{17}$$

The notation and geometrical interpretation of the two inverted arcs are presented in Fig.

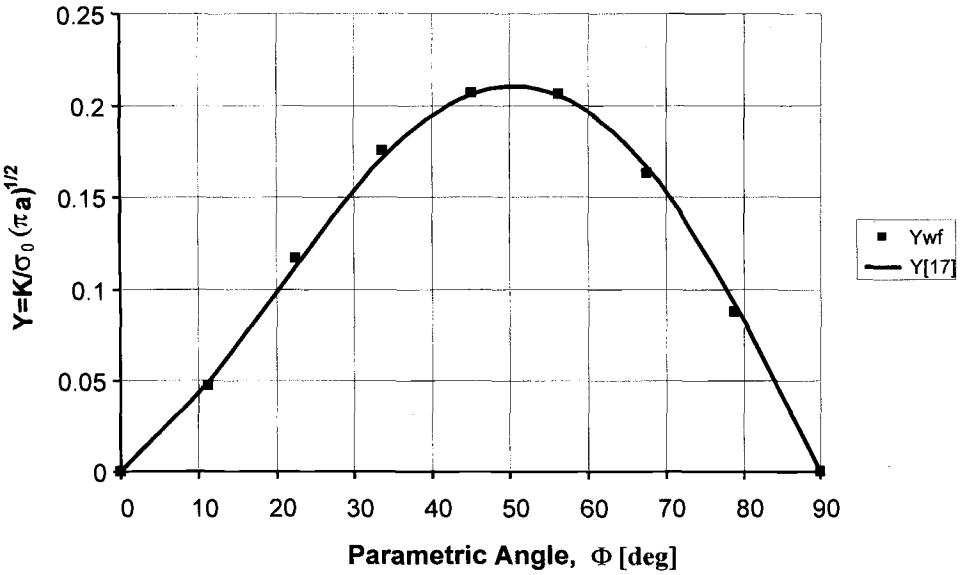


FIG. 9—*Comparison of SIF values with Kobayashi's data [17] obtained for an elliptical crack subjected to 2-D stress field,* a/c = *0.2.*

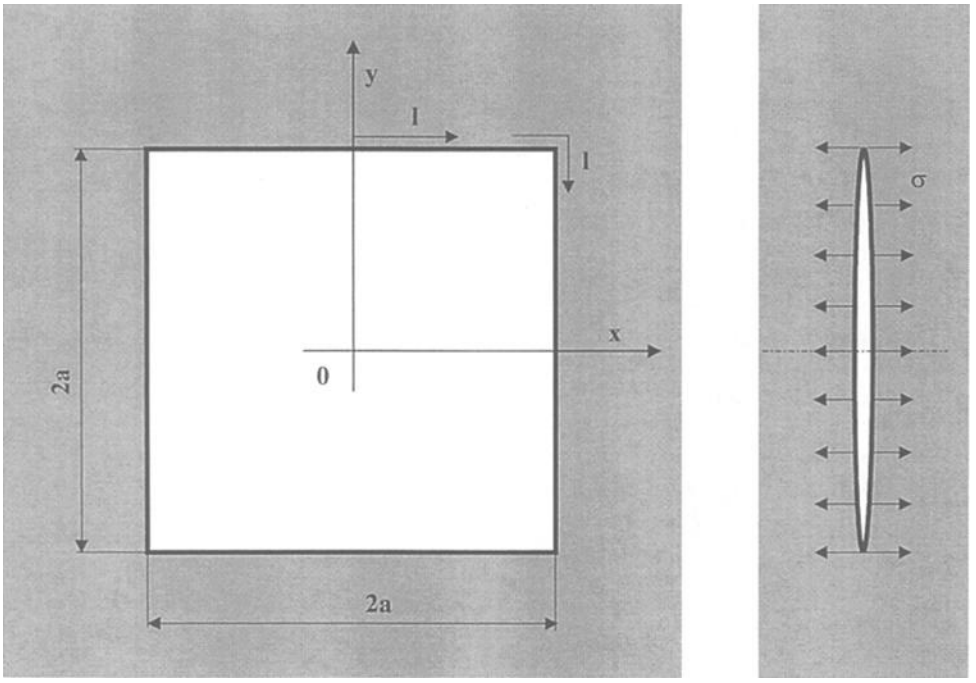


FIG. 10—*Square crack in an infinite body subjected to uniform tension.*

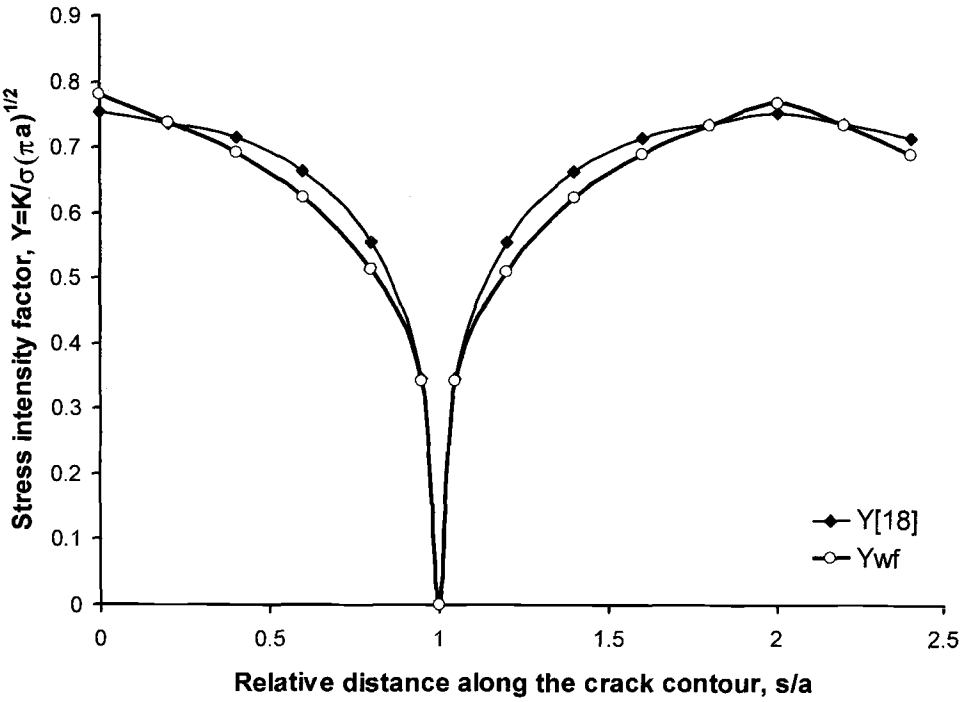


FIG. 11—*Comparison of the weight function, Eq 16, based stress intensity factors for a square crack under uniform tension and the finite-element data [18].*

12. In the case of cracks with circular or straight and parallel front lines the weight function, Eq 17, reduces to the simpler form of Eq 18.

$$K_A = m_A(x, y; F) = \frac{F\sqrt{2}}{\pi\rho^2} \times \frac{\sqrt{\Gamma_c + \Gamma_b}}{\Gamma_c} \tag{18}$$

There are very few point load weight functions for cracks in semi-infinite bodies and all of them are for infinite straight front edge cracks. Point load weight functions for planar circular or elliptical cracks in finite bodies do not exist in closed forms. However, some of them can be derived from the general weight function, Eq 18.

Infinite Straight Edge Crack Approaching a Straight Free Boundary

The geometrical configuration and generic dimensions for an infinite edge crack approaching a free boundary are shown in Fig. 13. Because the crack contour, G_c, and the free boundary, G_b, are straight lines then their inverted contours, Γ_c, and, Γ_b, respectively, form circles. The diameters of these circles are $D_c = 1/s$ and $D_b = 1/d$ for the inverted contour Γ_c, and Γ_b, respectively. Knowing that the inverted contours are circles, the arc length of each contour can be calculated as:

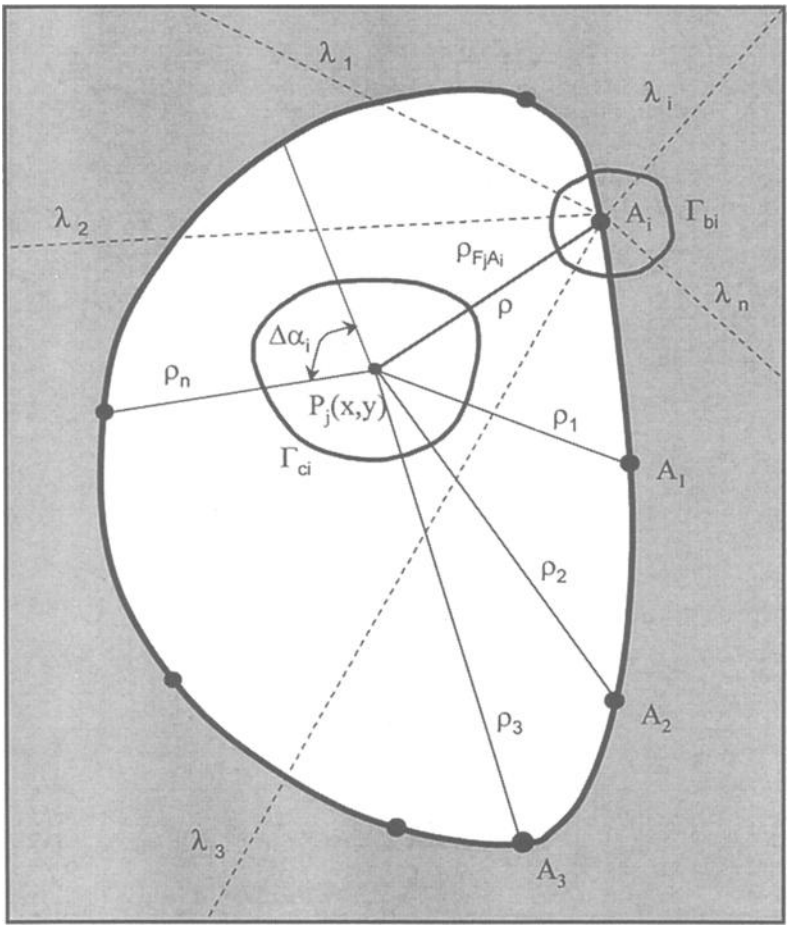


FIG. 12—*Notation for the generalized point load weight function for an arbitrary planar crack in a finite body.*

$$\Gamma_c = \pi D_c = \frac{\pi}{s} \quad \text{and} \quad \Gamma_b = \pi D_b = \frac{\pi}{d} \tag{19}$$

After substitution of Eq 19 into Eq 18 and rearrangement, the 2-D point load weight function for an infinite edge crack approaching a free boundary is derived.

$$m_A(x, y; F) = \frac{F\sqrt{2s}}{\pi^{3/2}\,\rho^2}\sqrt{1 + \frac{s}{d}} \tag{20}$$

Equation 20 can be further integrated along the line $x = 0$ resulting in the 1-D line load weight function for an edge crack approaching a free straight boundary.

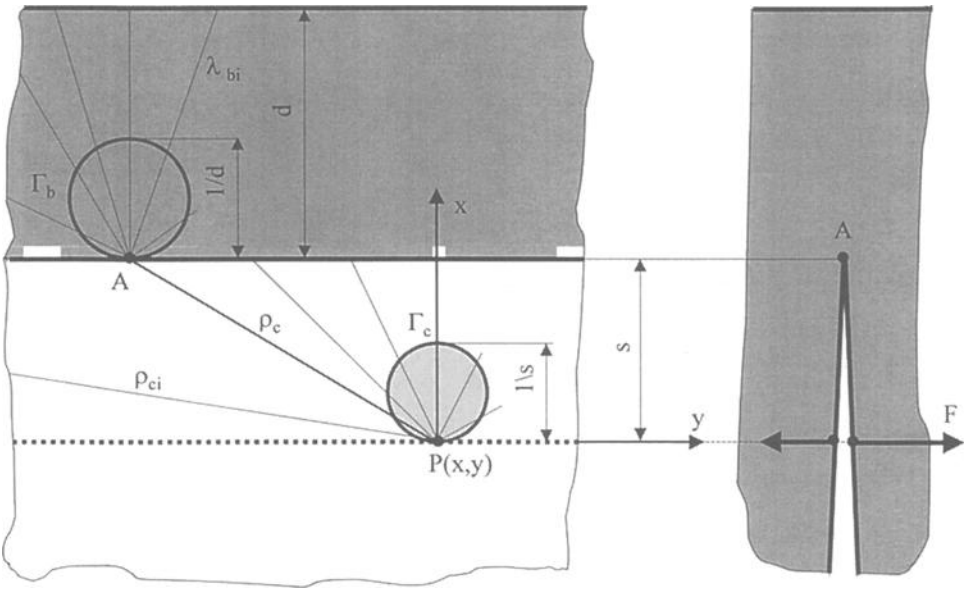


FIG. 13—*An infinite edge crack approaching a straight free boundary; the weight function notation.*

$$m_A(s; F) = \oint_{x=0} \frac{F\sqrt{2s}}{\pi^{3/2}\,\rho^2}\sqrt{1+\frac{s}{d}}\,dy = \frac{F\sqrt{2}}{\sqrt{\pi s}}\sqrt{1+\frac{s}{d}} \tag{21}$$

The final form of Eq 21 is the same as the exact line weight function for an infinite edge crack approaching a free boundary derived by Tada [*4*]. However, the weight function, Eq 21, is restricted to cases where the bending contribution from the load F is negligible, i.e., when the crack surfaces do not experience significant rotation with respect to "y" axis. It means that the weight function, Eq 21 accounts for the contribution of tension but does not account for the rotation (bending) induced by the load applied to the surface of an edge crack. Therefore, the application of the general weight function, Eq 17, seems to be limited to embedded and shallow surface breaking cracks where the crack surface rotation effect is negligible.

Two Infinite Edge Cracks Under Symmetric Loading and Separated by a Finite Thickness Ligament

The general weight function, Eq 18, can also be used to derive the point load weight function for symmetrically loaded two infinite edge cracks (Fig. 14) separated by a ligament of finite thickness d. The crack front opposite to point A was considered to be a free boundary. The weight function expression has to account for contributions from both symmetric forces F and the opposite crack front treated here as a free boundary. Therefore there are two identical inverted crack contours, Γ_c, and one inverted free boundary contour, Γ_b. The lengths of these contours are the same as those given by Eq 19. The leading radii ρ_1 and ρ_2 and other important parameters are denoted in Fig. 14. The point load (2-D) weight function derived for the geometrical configuration shown in Fig. 14 is given in the form of Eq 22.

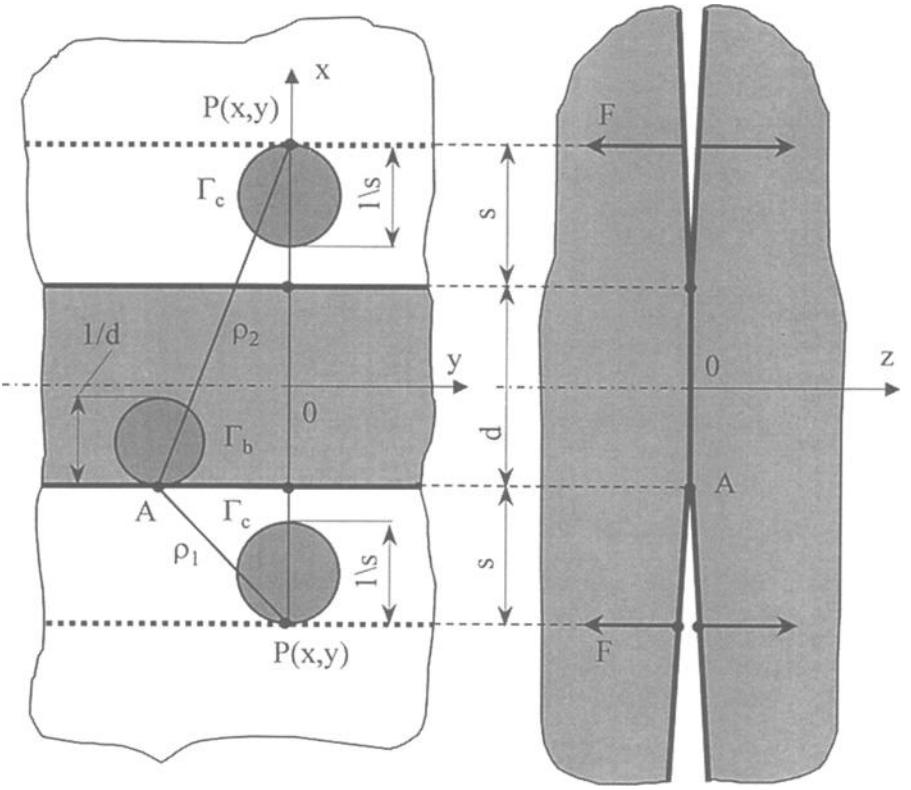


FIG. 14—*Weight function notation for two infinite edge cracks loaded symmetrically by line load* F *and separated by finite thickness ligament* d.

$$m_A(s, d; F) = \left(\frac{F\sqrt{2}}{\pi\rho_1^2} + \frac{F\sqrt{2}}{\pi\rho_2^2}\right) \times \frac{\sqrt{\Gamma_c + \Gamma_b}}{\Gamma_c} = \frac{F\sqrt{2s}}{\pi^{3/2}} \sqrt{\frac{d+s}{d}} \left(\frac{1}{\rho_1^2} + \frac{1}{\rho_2^2}\right) \tag{22}$$

Integration of Eq 22 for uniformly distributed load P (Fig. 14) along the two lines of $x = ABS(d/2 + s)$ resulted in the 1-D line weight function, Eq 23.

$$m_A(s, d) = \frac{F\sqrt{2}}{\sqrt{\pi s}} \times \frac{d+s}{\sqrt{d(d+s)}} \tag{23}$$

Equation 23 is the same as the exact analytical line weight function derived by Tada [*4*] for the same geometrical configuration.

The fact that all the 1-D line weight functions above were derived from previously unknown 2-D point-load weight function, Eqs 20 and 22 confirms that the general point weight function, Eq 18, is the correct one for all problems analyzed to date. The results obtained for the latest configuration (Fig. 14) indicate that the edge and also surface-breaking cracks can be analyzed with sufficient accuracy providing the stress field is symmetric resulting in negligible rotational displacements of crack surfaces.

Stress Intensity Solutions for Planar Cracks of Variable Curvature Embedded in Finite Bodies

In order to check the validity and accuracy of the general weight function, Eq 17, for cracks in finite bodies, several numerical tests were carried out. The assessment of the accuracy of the proposed weight function was based on the comparison of stress intensity factors obtained from the finite-element method (FEM) and those calculated by the integration of the general weight function.

Embedded Elliptical Cracks in Finite Thickness Plates

There are no closed form analytical SIF solutions for planar cracks in finite bodies subjected to complex 2-D stress distributions. Raju and Newman [*19*] have derived the first solution for embedded elliptical crack in a finite thickness plate subjected to uniform tensile stress using the FEM method. Two elliptical crack configurations shown in Fig. 15 were analyzed here. The stress intensity factors were calculated by numerical integration of the constant stress, σ_0, and the weight function, Eq 17, over the crack surface area Ω.

$$K_A = \iint_{\Omega} \frac{\sigma_0(x, y)\sqrt{2}}{\pi\rho^2} \times \frac{\sqrt{\Gamma_c \left(\frac{r_A}{r_F}\right)^2 + \Gamma_b}}{\Gamma_c \left(\frac{r_A}{r_F}\right)^2} dxdy \tag{24}$$

The calculated SIFs and those obtained by Raju and Newman [*19*] by the FEM method are presented in Fig. 16. The parametric angle was assumed to be $\Phi = 0$ at the end of the semi-minor axis and $\Phi = \pi/2$ at the end of the semi-major axis. In both cases the weight function based SIFs were no more than 3 to 6% different from the Raju and Newman data. The agreement is good for both cracks regardless of their location with respect to the free boundaries.

Stress Intensity Factors for Embedded Circular and Elliptical Cracks in a Solid Cylinder

The numerical SIF data concerning circular and elliptical cracks (Fig. 17) in a circular cross section were borrowed from Refs *20* and *21*. Unfortunately, the SIF data were given only for points *A* and *B* (Fig. 17) on the crack contour. Therefore the comparison of the literature and the weight function based SIFs, obtained for several crack configurations, is given in a tabular form (Table 1). It can be seen that the differences between the weight function based SIFs and the FEM literature data do not exceed 5%.

Conclusions

The proposed general weight function expression and the numerical integration procedure make it possible to calculate stress intensity factors for a variety of convex planar cracks subjected to any Mode I stress distribution. The comparison with exact and numerical SIF data has revealed that the proposed methodology predicted correctly the SIF distribution along the crack contour for several geometry and load configurations. The agreement between analytical and numerical data was within 5% of error for the majority of cases analyzed to date. The method is particularly suitable for simulating fatigue growth of cracks subjected

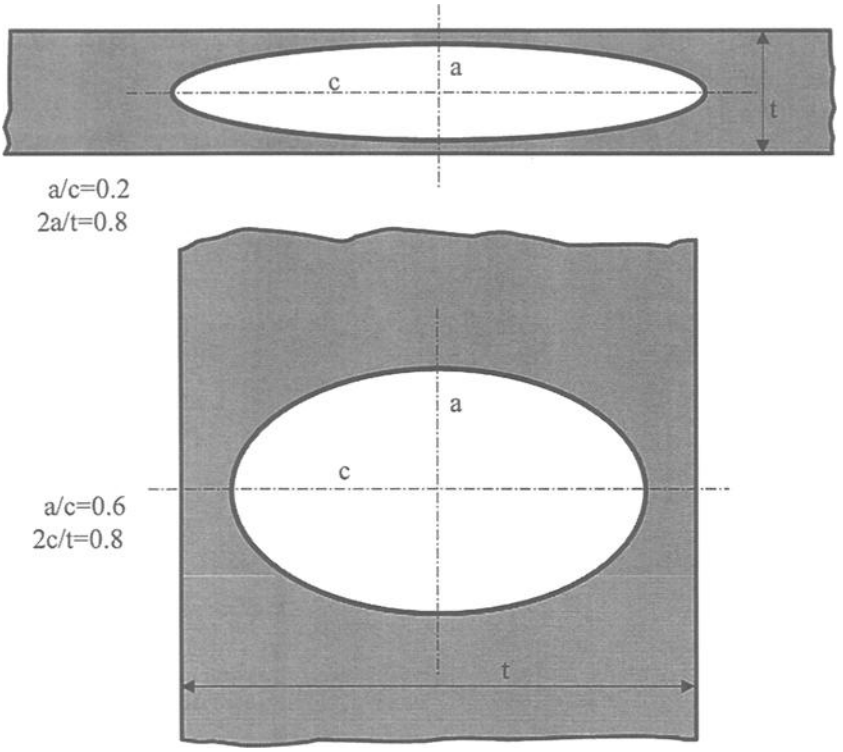


FIG. 15—*Elliptical cracks in finite thickness plates subjected to uniform tension.*

to complex nonlinear stress fields such as residual or thermal stress. The method can also be extended for surface breaking cracks.

APPENDIX

Numerical Integration Technique for Calculating Stress Intensity Factors

The stress intensity factor due to a continuous stress field applied to the crack surface is calculated by integrating the product, Eq 24, of the weight function and the stress field over the entire crack area. In the case of numerical calculations the continuous stress field has to be replaced (Fig. A1) by a finite number of discrete forces, F_j.

$$F_j = \iint_{\Delta\Omega_j} \sigma(x, y)dxdy = \sigma(x_j, y_j) \times \Delta\Omega_j \tag{A1}$$

where: $\Delta\Omega_j$ is the area of the crack surface segment over which the average stress, $\sigma(x_j, y_j)$, is acting.

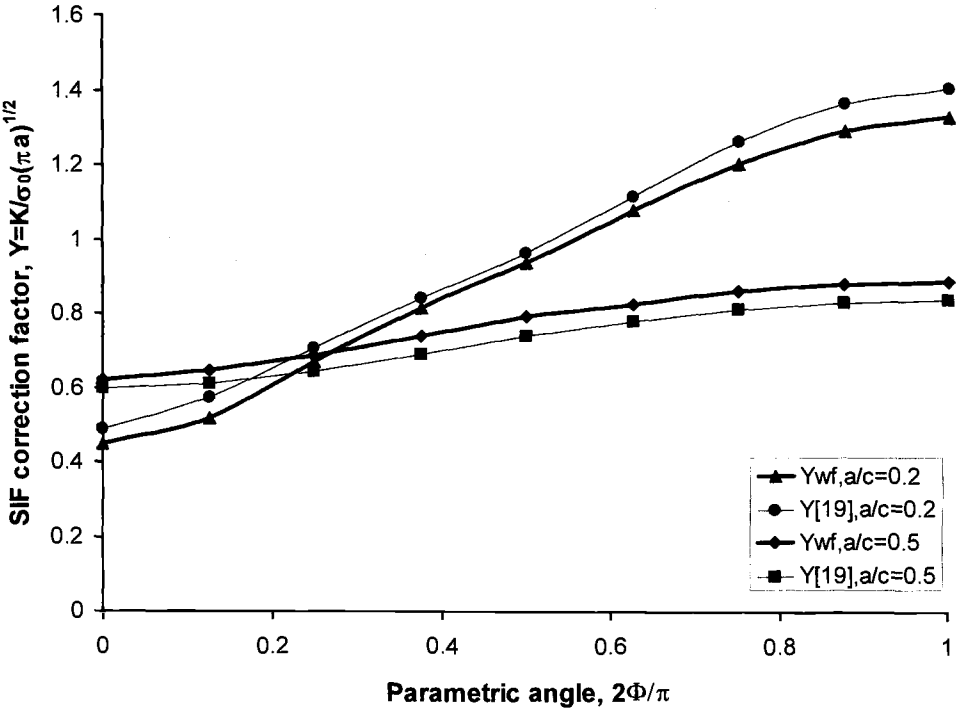


FIG. 16—*Comparison of the weight function based SIF with the FEM data of Raju and Newman [19].*

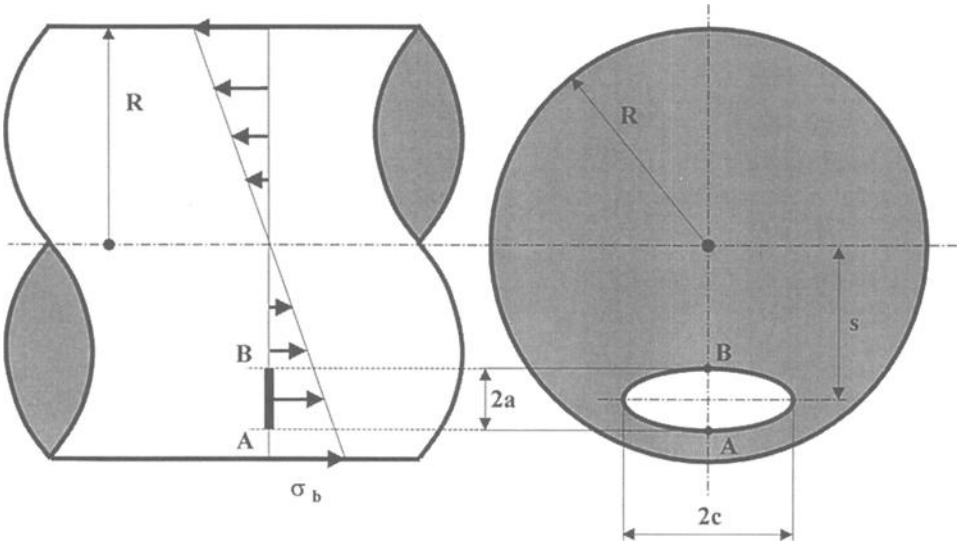


FIG. 17—*Eccentric circular and elliptical cracks in a cylinder; uniform tension, and bending load.*

TABLE 1—*Stress intensity factors for embedded circular and elliptical cracks in a solid cylinder.*

a/c, s/R, a/R	$Y_{A,wf}$	$Y_{A,[14]}$	$Y_{B,wf}$	$Y_{B,[14]}$
		Uniform Tensile Stress		
1.0, 0.0, 0.2	1.665	1.601	1.665	1.601
1.0, 0.0, 0.5	2.776	2.681	2.776	2.681
1.0, 0.0, 0.8	3.987	3.848	3.987	3.848
1.0, 0.7, 0.2	1.797	1.705	1.679	1.599
		Bending Stress		
1.0, 0.7, 0.2	1.481	1.421	0.961	0.966
0.5, 0.7, 0.2	1.884	1.849	1.244	0.1.245

The stress intensity factor induced by such a force (Figs. 12 and A1) is equal to the weight function value associated with that point. After substitution of Eq A1 into Eq 17 we can write the weight function in terms of stresses applied to the crack surface.

$$m_A(x_A, y_A; F_j) = \frac{\sigma(x_j, y_j) \times \Delta\Omega_j \times \sqrt{2}}{\pi\rho_{FjA}^2} \times \frac{\sqrt{\Gamma_{c,j}\left(\frac{r_A}{r_F}\right)^2 + \Gamma_{b,i}}}{\Gamma_{c,j}\left(\frac{r_A}{r_F}\right)^2} \tag{A2}$$

The stress intensity factor K_A at point A on the crack contour, induced by the entire stress field $\sigma(x, y)$ acting over the crack area, has to be calculated as the sum of contributions from all crack area segments $\Delta\Omega_j$.

$$K_A = \sum_{j=1}^{j=N} \left\{ \frac{\sigma(x_j, y_j) \times \Delta\Omega_j \times \sqrt{2}}{\pi\rho_{FjA}^2} \times \frac{\sqrt{\Gamma_{c,j}\left(\frac{r_A}{r_F}\right)^2 + \Gamma_{b,i}}}{\Gamma_{c,j}\left(\frac{r_A}{r_F}\right)^2} \right\} \tag{A3}$$

The dimensions of the crack surface segments, $\Delta\Omega_j$, have to be small in order to approximate sufficiently accurately the stress gradient and the crack geometry. The most important is the accurate integration in close proximity to the point A, where the radius ρ_{PjA} tends to zero. If possible the integration over the segments adjacent point A should be carried out analytically.

The stepwise procedure necessary for the calculation of stress intensity factors by using the weight function technique described above requires the execution of the following tasks.

- Determine the stress distribution, $\sigma(x, y)$, in the prospective crack plane using linear elastic analysis of uncracked body; i.e., perform the stress analysis ignoring the crack (Fig. 1) and determine the stress distribution $\sigma(x, y) = \sigma_0 * f(S, x, y)$.
- Apply the "uncracked" stress distribution, $\sigma(x, y)$, to the crack surfaces as traction.
- Choose point A on the crack front where the SIF is to be calculated (Fig. 12).
- Calculate the length of the inverted external boundary contour Γ_b associated with point A on the crack front.
- Calculate the length of the inverted crack contour, Γ_{cj}, associated with the point load at location, $F_j(x_j, y_j)$, where the stress, $\sigma_j(x_j, y_j)$, is acting.

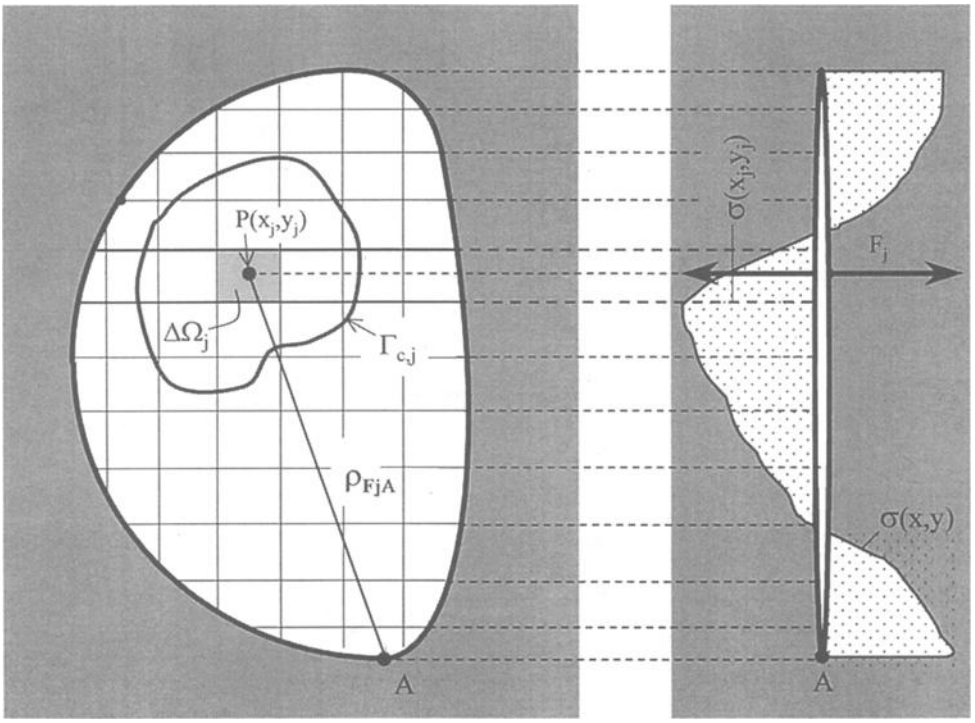


FIG. A1—*Approximation of the crack area with rectangular and triangular elements.*

- Calculate the stress intensity factor contribution (the weight function) due to the stress, $\sigma_j(x_j, y_j)$, applied at point, $P_j(x_j, y_j)$, on the crack surface (Eq A2).
- Repeat the calculations for point A over the entire crack surface area substituting appropriate values for stress $\sigma_j(x_j, y_j)$ and the length of arc Γ_{cj} and add all the contributions (Eq A3).

References

[1] Bueckner, H. F., "A Novel Principle for the Computation of Stress Intensity Factors," *Zeitschrift fur Angewandte Mathematik und Mechanik,* Vol. 50, 1970, pp. 529–546.
[2] Rice, J. R., "Some Remarks on Elastic Crack-Tip Stress Field," *International Journal of Solids and Structures,* Vol. 8, 1972, pp. 751–758.
[3] Broek, D., *The Principal Use of Fracture Mechanics,* 1988, Amsterdam, Kluwer.
[4] Tada, H., Paris, P., and Irwin, G., *The Stress Analysis of Cracks Handbook,* 2nd ed., Paris Production Inc., 1985, St. Louis, MO.
[5] Wu, X. R. and Carlsson, A. J., *Weight Functions and Stress Intensity Factor Solutions,* 1991, Pergamon Press, Oxford, UK.
[6] Fett, T. and Munz, D., "Stress Intensity Factors and Weight Functions for One-Dimensional Cracks," Report No. KfK 5290, Kernforschungszentrum Karlsruhe, Institut fur Materialforschung, Dezember 1994, Karlsruhe, Germany.
[7] Glinka, G. and Shen, G., "Universal Features of Weight Functions for Cracks in Mode I," *Engineering Fracture Mechanics,* Vol. 40, No. 6, 1991, pp. 1135–1146.

[8] Shen, G. and Glinka, G., "Determination of Weight Functions from Reference Stress Intensity Factors," *Theoretical and Applied Fracture Mechanics,* Vol. 15, No. 2, 1991, pp. 237–245.

[9] Shen, G. and Glinka, G., "Weight Functions for a Surface Semi-Elliptical Crack in a Finite Thickness Plate," *Theoretical and Applied Fracture Mechanics,* Vol. 15, No. 2, 1991, pp. 247–255.

[10] Zheng, X. J., Glinka, G., and Dubey, R., "Calculation of Stress Intensity Factors for Semi-Elliptical Cracks in a Thick-Wall Cylinder," *International Journal of Pressure Vessels and Piping,* Vol. 62, 1995, pp. 249–258.

[11] Zheng, X. J., Glinka, G., and Dubey, R., "Stress Intensity Factors and Weight Functions for a Corner Crack in a Finite Thickness Plate," *Engineering Fracture Mechanics,* Vol. 54, No. 1, 1996, pp. 49–62.

[12] Wang, X. and Lambert, S. B., "Stress Intensity Factors for Low Aspect Ratio Semi-Elliptical Surface Cracks in Finite-Thickness Plates Subjected to Non-Uniform Stresses," *Engineering Fracture Mechanics,* Vol. 51, No. 4, 1995, pp. 517–532.

[13] Wang, X. and Lambert, S. B., "Stress Intensity Factors and Weight Functions for High Aspect Ratio Semi-Elliptical Surface Cracks in Finite-Thickness Plates," *Engineering Fracture Mechanics,* Vol. 57, No. 1, 1997, pp. 13–24.

[14] Rice, J., "Weight Function Theory for Three-Dimensional Elastic Crack Analysis," *Fracture Mechanics Perspectives and Directions (20th Symposium), ASTM STP 1020,* American Society for Testing and Materials, 1989, pp. 29–57.

[15] Oore, M. and Burns, D. J., "Estimation of Stress Intensity Factors for Embedded Irregular Cracks Subjected to Arbitrary Normal Stress Fields," *Journal of Pressure Vessel Technology,* ASME, Vol. 102, 1980, pp. 202–211.

[16] Sih, G. C., "Mathematical Theories of Brittle Fracture," *Treatise on Fracture,* H. Liebowitz, Ed., Vol. II, Academic Press, New York, 1968, p. 69.

[17] Shah, R. C. and Kobayashi, A. C., "Stress Intensity Factor for an Elliptical Crack Under Arbitrary Normal Loading," *Engineering Fracture Mechanics,* Vol. 15, 1971, pp. 71–96.

[18] Murakami, Y., *Stress Intensity Factors Handbook,* JSME and Pergamon Press, Oxford-Tokyo, 1992.

[19] Newman, J. C. and Raju, I. S., "Stress-Intensity Factor Equations for Cracks in Three-Dimensional Finite Bodies Subjected to Tension and Bending Loads," *Computational Methods in the Mechanics of Fracture,* S. N. Atluri, Ed., North-Holland, 1986, pp. 311–334.

[20] Chen, D., Nisitani, H., and Mori, K., "Stress Intensity Factors for a Fish-Eye in a Shaft," *Transactions of Japan Society of Mechanical Engineers,* Vol. 57, No. 540, 1991, pp. 1768–1774.

[21] Benthem, J. P. and Koiter, W. T., *Mechanics of Fracture 1, Method of Analysis and Solutions of Crack Problems,* G. C. Sih, Ed., Noordhoff International Publishing Leyden, 1973, pp. 131–178.

D. C. Slavik,[1] *R. D. McClain,*[1] *and K. Lewis*[1]

Stress Intensity Predictions with ANSYS®[1] for Use in Aircraft Engine Component Life Prediction

REFERENCE: Slavik, D. C., McClain, R. D., and Lewis, K., **"Stress Intensity Predictions with ANSYS®[1] for Use in Aircraft Engine Component Life Prediction,"** *Fatigue and Fracture Mechanics: 31st Volume, ASTM STP 1389,* G. R. Halford and J. P. Gallagher, Eds., American Society for Testing and Materials, West Conshohocken, PA, 2000, pp. 371–390.

ABSTRACT: Stress intensity (K) predictions are presented using crack opening displacements with ¼ points elements at the crack tip to simulate the crack tip singularity. These results are compared to available literature values under remote applied tension for a 2D thru-crack and a 3D semi-elliptical surface crack geometry. Crack-opening displacements with ANSYS were found to calculate K for the 2D thru-crack geometry to within 1% of an available reference solution and were not strongly influenced by the crack tip mesh parameters evaluated. Predicted stress intensities with crack-opening displacements were then considered for the surface flaw geometry for a range of crack aspect ratios ($0.2 \leq a/c \leq 2.0$) and crack depths ($0.01 \leq a/T \leq 0.8$). K for the surface flaw geometry was also not significantly influenced by the crack tip mesh refinement and matched literature solutions to within ±5% of predicted K for the crack depth position. Predicted stress intensities at the surface position using crack-opening displacement approaches were: (a) not strictly valid given the nature of the crack tip singularity, (b) dependent on the stress state assumption, and (c) dependent on the degree of mesh refinement. These difficulties were avoided by selecting a 2° angular position below the surface with a plane strain assumption to calculate K from predicted crack-opening displacements. This approach produced a stress intensity that was reasonably assumed to be representative of K at the surface position and was not significantly influenced by the mesh refinement or stress state assumptions. K with this approach was somewhat higher than results using alternative approaches in the literature. The implication of these results compared to other finite element based results with respect to Raju-Newman interpolation equations are discussed with probability plots. Examples with crack opening models in specific aircraft engine components are also provided.

KEYWORDS: stress intensity, semi-elliptical surface flaw, and crack-opening displacements

Aircraft engine components are required to safely and economically meet engine performance requirements. These needs require an understanding of how a component is utilized in service along with life prediction methods to establish safe limits of operation. As an example, fracture mechanics methods are one of the tools used in design to predict the residual life of a component that may contain small flaws or defects. This approach requires a crack tip driving force that can be defined as a function of the stresses, crack dimensions, component dimensions, and crack displacement mode type [*1*]. Life prediction for critical aircraft engine rotating components typically focuses on linear elastic stress intensity (K) methods. K is the relevant parameter given that plasticity and creep zones are well contained within

[1] GE Aircraft Engines, Cincinnati, OH 45215.

Copyright® 2000 by ASTM International www.astm.org

elastic fields to meet component life goals. Additionally, the problems of interest can be simplified to that of the crack opening problems (Mode I). Mode II/III fracture parameters can become important for very small cracks on the order of the grain size or in materials that are highly anisotropic. But these issues are not relevant for today's critical rotating engine components of monolithic materials for the crack sizes of engineering interest utilizing fracture mechanics methods. Examples using Mode I K to establish life prediction methods for stresses, temperature, and crack sizes of relevance for aircraft engine components under mission cycling conditions are described elsewhere [*2*]. These cases are typical of many instances where the total load through the cross-sectional area remains constant and K solutions can be obtained from handbooks [*3,4*]. These approaches can be further generalized to account for complex stress gradients through influence or weight function approaches [*5,6*]. This approach is ideal for rotating aircraft engine components that are typically load-control with simple stress gradients.

More general analytical approaches may be required to obtain an accurate stress intensity prediction for components with irregular geometries or redundant load paths where displacement control boundary conditions can dominate. In these instances, K still applies but handbook solutions are unavailable and predictions from load-control K-solutions can provide highly conservative life estimates. More accurate approaches for these conditions can be best analyzed using analytical fracture mechanics approaches. This incorporates the influence of the crack directly into the component models. The main advantages of these techniques are that they are completely general so that all features of a particular problem can be incorporated directly into the prediction of K for use in life analysis. This approach does, however, requires crack tip elements that capture the crack tip $1/\sqrt{r}$ singularity [*7–11*]. Tracey originally developed a crack tip triangular element that produced reasonable predictions for KI [*7*], but this approach has limitations for thermal stress problems [*8*]. Additional work using parabolic elements with the mid-side nodes located at ¼ of the element edge length (quarter-point elements) were also found to produce reasonable predictions for K from crack opening displacements [*8,9*] without limitations concerning thermal stress problems. Alternative approaches using nodal forces have also been presented in the literature [*11*], but these approaches are not easily used for crack tip models that contain quarter-point elements.

The main objectives of this study are to understand crack-meshing guidelines with ANSYS to predict opening mode stress intensities for thru-crack and semi-elliptical surface flaw geometries. Included are the steps that are indicative of what is done in industry prior to utilizing a technology for component life prediction. First, the structural finite element code ANSYS was selected for the examination since this code is heavily used within GE Aircraft Engines and throughout the world. Then meshing macros were established to quickly build crack tip models for a 2D thru-crack geometry to predict the stress intensity from crack-opening displacements. This geometry was selected so that results could be compared to the nearly exact 2D solution in the literature. The crack opening approach was then evaluated with a 3D semi-elliptical surface crack geometry for comparison to literature solutions. The surface crack is evaluated since this geometry is typically the main case of interest when predicting life limits for aircraft engine components or field-cracking incidents. Statistical comparisons between different approaches are provided to indicate differences between the mean and standard deviation. Finally, meshing best practices with ANSYS macros are described that minimize crack tip modeling efforts that can be applied to component geometries that are representative of aircraft engine components. Examples are given below.

Approach

Baseline Solutions

A 2D centered thru-crack geometry in a flat plate is used to evaluate different analytical fracture mechanics approaches with ANSYS. The model geometry for the thru-crack is given in Fig. 1*a*. 2*H* is the specimen total height, 2*W* is the total width, 2*a* is the total crack length, and *K* is the stress intensity. The Mode I stress intensity equation with a remote applied tensile load (σ) is given in Eq 1.

$$K = Y\sigma\sqrt{\pi a} \tag{1}$$

where *Y* is the normalized stress intensity that has been established in the literature with a high degree of accuracy by Isida [*13*]. A correlation equation for this geometry has also been established in the literature with an accuracy to within 0.1% [*13*] that can also be used to compare the predictive capabilities of ANSYS results for $H/W = 3$ for this 2D geometry.

A surface flaw crack with a semi-elliptical crack shape is next used to evaluate crack meshing requirements and to assess the predictive capabilities of ANSYS for a 3D geometry. The model features, surface flaw geometry, and dimensions are described in Fig. 1*b*. *T* defines the specimen thickness, 2*H* is the total height, 2*W* is the total width, *a* is the crack depth, 2*c* is the crack length on the surface, K_a is the stress intensity at the crack depth position, and K_c is the stress intensity at the surface position. The Mode I stress intensity equation [*14*] used for semi-elliptical surface flaws with a remotely applied tension is given in Eq 2.

$$K_a = Y_a\sigma\sqrt{\pi a/Q}, \qquad K_c = Y_c\sigma\sqrt{\pi a/Q} \tag{2}$$

where σ is the remote applied stress, Y_a is the normalized stress intensity at the a-position, Y_c is the normalized stress intensity at the *c*-position, and *Q* is obtained from the elliptical integral of the second kind. The approximate empirical expression for *Q* as developed by Rawe [*11,14–16*] is given in Eq 3.

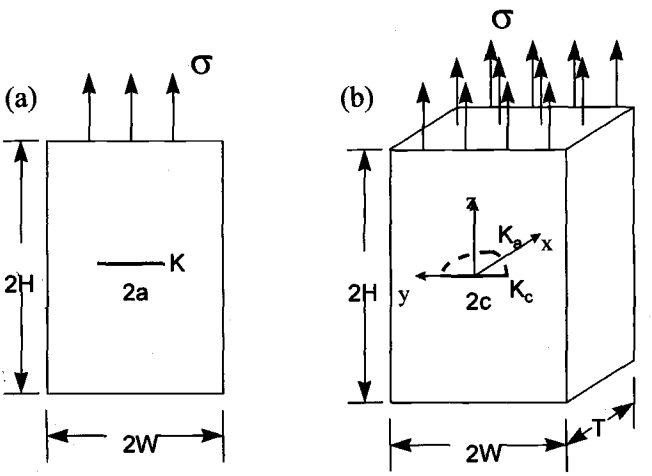


FIG. 1—*Crack geometries evaluated:* (a) *thru-crack in a center crack panel and,* (b) *a semi-elliptical surface crack in a flat plate.*

$$Q = 1.0 + 1.464(a/c)^{1.65} \text{ for } (a/c \leq 1)$$

$$Q = 1.0 + 1.464(c/a)^{1.65} \text{ for } (a/c > 1) \tag{3}$$

Predictions will focus on the normalized stress intensity at both a and c positions and for a/c = 0.2, 0.4, 0.6, 1.0, and 2.0. These cases have been evaluated in the literature by Raju-Newman [*11,15,16*] and Shiratori [*17*]. Crack depths were varied from $0.01 \leq a/T \leq 0.8$. The model height and width ($H = W = 5c$) were selected to be large and match the dimensions used in the finite element study by Raju and Newman [*11,15,16*]. All finite element predictions will also be compared to the interpolation equations for K established by Raju and Newman [*18*] that correlate K for a wide range of crack sizes and shapes to predict component life or analyze crack growth rate data with laboratory specimens.

K *Calculation Using Crack Opening Displacements*

A number of different approaches have been used in the literature to obtain the stress intensity from finite element results [*7–11*]. The approach readily available using ANSYS post-processing commands calculates K from the crack opening displacements. K is related to the crack-opening displacements based on the derivations from Paris and Sih [*1*] for linear elastic-plastic materials as given in Eq 4.

$$\frac{V}{\sqrt{r}} = \frac{K}{2G}\frac{(1 + \kappa)}{\sqrt{2\pi}} \tag{4}$$

where V is the crack opening displacement near the crack tip, r is the distance from the crack tip, G is the elastic shear modulus, κ is an elastic constant defined in Eq 5, and ν is Poisson's ratio.

$$\kappa = 3 - 4\nu \quad \text{for plane strain}$$

$$\kappa = \frac{3 - \nu}{1 + \nu} \quad \text{for plane stress} \tag{5}$$

Since $V/\sqrt{r}$ is not defined at the crack tip ($r = 0$), crack opening displacements from the nodes on the crack face just beyond the crack tip are used to define Constants A and B as given in Eq 6.

$$\frac{V}{\sqrt{r}} = A + Br$$

$$\lim_{r \to 0} \frac{V}{\sqrt{r}} = A \tag{6}$$

Equations 4 to 6 are combined using the ANSYS KCALC command to calculate K from the calculated crack opening displacements [*12*]. Disadvantages of this approach are that: (a) it may not be as accurate as other approaches to calculate K, and (b) it is difficult to predict K where neither plane stress or plane strain conditions strictly apply. First, the accuracy of the approach will be evaluated with the 2D thru-crack geometry under identically

plane stress and plane strain conditions. Then, the ability of the approach will be evaluated for semi-elliptical surface flaws to establish guidelines to use the approach over a range of crack depths and crack shapes as compared to approximate solutions in the literature [*11,15–17*]. Poisson's ratio has been taken as 0.3. E is 206 850 MPa.

ANSYS Crack Meshes for 2D Centered Thru-Cracks

2D thru-cracks were first analyzed with relatively fine and coarse crack tip meshes for $a/W = 0.2$. Only ¼ of the specimen and crack geometry were modeled with symmetry boundary conditions. The crack tip meshing for the 2D geometry was broken down into two steps. First, the mesh around the crack tip was generated. Two corners of the element are collapsed at the crack tip with the mid-sided nodes moved toward the crack tip to the quarter point position to simulate the crack tip $1/\sqrt{r}$ singularity [*8,9*]. Crack tip elements with quarter point nodes were automatically selected in ANSYS with the KCON command [*12*]. The additional specimen geometry was then meshed by ANSYS using tetrahedral elements. Representative very fine and fairly coarse meshes around the crack tip for $a/W = 0.2$ are shown in Fig. 2. The ability of the crack-opening approach with quarter point elements to calculate K for idealized plane stress and plane strain conditions are discussed below.

ANSYS Crack Meshes for Semi-Elliptical Surface Cracks

An ANSYS macro was developed to mesh semi-elliptical surface cracks in rectangular geometries. Only ¼ of the specimen and crack geometry were modeled with symmetry boundary conditions. The mesh generation has been broken into three basic steps. First, a small circular tunnel is modeled around the semi-elliptical crack front. The crack tunnel is idealized with a 2D representation of the mesh at the crack depth position. The 2D model is then dragged along a line defined by the crack front from the a to the c position in an elliptical coordinate system defined by the crack aspect ratio (a/c) along the crack front. This approach automatically positions nodes within very small tolerances to be normal to the crack front. This is crucial to obtain accurate stress intensities from crack opening displacement approach. The outer diameter of the tunnel around the crack front was selected as 10% of the smaller of a or c. A typical tunnel mesh around the crack tip as generated with ANSYS for $a/c = 1.0$ as shown in Fig. 3. CSZ defines the outer diameter of the tunnel around the crack tip and WSZ defines the inner row of elements around the crack tip. The total number of elements (NELM) around the crack front was varied from 10 to 60. Crack elements were skewed toward the c-position. NELM and the spacing of the elements near the c-position were found to be the main crack meshing parameter that had a significant influence on subsequent stress intensity predictions using the crack opening displacement approach.

The next meshing step focused on building a small rectangular box around the crack tunnel mesh. The dimension for the box that contained the tunnel mesh was a function of the crack size defined by the dimensions: $(a + 2 \times \text{CSZ})$ by $(c + 2 \times \text{CSZ})$ by $(2 \times \text{CSZ})$. Pyramid elements were used in the box for elements adjacent to the tunnel mesh; the remaining volume within the inner box was free-meshed with tetrahedron elements. The final meshing step was to mesh the remaining area of the specimen model. Element sizes and spacing were selected to smoothly transition elements from the inner rectangular box to the relatively coarse elements far away from the crack location. A typical mesh for $a/c = 0.6$ and a relatively short crack ($a/T = 0.2$) is shown for NELM = 10 and 30 in Figs. 4*a-b*. A typical mesh for $a/c = 0.6$ and a relatively deep crack ($a/T = 0.8$) is shown for NELM = 10 and

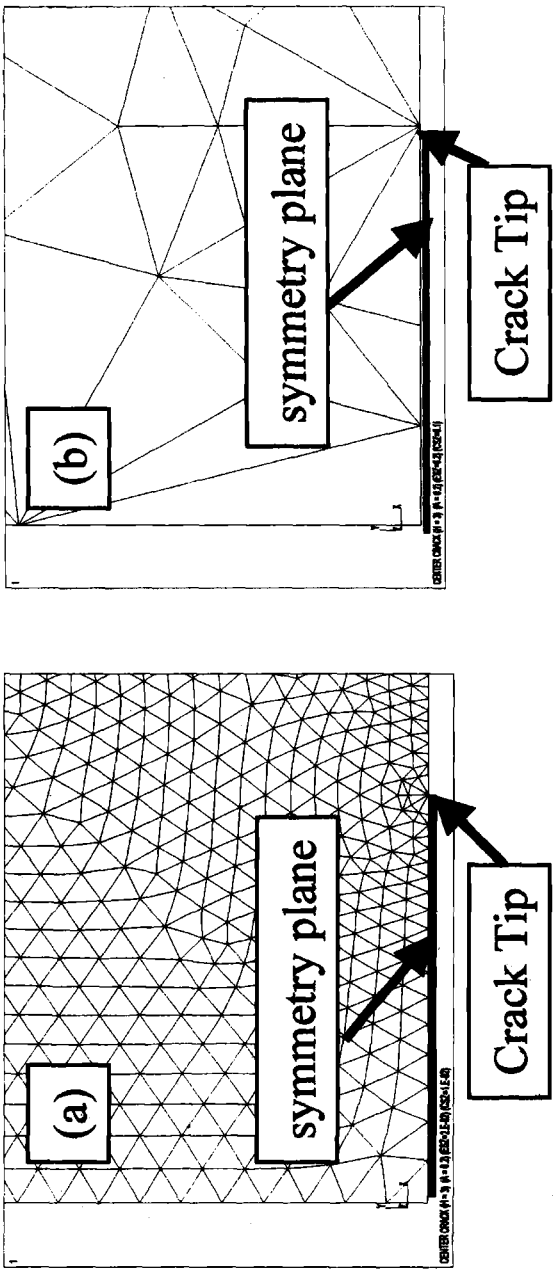


FIG. 2—*Representative coarse and fine crack tip mesh for a centered thru-crack* (a/W = *0.2*).

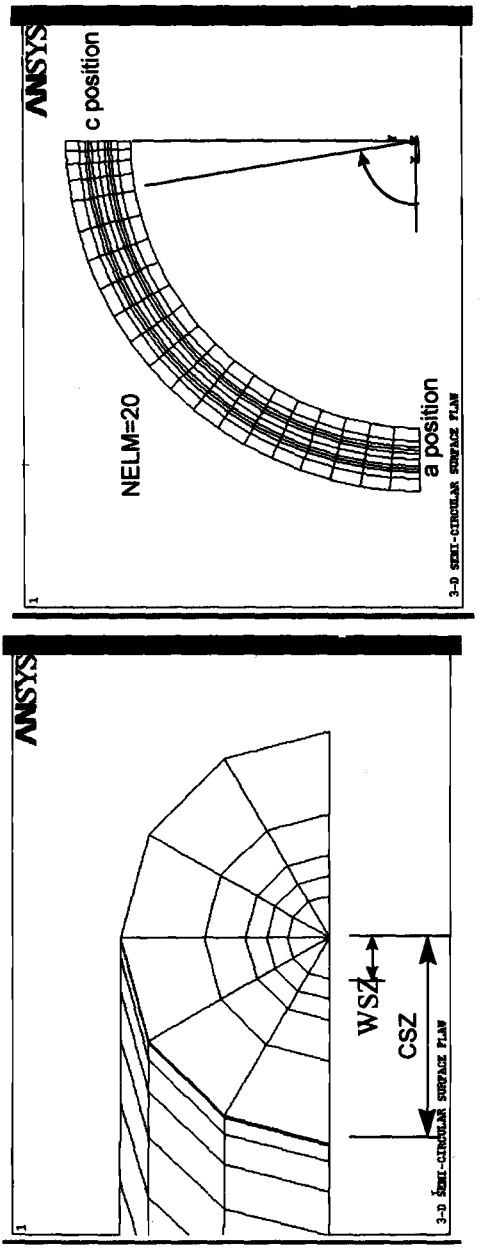


FIG. 3—*Crack tip meshing parameters for a circular crack mesh.*

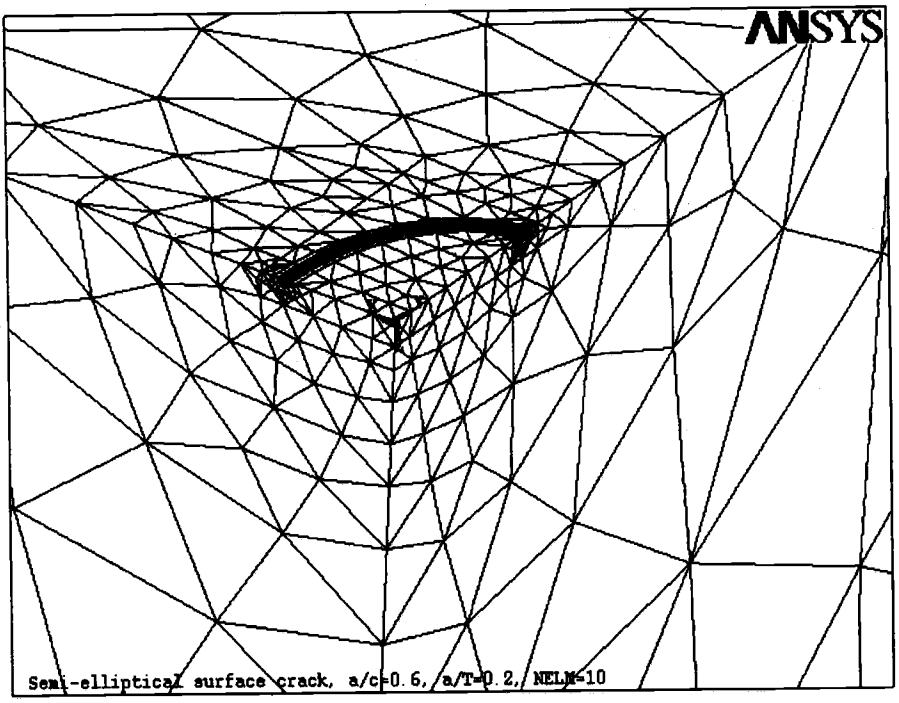


FIG. 4*a*—*Semi-elliptical surface crack mesh for* a/c = *0.6,* a/t = *0.2, and NELM = 10.*

30 in Figs. 5*a-b*. Only ¼ of the specimen geometry was modeled assuming symmetry boundary conditions. Results for these models will be used to obtain stress intensities at the *a* and *c* positions under a remote applied pressure load.

Results

Stress Intensities for the Centered Thru-Crack Geometry

A centered thru-crack geometry was used to evaluate potential limitations of the crack opening approach with ANSYS for a 2D geometry. The predicted K with ANSYS was found to be relatively insensitive to mesh refinement and accurate to within 1% of the Tada solution for a/W = 0.2 and H/W = 3.0 (Table 1). This approach was evaluated further for intermediate crack mesh dimensions for a/W from 0.1 to 0.9 for plane stress and plane strain conditions (Fig. 6, Table 2). The results using the crack opening displacements match the Tada solution to within 0.4%. Also note that the plane stress/plane strain stress state condition had essentially no impact on the predicted K. The predicted crack opening varied by ~9%, but this difference was offset with the elastic constant terms given in Eq 5. The net result of this was that predicted K was nearly independent of the 2D stress state assumption from the crack opening displacement approach. Given the crack opening approach was found to be very accurate when compared to the 2D solution and relatively insensitive to the crack tip parameters evaluated, this approach was extended to the 3D semi-elliptical surface crack geometry.

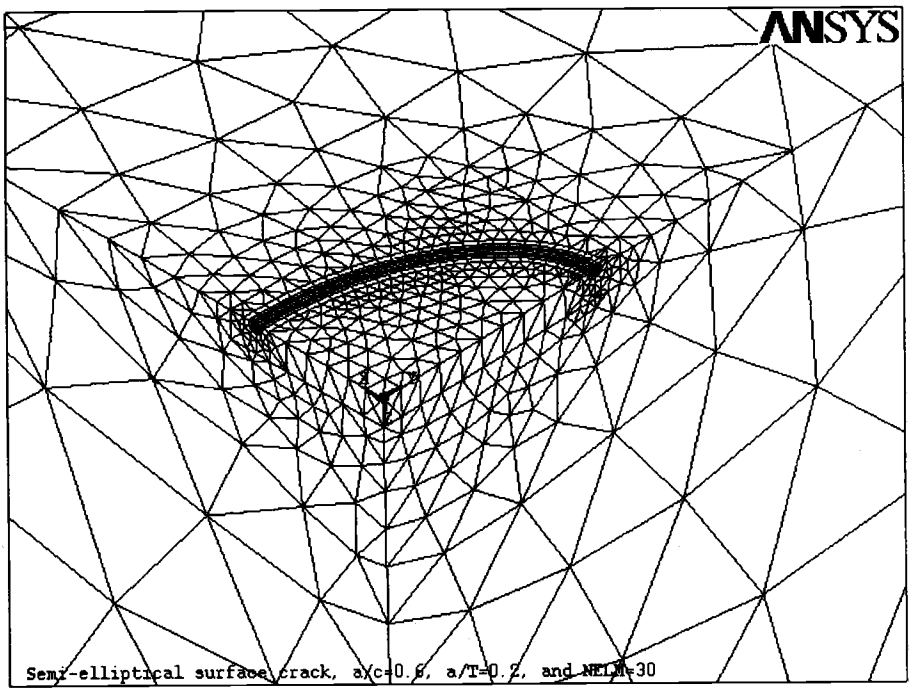


FIG. 4*b*—*Semi-elliptical surface crack for* a/c = *0.6,* a/t = *0.2, and NELM = 30.*

Stress Intensities at the Depth Position for the Semi-Elliptical Surface Crack

Predicted K for the semi-elliptical surface crack at the a and c crack positions are given with NELM = 15 and 30 in Table 3. Analysis was performed at a/c = 0.2, 0.4, 0.6, 1.0, 2.0 for a/T = 0.01 to 0.8. Normalized stress intensities at the a-position (Y_a) are shown in Fig. 7. The solid line corresponds to Y_a as calculated with the Raju-Newman interpolation equations given in Refs *18*. Symbols correspond to Y_a calculated from finite element results in the literature from Raju-Newman [*11,15,16*] and Shiratori when available [*17*]. Y_a calculated from crack opening displacements with a plane strain assumption are also shown for NELM = 15 and 30. Agreement among the different approaches and the interpolation equations are typically good for all crack aspect ratios and crack sizes. The comparison of the different finite element based approaches as compared to the Raju-Newman interpolation equation at the crack depth position are shown with a probability plot in Fig. 8. Probability plots can be used to establish the average and statistical difference between an existing process (FEM results) and a reference case (Raju-Newman equations). The y-intercept at (K FM/K RN equ) = 1 is a measure of differences in the mean between the different finite element approaches and the interpolation equations of Raju-Newman [*18*]. The slope of the line is a measure of the variation of the FEM results with respect to the reference interpolation equations. Probability plots are used heavily throughout GE for a wide range of manufacturing and analytical processes. These plots allow one to understand the average and minimum capability of a process as judged against a standard reference case. Predictions with the ANSYS crack-opening approach at the a-position are similar in mean and variation to other FEM results in the literature. ANSYS predictions with NELM = 30 are similar in mean and variation to the NELM = 15 results plotted in Fig. 8 and are therefore not shown.

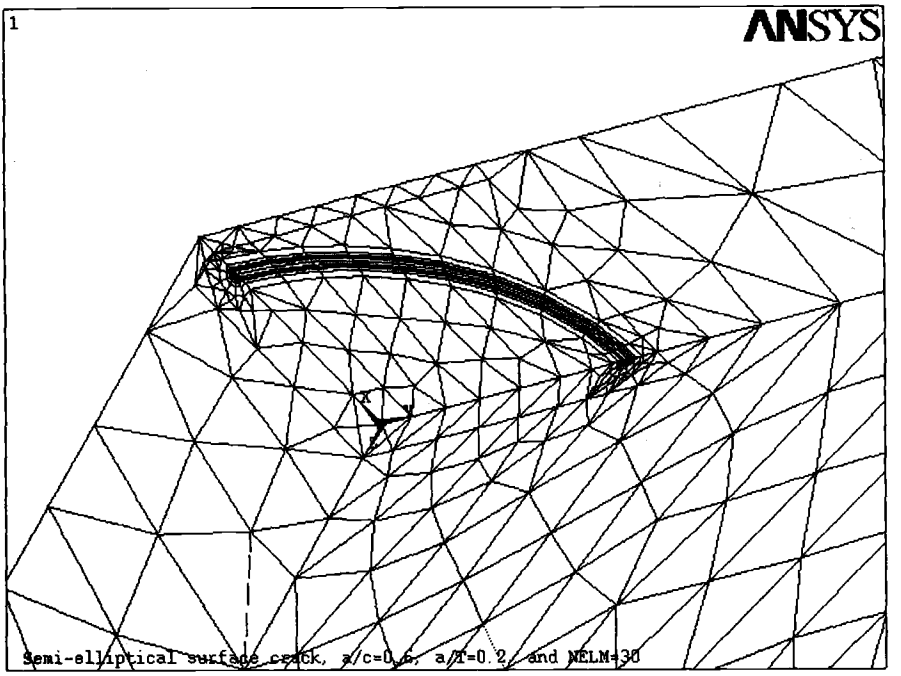


FIG. *5a—Semi-elliptical surface crack mesh for* a/c = *0.6 and* a/t = *0.8, and NELM = 10.*

Stress Intensities at the Surface Position for the Semi-Elliptical Surface Crack

Obtaining K at the surface position using analytical fracture mechanics approaches requires special attention since the analytical approach does not strictly apply at the surface as the character of the stress singularity changes [*19,20*]. Different extrapolation approaches/mesh densities have been employed to obtain representative stress intensities at the surface position. Predicted Y for $a/T = 0.2$ as a function of the angular Cartesian position away from the surface position are given for $a/c = 1.0$ and $a/c = 0.2$ in Figs. 9*a* and 9*b*, respectively. The number of elements around the crack front (NELM) was varied from 10 to 60. The normalized stress intensity was calculated using the crack-opening displacements with the plane strain assumption at all positions around the crack tip to obtain K. Plane strain was selected to avoid discontinuities in predicted K. The number of elements near the surface position was found to impact the predicted stress intensity for angular positions very close to the surface. The impact of the mesh density and the stress state assumptions are minimized by assuming a plane strain stress state at the 2° position as representative of the stress intensity at the surface. This approach is reasonable given that the stress state is not well defined at positions just below the surface. It also provides a standard approach to obtain K at a position representative of the surface while avoiding theoretical issues associated with a boundary layer of elements very close to the surface [*19,20*]. Normalized stress intensities with crack opening displacements at the 2.0° position for the range of a/c and a/T are shown in Fig. 10. Predictions of K_c with the crack opening approach at the 2.0° position are higher than other solutions with a similar standard deviation (Fig. 11). The impact of these results for component life predictions is discussed below.

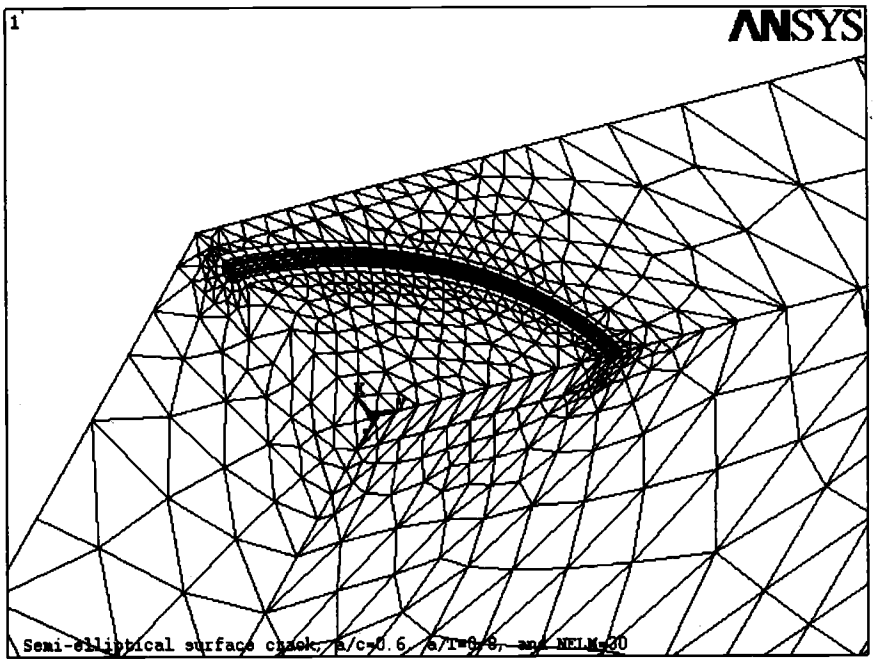


FIG. 5*b*—*Semi-elliptical surface crack mesh for* a/c = *0.6 and* a/t = *0.8, and NELM = 30.*

Discussion

The crack-opening displacement approach was found to be highly accurate and relatively insensitive to crack tip meshing parameters for a centered thru-crack geometry. A drawback of this approach is that it is only strictly valid for identically plane stress or plane strain stress states. Calculating K from crack tip stresses does not require stress state assumptions and was therefore briefly considered. But this approach was highly dependent on crack tip mesh refinement. J-integral and virtual crack tip displacement approaches that utilize stresses and displacements to calculate K were also briefly considered. But these approaches also require stress state assumptions to obtain K to use $da/dN - \Delta K$ material data for life prediction. Given the crack opening approach was found to compare favorably to the known 2D reference solution for a center crack using reasonable crack tip meshes, alternative approaches were not considered further.

TABLE 1—*Predicted* K *with crack opening compared to the Tada reference solution for a centered center crack panel under remote applied tension* ($a/W = 0.2$, $H/W = 3.0$).

Mesh Refinement	Y	Y/Ytada
coarse	1.0348	1.0100
fine	1.0269	1.0023
Tada	1.0245	1.0

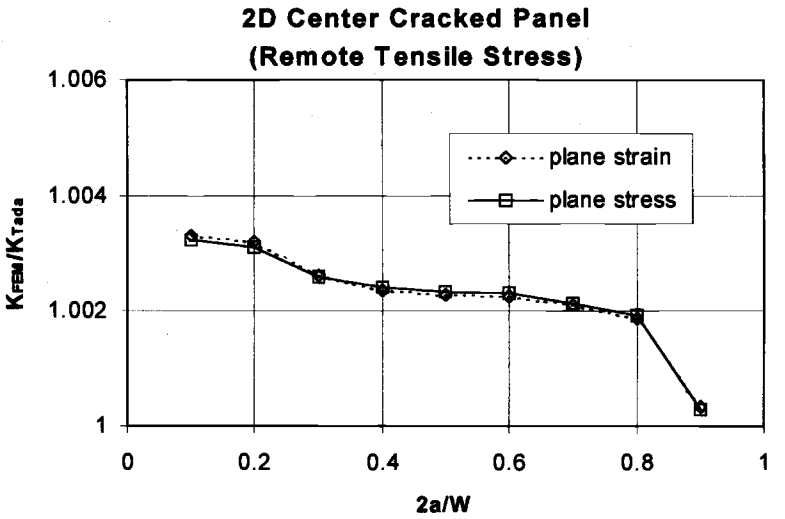


FIG. 6—*Normalized stress intensity for the 2D centered thru-crack compared to Tada.*

Semi-elliptical surface flaws were next successfully modeled in flat planes with ¼ point elements to simulate the crack tip singularity for a wide range of crack aspect ratios ($0.2 \leq a/c \leq 2.0$) and crack depths ($0.01 \leq a/T \leq 0.8$). These models have been used to predict the stress intensity at the crack depth and near-surface positions from the crack tip opening displacements assuming a plane strain stress state. This approach has proved to be fairly robust with converged stress intensity predictions observed for even reasonably coarse crack tip models. The potential limitation associated with the plane strain stress state to predict K for the semi-elliptical crack depth position is of little concern since: (a) the solution proves relatively insensitive to the crack tip meshing, and (b) the results match the mean and standard deviation of other finite element solutions in the literature as compared to Raju-Newman interpolation equations for K.

Predicting the stress intensity for the crack surface position proved more problematic and required more attention. Though plane stress applies at the surface position, the $[r]^{-0.5}$ sin-

TABLE 2—*Predicted* K *with crack opening compared to the Tada reference solution for a centered crack panel under remote applied tension (intermediate mesh refinement).*

	ANSYS Crack Opening				
a/W	*Y*tada	*Y*plane ε	*Y*plane σ	*Y*planeε/*Y*tada	*Y*planeσ/*Y*tada
0.1	1.00597	1.00930	1.00921	1.0033	1.0032
0.2	1.02448	1.02777	1.02765	1.0032	1.0031
0.3	1.05753	1.06029	1.06026	1.0026	1.0026
0.4	1.10905	1.11166	1.11172	1.0024	1.0024
0.5	1.18623	1.18893	1.18900	1.0023	1.0023
0.6	1.30274	1.30568	1.30574	1.0023	1.0023
0.7	1.48735	1.49048	1.49053	1.0021	1.0021
0.8	1.81433	1.81773	1.81782	1.0019	1.0019
0.9	2.57666	2.57752	2.57741	1.0003	1.0003

TABLE 3—*Predicted* K *with ANSYS using crack opening displacements compared to Raju-Newman interpolation equations, Raju-Newman finite element results, and Shiratori et al. finite element results (uniform remote tension,* W = H = 5c).

Remote Applied Tension, W=H=5c											
								(NELM=15)		(NELM=30)	
		Raju-Newman Eq		Raju-Newman FEM		Shiratori FEM		ANSYS FEM		ANSYS FEM	
a/T	a/c	Ya	Yc	Ya	Yc	Ya	Yc	Ya	Yc	Ya	Yc
0.010	0.2	1.112	0.547					1.105	0.599	1.104	0.590
0.030	0.2	1.114	0.548					1.106	0.599	1.105	0.591
0.100	0.2	1.132	0.558			1.119	0.512	1.118	0.606	1.117	0.597
0.200	0.2	1.184	0.590	1.173	0.617	1.162	0.582	1.169	0.631	1.170	0.624
0.400	0.2	1.380	0.713	1.359	0.724	1.371	0.688	1.398	0.747	1.397	0.738
0.600	0.2	1.664	0.913	1.642	0.899	1.651	0.882	1.705	0.950	1.705	0.940
0.800	0.2	1.980	1.172	1.851	1.190	1.787	1.201	1.897	1.247	1.894	1.238
0.010	0.4	1.094	0.761					1.084	0.771	1.085	0.766
0.030	0.4	1.096	0.763					1.085	0.771	1.085	0.766
0.100	0.4	1.106	0.772			1.087	0.794	1.089	0.775	1.091	0.771
0.200	0.4	1.137	0.801	1.138	0.767	1.119	0.810	1.115	0.798	1.117	0.793
0.400	0.4	1.246	0.911	1.225	0.896	1.216	0.911	1.226	0.908	1.227	0.903
0.600	0.4	1.396	1.082	1.370	1.080	1.327	1.060	1.356	1.093	1.360	1.088
0.800	0.4	1.543	1.292	1.447	1.318	1.379	1.320	1.418	1.329	1.422	1.322
0.010	0.6	1.076	0.917					1.069	0.940	1.069	0.937
0.030	0.6	1.077	0.918					1.069	0.940	1.069	0.937
0.100	0.6	1.084	0.927			1.069	0.933	1.071	0.943	1.071	0.939
0.200	0.6	1.104	0.953	1.110	0.916	1.090	0.954	1.086	0.961	1.088	0.959
0.400	0.6	1.172	1.049	1.145	1.015	1.143	1.025	1.153	1.057	1.153	1.053
0.600	0.6	1.262	1.198	1.230	1.172	1.206	1.192	1.223	1.215	1.224	1.213
0.800	0.6	1.346	1.381	1.264	1.353	1.228	1.366	1.252	1.409	1.253	1.404
0.010	1	1.040	1.144					1.047	1.200	1.048	1.194
0.030	1	1.041	1.145					1.047	1.200	1.047	1.194
0.100	1	1.045	1.153			1.039	1.133	1.047	1.200	1.047	1.195
0.200	1	1.053	1.173	1.049	1.174	1.047	1.145	1.055	1.212	1.055	1.207
0.400	1	1.080	1.249	1.062	1.229	1.083	1.220	1.084	1.281	1.085	1.277
0.600	1	1.115	1.368	1.107	1.355	1.106	1.318	1.108	1.394	1.111	1.389
0.800	1	1.148	1.520	1.112	1.464	1.107	1.441	1.119	1.526	1.121	1.520
0.010	2	0.510	0.794					0.518	0.820	0.516	0.826
0.030	2	0.510	0.794					0.519	0.821	0.516	0.827
0.100	2	0.511	0.797			0.510	0.764	0.519	0.820	0.516	0.826
0.200	2	0.513	0.803	0.495	0.821	0.506	0.774	0.518	0.820	0.516	0.827
0.400	2	0.516	0.824	0.501	0.848	0.504	0.769	0.522	0.836	0.519	0.842
0.600	2	0.520	0.856	0.501	0.866	0.515	0.816	0.523	0.867	0.521	0.873
0.800	2	0.524	0.898	0.496	0.876	0.508	0.834	0.522	0.900	0.521	0.906

gularity is not strictly valid [*19,20*]. This behavior results in stress intensities at the surface position that can be highly dependent on crack tip mesh refinement [*11,16*]. Different engineering approaches that obtain a representative K at the surface position for surface flaws have been considered but they can be difficult to apply in general for particular applications of interest for aircraft engine components. One approach of establishing an averaged K near the surface with coarse models avoids steep K-gradients near the surface and is reasonable in many instances. However, this approach was abandoned given components with small geometric features with steep stress gradients can require fine models for the evaluation. A second approach of obtaining surface K from an extrapolation of near-surface results was also considered. This approach was rejected given it can be difficult to standardize on the

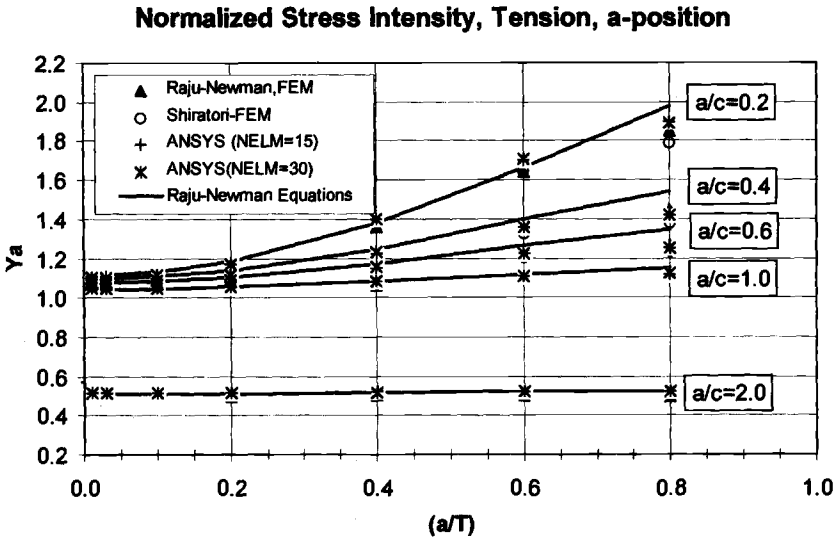


FIG. 7—*Normalized stress intensity at the crack depth position as compared to the Raju-Newman reference equations.*

near-surface points used for the fitting routine to obtain K. These difficulties led to a standard process that involved selecting the 2° position to be representative of K at the surface position. This position was typically beyond the boundary layers where steep gradients in K can exist. It also produced a near-surface stress intensity that was relatively insensitive to the mesh density using the crack opening displacements with the plane strain assumption. Predicted stress intensities with this approach were on average higher than other finite element predictions in the literature but with comparable standard deviations as compared to the Raju-Newman equations. This effect seems to reflect differences in approximate ways to obtain

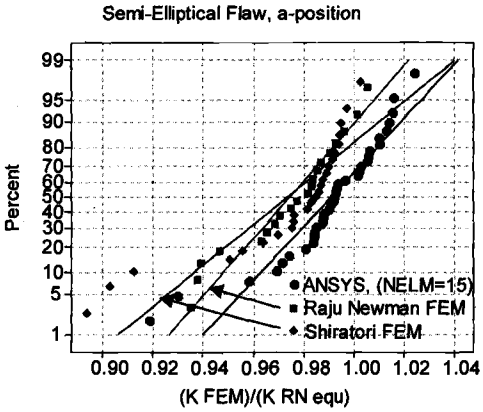


FIG. 8—*Normal probability plot of stress intensity predictions using finite element models as compared to the Raju-Newman interpolation equations for the crack depth position. ANSYS results for NELM = 15 shown are similar to the ANSYS results for NELM = 30 (Table 3).*

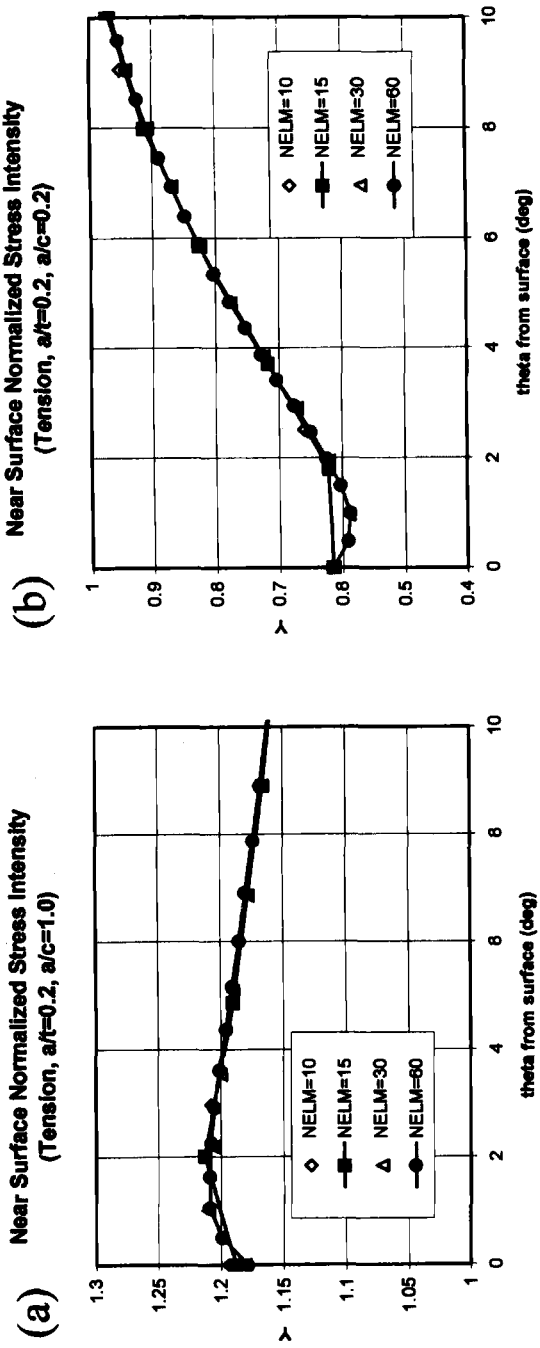


FIG. 9—*Normalized stress intensity as a function of position from the free surface and the number of elements around the crack front for* a/T = 0.2. (a) a/c = *1.0, and* (b) a/c = 0.2.

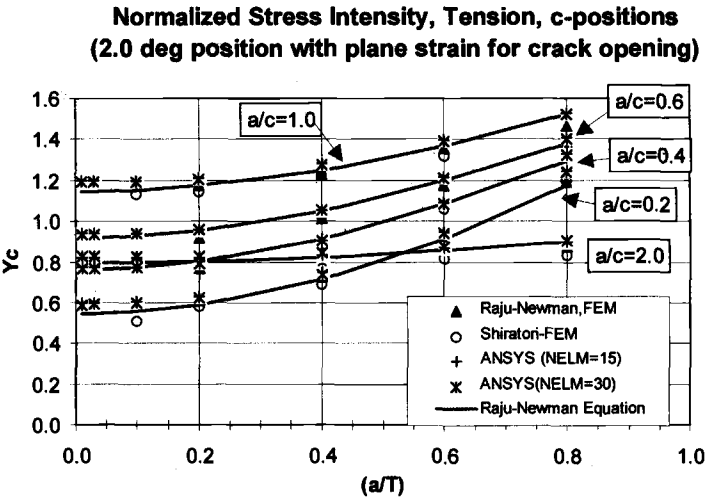


FIG. 10—*Normalized stress intensity at the crack surface position as compared to the Raju-Newman reference equations. Note that crack opening approach to calculate* K *with ANSYS uses the 2.0° position.*

stress intensities near the surface positions as opposed to an inaccuracy of any specific approach. The offset is small and can be ignored or accounted for empirically in life analysis models. Material models based on crack growth test data from semi-elliptical surface flaws have been developed that require corrections to K at the surface position of ~0.88 to 0.91 as predicted from the Raju-Newman equations. These models have been developed to ac-

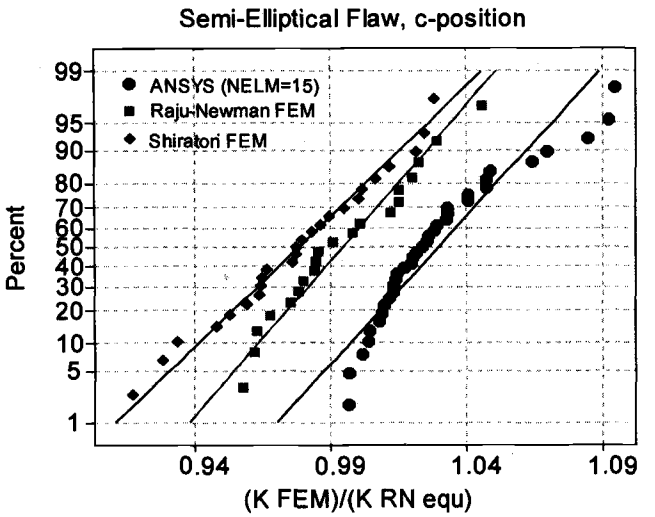


FIG. 11—*Normal probability plot of stress intensity predictions using finite element models as compared to the Raju-Newman interpolation equations at the* c *position. Note that crack opening approach to calculate* K *with ANSYS uses the 2.0° position for* Kc. *ANSYS results for NELM = 15 shown are similar to the ANSYS results for NELM = 30 (Table 3).*

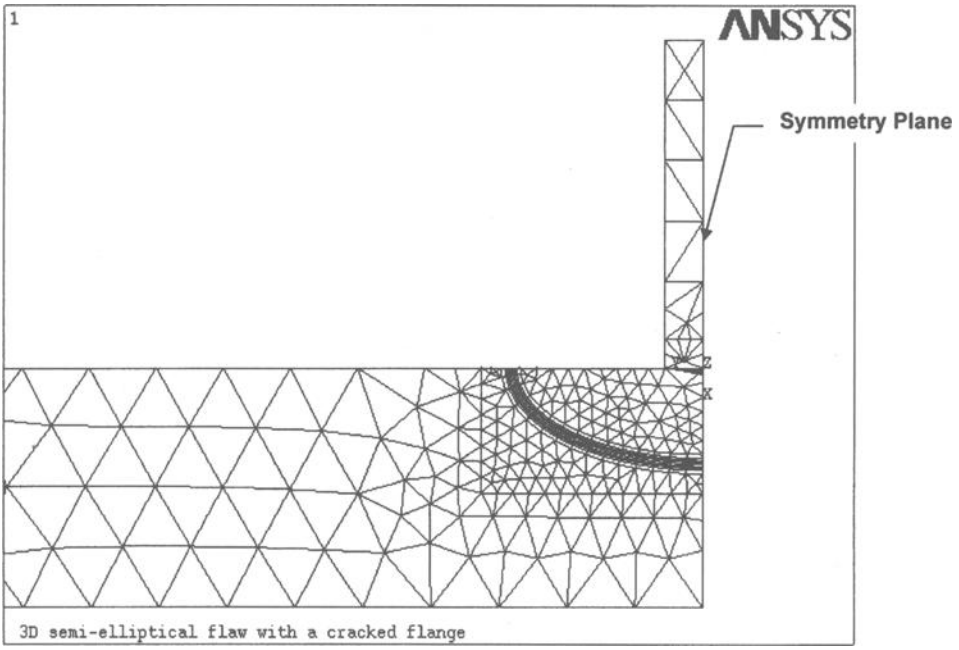


FIG. 12—*Example of a semi-elliptical surface crack in a back wall that originates in a thin attachment arm. One ¼ of the geometry is modeled with symmetry boundary conditions.*

curately predict crack growth in the surface direction for a number of different aircraft engine materials [*2,5*]. Though the exact source of this correction is difficult to identify given the difficulties in obtaining K near the free surface, a small additional adjustment could be used to maintain the consistency with K from ANSYS as compared to test data reduced with K from readily available Raju-Newman interpolation equations.[2]

Using crack meshing tools with comparisons to available solutions for rectangular geometries to interpret the results, the same tools can be used to begin modeling cracks into components with complex boundary geometries or boundary conditions. An example of a crack tip model for an edge crack growing into a rectangular back wall as a semi-elliptical surface crack is shown in Fig. 12. The geometry was modeled with symmetry conditions. These models were generated relatively quickly for a wide range of model dimensions and crack shapes that are generic to a number of different aircraft engine components. A second example of a circular corner crack model in a complex feature under predominately hoop stress is shown in Fig. 13. The outer dimensions of the crack tip model were selected to replace a small set of elements that were extracted from the existing component model. The crack model was tied into the component model with constraint equations to enforce dis-

[2] This has been justified based on limited additional work predicting K using crack opening displacements and K from the stresses ahead of the crack under both tension and bending applied loads. Kc for the 2° position was typically overpredicted by 3–5% as compared to the Raju-Newman interpolation equations. These predictions suggest that a constant adjustment to Kc as calculated from crack opening displacements may be acceptable for both tension and bending gradients. These assumptions for more complex stress gradients are an area for future work.

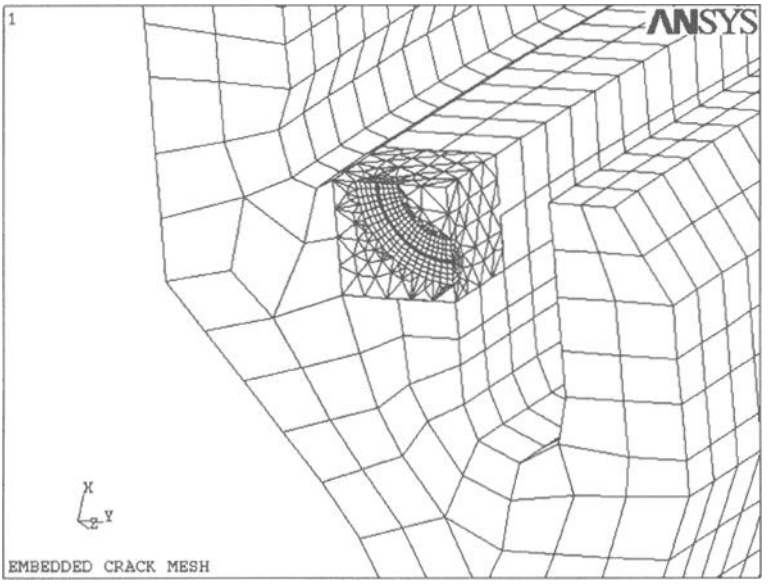


FIG. 13—*Example of a semi-circular corner crack in a complex disk geometry.*

placement continuity across the boundary between the component model and the crack model. Using this procedure a prediction for K for a complex 3D geometry with the component boundary conditions could be obtained relatively easily. This approach was advantageous since crack tip models can be quickly generated with ANSYS crack tip model macros. While this approach does introduce a stress discontinuity at the outer boundary of the crack tip model, it does not introduce significant errors in K calculated from the displacement field, which is continuous. Additional areas of interest that are currently under evaluation include: (a) a detailed evaluation of the crack opening displacement technique with a 2° position for K at the surface position for complex gradients; (b) prediction of K for anisotropic materials, and (c) enhanced meshing for simple 3D features.

Concluding Remarks

ANSYS macros can be used to build thru-crack and semi-elliptical crack models for analysis of both specimens and component geometries. The predicted stress intensity using the crack-opening displacements from ANSYS compares favorably to the nearly exact Isida solution for the centered thru-crack geometry. The results were relatively insensitive to the crack tip meshing parameters considered and were within 1% of the reference solution.

The predicted stress intensities from crack-opening displacements for the semi-elliptical surface crack geometry also compared favorably with other finite element predictions in the literature and Raju-Newman interpolation equations. Crack-opening displacements with the plane strain assumptions produced stress intensities at the crack depth position that were typically within ±5% of literature values with similar standard deviations as compared to other finite element based predictions and the Raju-Newman equations.

Crack-opening displacements produced consistent stress intensities that were relatively unaffected by mesh refinement at the near-surface position of 2.0° assuming plane strain

conditions apply. This approach produced a stress intensity that is representative of the surface position with a similar standard deviation as compared to other approximate finite element solutions in the literature. Surface K from ANSYS was on average higher than other finite element solutions. This effect can be incorporated into existing empirical models that require adjustments to existing solutions at the surface position to accurately model fatigue crack growth for aircraft engine materials.

Crack-meshing macros have been used to generate a crack tip model that can be used to predict K in specimen and more complicated component models with component boundary conditions. This is particularly important when geometries or displacement control boundary conditions exist that require analysis where reference solutions typically do not exist.

Acknowledgments

The authors would like to acknowledge Ahmet Kaya of GE Corporate Research and Development for consultations based on his substantial experience with finite elements and analytical fracture techniques. The additional GE Aircraft Engine team members Paul Domas, Sue Gilbert, Gary Mihlbachler, and Bob VanStone are also acknowledged for their helpful discussion and shared experience.

References

[1] Paris, P. C. and Sih, G. C., "Stress Analysis of Cracks," *Fracture Toughness and Testing and Its Applications, ASTM STP 381,* 1965, pp. 30–83.

[2] VanStone, R. H. and Slavik, D. C., "Prediction of Time Dependent Crack Growth with Retardation Effects in Nickel Base Superalloys," *The 31st Fatigue and Fracture Mechanics Conference,* Cleveland, OH, this publication.

[3] Rooke, D. P. and Cartwright, D. J., "Compendium of Stress Intensity Factors," 1974.

[4] Tada, H., Paris, P. C., and Irwin, G. R., "The Stress Analysis of Cracks Handbooks," DEL Research Group, 1985.

[5] Yau, J. F., "An Empirical Surface Crack Solution for Fatigue Propagation Analysis of Notched Components," in *ASTM STP 905,* 1986, pp. 601–624.

[6] Shen, G. and Glinka, G., "Determination of Weight Functions from Reference Stress Intensity Factors," *Theoretical and Applied Fracture Mechanics,* Vol. 15, 1991, pp. 237–245.

[7] Tracey, D. M., "Finite Elements for Determination of Crack Tip Elastic Stress Intensity Factors," *Engineering Fracture Mechanics,* Vol. 3, 1971, pp. 255–265.

[8] Barsoum, R. S., "On the Use of Isoparametric Finite Elements in Linear Fracture Mechanics," *International Journal for Numerical Methods in Engineering,* Vol. 10, 1976, pp. 25–37.

[9] Ingraffea, A. R. and Manu, C., "Stress-Intensity Factor Computation in Three Dimensions with Quarter-Point Elements," *International Journal of Numerical Methods in Engineering,* Vol. 15, 1980, pp. 1427–1445.

[10] Shih, C. F., deLorenzi, H. G., and German, M. D., "Crack Extension Modeling with Singular Quadratic Isoparametric Elements," *International Journal of Fracture,* Vol. 12, 1976, pp. 647–651.

[11] Raju, I. S. and Newman, J. C., Jr., "Stress-Intensity Factors for a Wide Range of Semi-Elliptical Surface Cracks in Finite-Thickness Plates," *Engineering Fracture Mechanics,* Vol. 11, 1979, pp. 817–829.

[12] ANSYS User's Manual, Vol. IV, Vol. 19, 1994, pp. 32–35.

[13] Isida, M., "Analysis of Stress Intensity Factors for the Tension of a Centrally Cracked Strip with Stiffened Edges," *Engineering Fracture Mechanics,* Vol. 5, 1973, pp. 647–655.

[14] Merkle, J. G., "A Review of Some of the Existing Stress Intensity Factor Solutions for Part-Through Surface Cracks," ORNL-TM-3983, Oak Ridge National Laboratory, 1973.

[15] Raju, I. S. and Newman, Jr., J. C., "An Empirical Stress-Intensity Factor Equation for the Surface Crack," *Engineering Fracture Mechanics,* Vol. 15, 1981, pp. 185–192.

[16] Newman, Jr., J. C. and Raju, I. S., "Analysis of Surface Cracks in Finite Plates Under Tension or Bending Loads," NASA Technical Paper 1578, 1979.

[17] Shiratori, M., Miyoshi, T., and Tanikawa, K., "Analysis of Stress Intensity Factors for Surface Cracks Subjected to Arbitrarily Distributed Surface Stress," 2nd report, "Analysis and Application of Influence Coefficients for Flat Plates with a Semielliptical Surface Crack," *Transactions of the Japan Society of Mechanical Engineers,* Vol. 52, No. 474, 1986, pp. 390–398.

[18] Newman, Jr., J. C. and Raju, I. S., "Stress-Intensity Factor Equation for Cracks in Three-Dimensional Finite Bodies Subjected to Tension and Bending Loads," NASA Technical Paper 85793, 1984.

[19] Benthem, J. P., "State of Stress at the Vertex of a Quarter-Infinite Crack in a Half-Space," *International Journal of Solids and Structures,* Vol. 13, 1977, pp. 479–492.

[20] Bazant, Z. P. and Estenssoro, L. F., "Surface Singularity and Crack Propagation," *International Journal of Solids and Structures,* Vol. 15, 1979, pp. 405–426.

Wyman Z. Zhuang[1] *and Bryon J. Wicks*[1]

Fracture Parameters of Surface Cracks in Compressor Disks

REFERENCE: Zhuang, W. Z. and Wicks, B. J., **"Fracture Parameters of Surface Cracks in Compressor Disks,"** *Fatigue and Fracture Mechanics: 31st Volume, ASTM STP, 1389,* G. R. Halford and J. P. Gallagher, Eds., American Society for Testing and Materials, West Conshohocken, PA, 2000, pp. 391–404.

ABSTRACT: The elastic and elastic-plastic fracture mechanics parameters of surface cracks in compressor disks of aircraft engines are evaluated using both the finite element method and the weight function method. First, a three-dimensional finite element model of a low-pressure compressor disk containing a surface crack at the snap radius is developed. The stress intensity factor distributions along the surface crack front with various crack shapes and sizes in the disk under a typical engine operation condition are calculated. Then, the effect of biaxial stresses on the stress intensity factor of a crack emanating from a tie bolt hole in a representative compressor disk is investigated using the weight function approach. Emphasis is given to determining the effect of the bolt hole plastic zone on the fracture parameters when the compressor disk is highly loaded. Finally, a new theoretical model for the estimation of the fracture parameters of a through-thickness crack in the web region is proposed using a definition of local biaxial stress ratio. The studies show that the developed model can provide better estimation of the plastic zone size and the crack-tip opening displacement than those existing models.

KEYWORDS: aircraft engine, fracture mechanics, fatigue crack, stress intensity factors, plastic yielding, crack opening displacement, biaxial loading

Nomenclature

a	Crack depth (or half-length of a center crack)
B	Specimen thickness
c	Half crack length
E	Young's modulus
K	Stress intensity factor
r	Snap radius
r_p	Crack tip plastic zone size
R	Bolt hole radius
S_{max}	Maximum far-field stress normal to the crack
S_{min}	Minimum far-field stress normal to the crack
S_x, S_y	Far-field stress parallel to the crack, normal to the crack
T	T stress

[1] Research scientist and principal research scientist, respectively, Airframes and Engines Division, Aeronautical and Maritime Research Laboratory, Defence Science and Technology Organisation, 506 Lorimer St., Fishermens' Bend, Victoria 3207, Australia. W. Zhuang is currently attached to the NASA Glenn Research Center as a visiting scientist for a year. His corresponding address is Mail Stop 49-7, 21000 Brookpark Road, Cleveland, OH 44145-3191.

Copyright© 2000 by ASTM International www.astm.org

W	Specimen width (half-width for specimen with center crack)
β	Local biaxial stress ratio ($= \sigma_{xx}/\sigma_{yy}$)
δ	Crack-tip opening displacement
λ	Far-field biaxial stress ratio ($= S_x/S_y$)
ν	Poisson's ratio
σ_o	Cohesive stress
σ_{rr}	Local stress component in the polar coordinate system
σ_{xx}, σ_{yy}	Local stress parallel to the crack, normal to the crack
σ_y	Yield stress
$\sigma_{\theta\theta}$	Local stress component in the polar coordinate system

Introduction

Most failure critical areas in aircraft engine compressor disks are subjected to biaxial or multiaxial loading conditions. These areas are normally adjacent to geometrical features, such as snap fillet (or snap radius), web bolt hole, and web as shown in Fig. 1. There is sound experimental evidence in the literature that demonstrates that the fatigue crack growth rate is strongly influenced by the biaxial loading condition [*1–4*]. Furthermore, previous research results have shown that the effect of biaxial loading on fatigue crack growth rates can be significant, depending on the level of the biaxial loading stresses compared to the yield stress of the material [*5*]. In order to predict the lives of the disks under low-cycle fatigue conditions representative of the engine usage, it is necessary to determine fracture parameters of surface cracks at the snap radius, web bolt holes, and webs considering the effect of biaxial loading.

In elastic-plastic fracture mechanics, the crack-tip plastic zone size and the crack-tip opening displacement (CTOD) are two key fracture parameters governing the fatigue crack growth. To estimate the plastic zone size and the CTOD of a crack under biaxial loading conditions, equations were derived using the Dugdale strip yielding model by Rice [*6,7*] in small-scale yielding. Under the large-scale yielding condition, by using the von Mises yielding criterion plus introducing a cohesive stress, Brown and Miller [*1,2*] proposed a model to estimate the plastic zone size and the CTOD under biaxial loading conditions. However, the accurate determination of these two parameters is far from complete. First, it has been

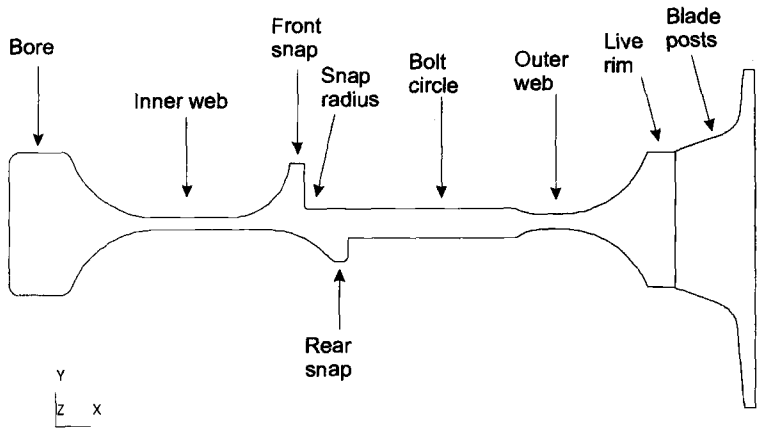


FIG. 1—*Terminology and cross section of a compressor disk.*

found that Rice's small-scale yielding model underestimates the biaxial loading effect significantly as shown in Fig. 2*a*. Second, Brown and Miller's large-scale yielding model does not simplify to the Dugdale model under the uniaxial loading condition and significantly overestimated the biaxial loading effect indicated in Fig. 2*b*. Third, both models ignore an important fact that the local biaxial stress ratio at the crack tip is not constant and further crack-length dependent [*8*].

To estimate fracture parameters, such as stress intensity factors used in linear elastic fracture mechanics is relatively easy. But accurate determination of stress intensity factor distributions for surface cracks adjacent to the complex geometries such as snap radii is certainly not trivial. Because of the complexities of the structural geometries of the disks under complex loading conditions, there are no exact solutions available for the cracks in real gas turbine engine disks. Among the available methods for calculating elastic and elastic-plastic fracture mechanics parameters of surface cracks, the finite element method is found to be a good candidate. First, the elastic plastic finite element method was applied successfully by several authors [*3,9*] to study crack behavior. Second, the finite element method can also be regarded as a powerful tool for three-dimensional complicated geometries subjected to complex loading conditions.

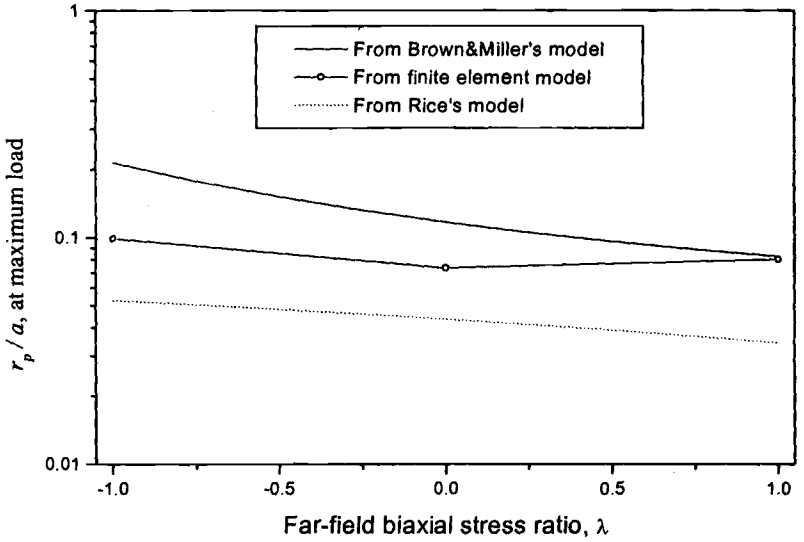
The main objective of this paper is to evaluate the elastic and elastic-plastic fracture mechanics parameters in cracked compressor disks using the finite element method and the weight function method. First, a three-dimensional finite element model of the disk containing a surface crack at the snap radius is developed. The stress intensity factor distributions along the surface crack front with various crack shapes and sizes in the disk under a typical engine operation condition are determined. Then, the effect of biaxial stresses on the stress intensity factor of a crack emanating from tie bolt holes (short for bolt holes) in the representative compressor disk is investigated using the weight function approach. Emphasis is given to determining the effect of the bolt hole plastic zone on the fracture parameters when the compressor disk is highly loaded. Finally, a new theoretical model for the estimation of the plastic zone size and the CTOD of a through-thickness crack in the web region is proposed using the definition of the local biaxial stress ratio. The studies show that the new model can provide better estimation than those existing models.

Stress Intensity Factors of Surface Cracks in Snap Radius

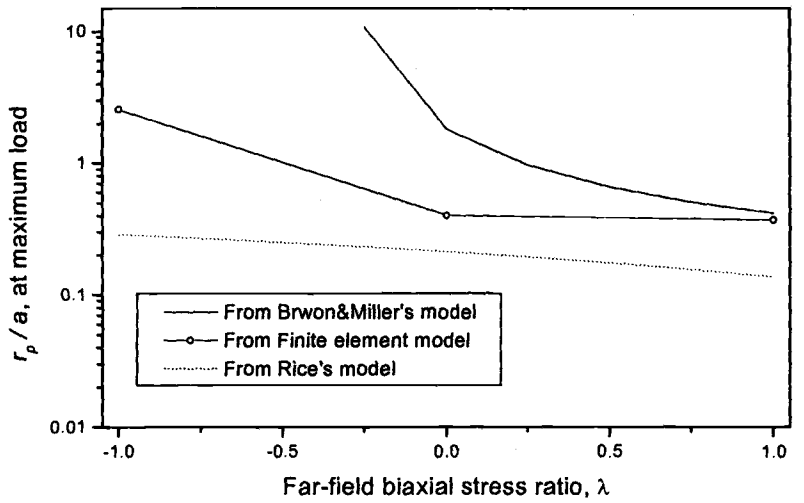
Because of the complexities of the structural geometries of compressor disks under complex loading conditions, there are no exact solutions available for the determination of the stress intensity factors of surface cracks in a disk of interest. As mentioned in the introduction, accurate determination of stress intensity factor distributions of surface cracks in a compressor disk relies heavily on a sophisticated three-dimensional finite element analysis so that an empirical equation can be established.

In this study, a three-dimensional cracked finite element model of a $\pm 5.625°$ segment of the low-pressure compressor disk was generated as shown in Fig. 3. The initial crack aspect ratio (a/c) is 1.0 with a half-crack length of $c = 0.2$ mm and located at snap radius. In the crack front, crack-tip elements were used so stress singularity at the crack tip can be accurately calculated. The model was subjected to a typical engine operation condition, including centrifugal force, installation loads, and temperature distribution. In this study, no vibrational loads were considered. The low-pressure compressor disk being studied is made of a duplex annealed Ti-8Al-1Mo-1V titanium alloy. Details of its properties are shown in Table 1.

The effect of snap radius on the stress intensity factor distributions for the crack has been investigated. The results are shown in Fig. 4. The three values of snap radius represent



(a) In small-scale yielding (S_{max}/σ_y=0.25)



(b) In large-scale yielding (S_{max}/σ_y=0.50)

FIG. 2—*Prediction of plastic zone size by the different models.*

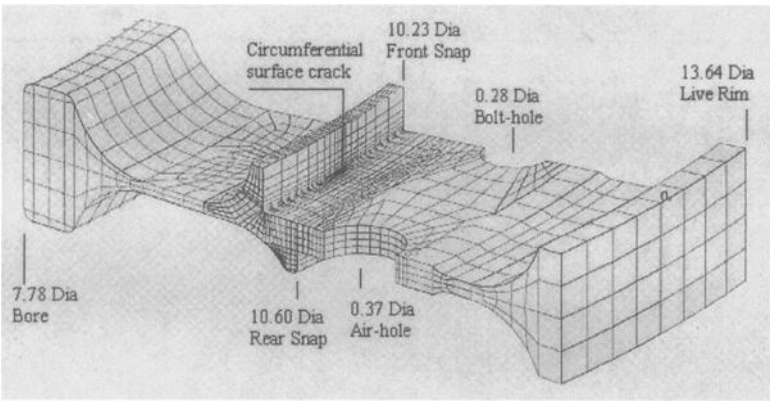


FIG. 3—*3D finite element mesh of a compressor disk.*

manufacturing tolerances from 0.203 to 0.457 mm. The dimensionless stress intensity factor F is given by

$$F = \frac{K}{K_o} \tag{1}$$

where K_o is the stress intensity factor for a crack in a disk with radius of disk R_d rotating at an angular velocity ω. K_o can be in turn written as the following [*10*].

$$K_o = \frac{\rho_m \omega^2 R_d^2}{8} \left(\frac{3 - 2\nu}{1 - \nu}\right) \sqrt{\pi c} \tag{2}$$

where ρ_m is the density of the disk material. It is worth noting that Eq 2 is used only for the plane strain condition, close to the case of a surface crack in the snap radius in the disk.

In the study, stress intensity factors along the crack front for c = 0.2 to 0.8 mm were calculated. The stress intensity factors shown in Fig. 4 are obtained for a semi-circular surface crack with a half crack length c = 0.2 mm. It clear indicates that there are two distinct peaks of SIFs along the crack front. The first peak, F_a, is located at both free surface ends of the crack; the second, F_b is at the center of the crack front. It demonstrates that the stress intensity factors along the crack front are very sensitive to the snap radius of the disk.

TABLE 1—*Mechanical properties of T1-8A1-1Mo-1V.*

Property	Value
Elastic modulus, E	131.0 GPa
Ultimate tensile stress	1049 MPa
0.2% proof stress	922 MPa
Poisson's ratio, ν	0.3
Density, ρ_m	4373 kg/m^3
Coefficient of thermal expansion	8.5 × 10^{-6} 1/°C

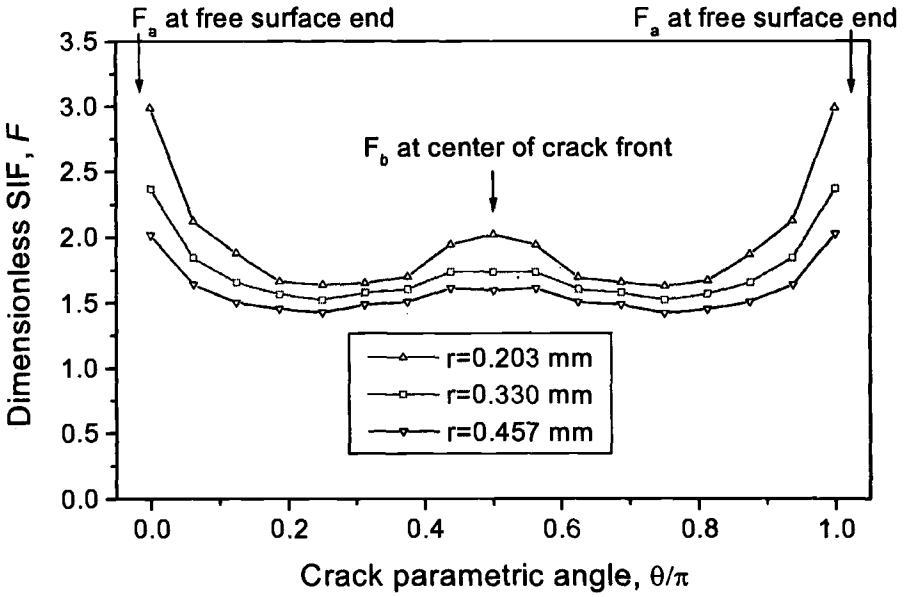


FIG. 4—*The SIFs for a semi-circular surface crack* (a/c = *1 and* c = *0.2 mm*).

The combined effect of snap radius and crack aspect ratio on the two distinct peaks of SIFs is shown in Fig. 5. Assuming the shape of the initial surface crack is semi-circular (crack aspect ratio is 1.0) and because the first peak is always higher than the second, as the crack propagates the crack aspect ratio will most likely reduce. Although the second peak may develop and increase considerably at the early stage of crack growth, it finally slows down as the crack aspect ratio reduces.

Effect of Bolt Hole Plastic Zone on Stress Intensity Factors

From the previous section, it has been seen that to determine stress intensity factors in a compressor disk theoretically or numerically is often difficult and time consuming. If the variation of a disk thickness in the particular interesting region is small (web bolt hole), it may be assumed that the stress intensity factor of a crack emanating from a bolt hole in a rotating disk could be approximated by the stress intensity factor of a crack emanating from a circular hole in an infinite plate subjected to biaxial stresses (radial and tangential stresses) because the contribution of non-singularity body force to the *J*-integral is negligible. The biaxial stresses used in calculation of the stress intensity factor are the radial and tangential stresses at the center of the bolt hole in an uncracked rotating disk.

The biaxial stress ratio in the bolt hole region of a representative compressor disk used in this study was found to be equi-biaxial ($\lambda = 1$) by finite element stress analysis. Furthermore, it was found that plasticity occurred around the bolt holes in a highly stressed rotating disk [*5*]. The effect of this bolt hole plastic zone on crack growth was later found to be significant [*11*]. There is a need to quantify the influence of the plasticity on stress intensity factors when the crack is entirely or partially engulfed in the bolt hole plastic zone, as illustrated in Fig. 6. Since stress distributions near the crack tip vary in elastic and plastic

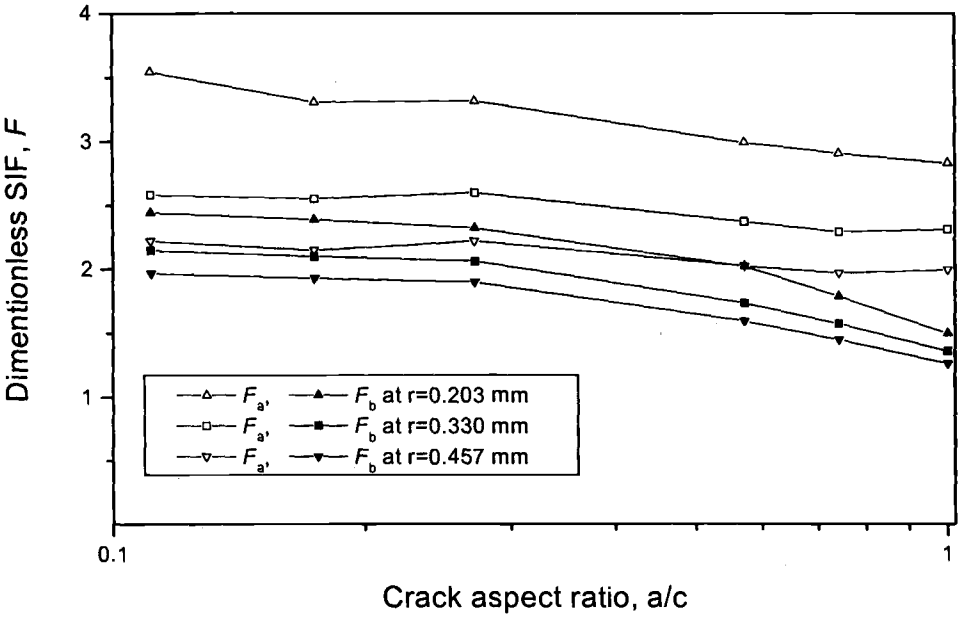


FIG. 5—*Combined effect of snap radius and crack aspect ratio on SIFs.*

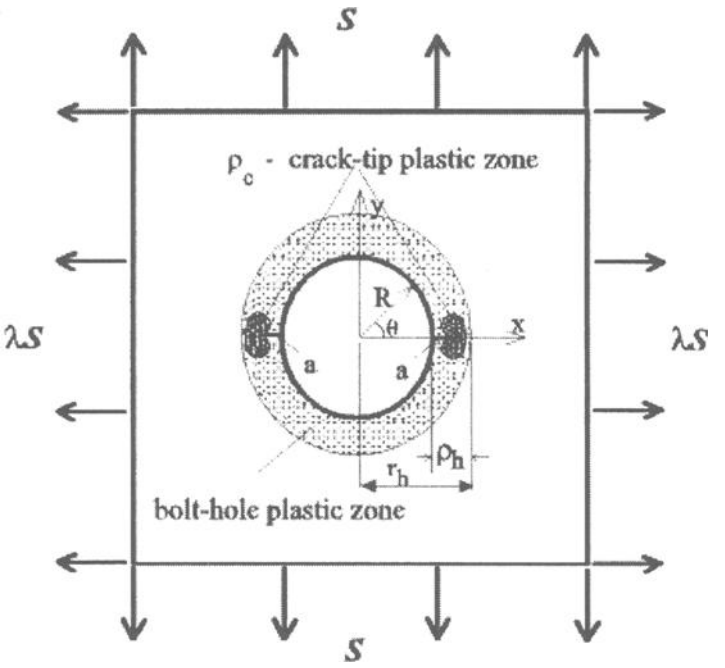


FIG. 6—*Stress state and notations for a crack emanating from a bolt hole.*

materials, the stress intensity factors determined by the following weight function method will be different to present the effect of the bolt hole plastic zone.

In Fig. 6, there exists a bolt hole plastic zone when far-field stress $S > \sigma_y/2$. Let us designate the size of the bolt hole plastic zone as ρ_h, which is measured from the edge of the hole. Then the normalized bolt hole plastic zone size, $\rho = \rho_h/R$ is obtained and can be written as the following:

$$\rho = \frac{1}{2(1 - S/\sigma_y)} - 1 \tag{3}$$

where R denotes the radius of the bolt hole and σ_y the material's yield stress. Obviously, when the far-field applied stress S reaches the material yield stress the entire plate would yield (or $r_p = \infty$). With x denoting the distance measured from the center of the hole, the radial stress $\sigma_{rr}(x)$ and the hoop stress $\sigma_{\theta\theta}(x)$ outside the bolt-hole plastic zone ($x \geq r_p$) are

$$\sigma_{rr}(x) = S - (\sigma_y - S)\frac{r_p^2}{x^2} \qquad \text{for} \quad x \geq r_p \tag{4}$$

and

$$\sigma_{\theta\theta}(x) = S + (\sigma_y - S)\frac{r_p^2}{x^2} \qquad \text{for} \quad x \geq r_p \tag{5}$$

In the plastic zone ($x \leq r_p$), the radial stress and hoop stress distributions are

$$\sigma_{rr}(x) = \left(1 - \frac{R}{x}\right)\sigma_y \qquad \text{for} \quad x \leq r_p \tag{6}$$

and

$$\sigma_{\theta\theta}(x) = \sigma_y \qquad \text{for} \quad x \leq r_p \tag{7}$$

It should be noted that although the von Mises yield criterion could produce more accurate elastic-plastic stress distributions around the bolt hole, the Tresca solutions in Eqs 4 to 7 can provide the same accuracy with much simpler expressions for the elastic perfectly plastic material [*12*].

For an elastic structure containing a crack, the stress intensity factor can be determined by a weight function method [*13*]. In principle, the weight function method is applicable only for elastic problems where there is no plastic deformation. However, this approach has been used extensively, due mainly to its simplicity, to handle cases where plastic deformation does occur [*14*], provided the effect of plastic deformation has been taken into account in deriving the prospective stress distribution. Based on the principle of superposition, the stress intensity factor of a crack embedded partially in the bolt hole plastic zone than can be determined as

$$K = \int_0^{\rho_h} \sigma_{\theta\theta}(t)\, G(t, a)dt + \int_{\rho_h}^{a} \sigma_{\theta\theta}(t)\, G(t, a)dt \tag{8}$$

where $G(t, a)$ is the weight function representing the stress intensity factor of the crack, with length a, caused by a pair of concentrated unit forces acting at position t (t measured from the edge of the crack). The $\sigma_{\theta\theta}(t)$ is given by Eqs 5 and 7. Normally, the stress intensity factors are written in the following form:

$$K_{max} = F_{max} S_{max} \sqrt{\pi a} \tag{9}$$

where S_{max} is the maximum applied stress, and F_{max} is the non-dimensional stress intensity factor. The non-dimensional stress intensity factor can be determined numerically using Eqs 8 and 9.

To determine the bolt hole plastic zone effect on the stress intensity factor, the non-dimensional stress intensity factors for three different load ratios (S/σ_y = 0.5, 0.6, and 0.7) are calculated using Eqs 8 and 9 and presented in Fig. 7. The results indicated that in the elastic case, the present results for equi-biaxial loading, i.e., the dashed line with an open square symbol for S/σ_y = 0.5, are consistent with those obtained using the theory of elasticity [5] (dashed line with open triangular symbol). It is also shown that for cracks of short length compared with the bolt hole plastic zone size, the bolt hole plastic zone has a significant influence on the stress intensity factor. Furthermore, compared with the stress intensity factor under the uniaxial loading condition, the biaxial loading significantly lowered the stress intensity factors, suggesting that analysis ignoring the biaxial stress may be overly conservative. As the crack gets longer, the effect of biaxial loading gradually diminishes under

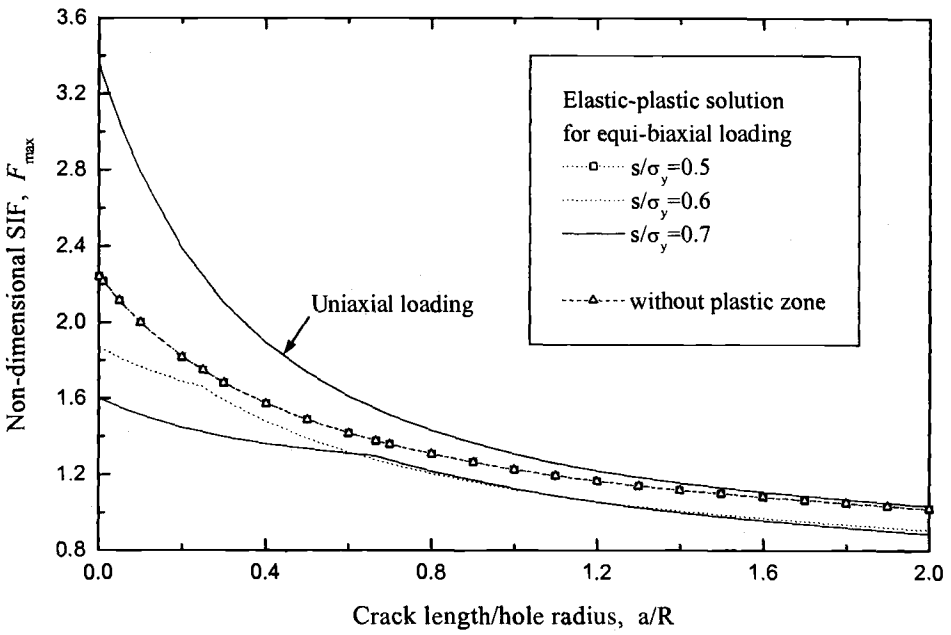


FIG. 7—*Bolt hole plastic zone effect on non-dimensional stress intensity factors.*

elastic conditions because the lateral stress (T-stress) does not contribute to the elastic stress intensity factors. However, the effect of the bolt hole plastic zone still remains, probably due to the reduction of the maximum stress.

Crack Tip Plastic Zone Size and the CTOD under Biaxial Loading

In a compressor disk, normally the cross section in the web region is quite uniform. Stress analysis shows that the state of stresses in the region is biaxial, that is, the structure is subjected to both radial and tangential (or hoop) stresses. To predict plastic zone size and the CTOD of a crack in the web, therefore, one could calculate the plastic zone size and the CTOD of a center-cracked panel under biaxial loading conditions as shown in Fig. 8. To predict the crack tip plastic zone size and the CTOD of a center-cracked panel under biaxial loading conditions, it is useful to introduce local biaxial stress ratio $\beta(x)$ with coordinates originated at the crack tip.

$$\beta(x) = \frac{\sigma_{xx}}{\sigma_{yy}} \tag{10}$$

where σ_{xx} and σ_{yy} are the local stress components. In Fig. 8, λ is the far-field biaxial stress ratio, which is equal to the ratio of the far-field stress parallel to the crack plane to the far-field stress perpendicular to the crack plane. Normally, $\lambda = 0$ stands for uniaxial loading, $\lambda = 1$ for equibiaxial, and $\lambda = -1$ for shear loading.

Local stress components around the crack-tip in a center-cracked panel under biaxial loading as shown Fig. 8 were derived by Eftis et al. [*8*]. For $\theta = 0$, the local stress components are

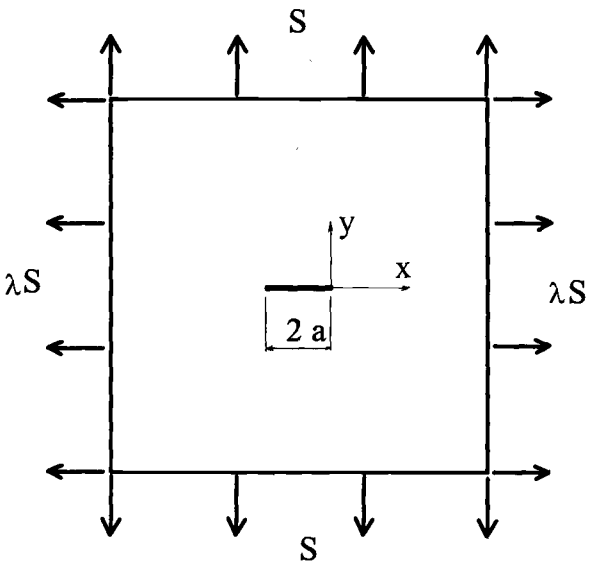


FIG. 8—*Center-cracked panel under biaxial loading.*

$$\sigma_{xx} = \frac{K}{\sqrt{2\pi x}} - (1 - \lambda)S \tag{11a}$$

$$\sigma_{yy} = \frac{K}{\sqrt{2\pi x}} \tag{11b}$$

Thus, the relationship of the local biaxial stress ratio and the far-field biaxial stress ratio is obtained by substituting the local stress components into Eq 10.

$$\beta(x) = 1 + (\lambda - 1)\sqrt{\frac{2x}{a}} \tag{12}$$

Obviously, the far-field biaxial stress ratio is geometry-independent. But, the local biaxial stress ratio in Eq 12 is crack-length dependent and a function of x as suggested by Leevers and Radon [*15*]. It implies that the assumption of constant T-stress used in the development of the existing model for the determination of plastic zone size and the CTOD is no longer held.

To be able to use the strip yielding model developed by Dugdale [*16*] for the determination of the plastic zone size and the CTOD, the relationship between the local stress component σ_{xx} and the cohesive stress σ_o needs to be determined. The cohesive stress was defined by Dugdale [*16*]. It is approximately equal to the average value of material yield stress and ultimate strength [*17*]. The relationship can be derived using the von Mises yield criterion for the plane stress condition. Since the cohesive stress is a function of the local biaxial stress ratio, the plastic zone size r_p would be obtained by numerical integration.

$$r_p = \frac{1}{\pi S}\left[\int_a^{r_p} G(x, a)\sigma_o\,(x - a)dx\right]^2 - a \tag{13}$$

where $G(x, a)$ is the weight function. For the sake of engineering application, one could use the local biaxial stress ratio at $x = a/2$ to avoid the complicated numerical integration. It is because that at the location ($x = a/2$) the local biaxial stress ratio represents the average value. Therefore, the plastic zone size can be written as:

$$r_p = a\left[\sec\left(\frac{\pi}{\lambda + \sqrt{4(\sigma_y/S)^2 - 3\lambda^2}}\right) - 1\right] \tag{14}$$

and the CTOD is

$$\delta = \frac{4a}{\pi E'}\left[\lambda S + \sqrt{4\sigma_y^2 - 3\lambda^2 S^2}\right] \ln\left[\sec\left(\frac{\pi}{\lambda + \sqrt{4(\sigma_y/S)^2 - 3\lambda^2}}\right)\right] \tag{15}$$

For the model verification, a finite element study is conducted on the same crack panel. Figure 9 shows the combined effect of the maximum applied load and the far-field biaxial stress ratio on the normalized plastic zone size, indicating good agreement between the developed model with finite element results. The present results reveal that only at the high ratio of S_{max}/σ_y (about 0.40 and 0.50) do the biaxiality have a significant influence, which is consistent with that obtained by McClung [*3*].

Figure 10 shows the CTOD under biaxial loading predicted by the developed model and calculated by the finite element model. In finite element analysis, the value of the CTOD is determined by the separation between crack faces where the two 45° lines emanating from the crack tip intercept the crack faces. This operational definition of the CTOD was suggested by Tracey [*18*]. As can be seen from Fig. 10, similar to the plastic zone size under biaxial

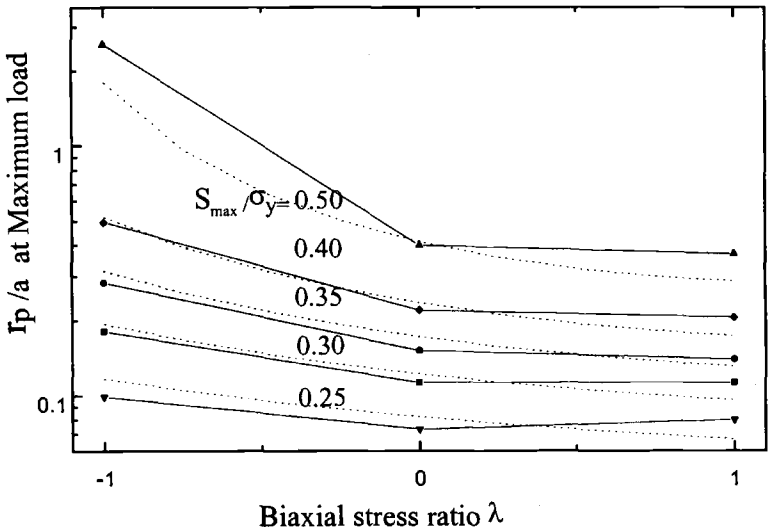


FIG. 9—*Combined effect of biaxiality and applied load on plastic zone size.*

loading, the CTOD is also not very much dependent on the biaxiality ratio until the ratio of S_{max} to σ_y is reaching to 0.5.

Conclusions

The elastic and elastic-plastic fracture mechanics parameters in cracked compressor disks have been investigated using the finite element method and the weight function method. The

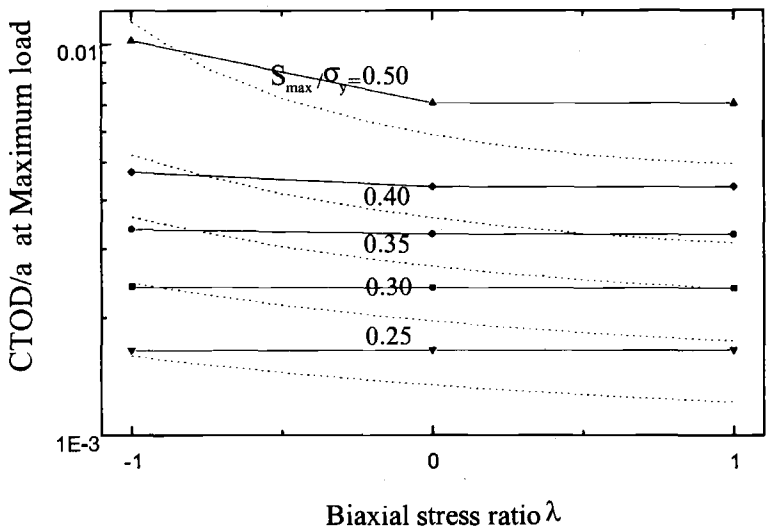


FIG. 10—*Combined effect of biaxiality and applied load on CTOD.*

stress intensity factor distributions along the surface crack front with various crack shapes and sizes in a gas turbine compressor disk under a typical operation condition were determined. Then, the effect of biaxial stresses on the stress intensity factor of a crack emanating from tie bolt holes in a representative compressor disk was determined using the weight function approach. Finally, a new theoretical model for the estimation of the crack tip plastic zone size and the CTOD of a through-thickness crack in the web region was proposed using the definition of local biaxial stress ratio. The developed model is able to recover the Dugdale model under the uniaxial loading condition. Furthermore, under the biaxial loading conditions, the developed model can give better estimation of the plastic zone size and the CTOD assessed with the FE prediction results.

References

[1] Brown, M. W. and Miller, K. J., "Mode I Fatigue Crack Growth under Biaxial Stress at Room and Elevated Temperature," *Multiaxial Fatigue, ASTM STP 853,* K. J. Miller and M. W. Brown, Eds., American Society for Testing and Materials, Philadelphia, 1985, pp. 135–152.

[2] Brown, M. W., de los Rios, E. R., and Miller, K. J., "A Critical Comparison of Proposed Parameters for High-Strain Fatigue Crack Growth," *Basic Questions in Fatigue: Volume I, ASTM STP 924,* J. T. Fong and R. J. Fields, Eds., American Society for Testing and Materials, Philadelphia, 1988, pp. 233–259.

[3] McClung, R. C., "Closure and Growth of Mode I Cracks in Biaxial Fatigue," *Fatigue Fract. Engng Mater. Struct.,* Vol. 12, No. 5, 1989, pp. 447–460.

[4] Shanyavskii, A. A., "Development of Semi-Elliptic Fatigue Cracks in AK6 Aluminium Alloy Under Biaxial Loading," *Fatigue Fract. Engng Mater. Struct.,* Vol. 19, No. 12, 1996, pp. 1445–1458.

[5] Zhuang, W. Z., Stocks, G. J., and Wang, C. H., "Prediction of Fatigue Crack Growth from Bolt Holes in a Titanium Disk," *Proceedings of The 21st Congress of the International Council of the Aeronautical Sciences,* Melbourne, Australia, 1998.

[6] Rice, J. R., "A Path Independent Integral and the Approximate Analysis of Strain Concentration by Notches and Cracks," *Journal of Applied Mechanics,* Vol. 35, 1968, pp. 379–386.

[7] Rice, J. R., "Limitations to the Small Scale Yielding Approximation for Crack Tip Plasticity," *Journal of the Mechanics and Physics of Solids,* Vol. 22, 1974, pp. 17–26.

[8] Eftis, J., Subramonian, N., and Liebowwitz, H., "Crack Border Stress and Displacement Equations Revisited," *Engineering Fracture Mechanics,* Vol. 9, 1977, pp. 189–210.

[9] Newman, J. C., "A Crack Opening Stress Equation for Fatigue Crack Growth," *International Journal of Fracture,* Vol. 24, 1984, pp. R131–R135.

[10] Rooke, D. and Cartwright, D., *Compendium of Stress Intensity Factors,* HMSO, London, 1976.

[11] Zhuang, W. Z. and Wang, C. H., "Bolt-Hole Plastic Zone Effect on Crack Growth in a Compressor Disc," *Structure Integrity and Fracture,* Dr. C. Wang, Ed., Australian Society for Fracture Mechanics, Australia, 1998.

[12] Chakrabarty, J., *Theory of Plasticity,* McGraw-Hill Book Company, New York, 1987.

[13] Wu, X. R. and Carlsson, A. J., "Weight Functions and Stress Intensity Factor Solutions," Pergamon Press, 1991.

[14] Beghini, M., Bertini, L., and Vitale, E., "Weight Functions Applied to Fatigue Crack Growth Analysis," *Fatigue Fract. Engng Mater. Struct.,* Vol. 20, No. 8, 1997, pp. 1093–1104.

[15] Leevers, P. S. and Radon, J. C., "Inherent Stress Biaxiality in Various Fracture Specimen Geometries," *International Journal of Fracture,* Vol. 19, 1982, pp. 311–325.

[16] Dugdale, D. S., "Yielding of Steel Sheets Containing Slits," *Journal of the Mechanics and Physics of Solids,* Vol. 8, 1960, 100–104.

[17] Newman, J. C., Jr., "FASTRAN-II—A Fatigue Crack Growth Structural Analysis Program," NASA TM 104159, 1992.

[18] Tracey, D. M., "Finite Element Solutions for Crack-Tip Behavior in Small-Scale Yielding," *Transactions of ASME, Journal of Engineering Materials and Technology,* Vol. 98, 1976, pp. 146–151.

Bibliography

Elber, W., "The Significance of Fatigue Crack Closure," *Damage Tolerance in Aircraft Structures, ASTM STP 486*, 1971, pp. 230–242.

Finney, J. M. and Beaver, P. W., "The Need for Biaxial Fatigue Testing at ARL," Aeronautical Research Laboratories, ARL-STRUC-TM-380, 1984.

R. H. Van Stone[1] *and D. C. Slavik*[1]

Prediction of Time-Dependent Crack Growth with Retardation Effects in Nickel Base Alloys

REFERENCE: Van Stone, R. H. and Slavik, D. C., **"Prediction of Time-Dependent Crack Growth with Retardation Effects in Nickel Base Alloys,"** *Fatigue and Fracture Mechanics: 31st Volume, ASTM STP 1389,* G. R. Halford and J. P. Gallagher, Eds., American Society for Testing and Materials, West Conshohocken, PA, 2000, pp. 405–426.

ABSTRACT: Accurate crack growth prediction methods are playing an increasing role in the design and evaluation of rotating gas turbine engine components. Fracture mechanics methods used to predict the cyclic lives (without time-dependent effects) are well established. As mission times and temperature increase, nickel base superalloys experience time-dependent crack growth where the crack growth response is a function of time under load (hold time) as well as overpeaks that occur prior to hold times. Linear elastic fracture mechanics methods have been developed that accurately predict the acceleration associated with hold times at elevated temperatures using a linear superposition of cyclic and static crack growth rates. The beneficial effects of retardation induced by overpeaks can be predicted using a modified Willenborg retardation model. Results of subcomponent validation tests for a variety of conditions and materials used to validate these methods are reported. Applicability of these model to predict complex missions and combinations of complex missions is also discussed.

KEYWORDS: nickel base alloys, crack growth, turbine engines

Critical rotating parts in advanced gas turbine engines such as turbine disks frequently operate at high temperature and stresses for rather long periods of time. Life prediction of these components includes evaluation using linear elastic fracture mechanics. These types of assessments are used to evaluate damage tolerance [*1*,*2*], setting of inspection intervals [*1*,*2*], and probabilistic fracture mechanics evaluations [*3*]. A key element of these types of analyses includes the consideration of the details of the stress-time history, which can affect the accuracy of the fracture mechanics predictions.

In advanced aircraft engines, these critical parts are frequently manufactured from high-strength nickel base superalloys. Examples of these alloys include Rene'95 [*4*] and Rene'88DT [*5*]. These alloys were developed to provide a balance between strength, creep, low-cycle fatigue, and crack growth properties. It has also been documented that cracks in the presence of sustained loads at elevated temperature can grow in a time-dependent fashion [*6–28*]. This type of a crack growth phenomena becomes more important as engine operating temperatures increase and as components are designed for static loading for longer periods of time.

A key element of fracture mechanics technology within the aircraft engine businesses is the ability to accurately calculate the lives of components using the actual missions account-

[1] GE Aircraft Engines, Cincinnati, OH 45215.

Copyright© 2000 by ASTM International www.astm.org

ing for cycle-dependent crack growth, time-dependent crack growth, and overpeak retardation. The subject of cycle-dependent crack growth is well established and its use by the aircraft engine business has been documented elsewhere [*29,30*]. The subject of this paper is the description of fracture mechanics models to assess the impact of time-dependent crack growth and overpeak retardation, individually and in combination.

Design System Requirements

Before discussing the models, it is useful to review the requirement of a fracture mechanics design system within an aerospace engineering organization. The system must be:

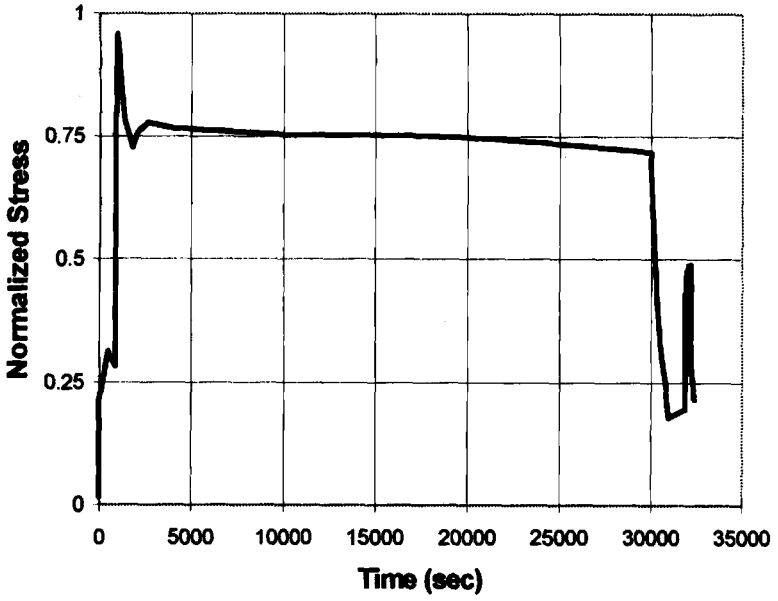
1. Accurate
2. Capable of determining stress intensity factors for complex component shapes with non-linear stress gradients containing various crack types (through cracks, surface cracks, corner cracks, etc.) having a variety of crack aspect ratios.
3. Easy to use by design engineers.
4. Able to utilize input material properties determined from laboratory tests.
5. Applicable to the full range of missions, temperatures, and stresses in operating components.

The mission issue has a direct impact on the development of the overpeak retardation model discussed later in the paper. Figure 1 shows an example of two missions for the same critical location on the same part for different types of aircraft usage. The stresses in these figures were normalized by the maximum stress experienced at this location. The mission shown in Fig. 1*a* has an overpeak stress very early in the mission followed by a sustained stress for a long cruise. The mission shown in Fig. 1*b* has an even higher overpeak stress followed by a series of cyclic loads. Design engineers must have the ability to analyze each contribution independently and also to determine how the combination of the different mission types impacts component lives. This process is known as mission mixing, and it is not unusual that between 9 and 28 different missions are mixed based on the documented history of a customer's engine operating experience. As the retardation model was developed, this ability to perform a mission mixing residual life calculation for missions with significantly different maximum stress (and therefore overpeaks) and highly different mission mix fractions was a key consideration. The models developed must be able to accurately predict residual lives for locations with significant variations in maximum stress, length of missions, cyclic and static variations in stress, overpeaks, temperatures, and mission mixing.

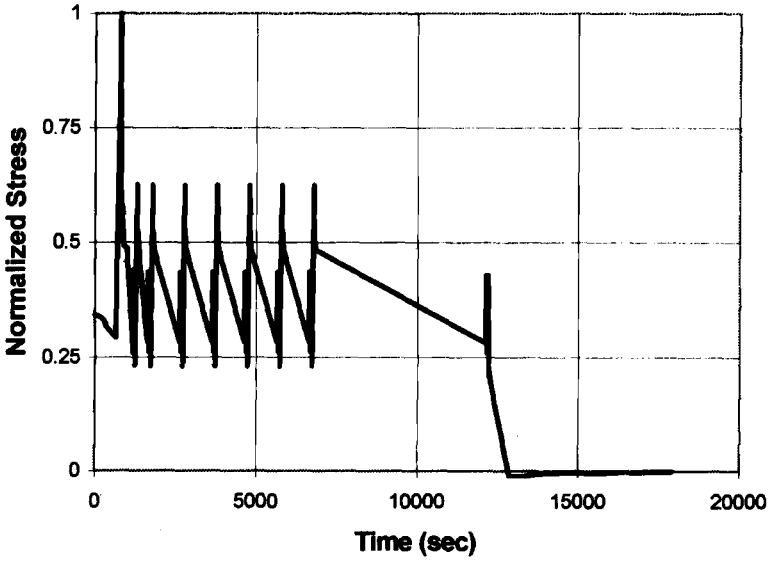
Each of the missions shown in Fig. 1 has a significant overpeak. The overpeaks in aircraft engine components are most often caused by a combination of engine system temperature variations and the high engine speed at and near takeoff conditions. As the engine heats up and metallic components expand by different amounts, they often induce significant thermal stresses that dissipate as the engine approaches its steady state temperature distribution. This source of overpeaks is significantly different from the often random types of operational overpeaks experienced by airframe members due to maneuvering and aerodynamic considerations. Within an engine, these overpeaks occur due to the thermal environment that occurs reproducibly on each flight.

Time-Dependent Crack Growth

Time-dependent crack growth is a well-documented elevated temperature crack growth mechanism in nickel base superalloys [*6–28*]. Time-dependent crack growth refers to growth



(a)



(b)

FIG. 1—*Examples of missions experienced in a range of aircraft engine applications.*

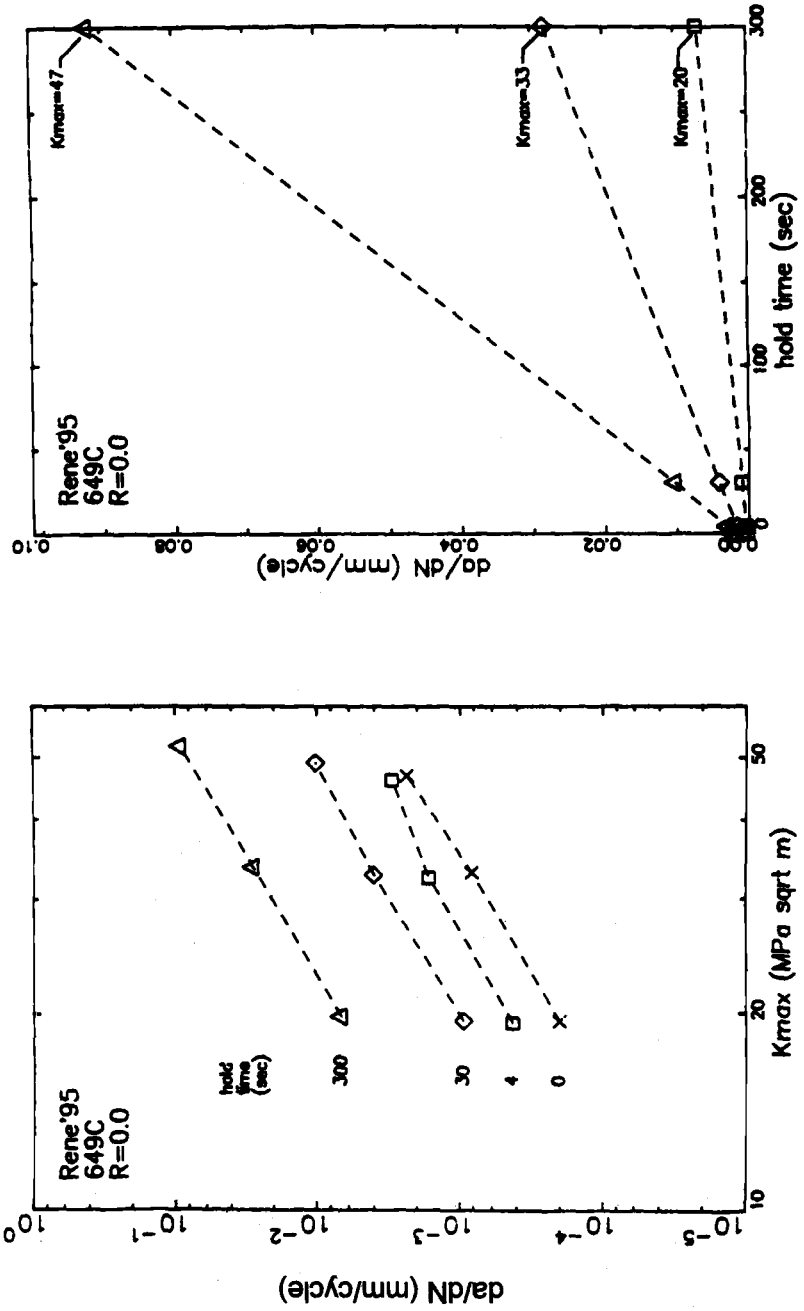


FIG. 2—*Rene'95 time-dependent crack growth data plotted as* (a) da/dN *as a function of* K_{max} *(logarithmic scale) and* (b) da/dN *plotted as a function of hold time (linear scale) [28].*

of cracks under static loads with no need for fatigue cycling to grow the crack. This crack growth mechanism is very similar to stress corrosion cracking in high-strength steels [*31*]. This type of crack growth occurs under nominally elastic loading conditions and does not require large-scale creep as in pressure vessel steels [*32*]. When superalloys crack in this fashion, the crack path is very often intergranular. Laboratory tests covering a range of hold times and environments (including high vacuum) strongly suggest that both the presence of oxygen and localized creep at the intense plastic zone size at the tip of the crack is required to induce this type of crack growth [*21*,*27*]. It has also been documented that time-dependent crack growth is very sensitive to overpeaks at stresses above the hold time stress. Overpeaks on the order to 10 to 20% significantly retard the crack growth, and overpeaks on the order of 50% are sufficient to suppress this type of crack growth [*27*].

An example of the impact of time-dependent crack growth is shown in Fig. 2 [*28*]. Figure 2*a* shows the variation in crack growth rates of Rene'95 at 1200°F with hold times of 0, 4, 30, and 300 s. These tests were performed in K control tests in edge crack specimens. The specimens loaded from zero to maximum loads with ramps having 1.5 s in duration (the 0 second hold time cycle lasted 3 s). In this figure, the results are plotted in the typical logarithmic scales. Hold time cycles of 300 s resulted in an acceleration of crack growth rates of more than an order of magnitude relative to the 3 s cycle test. These data are replotted in Fig. 2*b* showing the crack growth rates as a function of hold time for constant values of K_{max}. In this figure, the crack growth rates are plotted on a linear scale and show that time-dependent crack growth rates are proportional to the hold time. This linear relationship between time-dependent crack growth rates and hold time has been observed for a variety of high-strength nickel base superalloys at elevated temperatures [*14*,*15*,*16*,*27*,*28*,*34*,*35*].

As a result, time-dependent crack growth has been modeled using the linear superposition model originally proposed by Wei and Landes [*33*] for use in stress corrosion cracking in high-strength steels. Since then, numerous workers [*14*,*15*,*16*,*27*,*28*,*34*,*35*] have successfully applied this model to time-dependent crack propagation in materials including nickel base superalloys. The linear superposition model can be expressed as:

$$\Delta a_{mission} = \Delta a_{cyclic} + \Delta a_{td} \tag{1}$$

The crack growth increment for cyclic growth (Δa_{cyclic}) is calculated using conventional fatigue crack growth rate data (da/dN). The time-dependent crack growth increment (Δa_{td}) is calculated using the following equation:

$$\Delta a_{td} = \int (da/dt)dt \tag{2}$$

where the static growth rates (da/dt) represent the time-dependent crack growth rates. In most formulations, it is assumed that the static crack growth rates can be described using a Paris law.

$$da/dt = AK^n \tag{3}$$

If it is further assumed that all the static crack growth occurs at constant K at the maximum load in the mission cycle, the value of (Δa_{td}) becomes

$$\Delta a_{td} = AK^n \Delta t \tag{4}$$

Substitution of Eq 4 into Eq 1 results in:

$$\Delta a_{mission} = (da/dN)_{cyclic} \cdot (1cycle) + AK^n \Delta t \quad (5)$$

This expression accurately represents the Rene'95 test data shown in Fig. 2*b*. The variation in crack growth rates with hold time in this data set will only be dependent on the hold time. The data represented at zero hold time in Fig. 2*b* will have the contribution of both the cyclic and time-dependent crack growth during the 3 s loading ramps.

A significant database has been established using surface crack specimens performed for a range of materials, temperatures, and hold times. These data have been used to create temperature-dependent crack growth (*da/dt*) models. The linear superposition model has been implemented into internal fracture mechanics life prediction codes. The lives of Rene'95 hold time crack growth tests have been predicted with this approach. Predictions of these tests are shown in Fig. 3 and show that the linear superposition method is capable of predicting time-dependent crack growth behavior well within a factor of 3. The test data rep-

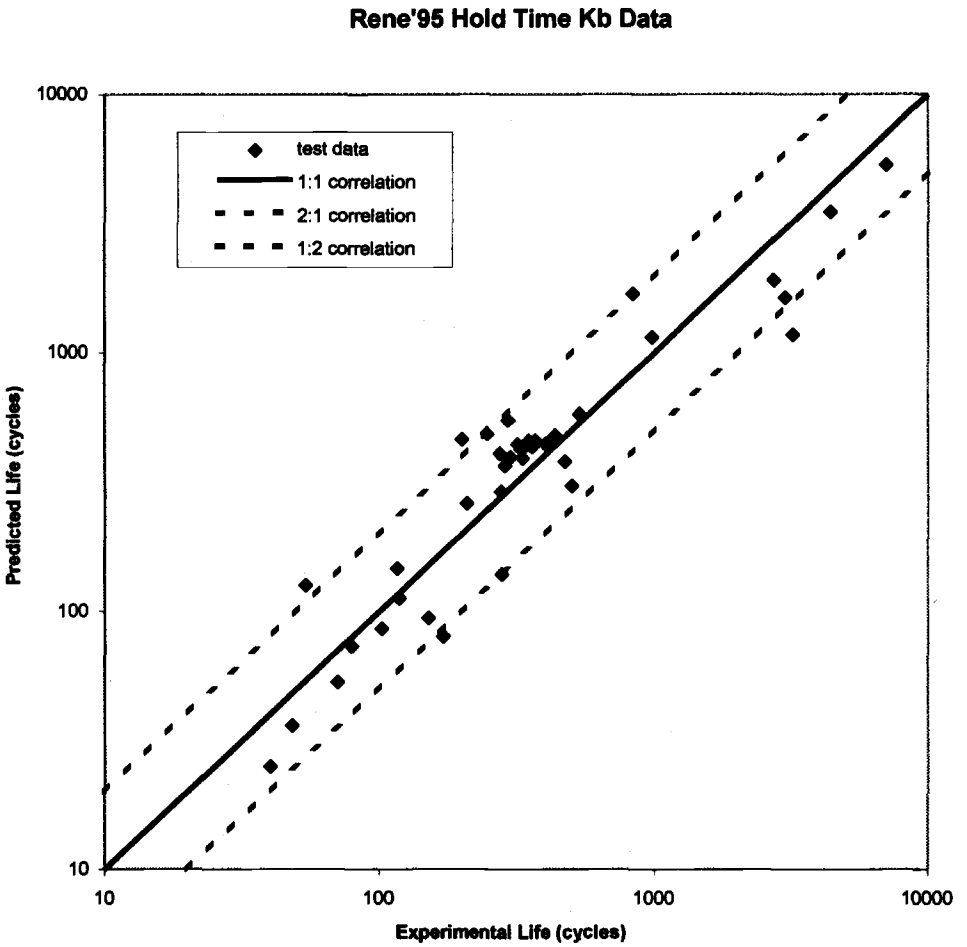


FIG. 3—*Comparison of predicted and observed crack propagation lives in Rene'95 surface crack tests specimens with hold times at the maximum load.*

resented in Fig. 3 cover a significant range in test temperature and hold time. Figure 4 shows the variation in predicted to experimental life ratio of these tests as a function of test temperature and hold time. These data show that there is very little bias in this life prediction method from these two key variables over the range of experimental variables evaluated experimentally (temperatures up to 1200°F and hold times up to 11 000 s).

The results shown in Figs. 3 and 4 could be critiqued as being misleading because these same tests were used to establish the da/dt crack growth models used to predict the lives of the specimens. As a separate validation of the linear superposition method, validation was performed using feature tests. The materials data and details of the linear superposition method were fixed prior to running these tests, so they are truly life prediction methodology validation tests. The feature specimen geometry used for this study was a double edge notch specimen shown schematically in Fig. 5. This specimen has a K_t of 1.76 and has a surface crack introduced in the center of the notch root on one side of the specimen. It was used for this evaluation because it has a stress gradient that simulates the stress gradients typical of turbine disk-turbine blade attachments. A series of hold time crack growth tests were performed with test cycles at various temperatures, stresses, and hold times. The predicted-to-observed life ratios of these tests are shown as a function of the elastic concentrated stress (net section stress $\times$ K_t) in Fig. 6. The linear superposition method was combined with K solutions in the presence of stress gradients that are standard within the aircraft engine business [*29,30*]. These results, similar to those in Fig. 4, show that the linear superposition method can be used to predict that the crack propagation lives of missions including the effects of hold time are well within a factor of 3.

Overpeak Retardation

A significant factor that can affect mission lives is the presence of overpeaks in missions such as those shown in Fig. 1. Such overpeaks cause significant retardation of crack growth rates for a relatively small amount of crack growth immediately after an overpeak. An example of this type of behavior is shown in Fig. 7*a* for a single overpeak test where a single overpeak is followed by repetitive cycles with smaller amplitudes. These repetitive cycles with smaller amplitudes are repeated until the crack grows through the retardation zone and the crack growth rates approach the steady state crack growth rate behavior. The value of K_{max} increases as the crack grows in a load control test. Figure 7*b* shows the measured crack growth rates in a 60% single load control overpeak test (K_{ol} is 1.60 times greater than K_{max}) in Rene'88DT. Crack growth rates are shown as a function of the crack advance after the overpeak cycle was performed. The solid line in this figure shows the predicted steady state crack growth response in the absence of overpeak retardation. The overload affected crack growth rate decreased to minimum shortly after the overpeak. For this particular test condition, the minimum crack growth rate is lower than the predicted steady state behavior (solid line) by a factor of five. The measured crack growth rates approach steady state behavior after the crack has grown approximately 0.02 in., which is a relatively small distance, but is large relative to the crack growth increment per cycle for small crack sizes. This is very significant, because repetitive overpeaks from engine thermal cycling can continue to significantly retard the crack growth.

The impact of overpeaks on time-dependent crack growth is even more significant. Previous work on Rene'95 and Alloy 718 [*27*] have shown that overpeaks on the order of 20 to 50% can completely suppress time-dependent crack growth for small cracks. The remainder of the paper will discuss the development of overpeak retardation methods that can be used to predict the response of aircraft engine components experiencing both cycle-dependent and time-dependent crack growth. A key requirement for such a model is that it can be used

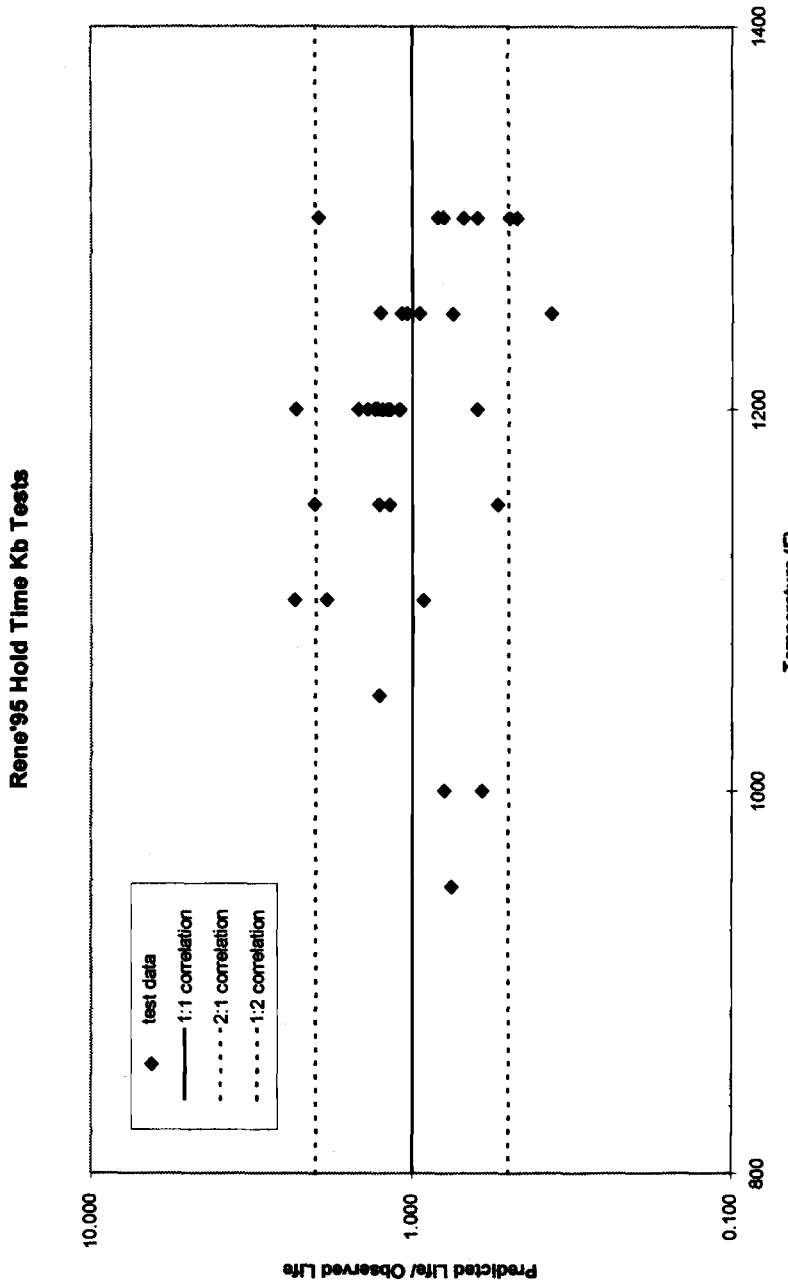


FIG. 4—*Variation in the predicted to observed lives in Rene'95 surface crack tests specimens with hold times at the maximum load as a function of* (a) *temperature and* (b) *hold time.*

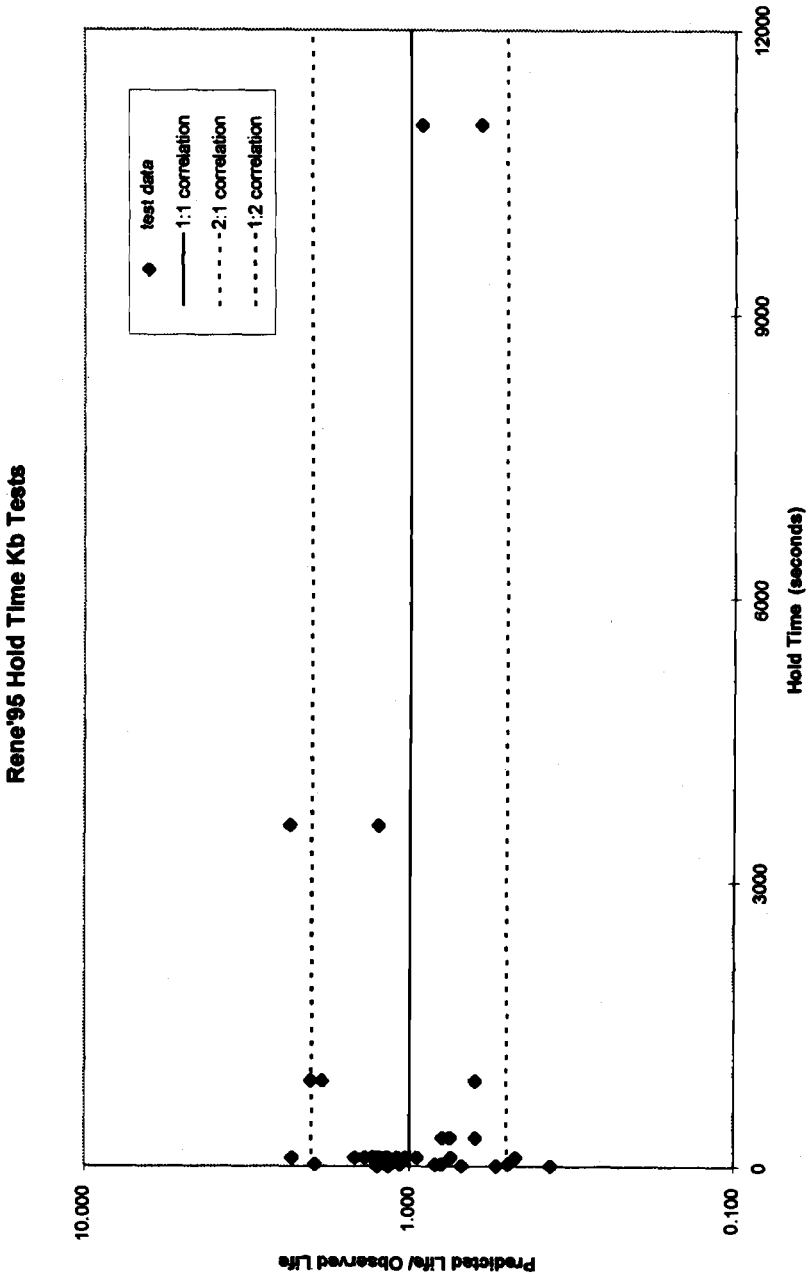


FIG. 4—*Continued.*

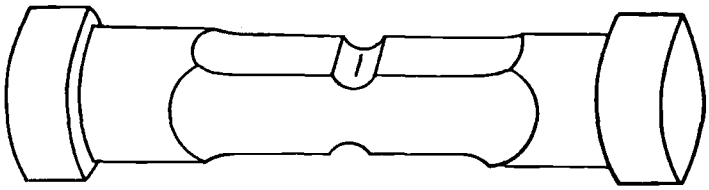


FIG. 5—*Schematic drawing of double edge notch specimen simulating the stress gradients in disk attachment regions.*

on very complex missions and with mixing of mission types. It is not unusual that missions with the largest overpeaks are experienced relatively infrequently. The retardation model should take this type of infrequent overpeak into consideration, but also not permit the overestimation of lives due to such an event. This will be discussed in more detail during the discussion portion of the paper.

The form of the model used to predict overpeak retardation was originally proposed by Willenborg [*36*]. He presented his model based on a reduced stress, but Gallagher and co-workers [*37,38*] later represented it on a reduced K basis. The reduced K approach has two very appealing characteristics that are consistent with the methods currently used to predict crack growth [*30*]:

1. The retardation model is based on calculating a reduced K (K_{red}) that can be applied to both the maximum and minimum K in a cycle. In this way ΔK is not changed, but

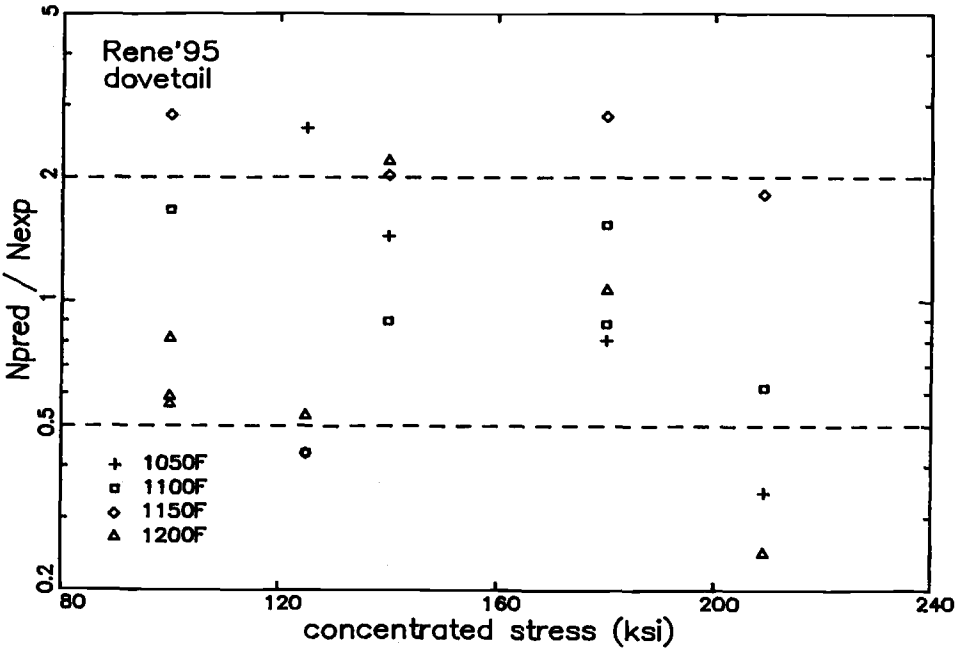
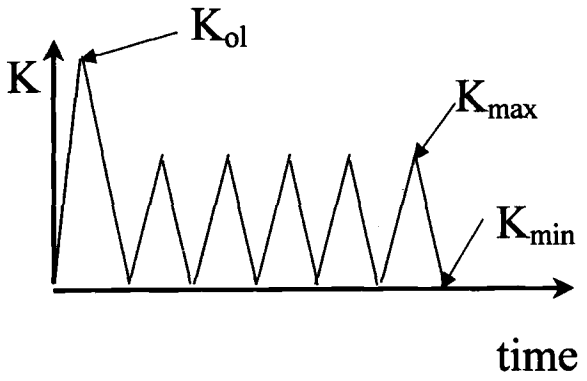


FIG. 6—*Variation in the predicted to observed lives in Rene'95 surface crack double edge notch specimen tests with hold times at the maximum load as a function of concentrated elastic stress.*



(a)

FIG. 7—*The results of a single overpeak retardation cycle* (a) *on the cyclic crack growth rates* (b) *measured in Rene'88DT.*

there can be significant changes to the R ratio (K_{min}/K_{max}) that can alter crack growth rates. In this way the mean stress (or K) models and data already in existence can be used to predict the crack growth behavior. For the predictions shown later in the paper, the dual Walker exponent method [*30*,*39*,*40*] for the cyclic crack growth and the reduction in K was used directly in the time-dependent model.

2. The retardation model alters the value of the reduced K as it grows through the plastic zone sizes. This is shown schematically in Fig. 8. The value of the reduced K becomes zero when the current plastic zone reaches the extent of the overload plastic zone due to either increases in load (higher K and plastic zone size) and/or growth of the crack through the overload plastic zone. As will be demonstrated later, the size of these zones can be adjusted based on experimental measurements like those in Fig. 7*b*.

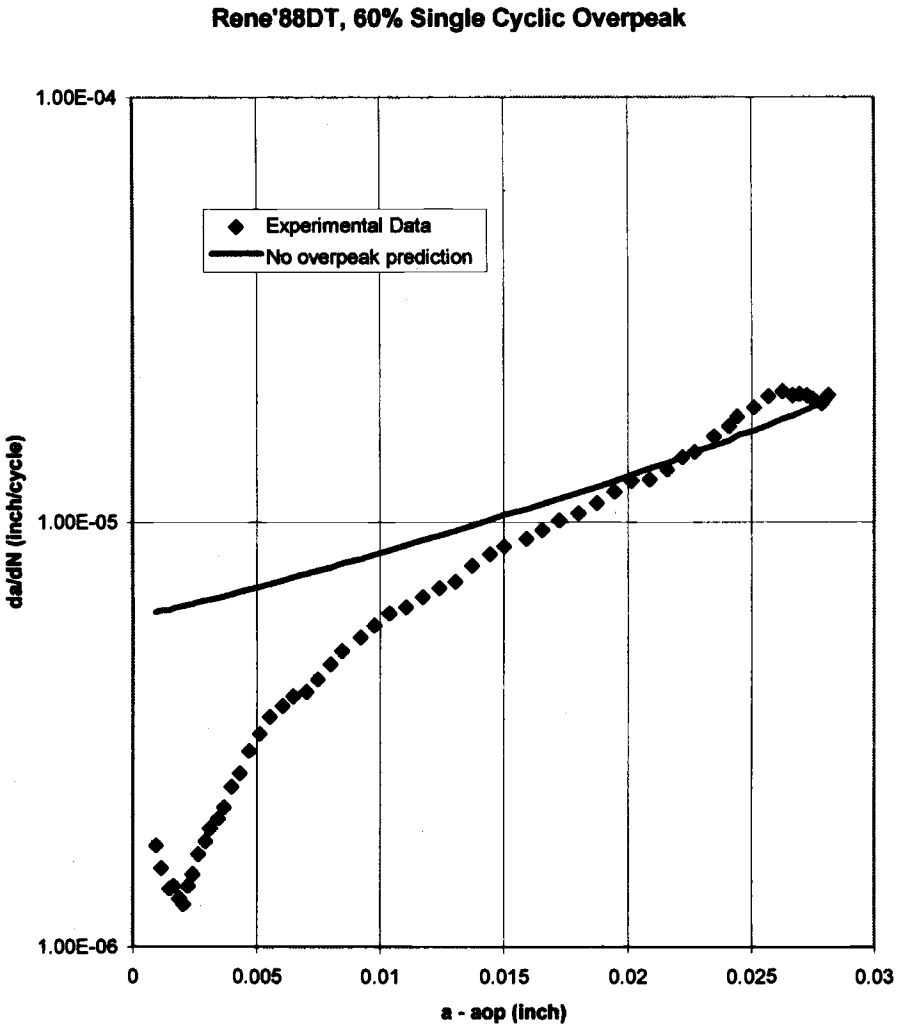
The reduced K Willenborg model [*37*,*38*] is described by the following equation:

$$K_{red} = K_{max}\left[\sqrt{\frac{r_{ol} - \Delta}{r_{max}}} - 1\right]\Phi \tag{6}$$

where

K_{red} = value by which non-related K values are reduced,
Φ = Willenborg retardation scaling constant,
K_{ol} = value of K at the overload (see Fig. 7*a*),
K_{max} = current value of K_{max} (see Fig. 7*a*),
Δ = increment of crack growth since the overpeak occurred,
r_{ol} = overpeak plastic zone size, and
r_{max} = current plastic zone size.

In the initial Willenborg formulation [*36*], no scaling was used ($\Phi = 1$). This model uses the Irwin plastic zone equations:



(b)

FIG. 7—*Continued.*

$$r_{ol} = \left(\frac{1}{2\pi}\right)\left(\frac{K_{ol}}{\sigma_{ys}^{ol}}\right)^2 \tag{7}$$

$$r_{\max} = \left(\frac{1}{2\pi}\right)\left(\frac{K_{\max}}{\sigma_{ys}^{\max}}\right)^2 \tag{8}$$

Note that the yield strength (σ_{ys}) in these equations may have different values because the temperature of the current mission point may be different from that at which the overpeak

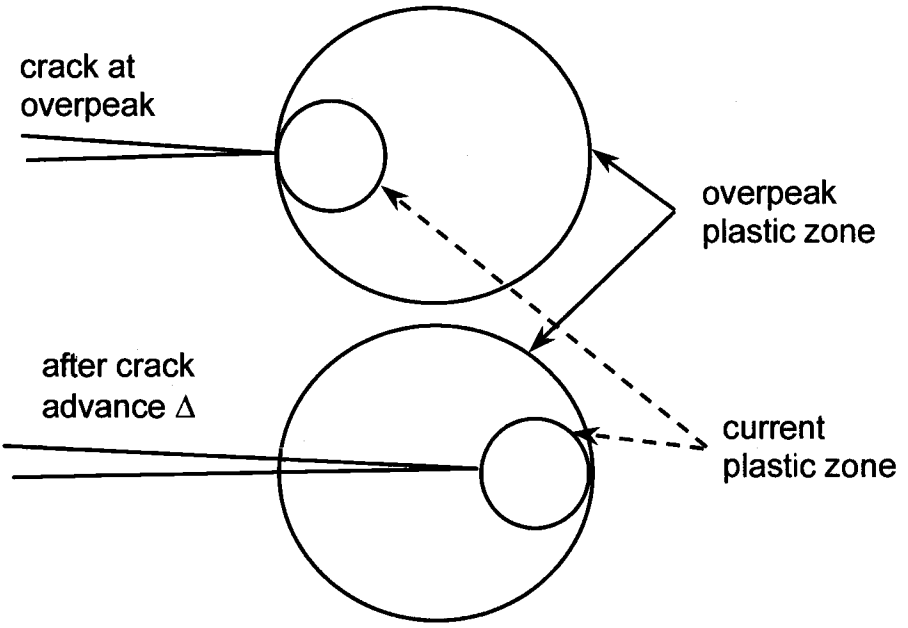


FIG. 8—*Concept of Willenborg retardation model.*

occurred. The key features of this model are that immediately after the overpeak ($\Delta = 0$), $K_{red} = K_{ol} - K_{max}$ and the extent of the overload zone (value of Δ when $K_{red} = 0$) equals $r_{ol} - r_{max}$.

The form of this relationship was modified based on the experimental observation of the crack growth data measured as cracks grew through the overload zone and requirements to calibrate the model based on experimental data:

1. There appears to be a gradual reduction in the crack growth rate as shown in Fig. 7*b* and not an instantaneous one as predicted by the Willenborg equation; at $\Delta = 0$, $K_{red} = \Phi (K_{ol} - K_{max})$. The minimum in crack growth rate is defined to occur at $\chi\, r_{ol}$ (see Fig. 9)
2. The extent of the overload plastic zone in not always well predicted by the Irwin equations, so a coefficient λ was introduced before the plastic zone size terms in the denominator. The extent of the overload zone now becomes $\lambda (r_{ol} - r_{max})$.
3. The measured crack growth was not well predicted by the Willenborg functional form. Evaluation showed that this relationship more accurately predicted the measured crack growth rate response when the dimensional term was altered and raised to the exponent ρ.

The resulting modified Willenborg equation is:

$$K_{red} = (K_{ol} - K_{max}) \left[1.0 - \left(\frac{\Delta}{\lambda r_{ol} - \lambda r_{max}} \right) \right]^{\rho} \Phi \quad \text{for } \chi r_{ol} \leq \Delta + \lambda r_{max} \leq \lambda r_{ol} \qquad (9)$$

In the region where Δ varies between zero and $\chi\, r_{ol}$, a relationship for K_{red} must be estab-

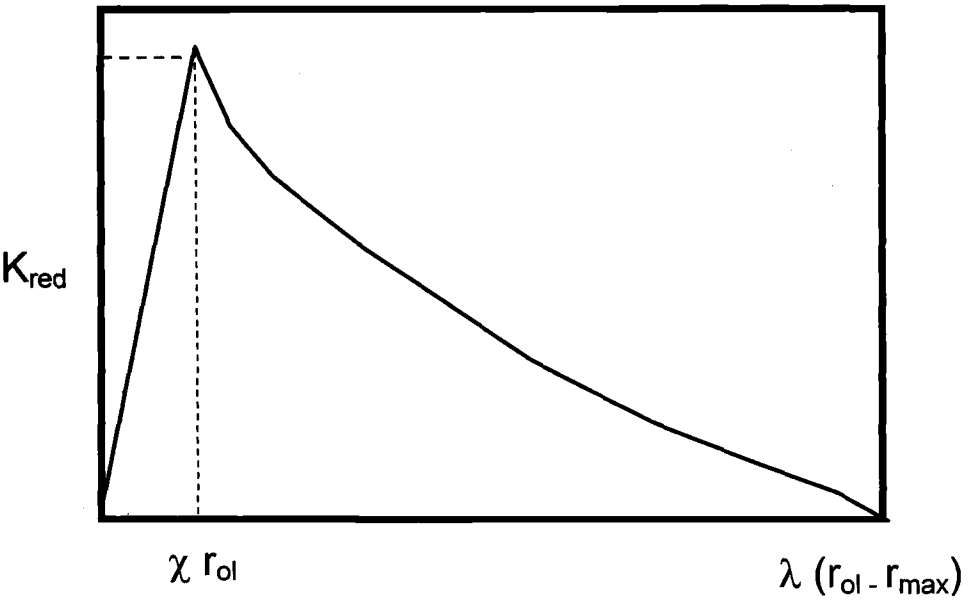


FIG. 9—*Physical significance of constants in modified Willenborg retardation model.*

lished. Based on the results of a single overpeak test (Fig. 7), one would expect that K_{red} would increase with Δ for values of Δ between zero and $\chi\ r_{ol}$ (solid line in Fig. 9). If this type of model were to be used, the value of K_{red} would be set to zero every time that an overpeak occurred. When this is applied to repetitive missions with little crack growth between overpeaks, there would be little influence of retardation on calculated lives. This is not the observed behavior. Another approach would be to maintain the current value of K_{red} at its current value and not set back to zero. Significant effort was spent attempting to find a computationally robust method to treat this region of the K_{red} curve for an arbitrary mission that might be provided in a design environment. Previous forms of models of this type [*27*] were shown to lack robustness. The resolution of this issue was to set the value of K_{red} to the value of K_{red} at $\chi\ r_{ol}$. This is shown schematically in Fig. 9 by the horizontal line for values of Δ between zero and $\chi\ r_{ol}$. Evaluation of typical missions showed that this was a good engineering approximation because overpeaks were often reset within this zone after very small increments of crack growth. The value of K_{red} builds up very quickly to values close to the maximum value of K_{red} (at $\chi\ r_{ol}$).

This modified Willenborg model has four adjustable constants (Φ, λ, χ, and ρ) that can be calibrated using data from single overpeak tests as shown schematically in Fig. 10. The left side of Fig. 10 includes the data previously shown in Fig. 7. The value of χ is determined from the crack advance at the minimum in crack growth rate. The value of λ is set on the value of crack advance where measured crack growth rate returns to the nonretarded crack growth rate. The values of Φ and ρ are determined by analysis of the crack growth data between $\chi\ r_{ol}$ and $\lambda(r_{ol} - r_{max})$. The modified Willenborg equation can be transformed to the following expression:

$$K_{red}/(K_{ol} - K_{max}) = \Phi \left[1.0 - \left(\frac{\Delta}{\lambda r_{ol} - \lambda r_{max}} \right) \right]^{\rho} \tag{10}$$

The value of K_{red} can be determined from the measured crack growth rate and the materials

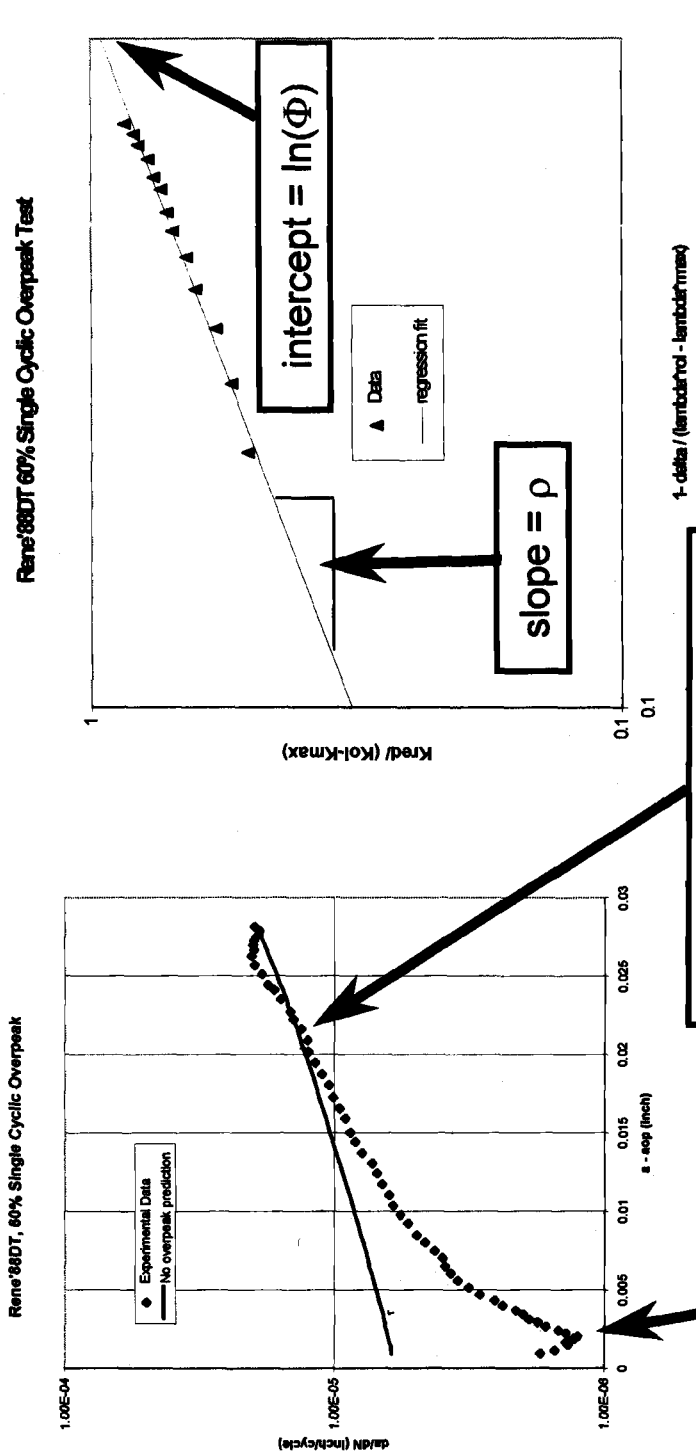


FIG. 10—*Method of determination of material constants in modified Willenborg retardation model.*

crack growth rate data including the Walker mean K model exponent m. The Walker model in the absence of retardation can be expressed as:

$$K_{eff} = K_{\max} (1 - R)^m = K_{max} (1 - K_{\min}/K_{\max})^n \tag{11}$$

In the overpeak retardation zone, each of the $K_{\min}$ and $K_{\max}$ terms must be reduced by the value of K_{red}. This results in the following expression:

$$K_{eff} = (K_{\max} - K_{red})\{1 - (K_{\min} - K_{red})/(K_{\max} - K_{red})\}^m \tag{12}$$

The value of K_{eff} is determined from the material's crack growth rate curve determined in the absence of retardation. Knowing the values of K_{eff}, $K_{\min}$, $K_{\max}$, and m, the value of K_{red} for any given crack growth data point can be calculated. Knowing all these values, the left side of the modified Willenborg equation can be evaluated. The values of the quantity $\{1 - \Delta/[\lambda(r_{ol} - r_{\max})]\}$ can be calculated knowing the crack advance (Δ) and the values of r_{ol} and $r_{\max}$ (from K_{ol} and $K_{\max}$). The values of λ are determined from the single overpeak test as shown in Fig. 7. The right side of Fig. 10 shows $K_{red}/(K_{ol} - K_{\max})$ plotted as a function of $\{1 - \Delta/[\lambda(r_{ol} - r_{\max})]\}$ on logarithmic axes. In this representation, the slope of the data represents the value of ρ and the intercept represents the value of Φ. This is shown on the right side of Fig. 10.

This process was used to analyze several single overpeak segments, and several difficulties were encountered. It was very difficult to reproducibly determine the values of λ and χ due to the variability in crack growth rates and the lack of precision in determining the minimum and asymptotic crack growth behavior within the retardation zone. In addition, the values of K_{red} when the crack growth rates were approaching the nonretarded crack growth rates need to be excluded from the regression analysis because of the small value and large variability in K_{red}. In order to better understand the relative importance of the modified Willenborg retardation constants, an analytical design of experiments (DoE) was performed. The DoE analytically evaluated surface cracks combining a variety of overpeaks (0 to 60%) and hold times (0 to 5 h) that bounded a significant fraction of the turbine engine mission characteristics. The values of the four retardation constants were permitted to vary outside the ranges that had been determined from the single overpeak tests. Analysis of this analytical DoE concluded that the variation of Φ overwhelmed the influence the other three variables had on predicted lives. The individual impact of those three variables (λ, χ, and ρ) were generally less than 10% in predicted lives. Collectively, the impact of these three variables slightly exceeded 20% in life, but these larger variations were systematic. These types of variations will be minimized by selecting the constants from the experimental data. The results of this DoE strongly suggest that small errors in selection of the values of λ, χ, and ρ will not significantly contribute to inaccurate life predictions. For the materials and temperatures studied in this investigation, the values of χ and λ were close to 0.4 and 5, respectively, and the values of ρ varied between 1.9 and 5.6 and were highly temperature dependent.

On the other hand, it also showed that it is very important to accurately determine the value of Φ. Based on this analysis, the values of λ, χ, and ρ are determined from single overpeak tests as shown in Fig. 10. The values of Φ for cyclic (Φ_{cyclic}) and time-dependent (Φ_{td}) crack growth are determined from simple missions laboratory tests with repetitive overpeaks.

Application of this model to missions with repetitive overpeaks also requires a criteria for defining when a new overpeak has occurred. The criteria selected was that a new overpeak

is defined when the extent of the overpeak plastic zone exceeds the current value, i.e., when $\lambda\ r_{max}$ exceeds $\lambda\ r_{ol} + \Delta$.

This modified Willenborg model was successfully calibrated for a range of materials, temperatures, and mission contents. The method was validated for Rene'95 using the double edge notch specimen geometry shown in Fig. 5 cycled with simple hold time missions at 1100 and 1200°F. The overpeak cycles were comprised of a 15 s ramp to maximum overpeak load, followed by unloading to the hold time load in 15 s, holding at that load for 90 s, followed by a 15 s unload to zero load. These tests were performed for a range of stress and overpeak levels. After completion of the tests, a fracture mechanics analysis of each test was performed in three different ways:

1. *Cyclic analysis.* This process considered only the cyclic crack growth and ignored any influence of either the hold time or the retardation effect. For this mission, the only fatigue cycle would be the loading between zero and the overpeak load.
2. *Cyclic + static analysis.* This process modeled both the cyclic and time-dependent crack growth, but ignored any potential benefit from overpeak retardation. The time-dependent analysis included any time-dependent crack growth that would be predicted to occur during the loading and unloading ramps.
3. *Cyclic + static + retardation.* This process modeled the cyclic, time-dependent, and retardation effects.

Figure 11 schematically illustrates the values of K used in these predictions. The same K values would be used for the maximum load (overpeak) mission point. For the cyclic analysis, the damaging effects of hold time will not be considered. In the case of the retardation

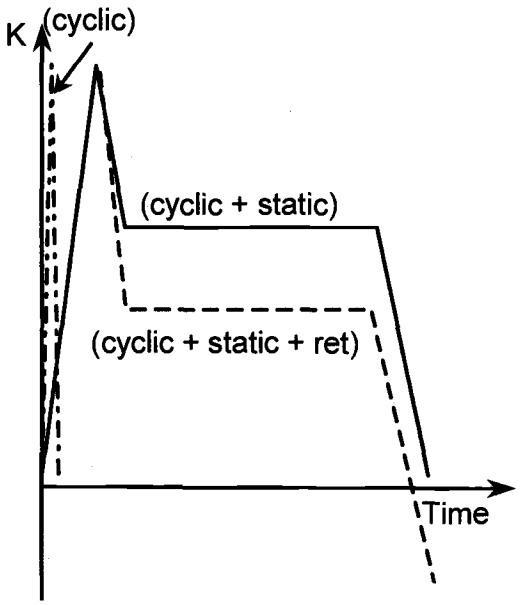


FIG. 11—*Schematic representation of an overpeak hold time cycle indicating the impact of time dependent and retardation models on the values of* K *used in the life prediction.*

model, the values of K for both ramps and the hold time will be reduced with the exception of the maximum load case ($K_{red} = 0$ because $K_{max} = K_{ol}$).

Figure 12 compares the experimentally measured crack propagation lives with those predicted by each of these three methods, so for each specimen there are three predictions for a given experimental result. Figure 12*a* shows the predictions for the 1100°F tests and Fig. 12*b* shows the predictions for the 1200°F tests. In both cases, the cyclic predictions (diamonds) are more than twice the observed lives. When hold time is considered without the retardation benefit, the predicted lives are significantly shorter than the observed lives. Comparison between Figs. 12*a* and 12*b* illustrates the larger influence of time-dependent crack growth at the higher temperatures. When the modified Willenborg retardation model is included in the analysis, the predicted lives are close to being within a factor of two of the experimental data, similar to those previously shown in Figs. 3 and 6. These results illustrate that for conditions where material is cycled with complex missions and also sensitive to time-dependent crack growth that it is important to include both the beneficial impact of overpeak retardation along with the damaging effects of hold time crack growth in order to accurately estimate crack propagation lives.

Figure 13 shows a comparison of the predicted and experimental lives for a significant number of Rene'95 and Rene'88DT tests. The predictions shown in this figure include cyclic and time-dependent crack growth along with the benefits of crack growth retardation. The tests labeled as cyclic were conducted under conditions with a very small to no component of time-dependent crack growth. The hold time mission tests are those previously shown in Fig. 12. The thermal mechanical fatigue (TMF) tests are similar to the isothermal Rene'95 overpeak-hold time mission cycles shown in Fig. 11 except that the overpeak occurred at a much lower temperature. This type of a cycle is typical for gas turbine disk applications. The results shown in Fig. 13 show that inclusion of retardation results in the accurate prediction of crack propagation during mission cycling.

Discussion

The modified Willenborg retardation model described in this paper was developed to a large extent based on the requirements of the design system described earlier. A key attribute of the model is its applicability to mix missions with significantly different overpeaks. These differences often occur due to variables such as the temperature at takeoff, which has a significant influence on the maximum stress during the early of a mission. For example, surveys of aircraft usage may indicate that a hot day takeoff occurs in 17% of the flights (mission mix fraction = 0.17). This information needs to be combined with all the other information including the length of the flight, which can significantly influence the hold time. One way to treat mission mixing is to increment the crack by the calculated increment times the mission mix fraction. For the case of hot day takeoff, this would be 17% of the calculated crack growth increment. This process accurately treats all the parts of the mission that do not have any history dependence (cyclic and time-dependent crack growth). This is not the case for retardation.

The application of the modified Willenborg model to the mixing of missions could result in providing excessive benefit from a single very low fraction mission with a high overpeak to the remainder of the missions. This possibility was rectified by multiplying the extent of the retardation zones ($\chi\ r_{ol}$ and $\lambda\ (r_{ol} - r_{max})$) by the mission mix fraction. This process has no influence of the initial values of K_{red}, but changes the range of crack growth increments over which it occurs. The ability of the modified Willenborg model to treat mixing of missions appears to be a distinct advantage relative to closure-based models where there is little to no control over the extent of the retardation zone.

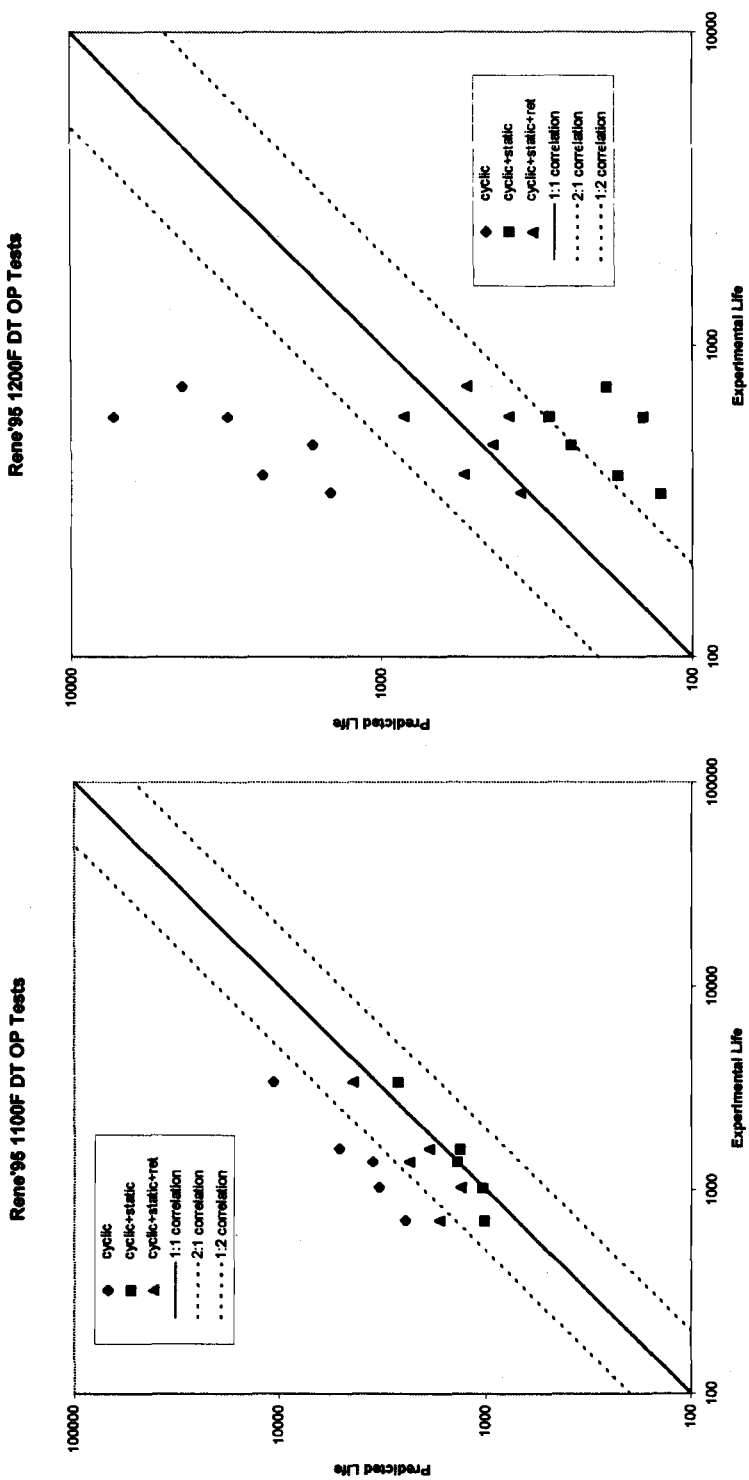


FIG. 12—*Comparison of predicted and observed lives in double edge notch feature crack growth tests under the combined influence of overpeaks and hold times.*

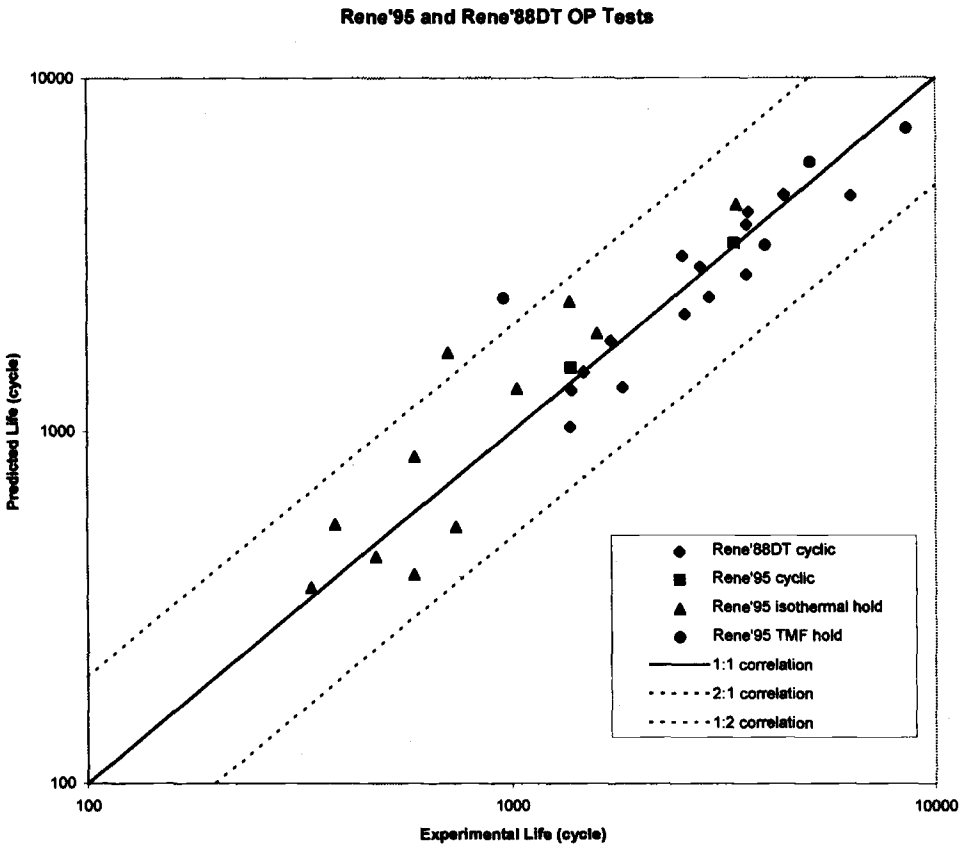


FIG. 13—*Comparison of predicted and observed crack propagation lives in Rene'95 and Rene'88DT surface crack specimens with overpeak test cycles.*

Conclusions

Time-dependent crack growth and overpeak retardation are very complex phenomena. The models described in this paper were developed to be both accurate and have the ability to be used by engineers in a design environment. The linear superposition of cyclic and static damage was extended from previous work on high-strength steels. Laboratory tests were performed to show that this type of a model can be used to accurately predict lives over a wide range of temperatures, stresses, and hold times. The method was validated with feature tests simulative of stress gradient in gas turbine components. The modified Willenborg retardation model was developed based on observations made of the crack growth rates through overpeak retardation zones. Starting with this concept the model was altered to provide computational robustness and to be able to accurately analyze the mixing of missions with much different overpeak and overall mission content. The accuracy of this model has been demonstrated through the evaluation of laboratory crack growth tests including significant variation in mission content, hold times, thermal mechanical fatigue cycles, and stress gradients.

Acknowledgments

The authors would like to acknowledge GE Aircraft Engines for supporting much of the work presented in this paper. We are indebted to Paul Domas, Sue Gilbert, Barney Lawless, and Dave Miller for the help in conducting much of this work. Marsha Tufft rigorously performed the analytical retardation DoE. The authors would also like to acknowledge helpful discussions with Jack Telesman and Tim Gabb of NASA Glenn Research Center.

References

[1] King, T. T., Cowie, W. D., and Reimann, W. H., "Damage Tolerant Design Concepts for Military Engines," NATO AGARD Structures and Materials Panel Specialists' Meeting on Damage Tolerance Concepts for Critical Engine Components, San Antonio, TX, April 1985.
[2] "Engine Structural Integrity Program (ENSIP)," MIL-STD-1783 (USAF), 30 Nov. 1984.
[3] Domas, P. A. and Roth, P. G., "Probabilities Life Prediction Methods—Meeting the Challenges for Practical Application," *Fatigue '96, Proceedings of the Sixth International Fatigue Congress,* Berlin, Germany, 6–10 May 1996, pp. 1251–1262.
[4] Chang, D. R., Krueger, D. D., and Sprague, R. A., *Superalloys 1984,* The Metallurgical Society of the American Institute if Mining, Metallurgical, and Petroleum Engineers, Warrendale, PA, 1984, pp. 245–273.
[5] Kissinger, R. D. and Huron, E., *Superalloys 1988,* The Metallurgical Society of the American Institute if Mining, Metallurgical, and Petroleum Engineers, Warrendale, PA, 1984.
[6] Clavel, M. and Pineau, A., *Metallurgical Transactions,* Vol. 9A, 1978, pp. 471–480.
[7] Pelloux, R. M. and Huang, J. S., *Creep-Fatigue-Environment-Interactions,* Pelloux, R. M. and Stoloff, N. S., Eds., TMS-AIME, 1980, p. 151.
[8] Pedron, J. P. and Pineau, A., *Materials Science and Engineering,* Vol. 56, 1982, pp. 143–156.
[9] Bain, K. R. and Pelloux, R. M., *Metallurgical Transactions,* Vol. 15A, 1984, pp. 381–388.
[10] Dibone, A. and Pineau, A., *Fatigue and Fracture of Engineering Materials and Structures,* Vol. 10, 1987, pp. 141–151.
[11] Sadananda, K. and Shahinian, S., *Metallurgical Transactions,* Vol. 8A, 1977, pp. 439–449.
[12] Sadananda, K. and Shahinian, S., *Engineering Aspects of Creep,* Vol. 2, 1980, p. 1.
[13] Sadananda, K. and Shahinian, S., *Metals Technology,* 1982, pp. 18–25.
[14] Larsen, J. M. and Nicholas, T., *Engineering Fracture Mechanics,* Vol. 22, 1985, pp. 713–730.
[15] Nicholas, T., Weerasooriya, T., and Ashbaugh, N. E., *Fracture Mechanics: Sixteenth Volume, ASTM STP 905,* ASTM, 1986, Philadelphia, PA, pp. 169–180.
[16] Nicholas, T., Weerasooriya, T., and Ashbaugh, N. E., *Fracture Mechanics: Sixteenth Volume, ASTM STP 905,* ASTM, 1986, Philadelphia, PA, pp. 155–168.
[17] Solomon, H. D. and Coffin, Jr., L. F., *ASTM STP 520,* ASTM, 1973, pp. 112–122.
[18] Solomon, H. D., *Metallurgical Transactions,* Vol. 4, 1973, pp. 341–347.
[19] Floreen, S., *Metallurgical Transactions,* Vol. 6A, 1975, pp. 1741–1749.
[20] Coles, A., Johnson, R. E., and Popp, H. G., *Journal of Engineering Materials Technology,* Vol. 98, 1976, pp. 305–315.
[21] Floreen, S. and Kane, R. H., *Metallurgical Transactions,* Vol. 10A, 1979, pp. 1745–1751.
[22] James, L. A. and Mills, W. J., *Engineering Fracture Mechanics,* Vol. 22, 1985, pp. 787–818.
[23] Cowles, B. A., Sims, D. L., and Warren, J. R., "Evolution of the Cyclic Behavior of Aircraft Turbine Disk Alloys," NASA-CR-1594039, October 1978.
[24] Utah, D. A., "Crack Modeling in an Advance Powder Metallurgy Alloy," AFWAL-TR-80-4098, Air Force Materials Laboratory, Wright-Patterson Air Force Base, Ohio 45433, July 1981.
[25] Donath, R. C., "Crack Growth Behavior of Alloy IN100 Under Sustained Loads at 732C (1350F)," AFWAL-TR-80-4131, Air Force Materials Laboratory, Wright-Patterson Air Force Base, OH 45433, April 1981.
[26] Larsen, J. M. and Nicholas, T., *ASTM STP 791,* ASTM, Philadelphia, PA, 1983, pp. II-536–II-552.
[27] VanStone, R. H., Gooden, O. C., and Krueger, D. D., "Advanced Cumulative Damage Modeling," AFWAL-TR-88-4146, Air Force Materials Laboratory, Wright-Patterson Air Force Base, OH 45433, September 1988.
[28] VanStone, R. H., "Comparison of Interpolation and Superposition Models to Predict Time Dependent Crack Growth in Rene '95," *Elevated Temperature Crack Growth,* ASME, MD-Vol. 18, 1990, pp. 53–68.

[29] Cowles, B. A., "Life Prediction in High Temperature Environments: Overview of a Current Gas Turbine Engine Approach," *Materials Science and Engineering,* Vol. A103, 1988, pp. 63–69.
[30] VanStone, R. H., "Residual Life Prediction Method for Gas Turbine Components," *Materials Science and Engineering,* Vol. A103, 1988, pp. 49–61.
[31] Gangloff, R. P., "Crack Tip Modeling of Hydrogen Environment Embrittlement: Application to Fracture Mechanics Life Prediction," *Materials Science and Engineering,* Vol. A103, 1988, pp. 157–166.
[32] Saxena, A., "Creep Crack Growth under Transient Conditions," *Materials Science and Engineering,* Vol. A103, 1988, pp. 125–129.
[33] Wei, R. P. and Landes, J. D., *Materials Research Standards,* Vol. 9, 1969, pp. 25–46.
[34] Gallagher, J. P. and Wei, R. P., *Corrosion Fatigue,* NACE-2, NACE, 1972, pp. 409–423.
[35] Solomon, H. D., *Corrosion Fatigue,* NACE-2, NACE, 1972, pp. 420–421.
[36] Willenborg, J., Engle, R., and Wood, H., "A Crack Growth Retardation Model Using an Effective Stress Concept," AFFDT-TR-71-1-FBR, Wright-Patterson Air Force Base, Ohio, January 1971.
[37] Petrak, G. J. and Gallagher, J. P., "Prediction for the Effect of Yield Strength in Fatigue Crack Growth Retardation in HP 9Ni-4Co-30C Steel," *Transactions of ASME, Journal of Engineering Materials and Technology,* Vol. 97, Series H, No. 3, July 1975, pp. 206–213.
[38] Gallagher, J. P. and Stalnaker, H. D., "Predicting Flight-by-Flight Fatigue Crack Growth Rates," *AIAA Journal of Aircraft,* Vol. 12, No. 9, September 1975, pp. 699–705.
[39] VanStone, R. H., Gilbert, M. S., Gooden, O. C., and Laflen, J. H., *Fracture Mechanics: Nineteenth Symposium ASTM STP 969,* ASTM, Philadelphia, PA, 1988, pp. 637–656.
[40] VanStone, R. H. and Krueger, D. D., *Fracture Mechanics: Nineteenth Symposium, ASTM STP 969,* ASTM, Philadelphia, PA, 1988, pp. 883–906.

Monty A. Moshier,[1] *Theodore Nicholas,*[1] *and Ben M. Hillberry*[2]

The Effect of Low Cycle Fatigue Cracks and Loading History on High Cycle Fatigue Threshold

REFERENCE: Moshier, M. A., Nicholas, T., and Hillberry, B. M., **"The Effect of Low Cycle Fatigue Cracks and Loading History on High Cycle Fatigue Threshold,"** *Fatigue and Fracture Mechanics: 31st Volume, ASTM STP 1389*, G. R. Halford and J. P. Gallagher, Eds., American Society for Testing and Materials, West Conshohocken, PA, 2000, pp. 427–444.

ABSTRACT: The high cycle fatigue (HCF) resistance of Ti-6A1-4V for gas turbine engine applications is studied when the material is first subjected to low cycle fatigue (LCF). The high cycle fatigue (HCF) threshold is determined after small LCF surface cracks are formed in notch tension specimens. LCF loading at two stress ratios, $R = 0.1$ and $R = -1.0$, is used to initiate the LCF cracks, which are detected using direct current potential difference (DCPD). The surface crack sizes are measured under load using a static loading fixture and a scanning electron microscope (SEM). In addition to the SEM surface measurements, heat tinting is used to mark the crack profiles before HCF testing so that fractography can be used after failure to measure the 2D crack geometry. The LCF surface-cracked specimens are tested at room temperature in lab air at 600 Hz using a step-loading procedure at two stress ratios, $R = 0.1$ and $R = 0.5$. The LCF loading history is found to affect the HCF threshold compared to what is predicted from long crack threshold values obtained from other crack geometries. Variations in HCF crack growth thresholds obtained on specimens with LCF crack sizes from 25 to 175 μm are attributed to overload and underload effects from the LCF precracking.

KEYWORDS: high cycle fatigue, threshold, stress intensity, overloads, loading history, small cracks, Ti-6A1-4V, fracture mechanics

High cycle fatigue (HCF) is a major concern for the USAF because it has accounted for 55% of the USAF's engine-related fighter aircraft failures that have resulted in $1 million in damage or loss of the aircraft [*1*]. Low cycle fatigue (LCF), on the other hand, has been successfully addressed using a damage-tolerant approach. For LCF, the Air Force's Engine Structural Integrity Program (ENSIP) requires critical engine components to demonstrate sufficient damage tolerance in the presence of inspectable flaw sizes [*2*]. The remaining LCF component life is based on the crack propagation of the inspectable flaw size. However, HCF introduces fatigue at high mean loads and frequencies upwards of 1 KHz. The high frequency and current size limitation of non-destructive inspection capabilities prohibit the direct application of a damage-tolerant approach for HCF [*3*]. Additionally, due to the lack of detailed information on the HCF capability of materials and dynamic response and vibratory loading of components, particularly in the presence of initial or in-service damage, anything but a highly empirical approach seems impractical at this time [*3*].

[1] Air Force Research Laboratory, Materials and Manufacturing Directorate (AFRL/MLLN), Wright-Patterson AFB, OH 45433-7817.
[2] Purdue University, School of Mechanical Engineering, West Lafayette, IN 47907.

Copyright© 2000 by ASTM International www.astm.org

Many of the HCF failures are the result of in-service damage due to fretting, foreign object damage (FOD), LCF, or others [*4*]. In the presence of damage and due to the large numbers of cycles applied in short periods of time, the idea of a threshold below which HCF does not occur is necessary. Damage tolerance for HCF when initial cracks are present would therefore require the determination of a crack growth threshold applicable to the conditions under which the crack was formed. In particular, cracks formed under LCF at notches or other stress concentrations pose one problem of practical interest. LCF damage can be associated with the major/minor cycle interaction as well as naturally initiating cracks due to the LCF loading. This study investigates the high cycle fatigue (HCF) threshold of a typical fan blade material, Ti-6A1-4V, when naturally initiated fatigue cracks, which have been created using different LCF loading sequences, are present.

Background

LCF can often result in the formation of cracks which will alter the high cycle fatigue (HCF) resistance of a material. In the presence of cracks, the criterion for further propagation of the crack is governed by fracture mechanics (crack growth threshold). On the other hand, the criterion for crack nucleation and subsequent propagation in an uncracked body is governed by stress (endurance limit). As cracks become smaller and smaller, it becomes unclear as to which criterion should govern.

Studies investigating the interaction of naturally initiated LCF cracks and HCF threshold have not been conducted. However, there have been studies that address major/minor cycle interaction, lower-bound HCF threshold, and crack growth of both long cracks and artificially induced small cracks including history effects. Akita et al. [*5*] demonstrated in Ti-6A1-4V with C(T) specimens that repeated loading blocks containing a single overload caused the da/dN crack growth curve to shift down, producing an increase in the threshold level.

Traditional methods for managing high cycle fatigue rely heavily on the Goodman diagram approach. The Goodman diagram approach requires smooth bar fatigue data over a range of stresses and stress ratios in order to define a material's fatigue endurance limit. The endurance limit, defined as the stress range below which failure doesn't occur within a specified lifetime, is then used to specify allowable design stresses. The shortcoming of this approach is that it does not account for any type of defect such as that caused by FOD, fretting fatigue, or cracking due to LCF or combined loading.

Threshold is a fracture mechanics concept for determining a stress level below which a crack of a given size will not grow. Threshold can be used to determine an allowable stress as a function of crack size and is seen as a viable alternative design parameter to the allowable design stress as determined from the Goodman diagram approach. As with the Goodman diagram approach, threshold is material specific and must be determined under a variety of conditions. The experimental method by which a threshold is determined, and the applicability of that value of threshold to different methods of creating a crack, are issues that have not been completely resolved within the technical community.

Sheldon et al. used artificially created surface cracks in K_b specimens to study the effect of specimen geometry and shed rate in Ti-6A1-4V [*6*]. They found that increased shed rates could be used to arrive at valid thresholds. However, they also noted that the choice of the starting K_{max} had an effect on the allowable shed rate that could be used and still measure valid thresholds. As K_{max} was increased, the absolute value of the gradient needed to be decreased in order to distance the crack tip stress field from the plastic wake. Sheldon et al. also found that specimen thickness ranging from 2.54 to 6.35 mm did not influence the measured threshold at $R = 0.1$ and $R = 0.8$.

Lenets and Nicholas [*7*] used two different methods for determining the fatigue crack growth threshold in titanium alloy IMI 834. The first test method used a transition from no-growth to growth while the second used a growth to no-growth approach. A consistent difference between the two thresholds for each test method was found. Increasing ΔK applied to the initially dormant crack produced the higher fatigue crack growth thresholds as compared to the situation when decreasing ΔK values were applied to a growing crack. Lenets and Nicholas concluded this difference in measured thresholds was attributed to the crack tip shielding associated with residual stresses in front of the crack tip caused by the two different loading histories. Both of these cited studies indicate that loading history is an important consideration when determining a threshold for crack propagation and that a single number for a material threshold may not be a valid consideration.

Loading history effects associated with LCF/HCF interactions is another crucial element in establishing allowable limits for HCF loading. Most of the work in this area has been associated with combined cyclic fatigue (CCF), that is, HCF, generally at high R, which is accompanied by periodic underloads to zero or near-zero stress. Several studies have shown that superimposed HCF cycling adversely affects the LCF life of steel [*8,9*] and superalloys [*10*]. Some of the first work in crack growth under combined HCF/LCF was conducted on Inconel 718 at 650°C [*11*]. The data showed that the crack growth rate was dominated by time-dependent behavior for the LCF cycles and cycle-dependent behavior for HCF. The minor (HCF) cycles had a threshold stress intensity, dependent on stress ratio, below which they had no effect on LCF growth rates, and above which the HCF growth dominated.

Guedou and Rongvaux [*12*] examined the effect of superimposed HCF on the LCF life of Ti-6A1-4V at 20°C and Inconel 718 at 550°C. They examined both initiation life (to a crack depth of a 50 μm) and crack propagation life and found that superimposing HCF cycles (R = 0.60, 0.80, and 0.85) on LCF cycles significantly reduced both the initiation and propagation life relative to those measured for LCF-only loading. In agreement with Ouyang et al. [*10*], the crack propagation life was reduced significantly more than initiation life.

Perhaps the greatest amount of research on combined HCF and LCF loading has been conducted by Powell, Duggan, and coworkers [*13–16*], who have examined the crack growth rate of titanium alloys and other materials under combined HCF and LCF loading. The earliest investigations [*13,14*] were conducted on Ti-6A1-4V and demonstrated the existence of an onset stress intensity, ΔK_{onset}, below which HCF had no effect on LCF growth rate and above which it dominated the growth rate under combined loading. The linear summation of growth rates obtained from LCF and HCF loadings alone was shown to predict the combined behavior for this material. Thus, ΔK_{onset} was essentially equivalent to ΔK_{th} for HCF alone, provided that the ratio of number of HCF to LCF cycles was large enough so that HCF growth rates per block exceeded those due to LCF alone. This condition has led to the requirement for using very high frequency testing apparatus in order to perform these types of tests in a reasonable time. Subsequent work shows Ti-6A1-4V [*15*] to be less sensitive to load history effects than nickel-base superalloys. The latest work in Ti-6A1-4V [*16*] shows the effects of multiple LCF underloads and overloads combined with high stress ratio HCF loading on crack growth. The linear summation model showed that the introduction of overloads caused the fatigue crack growth curves to shift to lower values of ΔK_{HCF} when compared with multiple underloads.

Most of the published literature on underloads and overloads in crack growth modeling deals with spectrum loading and the retardation or acceleration of growth rates. Little attention has been paid to the effect of such transients on the threshold for continued crack propagation. Hopkins et al. [*17*] used an increasing load step test to determine the overload

modified long crack threshold, ΔK^*_{th}, in both a nickel-base alloy and Ti-6A1-4V. They found that for high values of prior overloads that ΔK^*_{th} increased exponentially with the magnitude of the prior applied overload. It was also found that the ΔK^*_{th}/overload data could be extrapolated to obtain the basic threshold at low stress ratios where valid precracking is impractical. Gallagher and coworkers [*18,19*] investigated load interaction models to predict crack growth under different types of overloads resulting from spectrum loading. They showed it was possible to generalize the stress intensity to account for the overloaded generated arrest or threshold condition using an overload shut-off ratio. The overload shut-off ratio was the experimentally determined overload ratio above which crack arrest occurred. This approach and other methods like it provide models that work well in describing crack retardation regions where crack growth is retarded. However, these approaches require experimentally determined inputs such as the overload shut-off ratio and a baseline K_{th} to successfully correlate such data. Little work dealing directly with the determination of load interaction effects on threshold is available and even less with small cracks.

Another consideration in the determination of thresholds for HCF crack propagation is crack length. Ritchie points out the importance of the small fatigue crack phenomenon when determining HCF thresholds [*20*]. Any number of variables including crack size and geometry, mode mixity, applied loading spectra, and residual stress may affect the HCF threshold. Boyce and Ritchie [*21*] propose a high-stress-ratio large-crack-growth test to determine a lower bound HCF threshold. The long-crack lower-bound threshold was presented as a way of describing the onset of small crack growth from natural crack initiation and FOD sites. Frequencies of 50 to 1 kHz were used to study large-crack propagation in Ti-6A1-4V using C(T) specimens. The high-stress-ratio large-crack-growth test is used to simulate the closure-free small crack behavior and determine a lower-bound-long crack threshold of 1.9 MPa$\sqrt{m}$. Comparisons were done with closure-corrected lower-stress-ratio long-crack-growth threshold tests to verify the determined lower-bound long-crack threshold. The comparisons, however, indicated that the higher stress ratio threshold was less than the closure-corrected over-stress ratio test due to an additional mechanism such as room temperature creep or slip-step oxidation. Although an additional mechanism caused the measured higher stress level threshold to be less, it is in any event still a conservative estimate and thus a lower-bound threshold for Ti-6A1-4V. Additionally, Boyce and Ritchie found that thresholds for Ti-6A1-4V were frequency independent over the range of 50 to 1000 Hz. Campbell et al. [*22*] investigated mixed mode crack growth thresholds using through cracks in Ti-6A1-4V plate material. They determined that a slight increase in Mode I threshold results when the crack kinking direction increases from zero to 30° as compared to the pure Mode I case. Crack kinking angles greater than 30° produced lower Mode I thresholds.

Experiments

Material and Specimens

All specimens were machines from forged Ti-6A-4V plate. The plate was forged from a parent bar produced in accordance with AMS 4928. After forging, the plate was preheated at 938°C (±°C) for a minimum of 30 min, solution heat treated to 932°C (±14°C) for 75 min, and fan air cooled. The plate was then mill annealed in vacuum at 704°C (±14°C) for 24 and fan cooled in argon. The result was a titanium alloy with an alpha-beta microstructure for approximately 60% primary alpha was the remainder transformed beta. The mechanical properties of the Ti-6A1-4V plate are σ_y = 930 MPa and σ_{UTS} = 978 MPa.

Double notch tension test specimens were machined from the plate to the dimensions

shown in Fig. 1. After machining, all specimens were subjected to a stress relief by heating them to 704°C for 1 h in vacuum and then electropolishing the gage section in the vicinity of the notches. Stress concentration factors and notch depths of the two notches were chosen so that failure could be confined to the more severe notch having an elastic stress concentration factor, K_t, of 2.2. Finite element analysis of the specimen geometry confirmed that the use of equal depth for the two notches produced essentially no bending in the specimen whether fixed or pinned grips were used. In the experiments, nominally fixed grips were used.

LCF Cracks

LCF precracking was conducted under load control using a sinusoidal wave form at a frequency of 10 Hz with a superimposed hold time of 0.5 s on each cycle during which the DCPD measurements could be made. Stress ratios of -1.0 and 0.1 were utilized at maximum stress levels, which corresponded to approximately 250 000 cycles to failure. Several techniques were considered for measuring the small LCF cracks. It is recognized that detecting the initiation of small surface cracks 50 to 350 μm is more difficult than collecting crack measurements. Optical microscopy, acetate replica method, the in-situ scanning electron microscope (SEM) method, and direct current potential drop (DCPD) are all suitable methods for detecting initiation. In this investigation, DCPD, which is an accepted method for collecting long crack growth data [*23*], was used. This technique is based on the changing direct current potential as a function of crack length. Kalluri and Telesman [*24*] developed a DCPD system for the characterization of fatigue crack initiation in Ti-6AL-4V with which they successfully quantified the number of cycles to fatigue crack initiation. Depending on the specimen geometry, others have had success in quantifying crack growth increments from 2 to 50 μm [*25,26*]. In the present study, cracks were typically detected with DCPD at cycle counts between 20 000 and 100 000, at which point the tests were stopped and the specimens inspected in the SEM to confirm the existence of a crack.

To fully characterize the geometry of these cracks in order to determine ΔK_{th}, the crack shape had to be determined. To accomplish this, specimens with LCF cracks were heat tinted prior to HCF threshold testing. Heat tinting marks the crack profile for post-fracture measurement of the crack geometry without affecting any subsequent crack growth properties. Ravichandran and Larsen [*27,28*] demonstrated the effective use of heat tinting to mark the specimen crack profile in titanium alloys after a surface crack was initiated and before fracture occurred. In the present study, heat tinting of Ti-6A1-4V was conducted at 400°C for 4 h.

HCF Threshold Testing

Because of the large numbers of cycles associated with HCF, generation of HCF data takes considerable time in the laboratory. To overcome this problem, a step test procedure developed by Maxwell and Nicholas [*29*] for the rapid generation of HCF data was used. The method involves subjecting a specimen to 10^7 cycles at a stress level below the anticipated failure level. If the specimen does not fail within 10^7 cycles, the stress level is increased 5% and the test repeated until the specimen fails. The effective stress to cause failure is then determined by interpolating between the previous loading block stress level and the stress level that caused failure. In this investigation the step-loading procedure was used for both cracked and uncracked specimens. One concern in using this method is the potential for the existence of coaxing. However, Nicholas and Maxwell [*30*] showed good correlation between

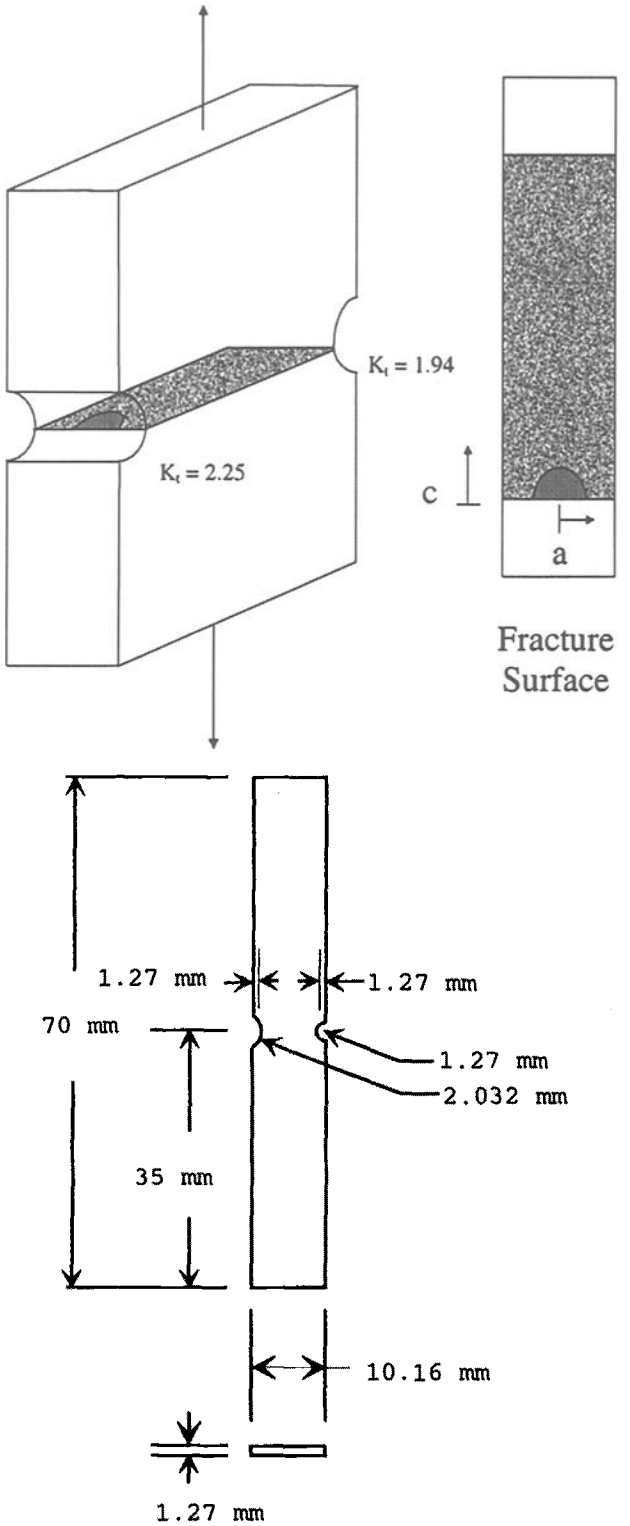


FIG. 1—*Double notch tension specimen and crack shape nomenclature.*

data collected using the step method and data collected using traditional data collection techniques. Bellows et al. [*31*,*32*] completed similar studies to investigate the viability of the step test method. They found that the step test method was valid for determining endurance limits in Ti-61A-4V for both smooth and notched specimen geometries. Others have also found coaxing to be minimal in titanium alloys [*33*,*34*].

Thresholds in the form of values of ΔK were determined from the results of the step testing, which established the load for crack extension to occur, and from the measurements of the initial crack size using heat tinting. Although stress intensity factor solutions have been developed for numerous crack and geometry configurations, no solution was found for the specific geometry used here. For this investigation, the finite element method was used to modify existing solutions developed for a semi-elliptical surface crack and corner crack in a single-edged notch tension specimen. In this work, ΔK_{th} is defined as the value of ΔK where propagation begins from a no-growth state. ΔK_{th} is then calculated using the crack measurements made from the fracture surfaces, the interpolated threshold stress, and the modified stress intensity factor solution. The ΔK_{th} determined here represents the onset of crack propagation and is identical to the terminology ΔK_{onset} used by Powell and coworkers [*13–16*] or ΔK_{th}^{*} used by Hopkins et al. [*17*] as an "overload modified threshold" determined from increasing load step testing on precracked specimens.

The crack shapes developed under LCF loading were taken into consideration when calculating the values of ΔK for each crack geometry. To show the trends for all crack sizes, data on crack aspect ratio were obtained for each crack from the fracture surface. These data are plotted in Fig. 2 along with a piecewise linear fit, which best represents the experimental data. Both the actual aspect ratios, as well as the trend line, were used in subsequent calculations of threshold values of ΔK as described in the next section.

Results and Discussion

Cracks initiated under LCF were detected using the DCPD method and verified by observing them under load using SEM. This allowed the determination of surface crack length,

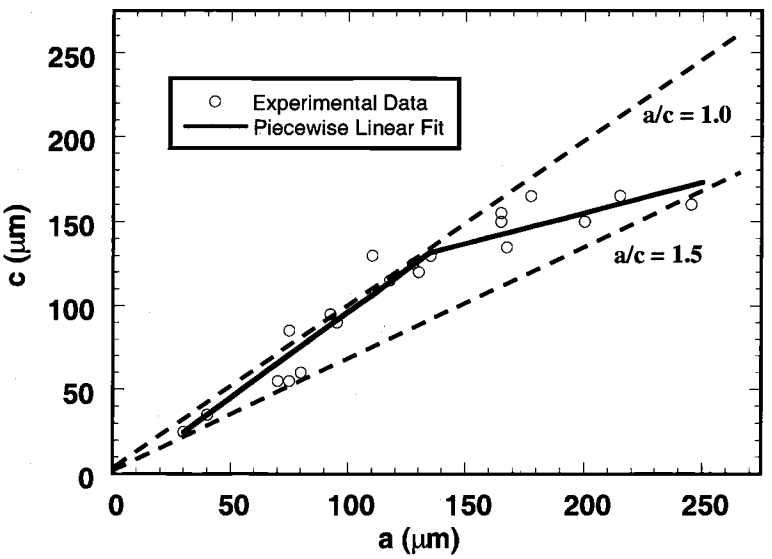


FIG. 2—*Experimental results for measured crack geometries.*

$2a$. The depth of the crack was determined from the fracture surface that showed the heat-tinted pattern of the crack after LCF but before HCF. Figure 3 shows a surface crack under load in the SEM. The surface crack length, projected onto an axis normal to the load direction (vertical in the figure), was $2a$ = 195 μm. The same crack is seen on the fracture surface after HCF in Fig. 4. That crack measurement from the fracture surface provides a crack size of $2a$ = 190 μm for the surface length and c = 95 μm for the crack depth into the notch. In all of the measurements of surface crack length, the values from surface measurements prior to HCF were very close to those from the heat-tinted fracture surface after HCF. For consistency, and since initial crack depths could not be measured prior to HCF testing, the values from the fracture surface were used throughout the investigation. For some of the smaller cracks, such as one shown in Fig. 5, the crack as somewhat inclined to the plane normal to the loading direction. In all cases, the crack length is the projected length normal to load direction and no attempt was made to account for Mode II contribution to the K analysis. In Fig. 5, the projected length was measured to be $2a$ = 60 μm. For comparison, the crack length determined from the fracture surface was $2a$ = 55 μm.

Comparisons are made between the fatigue limit stress in notched specimens that are tested without any loading history and those that have a limited number (30) of LCF cycles.[3] The results, obtained from HCF testing at stress ratios of 0.1 and 0.5, are presented in Fig. 6. The LCF cycling was conducted at either R = 0.1 and R −1.0 at maximum stresses of 430

[3] It was inconvenient to apply a smaller number of cycles even though stress redistribution is expected during the first complete cycle.

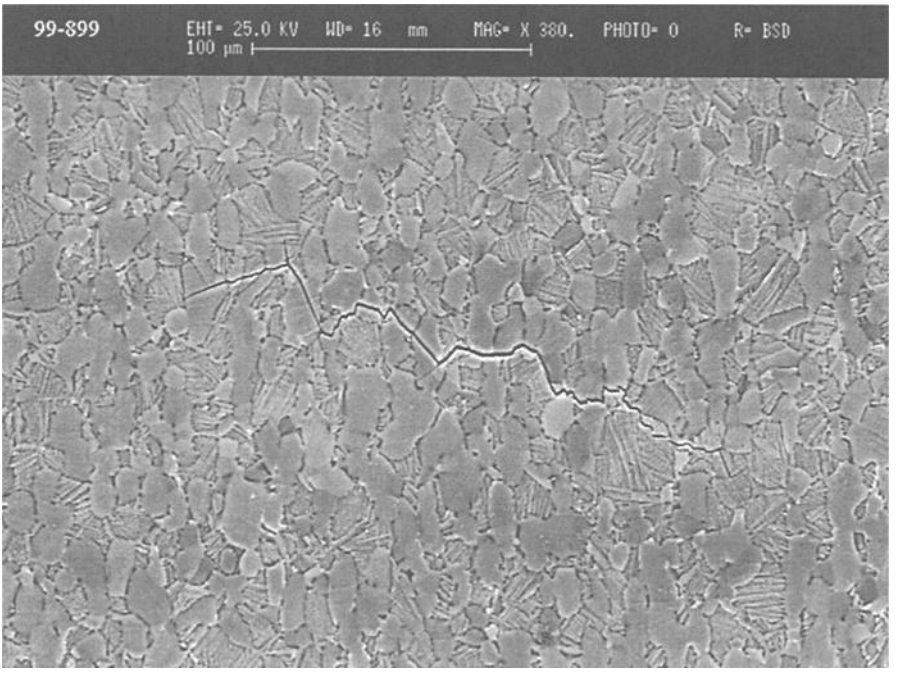


FIG. 3—*Surface crack under load in SEM.*

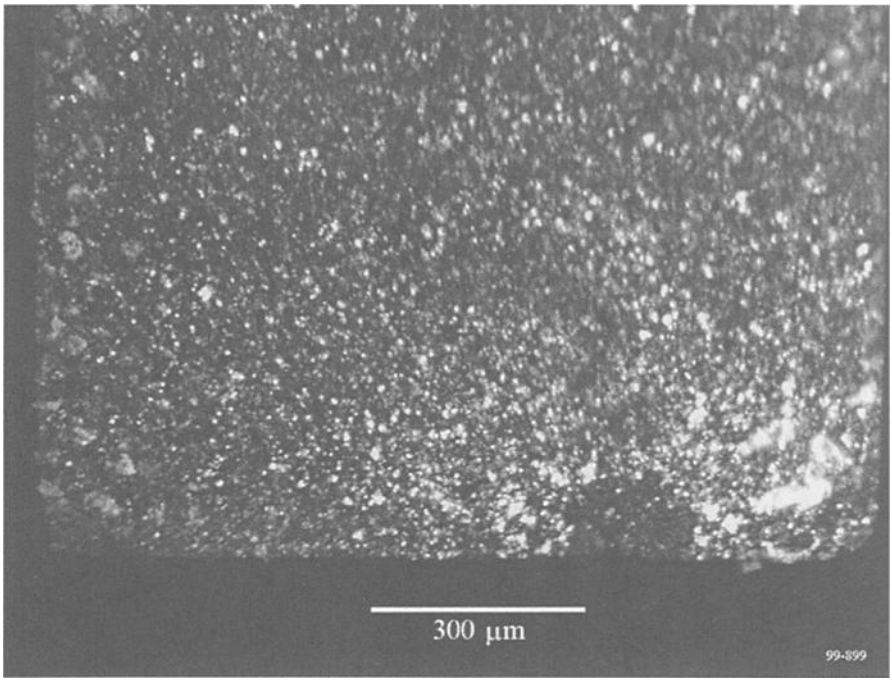


FIG. 4—*View of heat-tinted crack of Fig. 3 on fracture surface.*

or 265 MPa, respectively. For this material, with a yield stress of 930 MPa and a notch stress concentration factor of 2.2, one expects a small amount of notch plasticity and stress redistribution for the LCF loading at $R = 0.1$ since the calculated elastic stress of 930 MPa slightly exceeds the yield stress. Since this cycling under load control is at $R = 0.1$, the stress range at the notch is 0.9×946 (851), which is well within the elastic range of the material. Further, stress redistribution should occur only within the first load cycle and results in a local stress ratio for this elastic perfectly plastic material of $(930 - 851)/930 = 0.085$, which is only slightly below the applied $R = 0.1$. Plasticity is not expected for the fully reversed LCF loading because maximum stress is significantly below the material yield stress. Examination of the data in Fig. 6, particularly for LCF at $R = 0.1$, shows that there is no effect of the prior LCF on the HCF fatigue limit when compared to the baseline. From this, it is concluded that any effects due to stress redistribution at the notch can be neglected when assessing the effects of LCF-induced cracks on the threshold for HCF crack propagation.

An interesting observation is made when evaluating the data from the step test method on specimens with LCF cracks compared to data on specimens with no cracks. The last loading block, defined as the block of 10^7 cycles during which failure occurred, can have a cycle count anywhere from 1 to 10^7. The data for number of cycles to failure in this block are normalized with respect to 10^7 to show at what fraction of the block failure occurred. The results, presented in Fig. 7, show that for specimens with no prior cracks, the failure can occur anywhere in the block. When cracks are present, however, failure always occurs early in the loading block. These data show that there appears to be a very well defined HCF threshold for a cracked specimen for which failure occurs within a short time, typically under

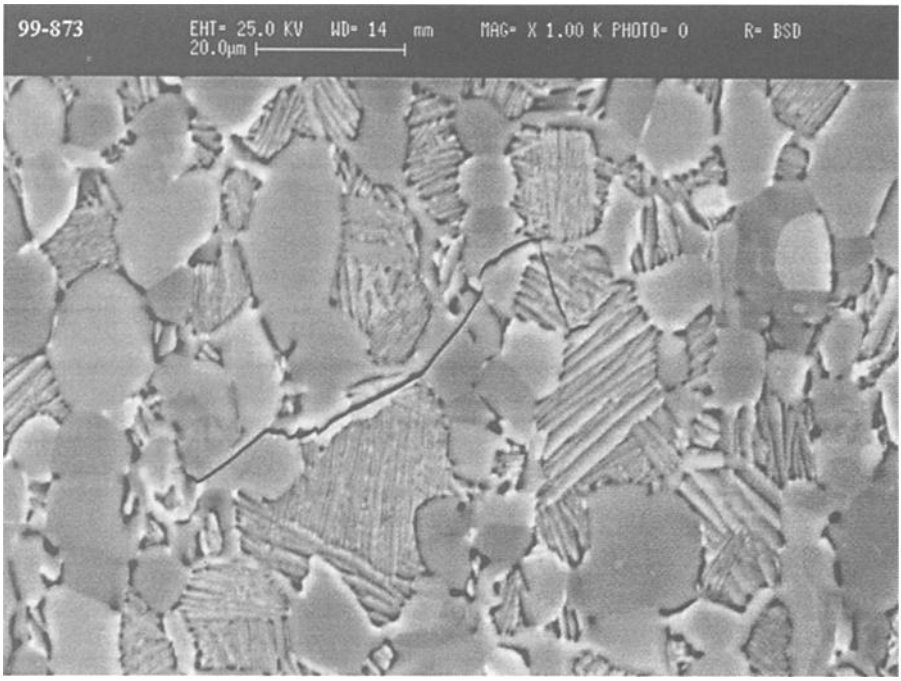


FIG. 5—*Small crack (2a = 55 μm) on surface under load in SEM.*

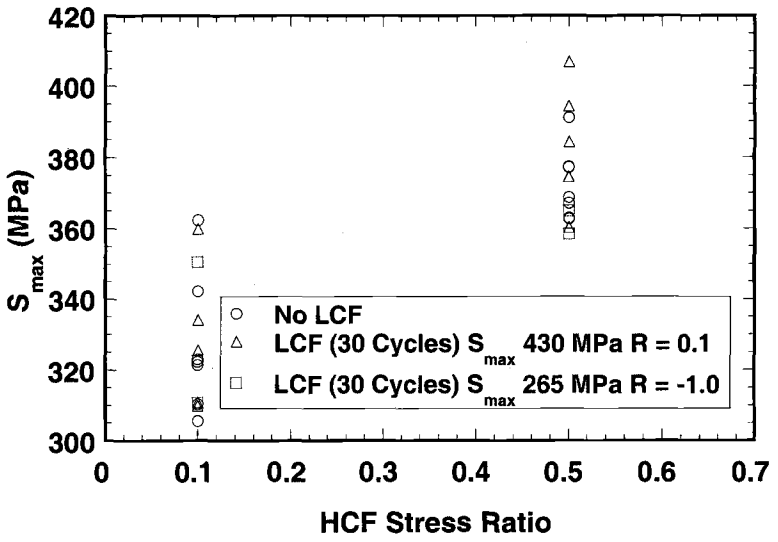


FIG. 6—*HCF endurance limit stresses.*

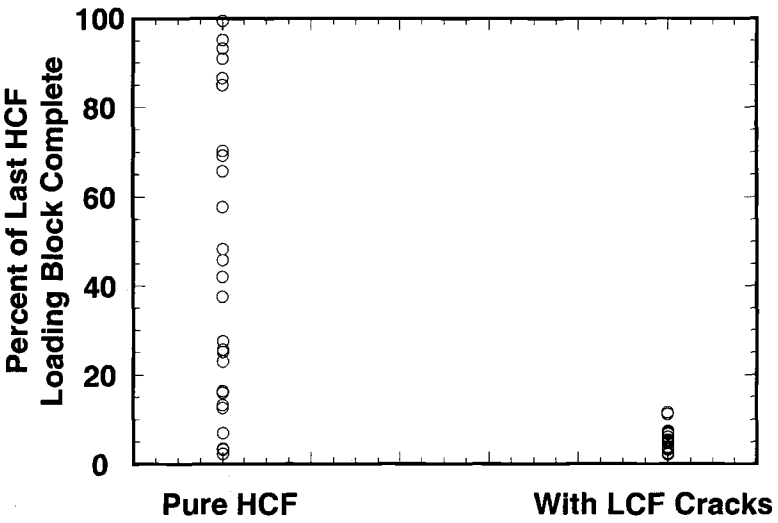


FIG. 7—*Comparison of number of cycles in last loading block of step test for under HCF with and without LCF precrack.*

one million cycles, or does not occur at all for a given applied stress (or K). Alternately, these data show that when a crack is present, we are dealing only with the propagation phase of fatigue that is small compared to the nucleation phase that dominates the HCF life in an uncracked specimen.

HCF crack threshold data are summarized in Fig. 8. All of the data are obtained at either $R = 0.1$ or $R = 0.5$, whereas the LCF cracks are generated at $R = 0.1$ or $R = -1.0$. To facilitate the explanation of an underload or an overload effect when going from LCF to HCF, a schematic of each of the four conditions considered is also presented in the figure. Each schematic shows the maximum stress for LCF, during which the crack is formed and starts to propagate, and the subsequent HCF maximum stress during which the crack propagates to failure. The data corresponding to each of the four conditions of combined LCF/HCF loading, as well as long crack threshold data, are presented in the figure and summarized in Table 1. Using the long crack threshold as a reference, the figure indicates that LCF at $R = 0.1$ produces cracks that have a higher threshold in subsequent HCF, whereas LCF at $R = -1.0$ produces anywhere from no change to a slightly lower threshold than obtained from long crack data. In terms of the loading schematics, this seems to indicate that an overload type condition (LCF at $R = 0.1$) retards the subsequent HCF propagation, while an underload (LCF at $R = -1.0$) might tend to slightly accelerate the subsequent HCF propagation. The apparent overload effect from precracking at a higher stress than that required to propagate the crack under HCF is the result of multiple "overloads" since constant amplitude loading was used to precrack the specimens. The apparent multiple overload effect is consistent with observations such as those of Frost [*35*], who noted that crack formed by precracking at a higher alternating stress are all stronger than expected and that the "propagation stress" (stress to obtain ΔK_{th}) is increased if the initial loading conditions are such as to induce compressive residual stresses at the crack tip. It should also be noted here that the overload ratios (OLR = ratio of precrack stress to fatigue limit stress) are relatively small (see Table 1) compared to those used in studies of overload effects, where values of OLR typically exceed 1.5 to produce noticeable effects [*36*]. While it is not the purpose of this

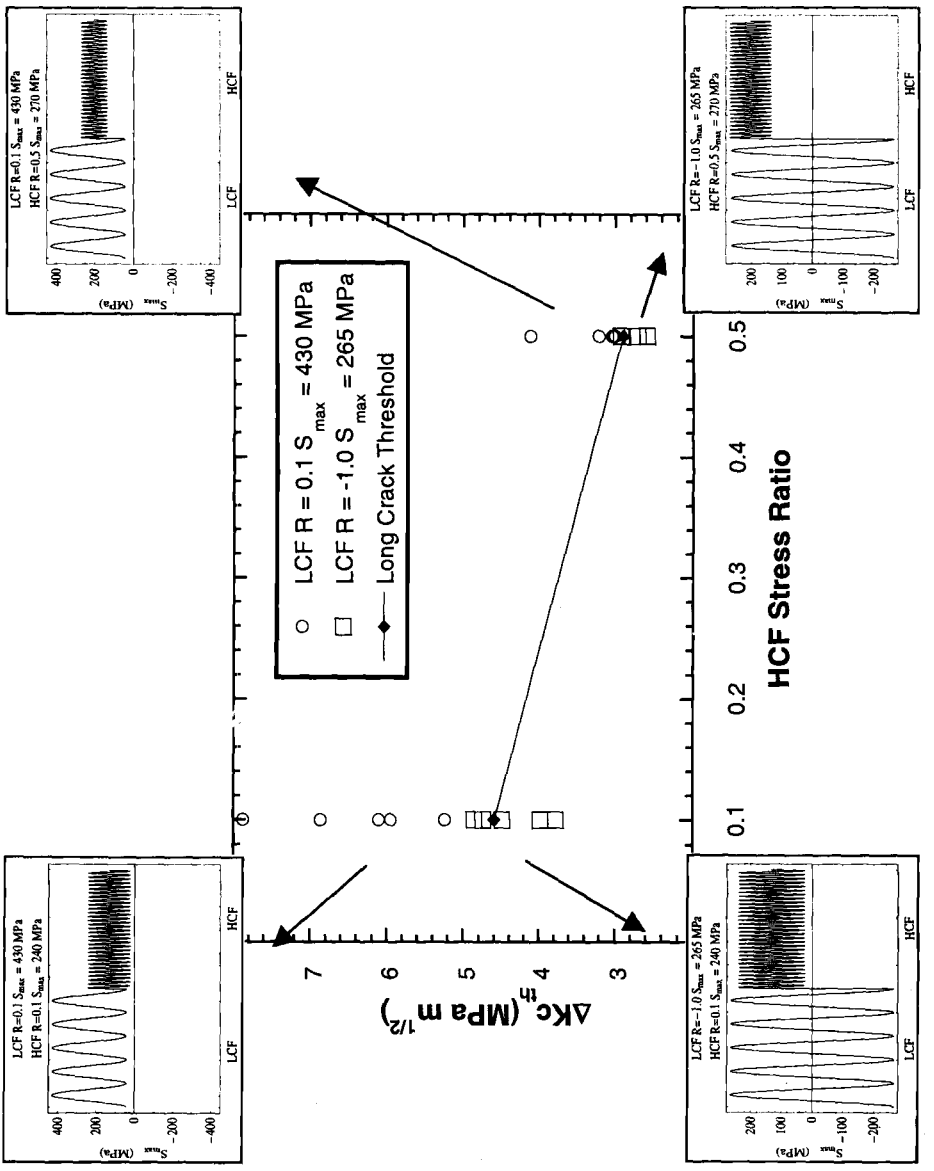


FIG. 8—*HCF threshold stress intensity range for LCF precracked specimens.*

TABLE 1—*Fatigue data.*

HCF R=0.1			HCF R=0.5		
	LCF R=0.1			*LCF R=0.1*	
c (μm)	Fatigue Limit (MPa)	OLR	c (μm)	Fatigue Limit (MPa)	OLR
160	250.3	1.7	130	235.3	1.8
165	225.6	1.9	150	230.5	1.9
125	270.4	1.6	85	300.4	1.4
120	234.4	1.8	135	288.0	1.5
95	260.6	1.7	150	250.7	1.7
110	220.2	2.0	130	265.4	1.6
	LCF R=-1.0			*LCF R=-1.0*	
165	155.3	1.7	35	346.1	0.8
60	246.9	1.1	55	305.6	0.9
25	305.7	0.9	155	181.0	1.5
55	247.6	1.1	95	234.6	1.1
55	224.0	1.2			

paper to discuss the governing mechanisms of retardation due to overloads, the reader is referred to the review article by Sadananda et al. [*36*], who address that subject.

An alternate method for looking at threshold crack growth data is to compare stresses for a given crack size against crack length for LCF-generated cracks and data extrapolated from a long crack growth threshold test. Such information can be presented in the form of a Kitagawa diagram [*37*], shown schematically in Fig. 9, which plots stress against crack size. Using logarithmic scales, a crack growth threshold for a geometry where K is proportional

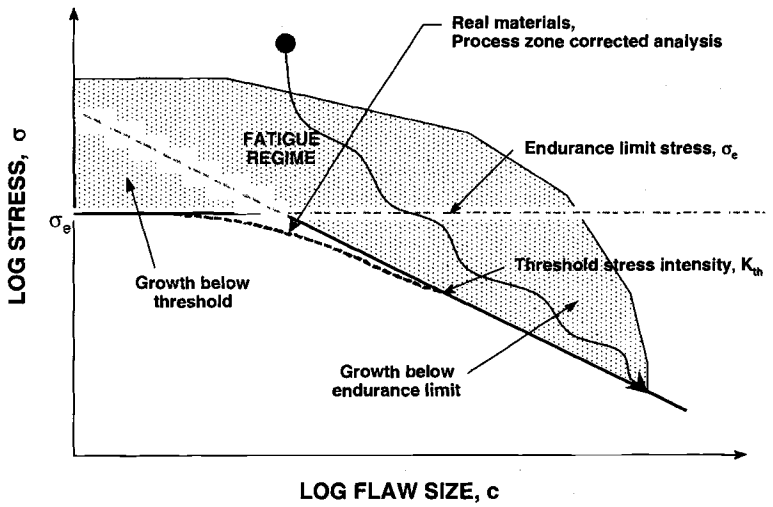


FIG. 9—*A Kitagawa type diagram showing thresholds as function of stress and flaw size.*

to $\sqrt{c}$ (c is flaw size) produces a straight line of slope = −0.5 as shown in the figure. Concurrently, the endurance limit of an uncracked material is a stress, σ_e, which has meaning only for arbitrary small flaw size, but can be indicated by a horizontal line in the figure.

For any given geometry, all combinations of crack length and stress corresponding to a K solution equal to the threshold value an be plotted to establish the threshold crack growth line. This line now represents the fracture mechanics solution down to arbitrarily short crack lengths and makes no assumptions about the lack of validity of the solution for such short cracks. In fact, the diagram shows clearly that the threshold value from the K solution cannot be valid for arbitrarily short cracks because there is a region above the endurance limit yet below the crack growth threshold. Much more important is the concept of data points below the endurance limit that represent a threshold for cracks of a particular size. It is clear that such cracks could not be naturally initiated since they represent stress levels below the endurance limit. While such cracks could be preexisting in the material in the form of initial defects, material with such defects would have a lower endurance limit. It follows, therefore, that data plotted on a Kitagawa diagram representing a crack length and stress below the endurance limit generally represent a condition where the crack was initiated above the endurance limit and then followed some path as depicted schematically in Fig. 9. While another explanation might be that a complex stress field allows the initiation, but not propagation of a crack, then the simple K solution that produces the line of constant K is no longer valid and the actual K solution has to be represented in the diagram. With this in mind, the question is raised as to whether any point on a Kitagawa diagram is unique or, instead, is dependent on the history of loading in getting to that point. The long crack threshold, whose loading path is depicted schematically in Fig. 9, is clearly an example of a data point that may be dependent on loading history. Wile standards have been set for determining this threshold by following a predetermined history, the history dependence and the existence of a unique long crack threshold still have to be questioned.

The data for the HCF threshold after a LCF crack has been initiated, shown in Fig. 8, are replotted in a Kitagawa-type diagram in Figs. 10 and 11 for HCF values of R = 0.1 and R = 0.5, respectively. In each of the figures, three lines are drawn representing the long crack threshold of K_{max} = 5.1 MPa$\sqrt{m}$ for R = 0.1 (Fig. 10) and K_{max} = 5.8 MPa$\sqrt{m}$ for R = 0.5 (Fig. 11). The three lines represent the bounds of a/c that were observed experimentally, and the best fit used to represent the actual data as shown in Fig. 2. The horizontal line in each figure represents the experimentally determined endurance limit corresponding to 10^7 cycles. It can be seen in both figures that the data that were obtained using LCF at R = −1.0 (triangles) tend to fall slightly below the projected long crack threshold, the type of effect being representative of what one would expect when a material sees an underload during prior cycling. Conversely, the circles that represent data obtained under LCF at R = 0.1 show what appears to be equivalent to an overload effect since the threshold values of stress are consistently above the extrapolated long crack threshold. The data cover only a limited range of crack sizes and are insufficient in number to draw any conclusions about the effect of crack length on the overload or underload effect on the HCF threshold.

Conclusions

Notched tension specimens were subjected to sequential LCF and HCF loading conditions. HCF threshold were determined for cracks formed under LCF loading at stress ratios of 0.1 and −1.0. The HCF thresholds, obtained using a step-loading technique, were obtained at stress ratios of 0.1 and 0.5. Comparisons between the values of ΔK_{th} obtained elsewhere using long crack data and those obtained here show an effect of the prior LCF loading history. LCF conducted at R = 0.1 prior to HCF produces an apparent overload effect which,

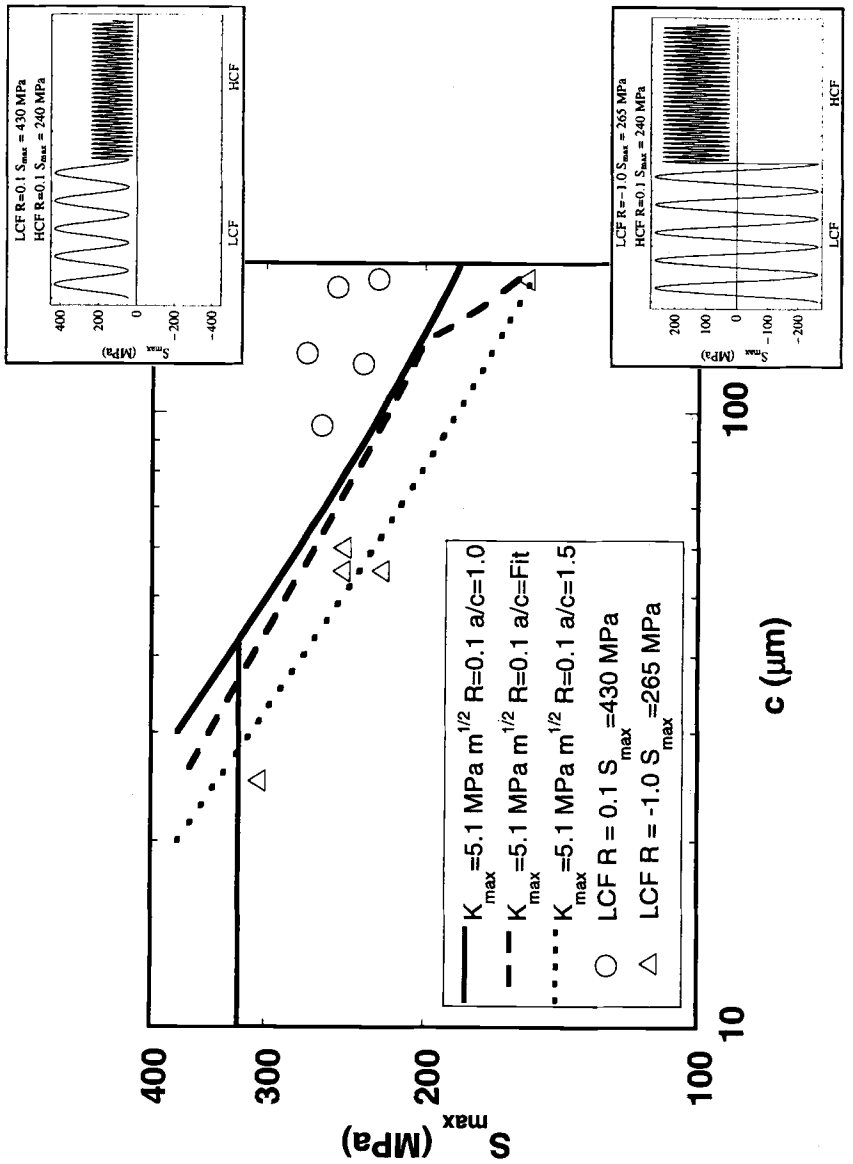


FIG. 10—*HCF thresholds at* R = *0.1 on a Kitagawa type diagram.*

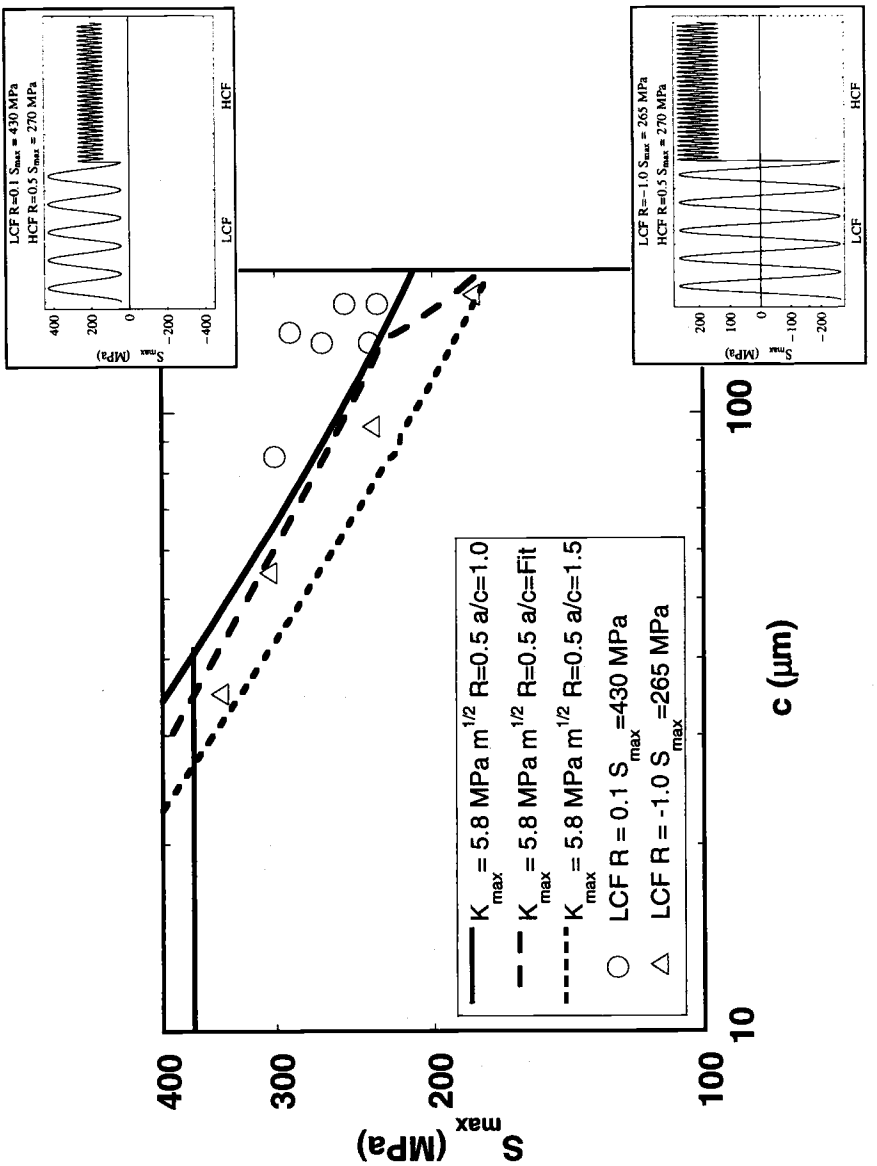


FIG. 11—*HCF thresholds at* R = *0.5 on a Kitagawa type diagram.*

in turn, increases the subsequent HCF threshold. On the other hand, LCF at $R = -1.0$ produces what appears to be a slight underload effect, tending to lower the subsequent HCF threshold. These results indicate that values of crack growth threshold, plotted on a Kitagawa-type diagram, are not unique but instead an depend on the loading history used to produce the cracks whose thresholds are subsequently determined. Very limited data show no dependence of threshold on crack size within the limits of crack sizes obtained in this investigation.

Acknowledgments

This research was conducted at the Air Force Research Laboratory Materials and Manufacturing Directorate. The support of Mr. Richard Goodman of UDRI in the HCF testing, Mr. Ken Goecke of UDRI in the LCF testing, Mr. George Hartman of UDRI in the DCPD measurements, and Mr. Bob Lewis of UES in electropolishing is gratefully appreciated.

References

[1] Thomson, D. E. and Griffin, J. T., "The National Turbine Engine High Cycle Fatigue Program," *Global Gas Turbine News,* Vol. 39, ASME International, 1999, pp. 14–17.

[2] *Engine Structural Integrity Program,* USAF MIL-STD-1783, November 1984.

[3] Nicholas, T., "Critical Issues in High Cycle Fatigue," *International Journal of Fatigue,* Vol. 21, Supp. 1, 1999, pp. S221–S231.

[4] Nicholas, T. and Zuiker, J. R., "On the Use of the Goodman Diagram for High Cycle Fatigue Design," *International Journal of Fracture,* Vol. 80, 1996, pp. 219–235.

[5] Akita, K., Misawa, H., Tobe, S., and Kodama, S., "Fatigue Crack Propagation Behavior of Ti-6A1-4V Alloy under Simplified Loading with a Single Overload," *Fatigue '93,* J. P. Bailon and J. I. Diskson, Eds., Vol. 3, EMAS, Warley U.K., 1993, pp. 1575–1580.

[6] Sheldon, J. W., Bain, K. R., and Donald, K. J., "Investigation of the Effects of Shed-Rate, Initial K_{max}, and Geometric Constraint on ΔK_{th} in Ti-6A1-4V at Room Temperature," *International Journal of Fatigue,* Vol. 21, 1999, pp. 733–741.

[7] Lenets, Y. N. and Nicholas, T., "Load History Dependence of Fatigue Crack Thresholds for Ti-Alloy," *Engineering Fracture Mechanics,* Vol. 60, 1998, pp. 187–203.

[8] Makhutov, N., Romanov, A., and Gadenin, M., "High-Temperature Low-Cycle Fatigue Resistance Under Superimposed Stresses at Two Frequencies," *Fatigue of Engineering Materials and Structures,* Vol. 1, 1979, pp. 281–285.

[9] Zaitsev, G. Z. and Faradzhov, R. M., *Metallovedenie i Termicheskaya Obrabotka,* Vol. 2, 1970, pp. 44–46.

[10] Ouyang, J., Wang, Z., Song, D., and Yan, M., "Influence of High Frequency Vibrations on the Low Cycle Fatigue Behavior of a Superalloy at Elevated Temperature," *Low Cycle Fatigue, ASTM STP 942,* American Society for Testing and Materials, Philadelphia, PA, 1988, pp. 961–971.

[11] Goodman, R. C. and Brown, A. M., "High Frequency Fatigue of Turbine Blade Material," AFWAL-TR-82-4151, Wright-Patterson AFB, OH, October 1982.

[12] Guedou, J. Y. and Rongvaux, J. M., "Effect of Superimposed Stresses at High Frequency on Low Cycle Fatigue," *Low Cycle Fatigue, ASTM STP 942,* American Society for Testing and Materials, Philadelphia, PA., 1988, pp. 938–960.

[13] Powell, B. E., Duggan, T. V., and Jeal, R., "The Influence of Minor Cycles on Low Cycle Fatigue Crack Propagation," *International Journal of Fatigue,* Vol. 4, 1982, pp. 4–14.

[14] Powell, B. E., Henderson, I., and Duggan, T. V., "The Effect of Combined Major and Minor Stress Cycles on Fatigue Crack Growth," *Second International Congress on Fatigue (Fatigue '84),* 1984, pp. 893–902.

[15] Hawkyard, M., Powell, B. E., Hussey, I. and Grabowski, L., "Fatigue Crack Growth under Conjoint Action of Major and Minor Stress," *Fatigue & Fracture of Engineering Materials & Structures,* Vol. 19, 1996, pp. 217–227.

[16] Hall, R. F. and Powell, B. E., "The Effects of LCF Loadings on HCF Crack Growth," US AFOSR Annual Report for Phase II, Report Number F567, University of Portsmouth, England, May 1999.

[17] Hopkins, S. W., Rau, C. A., Leverant, G. R., and Yuen, A., "Effect of Various Programmed Overloads on the Threshold for High-Frequency Fatigue Crack Growth," *Fatigue Crack Growth Under Spectrum Loads, ASTM STP 595,* American Society for Testing and Materials, Philadelphia, 1976, pp. 125–141.

[18] Petrak, G. J. and Gallagher, J. P., "Predictions of the Effect of Yield Strength on Fatigue Crack Growth Retardation in HP-9NI-4Co-30C Steel," *Journal of Engineering Materials and Technology,* Vol. 97, 1975, pp. 206–213.

[19] Gallagher, J. P. and Stalnaker, H. D., "Predicting Flight by Flight Crack Growth Rates," *Journal of Aircraft,* Vol. 12, 1975, pp. 699–705.

[20] Ritchie, R. O., "Small Cracks and High Cycle Fatigue," *Proceedings of the ASME Aerospace Division,* J. C. I. Chang, Ed., AMD—Vol. 52, ASME, New York, NY, 1996, pp. 321–333.

[21] Ritchie, R. O., Boyce, B. L., Campbell, J. P., Roder, O., Thompson, A. W., and Milligan, W. W., "Thresholds for High-Cycle Fatigue in a Turbine Engine Ti-6A1-4V Alloy," *International Journal of Fatigue,* Vol. 21, 1999, pp. 653–662.

[22] Campbell, J. P., Thompson, A. W., and Ritchie, R. O., "Mixed-Mode Crack-Growth Thresholds in Ti-6AL-4V under Turbine-Engine High-Cycle Fatigue Loading Conditions," *4th National Turbine Engine High Cycle Fatigue Conference,* USAF, Monterey, CA, 1999.

[23] Standard Test Method for Measurement of Fatigue Crack Growth Rates, *Annual Book of ASTM Standards,* ASTM E 647-95a, 1995, pp. 562–599.

[24] Kalluri, S. and Telesman, J., "Characterization of Fatigue Crack Initiation and Propagation in Ti-6A1-4V with Electrical Potential Drop Technique," NASA Technical Memorandum 100877, Cleveland, OH, July 1988.

[25] Ghonem, H. and Rosenberger, A., "Results from the Experimental Calibration of a DC Electrical Potential Drop System for the Measurement of Surface Flaws," University of Rhode Island, Kingston, RI, October, 1989.

[26] Mom, A. J. A. and Raizenne, M. D., "AGARD Engine Disc Cooperative Test Programme," AGARD R-766, 1988.

[27] Ravichandran, K. S. and Larsen, J. M., "An Approach to Measure the Shapes of Three-Dimensional Surface Cracks During Fatigue Crack Growth," *Fatigue & Fracture of Engineering Materials and Structures,* Vol. 16, 1993, pp. 909–930.

[28] Ravichandran, K. S. and Larsen, J. M., "Behavior of Small and Large Fatigue Cracks in Ti-24A1-11Nb: Effects of Crack Shape, Microstructure, and Closure," *Fracture Mechanics: 22nd Symposium, ASTM STP 1131,* H. A. Ernst, A. Saxena, and D. L. McDowell, Eds., American Society for Testing and Materials, Philadelphia, PA, 1992, pp. 727–748.

[29] Maxwell, D. C. and Nicholas, T., "A Rapid Method for Generation of a Haigh Diagram for High Cycle Fatigue," *Fatigue and Fracture Mechanics: 29th Volume, ASTM STP 1321,* T. L. Panontin and S. D. Sheppard, Eds., American Society for Testing and Materials, West Conshohocken, PA, 1999, pp. 626–641.

[30] Nicholas, T. and Maxwell, D. C., "Evolution and Effects of Damage in Ti-6A1-4V under High Cycle Fatigue," *Progress in Mechanical Behaviour of Materials,* Proceedings of the Eighth International Conference on the Mechanical Behaviour of Materials, ICM-8, F. Ellyin and J. W. Provan, Eds., Vol. III, 1999, pp. 1161–1166.

[32] Bellows, R. S., Muju, S., and Nicholas, T., "Validation of the Step Test Method for Generating Haigh Diagrams for Ti-6A1-4V," *International Journal of Fatigue,* Vol. 21, 1999, pp. 687–697.

[32] Bellows, R. S., Bain, K. R., and Sheldon, J. W., "Effect of Step Testing and Notches on the Endurance Limit of Ti-6A1-4V," *Mechanical Behavior of Advanced Materials, MD—Vol. 84,* D. C. Davis et al., Eds., ASME, New York, 1998, pp. 27–32.

[33] Vitovec, F. H. and Lazan, B. J., "Strength, Damping and Elasticity of Materials Under Increasing Reversed Stress with Reference to Accelerated Fatigue Testing," *ASTM Proceedings,* Vol. 55, American Society for Testing and Materials, 1955, pp. 844–862.

[34] Vasserman, N. N., Gladkovskii, V. A., Lukyanov, O. P., Kozlov, I. V., and Zgogurin, V. V., "Investigation of the Cyclic Strength of VT6 Titanium Alloy," *Strength of Materials,* Vol. 8, 1976, pp. 1288–1293.

[35] Frost, N. E., "Notch Effects and the Critical Alternating Stress Required to Propagate a Crack in an Aluminum Alloy Subject to Fatigue Loading," *J. Mech. Eng. Sci.,* Vol. 2, 1960, pp. 109–119.

[36] Sadananda, K., Vasudevan, A. K., Holtz, R. L., and Lee, E. U., "Analysis of Overload Effects and Related Phenomena," *International Journal of Fatigue,* Vol. 21, 1999, pp. S233–S246.

[37] Kitagawa, H. and Takahashi, S., "Applicability of Fracture Mechanics to Very Small Cracks or the Cracks in the Early Stage," *Proceedings of the Second International Conference on Mechanical Behaviour of Materials,* Boston, MA, 1976, pp. 627–631.

Kenneth R. Bain[1] *and David S. Miller*[1]

Fatigue Crack Growth Threshold Stress Intensity Determination via Surface Flaw (Kb Bar) Specimen Geometry

REFERENCE: Bain, K. R. and Miller, D. S., **"Fatigue Crack Growth Threshold Stress Intensity Determination via Surface Flaw (Kb Bar) Specimen Geometry,"** *Fatigue and Fracture Mechanics: 31st Volume, ASTM STP 1389,* G. R. Hilford and J. P. Gallagher, Eds., American Society for Testing and Materials, West Conshohocken, PA, 2000, pp. 445–456.

ABSTRACT: Many aircraft component failures originate from small-surface flaw cracks in highly stressed locations. It is therefore desirable to measure the threshold stress intensity factor that simulates the key conditions of high-stress and small semicircular surface crack shape. Such a technique has been developed and demonstrated on multiple titanium and nickel-base alloys. This technique is effective at both room and elevated temperatures and at both low and high mean stress.

The test method is described in detail, but in brief a small EDM flaw is made on the surface of a rectangular specimen. The crack length is monitored via electrical potential drop technique. The crack length and aspect ratio versus the change in electrical potential across the crack tip has been measured and is used to control the load shed during the experiment. Load sheds up to $C = -1181\ m^{-1}$ have been demonstrated to give comparable thresholds to those measured using single edge notch or compact tension geometries with lower shed rates. Typical experimental results on both Ti-6Al-4V and an advanced nickel-base superalloy (KM4) are shown at both room temperature and elevated temperatures. This technique allows a rapid determination of threshold stress intensity factor for a material in a manner simulating the types of constraint experienced in components.

KEYWORDS: threshold stress intensity, experimental procedure, titanium alloy, nickel alloy, fatigue crack growth

Objective

The research presented in the following paper details the test procedure and some initial results obtained using a surface flaw specimen (Kb-Bar specimen) to measure the threshold stress intensity for crack growth of high-strength nickel and titanium alloys. The test technique was developed to allow a better simulation of the loads and physical crack sizes commonly expected in naturally initiated cracks in high-stress components. The change in constraint associated with such physically small cracks was feared to affect the threshold measurement and therefore the subsequent calculated lives of components. Research on this type of test has recently been presented by Sheldon et al. [*1*] for Ti-6Al-4V alloy. The results indicate that this type of test yields valid threshold measurements, but does not go into other materials or the specifics of the test procedure.

[1] Senior staff engineer and lead specialist, respectively, General Electric Aircraft Engines, Mail Stop G50, One Neumann Way, Cincinnati, OH 45215-6301.

Copyright© 2000 by ASTM International www.astm.org

The use of surface flaw specimens to measure the crack growth behavior of high-strength turbine materials has been detailed by VanStone et al. [2]. The cracks were measured using an electrical potential drop technique similar to that described by Gangloff [3]. Most other features of the test procedure are the same as those detailed in ASTM Test Method for Measurement of Fatigue Crack Growth Rates (E 647) [4] with the exception of the need to increase the rate of load shed far faster than that recommended in ASTM E 647. Experimental test results on the rate of shed on measured threshold stress intensity are shown with the conclusion that for high-strength materials far faster shed rates are acceptable.

The following sections will describe how the test is conducted, typical test results, and present a number of conclusions and recommendations for future changes in ASTM E 647 to allow the use of a surface flaw specimen to measure threshold.

Experimental Procedure

General Requirements

All tests are to be performed in accordance with the requirements of ASTM E 647 unless otherwise specified. The standard specimen is a rectangular cross-section specimen with buttonhead ends to facilitate rigid gripping and minimum bending loads (see Fig. 1).

The four sequential steps in the test procedure are detailed in Table 1 along with the tasks associated with each step. It is required that the electrical potential drop (EPD) method of crack growth measurement be used to measure the crack growth. The general method used was described by Gangloff [3]. The EPD system should, as a minimum, incorporate the following:

- *Current Power Supply*—The power supply for the EPD system is capable of supplying the constant current required across the gage section (uniform reduced section) of the specimen to provide 200 to 300 μV. The power supply must provide a stability of less than 25 mA throughout the duration of the test.
- *Digital Data Acquisition*—Digital data acquisition is synchronized with the command signal of the test frame to provide potential drop and load measurements taken at the maximum and minimum peaks of the loading cycle. Switching current on/off or reversing to eliminate thermocouple effects in the potential readings is required. All data

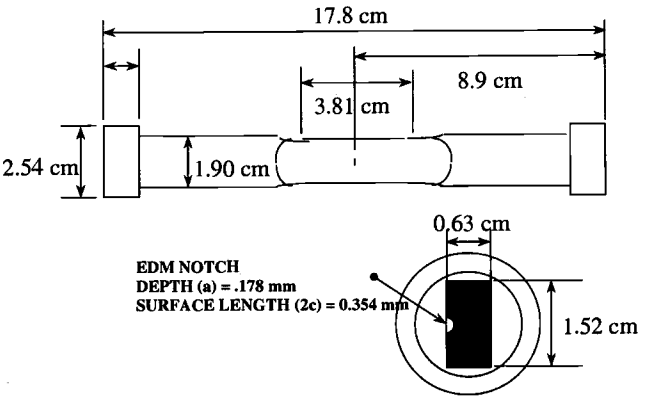


FIG. 1—*Standard surface flaw specimen (Kb-Bar) geometry.*

TABLE 1—*Typical test sequence from specimen preparation through analysis for a surface flaw threshold test (KB-Bar) of a titanium alloy.*

Step One	Step Two	Step Three	Step Four
Specimen Preparation	Pre-Crack of Specimen	Test of Specimen	Post Test Analysis
1. EDM notch in specimen dimensions 0.178 mm by 0.356 mm 2. Locate sensing leads 0.406 mm above and below notch 3. Measure width and thickness of the notch region 4. Attach current leads and sensing leads 5. Load specimen into the test stand 6. Connect EPD system; check sensing voltage stability	1. Input parameters Mode: constant load frequency: 10 Hz waveform: Sine *a* initial: 0.178 mm *a* final: 0.508 mm *K* initial: 8.25 $mPa*m^{-0.5}$ *K* final: 15.4 $mPa*m^{-0.5}$ Temperature: ambient *R* ratio: 0.1 2. Data acquisition block average: 300 cycles 3. Upon completion heat tint specimen 4 h at 371°C at zero load	1. Input parameters Mode: *K* shed frequency: 0.33 Hz waveform: Triangular *a* initial: 0.508 mm *K* initial: 15.4 $mPa*m^{-0.5}$ *C* gradient: −1181 m^{-1} Temperature: ambient *R* ratio: 0.1 2. Data acquisition block average: variable *da/dN* termination: $2.5e^{-10}$ m/cycle 3. Upon completion heat tint specimen 2 h at 343°C at zero load	1. Break specimen apart to reveal crack surface 2. Measure crack depth and surface length at several locations as indicated by heat tints or other fractographic markers 3. Calculate depth to half surface length aspect ratio (*a*/*c*) 4. Run data analysis software 5. Plot *da/dN* vs. delta *K* and plot effective *C* gradient

readings correspond to the cumulative cycle count of the test. The test system is capable of resolving 0.5 μV or less. The stability of the unit has been shown to be the lesser of 1% or 2 μV of the measured signal averaged over no more than 1 min. If additional amplification or filtering is required, the net result of all devices used must still meet the 1% or 2 μV specification. In addition, any aliases or biases caused by equipment response should be investigated and resolved before testing is started. These equipment response issues can include interchannel or intermodule skew, which is defined as the time delay between simultaneously sampled channels or modules. The skew is multiplied by the number of channels being sampled, which provides the system skew rate. This rate shall not exceed more than 1% of the mechanical cycle's period.

- *Software*—The logic used by the software to control the test is shown schematically in Fig. 2. A key experimentally determined relationship is required to convert the measured potentials into crack length. A typical result is shown in Fig. 3. The relationship can vary with the aspect ratio of the crack during growth. Aspect ratio is the ratio of crack depth (*a*) to the half surface length (*c*). The aspect ratio tends to be a constant for a given material at a test temperature (Fig. 1 also describes the EDM notch and the starting *a* and 2*c* dimensions). The software should be capable of recording data, making computations, and monitoring for interrupts within the time frame of a cycle. This is required for the computer to monitor the crack growth and to actively control the shed rate during the test. The software should also be capable of controlled shutdowns on a predetermined schedule to allow for marking of the crack front through means of a heat tint or by other requested methods. The software should allow for a seamless restart after such an event with continuation of the cycle count and reference back the test's

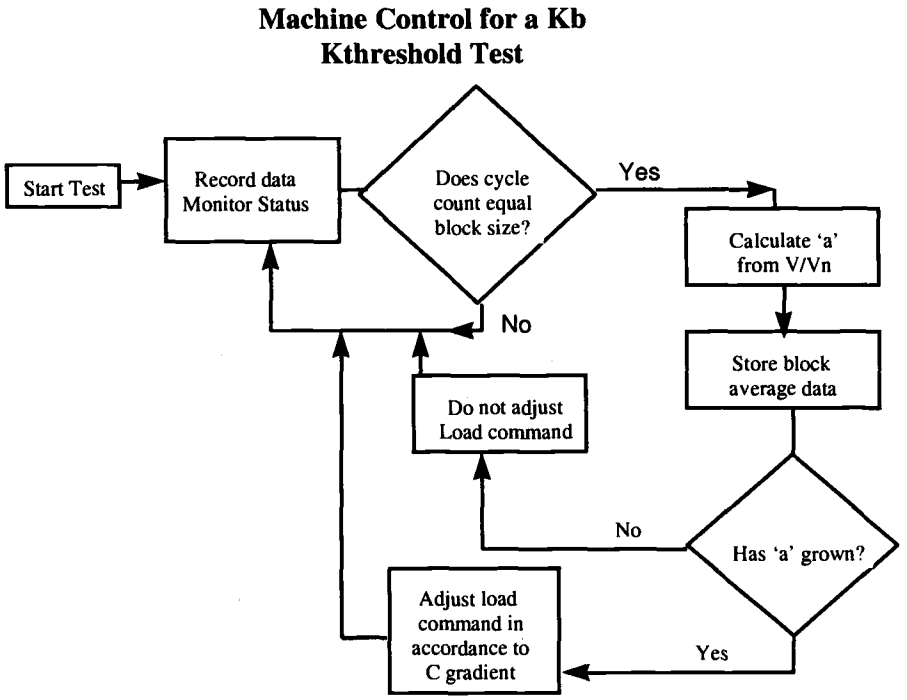


FIG. 2—*Schematic of what threshold program does to control load shed during a surface flaw threshold test.*

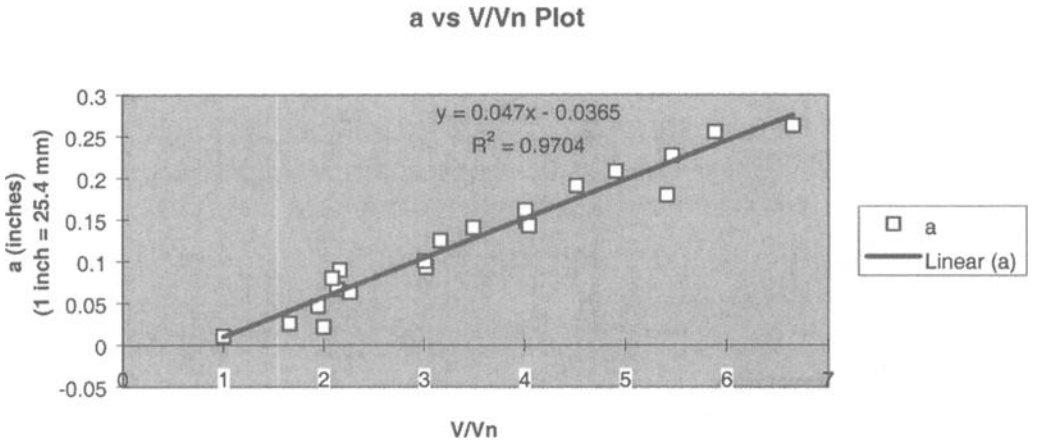


FIG. 3—*Relationship between measured crack depth* (a) *and observed EPD voltage change for surface flaw specimens. Measurements of depth were accomplished post-test using both fractography changes and heat tints to mark crack shape and size.*

first cycle block VDA (voltage difference average) for determination of the voltage change ratio (renormalized voltage). A data collection algorithm should be in place to allow the requester to choose the amount of data attained for each test. The algorithm should be based on cycle count. An additional method based on crack growth or growth rate may be desirable.

Specimen Preparation

An initial starter notch is cut into the specimen via electrical discharge machining (EDM). A smaller razor blade with a ground tip is used to precisely machine the small semi-elliptical notch (notch dimensions in Fig. 1.). The specimen is marked using a dual point scribe tool with a 0.032 in (0.81 mm) total spacing with the EDM notch located in the middle of the two scribe marks. These marks are used to locate the potential lead attachments. Installation of the current source leads and sensing leads for the electrical potential drop (EPD) monitoring is accomplished using capacitance welding. The sensing leads are located within 0.025 mm of the scribe marks. The current leads are capable of handling the current required to provide the proper voltage across the sensing leads (200 to 300 μV) and placed to provide an uninterrupted current path through the notched test area where the sensing leads have been placed. Current leads are typically made of copper wire. The sensing leads will be of a highly conductive material (Alumel or platinum) capable of withstanding, without physical or electrical property change, the time and temperature requirements of the test including heat tinting or other benchmarking method used to define the fatigue crack location at specified cycle intervals. The sensing leads are placed above and below the notch on the scribe marks provided and measured to three places from the center to center of the attachment tack welds. Both current and sensing leads should be fastened in a low stress area to prevent accidental breakage during specimen loading.

Pretest EPD Stability Check

After the specimen has been installed in the test frame using the lab's standard procedures and the EPD current source and monitoring system leads have been attached, the specimen is brought to the test temperature. Once the specimen reaches test temperature the specimen is cycled from 0 to 7 mPa (0 to 1 ksi) in load control at 20 to 30 cpm for 1 h prior to testing. The pre-test's recorded data are block averaged to provide data at a 20-cycle block interval. The data from this pre-test indicates the setup's ability to meet the stability requirements of the lesser of 1% of the acquired average potential voltage difference (VDA) or 2 μm of potential voltage. If the setup is not capable of meeting the stability check, the cause must be determined, repaired, and checked again before proceeding to test.

Pre-Cracking

The test bar is pre-cracked prior to undergoing the test. Pre-cracking conditions are typically done at ambient air temperature. Pre-cracking may occur at other temperatures if room temperature crack growth is difficult to control. No thermocouple attachment should be made prior to the completion of the pre-crack as the precrack cycling may result in crack initiation from the weld pool associated with the thermocouple attachment, thus voiding the experiment. The pre-crack is generated in load control with constant cyclic stress intensity. This is accomplished via a closed loop test system that calculates the crack length and then decreases the load range to maintain a constant cyclic stress intensity. The constant stress

intensity range used during pre-crack is also the initial stress intensity range at the start of the threshold test.

Instrumentation for Temperature

Upon the completion of the pre-crack the specimen is instrumented for temperature monitoring. Presently, only two methods for temperature measurement are acceptable. The first method, the preferred method, is direct thermocouple attachment tack welded directly behind the sensing lead welds making sure not to contact the sensing leads. The second method is identical to a method used in LCF testing with induction heating. The method uses a representative bar with thermocouples spaced evenly throughout the gage section and radii to map thermal gradients throughout the specimen providing a pair of control locations (top and bottom) whose temperatures are within 10% or 100° (the lesser of the two) of the notch temperature. These control locations are located in a lower stress area on the specimens such as the shank-radius interface.

Crack Front Marking Procedure

The schedule for benchmarking the crack front will be provided by the requesting engineer and are specific for each material and test temperature used. The standard procedure for Region II crack growth consists of a series of three to four heat tints applied at zero load at specified renormalized voltages. Threshold tests are heat tinted only at threshold to mark the crack size at threshold. A heat-tinting schedule for a material is based on the knowledge of the pre-conditioning of the material and past heat tinting experience. The temperature and duration of the heat tint is varied to produce a distinguishable marking at the conclusion of the cracking segment. The time and temperatures required to develop the heat tints has to be developed for each new material, but once established can easily be used on similar materials. Another means of marking the crack front is the change in the fractography of the crack plane. Through experience it was known that the 10 Hz frequency used during pre-cracking out of the EDM starter notch would provide an unique marking of the crack front as compared to the other segments so no heat tint was used following the initial pre-crack. There are many possible heat tint schedules, but a typical schedule is presented in Table 2. The heat tints are typically applied at the minimum load in the cycle. The tints are

TABLE 2—*Recommended heat tint schedules for a titanium alloy and a nickel base alloy.*

Ti-6Al-4V Alloy			
Test Temperature	Mode	Tint Temperature	Tint Duration
Ambient	Pre-crack	none	
Ambient	K decreasing	371°C	4 h
Ambient	K increasing	343°C	2 h
KM4—PM Nickel Base Superalloy			
Test Temperature	Mode	Tint Temperature	Tint Duration
Ambient	Pre-crack	none	
371°C	K decreasing	650°C	4 h
371°C	K increasing	650°C	2 h

applied after threshold is achieved to allow a determination of crack dimensions at threshold and again at the end of the K increasing segment of the test to allow an accurate determination of crack dimensions at the end of the test. In the case of the crack shown in Fig. 4 a 1 h tint at a higher temperature of 427°F was employed. The heat tint was only performed at the end of the K decreasing segment for this test.

Post Test Crack Length Measurement

Following completion of the test, the actual crack length and aspect ratio can be measured from the failed specimen using the heat tint applied during the running of the test. Figure 4 is a fractograph showing a Ti-6Al-4V specimen. The heat-tinted fracture surface can be used to determine the precise size and shape of the crack at the cycle count and voltage potential at the point where the tint was conducted. This information is used to correct the potential drop measurement results to allow for changes in crack shape that may have occurred during the test. Potential difference calculations typically assume that shape is maintained constant throughout a test, but this is rarely observed. The shape information is required to posttest correct the crack depth and surface lengths based on the measured sizes made possible by the periodic marking of the crack via the heat tints.

Data Analysis

Following the completion of the test a relationship between measured potential and crack length is determined using the information on crack size obtained from the heat tints. The actual procedure is detailed in a paper by Gangloff [*3*]. The stress intensity is calculated using a relationship developed by Newman and Raju [*5*].

When starting a test program is often saves both time and specimens if the planned tests are simulated. A simple spreadsheet can be constructed that calculates the crack size versus cycle count given the initial stress intensity range, initial crack size, and shed rate to be used during the planned test. This will ensure that the test conditions selected will in fact allow the test system to shed to threshold before the crack size exceeds the specimen size. This is

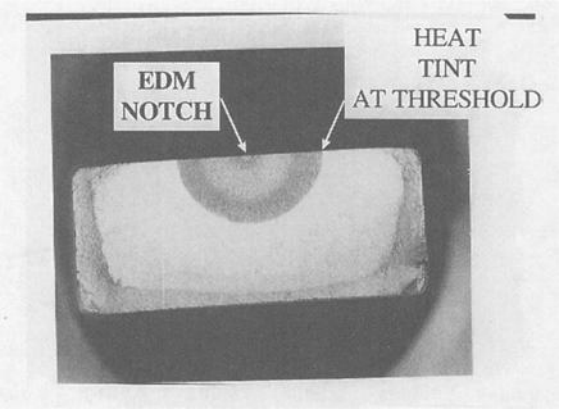


FIG. 4—*Typical fracture surface of a room temperature threshold test conducted in air using the Kb-bar specimen in Fig. 1. This heat tint was performed at 427°C, for 1 h once the crack had stopped at threshold, allowing a precise measurement of final crack length and aspect ratio for calculating threshold stress intensity factor.*

a particular worry for tests with a high mean stress. The results of such a simulation are shown in Fig. 5. These test results indicate that threshold should be obtained before the crack reaches a depth of 1.25 mm (0.05 in.) for the test conditions selected for that test. The analysis of the test results once the crack depth (a) versus cycles (N) relationship and stress intensity calculations are made is identical to that recommended in ASTM E 647.

Initial Test Results

Shed Rate Effects on Threshold

The shed rate recommended in ASTM E 647 is $C = -79\ m^{-1}$. The very gradual shed recommended in ASTM E 647 cannot be used with the surface flaw specimen geometry. Reasonable-size specimens are not physically large enough to allow the stress intensity factor to be shed at this rate to threshold before the crack would break through the back face of the rectangular specimen. Larger specimen sizes that would allow the use of a slow shed rate would require tremendous loads to be applied to the specimen due to the increased area of the specimen.

The recommendation for a shed rate of $-79\ m^{-1}$ was developed for use on all materials including relatively low-strength aluminum alloys. High-strength turbine disk materials such as Ti-6Al-4V or nickel-base superalloys have yield strength values three or four times greater than common aluminum alloys and therefore have a much smaller plastic zone at the tip of the crack. The smaller plastic zone size should allow a much faster shed rate to be used without prematurely retarding the crack growth that would result in a false high threshold determination. Experiments using shed rates from $C = -295\ m^{-1}$ to $C = -1181\ m^{-1}$ were conducted on Ti-6Al-4V titanium alloy. The results are shown in Fig. 6. The threshold measured was similar to that obtained using a compact tension specimen with a shed rate

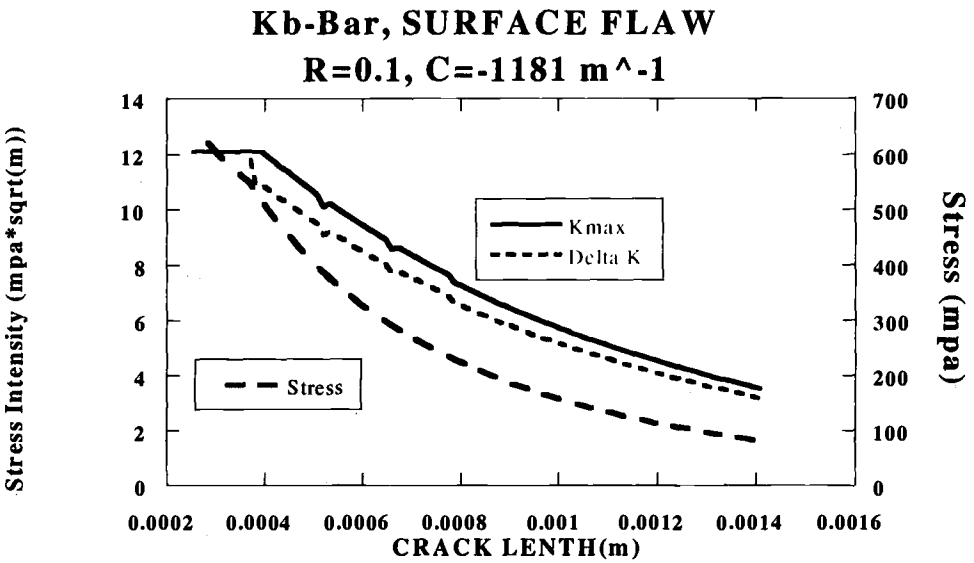


FIG. 5—*Before beginning a test, it is best to simulate the test via a spreadsheet program or similar analytical method. Threshold was obtained at a cyclic stress intensity of 4 ksi$\sqrt{in.}$ (4.4 mPa$\sqrt{m}$) or a crack length of 1.25 mm (0.05 in.).*

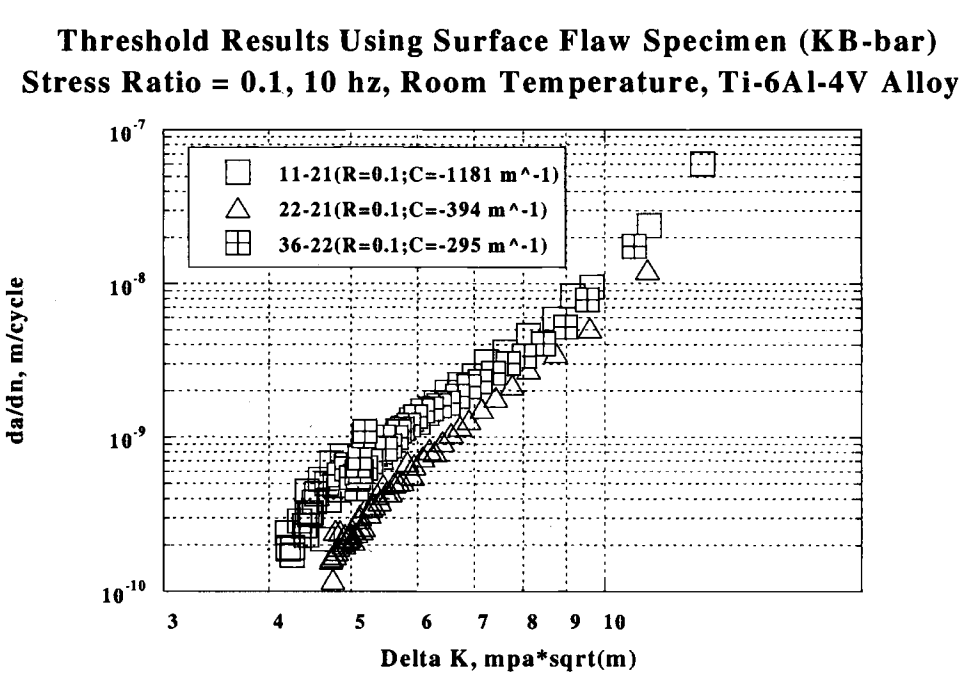


FIG. 6—*A study of the effect of shed rate on observed threshold indicated that shed rate up to* C = $-1181\ m^{-1}$ *was still producing valid threshold values. Threshold occurred between 4.2 mPa*$\sqrt{m}$ *for the fastest shed rate (Specimen 11-21) and 5.0 mPa*$\sqrt{m}$ *for the slowest shed rate (Specimen 36-22).*

of $C = -79\ m^{-1}$ as reported by Sheldon et al. [*1*]. Attempts to use lower shed rates at high *R* ratios were unsuccessful in achieving threshold before the crack began to break through the backface of the specimen. A typical result for a stress ratio of 0.8 series of experiments is shown in Fig. 7.

Effect of Grain Size on Threshold

The surface flaw test procedure was also used to measure threshold stress intensity values for crack growth on an experimental high-strength superalloy, KM4, at elevated temperatures. These tests were conducted as part of the NASA Enabling Propulsion Materials contract. KM4 is a nickel-base superalloy produced via powder metallurgy processes and was developed for advanced turbine disk applications. Results were obtained for alloy processed to produce either a fine grain size (ASTM grain size 10 to 12) or a coarse grain size (ASTM grain size 5 to 6). The results are shown in Fig. 8. The results indicated that increasing grain size (open symbols in Fig. 8) increases the threshold for Alloy KM4.

Statistical Review of Specimen Geometry on Threshold

Results on Ti-6Al-4V titanium alloy when tested at room temperature at a variety of stress ratios and using several different specimen geometries were compared statistically, and the results are presented in Table 3. The lower average threshold value of the surface flaw specimen (Kb-bar) is statistically significant based on a T-test of the means at a 0.05 level of significance.

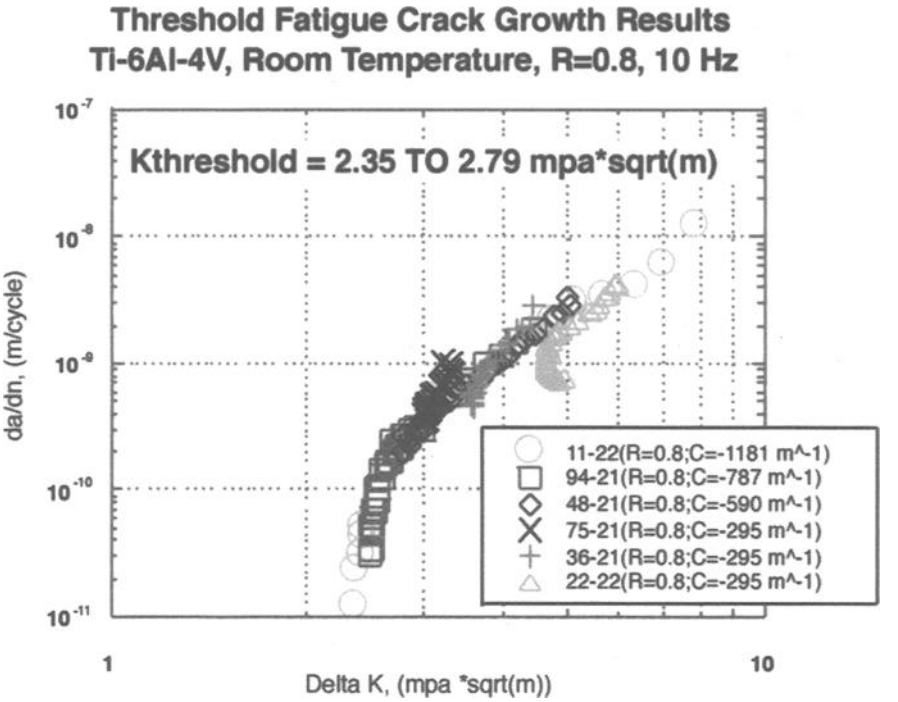


FIG. 7—*The need for a high shed rate is shown in the results gathered on a Ti-6Al-4V tested stress ratio of 0.8. The tests conducted at a lower shed rate of −295 m^{-1} could not be shed to threshold before the crack length became excessive. Tests conducted at −1181 m^{-1} shed rate did achieve threshold.*

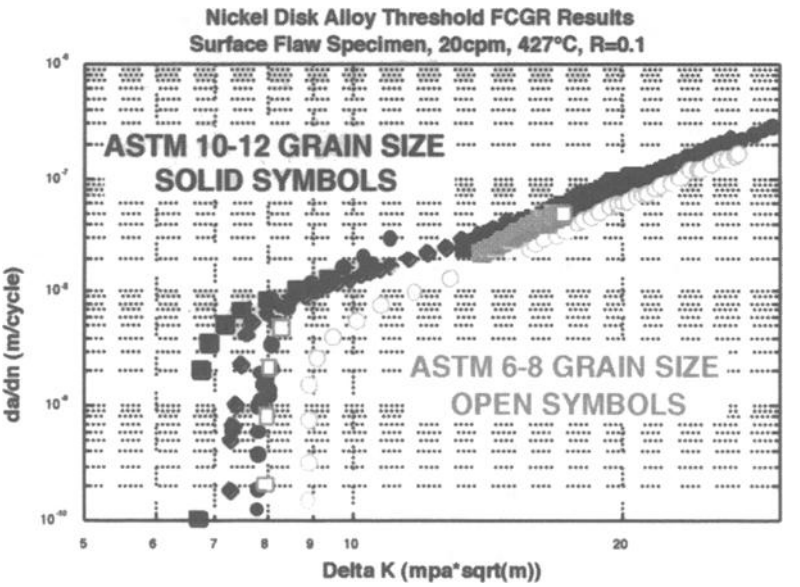


FIG. 8—*Threshold test results for a nickel-base alloy. Coarse grain size appears to increase threshold.*

TABLE 3—*Comparison of threshold results on Ti-6Al-4V alloy at room temperature using three different specimen configurations at a stress ratio of 0.10.*

Specimen Type	Range of Shed Rate, C (m^{-1})	Number of Tests	Low Value mPa*$\sqrt{m}$	High Value mPa*$\sqrt{m}$	Average mPa*$\sqrt{m}$	−3 Standard Deviation Minimum, mPa*$\sqrt{m}$
Single edge notch	−1181	13	3.83	5.98	4.58	3.18
Compact tension	−236 to −1181	11	4.14	5.34	4.70	3.67
Kb-BAR	−295 to −1181	5	3.87	4.60	4.23	3.46

The Kb-Bar surface flaw specimen with a shed rate of $C = -1181$ m^{-1} results has similar scatter and observed threshold results as compared to those obtained using either compact tension or single-edge-notched specimens. The use of higher shed rates does result in a faster determination of threshold.

Concluding Remarks

The surface flaw threshold specimen has many advantages over more commonly used specimen geometries when determining the threshold stress intensity for fatigue crack growth. It better simulates the small crack size, loading, and constraint experienced by cracks naturally initiated on modern turbine components. The thresholds obtained are typically 5 to 10% lower (see Table 3) than those obtained using specimen configurations that require longer fatigue cracks such as those on compact tension specimens or single-edge-notched specimens.

The technique requires the use of aggressive load shed rates to achieve threshold before breaking through the back face of the specimen. This is especially true for testing with a high mean stress. Testing has shown that for a high-strength nickel disk alloy and high-strength titanium alloy the shed constant C can be as severe as -1181 m^{-1}. This is far steeper than the -79 m^{-1} value recommended in ASTM E 647, and review of this requirement should be undertaken for high-strength alloys.

Acknowledgments

The authors would like to thank GE Aircraft Engines, the Air Force, for support from the High Cycle Fatigue Initiative (Air Force Contract 33615-96-C-5269), and NASA for support from the Enabling Propulsion Material Program (Contract NAS3-26385). In addition, the authors would like to thank Dr. Robert VanStone and Barney Lawless for their support and discussions throughout the development of this new threshold test procedure.

References

[*1*] Sheldon, J., Brain, K. R., and Donald J. K., "Investigation of the Effects of Shed-rate, Initial Kmax, and Geometric Constraint on ΔKth in Ti-6Al-4V at Room Temperature," *International Journal of Fatigue,* Vol. 21, No. 7, 1999, pp. 733–741.

[*2*] VanStone, R. H. and Richardson, T. L., "Potential-Drop Monitoring of Cracks in Surface-Flawed Specimens," *ASTM STP 877,* 1985, pp. 148–166.

[3] Gangloff, R. P., "Electrical Potential Monitoring of Crack Formation and Subcritical Growth of Small Defects," *Fatigue and Engineering Materials and Structures,* Vol. 4, No. 1, 1981, pp. 15–33.
[4] ASTM Specification E 647, "Standard Test Method for Measurement of Fatigue Crack Growth Rates," *ASTM Standards and Specifications Volume 3.01.*
[5] Newman, J. C. and Raju, I. S., "Analysis of Surface Cracks in Finite Plates Under Tension or Bending Loads," NASA TP 1578, 1979.

Yoshio Kitsunai,[1] *Yutaka Maeda,*[2] *Etsuji Yoshihisa,*[2] *Takashi Honda,*[2] *and S. Ganesh Sundara Raman*[2]

Fatigue Strength of Weld Repair Specimens Under Simulated Program Loading of an Overhead Traveling Crane

REFERENCE: Kitsunai, Y., Maeda, Y., Yoshihisa, E., Honda, T., and Sundara Raman S. G., **"Fatique Strength of Weld Repair Specimens Under Simulated Program Loading of an Overhead Traveling Crane,"** *Fatigue and Fracture Mechanics: 31st Volume, ASTM STP 1389,* G. R. Halford and J. P. Gallagher, Eds., American Society for Testing and Materials, West Conchohocken, PA, 2000, pp. 457–474.

ABSTRACT: Service stresses acting on an overhead traveling crane were monitored and analyzed by the rain flow method. To assess the effectiveness of various repair schemes for components of aged overhead traveling cranes, weld-repaired gusset specimens, several kinds of plate specimens with cracks repaired by welding, and cover plate specimens were fabricated, and the fatigue strength of the weld-repaired specimens was evaluated under a program loading determined from the monitored service stresses. The fatigue strength of weld-repaired gusset plate specimens was approximately the same as that of uncracked gusset plate specimens, because the fatigue crack always initiated from the weld toe of the as-welded side in both specimens. The fatigue strength of one-surface repaired specimens decreased with an increase in the initial crack length. In case of one-surface repaired specimens with the initial crack length beyond half of the specimen width and one-surface cover plate specimens, the fatigue strength did not satisfy the design requirement. On the other hand, the specimens with cracks repaired completely by welding on both surfaces displayed sufficient fatigue strength to satisfy the requirement. The fatigue crack growth rate of the weld-repaired gusset specimens under the program loading was correlated with an effective stress intensity factor range, which considered the effect of residual stresses.

KEYWORDS: weld repair, fatigue strength, crack growth, overhead traveling crane, program loading, stress concentration, residual stress, fracture mechanics, effective stress intensity factor

Fatigue life of overhead traveling cranes in Japan has generally been designed as 2×10^6 cycles. Recently, some cranes have been used beyond the designed operation ratio because of demands of increasing transportation quantities. As a result, fatigue cracks are sometimes found in highly stressed regions, such as a weld toe of a gusset plate and a cover plate, and occasionally lead to serious accidents such as collapse of cranes. According to our survey on the degradation of overhead traveling cranes, fatigue cracks begin to appear after five years of service, and half of the cranes surveyed were found to have some damage after 15 years of service [*1*]. Hence, to maintain the integrity of cranes throughout their service lives, it is necessary to establish rational methods of maintenance as well as design. From historical background, specifications or standards of maintenance and reinforcement for highway

[1] Research engineer, Japan Crane Association, 1-13-12 Higashi-Gotanda, Shinagawa-ku, Tokyo 141-0022, Japan.
[2] Researcher, National Institute of Industrial Safety, 1-4-6 Umezono, Kiyose, Tokyo 204-0024, Japan.

Copyright© 2000 by ASTM International www.astm.org

bridges and railway bridges have been established already and applied to components of the structures [2–5]. Studies on the maintenance of cranes, however, have been limited [6–8], in spite of an increasing number of aged cranes. When a crack is found in a structural member of a crane, welding has often been applied to repair the crack because of ease of handling. The repair job for cranes often demands the work to be done at a narrow place or a high location under insufficient lighting, so that welding defects are sometimes introduced during the operation. Moreover, inadequate weld repair may lead to a significant reduction in the remaining fatigue life of the components. Therefore, a minimum requirement for the quality of the repair welding is necessary. However, the influence of the weld repair method on the fatigue strength of cranes is not fully understood. In order to get a reliable estimate on the fatigue life of the repaired crane components, the loads used in laboratory tests should simulate the actual service loads acting on the crane as closely as possible.

In this study, the monitoring of stresses acting on the components in an overhead traveling crane was carried out to determine the test loading. To assess the effectiveness of various repair schemes for damages in overhead traveling cranes, fatigue tests on several kinds of specimens with artificial cracks repaired by welding were carried out under a program loading that was determined based on the monitored service load history of the crane.

Monitoring of Service Loading of an Overhead Traveling Crane and Determination of Testing Load

To determine the testing load, monitoring of service stresses of an overhead traveling crane was carried out. The overhead traveling crane used was of a conventional pipe structure, as shown in Fig. 1. The specifications of the overhead traveling crane were: a maximum hoisting load of 50 kN, a crane span of 16.3 m, and a crab trolley wheel base of 3.25 m. The stress measurement was carried out using strain gages pasted on the selected components of the crane. The rain flow method was applied as a stress-counting technique. The stresses acting on a crane are dependent on the hoisting load, movement of the load, and the operation rate of the crane. A 50-kN weight corresponding to the rated load of the crane was used during the stress measurement. The typical movement of the crane was as follows: the test weight was hoisted by a crab trolley at one end of the crane span, the trolley traversed from one side to the opposite side of the span, then the crane traveled approximately 20 m on the runway girder, subsequently returned to the starting position retracing its original route, and the weight was lowered. This sequential movement of the crane was repeated 20 times during

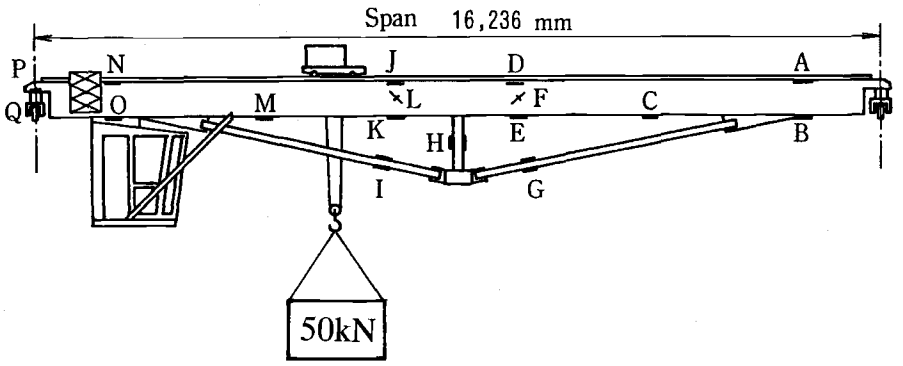


FIG. 1—*Overhead traveling crane used to monitor service loading.*

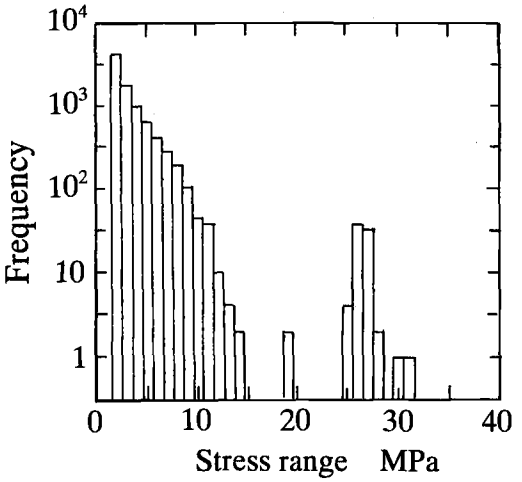


FIG. 2—*Histogram of stress range for a component of crane.*

the test. Figure 2 shows a histogram of stress range measured at Location *G* in Fig. 1, which recorded the highest stress range in the crane. It can be seen in the figure that relatively low stress ranges below 15 MPa occupied a major portion of the histogram. The program block loading was determined based on the histogram of stress range acting on the crane girder. Stress ranges below 20 MPa, which had a high frequency of occurrence in the histogram, were neglected because of their insignificant influence on the fatigue strength and to achieve high efficiency of the fatigue tests. This cut-off level was chosen merely as a matter of judgment. Therefore, the Weibull distribution was applied for the stress ranges above 20 MPa in the histogram. The result is given by:

$$f(x) = 0.219\ (x - 25)^{1.41}\ e^{-\frac{(x-25)^{2.42}}{11.07}} \tag{1}$$

where $f(x)$ is the cumulative frequency distribution of the stress range, and x is the stress range.

From Eq 1, a testing program load, which is composed of five steps in one block, was determined. The total number of steps in one block was 100 cycles, based on an average operation rate of an overhead traveling crane per day in steelworks. The ratio between stress range in each step, $\Delta\sigma_i$, and the maximum stress range in a block, $\Delta\sigma_{max}$, and the number of elapsed cycles at each step, n_i, are given in Table 1.

TABLE 1—*Program loading used in fatigue tests.*

Step No.	$\Delta\sigma_i/\Delta\sigma_{max}$	n_i
1	0.846	34
2	0.884	41
3	0.923	19
4	0.961	5
5	1.000	1

Material and Specimens

The material used in this study was JIS SB410 steel plate. The mechanical properties of the material used were: a yield strength of 333 MPa, a tensile strength of 461 MPa, and an elongation of 29%. Gusset plate specimens [see Fig. 3*a*] were fabricated as basic specimens, because fatigue cracks often tend to initiate from weld toes of gusset plates in a crane. They will be referred to as Type A specimens. In some gusset plate specimens, an artificial crack of approximately 30 mm in length was introduced at one of four weld toes of gusset welds using a handsaw, and, subsequently, the crack was filled with weld metal, as shown in Fig. 3*b*. These weld-repaired gusset specimens will be referred to as Type B specimens. Plate specimens were introduced with a saw cut crack 10 or 50 mm in length in the width direction at the center, and the crack was repaired on one surface or both surfaces by welding [Fig. 4*a*, 4*b*, and 4*c*]. The specimens with 10-mm-long crack repaired on one surface, 50-mm-long crack repaired on one surface, and 50-mm-long crack repaired on both surfaces will be

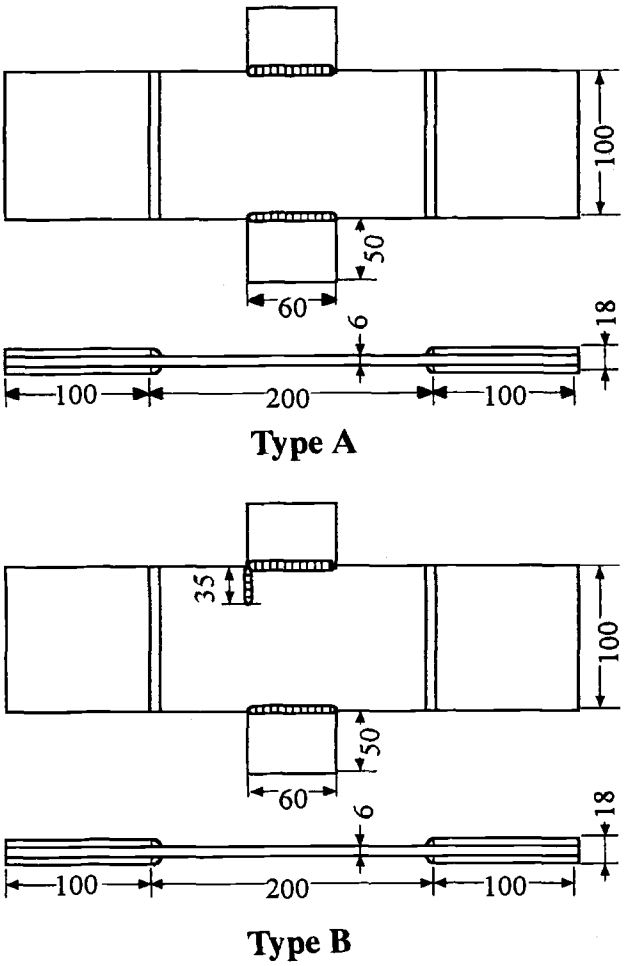


FIG. 3—*Gusset specimen and weld-repaired gusset specimen:* (a) *Type A specimen;* (b) *Type B specimen.*

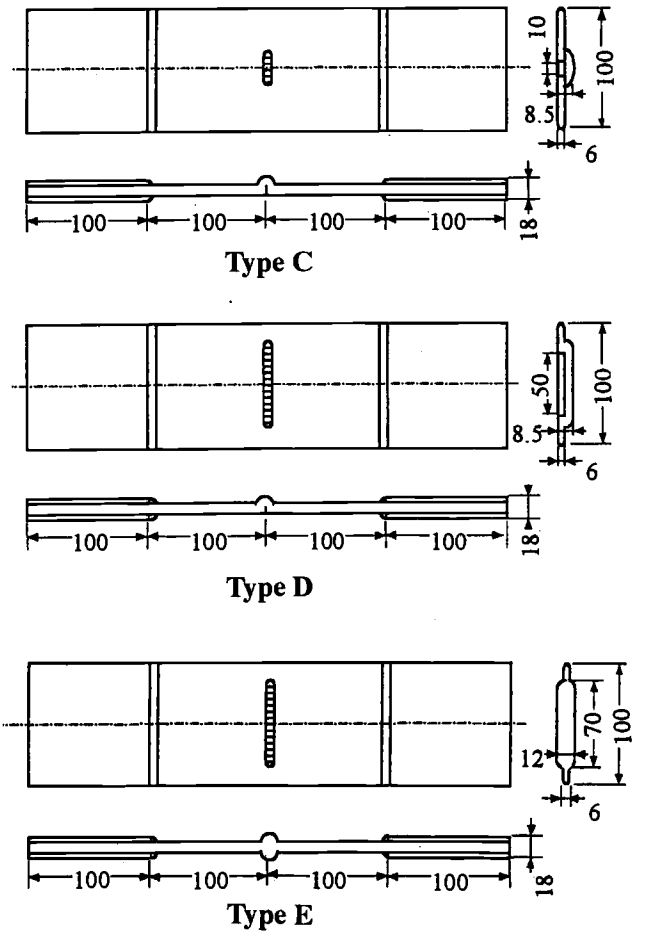


FIG. 4—*Configurations of weld-repaired specimens:* (a) *Type C specimen;* (b) *Type D specimen;* (c) *Type E specimen;* (d) *Type F specimen;* (e) *Type G specimen.*

referred to as Types C, D, and E, respectively. The Type C and D specimens had a surface crack on the non-repair side, while the Type E specimen did not have a crack because an artificial crack in the specimen was repaired completely from both surfaces by welding. Also, two types of cover plate specimens as shown in Figs. 4*d* and 4*e* were prepared. These specimens will be referred to as Types F and G.

The welding was done manually using covered electrodes of 4-mm diameter corresponding to JIS D4326. The main welding parameters were: a welding current of 160 A, an arc voltage of 25 V, a heat input of about 12 kJ/cm, and a flat welding position.

Stress Distributions and Profiles near the Weld Toe of Specimens

The stress concentration factor, K_t, of the gusset specimens (Type A) was examined using strain gages pasted near welds of the specimens. An average value of K_t was found around 2.1. A dental mold method was applied to assess the profiles of weld toes of the gusset

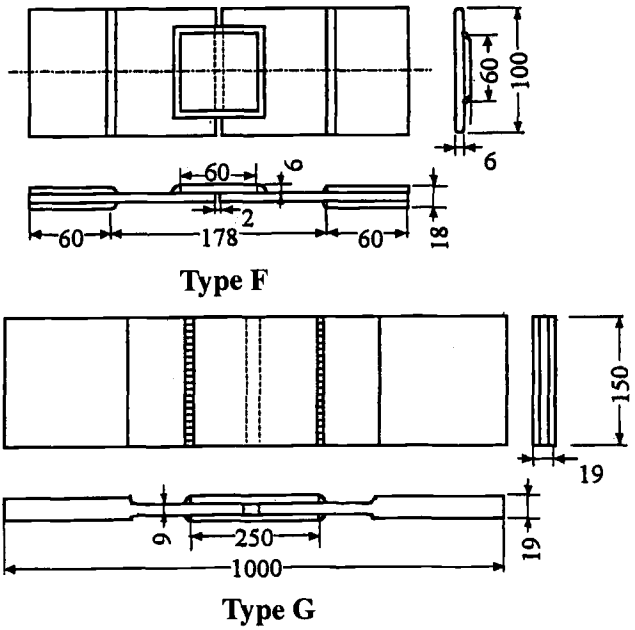


FIG. 4—*Continued.*

specimens (Type A) and weld-repaired gusset specimens (Type B). The molds of the specimens were examined by an inspection projector of 10 magnification, and the radius of curvature at the weld toe, ρ, and the tangent angle, θ, were determined. A considerable scatter was found in the result, as shown in Fig. 5. In the case of the Type B specimen, the average value of ρ and θ of the weld-repaired side was 2.2 mm and 33.3°, respectively. The stress distributions near the weld toe of the weld-repaired side and that of the as-welded side in a Type B specimen were examined using an infrared stress analysis technique [*9*]. As can be seen in Fig. 6, the stress on the as-welded side was higher than that of the repair-welded side. This result may be explained by the fact that the curvature of the weld toe became larger and the thickness of the plate near the weld toe increased partially, because the artificial crack was covered by molten weld metal.

Residual Stresses in Weld-Repaired Specimens

The residual stresses in weld-repaired specimens were measured by an X-ray diffractometer with a chromium X-ray tube. The value of residual stress was determined by the $\sin^2 \psi$ method. The experimental conditions for the residual stress measurement were: a characteristic X-ray of CrKα, a diffraction plane of (211), a vanadium filter, a tube voltage of 30 kV, a tube current of 10 mA, and an irradiated area of 3×3 mm^2. Figure 7 shows the distribution of longitudinal residual stress, in the direction of the externally applied load, measured in the width direction of a Type B specimen. The residual stresses on the as-welded side (non-repaired side) shown in Fig. 7*a* were almost symmetrical with respect to the center of the specimen width. Tensile residual stresses existed on both sides of the specimen, whereas compressive residual stresses existed in the neighborhood of the middle

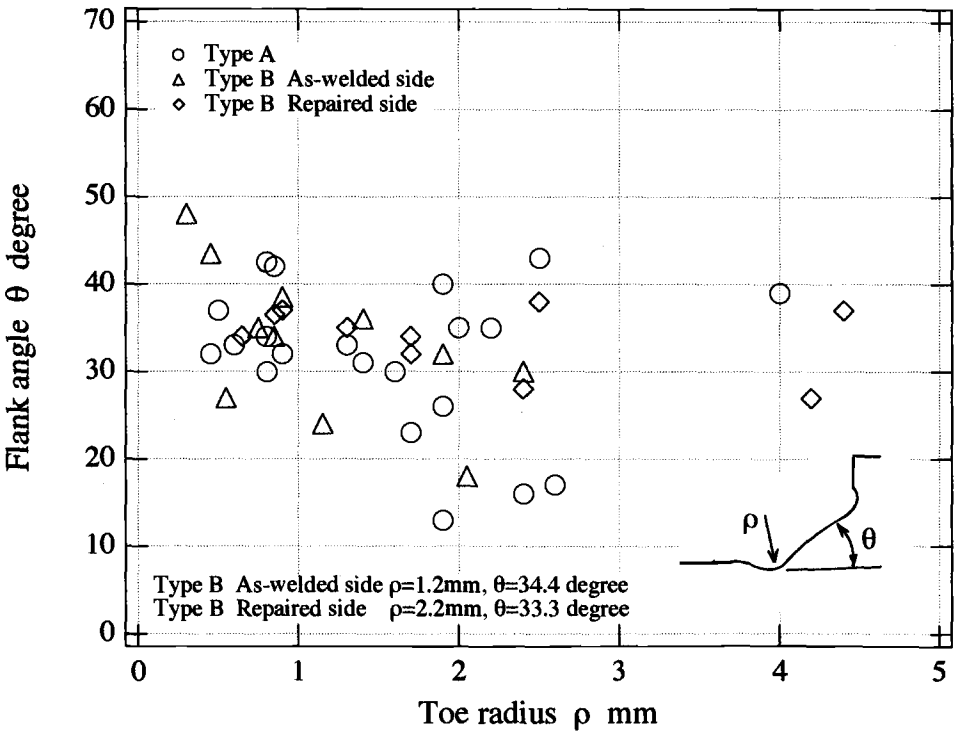


FIG. 5—*Distribution of toe angle and toe radius for gusset specimen.*

part of the width of the specimen. In the case of the weld-repaired side as shown in Fig. 7*b*, considerably complex residual stress distributions were found because of an interaction between longitudinal residual stress resulting from welding of gusset and horizontal residual stress in the specimen's width direction, resulting from repair welding of the crack. The circular symbol in Fig. 7 corresponds to the data obtained on the front surface (Side A) of the specimen, whereas the triangular symbol represents the data obtained on the opposite surface (Side B). Figure 8 shows the residual stress distributions of one-surface weld-repaired plate specimens (Types C and D). Comparing residual stresses between a Type C specimen with an initial artificial crack length of 10 mm and a Type D specimen with a crack length of 50 mm, higher residual stresses were found in the Type C specimen. This difference may be associated with the magnitude of restraint of thermal strain resulting from the repair welding. Comparing the magnitude of residual stresses between the repaired side and the non-repaired side in the Type C and Type D specimens, higher tensile residual stresses existed near the tip of the artificial crack of the non-repaired side of the specimens. This discrepancy is related to the difference in the thermal transfer of welding heat between the non-repaired side and repaired side. This result suggests that higher residual stresses are generated on the non-repaired side with a crack when the weld repair is performed on one surface alone. From the above result, it may be said that the repair of one surface is an inadequate repair method due to high residual stresses and high stress concentration existing on the non-repaired surface.

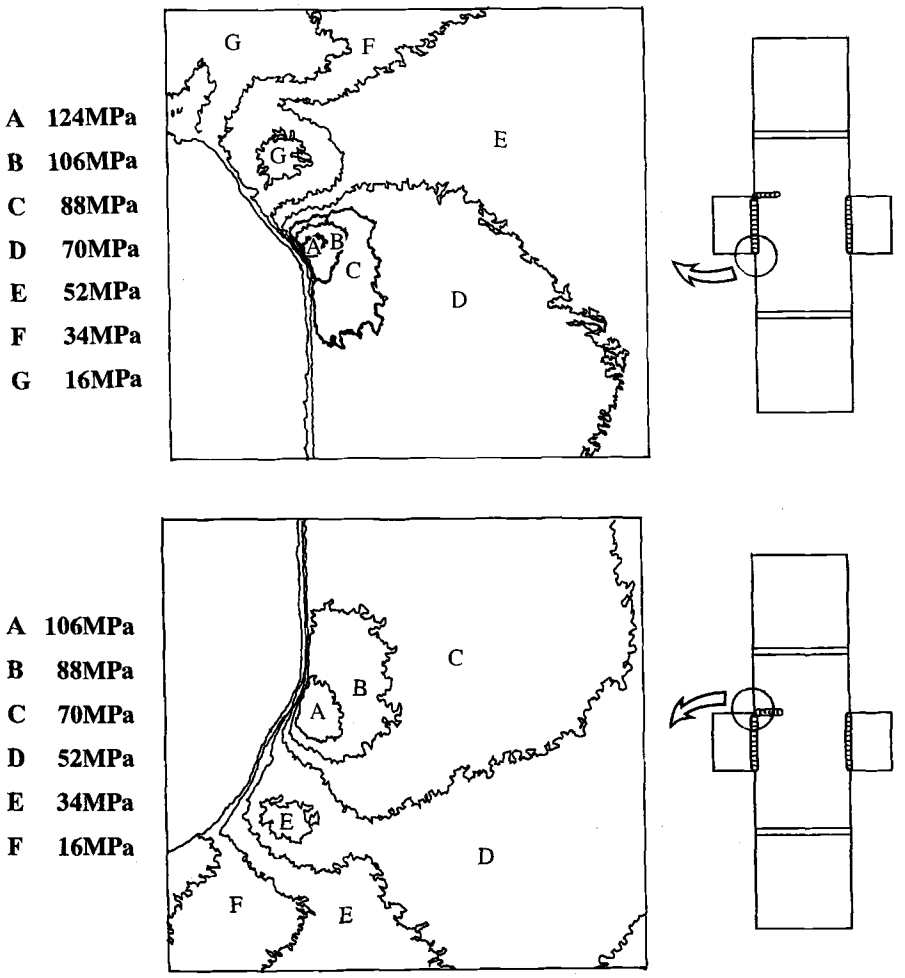


FIG. 6—*Comparison of stress distributions near weld toe as welded side and weld-repaired side in Type B specimen. Stress was measured by infrared method:* (a) *as welded side;* (b) *weld-repaired side.*

Fatigue Test Procedure

Fatigue tests under a program block loading shown in Table 1 and a constant loading were carried out using computer-controlled servohydraulic testing machines. A sinusoidal loading waveform with a stress ratio, R, of 0.05 was employed, and the test frequency was in the range from 0.5 to 10 Hz. The fatigue tests using the program loading were carried out under the load-increasing sequence. For the Type G specimen, constant loading tests were carried out at a stress ratio of 0.05 using a 1500-kN capacity servohydraulic testing machine.

Fatigue Strength of Weld Repaired Specimens

The results of fatigue tests on the Type A and Type B specimens under the program loading are shown in Fig. 9. The ordinate in the figure, $\Delta\sigma e$, is the equivalent stress range that is given by

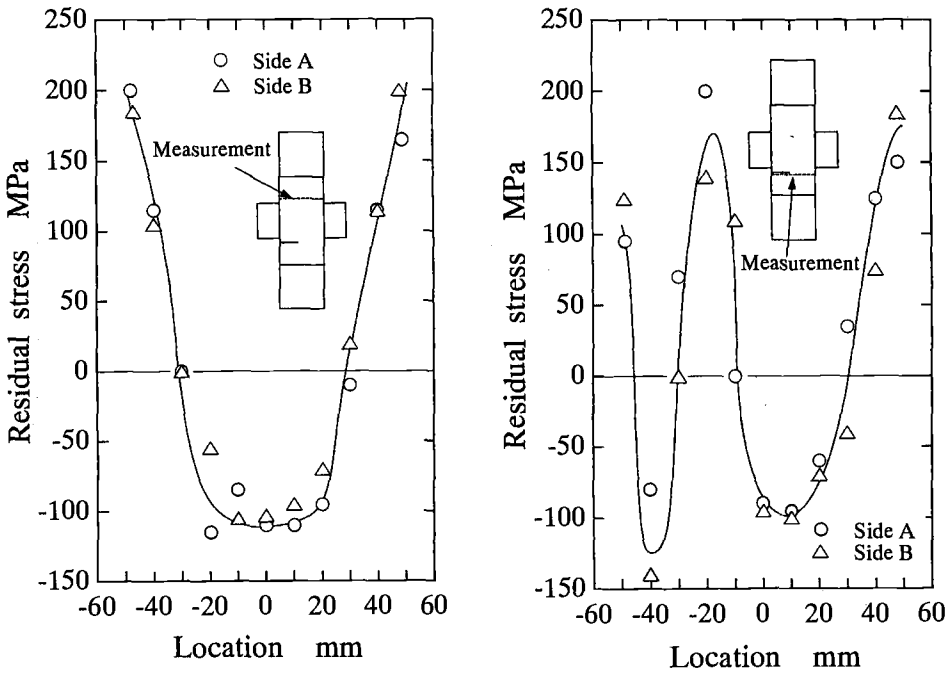


FIG. 7—*Residual stress distributions of Type B specimen:* (a) *as-welded side;* (b) *weld-repaired side.*

$$\Delta\sigma e = \left(\sum \Delta\sigma_i^q \frac{ni}{\sum ni}\right)^{1/q} \tag{2}$$

where q is a constant, $\Delta\sigma_i$ is the stress range in each step, and n_i the number of elapsed cycles in each step. The value of q was adopted as 3, with reference to a fatigue design recommendation proposed by JSSC [*10*]. The fatigue strength of welds in steel structures are classified depending on the constructional details. The fatigue design curve for the gusset plate that has been proposed by ISO 10721-1 [*11*] is also shown in Fig. 9. In this case, the fatigue strength corresponding to 2×10^6 cycles is 45 MPa.

There was not any appreciable difference between the lives of Type A and B specimens. This may be due to the fact that the fatigue crack always initiated from the weld toe of the as-welded side in both types of specimens. The fatigue crack did not initiate from the weld-repaired location in Type B specimens. This result can be explained by the fact that stress concentration and residual stresses at weld toe on the weld-repaired side were smaller than those on the as-welded side in Type B specimens. This was because of relaxation of residual stresses due to re-heating and reduction of stress concentration at the weld toe due to a decrease in the curvature of the weld toe resulting from weld repair. Both types of specimens satisfied the design requirement. The ratio between fatigue crack initiation life, N_c, and total fatigue life, N, for Type A and B specimens was in the range from 0.64 to 0.75. Hence, the crack initiation life rather than the crack propagation life dominated the fatigue life of the gusset-welded specimens with a K_t of around 2.1.

The results of fatigue tests on the Type C, D, E, and F specimens under the program loading and the Type G specimens under constant amplitude loading are shown in Fig. 10.

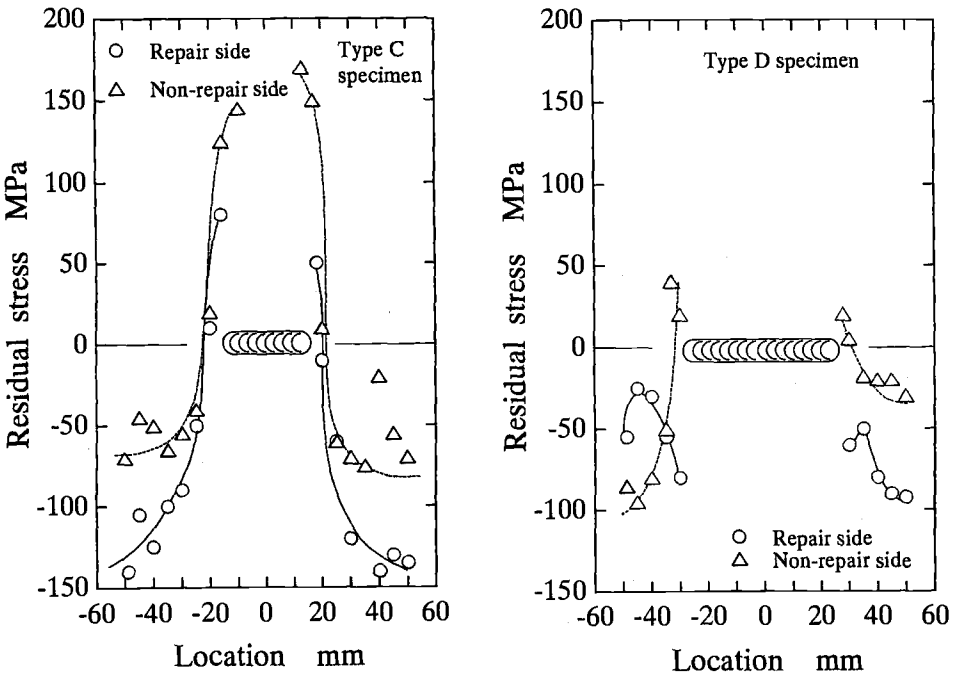


FIG. 8—*Comparison of residual stress distributions of weld repaired between Type C and Type D specimens:* (a) *Type C specimen;* (b) *Type D specimen.*

The best fit regression for N-$\Delta\sigma e$ relations of different types of the specimens is given in Table 2. The $\Delta\sigma e$-N curve of Type E specimens with crack repaired on both surfaces and Type C specimens with a relatively smaller crack repaired on one surface were well above the design curve shown in the figure. The design curve shows the lowest classification for the fatigue strength of crane components proposed by ISO 10721-1 [*11*]. Similarly, Type G specimens with cover plates welded on both surfaces tested under constant amplitude loading also satisfied the design requirement. In the case of Type D specimens with a long crack repaired on one surface, the data points were close to the design curve of the lowest classification. On the other hand, in the case of Type F specimens with a cover plate welded on one surface, the $\Delta\sigma e$-N curve was well below the design curve and hence failed to satisfy the design requirement. The fatigue strength of Type F specimens corresponding to 2×10^6 cycles was about 25 MPa against the lowest design value of 36 MPa, shown in ISO 10721-1 [*11*].

Figure 11 shows the stress sum contours of a Type F specimen determined by the infrared technique. As can be seen in the figure, the throat section of the fillet welds, which was the fatigue crack initiation site, was subjected simultaneously to both tension and bending. The maximum stress reached 250 MPa when a nominal stress range of 30 MPa was applied. From the present results it can be said that the weld repair method using a cover plate on one surface is not a suitable method for the crane components. When two types of specimens having the same initial crack length but different weld-repaired methods were compared in terms of the fatigue strength at 2×10^6 cycles, the fatigue strength of Type D specimens with crack repaired by welding on one surface was about one third of that of Type E

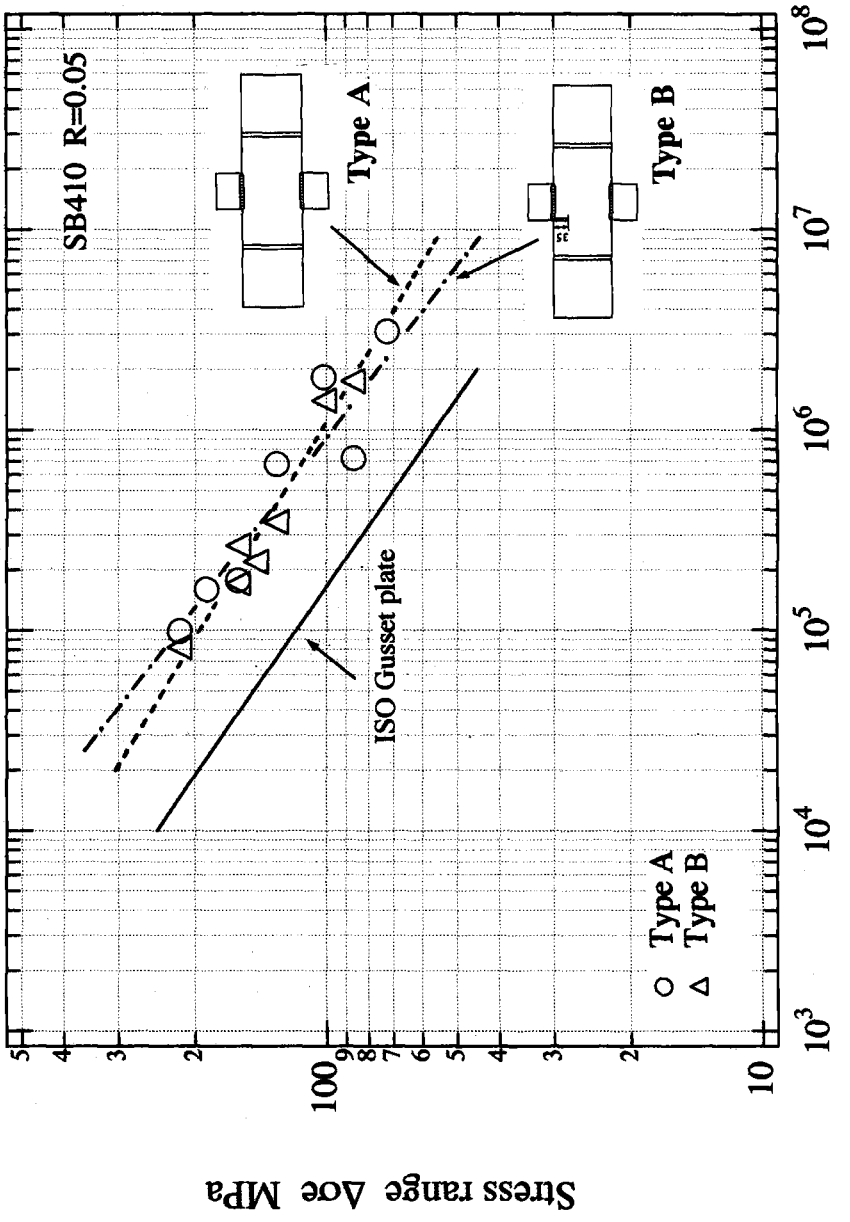


FIG. 9—*Comparison of fatigue strength between Type A and Type B gusset specimens.*

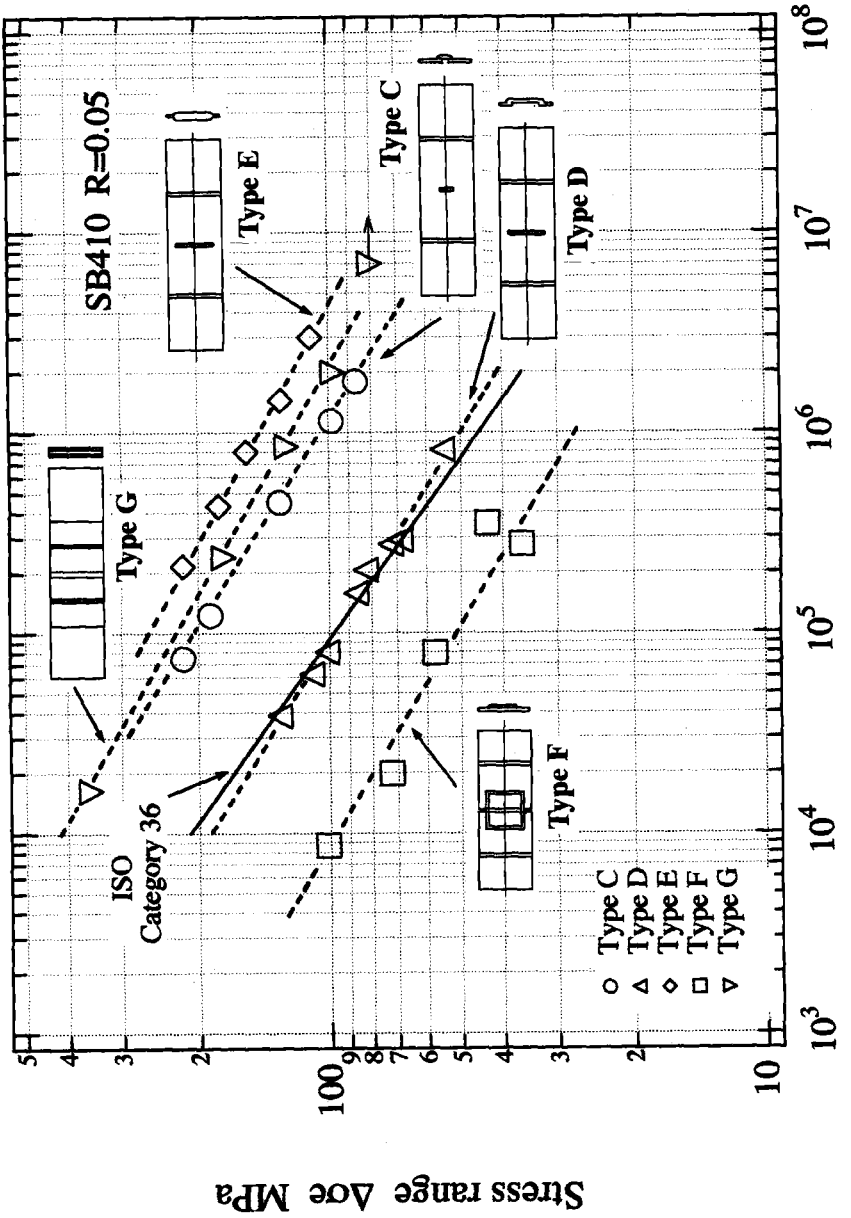


FIG. 10—*Relationship between weld-repaired method and fatigue strength.*

TABLE 2—*Regression constants for* N-$\Delta\sigma$e *relation* N-Q($\Delta\sigma$e)$^{\gamma}$.

Specimen Type	Q	γ
A	4.56×10^{11}	−2.84
B	1.68×10^{13}	−3.59
C	9.23×10^{12}	−3.46
D	1.02×10^{12}	−3.52
E	2.89×10^{14}	−3.92
F	2.29×10^{11}	−3.70
G	7.72×10^{13}	−3.78

specimens with crack repaired by welding on both surfaces. From the results obtained in the present investigation, it can be said that the one surface weld repair method may be employed only in case of crane components with short cracks. In case of crane components with cracks of length beyond half the plate width, both surface weld repair methods must be used to obtain satisfactory fatigue strength.

Fatigue Crack Growth Behavior

Figure 12 shows the relationship between the fatigue crack growth rate, da/dN, under the program loading and the stress intensity factor range, ΔK, for Type A and B specimens, da/dN was the average fatigue crack growth rate in one block of the program loading. ΔK was calculated from

$$\Delta K = \left(\sum \Delta K_i^m \frac{n_i}{\sum n_i} \right)^{1/m} \tag{3}$$

where ΔK_i is the stress intensity factor range in each step of a block of the program loading,

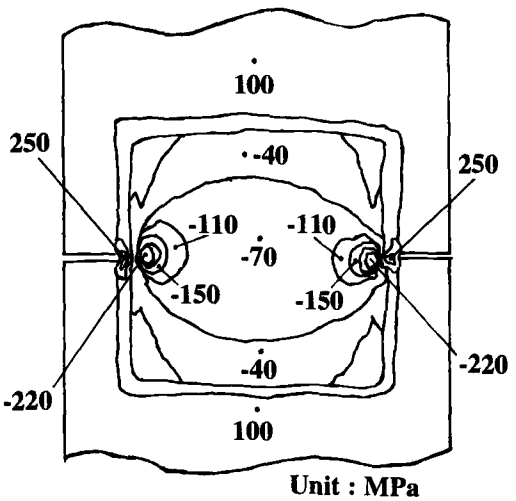


FIG. 11—*Stress distribution of Type F specimen (one-surface cover plate specimen) measured by infrared method.*

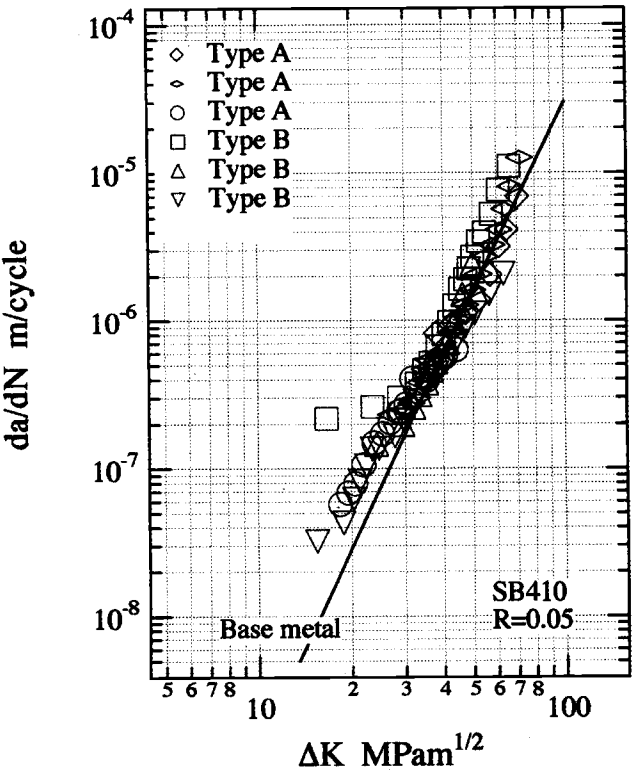


FIG. 12—*Relationship between* da/dN *and* ΔK for Type A and B specimens.

and m is a constant. The value of m adopted was 2.7, on the basis of the exponent of the da/dN-ΔK relation of the base metal under constant load. ΔK_i is given as [*10*]

$$\Delta K_i = M_k F_k \Delta\sigma_i \sqrt{\pi a}\, F(a/W) \tag{4}$$

where M_k is a shape parameter considering stress concentration, F_k is a constraint parameter, a is the crack length, and W is the width of the specimen.

As can be seen in Fig. 12, the da/dN of Type A and B specimens is slightly higher than that of the base metal shown by a solid line, because of the presence of tensile residual stresses near the gusset of Type A and B specimens. When a crack propagates in the residual stress field under a program loading, an effective stress intensity factor range that takes into account residual stress, ΔK_{eff}, is given by [*12*]:

$$\Delta K_{eff} = \left(\sum_{i=1}^{5} \Delta K_{ieff}^{m} \frac{n_i}{\sum n_i} \right)^{1/m} \tag{5}$$

where $\Delta K_{ieff} = K_{imax} - K_{op}$, K_{imax} is the maximum stress intensity factor considering the residual stress at each step, K_{op} is the crack opening stress intensity factor, and m is a constant. The K_{op} is given by

$$K_{op} = K_{imax} + K_{res} - (\gamma + \delta R_{ires}) \Delta K_i \quad (6)$$

where K_{res} is the stress intensity factor due to residual stresses, and γ and δ are constants given as 0.82 and 0.3, respectively, from crack closure measurement of the base metal [*1*]. R_{ires} is the stress ratio considering the residual stress at Step *i*. Detail has reported elsewhere [*1*].

The *da/dN* shown in Fig. 12 were replotted in Fig. 13 against the ΔK_{eff} expressed by Eq 5. As can be seen in the figure, the *da/dN* for the Type A and B specimens with residual stresses under the program loading were correlated closely with ΔK_{eff} and coincided with that for the base metal shown by a straight line. The best fit regression for $da/dN - \Delta K_{eff}$ in Fig. 13 is given by the following equation.

$$da/dN = 1.494 \times 10^{-13} (\Delta K_{eff})^{4.28} \quad (7)$$

In the case of Type C specimens with a surface crack, it was difficult to measure directly the crack depth during the fatigue crack growth. Therefore, in a Type C specimen beach marks were periodically pressed under constant amplitude loading. The fracture surface of the Type C specimen formed with beach marks is shown in Fig. 14. From the shape of the beach marks, the relationship between the surface crack length, 2*c*, and the crack depth, *a*,

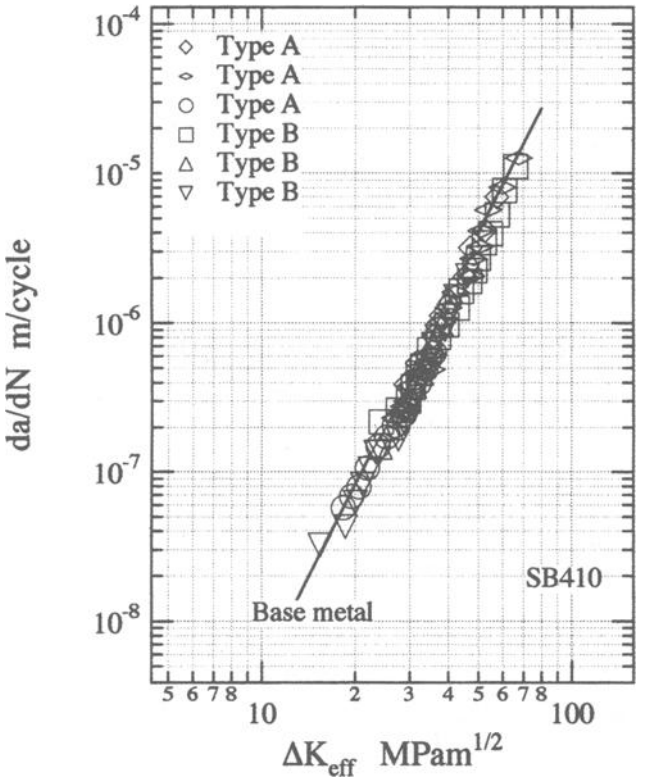


FIG. 13—*Relationship between* da/dN *and* ΔK_{eff} *for Type A and B specimens.*

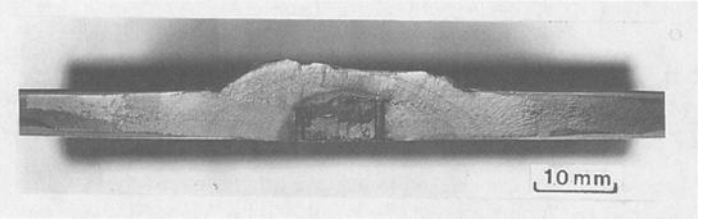


FIG. 14—*Fractograph showing beach marks formed on fracture surface of Type C specimen.*

was determined, and it is expressed by Eq 8. It was assumed that the same relationship will be valid for a Type C specimen under program loading, too. The ΔK for a surface crack is given by Eq 9 [*13*,*14*]:

$$a = 4.48 + 0.118(2c) \tag{8}$$

$$\Delta K = (\Delta\sigma_m + H\Delta\sigma_b)\sqrt{(\pi a/Q)} \cdot T \tag{9}$$

where: $\Delta\sigma_m$ is the membrane stress range; $\Delta\sigma_b$ is the bending stress range; H, Q, and F are correction factors depending on a, c, thickness, and distance to the nearest edge from the centerline of the crack.

Figure 15 shows the fatigue crack growth rate in the depth direction, da/dN, and surface crack growth rate, dc/dN, with ΔK of a Type C specimen. The dc/dN coincided with the crack growth rate of base metal, whereas the da/dN was slightly lower than the dc/dN. This difference may be due to error in crack depth measurement, deviation from the small-scale yielding condition, and the residual stress effect. However, the difference between both crack growth rates was not so significant. Hence, it may be possible to estimate the fatigue crack growth behavior of a component with a weld-repaired surface crack.

Conclusions

1. Comparing the magnitude of residual stresses between repaired side and non-repaired side in the one-surface weld-repaired specimens, higher tensile residual stresses existed near the tip of crack of the non-repaired side of the specimen.

2. The fatigue strength of weld-repaired gusset plate specimens (Type B) under the program loading was approximately the same as that of uncracked gusset plate specimens (Type A), because the fatigue crack always initiated from the weld toe of the as-welded side in both types of specimens. This result can be explained by the fact that stress concentration and residual stresses at the weld toe on the weld-repaired side were smaller than those on the as-welded side in weld-repaired gusset specimens.

3. When two types of specimens having the same initial crack length of about half of the specimen width by different weld-repair methods were compared, the fatigue strength of one-surface weld-repaired specimens was about one third of that of both surface weld-repaired specimens. Therefore, for crane components with cracks of length beyond half the plate width, both surface weld repair methods must be used to obtain satisfactory fatigue strength.

4. The fatigue strength of the specimens with a cover plate welded on one surface was about 25 MPa at 2×10^6 cycles, against the design value of 36 MPa of the lowest value

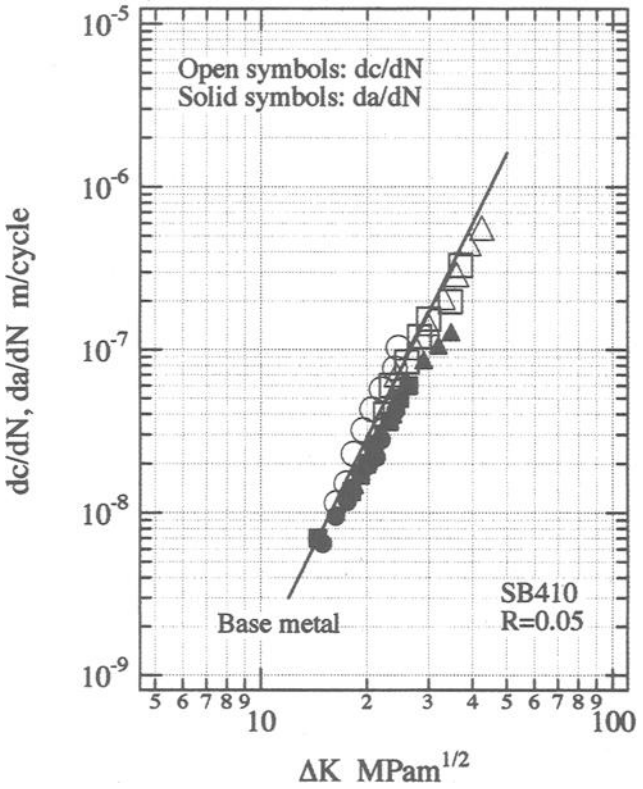


FIG. 15—*Relationship between* dc/dN, da/dN, *and* ΔK *for Type C specimen.*

proposed by ISO. Hence the weld repair method using a cover plate on one surface is not a suitable method for crane components.

5. The fatigue crack growth rate of the gusset plate specimens under the program loading was correlated with an effective stress intensity factor range estimated based on the linear accumulation of the stress intensity factor range, which considered the residual stress in each step of a block.

References

[1] Kitsunai, Y., Maeda, Y., and Yoshihisa, E., "Fatigue Strength of Gusset Welded Joints under Simulated Program Loading of Overhead Travelling Crane," *JSME International Journal,* Series A, Vol. 41, No. 1, 1998, pp. 112–120.

[2] Fisher, J. W., Haysammann, H., Sullivan, M. D., and Pense, A. D., "National Cooperative Highway Research Program Report 206," Transportation Research Board, 1979.

[3] Yamada, K., Sakai, Y., Kondo, A., and Kikuchi Y., "Weld Repair of Cracked Beams and Residual Fatigue Life," *Structural Engineering/Earthquake Engineering,* Vol. 3, No. 2, 1986, pp. 373s–382s.

[4] Miki, C. and Okukawa, A., "Fatigue Design, Quality Control and Maintenance of the Seto Ohashi Bridge," *Proceedings of International Conference on Mechanical Behavior of Materials,* Kyoto, Japan, Vol. 2, 1992, pp. 173–180.

[5] Miki, C. and Tateishi, K., "Fatigue Strength of Cope Hole Details in Steel Bridges," *International Journal of Fatigue,* Vol. 19, No. 6, 1997, pp. 445–455.
[6] Reemsnyder, H. S. and Demo, D. A., "Fatigue Cracking in Welded Crane Runway Girders: Causes and Repair Procedures," *Iron and Steel Engineer,* April 1978, pp. 52–56.
[7] Ingraffea, A. R., Gerstle, W. H. Mettam, K. I., Wawrzynek, P., and Hellier, A. K., "Cracking of Welded Crane Runway Girders: Physical Testing and Computer Simulation," *Iron and Steel Engineer,* December 1985, pp. 46–52.
[8] Kuwamura, H. and Hanazawa, M., "Inspection and Repair of Fatigue Cracks in Crane Runway Girders," *Proceedings of ASCE,* Paper No. 21967, 1987, pp. 2184–2197.
[9] Kitsunai, Y., Honda, T., and Sasaki, T., "The Determination of Stress Concentration Factors and Stress Intensity Factors by Means of Thermoelastic Stress Analysis," *Transactions of the Japanese Society Mechanical Engineers,* Vol. 64, No. 628, 1998, pp. 2782–2787 (in Japanese).
[10] Japan Society of Steel Construction, "Fatigue Design Recommendations for Steel Structures," JSSC Technical Report, No. 32, 1995.
[11] ISO 1072-1, Steel structures-Part 1: Materials and Design, 1997.
[12] Kitsunai, Y., Tanaka, M., and Yoshihisa, E., "Influence of Residual Stresses and Loading Frequencies on Corrosion Fatigue Crack Growth Behavior of Weldments," *Metallurgical and Materials Transactions A,* Vol. 29A, April 1998, pp. 1289–1298.
[13] Newman, J. C. and Raju, I. S., "Stress Intensity Factor Equations for Cracks in Three-Dimensional Finite Bodies," *Fracture Mechanics: 14th Symposium, ASTM STP 791,* 1983, pp. 238–265.
[14] The International Institute of Welding, *Fatigue Design of Welded Joints and Components,* A. Hobbacher, Abington Publishing, 1996, p. 111.

Thomas Siegmund[1] *and Wolfgang Brocks*[2]

Modeling Crack Growth in Thin Sheet Aluminum Alloys

REFERENCE: Siegmund, T. and Brocks, W., **"Modeling Crack Growth in Thin Sheet Aluminum Alloys,"** *Fatigue and Fracture Mechanics: 31st Volume, ASTM STP 1389,* G. R. Halford and J. P. Gallagher, Eds., American Society for Testing and Materials, West Conshohocken, PA, 2000, pp. 475–485.

ABSTRACT: The present study reports on the application of a cohesive zone model to the analyses of crack growth in a thin sheet specimen of a high-strength aluminum alloy. In addition to the elastic-plastic material properties, the parameters cohesive strength and cohesive energy describe material separation. For the sheet specimen under investigation, the cohesive energy is found to be close to the corresponding value of plane strain fracture toughness. The cohesive strength is approximately twice the yield strength. With these two additional material parameters being determined, crack growth experiments in center crack panels are analyzed. Good agreement with experimental records is found. Finally, the applicability of the model to study complex crack configurations as in multi-site damaged specimens is demonstrated.

KEYWORDS: ductile fracture, cohesive zone model, CTOA, aluminum, finite element analysis

Notation

$2L$	Specimen height
$2w$	Specimen width
t	Specimen thickness
$2a_i$	Initial length of lead crack
b_n	Length of nth-ligament
c_n	Length of nth-minor crack
x_i	Coordinate axes
h	Size of cohesive element
σ_t	True stress
ε_t	True strain
E	Elastic modulus
ν	Poisson's ratio
σ_0	Tensile yield stress
n	Hardening exponent
u_n	Normal displacement jump across crack surfaces
σ_n	Crack-opening stress
σ_{max}	Cohesive strength

[1] Assistant professor, School of Mechanical Engineering, Purdue University, West Lafayette, IN 47907, email: siegmund@ecn.purdue.edu.

[2] Professor, Institute of Materials Research, GKSS Research Center, D-21502 Geesthacht, Germany.

Copyright© 2000 by ASTM International www.astm.org

δ_c Cohesive length
Γ Cohesive energy
J_i J-integral at crack initiation
K_{IC} Plane strain fracture toughness
Σ_{22} Applied stress
Δa Crack extension
CTOA Crack tip opening angle

Introduction

In an assessment of the structural integrity of aircraft structures, the correct determination of the residual strength is a factor of vital importance [*1*]. Such an analysis requires an elastic-plastic stress analysis with the capabilities that allow for crack initiation and stable crack propagation. This implies the necessity for the knowledge on appropriate methods to characterize the crack growth resistance of the material under consideration. Methods being applied to analyze crack growth in fuselage structures include the use of stress intensity factors, the energy release rate, the J-integral, or the T^*-integral. For a recent overview on these methods, see Ref *2*. These integral measures of crack growth resistance can be applied to the predictions of the residual strength of real structures only if certain geometry requirements are fulfilled. The R-curves determined in the test program have to be from similar geometry as those encountered in the to-be-investigated structure. This issue of the lack of transferability of fracture data from one specimen geometry to another imposed important restrictions on the R-curve approach.

To solve the transferability problem, the so-called "local" approach to fracture provides solutions. Within this approach, fracture is described by a failure criterion locally at the crack tip. This approach is now very well established in the analysis of pressure vessel steels. In these ferritic steels the approach using the Gurson model together with the introduction of a material length-scale via the minimum element size in the uncracked ligament has been extremely successful [*3*]. While the complex crack propagation processes and 3D stress states found at the crack tips in sheet specimens in principle can be investigated by the Gurson model [*4*], this approach seem not practicable in the aluminum sheet material under investigation here. The main reason for this is that the material microstructure would require the element size for high-strength aluminum alloys to be approximately 10 to 20 μm only. Computations of crack growth extensions of up to 100 mm are, however, frequently required in the analysis of fracture of sheet specimens. Such crack growth analyses using these highly refined finite element meshes would be computational extremely extensive. As a consequence, most analyses of ductile tearing in sheet metal reported in the technical literature use a local deformation criterion to account for crack propagation. Two methods have been applied with success. One is a criterion based on a critical crack-tip-opening angle (CTOA) [*5,6*]. The other approach uses a crack opening displacement at a defined location relative to the crack tip [*7*]. These methods describe fracture by a local deformation measure. These two local fracture criteria can either be used within full-field finite element solutions or within approximate methods using the Dugdale model; for recent application, see Refs *8* and *9*. A material failure description by physically motivated parameters is, however, desired from a fundamental standpoint of fracture analysis. It is also of technological interest if the response of a structure is to be linked to the properties of the material itself. The present study reports on a step in this direction. Crack growth is described by the use of so-called "cohesive elements" [*10–12*]. These elements use a micromechanically and physically based constitutive equation for material separation embedded into the finite element method. The property of these elements is that they allow the description of crack propagation. Two

physically based material parameters are introduced: material separation strength and separation energy.

In the present paper a study on crack growth simulations performed on sheets of A1 2024-T3 Alclad is reported. The numerical results obtained are compared to experimentally determined data as published in the recent technical literature [*13*].

Problem Description

The cohesive surface formulation used in the investigation is based on the approach in Ref *10*. The difference of the present study to similar previous ones is that here the cohesive elements are embedded in a plane stress environment.

Computations are carried out for panel specimens either containing only a single center crack or a center crack plus additional minor cracks. The dimensions of the specimens are the height $2L$ and the initial width $2w$. The initial length of the center crack is $2a_i$, the length of the nth ligament between the additional cracks in front of the main crack is b_n, and the length of the minor nth cracks is c_n. Computations are performed under plane stress conditions. The geometry of the center cracked and of the multi-site-damaged panel is given in Fig. 1. In the finite element model only one quarter of the entire specimen is analyzed applying appropriate boundary conditions.

The constitutive relation used to describe the behavior of the plane stress volumetric elements is an isotropic elastic-plastic constitutive relation using the von Mises yield function. In this paper, the following representation of the true stress, σ_t, versus true strain, ε_t, curve is used:

$$\varepsilon_t = \begin{cases} \sigma_t/E & \text{for} \quad \sigma_t < \sigma_0 \\ (\sigma_0/E)(\sigma_t/\sigma_0)^n & \text{for} \quad \sigma_t > \sigma_0 \end{cases} \tag{1}$$

The material properties used in Eq 1 are those of 2024-T3 Alclad aluminum. The properties were taken to be $E = 71\ 400$ MPa, $\nu = 0.3$, $\sigma_0 = 285$ MPa, and $n = 8$, see Ref *8*.

The crack is constrained to grow along the initial crack line, i.e., along the x_1 coordinate axis. Since symmetry conditions prevail about that line, only normal separation is to be considered. In this case the crack opening stress, σ_n, can be related to the normal displacement jump across the crack surfaces, u_n, by the relation [*10*]:

$$\sigma_n = \sigma_{\max}\, ez\, \frac{u_n}{\delta_c} \exp\left(-z\,\frac{u_n}{\delta_c}\right) \quad \text{with} \quad e = \exp(1),\ z = \frac{16e}{9} \tag{2}$$

Here $\sigma_{\max}$ denotes the cohesive strength, i.e., the values describing the maximum stress-carrying capacity of the cohesive element. δ_c is the cohesive length, i.e., the value of the displacement jump across the crack surfaces at which the stress-carrying capacity of the cohesive elements falls to a small value. Figure 2 shows the dependence of the crack-opening stress in dependence of the displacement jump across the crack faces. Cohesive strength and cohesive length define the cohesive energy, Γ. In the case of small-scale yielding, the cohesive energy is identical to the value of the J-integral at crack initiation, J_i:

$$\Gamma = \frac{9}{16}\,\sigma_{\max}\delta_c = J_i \tag{3}$$

The path followed in the choice of cohesive zone material parameters is outlined in the

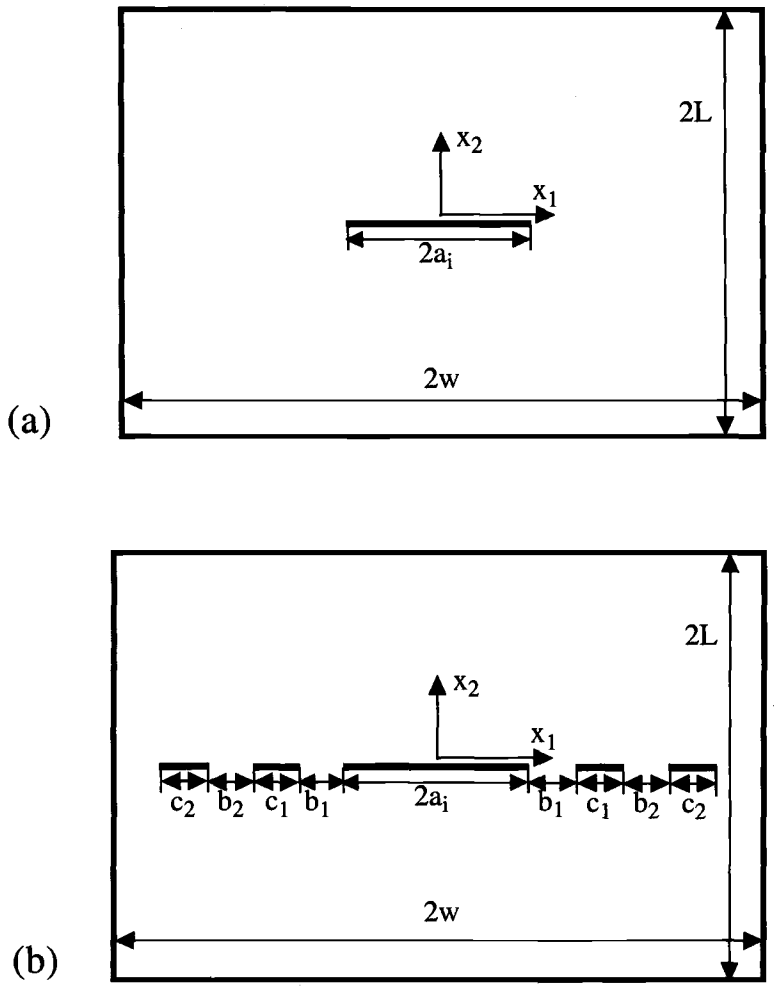


FIG. 1—*The geometry of the specimen under consideration: (a) center crack panel; (b) multi-site damage specimen.*

following. The values of the cohesive strength were taken to be $\sigma_{max}/\sigma_0 = 2$. This choice of cohesive strength used to characterize crack growth in the plane stress situation here is very different from those used to characterize ductile crack growth in plane strain situations. There, σ_{max}/σ_0 is between 3 and 4. The choice of $\sigma_{max}/\sigma_0 = 2$ for the current plane stress situation was motivated by results from numerical studies on the micromechanics of void growth. In Ref *14*, a study on the growth of large voids assisted by microvoid cavitation was presented for a material with σ_0/E as used here. From the peak stresses determined in this study, as assessment of the cohesive strength as used here can be made. In the material studied in Ref *14*, the peak stress was found to be approximately $3.5\sigma_0$ if the loading was at high-strain biaxiality, and void coalescence occurs in a plane normal to the principal loading direction. However, for low strain biaxiality, void coalescence takes place under 45° as in slant fracture, and the value of the peak stress drops to $2\sigma_0$. This result is confirmed

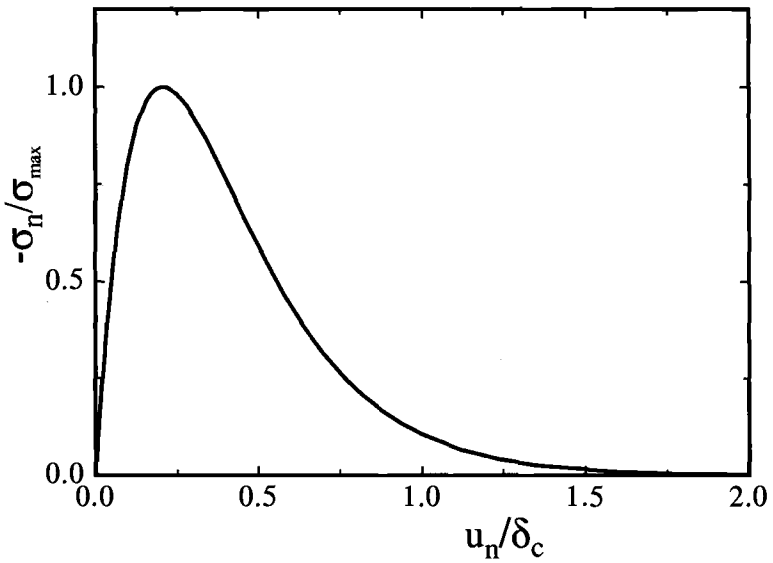


FIG. 2—*The traction-separation law employed in the cohesive zone model.*

by a study on crack propagation in a thin sheet of a model Gurson material [*4*]. There, the transition from normal to slant fracture was studied under dynamic loading and compared to numerical predictions of fracture processes under plane strain conditions. These authors also report a similar decrease of the level of peak crack opening stress when comparing the high constraint plane strain case to a case of slant fracture under 45° to the sheet plane. Finite element studies of the stress distribution in thin sheet were also reported in Refs *15* and *16*. These studies consider only elastic-plastic material properties. They again show that the specimen thickness average of the peak crack opening stress is approximately $2\sigma_0$. In Ref *15* also, little change in this average of stress is reported for a tearing crack. In the present study a single and constant value for σ_{max} is used for crack initiation and crack propagation.

The values of the plane strain fracture were used as the values of the initiation toughness in the plane stress simulations. This choice is motivated by the experimental results on high-resolution detection of crack tip process damage in thin aluminum sheet [*17,18*]. This result also is confirmed by a study of crack initiation in A1 2425-T351 as conducted by the present authors [*19*]. There, a damage-indicator-based void growth relation was calibrated on notched tensile specimens. The subsequent application of the damage indicator to crack initiation in center-cracked panels predicts crack initiation at stress intensity factors close to the plane strain fracture toughness. For the alloy 2024-T3 Alclad, the value of K_{IC} = 35 MPa $m^{1/2}$ was used. With $J = K^2/E$ and with Eq 3 the value for the cohesive length is δ_c = 0.05 mm.

Furthermore, in many fracture experiments on thin sheet specimens a transition from normal fracture to slant fracture is observed after small amounts of crack growth. Cracks subsequently often propagate in a plane under 45° to the loading plane at local mixed mode I/III. The mixed mode fracture mechanism maps presented in Ref *20* allow the determination of the expected mixed mode fracture toughness in dependence of J_I/σ_0. For the current material this ratio is close to 0.05. In this case, using the mixed mode fracture mechanism maps in Ref *20* the ratios between the mixed mode toughness for fracture under 45° and the

pure Mode I toughness is close to 1. As a consequence, the cohesive energy determined for the onset of crack propagation is used for the entire crack propagation stage.

The simulations reported here were performed using the finite element code ABAQUS [*21*]. Cohesive elements are incorporated into the numerical setup by means of user-defined elements (UEL). The numerical implementation uses an adaptive load control. Such a strategy is also implemented so that a single large load increase that properly resolved would cause several crack growth steps is subdivided appropriately. This adaptive load control strategy enforces the increase in material separation in a single load step to be at maximum $0.2\delta_c$. A violation of this requirement results in a 50% reduction of the increment size in the next solution step.

Crack Initiation and Crack Propagation

The first set of results presented here is on crack growth in center-cracked panels of A1 2024-T3 Alclad as reported in Ref *13*. The specimen under investigation there had specimen widths of $2w$ = 508 mm, a specimen thickness of t = 1.0 mm, and initial crack lengths of $2a_i$ = 101.6, 177.8, and 280 mm. The computer simulation uses 2652 plane stress elements surrounding 200 cohesive elements of length 0.25 mm. The ratio of the size of the cohesive elements to the cohesive length is thus h/d = 5. Results from previous investigations [*23,24*] demonstrated that this value for the h/d ratio leads to convergent predictions of fracture within the cohesive element approach.

While the experimentally examined specimens had saw cuts instead of fatigue cracks, the present investigation neglects this influence on the specimen behavior. Curves of applied stress, Σ_{22}, versus crack extension, Δa, for the three different crack lengths are depicted in Fig. 3. The increase of crack length results in a predicted decrease of the applied stress in very good agreement with the experimentally determined data of Ref *13*.

The crack tip opening angle, CTOA, was determined for these computations of crack growth. The distance behind the crack tip that was used to calculate CTOA was equal to the length of the cohesive elements. Results for the prediction of the evolution of CTOA in dependence of the crack extension are depicted in Fig. 4 for the three center crack panels of A1 2024-T3 Alclad. The evolution of CTOA is nearly identical for all three crack lengths. Values of CTOA are initially large but decrease substantially during the first 5 mm of crack extension. After that, only a small further reduction of CTOA occurs on further crack growth. The results on the evolution of CTOA with the crack extension as predicted here are in very good agreement with the CTOA measurements in Ref *22* for the same material. Furthermore, crack growth simulations of the same specimens as investigated here but using a crack growth criterion with a critical CTOA were reported in Ref *6*. A CTOA value for crack initiation and a different CTOA value for crack propagation were used. The values of CTOA reported there are depicted together with the current predictions in Fig. 4. Again, a good agreement on the CTOA values is obtained.

An issue of major interest with respect to residual strength analyses of metal sheet specimens is the prediction of the residual strength of multi-site damage structures; see Refs *2* and *25* for overviews and Refs *6*, *8*, and *9* for some recent developments. To demonstrate the predictive capabilities of the present crack growth model, one of the multi-site damage specimen of Ref *13* was analyzed. The specimen (P6 in Report *13*, A1 2024-T3 Alclad) has a width of $2w$ = 508 mm and a thickness of t = 1.0 mm. In addition to the lead crack of initial length $2a_i$ = 193 mm, two additional minor cracks in front of each initial lead crack tip were present such that b_1 = 6.35 mm, c_1 = 19.050 mm, b_2 = 12.70 mm, and c_2 = 31.75 mm. The computations use the modified Riks algorithm as implemented in the FE program ABAQUS [*21*]. Results of this simulation are depicted in Fig. 5 for the multi-site damaged

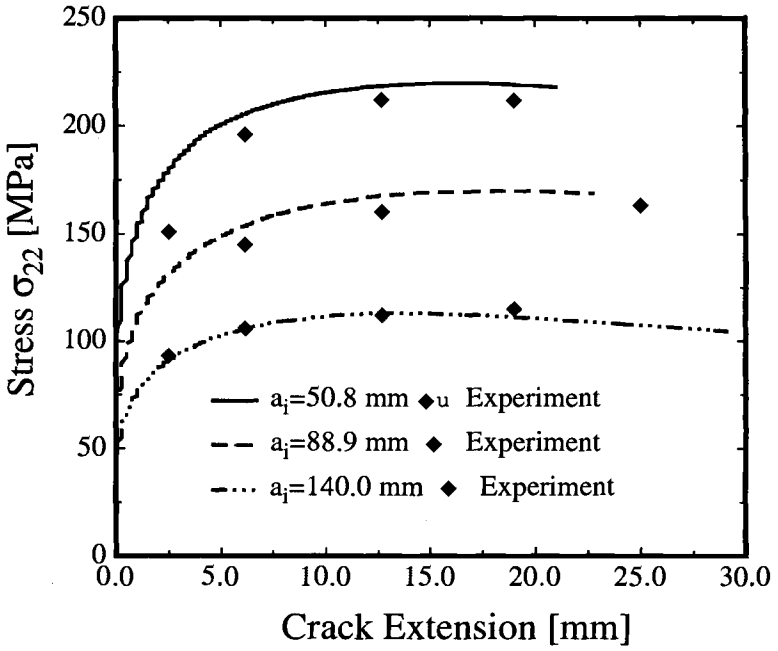


FIG. 3—*Applied stress versus crack extension for the center crack panels of A1 2024-T3 Alclad. Three different crack lengths are considered. Comparison of numerically determined values to the experimental data.*

panel and for a specimen containing only the lead crack. Figure 5 shows the applied stress, Σ_{22}, versus the extension of the lead crack only. The applied stress increases monotonically first as the main crack grows across the first ligament. As the main crack tip interacts with the first minor crack, the applied stress drops slightly. The crack then jumps across the first minor crack. Subsequently, crack growth is restarted within the second ligament. Again, as the main crack starts to interact with the second minor crack, a small decrease in the applied stress is predicted. Once the remaining ligament is reached, a peak in the applied stress is predicted again as the crack grows further. When compared to the specimen including the lead crack only a considerable reduction in the residual strength of the specimen is predicted. The experimental report in Ref *13* contains data on the peak applied stresses as indicated in Fig. 5. Again, the present crack growth model predicts the experimentally determined data reasonably well.

The evolution of the crack-tip-opening angle in dependence of the initial location of an element in the ligament was determined for the multi-site-damaged specimen, Fig. 6. Again, no constant CTOA is observed. CTOA has large values at each of the initial crack tips, and a rapid subsequent reduction from this large initial value is observed in all cases. For cracks growing to the right—including the lead crack—the reduction of CTOA is slower than for the cracks initially growing to the left. Once two cracks start to interact, a further strong reduction in CTOA is observed with CTOA falling nearly to zero. During this stage of interaction of the crack tips, the ratio between the length of the remaining ligament and cohesive length is reduced. From Fig. 6 the distance over which CTOA drops significantly is determined to approximately 5 mm during linkup of the lead crack with the two minor cracks. The ratio between this remaining ligament length and δ_c is approximately 100. For

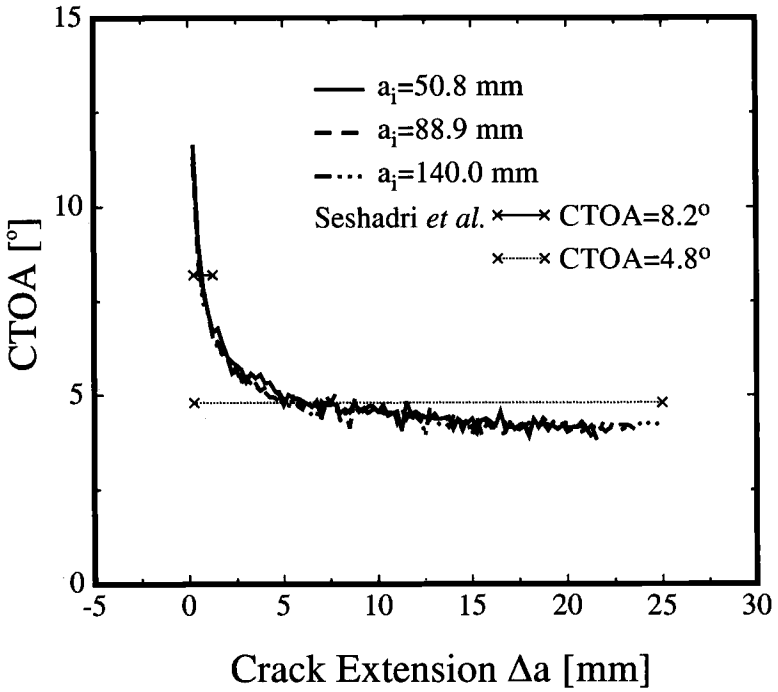


FIG. 4—*The evolution of the crack tip opening angle, CTOA, versus the crack extension in the three center crack panels of A1 2024-T3. Comparison to the CTOA values used in the simulation of the same specimens in Ref* 6.

the ratio of length scales in Ref *10*, a similar transition from a crack-like behavior to a uniform debonding behavior was observed.

Discussion

Crack growth in a thin sheet specimen of a high strength aluminum alloy has been analyzed by a computational method in which crack growth is determined within the deformation analysis of the specimen under consideration. This becomes possible since a cohesive constitutive relation accounts for the processes of material separation directly within the computations. The material under investigation is thus described by its elastic-plastic properties, and, in addition, by the parameters describing the material separation. An adaptive load control is used to avoid possible errors on the material separation due to too-large load steps, especially in cases of decreasing fracture resistance as it commonly occurs in the analysis of multi-site-damage specimens.

It is to be stressed here that the investigation presents an attempt to choose the cohesive material parameters prior to the analysis. Without employing a fitting procedure the current approach to the cohesive zone parameters results in good agreement between numerically predicted and experimentally determined data. An even closer fit between experiment and prediction could be obtained by further adjustment of the cohesive zone material parameters.

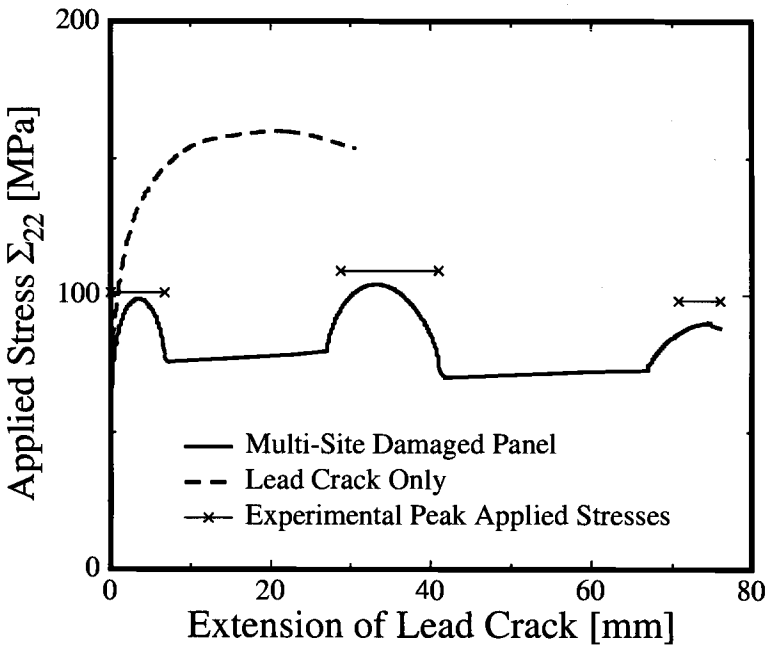


FIG. 5—*Applied stress versus crack extension for the multi-site damaged specimen of A1 2024-T3 Alclad. Comparison to a specimen containing the lead crack only. The experimentally determined values of the peak applied stresses as determined in Ref 13 are depicted as indicated.*

The current approach differs from other approaches to the analysis of crack growth in thin sheet metal describing fracture by physical material separation quantities only.

The current investigation predicts the experimentally determined evolution of the crack-tip-opening angle in good agreement with experiments. The assumption of a constant CTOA is violated, especially in the case where a multi-site-damaged specimen is investigated. In the regime of crack tip interaction via a short remaining ligament, the present approach predicts a change from a crack-like behavior to a situation of homogeneous debonding in agreement with results in Ref *10*. In this case the crack-tip-opening angle drops to zero. While a CTOA criterion is more readily available in commercial software packages, the present approach could provide the values of the critical *CTOA* being used in subsequent structural analyses.

The use of a cohesive zone model differs from the application of the Dugdale-model since it does not lump the effects of plasticity and material separation into a single strip. In comparison with the results of Ref *8* this is expressed in the different values of the parameters characterizing the maximum stress-carrying capacity within the two models. While the effective yield stress for the present material as used in the Dugdale model in Ref *8* is approximately $1.2\sigma_0$, the cohesive strength here is considerably larger, namely $2\sigma_0$. Given the computational advantages of the Dugdale approach, analyses as those presented here could provide means to identify the characteristic length needed in the crack-restart criterion of this approach.

To further improve the predictive capabilities of the approach presented here, more validation with experimental results is necessary. These further studies will especially have to

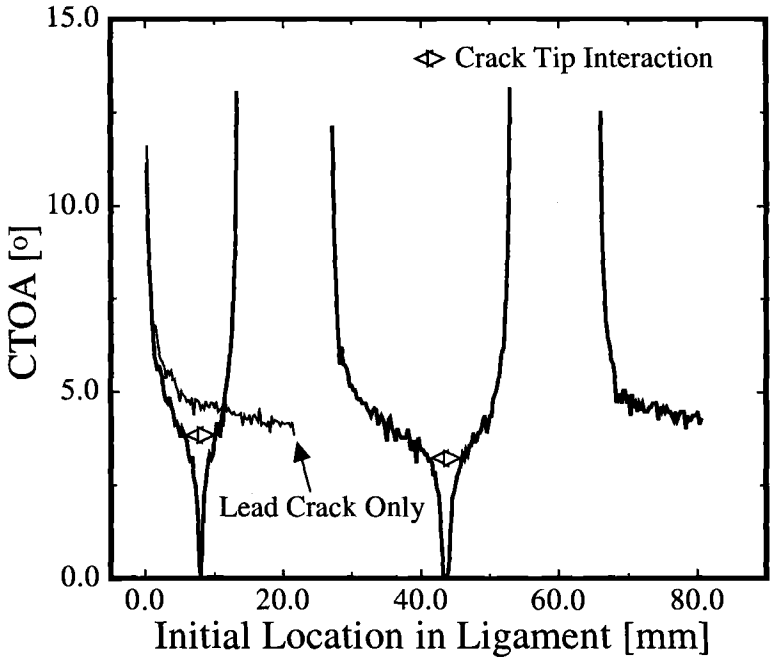


FIG. 6—*The evolution of the crack tip opening angle, CTOA, in dependence of the initial location of the cohesive element. Comparison to the evolution of CTOA in the specimen containing the lead crack only.*

take into account the effects of different specimen sizes and configurations. Furthermore, constraint effects due to buckling and bulging on the crack growth must be considered. It is strongly believed that the application of cohesive zone elements to these problems holds great promise to find solutions to these problems.

References

[1] *Proceedings of the FAA-NASA Symposium on Continued Airworthiness of Aircraft Structures,* July 1997.

[2] Harris, C. E., Newman, J. C., Jr., Piascik, R. S., and Starnes, J. H., Jr., "Analytical Methodology for Predicting Widespread Fatigue Damage Onset in Fuselage Structures," *Journal of Aircraft,* Vol. 35, No. 2, 1998, pp. 307–317.

[3] Xia, L., Shih, C. F., and Hutchinson, J. W., "A Computational Approach to Ductile Crack Growth under Large Scale Yielding Conditions," *Journal of the Mechanics and Physics of Solids,* Vol. 43, No. 3, 1995, pp. 389–413.

[4] Mathur, K. K., Needleman, A., and Tvergaard, V., "Three Dimensional Analysis of Dynamic Ductile Crack Growth in a Thin Plate," *Journal of the Mechanics and Physics of Solids,* Vol. 44, No. 3, 1996, pp. 439–464.

[5] Dawicke, D. S., Newman, J. C., Jr., and Bigelow, C. A., "Three Dimensional CTOA and Constraint Effects During Stable Crack Tearing in a Thin-Sheet Material," *Fracture Mechanics: 26th Volume, ASTM STP 1256,* W. G. Reuter, J. H. Underwood, and J. C. Newman, Jr., Eds., American Society for Testing and Materials, West Conshohocken, PA, 1995, pp. 223–242.

[6] Seshardri, B. R. and Newman, J. C., Jr., "Analyses of Buckling and Stable Tearing in Thin-Sheet Materials," *Fatigue and Fracture Mechanics, ASTM STP 1332,* T. L. Panontin and S. D. Sheppard, Eds., American Society for Testing and Materials, West Conshohocken, PA, 1998.

[7] Hellmann, D. and Schwalbe, K.-H., "Geometry and Size Effects on *J-R* and δ-*R* Curves under Plane Stress Conditions," *Proceedings, 15th National Symposium on Fracture Mechanics ASTM STP 833,* R. J. Sanford, Ed., American Society for Testing and Materials, West Conshohocken, PA, 1984, pp. 577–605.

[8] Deng, X. and Hutchinson, J. W., "Approximate Methods for Analyzing the Growth of Large Cracks in Fatigue Damaged Aircraft Sheet Material and Lap Joints," *Finite Elements in Analysis and Design,* Vol. 23, 1996, pp. 101–114.

[9] Nilsson, K.-F. and Hutchinson, J. W., "Interaction Between a Major Crack and Small Crack Damage in Aircraft Sheet Material," *International Journal of Solids and Structures,* Vol. 31, No. 17, 1994, pp. 2331–2346.

[10] Needleman, A., "An Analysis of Decohesion Along an Imperfect Interface," *International Journal of Fracture,* Vol. 42, 1990, pp. 21–40.

[11] Tvergaard, V. and Hutchinson, J. W., "The Relation Between Crack Growth Resistance and Fracture Process Parameters in Elastic-Plastic Solids," *Journal of the Mechanics and Physics of Solids,* Vol. 40, No. 6, 1992, pp. 1377–1397.

[12] Siegmund, T. and Needleman, A., "A Numerical Study on Dynamic Crack Growth in Elastic-Viscoplastic Solids," *International Journal of Solids and Structures,* Vol. 43, No. 7, 1997, pp. 769–787.

[13] Broek, D., Thomson, D., and Jeong, D. Y., "Testing and Analysis of Flat and Curved Panels with Multiple Cracks," *FAA-NASA International Symposium on Advanced Structural Integrity Methods for Airframe Durability and Damage Tolerance,* NASA Conference Publication 3274, Part I, September 1994, pp. 85–98.

[14] Faleskog, J. and Shih, C. F., "Micromechanics of Coalescence—I. Synergistic Effects of Elasticity, Plastic Yielding and Multi-Size-Scale Voids," *Journal of the Mechanics and Physics of Solids,* Vol. 45, No. 1, 1997, pp. 21–50.

[15] Newman, J. C., Jr., Crews, J. H., Jr., Bigelow, C. A., and Dawicke, D. S., "Variations of a Global Constraint Factor in Cracked Bodies under Tension and Bending Loads," *Constraint Effects in Fracture, Theory and Applications: Second Volume, ASTM STP 1244,* M. Kirk and A. Bakker, Eds., American Society for Testing and Materials, West Conshohocken, PA, 1995, pp. 21–42.

[16] Hom, C. L. and McMeeking, R. M., "Large Crack Tip Opening in Thin Elastic-Plastic Sheets," *International Journal of Fracture,* Vol. 45, 1990, pp. 103–122.

[17] Haynes, M. J. and Gangloff, R. P., "High Resolution *R*-curve Characterization of the Fracture Toughness of Thin Sheet Aluminum Alloys," *Journal of Testing and Evaluation,* Vol. 25, 1997, pp. 82–98.

[18] Schwalbe, K.-H., "Influence of Stress State on Static Crack Growth in AlZnMgCuO 5," *Engineering Fracture Mechanics,* Vol. 9, 1977, pp. 557–583.

[19] Siegmund, T., Brocks, W., Heerens, J., Tempus G., and Zink, W., "Modellierung von Rissausbreitung in Duennen Aluminiumblechen," *Bruchmechanische Bewertungskonzepte im Leichtbau, DVM-Report 231,* W. Brocks, Ed., Deutscher Verband fuer Materialforschung und -pruefung, 1999, pp. 33–40.

[20] Manoharan, M., "Development of a Mixed-Mode Fracture Mechanism Map and its Extension to Mixed-Mode Impact Fracture," *Recent Advances in Fracture,* R. K. Madhidhara et al., Eds., The Minerals, Metals & Materials Society, 1997, pp. 373–384.

[21] ABAQUS, User's Manual (1998) Version 5.8, Hibbitt, Karlson and Sorensen, Inc., Pawtucket, RI.

[22] Lloyd, W. R. and Piascik, R. S., "Three-Dimensional Crack Growth Assessment by Microtopographic Examination," *Fracture Mechanics: 26th Volume, ASTM STP 1256,* W. G. Reuter, J. H. Underwood, and J. C. Newman, Jr., Eds., American Society for Testing and Materials, Philadelphia, 1995, pp. 303–318.

[23] Needleman, A., "Numerical Modeling of Crack Growth under Dynamic Loading Conditions," *Computational Mechanics,* Vol. 19, 1997, pp. 463–469.

[24] Siegmund, T. and Brocks, W., "The Role of Cohesive Strength and Separation Energy for Modeling of Ductile Fracture," *Fatigue and Fracture Mechanics, ASTM STP 1360,* K. L. Jerina and P. C. Paris, Eds., American Society for Testing and Materials, West Conshohocken, PA, 1999.

[25] Schijve, J., "Multiple-Site Damage in Aircraft Fuselage Structures," *Fatigue and Fracture of Engineering Materials and Structures,* Vol. 18, No. 3, 1995, pp. 329–344.

B. R. Seshadri[1] *and J. C. Newman, Jr.*[2]

Residual Strength Analyses of Riveted Lap-Splice Joints

REFERENCE: Seshadri, B. R. and Newman J. C., Jr., **"Residual Strength Analyses of Riveted Lap-Splice Joints,"** *Fatigue and Fracture Mechanics: 31st Volume, ASTM STP 1389,* G. R. Halford and J. P. Gallagher, Eds., American Society for Testing and Materials, West Conshohocken, PA, 2000, pp. 486–504.

ABSTRACT: Aging aircraft may develop multiple-site damage (MSD) that can reduce the structural integrity of fuselage structures. The existence of small cracks emanating from adjacent rivet holes in a fuselage lap-splice joint is of major concern. The residual strength of a panel with a lead crack is greatly reduced by the presence of smaller collinear cracks compared to that of only a lead crack. Recent studies in predicting the residual strength of flat and curvilinear panels with riveted lap-splice joints gave quite encouraging results, but some difficulties arose in modeling small cracks at rivet-loaded holes. Thus, there was a need to conduct detailed fracture analyses of the crack-linkup phenomenon in lap-splice joints with rivet-loaded fasteners.

The objective of this paper was to analyze the crack-linkup behavior in riveted-stiffened lap-splice joint panels with small MSD cracks at several adjacent rivet holes. Analyses were based on the STAGS (STructural Analysis of General Shells) code with the critical crack-tip-opening angle (CTOA, Ψ_c) fracture criterion. To account for high constraint around a crack front, the "plane strain" core option in STAGS was used. The importance of modeling rivet flexibility with fastener elements that accurately model load transfer across the joint was discussed. Fastener holes were not modeled, but rivet connectivity was accounted for by attaching rivets to the sheet on one side of the cracks that simulated both the rivet diameter and MSD cracks. Residual strength analyses made on 2024-T3 alloy (1.6-mm thick) riveted-lap-splice joints with a lead crack and various-size MSD cracks were compared with test data from Boeing. Analyses were conducted for both restrained and unrestrained against buckling conditions. Comparison of these analyses with lap-splice-joint test panels, which were partially restrained against buckling, was generally bounded by the restrained and unrestrained failure loads.

KEYWORDS: lap-splice joint, rivets, cracks, crack growth, crack-tip-opening angle, buckling, multiple-site damage cracking, STAGS shell code

Nomenclature

B	Specimen thickness, mm
c_i	Initial half-length of crack, mm
D	Rivet diameter, mm
d	Minimum element size along crack line, mm
E	Young's modulus, GPa
h_c	Half-height of plane-strain core, mm
P	Applied load, kN

[1] National Research Council resident research associate, NASA Langley Research Center, MS 188E, Hampton, VA 23681.
[2] Senior scientist, NASA Langley Research Center, MS 188E, Hampton, VA 23681.

Copyright© 2000 by ASTM International www.astm.org

S Applied stress, MPa
S_f Failure stress, MPa
w Half-width of specimen, mm
X, Y, Z Cartesian coordinates
Δc Crack extension, mm
ν Poisson's ratio
σ_{ij} Stress components, MPa
Ψ_c Critical crack-tip-opening angle, degrees

Introduction

The damage-tolerant philosophy applied to aircraft fuselage structures requires that the structure retain adequate structural integrity in the presence of discrete source damage or fatigue cracks. Over the years of operation, an aircraft accumulates fatigue damage and the potential for fatigue cracks to develop at rivet-loaded joints. Economic factors have also encouraged the use of commercial and military aircraft beyond their original design requirements. Widespread fatigue damage in these aircraft are of great concern because the residual strength of a fuselage structure with a large two-bay crack may be significantly reduced by the existence of small cracks at adjacent rivet holes [*1*]. Whereas a single large crack in a fuselage structure may produce flapping (resulting in safe decompression), a fuselage with a large crack and multiple-site or multiple-element damage (MSD or MED) cracking may not flap and significantly degrade the residual strength of the structure [*2,3*]. It has become increasingly important to develop methodologies to predict flapping or failure in damaged fuselage structures in the presence of widespread fatigue damage [*4*]. Development of these methodologies for complex loading are essential to ensure the continued safe operation of the aging commercial transport fleet and aircraft for the next generation [*5*]. The approach is to use a finite-element shell code with hierarchical modeling strategies, appropriate local fracture criteria to predict progressive failure in complex structures, conduct material and geometric nonlinear analyses of stiffened shells subjected to complex loading, and conduct experiments to verify analyses and to identify critical behavioral characteristics.

In 1992, Maclin [*3*] conducted a series of tests on flat riveted-stiffened panels to study the performance of structural details in older airplanes relative to the pressurized fuselage sections. The study was initiated at Boeing to find out the degree to which structural integrity is maintained after the development of MSD. Flat panels were used in the test program to obtain the probable effects on residual strength of a common scenario—small fatigue cracks in a row of fastener holes. It was felt that the flat panels would give some indication on the effects of MSD, while avoiding the complexity of testing curved fuselage panels. Since then, test results in Ref *6* and analyses from Ref *7* have shown that the effects of MSD on residual strength are nearly the same for flat and curved panels. Several different crack configurations were considered in Ref *2*: (1) a wide M(T) specimen ($2w$ = 1219 mm) containing a large crack at the center, (2) a wide M(T) specimen ($2w$ = 1219 mm) with a large crack and a riveted hat stiffener parallel to the crack plane (no-load-transfer panel), and (3) wide riveted-stiffened lap-splice joint (load-transfer) panels with a large crack and various-size MSD cracks emanating from several adjacent rivet holes. All of these panels were tested with partial anti-buckling guide plates (positioned only along the cracked lap-joint region) to prevent buckling during the course of loading. It is very difficult to prevent total buckling of large, cracked panels with partial guide plates (see Ref *8*). Thus, the panels tested with only partial guide plates may have been buckling to some extent during the course of testing.

The objective of this paper was to analyze the crack-linkup behavior in riveted-stiffened lap-splice joint panels with small MSD cracks at several adjacent rivet holes. Analyses were based on the STAGS (STructural Analysis of General Shells) code [*9,10*] with the critical crack-tip-opening angle (CTOA, Ψ_c) fracture criterion. To account for high constraint around a crack front, the "plane strain" core (h_c) option in STAGS was used. The importance of modeling rivet flexibility with fastener elements that accurately model load transfer across the joint will be discussed. Fastener holes were not modeled, but rivet connectivity was accounted for by attaching rivets to the sheet on one side of the cracks that were used to simulate both the rivet diameter and MSD cracks. Analyses were conducted for both restrained and unrestrained against buckling conditions. Comparisons are made between measured and predicted applied stress against crack extension, crack opening displacement (COD), and crack-out-of-plane displacement (COPD) for specimens tested with and without anti-buckling guides. The influence of multiple-site damage on the buckling response of lap-splice joint specimens was also studied. The ability of the STAGS shell code and the CTOA fracture criterion to predict the influence of buckling on stable tearing behavior in riveted lap-splice joint panels was studied. Residual strength analyses made on 2024-T3 (TL) aluminum alloy (1.6-mm thick) riveted-lap-splice joints with a lead crack and various-size MSD cracks were compared with test data from Boeing.

Material and Specimen Configurations

Analyses were conducted on middle-crack tension M(T) specimens, a riveted-stiffened panel with a single crack, and riveted-stiffened lap-splice-joint panels with a large crack and various-size multiple-site-damage (MSD) cracks at adjacent rivet holes. All of the specimens were subjected to remote tension and had partial anti-buckling guides along the crack plane to prevent some buckling. The materials studied in the present study were aluminum alloy 2024-T3 (sheet) and 7075-T6 clad (stiffener). The material stress-strain behavior was approximated by piece-wise-linear curves, and they are given in Table 1.

STAGS Finite-Element Analyses

The STAGS finite-element shell code [*9,10*] and the critical crack-tip-opening angle (CTOA) failure criterion were used to model stable tearing of cracks in lap-splice joint

TABLE 1—*Material stress-strain properties.*

2024-T3 (TL) E = 71.5 GPa ν = 0.3		7075-T6 (LT) Clad E = 71.5 GPa ν = 0.3	
ε	σ, MPa	ε	σ, MPa
0.00434	311	0.00739	529
0.01	356	0.015	543
0.02	387	0.03	553
0.04	422	0.06	569
0.07	453	0.12	576
0.1	470	0.2	577
0.16	484		
0.2	485		

panels. The critical CTOA (Ψ_c) and the plane-strain core height (h_c) for the thin-sheet 2024 alloy were determined from failure loads on middle-crack tension specimens (restrained from buckling). The fracture constants were then used with the STAGS code to predict the fracture behavior of the riveted-stiffened lap-splice joint panels that were restrained or unrestrained against buckling. Rivet connectivity, rivet yielding, stiffener yielding, out-of-plane buckling, and stiffener-sheet connectivity were modeled during the stable tearing process. Single cracks and MSD cracks at simulated rivet holes were considered.

STAGS is a finite element program for the analysis of general shell-type structures [*9,10*]. The program has several types of analysis capabilities (static, dynamic, buckling, crack extension, material nonlinear, and geometric nonlinear behavior). STAGS has crack extension capability based on the critical crack-tip-opening angle or displacement (CTOA or CTOD) criterion [*11*], the T^*-integral [*12*], and the traditional K_R-curve. In the current study, quadrilateral shell elements with six degrees of freedom per node (three displacements and three rotations) were used in all models. The quadrilateral shell element was under "plane-stress" conditions everywhere in the model except for a "core" of elements along the crack plane that were under "plane strain" conditions [*11*]. Elastic-plastic material behavior of the sheet and stiffener were approximated by multi-linear stress-strain curves. The White-Besseling plasticity theory with a form of kinematic hardening was used to account for yielding and reverse yielding during unloading [*9*].

Modeling of the Sheet Material

To model the fracture process with the CTOA failure criterion, a finite-element mesh with an array of small elements was positioned along the crack plane. A minimum crack-tip element size (d) of about 1 mm, along the line of crack extension, was chosen to be the same for all crack configurations. From previous parametric and convergence studies, it was found that a minimum crack-tip element size of 1 mm (linear-strain element) was sufficient to model stable tearing under elastic-plastic conditions [*13*[. Crack growth was governed by monitoring the critical CTOA(Ψ_c) at a distance of 1 mm (one element) behind the crack tip. In general, the critical value (Ψ_c) was determined by matching the average failure load measured on several M(T) specimens (restrained from buckling), as will be discussed later. Typical finite-element models that were used in the STAGS analyses will be shown later.

Modeling of Multiple-Site Damage (MSD) Cracking

Small MSD cracks at adjacent structural details, such as in a riveted fuselage structure, have a strong influence on residual strength, see Swift [*1*] and Broek et al. [*14*]. The MSD crack sizes in the tests from Ref 2 ranged from 0.35 to 1.3 mm in length from the rivet holes. Because the MSD crack sizes were smaller than the minimum element size, the rivet holes were not modeled, but rivet connectivity was modeled. To model the holes and MSD cracks, the nodes along the symmetric plane over the diameter of the hole and MSD cracks were free to displace. Thus, the hole and MSD cracks were modeled as a "crack." One test was also conducted without MSD with only a lead crack and rivet-loaded holes. Here the riveted-loaded holes were modeled in two ways. First, the rivet hole was treated as a crack (equal to the hole diameter). In the second case, the rivets were treated as tight rivets and modeled only as normal rivet-to-sheet connections using rigid links.

The lead crack and MSD cracks had a constant tearing angle (Ψ_c) from initiation of tearing to linkup or failure. Crack linkup occurred under constant Ψ_c conditions for all crack tips. Thus, the cracks coalesced with each other, always maintaining a constant tearing angle. An option to have a crack-initiation displacement (δ_i), or initiation angle (Ψ_i), different than the

tearing angle Ψ_c has also been added to the STAGS code [*10*]. This option can be used to simulate fracture of "sawcuts" and stable tearing of cracks [*15*].

Modeling of Stiffeners and Rivets

Analyses of cracked-stiffened panels by Newman and Dawicke [*15*] indicated that a refined mesh was required in the region of the rivet connection to maintain proper load transfer. In the wide riveted-stiffened lap-splice joint panels, the elements in the rivet-connection region were 2-mm square. Larger elements were used away from the rivet connection and away from the crack plane to help reduce the number of degrees of freedom. The stiffeners were modeled separately and overlapped the sheet with an offset equal to the sheet thickness. Rivet holes were not modeled [*7,16*], but rivet connectivity was modeled. Rivet attachment to the sheet was placed on only one side of the cracks.

Rivet connections between the stiffener and sheet were modeled with fastener elements in STAGS. The fastener elements are nonlinear spring elements with six degrees of freedom (three translations and three rotations). For each degree of freedom, the user has to input the nonlinear load-displacement curve. Rigid links were used at the end of each fastener to distribute the load transferred across each rivet [*7,16*]. Rivet holes were not modeled (a tight fit between the rivet and hole was assumed). For more information on the fastener element capability in STAGS, refer to Refs *9* and *10*.

Modeling Stiffener-Sheet Contact and Buckling

Forman [*17*] has experimentally shown that buckling has a strong influence on the residual strength of cracked panels. Seshadri and Newman [*18*] have demonstrated that stable tearing in the presence of buckling can be predicted with STAGS and the CTOA fracture criterion. In the present study, a bifurcation analysis was conducted to determine the first buckling mode shape. This out-of-plane displacement shape (about 10% of the sheet thickness) was then introduced as an imperfection in the panels for the nonlinear analysis.

Modeling of Crack-Tip Constraint

A concept of defining plane-strain elements around the crack-front region [*11*] was adopted to simulate three-dimensional constraint conditions around a crack front. Previous analyses of wide flat panels [*19*] have shown that the high-constraint conditions around a crack front, like plane strain, have to be modeled in order for the critical CTOA criterion to predict wide panel failure from small laboratory tests. The plane-strain core capability has been added to the STAGS code [*10*]. The plane-strain core is defined as a strip of elements (h_c is half-height) parallel to the crack plane. In the present analyses, the core height was selected as 1 mm to help fit the failure loads on various width M(T) specimens, as will be discussed later.

Determination of Critical CTOA and Plane-Strain Core Height

A critical CTOA (Ψ_c) value was used to model the onset of crack growth and the stable tearing process. This criterion is equivalent to a critical CTOD (δ_c) value at a specified distance behind the crack tip. At each load increment, the CTOA was calculated and compared to a critical value Ψ_c. When the CTOA exceeded the critical value, the crack-tip node was released and the crack was advanced to the next node. This process was continued until crack growth became unstable under load control or until the desired crack length had been

reached under displacement control. For multiple-site-damage cracking analyses, all cracks were controlled by the same critical CTOA at each crack tip.

To carry out stable tearing analysis with STAGS, the critical CTOA that governs the onset of crack growth and the plane-strain core height that simulates the three-dimensional constraints around the crack-front region needed to be determined. For this purpose, the load-crack-extension results from the M(T) specimens (restrained from buckling) were used.

The specimen configuration and a typical mesh pattern used in the present study are shown in Figs. 1 and 2, respectively. As the configuration and loading are symmetric, only a quarter of the sheet was modeled, as shown in Fig. 2. The one-quarter model had 1495 elements and 2187 nodes for this specimen width ($2w$ = 610 mm). The minimum crack-tip element size (d) of 1 mm, all along the line of crack extension, was chosen to be the same for all meshes generated for the different crack configurations. In the M(T) specimen, the normal stress, σ_{xx}, parallel to the crack surface is compressive, as shown in Fig. 1. If the specimen is not restrained, the crack flanks will deform out of plane (buckle) and this behavior will greatly reduce the load-carrying capacity of the panel.

Figure 3 shows the failure stress S_f against specimen width ($2w$) for various M(T) specimens. The symbols show the test results on specimens with crack-length-to-width (c/w) ratios of 1/3. Using a critical angle of 5.0°, the failure stresses predicted under plane-stress conditions are shown as the dashed curve, whereas, the predicted results under plane-strain conditions are shown by the dash-dot curve. From these results, it was clear that the plane-strain analyses could not capture the experimental trends. For the thin-sheet alloy, the fracture behavior fell closer to the plane-stress behavior. In order to account for three-dimensional constraint effects in two-dimensional analyses, a plane-strain core region was defined around the crack tip [*11*]. In general, the plane-strain core height is equal to or less than the material

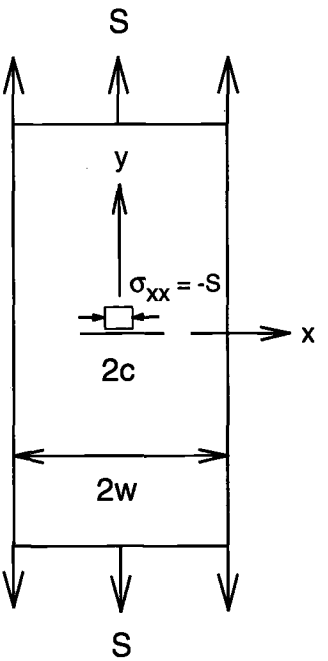


FIG. 1—*Middle-crack tension, M(T), specimen.*

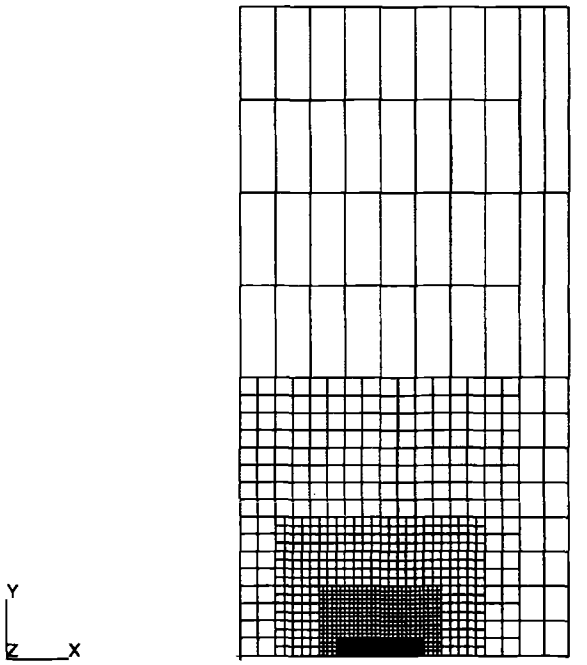


FIG. 2—*A typical finite-element model of one quarter of an M(T) specimen.*

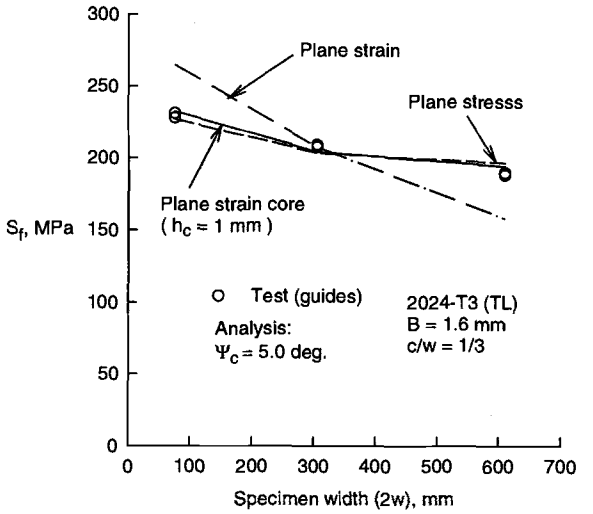


FIG. 3—*Measured and calculated failure stress for various width M(T) specimens.*

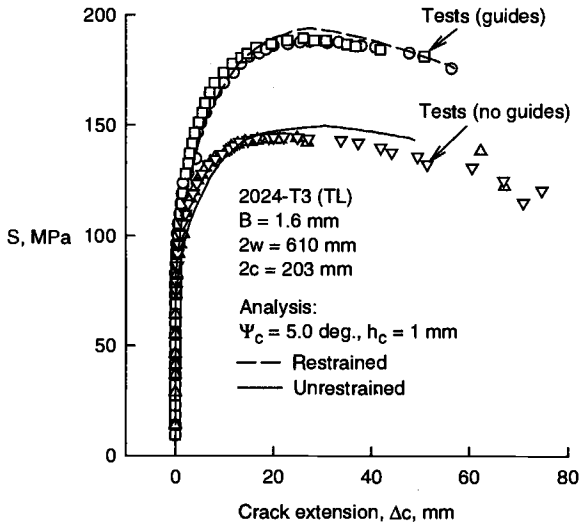


FIG. 4*a*—*Measured and predicted stable crack growth in M(T) specimens using CTOA fracture criterion.*

thickness. The solid curve with the same critical angle and a plane-strain core height of 1 mm captured the experimental trends slightly better than the plane-stress analyses. For thicker materials, the differences between the test data and plane-stress analyses have been greater [*20*] and the plane-strain core analyses were needed to fit the test data.

Figure 4*a* shows the load-against-crack extension results (symbols) from a 610-mm wide M(T) specimen with and without anti-buckling guides. Crack extension is the average crack

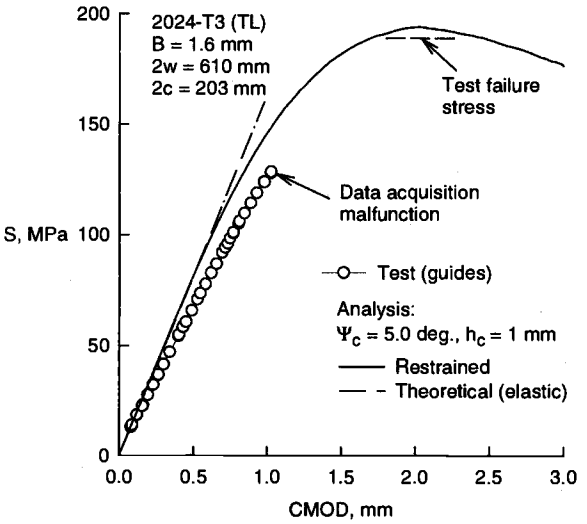


FIG. 4*b*—*Measured and predicted crack-mouth-opening displacement (CMOD) for M(T) specimen.*

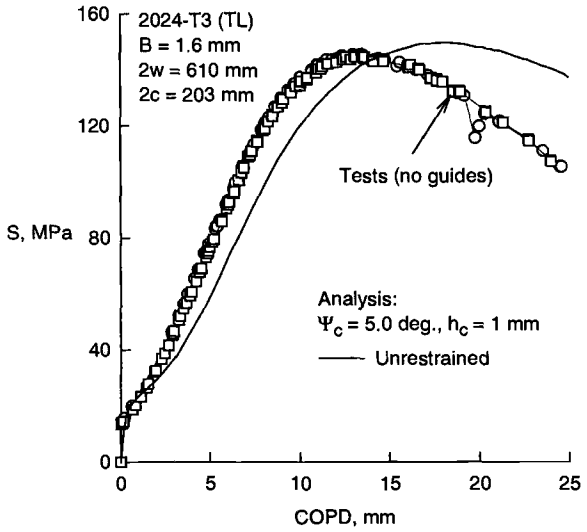


FIG. 4c—*Measured and predicted crack out-of-plane displacement (COPD) for M(T) specimens.*

extension measured at both crack tips. Square and circular symbols represent the tests conducted with guides, and the triangles show data where guides were not used and the sheet was allowed to buckle. An angle of $\Psi_c = 5.0°$ was used to fit the average of the experimental results on the M(T) specimens with guides. The dashed curve corresponds to the fracture simulation of the specimens that were restrained from buckling. The analysis was then repeated with the same angle, but buckling was allowed. The solid curve represents the numerical results when out-of-plane deformations were permitted. Both the tests and numerical results indicated a significant influence of buckling on stable tearing. The residual strength was reduced drastically when the sheet was allowed to buckle. The experimental and numerical results agreed well near the maximum load. But both analyses tended to slightly overpredict crack extension in the early stages of crack growth (between crack initiation and maximum load) than the tests. This behavior has been a general trend that has been observed on many other tests and analyses [*20–23*]. At first glance, a higher CTOA at initiation than during stable tearing would make the analysis fit the test data better. However, the plastic history generated during fatigue pre-cracking was not modeled because this capability had not been incorporated into STAGS. It was estimated that fatigue precracking would raise the initial portion of the predicted curve by about 10 kN in the early stages of tearing. But fatigue precracking is not expected to influence the failure load because of the large amount of stable tearing. Also, a crack in the thin-sheet material severely tunnels at crack initiation, as much as two times the sheet thickness, so the surface measurement of crack extension is low compared to the interior [*19*]. These two issues would tend to make the predicted results with a constant CTOA in better agreement with the test data.

Comparison of Measured and Predicted In-Plane Displacements—For the specimen tested with anti-buckling guides, the in-plane crack-opening displacement was measured at the centerline of the crack with a crack-mouth-opening displacement (CMOD) gage. A comparison of applied stress against CMOD from the test (symbols) and the STAGS analysis is shown in Fig. 4*b*. Only test results from one specimen with guides were available for comparison. Due to a malfunction of the data acquisition system, comparison with test data was

possible only up to an applied stress of about 130 MPa. The initial slope of the measured CMOD curve was bout 20% lower than the numerical analysis. The reason for the discrepancy is unknown. But the numerical analysis agreed well with the elastic theoretical value (dashed-dot line with E = 71.5 GPa). The upper dashed line shows the maximum failure stress from the test.

Measured and Predicted Out-of-Plane Displacements—For the specimen tested without anti-buckling guides, the out-of-plane displacement was measured using a laser gage at every load increment. The crack out-of-plane (or transverse) displacements (COPD) are plotted against applied stress in Fig. 4*c*. The symbols show the experimental measurements, and the solid curve shows the results from the numerical analysis. Both the test and analyses were conducted for unrestrained (buckling) conditions. Here the numerical analyses tended to overpredict the COPD at a given applied stress level, especially beyond the maximum applied stress. This may indicate that the plane-strain core height needed to be larger than 1 mm. Reference *8* has indicated that the load-CMOD results beyond maximum load were a strong function of the plane-strain core height. Further study is needed to help resolve these discrepancies.

Results and Discussions

In the following sections, the results from the numerical analyses are compared with the test data reported in Ref *2* and discussed in detail. Corresponding to the three specific panel configurations, detailed STAGS analyses were carried out with restrained boundary conditions to simulate the influence of guide plates and with unrestrained boundary conditions to simulate the influence of buckling on residual strength of the panel. The effects of a hat-stiffener (parallel to the crack plane) and riveted fasteners on the residual strength of the panel are discussed. Finally, the effects of buckling on stable tearing and the influence of multiple-site damage (MSD) cracking on crack growth behavior with and without buckling in riveted-stiffened lap-splice joint specimens are presented.

Fracture Simulations with Cracks

Prior to testing the riveted-stiffened lap-splice joint panels, a preliminary test was performed on a 1219-mm wide M(T) specimen. The test data helped in characterizing the fracture behavior of the material used in the lap-splice joint panels. In this section, the numerical results are compared with the preliminary test.

The specimen configuration and finite-element mesh pattern used in the present analysis were similar to those shown in Figs. 1 and 2, respectively. Only the failure stress was available from Ref *2* and is shown by the dashed line in Fig. 5. As previously determined from a similar material and thickness, a critical angle of Ψ_c = 5.0° and a plane-strain core height of h_c = 1 mm was used in the numerical analysis. Analyses on the 1219-mm wide M(T) specimens with and without buckling are plotted as applied stress against crack extension in Fig. 5. The dashed curve shows the fracture simulation of the specimens where out-of-plane displacements were restrained. The analysis was then repeated with the same angle but buckling was allowed. The solid curve represents the numerical results when out-of-plane deformations were permitted. The numerical results indicated a significant influence of buckling on stable tearing and residual strength. But the two analyses bounded the test failure stress (dashed line).

The discrepancy between the analyses and test data may be due to the following reasons. It is suspected that the use of the partial anti-buckling guide system, only along the crack plane, does not totally prevent buckling away from the crack plane. It has been found [*8*]

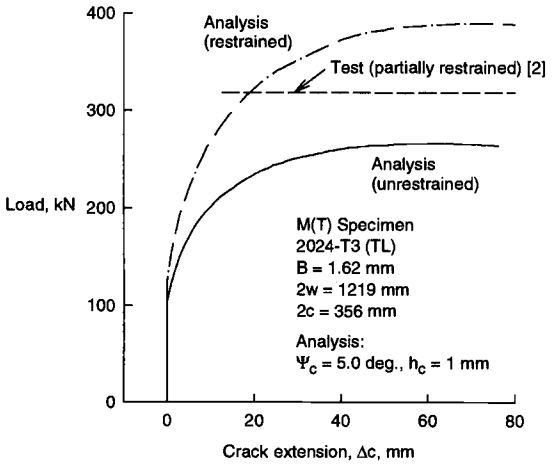


FIG. 5—*Measured failure stress and predicted crack extension for M(T) specimens.*

that it takes a massive guide-plate system to prevent buckling of wide panels with cracks. The specimen must be totally supported from the crack plane to the grip ends with guide plates that have many orders-of-magnitude greater stiffness than the sheet. The authors [*16,18*] have also shown that the STAGS code and the CTOA fracture criterion can predict stable tearing for wide panels under both restrained and unrestrained conditions. It is very difficult to accurately match the contact boundary conditions for a partially supported buckling panel. Thus, tests of wide cracked panels without guide plates, and the use of numerical fracture simulation to obtain material fracture properties, may be preferred. The analyses could then be conducted with restrained conditions to obtain the fracture behavior and stable tearing without the influence of buckling.

Fracture Simulations of Riveted-Stiffened Panels

The configuration for the riveted-stiffened (no-load-transfer) panel and a typical finite element mesh used in the present study are shown in Figs. 6 and 7. The specimen had a hat stiffener made of 7075-T6 clad located along the centerline of the specimen (parallel to the crack plane). The stiffener was connected to the sheet material through a series of rivets spaced about 30.5 mm apart. Rivets were made of 2024-T4 material and they were 4.8 mm in diameter. The finite-element mesh shown in Fig. 7 had an array of 1-mm size elements all along the horizontal symmetric plane ($Y = 0$) for stable crack growth analyses. The mesh element pattern used around the crack-tip region is shown in Fig. 7*a*. Here the one-quarter model had 5558 elements and 7372 nodes. A comparison of experimental and numerical results for the no-load-transfer panel is shown in Fig. 8. The dashed line shows the experimental failure stress for the partially restrained panel. Solid and dash-dot curves are the analysis results under unrestrained and restrained conditions, respectively. The analysis for the unrestrained case was about 3.5% higher than the test load. In contrast to the M(T) specimen (Fig. 5), the panel with the horizontal stiffener exhibited much less buckling, presumably because the stiffener prevented some in-plane contraction and supported some of the normal σ_{xx} stresses in the sheet.

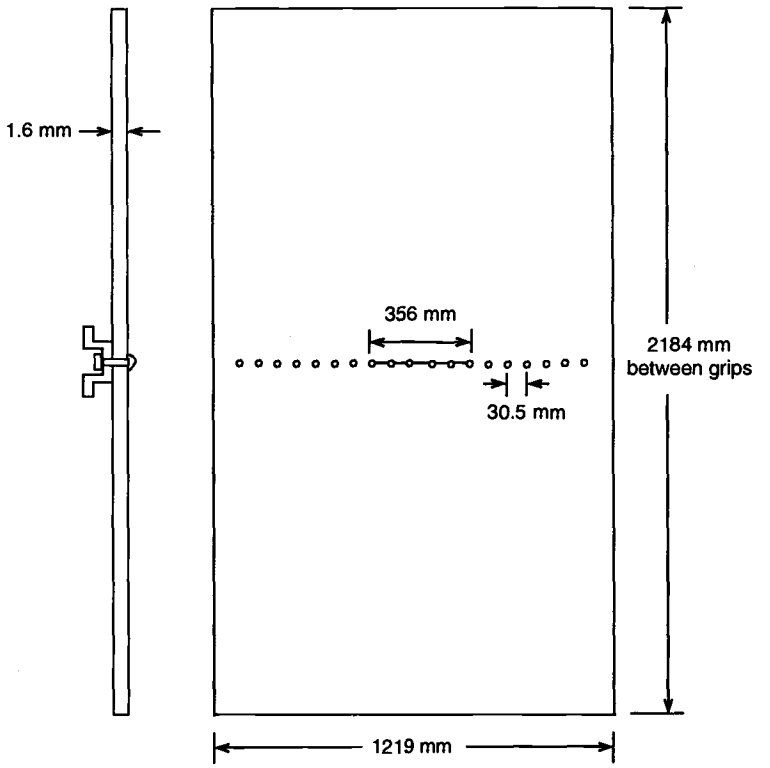


FIG. 6—*Riveted and stiffened wide panel with a single crack.*

Fracture Simulations of Riveted-Stiffened Lap-Splice Joint Panels with MSD

The typical riveted-stiffened lap-splice joint panel used in the Boeing test program [*2*] is shown in Fig. 9. The lap joint had three rows of 4.8-mm diameter rivets with a hat stiffener riveted to the central rivet row. The rivet pitch in the axial direction is 30.5 mm, and the rivet rows were spaced at 23 mm apart. The initial damage in the panel consisted of a 356-mm lead crack located at the center of the top row of rivets. Several panels were also tested with various-size MSD cracks emanating from adjacent fastener holes, as shown in Fig. 10*a*. Only the first four rivets immediately ahead of the lead crack had equal MSD crack sizes emanating from each hole. The other rivet holes were pristine. The specimens had MSD crack sizes ranging from 0.35 to 1.3 mm in length from each side of a hole.

In the analysis, two cases were considered to simulate the rivets and/or MSD. First, the rivet hole and MSD were approximated by a crack (length of rivet diameter plus MSD sizes), as shown in Fig. 10*b*. Rivet connections to the sheet were made on only one side of the crack using rigid links [*7*]. The particular crack length at each rivet would affect load transfer from each sheet layer. Second, for the case of no MSD cracks, rivets were considered either as cracks (length of rivet diameter), see Fig. 10*b*, or as a tight rivet with rigid links between adjacent sheets, as shown in Fig. 10*c*. It was expected that the analyses of the configurations shown in Figs. 10*b* and 10*c* would bound the behavior for an actual riveted joint.

A typical finite-element mesh used in the analysis of lap-splice joint is shown in the Fig. 11. The one-half model had 15 551 elements and 18 915 nodes. The finite-element mesh

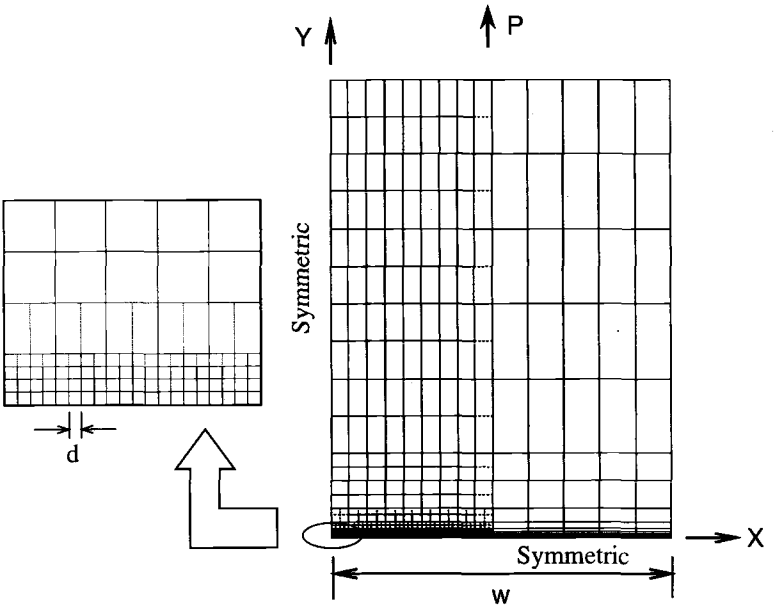


FIG. 7—*Typical finite-element model of riveted-stiffened panel.*

had a very refined mesh (1-mm size element) around the crack-tip region and all along the crack growth path (assumed to be straight along the rivet row). Around the fasteners, which transfer load from the outer skin to the inner skin, a refined mesh (2 mm in size) was used. The rivets were modeled with fastener elements. The nonlinear behavior of the fastener elements was based on the empirical relation developed by Swift [*1*] and represents the net shear stiffness of the fastener sheet connection and accounts for bearing deformation. The

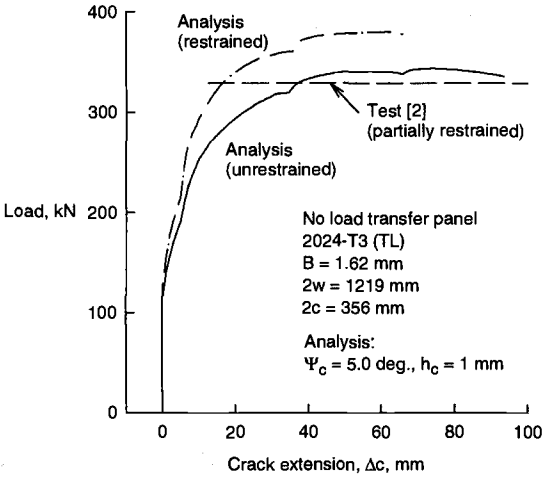


FIG. 8—*Measured failure stress and predicted crack extension for wide, riveted-stiffened panel.*

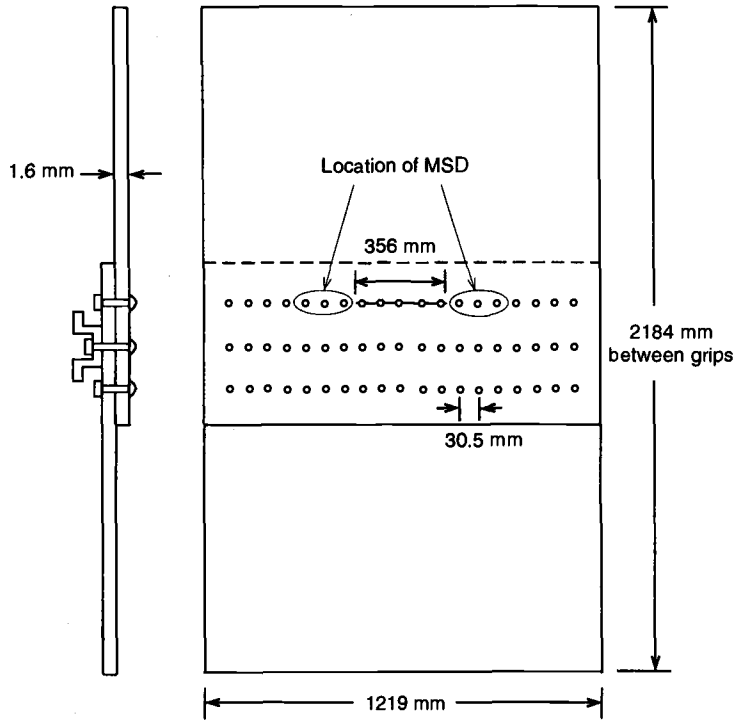


FIG. 9—*Typical riveted and stiffened lap-splice panel.*

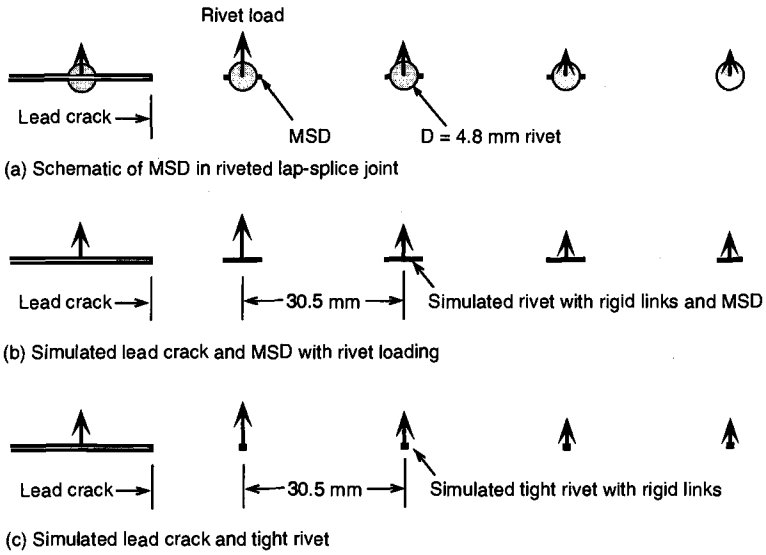


FIG. 10—*Schematic of lap-splice joint and simulation methods for rivets and MSD.*

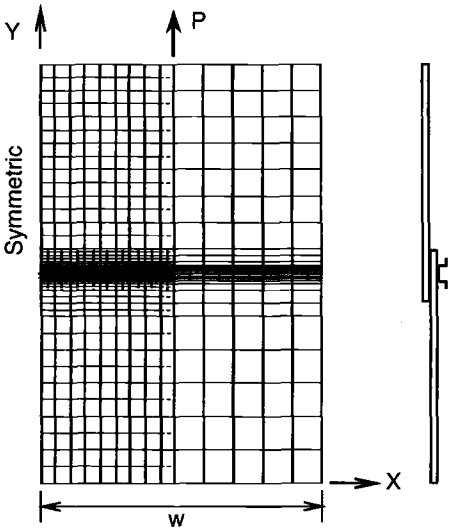


FIG. 11—*Typical finite-element model of riveted-stiffened lap-splice joint panel.*

finite-element mesh did not model the fastener holes. Rivet connectivity was accomplished by defining rigid links around the fastener and distributing the fastener loads over the fastener cross-sectional area [*7*].

Comparisons between the test results and fracture simulations on riveted-stiffened, lap-joint panels with and without MSD are shown in Figs. 12 and 13. The upper dashed line in both figures shows the test results for the lap joint with only a lead crack (c_i = 356 mm).

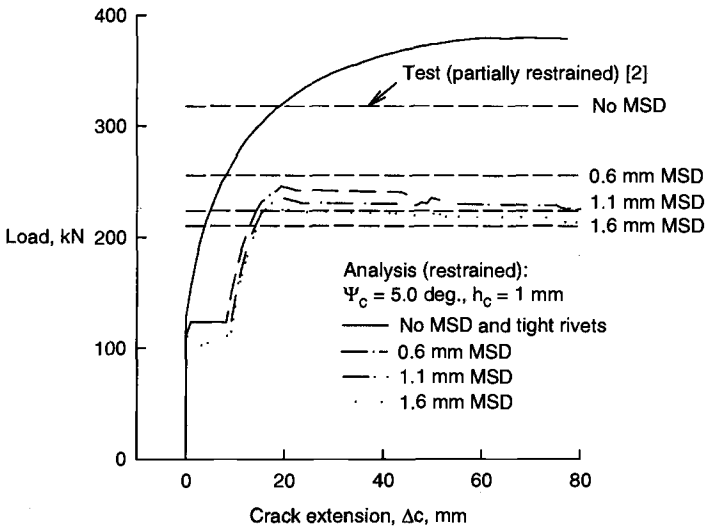


FIG. 12—*Measured failure stresses and predicted crack extension in wide restrained riveted-stiffened panels with and without MSD.*

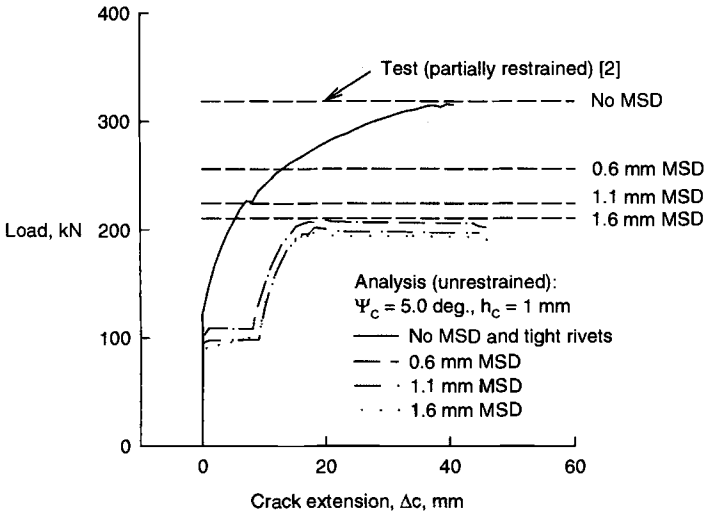


FIG. 13—*Measured failure stresses and predicted crack extension in wide unrestrained riveted-stiffened panels with and without MSD.*

The lower three dashed lines show failure loads extrapolated from the MSD test panels from Ref *2*. The three values of MSD (0.6, 1.1, and 1.6 mm) were chosen to match the values that could be simulated from the finite-element mesh. Because of the 1-mm element size, the 0.6-mm MSD was the smallest MSD size that could be simulated. This size was about one half of the standard damage-tolerant crack size (1.27 mm) and was below the current inspection limit for lap-splice joints [*24*]. The reason for repeating the analysis under both restrained and unrestrained conditions was to evaluate the bounds on the residual strength for these conditions. As the experiments were conducted under a partial restraint anti-buckling guide system, the exact simulation of the corresponding boundary conditions would have been difficult. But these bounds would define the limits within which the experimental results should fall. In Figs. 12 and 13, the loads against crack extension for the lead crack as it grows and links up with the MSD cracks are compared with the failure loads for various MSD crack sizes. The solid curve corresponds to the case of no MSD cracks (assumed tight rivets, see Fig. 10*c*. The presence of MSD cracks drastically reduces the residual strength of the panel. Larger MSD crack sizes caused a larger reduction in residual strength.

The analyses (three lower curves) were made on simulated lap joints with the crack configurations modeled like Fig. 10*b*. All rivets along the crack line were assumed to be cracks (length of rivet diameter). The results from the restrained analyses (Fig. 12) for MSD cracks matched the test data better than the results from the unrestrained analyses (Fig. 13). The reason may be due to the horizontal stiffener and the lap joint increasing the stiffness in the cracked region, in addition to the partial restrain system, and reducing the influence of buckling on residual strength.

Comparison of failure loads on panels with various MSD crack sizes is shown in Fig. 14. The test failure loads (open symbols) are plotted against the MSD crack sizes. Analysis results corresponding to the restrained and unrestrained cases are shown by solid circular and square symbols, respectively. For the larger MSD crack sizes considered in analyses, the experimental failure loads fell within the bounds of restrained and unrestrained conditions. But for all smaller MSD crack sizes, the test results fell between restrained analyses

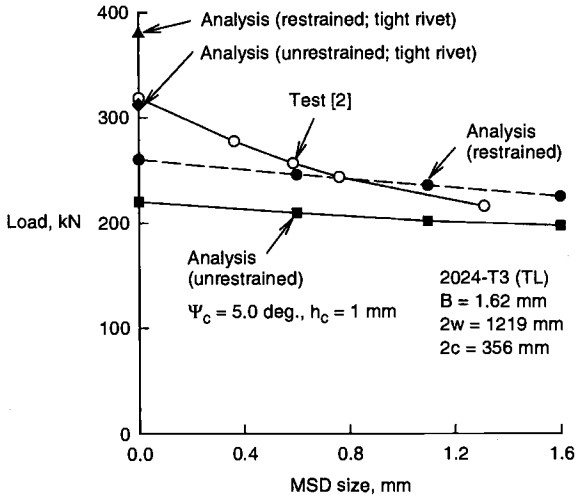


FIG. 14—*Measured and predicted failure loads for wide restrained and unrestrained riveted-stiffened panels with MSD.*

for tight rivets (solid triangular symbol, see Fig. 10*c*) and rivets simulated as cracks (solid circular symbols, Fig. 10*b*). To accurately model MSD crack sizes less than about 0.6 mm would require modeling the rivet hole and fastener contact.

Concluding Remarks

Results from the analyses of riveted-stiffened lap-splice joint panels were presented and discussed. Fracture simulations of these panels using the STAGS shell code and the critical crack-tip-opening angle (CTOA) fracture criterion produced quite reasonable results when compared with experimental measurements. The numerical analyses predicted the upper and lower bounds on failure loads corresponding to restrained and unrestrained boundary conditions. For most of the cases, the experimental test data (partial restrained against buckling) was within these bounds. The analyses predicted a significant influence of multiple-site damage (MSD) cracking and buckling on residual strength of the panels. Because the analyses were able to predict the failure loads quite accurately, testing of cracked wide panels without anti-buckling guide plates would be recommended. This would reduce the effort and costs involved in testing wide panels and provide tests with known boundary conditions. This study has demonstrated that the STAGS code and the CTOA fracture criterion can serve as an analysis tool for predicting the residual strength of built structures subjected to complex loading conditions.

Acknowledgment

This work was performed while the first author was a National Research Council Research Associate at the NASA Langley Research Center.

References

[1] Swift, T., "Damage Tolerance in Pressurized Fuselages," *New Materials and Fatigue Resistant Aircraft Design,* 14th Symposium of the International Committee on Aeronautical Fatigue (ICAF), Ottawa, Canada, June 1987.

[2] McGuire, J. F. and Goranson, U. G., "Structural Integrity of Future Aging Airplanes," International Conference on Aging Aircraft and Structural Airworthiness, C. E. Harris, Ed., NASA CP-3160, Washington, DC, 1992, pp. 33–48.

[3] Maclin, J., "Performance of Fuselage Pressure Structure," *International Conference on Aging Aircraft and Structural Airworthiness,* C. E. Harris, Ed., NASA CP-3160, Washington, DC, 1992, pp. 67–75.

[4] Harris, C. E. and Heyman, J. S., "Overview of NASA Research Related to the Aging Commercial Transport Fleet," *Journal of Aircraft,* Vol. 30, No. 1, 1993, pp. 64–68.

[5] Harris, C. E., Newman, J. C., Jr., Piascik, R., and Starnes, J. H., Jr., "Analytical Methodology for Predicting the Onset of Widespread Fatigue Damage in Fuselage Structure," *Journal of Aircraft,* Vol. 35, No. 2, 1998, pp. 307–317.

[6] Gruber, M. L., Wilkins, K. E., and Worden, R. E., "Investigation of Fuselage Structure Subject to Widespread Fatigue Damage," *Proceedings of FAA-NASA Symposium on the Continued Airworthiness of Aircraft Structures,* Atlanta, GA, 1996, pp. 439–459.

[7] Young, R. D., Rouse, M., Ambur, D. R., and Starnes, J. H., Jr., "Residual Strength Pressure Tests and Nonlinear Analyses of Stringer- and Frame-Stiffened Aluminum Fuselage Panels with Longitudinal Cracks," *Second Joint NASA/FAA/DoD Conference on Aging Aircraft,* C. E. Harris, Ed., Williamsburg, VA, 1998, pp. 408–426.

[8] Dawicke, D. S., Gullerud, A. S., Dodds, R. H., Jr., and Hampton, R. W., "Residual Strength Predictions with Crack Buckling," *Second Joint NASA/FAA/DoD Conference on Aging Aircraft,* C. E. Harris, Ed., Williamsburg, VA, 1998, pp. 565–574.

[9] Almroth, B., Brogan, F., and Stanley, G., "User's Manual for STAGS," NASA CR 165670, 1978.

[10] Rankin, C. C., Brogan, F. A., Loden, W. A., and Cabiness, H. D., "STAGS User Manual—Version 2.4," Lockheed Martin Advanced Technology Center, Report LMSC P032594, 1997.

[11] Newman, J. C., Jr., Booth, B. C., and Shivakumar, K. N., "An Elastic-Plastic Finite Element Analysis of the J-Resistance Curve using a CTOD Criterion," *Fracture Mechanics: Eighteenth Symposium, ASTM STP 945,* D. T. Read and R. P. Reed, Eds., 1988, pp. 665–685.

[12] Atluri, S. N. and Tong, P., "Computational Schemes for Integrity Analyses of Fuselage Panels in Aging Airplanes," *Structural Integrity of Aging Airplanes,* Springer-Verlag, 1991, p. 33.

[13] Dawicke, D. S. and Newman, J. C., Jr., "Residual Strength Predictions for Multiple-Site Damage Cracking using a CTOA Criterion," *Fatigue and Fracture Mechanics: 29th Volume, ASTM STP 1332,* T. L. Panontin and S. D. Sheppard, Eds., 1999, pp. 815–829.

[14] Broek, D., Thomson, D., and Jeong, D. Y., "Testing and Analysis of Flat and Curved Panels with Multiple Cracks," NASA Conference Publication 3274, Part II, September 1994, pp. 963–984.

[15] Newman, J. C., Jr. and Dawicke, D. S., "Fracture Analysis of Stiffened Panels under Biaxial Loading with Widespread Cracking," AGARD CP-568, 1995, pp. 3.1–3.16.

[16] Seshadri, B. R., Newman, J. C., Jr., Dawicke, D. S., and Young, R. D., "Fracture Analysis of FAA/NASA Wide Stiffened Panels," *Second Joint NASA/FAA/DoD Conference of Aging Aircraft,* C. E. Harris, Ed., Williamsburg, VA, 1998, pp. 513–524.

[17] Forman, R. G., "Experimental Program to Determine Effect of Crack Buckling and Specimen Dimensions on Fracture Toughness of Thin Materials," Technical Report AFFDL-TR-65-146, January 1966.

[18] Seshadri, B. R. and Newman, J. C., Jr., "Analyses of Buckling and Stable Tearing in Thin-Sheet Materials," *Fatigue and Fracture Mechanics: 29th Volume, ASTM STP 1332,* T. L. Panontin and S. D. Sheppard, Eds., 1999, pp. 114–134.

[19] Newman, J. C., Jr., Dawicke, D. S., and Bigelow, C A., "Finite-Element Analyses and Fracture Simulation in Thin-Sheet Aluminum Alloys," *Durability of Metal Aircraft Structures,* S. N. Atluri et al., Eds., Atlanta, Georgia, 1992, pp. 167–186.

[20] Kanninen, M., Rybicki, E., Stonesifer, R., Broek, D., Rosenfield, A., and Nalin, G. T., "Elastic-Plastic Fracture Mechanics for Two-Dimensional Stable Crack Growth and Instability Problems," *ASTM STP 668,* 1979, pp. 121–150.

[21] Dawicke, D. S., Sutton, M., Newman, J. C., Jr., and Bigelow, C. A., "Measurement and Analysis of Critical CTOA for an Aluminum Alloy Sheet," *Fracture Mechanics: 25th Volume, ASTM STP 1220,* F. Erdogan, Ed., 1995, pp. 358–379.

[22] Dawicke, D. S., Newman, J. C., Jr., and Bigelow, C. A., "Three-Dimensional CTOA and Constraint Effects during Stable Tearing in a Thin-Sheet Material," *Fracture Mechanics: 26th Volume, ASTM STP 1256,* W. G. Reuter, J. H. Underwood, and J. C. Newman, Jr., Eds., 1995, pp. 223–242.

[23] Newman, J. C., Jr., Dawicke, D. S., Sutton, M. A., and Bigelow, C. A., "A Fracture Criterion for Widespread Cracking in Thin-Sheet Aluminum Alloys," *Durability and Structural Integrity of Airframes,* Vol. I., A. F. Blom, Ed., 1993, pp. 443–468.

[24] Hagemaier, D., Rengel, K., Wincheski, B., and Namkung, M., "Evaluation of the Self-Nulling Rotating Eddy Current Probe System," *Second Joint NASA/FAA/DoD Conference on Aging Aircraft,* C. E. Harris, Ed., Williamsburg, VA, 1998, pp. 252–264.

Thomas J. Curtin[1] *and Robert A. Adey*[2]

Damage Repair Simulation of a Tension Panel and Pressurized Cylindrical Shell Using Adhesively Bonded Patches

REFERENCE: Curtin, T. J. and Adey, R. A., **"Damage Repair Simulation of a Tension Panel and Pressurized Cylindrical Shell Using Adhesively Bonded Patches,"** *Fatigue and Fracture Mechanics: 31st Volume, ASTM STP 1389*, G. R. Halford and J. P. Gallagher, Eds., American Society for Testing and Materials, West Conshohocken, PA, 2000, pp. 505–525.

ABSTRACT: The bonded patch repair performance of a cracked tension panel, and a pressurized cylindrical shell with longitudinal through-crack, is simulated using a commercially available boundary element code. Three-dimensional, quadrilateral-shaped, reduced-quadratic order, boundary elements are used to model the panel, cylindrical shell, and repair patch. The adhesive layer is modeled using a continuously distributed system of linear springs. A special boundary element is used to model the crack. The tension panel analysis is based on a single-sided repair configuration. The relationship between crack length and stress intensity factor (SIF) for both the unrepaired and repaired panel is presented. The reduction in SIF and change in stress field, for the repaired panel compared to the unrepaired panel, determined from the present analysis, are compared with FME and analytical results. The occurrence of out-of-plane bending and its impact on the through-thickness SIF variation in the panel is discussed. Crack growth simulation results show the crack front becoming curvilinear as the crack advances below the patch. The reduction in SIF for a pressurized cylindrical shell with a double-sided elliptical patch repair is presented as a special case.

KEYWORDS: bonded patch repair, three-dimensional boundary element analysis, stress intensity factor, crack propagation, pressurized cylindrical shell

Bonded repair techniques for damaged aircraft skin have become increasingly common given their advantage over more conventional repair methods that use mechanically fastened doublers; their major advantage is improved fatigue behavior. The ability to determine an acceptable fatigue life for the damaged structure has become increasingly important with the advent of the damage tolerance criteria mandated by FAA regulations for aging transport aircraft. In order to develop an effective bonded repair methodology it is important to be able to accurately determine the complex stress fields created by the repair as well as the resulting reduction in the stress intensity factor (SIF).

During the past decade extensive research has been conducted in the area of bonded patch repair performance. The majority of numerical analysis has been performed using the finite element method (FEM) [*1–4*] although some work has also been done using the boundary element method (BEM) [*5–8*].

The present work focuses on the use of a three-dimensional boundary element analysis to investigate the bonded repair performance of both an edge-cracked and center-cracked ten-

[1] Senior applications engineer, Computational Mechanics Inc., 25 Bridge Street, Billerica, MA 01821.
[2] Managing director, Computational Mechanics BEASY, Ashurst Lodge, Southampton, SO40 7AA, UK.

Copyright© 2000 by ASTM International www.astm.org

sion panel, and a pressurized cylindrical shell with a longitudinal through-crack. The crack is modeled using the dual boundary element method (DBEM) [*8,9*].

Previous BEM work has focused primarily on the use of two-dimensional elastostatic theory where the panel, patch, and adhesive have been assumed thin so that out-of-plane bending is not considered. Young [*7*] has performed patch repair studies using a BEM approach where both the patch and panel were discretized and the adhesive shear stresses were modeled as body forces acting on the patch and sheet. A straight crack in the sheet was modeled implicitly using a crack Green's function. Although this strategy avoids discretization of the crack surface it restricts the applications to straight cracks.

The present analysis extends the previous BEM work by performing a fully three-dimensional analysis and using the DBEM to model the crack. Although the DBEM method requires the crack surface to be discretized with special crack elements it also provides a means to analyze nonplanar cracks, investigate the out-of-plane behavior associated with single-sided patch repairs, and implement crack growth simulation studies. The present analysis also provides some preliminary results illustrating the use of the BEM to investigate the patch repair of an internally pressurized cylindrical shell.

Because the solution method and modeling technique of the BEM differ slightly from the FEM there are some inherent advantages and disadvantages in using the BEM for this type of analysis. Important advantages include simplified modeling of the adhesive layer, direct calculation of stress intensity factor (SIF) values, and accurate crack growth simulation. A disadvantage is that the BEM computer code used for this analysis is currently limited to geometrically linear analysis.

Three-Dimensional Boundary Element Model

The commercially available boundary element software, BEASY, is used to simulate the repaired behavior of a tension panel and pressurized cylindrical shell [*10*]. The plate and patch are modeled using a quadrilateral element topology and reduced-quadratic element order. The adhesive is modeled using a series of linear springs with stiffness values representing the adhesive material properties. The crack in the plate is simulated using a special boundary element capable of handling the discontinuous stress field located at the crack front. These important modeling features are discussed in detail in the following sections.

Simulation of Adhesive Layer

The adhesive is modeled as an interface boundary condition by applying internal springs on the surface shared between the patch and plate that are defined as different boundary element zones. The spring stiffness, specified in units of *pressure/displacement,* is defined in terms of the normal and tangential directions in a local coordinate system. The axial (k_{axial}) and shear (k_{shear}) spring stiffness are found from the following relationships:

$$k_{\text{axial}} = \frac{E_a}{t_a}$$
$$k_{\text{shear}} = \frac{G_a}{t_a} \tag{1}$$

The boundary element formulation for the internal spring relationship is defined by the following equation:

$$T_{i1} = k_i(u_{i2} - u_{i1}) \tag{2}$$

where

T_{i1} traction in the *ith* direction acting on Zone 1,
k_i spring stiffness in the *ith* direction,
u_{i1} displacement of Zone 1 in *ith* direction, and
u_{i2} displacement of Zone 2 in *ith* direction.

The traction applied to Zone 2 is the same in value as T_{i1}, but opposite in direction.

Simulation of Damage in the Plate

Cracks are modeled using the DBEM. The DBEM simultaneously imposed displacement and traction boundary integral equations on opposite sides of the crack surface. Both crack surfaces are discretized with discontinuous quadratic boundary elements. The SIFs are calculated from the crack opening displacements associated with node pairs on opposite crack surfaces using the near-tip displacement extrapolation method [*8*].

Discontinuous Elements—Discontinuous elements play an important role in the boundary element method because the problem variables are not forced to be continuous across elements. A discontinuous element is represented as an element where the mesh point and node locations are not coincident. As a result of this formulation the nodes are not shared between elements. The major benefit of discontinuous elements is their ability to model discontinuous stress results at a crack front.

Crack Propagation—Crack growth is simulated using an incremental-type analysis. For the present analysis the incremental direction and size along the crack front for each extension are determined using the minimum strain energy density criterion. For each increment of crack extension, a stress analysis is performed using the DEBM, and the SIF are evaluated. The crack front is remeshed and the next stress analysis is carried out for the new configuration. The theoretical aspects and detailed mathematical formulation of this crack growth method are described in the work by Mi [*11*].

Problem Description and Results

Computer modeling, using boundary element analysis, was performed to determine SIF solutions for a simple center-cracked plate and variety of patch repair configurations. Edge-cracked and center-cracked tension panels, repaired with composite and metallic patches, respectively, are analyzed as well as the metallic patch repair of a cylindrical shell containing a longitudinal through-crack. The work is useful in demonstrating the accuracy and feasibility of the BEM as a repair simulation tool.

SIF Solution for Center-Cracked Tension Panel

A computer model of a 3 mm thick tension panel, 500 by 500 mm in plan section, with a center crack, was created to determine the SIF for various crack lengths. The panel is loaded by a remote uniform tensile stress (1 MPa) applied normal to the crack. SIF solutions are determined for half-crack lengths ranging from 20 to 150 mm. In order to assess the accuracy of the boundary element solution the SIF values obtained from the present analysis are compared to analytical and FEM solutions for a similar configuration. The FEM solution

used for comparison is presented in the work by Callinan [*3*]. This work discusses results from a three-dimensional, geometrically linear, finite element analysis. The center-cracked panel was modeled using 20-noded isoparametric brick elements. The SIF was determined using isoparametric wedge-shaped elements at the crack tip with the mid-point nodes shifted to the quarter-point locations to account for the crack tip singularity.

Figure 1 shows a comparison of the SIF solutions obtained using the BEM, FEM, and analytical solutions. There is good agreement between the BEM, FEM, and analytical solutions for half-crack lengths less than 40 mm with the SIF values typically being within 1 to 3% of each other. For crack lengths between 40 and 120 mm the BEM solution agrees with the analytical solution almost exactly, whereas the FEM solution ranges between 3 to 8% higher than the analytical solution. At longer crack lengths, greater than about 120 mm, the analytical solution starts to diverge from the BEM solution. It should be noted that the analytical solution used to approximate the finite width boundary correction was determined by assuming a periodic array of collinear cracks in an infinite plate. Anderson [*12*] states that this analytical solution becomes less accurate for $a/W > 0.6$ (which in this case represents a half-crack length of 150 mm) and that numerical methods should be used to obtain a more accurate solution.

Bonded Patch Repair of Cracked Tension Panels

The following sections explore the feasibility of the BEM as an analysis/design tool for the bonded repair of thin sheet aluminum panels. Two different repair configurations are investigated and the results compared to either analytical or FEM solutions. Case 1 focuses on the modeling of an edge-cracked panel with a composite patch, and Case 2 involves the analysis of a center-cracked panel with a metallic patch. The geometry, material properties, loading, and solution results for these two cases are presented in detail in the following sections.

Edge-Cracked Panel with Bonded Composite Patch (Case 1)—A computer model was created to determine the SIF for an edge-cracked panel with a single-sided, adhesively bonded, composite repair. The patch was comprised of a glass-epoxy material with orthotropic elastic properties. The geometry and material properties are shown in Fig. 2. A uniform load (58.33 MPa) was applied to the remote ends of the panel in a direction normal to the crack surface. This repair configuration and loading is the same as that investigated by Umamaheswar and Singh [*2*].

Umamaheswar and Singh used finite element modeling to study the composite patch repair of an edge-cracked sheet. SIF solutions were obtained for the different combinations of brick, shell, and beam elements used to model the repair of the cracked sheet. The adhesive layer was modeled using both beam and brick elements. Brick elements were found to be more accurate and less labor intensive in terms of modeling time. Both geometrically linear and nonlinear FEM analyses were performed with results indicating that a geometrically nonlinear analysis provided a more accurate SIF solution. The SIF was determined by a modified crack closure integral method using the element nodal forces and displacements on the crack surface obtained from the FEM analysis.

A comparison of the SIF solutions, determined from the BEM and FEM analyses, is made in order to substantiate the accuracy of the boundary element solution and modeling approach. Table 1 shows the SIF result from the present analysis with comparison to the FEM result from the Umamaheswar and Singh study. The FEM case from Ref *2*, selected for comparison, used single-crack elements to model the plate, adhesive, and patch. This FEM model was solved using a geometrically nonlinear analysis. In order to match the FEM result, a convergence study was performed to determine the number of boundary elements required

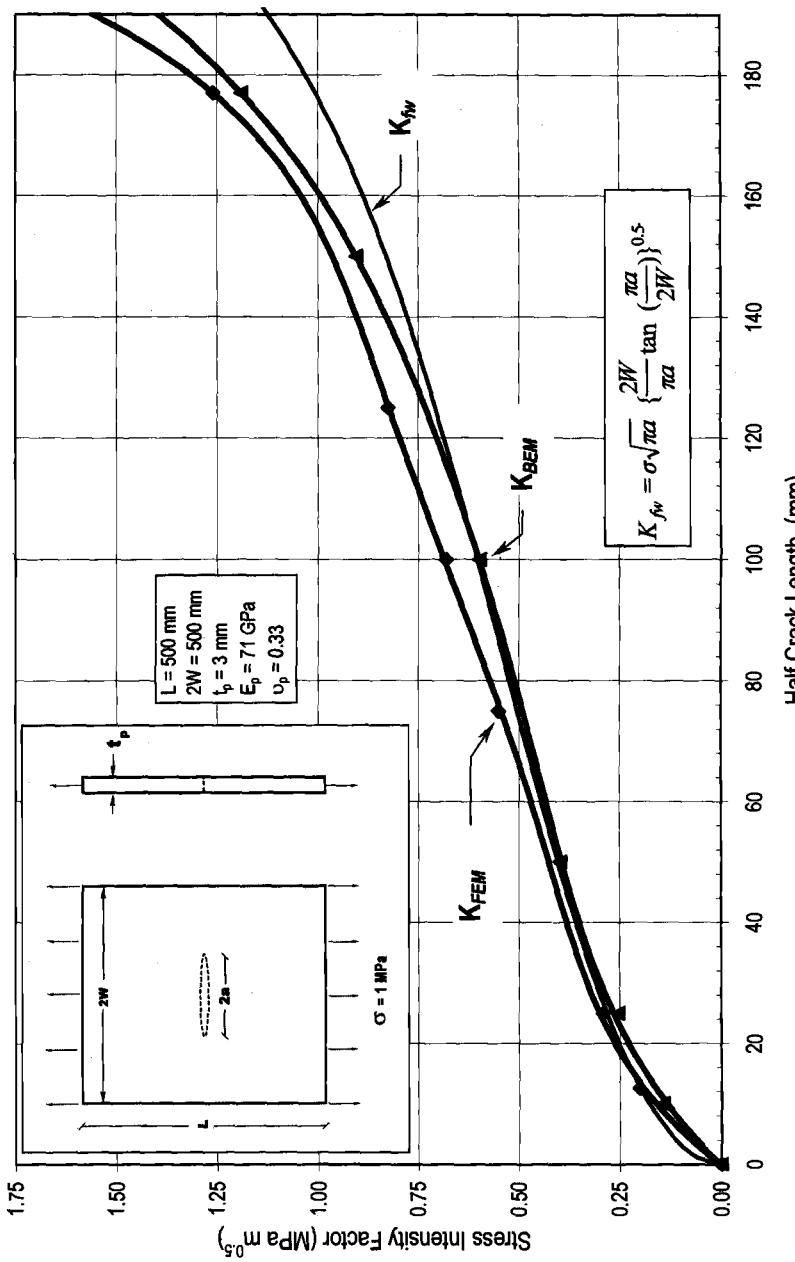


FIG. 1—*SIF solution for center-cracked plate.*

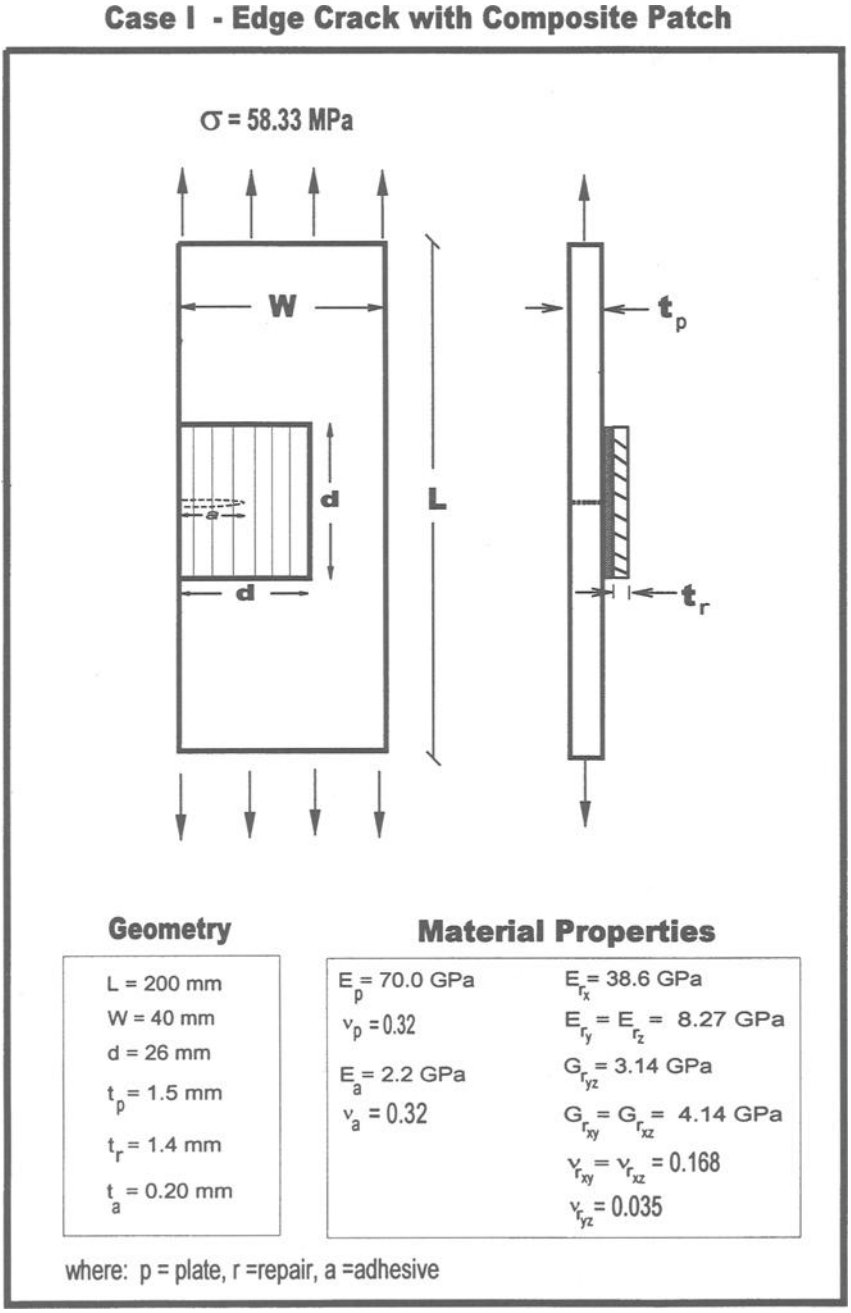


FIG. 2—*Composite and metallic patch repair configurations.*

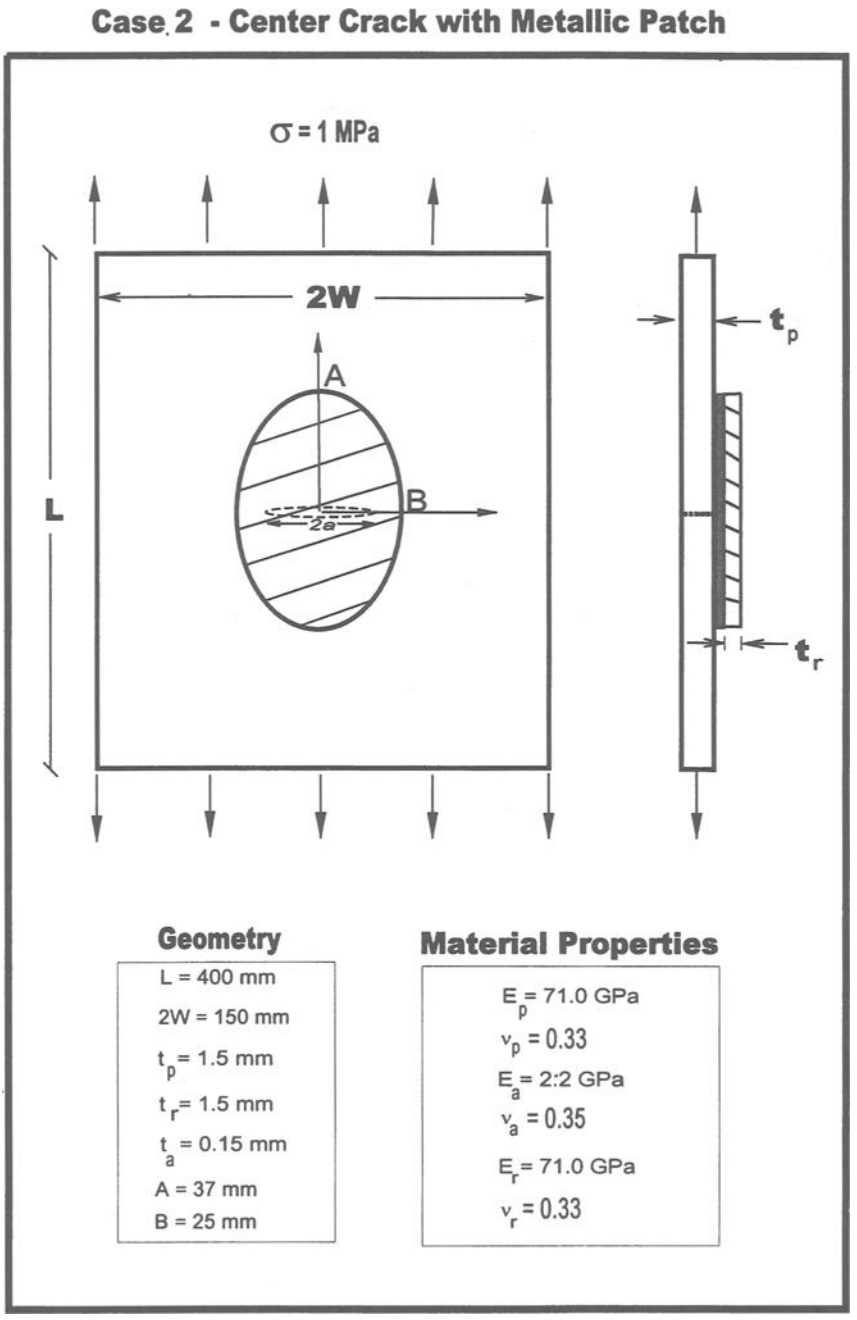


FIG. 2—*Continued.*

TABLE 1—*Comparison of SIF solutions for Case 1—edge crack with composite patch.*

SIF Component (Values in Units of MPa $\sqrt{m}$)	FEM Solution[a]	BEM Model 1	BEM Model 2	BEM Model 3	BEM Model 4
BEM element order[b]	...	Linear	Linear	Linear	Reduced-quadratic
No. of Crack Front Elements	...	2	4	8	8
K_{patch} (patch surface)[c]	4.73	3.89	3.68	3.78	4.70
K_{free} (free surface)[c]	13.43	10.59	11.37	13.09	13.59
K_b (bending)[d]	4.35	3.35	3.85	4.66	4.45
K_m (membrane)[d]	9.08	7.24	7.53	8.44	9.15
K_{rms} (root mean square)[e]	9.42	7.49	7.85	8.85	9.50
$\%K_{rms}$ deviation from FEM	...	20.5%	16.7%	6.1%	−0.7%

[a] Represents reference solution for comparison with BEM results. FEM solution from work by Umamaheswar and Singh [2] using 8-noded, 24 DOF brick elements and geometrically nonlinear analysis.

[b] Element order shown is for the tension panel and repair patch. Reduced-quadratic elements were used on the crack surface in all cases. Linear elements have four corner nodes. Reduced-quadratic elements have four corner nodes and four mid-side nodes.

[c] K_{patch} and K_{free} represent the SIF values determined at the respective locations on the crack front directly by the BEASY computer code.

[d] The bending (K_b) and membrane (K_m) SIF components are determined using the following relationships.

$$K_b = \left(\frac{K_{free} - K_{patch}}{2}\right)$$

$$K_m = \left(\frac{K_{patch} + K_{free}}{2}\right)$$

[e] The K_{rms} value [3] is determined using the following equation and assumes a linear through-thickness variation in the SIF.

$$K_{rms} = \sqrt{K_m^2 + \frac{1}{3}K_b^2}$$

on the crack front for accurate SIF solution. The results (shown in Table 1) for BEM Model 4 indicate a favorable comparison with the FEM results, with the SIF value within approximately 1% of the FEM solution. However, the comparison also raises the issue of the need for a geometrically nonlinear analysis. The following section attempts to quantify the error that results when using small displacement theory.

Solution Accuracy Using Small Displacement Theory—Typically the second order strain terms in the axial component of the strain field can be neglected for the configurations investigated in the present work if the out-of-plane bending effects are not significant. The complete axial component of the strain field for an isotropic plate can be simplified as shown in Eq 3 since the second order axial $(\partial u_1/\partial x_1)^2$ and transverse $(\partial u_3/\partial x_1)^2$ strain terms are small in comparison to the axial strain $(\partial u_1/\partial x_1)$.

$$\varepsilon_{11} = \frac{\partial u_1}{\partial x_1} + \frac{1}{2}\left(\frac{\partial u_2}{\partial x_1}\right)^2 \tag{3}$$

The remaining second order term that needs to be investigated is the out-of-plane strain component $(\partial u_2/\partial x_1)^2$. The magnitude of this out-of-plane strain component was evaluated

from displacement data obtained from the BEM analysis. The displacement data showed that an out-of-plane displacement of 0.091 mm occurred over a half patch length of 13 mm. This translates into a second order strain effect of 24.5 $\times$ 10^{-6} mm/mm in accordance with Eq 3. This value is small compared to the in-plane axial strain ($\partial u_1/\partial x_1$) value of 833 $\times$ 10^{-6} mm/mm. The error introduced by neglecting this second order strain term is approximately 2.9% for this particular analysis.

Center-Cracked Panel with Bonded Metallic Patch (Case 2)—A second slightly different repair configuration was evaluated to help further understand the mechanics of the repaired configuration as well as the efficacy of the patch in reducing the SIF. This configuration is shown in Fig. 2 and consists of a center-cracked panel repaired with a single-sided, adhesively bonded. elliptical, metallic patch. A remote uniform tensile stress of 1 MPa was applied to the panel in a direction normal to the crack surface. A detailed view of the boundary element mesh near the crack surface is shown in Fig. 3. The computer model takes advantage of the symmetry plane passing through the middle of the crack. SIF results are obtained for half-crack lengths of 1.25, 5, 10, 17.5, and 22.5 mm. These results are compared to Rose's analytical solution for a similar case [*13*]. The shear stress and principal stress in both the patch and tension panel are presented to show the stress redistribution resulting from the repair. Results from a numerical crack propagation simulation are also presented to explore the nature of the crack front advancing below the repair.

Stress Intensity Factor Solution—Rose derived an analytical solution for calculating the repaired stress-intensity factor (K_r) for a semi-infinite cracked plate with a bonded repair [*13*]. Rose's solution for a repaired stress-intensity factor is a function of both the joint flexibility and stress reduction under the patch. Rose has proposed an upper bound for the repaired stress intensity factor (K_∞) which is controlled primarily by the adhesive transfer length and applied stress. As such, K_∞ is very sensitive to the adhesive stiffness and the difference between the panel and repair patch stiffness.

For the single-sided repair configuration investigated, the difference in bending stiffness of the panel compared to the reinforced section results in a secondary bending moment. Rose provides an extension to his fundamental upper-bound analytical expression (K_∞) to account

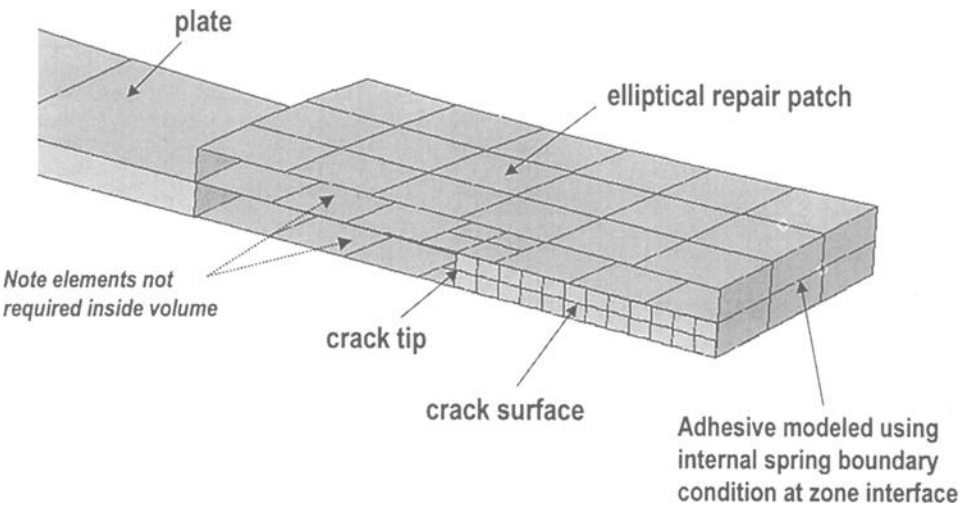


FIG. 3—*Boundary element mesh showing cut-away view of plate, repair patch, and crack surface.*

for this out-of-plane bending effect. The predicted SIF results and Rose's analytical solution for an upper bound limit with bending correction ($\overline{K}_\infty$) are shown in Fig. 4. These data indicate that the SIF solution approaches Rose's upper bound limit with increased crack length. The predicted SIF results shown on Fig. 4 represent root-mean-square (K_{rms}) values computed using the membrane and bending components of the SIF (Table 2). The root-mean-square value of K calculated using Eq 6, shown in Table 2, represents an average value that can be used for comparison with analytical estimates [*3*].

Figure 5 shows the deformed shape determined from the BEM analysis. The out-of-plane bending due to the one-sided reinforcement is well illustrated. The resulting shift in the neutral axis in the reinforced section creates a load path eccentricity and secondary bending moment in the repaired configuration.

The through-thickness variation in the SIF for various crack lengths is shown in Fig. 6. The plotted data represents SIF values computed automatically at crack element nodal points by the BEASY computer code. The data indicate a linear variation in the SIF with the difference in the value at the patch surface compared to the free surface increasing with increased crack length. These differences are 0.72, 1.21, and 2.33 MPa $mm^{0.5}$ for half-crack lengths of 1.25, 5, and 17.5 mm, respectively.

Changes in Stress Field—Stress results for the repaired configuration with a half-crack length of 10 mm are used to illustrate the stress redistribution resulting from the repair. Figure 7 shows a contour plot of the shear stress and maximum principal stress on the repair patch. The highest maximum principal stress (1.45 MPa) occurs on the bottom surface of the repair patch, directly above the crack line (Location A). This stress represents an increase of approximately 30% above the far field stress. The contour plots of shear stress indicate two zones of high shear stress. The first zone (Location B) occurs on the top surface of the patch opposite the crack tip and has a maximum shear stress of −0.16 MPa. The second zone occurs on the bottom edge of the patch [Location C] and has a maximum shear stress of 0.15 MPa.

Figure 8 shows the maximum principal stress distribution on the top and bottom surfaces of the tension panel near the patch boundary. The characteristic high stress at the crack tip (Location D) is apparent on the bottom surface of the panel. With increased mesh refinement the crack tip stress should trend toward an infinite value since there is a stress singularity at this location. The principal stress distribution near the crack tip below the repair patch (Location E) is characterized by a reduction in stress magnitude compared to the bottom surface of the panel. This is consistent with the load transfer from the cracked panel to the repair patch at this location.

A stress increase occurs on the bottom surface of the panel near the step change in thickness along the patch boundary (Location F). This stress increase is marked by the 1.40 MPa contour that follows the outline of the patch boundary. There is maximum compressive principal stress of −1.12 and 5.61 MPa on the bottom and top surface of the panel, respectively, near the high curvature edge of the patch (Locations G and H). This high stress gradient through the thickness of the panel below the patch suggests very localized bending at the patch tip.

Numerical Crack Propagation Simulation—Figure 9 shows the crack growth path for a through-the-thickness crack of crack length ($2a$) = 2.5 mm, advanced in four crack step increments. The crack growth distances vary slightly for each step and are controlled by the maximum element size adjacent to the crack front. The maximum crack growth extension (Δa_{max}) for each step is equal to the maximum element edge length on the crack front. Other points on the crack front are scaled relative to this maximum value. The crack growth increments displayed on Fig. 9 are therefore a consequence of the maximum crack front

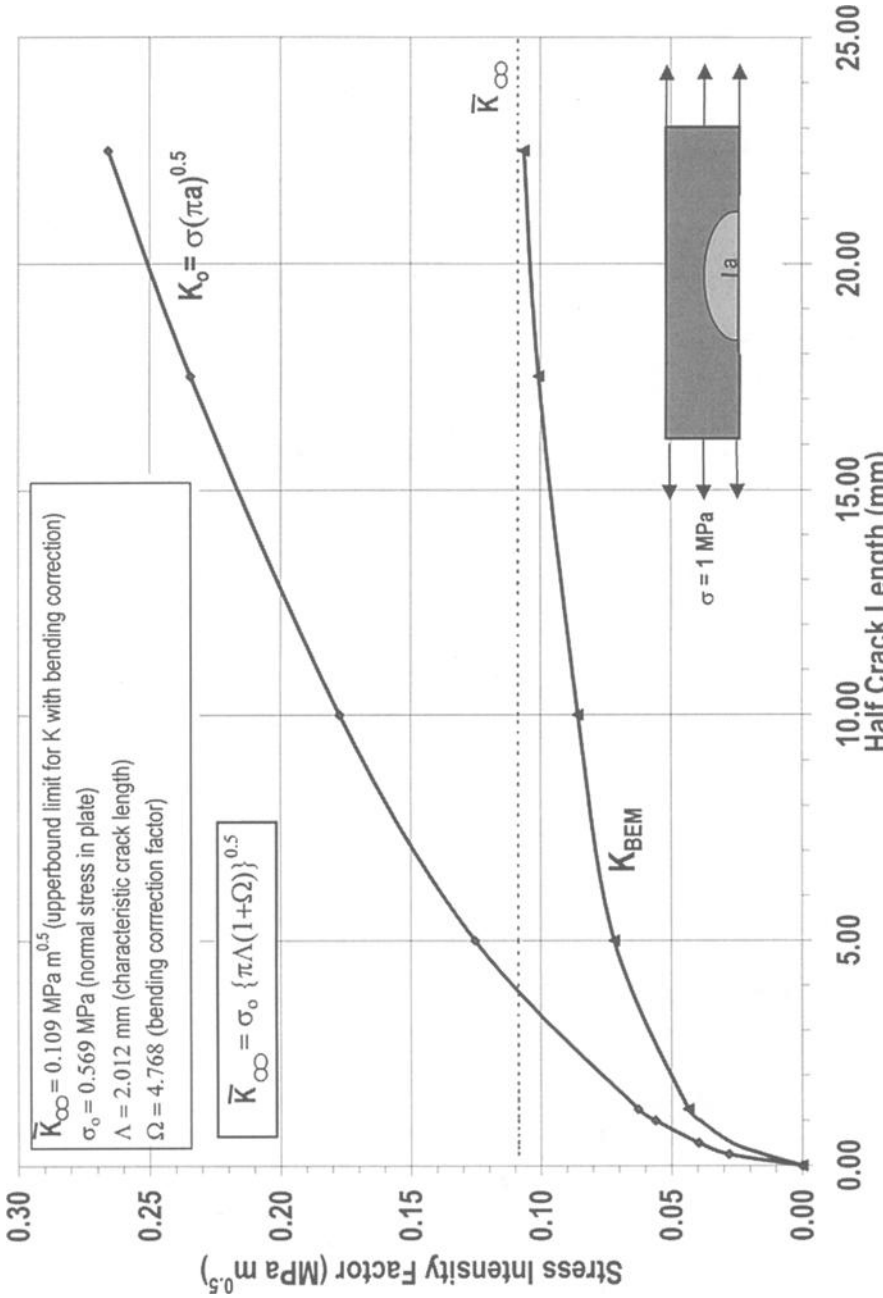


FIG. 4—*Plot showing reduced SIF for center-cracked panel with single-sided elliptically shaped metallic patch.*

TABLE 2—*BEASY SIF solutions for repaired tension panel.*

a, mm	K_{patch}	K_{free}	K_b	K_m	K_{rms}
1.25	0.032	0.054	0.011	0.043	0.044
5.00	0.052	0.090	0.019	0.071	0.072
10.00	0.058	0.111	0.026	0.084	0.086
17.50	0.062	0.135	0.037	0.099	0.101
22.50	0.064	0.144	0.040	0.104	0.106

[a] Units for SIF are MPa · $m^{0.5}$.

element size and not a true indication of changes in crack growth rate between successive increments.

The predicted crack fronts propagate in a nearly curvilinear fashion after the initial first step. This is consistent with the variation in the SIF along the crack front (Fig. 10). The crack front grows fastest near the free end of the panel with each subsequent crack front being nearly parallel to the preceding crack front. With the exception of localized SIF values near the patch and free surfaces it appears that the SIF distribution along the crack front is approaching a nearly constant value. Increased refinement of the crack front mesh and additional crack step increments may provide a more accurate representation. It should be noted that the accuracy of the SIF values determined at the intersection of the crack front with the free surface should be viewed with some caution given that the stress singularity at this location varies from the typical $1/\sqrt{r}$ stress singularity.

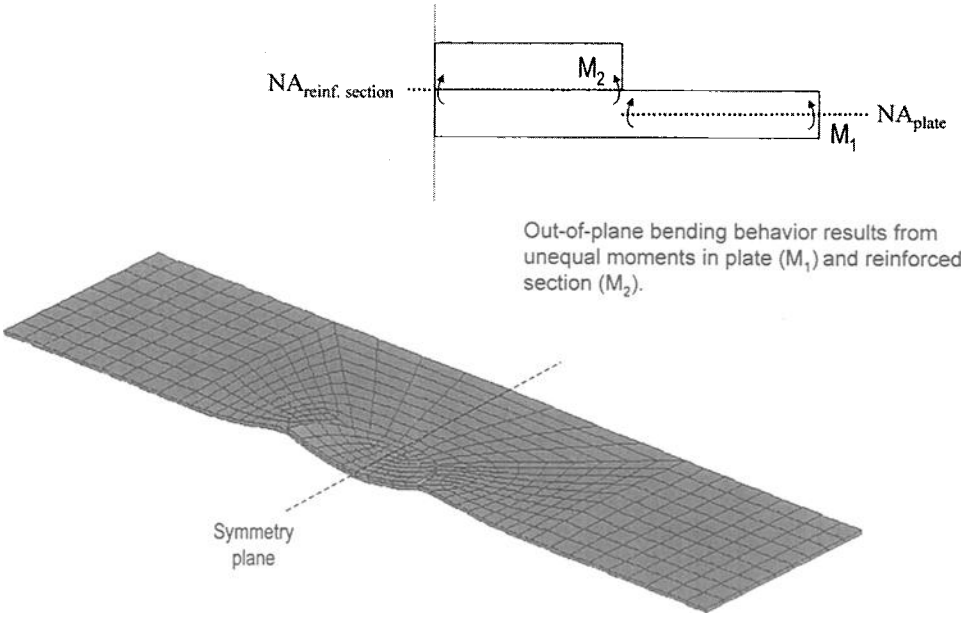


FIG. 5—*Deformed shape of center-cracked tension panel with single-sided elliptically shaped metallic patch.*

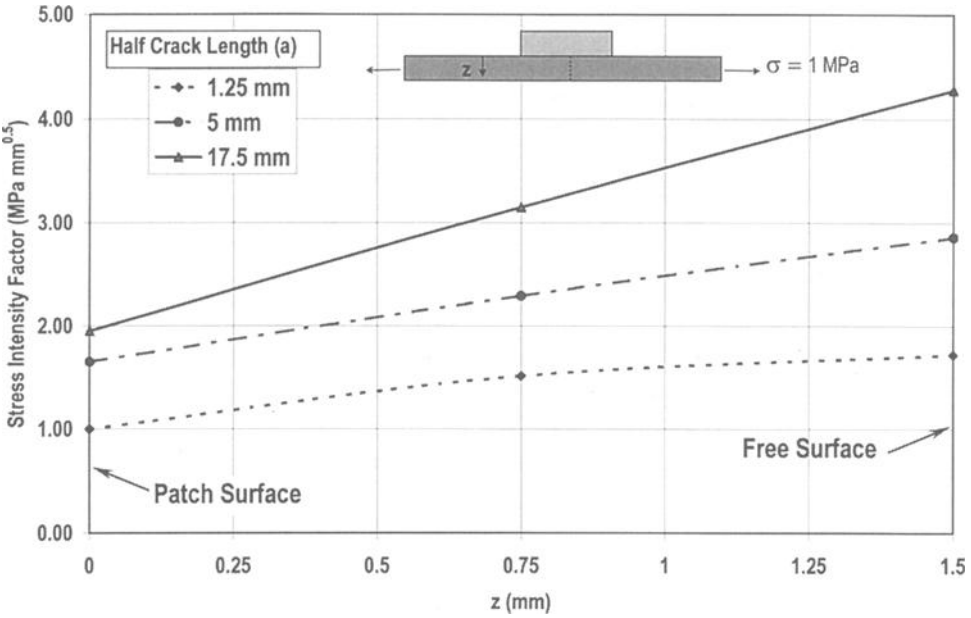


FIG. 6—*Through-thickness SIF variation for center-cracked panel with single-sided elliptically shaped metallic patch.*

Bonded Patch Repair of Pressurized Cylindrical Shell

The boundary element solution and modeling approach used in the previous sections to investigate repair of thin panels is extended to investigate the fracture behavior of a cylindrical shell, since this geometry is more representative of airframe structures. Computer models of both a cracked and repaired cylindrical shell are analyzed to determine the reduction in SIF. The numerical results provide data to help assess the influence of curvature on the SIF distribution and on the effectiveness of the bonded patch repair. The data presented in the following section are intended to characterize the variation in the SIF through-the-thickness of the shell for a single crack length.

Cylindrical Shell with Longitudinal Through-Crack

An internally pressurized cylindrical shell with a longitudinally oriented, 20 mm long, through-crack was analyzed to determine a SIF solution for this configuration. The nominal radius of the cylinder is 159.2 mm and the wall thickness is 3 mm. The shell is modeled using material properties representative of a 7075 T6 aluminum alloy. The computer model assumes two planes of symmetry, the first through the midplane of the cylindrical shell at the crack location, and the second through the long axis of the cylindrical shell. A uniform internal pressure of 1 MPa is applied to the inside face of the cylindrical shell. The SIF result is compared to the NASGRO solution for this configuration.

Figure 11 shows the through-thickness SIF distribution for a pressurized cylindrical shell with longitudinal through-crack ($2a$ = 20 mm). The data points shown in Fig. 11 represent the SIF values along the crack front (located at 0.00, 0.75, 1.50, 2.25, and 3.00 mm from

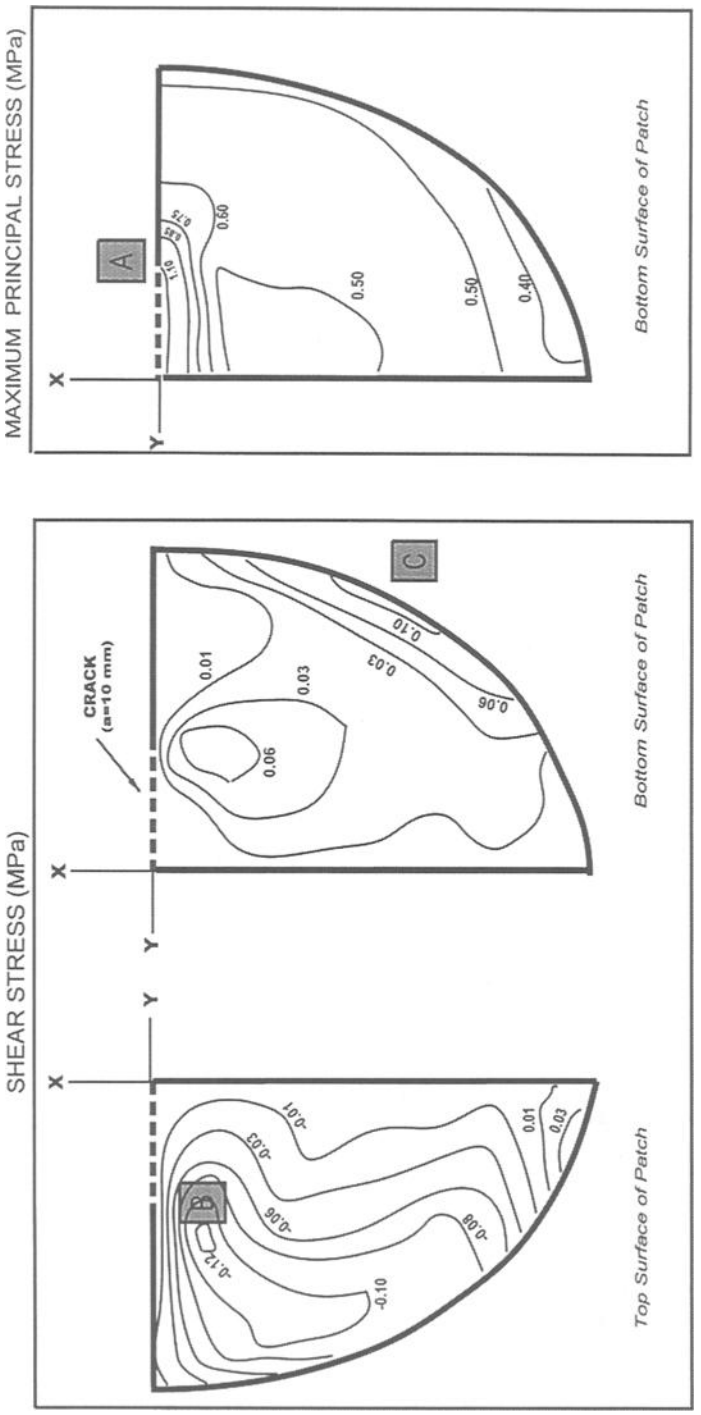


FIG. 7—*Contour plots of stress field in repair patch.*

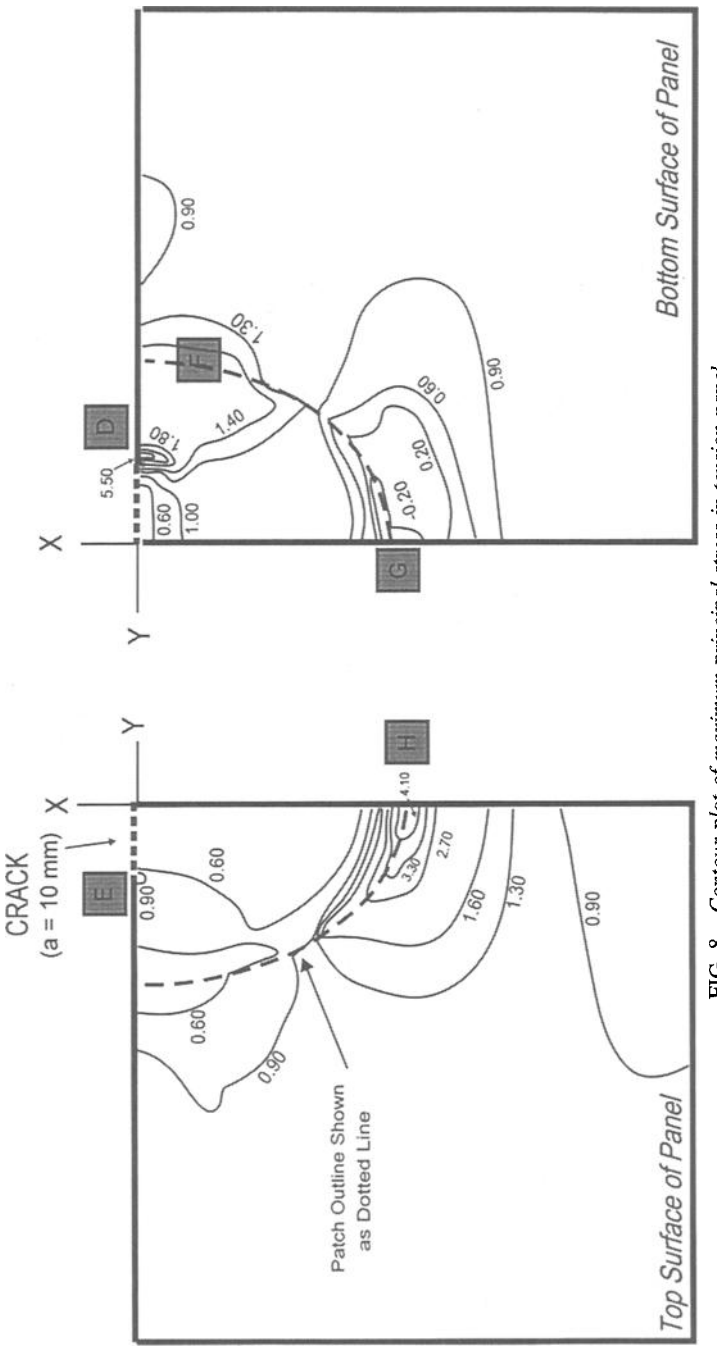


FIG. 8—*Contour plot of maximum principal stress in tension panel.*

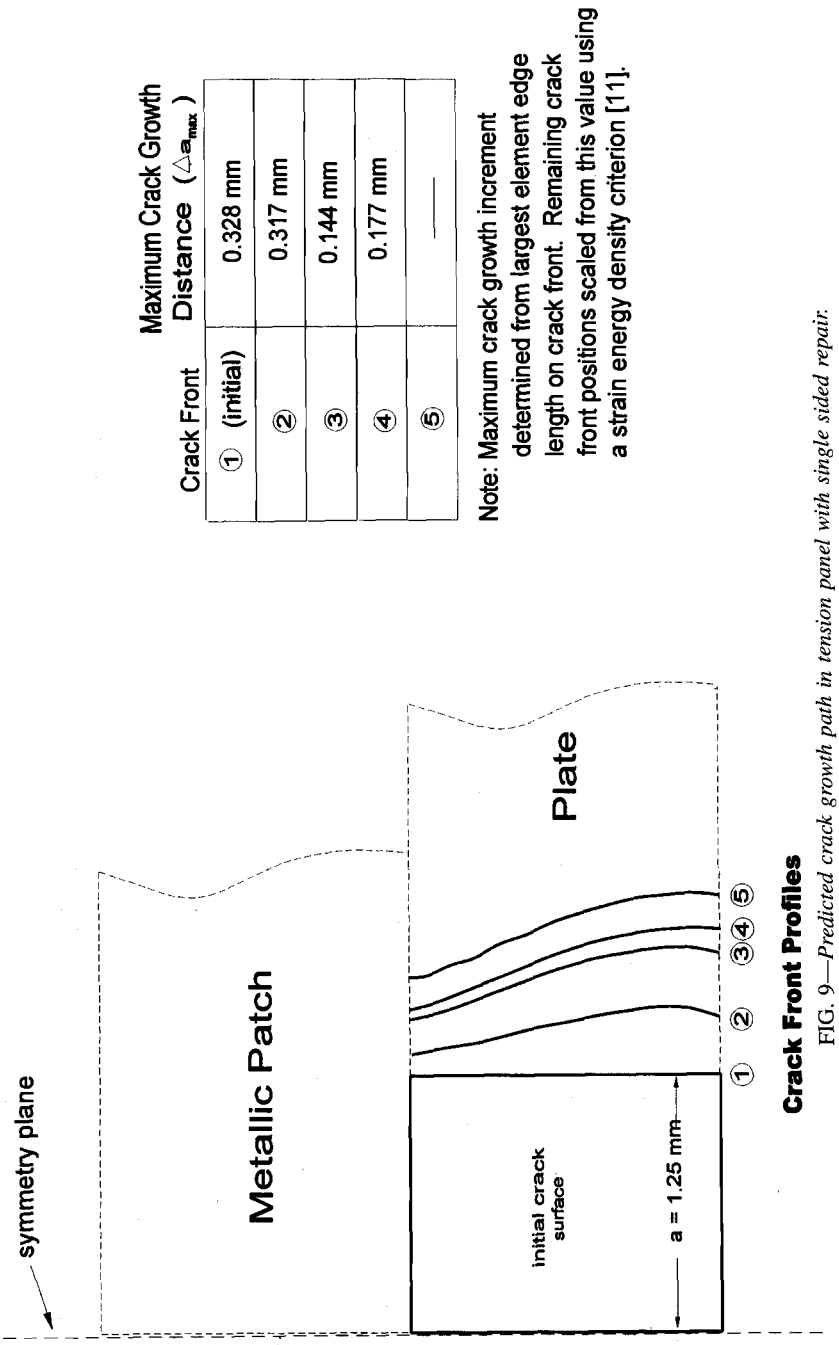


FIG. 9—*Predicted crack growth path in tension panel with single sided repair.*

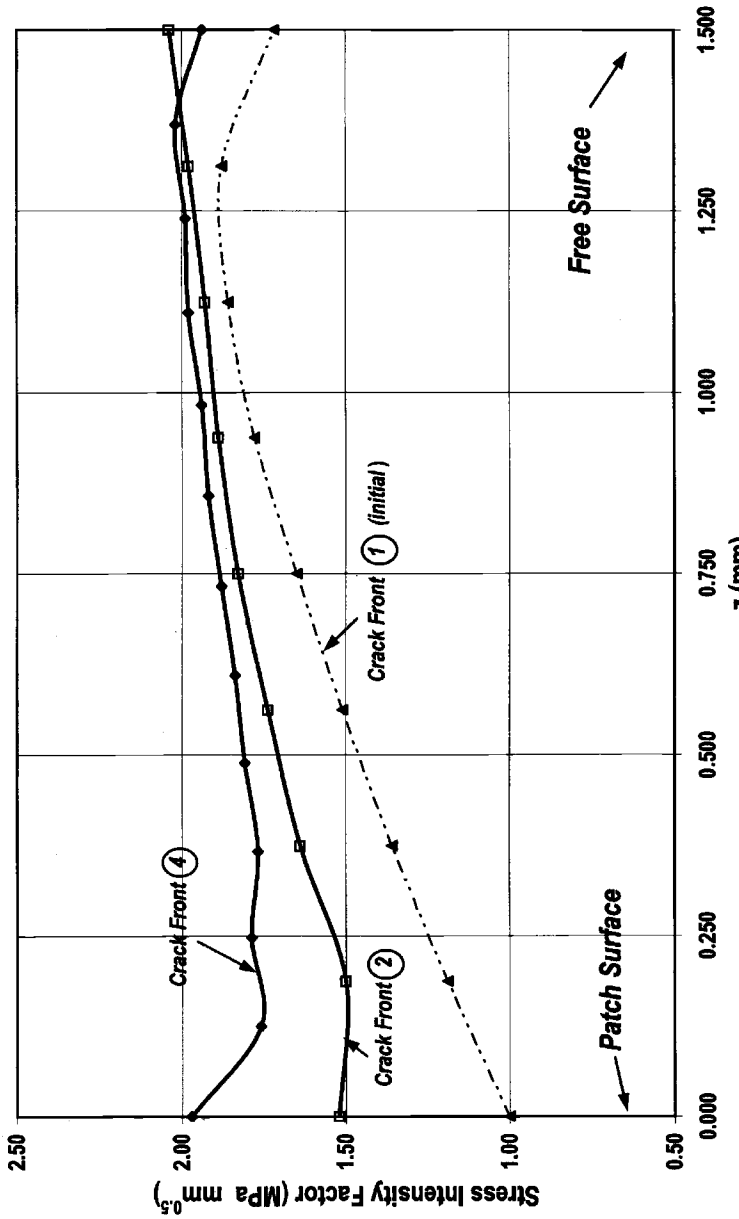


FIG. 10—*Change in SIF distribution for advancing crack front.*

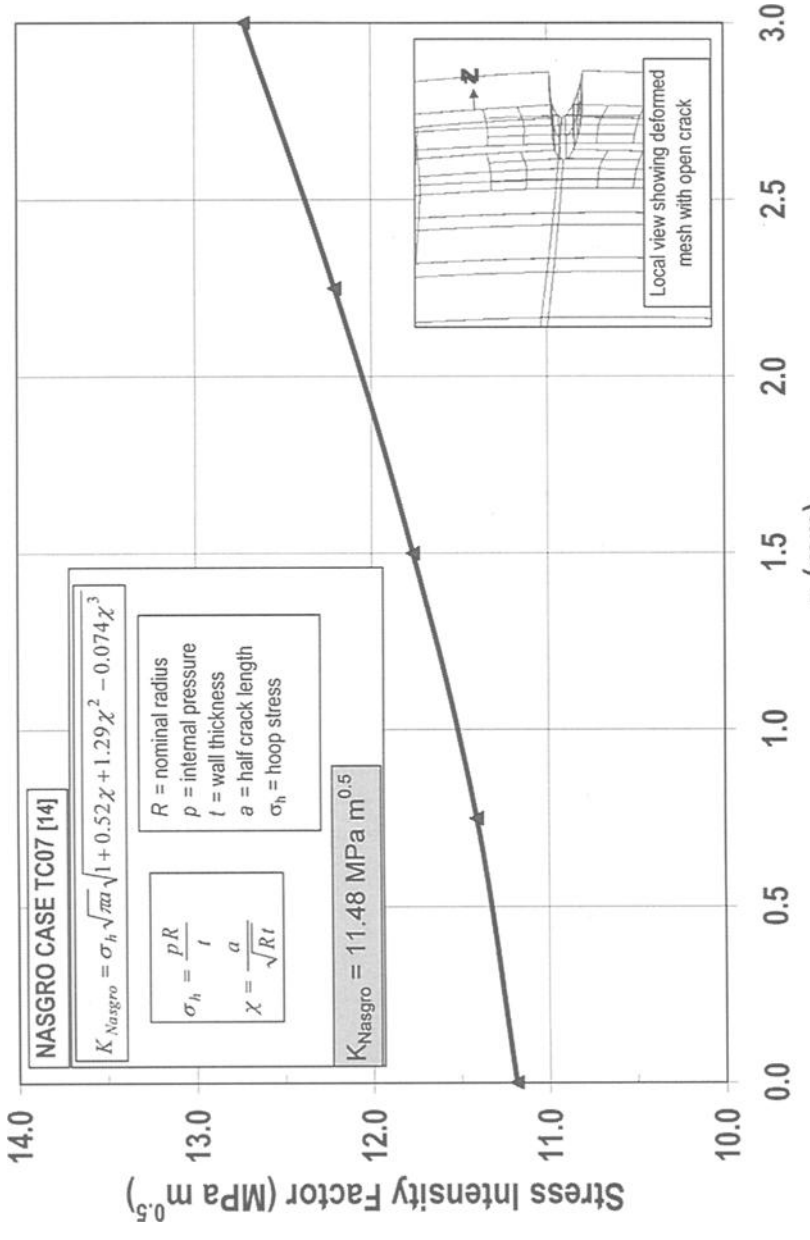


FIG. 11—*SIF solution for pressurized cylindrical shell with longitudinal through-crack of length* (2a) = 20 *mm.*

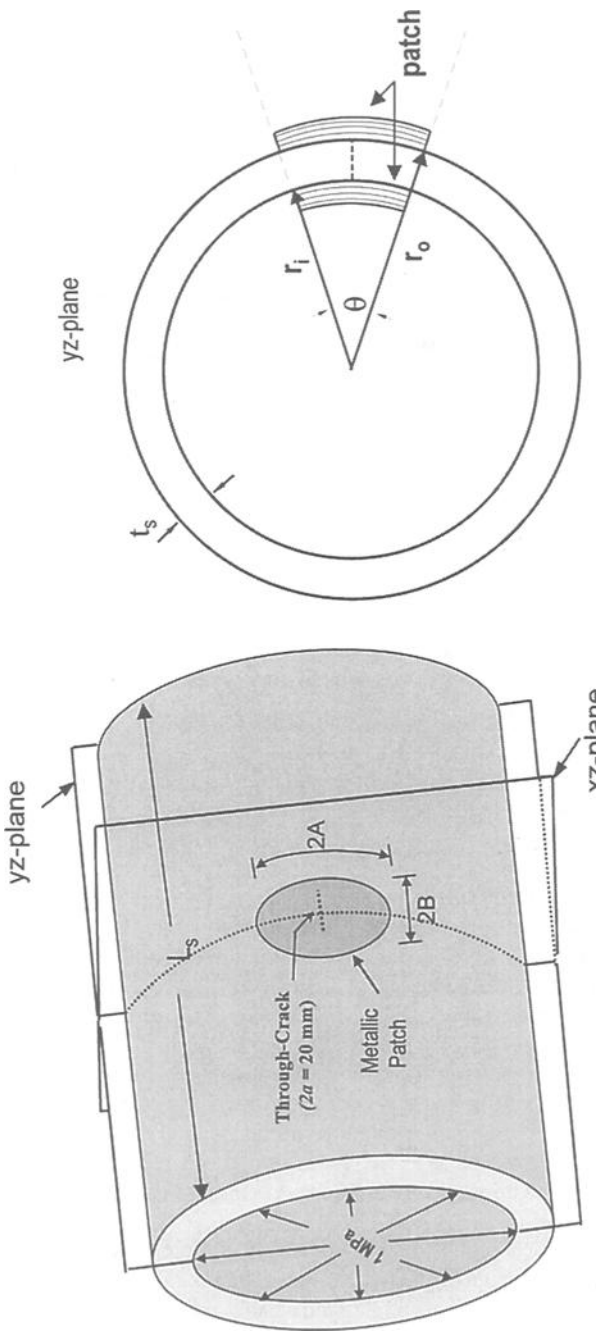


FIG. 12—*Metallic patch repair configuration for pressurized cylindrical shell.*

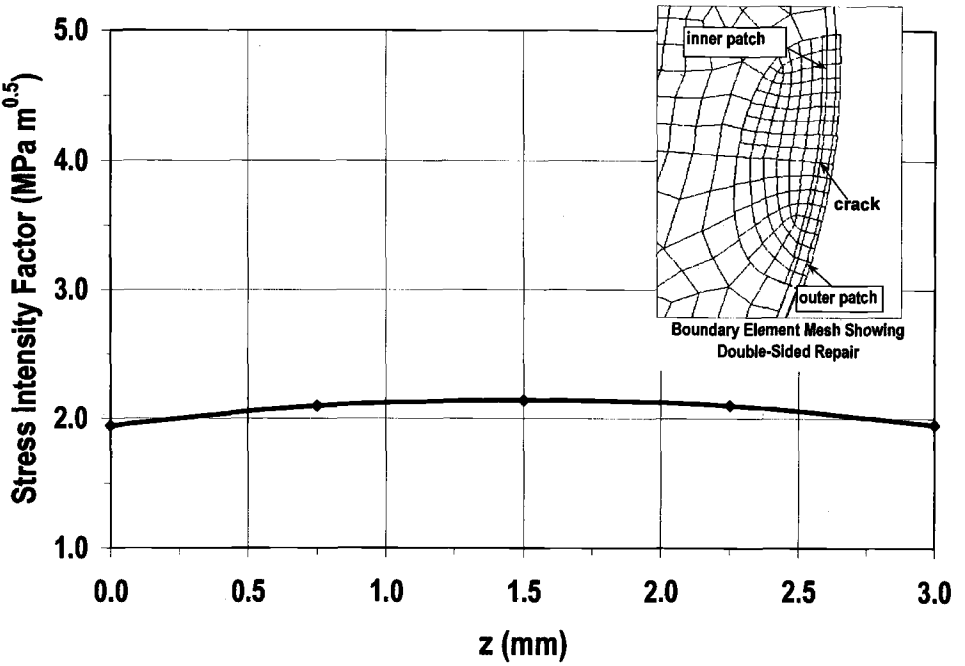


FIG. 13—*Through-the-thickness variation in SIF for a cracked (crack length* (2a) = 20 mm), *pressurized cylindrical shell with double sided metallic patch.*

inner surface of the cylinder) determined from the boundary element analysis. A regression analysis (least squares fit) was performed and a second-order polynomial curve was fit to these data as a trendline. The data shown in Fig. 11 indicate an approximately linear, through-thickness variation in the SIF solution. The SIF solution increases from the inside surface (11.16 MPa $m^{0.5}$) to the outside surface (12.71 MPa $m^{0.5}$) of the shell. Because the displacement in the circumferential direction controls Mode I crack opening, and the governing equations for a cylindrical shell define a linear increase in circumferential strain toward the outer shell surface, the SIF distribution obtained seems reasonable. The root-mean-square value (11.76 MPa $m^{0.5}$), computed from the data in Fig. 11, is within 2.4% of the NASGRO solution (11.48 MPa $m^{0.5}$) for this case [*14*].

This NASGRO solution was obtained by fitting a polynomial equation to three-dimensional, geometrically linear, FEM results for this configuration. The polynomial equation shown in the inset box on Fig. 11 is based on a relationship between crack length (*2a*), wall thickness (*t*), and nominal cylinder radius (*R*). The NASGRO result represents an average through-thickness value. Further details on this formulation can be found in the work by Newman [*15*].

Bonded Repair of Cylindrical Shell—The configuration described in the preceding section was modified to include a double-sided, elliptical, metallic patch. The repaired configuration and material properties are shown in Fig. 12. The double-sided patch reduces the SIF value in the cracked cylindrical shell by a factor of approximately 6 (see Fig. 13) and essentially eliminates the through-thickness variation in the SIF. Because of the symmetric nature of the repair the use of a geometrically linear analysis for this case appears reasonable.

Concluding Remarks

Computer modeling can be used to assess structural repairs made with bonded patches. The boundary element approach offers several advantages in this regard including:

1. Simplified modeling due to the surface only mesh requirement for the cracked structure and repair patch.
2. Efficient modeling of the adhesive using a zone interface boundary condition that eliminates the need for element discretization. Both the axial and shear properties of the adhesive can be modeled by simply creating a distributed system of springs with appropriate stiffness properties.
3. Direct computation of the SIF without the need to extract nodal forces or displacements for further postprocessing.
4. Crack propagation studies can be performed using the DBEM. The change in crack front morphology associated with growth below a bonded repair patch can be characterized.

The BEM modeling approach and solution methodology described in the present analysis provided good comparison with analytical and FEM solutions and should be explored further as means to conduct design assessment studies before implementing patch repairs.

References

[1] Kumar, A. M. and Singh, R., "3D Finite Element Modelling of a Composite Patch Repair," *Proceedings*, International Conference on Fracture, ICF-9, 1997, pp. 2159–2166.
[2] Umamaaheswar, T. V. R. S. and Singh, R., "Modelling of a Patch Repair to a Thin Cracked Sheet," to be published in *Engineering Fracture Mechanics*, Elsevier Science Ltd, 1998.
[3] Callinan, R. J., Rose, L. R. F., and Wang, C. H., "Three Dimensional Stress Analysis of Crack Patching," *Proceedings*, International Conference on Fracture, ICE-9, 1997, pp. 2151–2158.
[4] Sun, C. T., Lug, J., and Arendt, C., "Analysis of Cracked Aluminum Plates Repaired with Bonded Composite Patches," *AIAA Journal*, Vol. 34, 1996, pp. 369–374.
[5] Young, A., Cartwright, D. J., and Rooke, D. P., "Model Studies of Repair Patches," *Proceedings*, International Conference on Fatigue, Corrosion, Cracking, Fracture Mechanics and Failure Analysis, Salt Lake City, 1985, pp. 339–346.
[6] Salgado, N., "Boundary Element Methods for Damage Tolerance Design of Aircraft Structures," *Topics in Engineering Series*, Vol. 33, Computational Mechanics Publications, Southampton, UK, and Boston, 1998.
[7] Young, A., Rooke, D. P., and Cartwright, D. J., "Analysis of Patched and Stiffened Cracked Panels using the Boundary Element Method," *International Journal of Solid Structures*, Vol. 29, No. 17, 1992, pp. 2201–2216.
[8] Portela, A. and Aliabadi, M. H., "The Dual Boundary Element Method: Effective Implementation for Crack Problems," *International Journal for Numerical Methods*, Vol. 33, 1992, pp. 1269–1287.
[9] Portela A., Aliabadi M. H., and Rooke D. P., "Dual Boundary Element Incremental Analysis of Crack Propagation," *Computers & Structures*, Vol. 46, No. 2, 1993, pp. 237–247.
[10] *BEASY Reference Manual*, Computational Mechanics Inc., Billerica, MA, 1999.
[11] Mi, Y., "Three-Dimensional Analysis of Crack Growth," *Topics in Engineering Series*, Vol. 28, *Computational Mechanics Publications*, Southampton UK and Boston USA, 1996.
[12] Anderson T. L., *Fracture Mechanics, Fundamentals and Applications*, CRC Press Inc., Boca Raton, Florida, 1995.
[13] Rose, L. R. F., "Theoretical Analysis of Crack Patching," *Bonded Repair of Aircraft Structures*, A. Baker and R. Jones, Eds., Martinus Nijhoff Publishers, 1988, pp. 77–106.
[14] Fatigue Crack Growth Computer Program "NASGRO" Version 3.00, *Reference Manual, Revision B*, NASA, September 1998.
[15] Newman, J. C., Jr., "Fracture Analysis of Surface and Through Cracks in Cylindrical Pressure Vessels," NASA TN D-8325, December 1976.

Pizhong Qiao,[1] *Julio F. Davalos,*[2] *and Brent S. Trimble*[3]

Effect of Moisture on Fracture Toughness of Composite/Wood Bonded Interfaces

REFERENCE: Qiao, P. Z., Davalos, J. F., and Trimble, B. S., **"Effect of Moisture on Fracture Toughness of Composite/Wood Bonded Interfaces,"** *Fatigue and Fracture Mechanics: 31st Volume, ASTM STP 1389,* G. R. Halford and J. P. Gallagher, Eds., American Society for Testing and Materials, West Conshohocken, PA, 2000, pp. 526–544.

ABSTRACT: Current research on wood reinforcement has focused on the use of fiber-reinforced plastic (FRP) strips or fabrics bonded to wood members. Although significant increases in stiffness and strength have been achieved by this reinforcing technique, there is a concern about the reliable performance of the wood-FRP interface bond, which can be susceptible to delamination. The objective of this study is to present a combined analytical/experimental study to evaluate the effect of moisture on fracture toughness of composite/wood bonded interfaces under Mode I loading. A contoured double cantilever beam (CDCB) specimen is used to characterize the fracture toughness of both wood-wood and wood-FRP samples. The specimens are designed by the Rayleigh Ritz method to achieve a linear rate of compliance with respect to crack length and are calibrated experimentally and also analytically by the finite element method. Both wood-wood and wood-FRP samples are tested under dry and wet conditions, and bonded interface fracture toughness data under Mode I loading are obtained. The guidelines and procedures for the modeling and design of CDCB specimens for hybrid or dissimilar adherends using a Rayleigh-Ritz model are presented briefly, and a modified Rayleigh-Ritz method is further developed. The effect of moisture on fracture toughness is evaluated, and increases in interface fracture toughness are observed due to moisture absorption for wet wood-wood and wood-FRP samples; the toughening of the interface under moisture is due mainly to a much more plastic fracture failure mode of the interface.

KEYWORDS: fiber-reinforced plastics, wood, Mode I fracture, moisture effect, bonded interface, hybrid or dissimilar material adherends

Fiber-reinforced plastic (FRP) composites are being used for reinforcement of wood, concrete, and steel. Current research on wood reinforcement has focused on the use of fiber-reinforced strips or fabrics bonded to wood members (e.g., FRP has been used commercially for reinforcement of glulam timber beams). Although significant increases in stiffness and strength have been achieved by this reinforcing technique, there is concern about the reliable performance of the wood-FRP interface bond, which can be susceptible to delamination. An inadequate interface bond strength and integrity can lead to premature failure of a reinforced wood member. Several adhesive systems have been used successfully to reinforce wood

[1] Assistant professor, Department of Civil Engineering, The University of Akron, Akron, OH 44325-3905; Email: Qiao@uakron.edu.

[2] C. W. Benedum Distinguished Teaching Professor, Department of Civil and Environmental Engineering, West Virginia University, Morgantown, WV 26506-6103.

[3] Graduate research assistant, Department of Civil and Environmental Engineering, West Virginia University, Morgantown, WV 26506-6103.

Copyright© 2000 by ASTM International www.astm.org

materials with composites; however, there is little information on interface fracture toughness, particularly under exposed service conditions.

It has been shown that delamination of bonded interfaces can be described by fracture mechanics models [*1*], and although three distinct modes of fracture can be defined, an interface bond is less resistant to crack extension (delamination) under the action of normal load than under shear load, and, therefore, Mode I (opening mode) fracture is generally more critical than other modes of fracture. In this study, a newly developed contoured double cantilever beam (CDCB) specimen [*1*] is used to evaluate the fracture toughness of wood-FRP bonded interfaces. A bi-layer CDCB specimen is designed by the Rayleigh-Ritz method and used for fracture toughness tests of bonded wood-wood and wood-FRP interfaces. Using linear-slope CDCB specimens, fracture tests are performed for dry and wet specimens to determine critical loads for crack initiation and crack arrest, from which the critical strain energy release rates (G_{Ic}) are evaluated by making use of experimentally verified constant compliance rate changes over defined crack lengths. The effect of moisture on fracture toughness of bonded interfaces is evaluated; this information is useful in design of wood-FRP structures under exposed service conditions.

This paper is organized as follows: (1) material characterization and design of CDCB specimens, (2) experimental compliance calibration tests, (3) finite element modeling of specimens and verification of compliance rate change, and (4) evaluation of fracture toughness of bonded interfaces.

Material Characterization and Design of Contoured DCB Specimens

The theoretical developments used to design the CDCB specimens are described in Ref *1*. A typical CDCB sample is shown in Fig. 1. At the interface, the bi-layer laminate consists of Red Maple wood bonded to constant-thickness Phenolic FRP; for convenience of manufacturing the test samples, Red Maple is also used for the contour portions attached to the adherends. When testing moisture-saturated samples, the geometries of the samples are defined, accounting for the degraded stiffness properties of the materials due to moisture effects. In this section, a brief review of the theory and design procedure for CDCB specimens is presented first. Then, the material characterization of wood and FRP under dry and wet conditions is discussed. Finally, the contour shapes of CDCB specimens with different material/moisture combinations are designed by the Rayleigh-Ritz method.

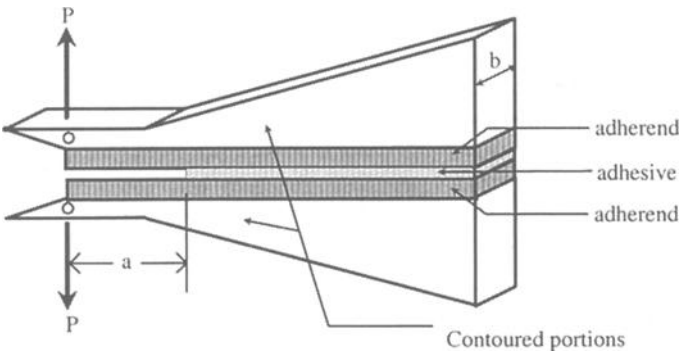


FIG. 1—*A schematic view of a contoured double cantilever beam (CDCB).*

Overview of Theory

The conventional method for determining the strength of an adhesive interface under Mode I fracture is by testing double cantilever beam (DCB) specimens under cleavage loading [2]. The critical strain energy release rate, G_{Ic}, which is a measure of the Mode I fracture toughness of an interface bond, is given by

$$G_{Ic} = \frac{P_c^2}{2b}\frac{dC}{da} \tag{1}$$

where P_c = critical load, b = thickness of the specimen, and dC/da = rate of change of compliance C with respect to crack length a (Fig. 1). The testing for fracture toughness of interface bonds obtained with conventional DCB specimens requires simultaneous measurements of critical load and crack length for each load step. The value of dC/da in Eq 1 depends on the accuracy of the crack length measurement, which is generally a difficult task. The measurement of crack length can be avoided by contouring the DCB specimen, such that dC/da is a constant, and, in this case, the specimen is known as the contoured double cantilever beam (CDCB). To use the CDCB specimen for interface bonds of dissimilar adherends, it is convenient to use constant-thickness adherends bonded to contoured portions made of a material that is easy to shape, such as wood-based materials. Due to the relative complexity of defining the shape of a CDCB specimen, a numerical method based on the Rayleigh-Ritz solution was recently developed [*1*] to design the shape of the test specimens. In the Rayleigh-Ritz solution [*1*], the variation of the displacement and rotational degrees of freedom in the beam are approximated by interpolation functions over the entire domain of the beam system, and, through the minimization of the total potential energy with respect to the unknown displacement vectors, the displacement parameters are computed, in which the compliance is obtained by computing the beam tip deflection. For a given crack length, the CDCB specimen is modeled as a cantilever beam to obtain its compliance; the expression for compliance of the specimen is derived using a Rayleigh-Ritz solution and defined as a function of the crack length and the slope of the contour. A first-order shear deformation theory [*3*] is used to account for shear deformation, which is important for materials such as FRP and wood.

Based on the compliance derived from the Rayleigh-Ritz solution, a methodology for the design of the contour of a CDCB specimen was proposed [*1*]. A graphical representation of the geometric parameters used in defining the CDCB specimen is shown in Fig. 2, where the constant height of the base adherend is h_b, and the bonded contoured portion of the CDCB specimen is assumed to have an initial constant height h_1 for an initial crack length a_1. This initial constant height should provide sufficient material to accommodate loading fixtures, such as an attached hinge or a pin through the specimen. The expression for dC/da is obtained by differentiating the expression for the compliance with respect to the crack length. For each discrete crack length ($a \geq a_1$), a linear shape of the contour is assumed. The following step-by-step procedure summarizes the methodology for the design of the contoured specimen:

1. Compute the compliance of the CDCB specimen by the Rayleigh Ritz method [*1*] as a function of crack-length and slope: $C = C(a,p)$.
2. Differentiate the compliance function to obtain dC/da.
3. Evaluate dC/da for a discrete value of a, say $a = a_2$ for $a_2 > a_1$ (Fig. 2).
4. Equate dC/da, evaluated at a discrete crack-length, to a predefined constant value K to solve for the slope, say $p = p_2$. That is, let $dC/da(a_2,p_2) = K$ and solve for p_2.

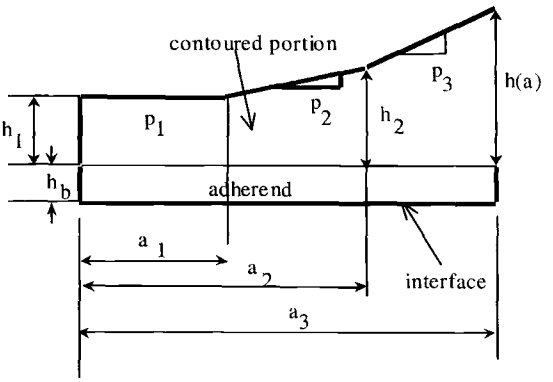


FIG. 2—*Geometric parameters of the contour of the CDCB specimen.*

5. Then, $h(a) = h_1 + p_2(a - a_1)$ for $a > a_1$, say $h_2 = h_1 + p_2(a_2 - a_1)$.
6. Repeat Steps 1 through 5 to solve for p_3.

This procedure is repeated for each incremental crack-length until the contour for the entire length of the CDCB specimen is obtained. When an interface of dissimilar materials is considered, the contour has to be developed for each adherend, since the stiffnesses of the adherends would be different, and the shape of the contour would be different on either side of the interface bond in order to achieve the same rate of compliance change for each half of the specimen.

The exact contour obtained from the above procedure has a convex shape [*1*], obtained by fitting a polynomial function through the discretized heights. However, the effort and cost involved in accurately manufacturing such a complex geometry can be significant, particularly since it is often necessary to test several specimens to obtain a good estimate of the fracture toughness of the interface. The exact contour can be simplified by a linear approximation function obtained through regression of the discrete heights [*1*]. Then, through experimental and analytical investigations of the compliance rate change of the simplified linear-slope CDCB specimens [*4*], the linearity of the compliance crack-length relationship of linear-slope CDCB specimens can be verified for specific ranges of crack lengths.

Material Characterization

To design the CDCB specimens for dry and wet conditions, the elastic properties of the wood material under the required moisture conditions must be obtained. For instance, the contoured shapes of the moisture-saturated samples should be defined accounting for the degraded stiffness properties of the materials due to moisture effects. The change in stiffness properties of pultruded phenolic FRP laminates due to moisture ingress can be neglected, and the properties of dry FRP samples are used for design of both dry and wet conditions.

The longitudinal-tensile and shear moduli of Red Maple were obtained from tension and torsion coupon tests, respectively. For dry tension tests, 12 specimens with dimensions of 25.4 by 12.7 by 508 mm (1 by 1/2 by 20 in.) were conditioned to 12% moisture content (MC) in an environmental chamber; for wet tension tests, another 12 specimens of the same dimensions were immersed in a water bath and subjected to one cycle of 40-min vacuum and 40-min pressure soak in a closed cylinder to saturate the wood samples with more than

TABLE 1—*Material properties of Red Maple under dry and wet conditions.*

	E, GPa	*G*, GPa
Dry Samples	13.714 (COV = 4.57%)	1.248 (COV = 5.40%)
Wet Samples	9.039 (COV = 12.24%)	0.586 (COV = 3.72%)

100% MC [*5*]; then, the samples were immediately tested. Similarly, eight dry and eight wet samples with dimensions of 38.1 by 38.1 by 432 mm (1-1/2 by 1-1/2 by 17 in.) were also prepared for the torsion tests. Table 1 lists the average tensile and shear moduli for Red Maple under both dry and wet conditions. Six pultruded phenolic FRP strips 2.54 mm (0.1 in.) thick were also tested under tension. The lay-up of the FRP laminate (V_f = 50.98%) consists of two continuous strand mat (CSM) layers (1 oz in weight) and one unidirectional roving layer (113 Yield). The CSM layers are located on both outside surfaces and provide desirable surface texture for bonding. In Table 2, the tensile modulus is compared with the micro-macromechanics model prediction [*6*]. The FRP strips were too flexible to test in torsion, and the shear modulus prediction by the micro/macromechanics model is used in design. The material properties in Tables 1 and 2 are used to design the tapered shapes of wood-wood, FRP-FRP, and wood-FRP CDCB specimens.

Tapered Shapes of the Designed CDCB Specimens

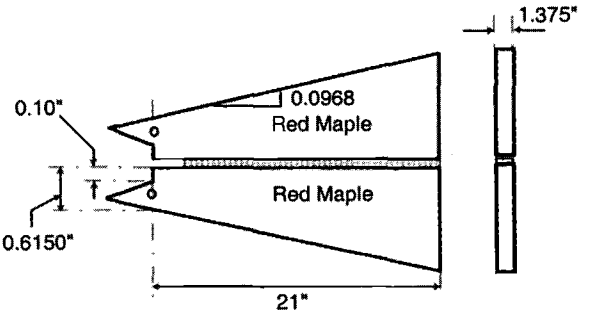
Based on the design procedures and material properties described above, four tapered shapes of the CDCB specimens (Figs. 3 and 4) are designed using the Rayleigh-Ritz method: (1) wood-wood/dry, (2) wood-wood/wet, (3) FRP-FRP/dry, and (4) FRP-FRP/wet. The compliance rate changes (dC/da) for the above four linear-slope specimens predicted by the Rayleigh-Ritz (RR) method [*1*] for crack lengths from 102 to 356 mm (4 to 14 in.) are listed in Table 3. Also, a modified Rayleigh-Ritz (MRR) method is developed further, in which higher-order shape functions for deflection and rotation are used to replace the quadratic shape functions used before. The improved values of dC/da are shown in Table 3.

Experimental Compliance Calibration of the CDCB Specimens

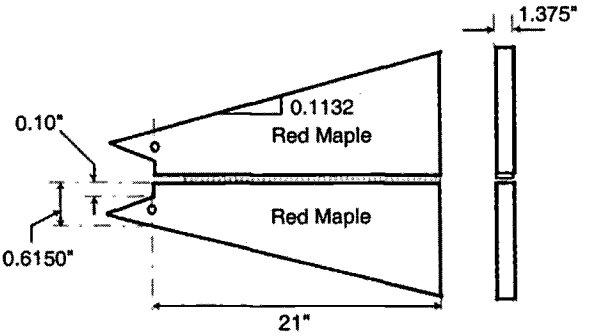
Once the geometries of linear-slope test specimens are defined by the Rayleigh Ritz method, the specimens are calibrated experimentally to verify the linearity of compliance rate-change with respect to crack length. Considering wood-wood and FRP-FRP interfaces. CDCB specimens for four material/moisture conditions were manufactured (see Figs. 3 and 4). The adhesive used to bond wood to wood, wood to FRP, and FRP to FRP was Resorcinol-Formaldehyde (RF, G-1131 from INDSPEC Chemical Corp., Pittsburgh, PA) resin, which is capable of curing at room temperature and providing strong and water-proof bonds. The RF

TABLE 2—*Material properties of phenolic FRP strips.*

	E, GPa	*G*, GPa
Experiment	30.407 (COV = 0.55%)	...
Micro/Macromechanics	30.186	4.482



(a) Geometry of wood-wood/Dry Specimen

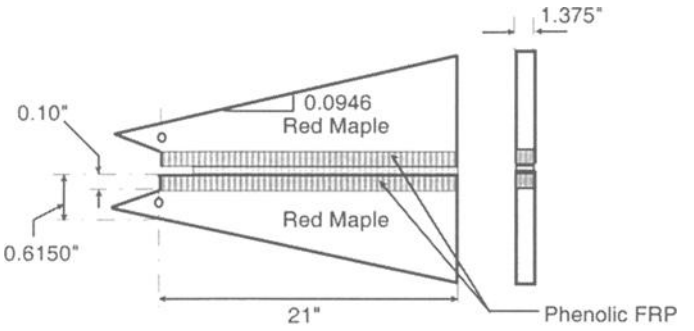


(b) Geometry of wood-wood/Wet Specimen

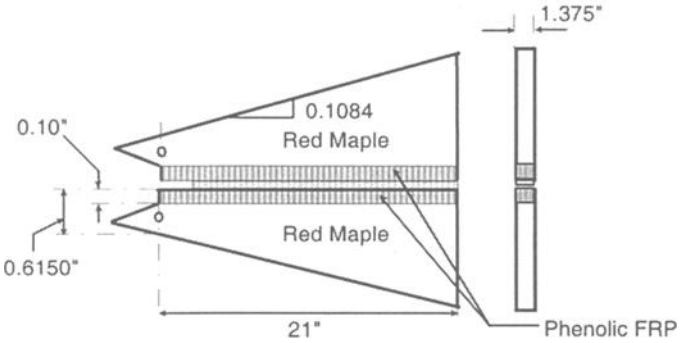
FIG. 3—*Contour shapes for CDCB wood-wood specimens.*

adhesive is a two-component resin and consists of resorcinol-formaldehyde polymer, which is a liquid resin, and paraformaldehyde, which is a powdered hardener. These two parts are mixed in the ratio of 5 to 1 by weight. Based on ASTM test results of bonded interface delamination studies [7], the best combination of pressure of 1448 kPa (210 psi) and open /closed assembly time of 5/30 min was used to bond the specimens.

For the compliance calibration of the specimens, various crack lengths have to be simulated to experimentally determine the compliance crack-length relationship. For both wood-wood and FRP-FRP bonded interfaces, these cracks were produced by sawing the interfaces to required lengths, starting from the smallest crack length of 50.8 mm (2.0 in.). The compliance calibration experiments were performed on a servo-hydraulic testing machine. The load was applied using a loading fixture made of aluminum, and this fixture was also later used in Mode I fracture tests. The tip of a specimen was connected to the load fixture, and the end of the specimen was supported by a plastic thread attached to the frame of the testing machine (Fig. 5). The experiment was conducted under displacement-controlled mode with the displacement rate of 0.051 mm/s (0.002 in./s). By monitoring the control console, a maximum load of approximately 100 lb was applied, and for every crack length the load and displacement data were continuously recorded. A crack-opening gage was clipped to the specimen tip, and it measured the transverse displacement of the specimen at the point of load application. For example, the compliance versus crack length relation for FRP-FRP wet specimen is shown in Fig. 6. The average compliance rate change values (dC/da) based on experimentally obtained compliance and linear regression for crack lengths from 101.6 mm (4 in.) to 355.6 mm (14 in.) are shown in Table 3.



(a) Geometry of FRP-FRP/Dry Specimen



(b) Geometry of FRP-FRP/Wet Specimen

FIG. 4—*Contour shapes for CDCB FRP-FRP specimens.*

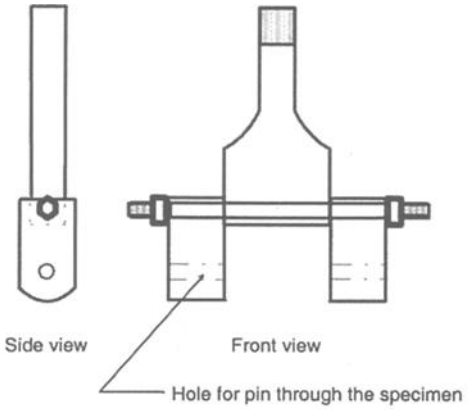
Finite Element Modeling of the CDCB Specimens

One of the major concerns with tests using the contoured DCB specimen is the linearity of the compliance versus crack length, which must be achieved over a significant length of the specimen. To validate the linearity of the compliance, specimens can be tested to define the crack length region over which the response is linear; however, the experimental effort can be minimized by predicting the response of the specimen by the finite element (FE) method or the modified Rayleigh-Ritz method. The finite element model represents, as ac-

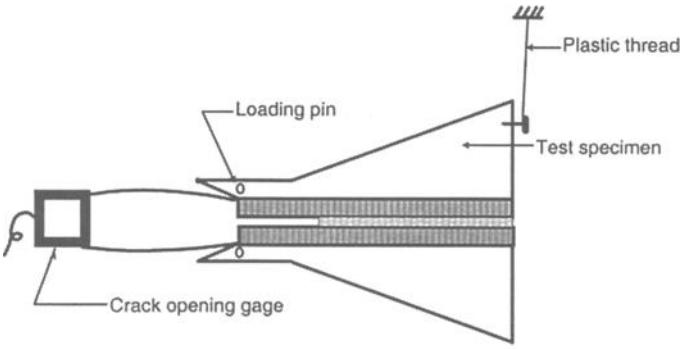
TABLE 3—*Compliance rate change of linear tapered specimens.*[a]

		dC/da ($\times 10^{-5}$ N^{-1})				% Diff.
Specimen Types	Slope	RR	MRR	Exp.	FE	Exp. vs. FE
Wood-Wood/Dry	0.0968	5.355	5.921	6.707	6.164	+8.81
Wood-Wood/Wet	0.1132	5.599	6.074	5.674	6.089	−6.82
FRP-FRP/Dry	0.0946	5.402	6.020	6.590	6.089	+8.23
FRP-FRP/Wet	0.1084	5.400	6.006	6.388	6.094	+4.82

[a] dC/da obtained for crack lengths from 101.6 mm (4 in.) to 355.6 mm (14 in.).



(a) Loading fixture for the CDCB specimen



(b) CDCB specimen and crack opening gage

FIG. 5—*Experimental setup for calibration and Mode I fracture tests.*

curately as possible, the actual behavior of the specimen. The CDCB specimens were modeled using plane-stress isoparametric eight-node quadrilateral elements in NISA [*8*]—a commercial finite element software. Similar to the experimental calibration of compliance change, the FE model was used to obtain compliance values with respect to crack lengths, and the compliance rate changes by FE predictions are also listed in Table 3. As indicated in Table 3, the compliance rate changes by the modified Rayleigh-Ritz (MRR) method are within 4% of the predictions by the FE model. For both experimental data and analytical predictions, the compliance crack-length relationship remains linear for crack lengths ranging from 101.6 mm (4 in.) to 355.6 mm (14 in.). The maximum difference of compliance rate change (dC/da) between experiment and FE model is about 8% for wood-wood/dry specimens. As shown in Table 3, the compliance rate change by the MRR method is more close to ones obtained by the FE prediction and experiment, and it indicates that the MRR method can be used with confidence to predict dC/da and to compute the fracture toughness values in Eq 1.

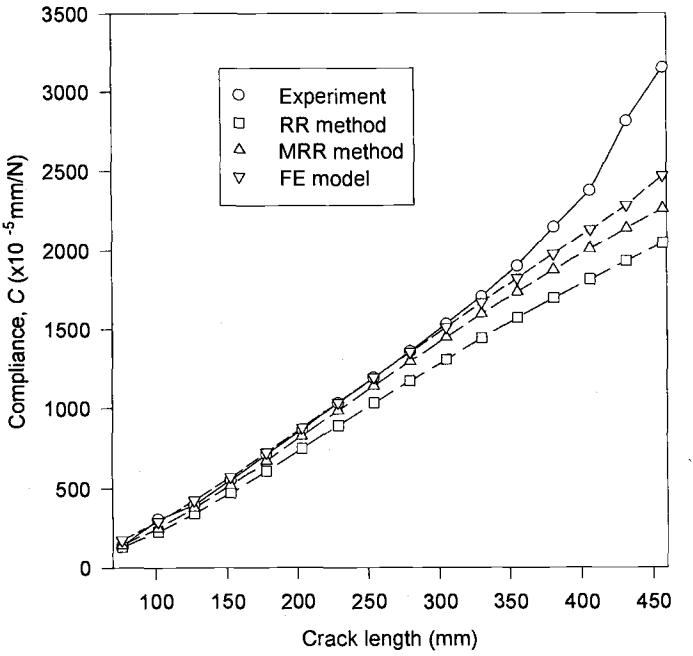


FIG. 6—*Compliance versus crack length for FRP-FRP/wet specimen.*

Experimental Evaluation of Fracture Toughness

Based on the calibration studies, both wood-wood and wood-FRP samples were manufactured and tested under dry and wet conditions, and the Mode I fracture toughness of the interface was evaluated. A set of 8 samples for each material/moisture condition was manufactured and tested, which resulted in a total number of 32 samples.

Material and Specimen Preparation

The CDCB specimens were manufactured based on the design of the contoured shapes shown in Figs. 3 and 4. The interface material/moisture condition combinations include: (1) wood-wood/dry (Fig. 3*a*), (2) wood-wood/wet (Fig. 3*b*), (3) wood-FRP/dry (Fig. 7*a*), and (4) wood-FRP/wet (Fig. 7*b*). Both the adherends and tapered portions for each side of the wood-wood interface consisted of an integral Red Maple piece (see Fig. 3). The wood-FRP bonded interface consisted of E-glass/Phenolic pultruded FRP strip and an integral Red Maple adherend-contour combination (Fig. 7). The adhesive used for all the bonded interfaces was Resorcinol Formaldehyde (RF, G-1131), and the optimum pressure of 1448 kPa (210 psi) and open/closed assembly time of 5/30 min [*7*] were used in the bonding process. Since the compliance rate change is approximately constant for crack lengths beyond an initial length of 101.6 mm (4 in.), the CDCB specimens were manufactured with an initial crack length of 101.6 mm (4 in.). For dry samples, the specimens were conditioned to 12% MC in an environmental chamber; whereas, the wet specimens were obtained by submerging the samples in a water bath under a 40-min vacuum and 40-min pressure soaking cycle, and the specimens were tested immediately after the end of the cycle. The vacuum/pressure soaking cycle was used to saturate the specimens with moisture contents beyond fiber sat-

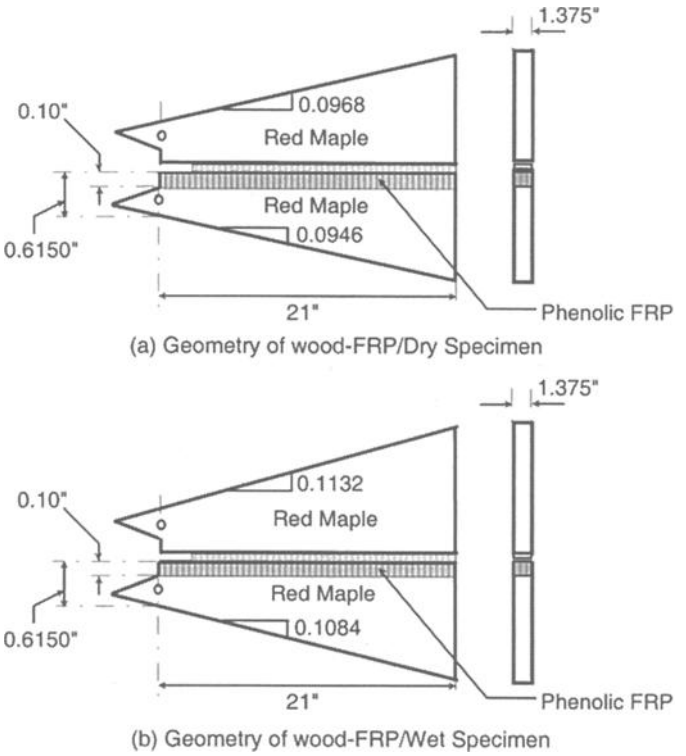


FIG. 7—*Contour shapes of CDCB wood-FRP specimens for Mode I fracture tests.*

uration point, and the wet samples obtained by this process exhibited more than 100% moisture contents by weight [*5*].

Testing Procedure

Similar to the compliance calibration tests, the fracture tests were also conducted using the servo hydraulic testing machine. The specimen was loaded using the same loading fixture shown in Fig. 5. The experiment was performed under displacement control mode with a loading rate of 0.051 mm/s (0.002 in./s). Under displacement control, the crack propagation is stable, since the energy required for crack extension is obtained from the release of elastic strain energy [*9*]. The load was applied continuously to initiate and sustain the crack propagation in the specimen. Since the compliance rate change (dC/da) was already established for the test specimens (see Eq 1 and Table 3), it was required to measure only the critical loads from which the fracture toughness could be evaluated. To monitor the crack propagation, the critical loads versus crack opening displacements were plotted. An accurate measurement of the crack opening displacements is not essential, and therefore the load grip displacements were recorded and used to interpret the test results.

Pattern of Crack Initiation and Arrest for CDCB Specimens

In general, for CDCB specimens with constant compliance rate change, the load versus crack length, or load versus crack opening displacement, during fracture tests can be char-

acterized by a function similar to that shown in Fig. 8. Initially, as the applied load increases, the elastic strain energy stored in the specimen increases until the internal elastic energy is equal to the energy required to initiate the crack. The crack initiation is characterized by a drop in the applied load as seen in Fig. 8. Each peak load value corresponds to the critical load of crack initiation (Points A, B, C, D, and E in Fig. 8). As the crack extends, the applied load is relaxed, and the stored elastic strain energy decreases, resulting in a crack arrest without complete fracture of the specimen. When the crack is arrested, the applied load increases once again. The critical load value at which the load-crack opening curve shows a "valley" is the critical load of crack arrest (Points a, b, c, d, and e in Fig. 8). This sequence of crack initiation and arrest continues as the crack extends, and, finally, a catastrophic failure of the interface bond is observed (at Point F in Fig. 8). Based on the design of a constant compliance rate change specimen, the assumed theoretical critical load values for crack initiation or arrest should remain constant along the bonded interface.

Fracture Failure Mode and Mode I Fracture Toughness of Bonded Interfaces

In the following four sections, the fracture patterns of specimens for four types of material/moisture conditions are described based on experimental observations, and their corresponding fracture toughness values are reported. For the dry and wet wood-wood and FRP-FRP specimens, the compliance rate changes obtained by Rayleigh-Ritz method, finite element model, and experiment are given in Table 3. Since the experimental values are assumed to be accurate, these are used to evaluate the Mode-I fracture toughness from Eq 1. For the dry and wet wood-FRP specimens, the average experimental values of dC/da for wood-wood and FRP-FRP specimens were used to evaluate the fracture toughness.

Wood-Wood Bonded Interface under Dry Condition—The linear-slope CDCB specimen shown in Fig. 3*a* was used for Mode I fracture test of wood-wood bonded interface under dry condition. Eight specimens numbered WWD1 through WWD8 were fabricated and then tested to obtain the critical loads for crack initiation and arrest. The experimental setup and a specimen under fracture are shown in Fig. 9. A representative test result is shown in Fig. 10 for specimen WWD1. As indicated in Fig. 10, several distinct crack initiations and arrests occurred during crack propagation. The fracture failure modes showed a combined wood cohesive failure and adhesive failure along the bond line, with an average cohesive failure

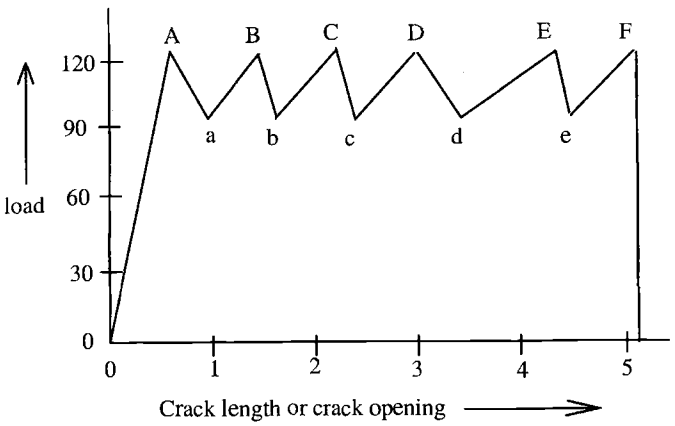


FIG. 8—*Idealized crack pattern for contoured double-cantilever beam test.*

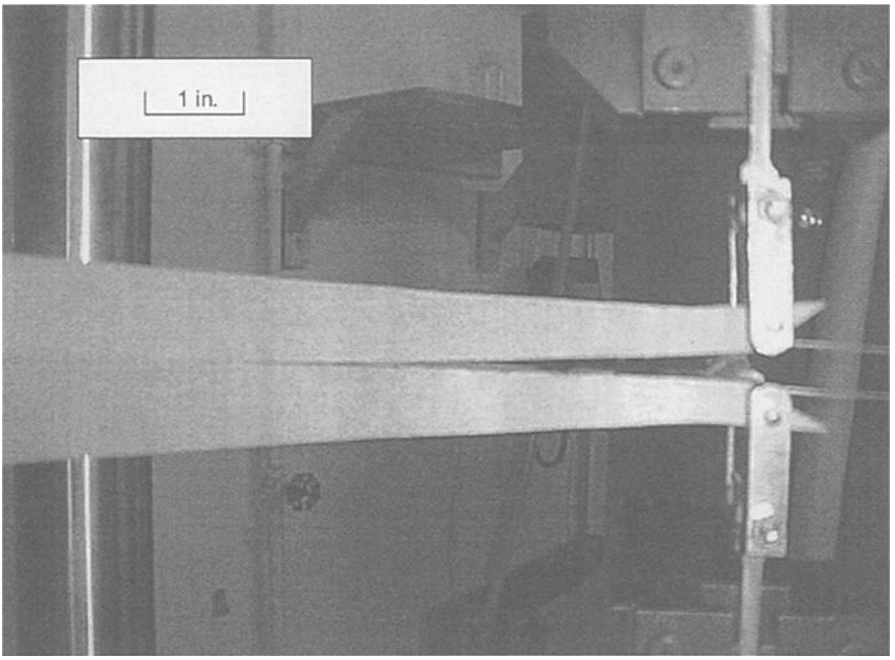
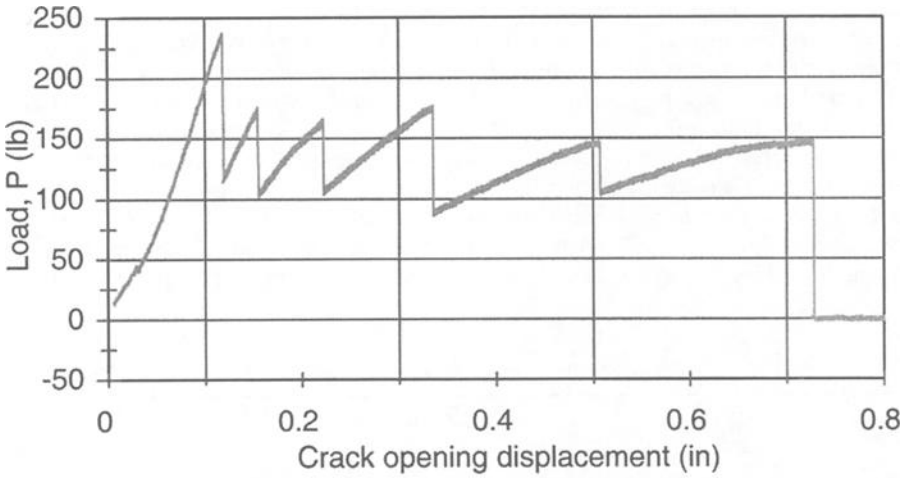


FIG. 9—*Fracture of wood-wood/dry interface for CDCB specimens.*



(1 lb = 4.45 N and 1 in =25.4 mm)

FIG. 10—*Load versus crack-opening displacement for specimen WWD1.*

TABLE 4—*Mean critical initiation and mean arrest loads for wood-wood and wood-FRP interface bonds.*

Specimen Type	Initiation Load, P_c^i (N)	Arrest Load, P_c^a (N)
Wood-Wood/Dry (WWD)	781.9 (COV = 14.1%)	586.1 (COV = 20.3%)
Wood-Wood/Wet (WWW)	885.1 (COV = 12.9%)	815.2 (COV = 14.8%)
Wood-FRP/Dry (WFD)	487.3 (COV = 15.4%)	445.0 (COV = 17.0%)
Wood-FRP/Wet (WFW)	700.9 (COV = 13.1%)	653.6 (COV = 15.1%)

of about 60% of the fracture surfaces. The data for two specimens (WWD2 and WWD6) were disregarded because the fracture occurred completely in the wood substrate, and the rational for neglecting these two specimens is that we intend to measure the fracture toughness along bonded interface under Mode I fracture and not the mixed mode fracture of wood materials. The critical loads for crack initiation and crack arrest were obtained for the remaining six specimens, and the mean crack initiation and arrest loads are given in Table 4. The critical strain energy release rates (fracture toughness, see Table 5) for crack initiation (G_{Ic}^i) and crack arrest (G_{Ic};^{a}) are computed by Eq 1 using the mean value of the critical loads and the compliance rate change, dC/da, obtained experimentally.

Wood-Wood Bonded Interface under Wet Condition—The linear-slope CDCB specimen for wood-wood bonded interface under wet condition is based on the design given in Fig. 3*b*. Eight specimens numbered WWW1 through WWW8 were fabricated and subjected to one cycle of water vacuum/pressure soaking that achieved a moisture content of over 100% by weight [*5*]. The specimens were tested immediately after water saturation, and the critical loads for crack initiation and arrest were obtained. A photograph of a wood-wood/wet interface specimen (WWW4) under fracture is shown in Fig. 11, and Fig. 12 shows the fractured interface of specimen WWW4. Observations of the fracture surface showed predominantly adhesive failure of nearly 60%. A representative test result of load versus crack opening is shown in Fig. 13 for specimen WWW7. Specimen WWW2 failed around the loading pin and was discarded. Similarly, the contour portion of specimen WWW3 failed after some initial crack propagation, and this specimen was also disregarded. The critical loads for crack initiation and crack arrest were obtained for six specimens, and the results are given in Table 4. Using Eq 1, the fracture toughness data for crack initiation (G_{Ic}^i) and crack arrest (G_{Ic}^a) are computed and shown in Table 5.

Wood-FRP Bonded Interface under Dry Condition—The linear-slope CDCB specimen shown in Fig. 7*a* was used for Mode I fracture test of wood-FRP bonded interface under dry condition. The specimen was designed by combining the contour shapes of wood-wood/

TABLE 5—*Fracture toughness of wood-wood and wood-FRP interface bonds.*

Specimen Type	Critical Strain Energy Release Rate		Brittleness Index
	G_{Ic}^i (J/m^2)	G_{Ic}^a (J/m^2)	I
Wood-Wood/Dry (WWD)	587.5	329.5	0.439
Wood-Wood/Wet (WWW)	636.4	539.8	0.152
Wood-FRP/Dry (WFD)	224.7	186.4	0.170
Wood-FRP/Wet (WFW)	449.4	391.1	0.130

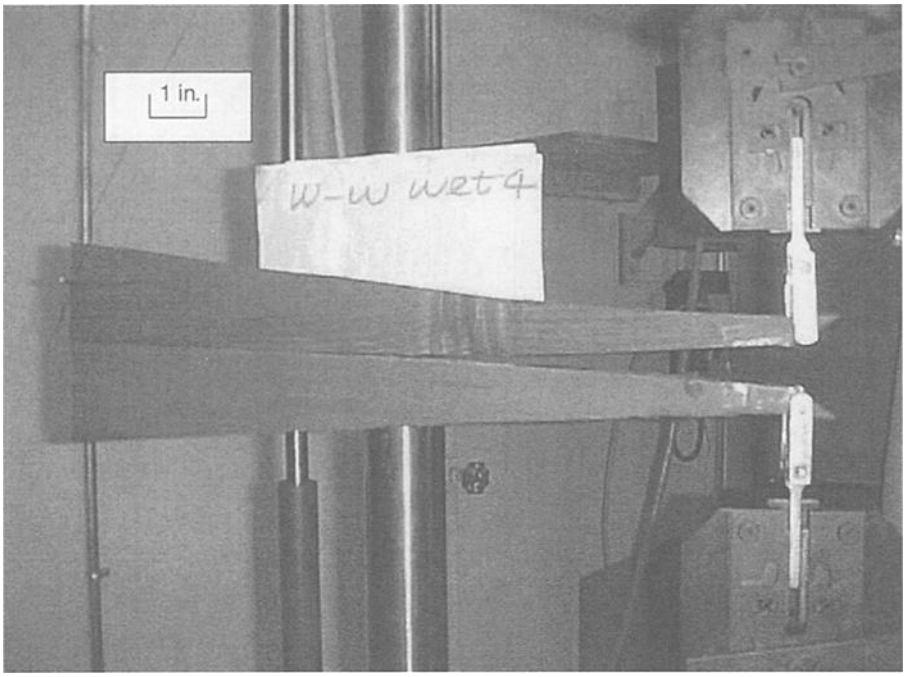


FIG. 11—*Fracture of wood-wood/wet CDCB specimen (WWW4).*

dry (Fig. 3*a*) and FRP-FRP/dry (Fig. 4*a*). Eight specimens numbered WFD1 through WFD8 were fabricated and then tested to obtain the critical loads for crack initiation and arrest. As observed in the tests, most of the interface fracture happened within the continuous strand mat (CSM) layer of the FRB substrate in combination with interface adhesive failure; for

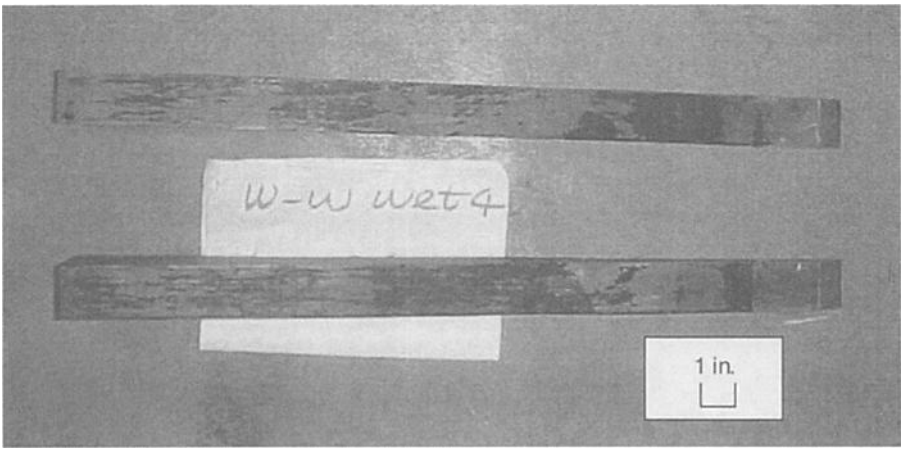
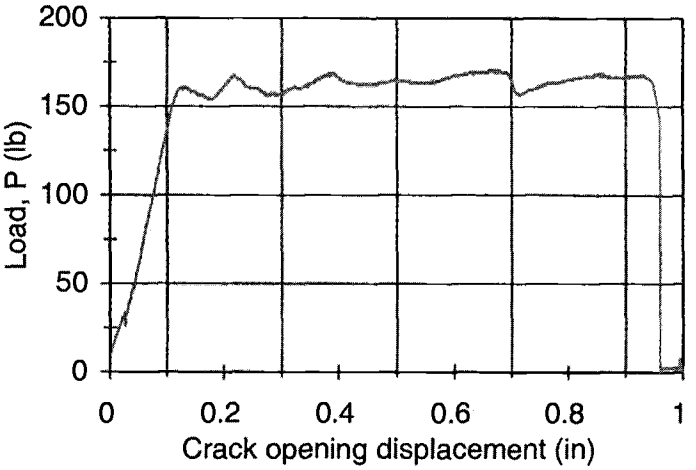


FIG. 12—*Fractured surface of wood-wood/wet specimen.*



(1 lb = 4.45 N and 1 in = 25.4 mm)

FIG. 13—*Load versus crack-opening displacement for specimen WWW7.*

several specimens, substantial fiber-bridging was evident during the fracture process, as a close-up photograph shows in Fig. 14 for Specimen WFD6. A representative test result is given in Fig. 15 for Specimen WFD4. The mean critical loads for all eight specimens are given in Table 4, and the fracture toughness values based on Eq 1 are shown in Table 5.

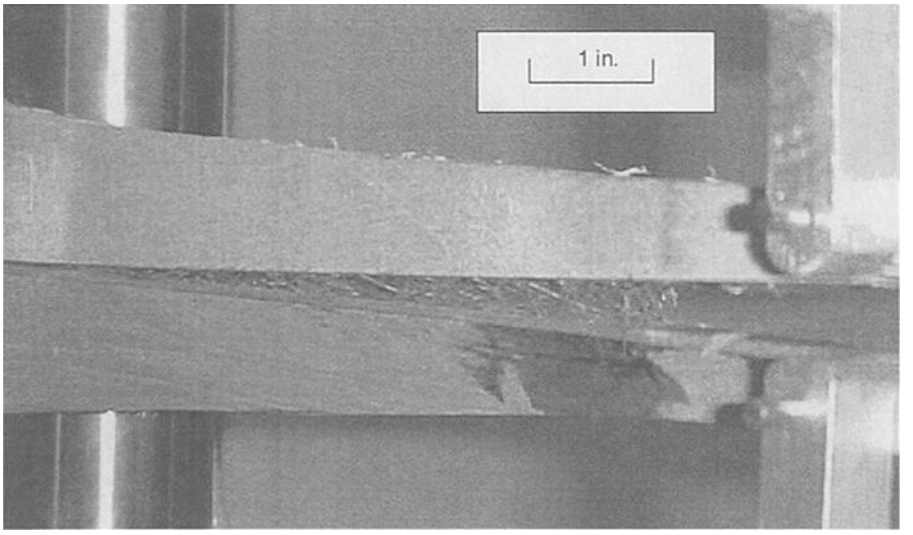
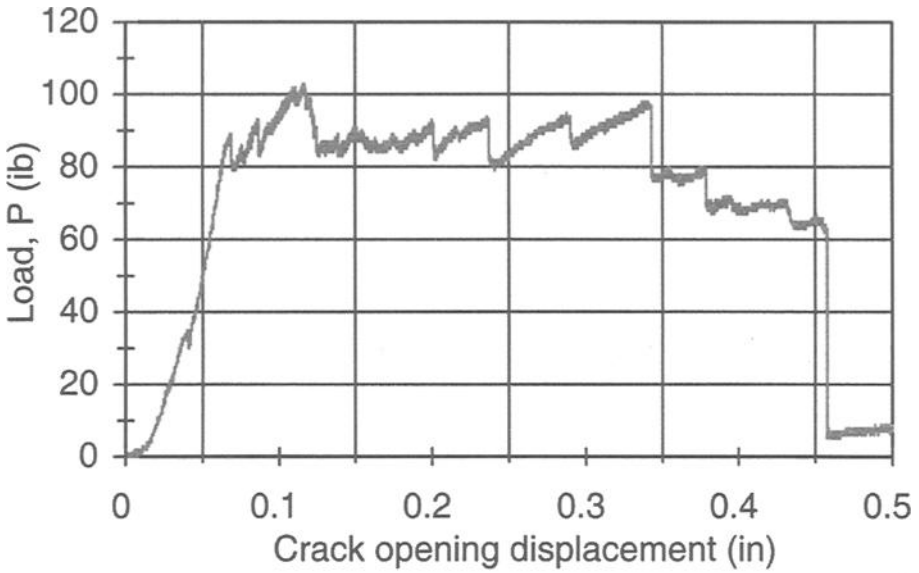


FIG. 14—*A close-up observation of fiber bridging along the interface (WFD6).*



(1 lb = 4.45 N and 1 in = 25.4 mm)

FIG. 15—*Load versus crack-opening displacement for specimen WFD4.*

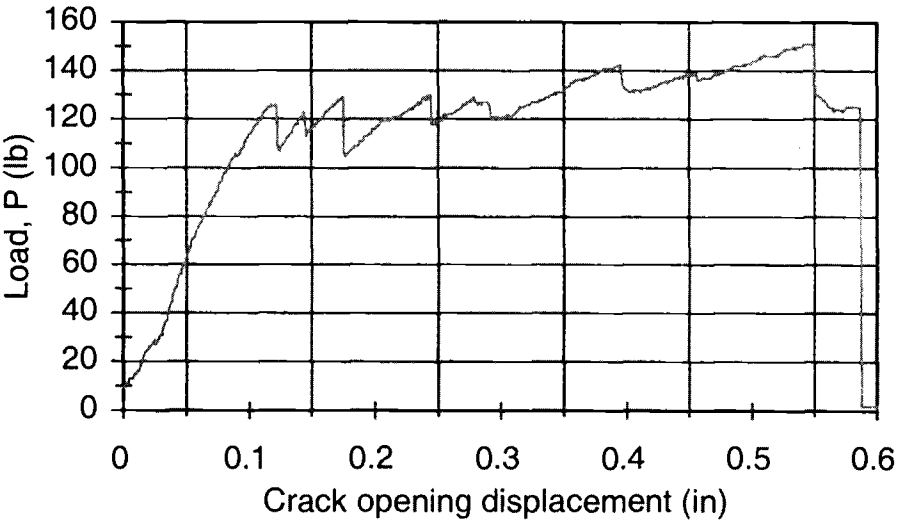
Wood-FRP Bonded Interface under Wet Condition—The linear-slope CDCB specimen shown in Fig. 7*b* was used for Mode I fracture test of wood-FRP bonded interface under wet condition. Eight specimens numbered WFW1 through WFW8 were fabricated and then tested to obtain the critical loads for crack initiation and arrest. For most of the specimens, the interface fracture failures happened mainly within the CSM layer in the FRP substrate and is similar to the wood-FRP/dry samples; we observed significant fiber-bridging at the interface during fracture propagation. A representative test result is shown in Fig. 16 for specimen WFW2. The critical loads for crack initiation and crack arrest were obtained for all the specimens, and the results are given in Table 4. Similarly, the fracture toughness for crack initiation ($G_{Ic}{}^{i}$) and crack arrest ($G_{Ic}{}^{a}$) are computed by Eq 1 (Table 5).

Brittleness Index

In addition to fracture toughness data, a "brittleness index, *I*" [*10*], which is the ratio of energy lost during crack growth to the energy required to initiate crack growth, can also be used to indicate stability of crack growth:

$$I = \frac{G_{Ic}{}^{i} - G_{Ic}{}^{a}}{G_{Ic}{}^{i}} \tag{2}$$

A large *I* value corresponds to a catastrophic and unstable crack growth that is independent



(1 lb = 4.45 N and 1 in = 25.4 mm)

FIG. 16—*Load versus crack-opening displacement for specimen WFW2.*

of the rate of loading, and a small I value indicates a slow tearing or growth in small increments. In the study conducted in Ref *10*, a value of $I = 0.43$ was considered to represent a strong and moderately unstable crack growth, and a value of $I = 0.06$ showed a moderately strong and stable crack growth. Based on the fracture toughness data obtained, the corresponding I values for both dry and wet samples are computed and given in Table 5. Except for wood-wood/dry interfaces with moderately unstable crack growth, a relatively stable crack propagation was observed for the rest of the specimens, and the crack growth in wet samples tended to be more stable than the corresponding ones in dry samples.

Summary and Discussions of Experimental Results

In this section, the experimental results of critical strain energy release rates (fracture toughness) for wood-wood/dry, wood-wood/wet, wood-FRP/dry, and wood-FRP/wet interfaces are summarized and discussed. As indicated in Table 4, the mean values of the critical loads for the wood-FRP interface bonds are less than the corresponding values for wood-wood interface bonds. The differences are the result of bonding two different adherends with distinct characteristics, resulting in lower bond strengths. Also, for the wood-FRP specimens, significant fiber-bridging was observed at the interface bond, and the failure occurred mainly within the CSM layer. The saturated (wet) samples show an increase in the fracture toughness, and this indicates that the absorption of water in the CDCB specimens had a tendency to toughen the interface bonds, especially for wood-FRP bond, for which the increase is over 100%. Although this increase may appear to be strange, it is a phenomenon that has been observed also for interlaminar delamination of graphite/epoxy composites [*11*]. Due to the moisture-induced plastification of both the polymeric adherends and adhesive, the failure

mode is much more plastic, resulting in higher critical loads and a relatively "smooth" crack propagation response; see the smaller variations in peaks and valleys shown in Fig. 13 (wood-wood/wet) and Fig. 16 (wood-FRP/wet).

Conclusions

In this paper, the fracture toughness of dry and wet wood-wood and wood-FRP bonded interfaces under Mode I fracture is evaluated using contoured double cantilever beam (CDCB) specimens. The guidelines and procedures for modeling and design of CDCB specimens for hybrid or dissimilar adherends using a Rayleigh-Ritz (RR) model are presented briefly; a modified Rayleigh-Ritz (MRR) method is further developed. The linearity of the compliance crack-length relationship of linear-slope specimens is theoretically verified using RR, MRR, and finite element models. A close correlation was achieved between the MRR method and finite element model, and the improved MRR method can be used with confidence to design the specimens and predict the compliance rate change. Through an experimental study of the compliance crack-length relationship of linear-slope specimens for wood-wood and FRP-FRP bonded interfaces under dry and wet conditions, it is shown that the linearized specimen can be used for Mode I fracture tests with reasonable confidence on the linearity of the compliance rate change. The fracture toughness values of wood-wood and wood-FRP bonded interfaces under dry and wet conditions are experimentally determined, and an increase in interface fracture toughness due to moisture absorption was obtained for wet wood-wood and wood-FRP interface samples; the toughening of the interface under moisture is due mainly to a much more plastic fracture failure mode of the interface.

Acknowledgments

This study was partially sponsored by the USDA National Research Initiative Competitive Grants Program (NRICGP-CSREES, Grant No. 98-35103-67579, PIs: Dr. Julio F. Davalos and Dr. Pizhong Qiao). The cooperation and suggestions provided by Russell Moody and Charles Vick of USDA Forest Service—Forest Product Laboratory are appreciated.

References

[1] Davalos, J. F., Madabhusi-Raman P., and Qiao, P. Z., "Characterization of Mode-I Fracture of Hybrid Material Interface Bonds by Contoured DCB Specimens." *Engineering Fracture Mechanics,* Vol. 58, No. 2, 1997, pp. 173–192.

[2] Carlsson, L. A. and Pipes, R. B. "Experimental Characterization of Advanced Composite Materials," Prentice Hall, Inc., Englewood Cliffs, NJ, 1987.

[3] Madabhusi-Raman, P. and Davalos, J. F., "Static Shear Correction Factor for Laminated Rectangular Beams," *Composites: Part B, Engineering Journal,* Vol. 27, No. 3-4, 1996, pp. 285–293.

[4] Davalos, J. F., Madabhusi-Ramn, P., Qiao, P. Z., and Wolcott, M. P., "Compliance Rate Change of Tapered Double Cantilever Beam Specimen with Hybrid Interface Bonds," *Theoretical and Applied Fracture Mechanics,* Vol. 29, 1998, pp. 125–139.

[5] Gardner, D. J., Davalos, J. F., and Munipalle, U. M., "Adhesive Bonding of Pultruded Fiber Reinforced Plastic (FRP) to Wood," *Forest Products Journal,* Vol. 44, No. 5, 1994, pp. 62–66.

[6] Davalos, J. F., Salim, H. A., Qiao, P. Z., Lopez-Anido, R., and Barbero, E. J., "Analysis and Design of Pultruded FRP Shapes under Bending," *Composites, Part B, Engineering Journal,* Vol. 27, No. 3-4, 1996, pp. 295–305.

[7] Davalos, J. F., Qiao, P. Z., and Trimble, B., "Fiber-Reinforced Plastic Composite-Wood Bonded Interfaces: Part 1. Durability and Shear Strength," *Journal of Composites Technology and Research, Journal of Composites Research & Technology,* Vol. 22, No. 4, 2000, pp. 224–231.

[8] Numerically Integrated Elements for System Analysis (NISA), Users Manual, Version 94.0, Engineering Mechanics Research Corp., Troy, MI, 1994.

[9] Anderson, T. L., *Fracture Mechanics: Fundamentals and Applications,* CRC Press, Boca Raton, Florida, 1995.

[10] River, B. H. and Okkonen, E. A., "Contoured Wood Double Cantilever Beam Specimen for Adhesive Joint Fracture Test," *Journal of Testing and Evaluation,* Vol. 21, No. 1, 1993, pp. 21–28.

[11] Hooper, S. J. and Subramanian, R., "Effects of Water and Jet Fuel Absorption on Mode I and Mode II Delamination of Graphite/Epoxy," *Composite Materials: Fatigue and Fracture, ASTM STP 1156,* W. W. Stinchcomb and N. E. Ashbaugh, Eds., American Society for Testing and Materials, 1993, pp. 318–340.

Author Index

A

Adey, Robert A., 505
Arimochi, Kazushige, 271
Aveline, C. R., Jr., 206, 221

B

Bain, Kenneth R., 445
Bass, B. Richard, 242
Bonacuse, Peter J., 110
Brocks, Wolfgang, 475

C

Chao, Y. J., 165
Chatterjee, Amit, 110
Chu, C.-C., 67
Curtin, Thomas J., 505

D

Daniewicz, S. R., 206, 221
Davalos, Julio F., 526
Dowling, Norman E., 3

G

Gabb, Timothy P., 110
Gallagher, Joseph P., ix
Ghosn, Louis J., 110
Glinka, G., 348
Green, Kenneth A., 110

H

Halford, Gary R., ix, 94
Hashida, Tomoyuki, 271
Hillberry, Ben M., 427
Honda, Takashi, 457

I

Iyer, N. C., 165

K

Kalluri, Sreeramesh, 94
Kim, K. S., 79
Kirk, Mark T., 183, 318
Kitsunai, Yoshio, 457
Kobayashi, Hideo, 128
Konda, Noboru, 271
Kumagai, Katsuhiko, 128

L

Lam, P.-S., 165
Landes, John D., 54, 305
Lee, B. L., 79
Lewis, K., 371
Lott, Randy G., 183
Louthan, M. R., 165

M

Maeda, Yutaka, 457
McAfee, Wallace J., 242
McClain, R. D., 371
McGaw, Michael A., 94
Miller, David S., 445
Minami, Fumiyoshi, 271
Moshier, Monty A., 427

N

Nakamura, Haruo, 128
Natishan, MarjorieAnn E., 318
Newman, James C., 39, 486
Nicholas, Theodore, 427
Nuel, Brian P., 143

O

Ochiai, Takao, 271

P

Park, J. C., 79
Phoenix, S. Leigh, 331

Q

Qiao, Pizhong, 526

R

Ranam, S. Ganesh Sundara, 457
Reinhardt, Wolf, 348
Rejda, Ed F., 143

Copyright© 2000 by ASTM International www.astm.org

S

Seshadri, B. R., 486
Siegmund, Thomas, 475
Slavik, D. C., 371, 405
Socie, Darrell F., 143
Sweeney, Joseph W., 110

T

TerMaath, Stephanie C., 331
Thangjitham, Surot, 3
Trimble, Brent S., 526

V

Van Stone, R. H., 405

W

Wagenhofer, Matthew, 318
Wicks, Bryon J., 391
Williams, Paul T., 242
Wilson, Christopher D., 305

Y

Yoshihisa, Etsuji, 457

Z

Zhuang, Wyman Z., 391
Zhu, X. K., 165

Subject Index

A

A302B steel, 305
Aircraft components, 445
  multiple site dama, 486
Aircraft engine, compressor disks, 391
Aluminum alloys, crack growth modeling, 475
ANSYS, 206
  stress intensity predictions, 371
ASTM E 1737, 165
ASTM E 1820, 183
ASTM E 1921, 305
Asymptotic solution, 165

B

Basis function, 331
Biaxial fatigue, irregular loading, 79
Biaxial loading, 242, 391
Bonded interface, 526
Bonded patch repair, 505
Boundary element analysis, 3D, 505
Branched cracks, 331
Brittle fracture, structural, 271
Buckling, 486
Bulk property evaluation, thermal barrier coating, 143

C

Cleavage fracture, 242
Cohesive energy, 475
Cohesive strength, 475
Cohesive zone model, 475
Compressor disks, surface cracks, 391
Constitutive behavior, 143
Constraint, 39
  surface-cracked plates, 206
Constraint effect, 165
Contoured double cantilever beam specimen, 526
Crack closure, 39
Crackface tractions, 331
Crack growth, 3, 39, 457
  ductile, 165
  J-controlled, 165
  modeling, 475
  riveted lap-splice joints, 486
  threshold stress intensity, 445
  time-dependent, 405
Crack propagation, 505
Cracks
  branched, 331
  complex geometry, 348
  kinked, 110, 331, 371
  nonlinear stress fields, 348
  part-through, 206, 221
  small, 427
  surface, 206, 221
Crack-tip field approach, 54
Crack-tip-opening angle, 475
  riveted lap-splice joints, 486
Crack-tip opening displacement, 371, 391
  critical, 271
Cruciform bend specimen, shallow-flaw, 242
Cyclic hardening, 94
Cyclic hysteresis, 143

D

da/dN versus ΔK curves, 3
Damage, incremental, 67
Damage cracking, multiple-site, 486
Damage curve approach, 94
Damage parameter, 67
Deformation limits, 183
Direct current potential difference, 427
Dislocation
  density distributions, 331
  mechanics, 318
Dissimilar material adherends, 526
Ductile crack growth, 165
Dynamic fracture toughness, 271

E

Eigenstrain, 128
Elastic-plastic finite element analysis, 206
Elastic-plastic fracture mechanics, Irwin's contributions, 54

F

Facets, 110
Fatigue
  incremental method, 67
  strain-based method, 67
Fatigue damage event, 67
Fatigue life prediction, *see* Life prediction
Fatigue strength, 457

Ferritic steels, 183
Fiber-reinforced plastics, 526
Finite element method, 128
  crack growth, 475
  3D model, 391
  3D dynamic FEM, 271
Flow stress, 67
Fracture mechanics, 39, 427, 457
  Irwin's contributions, 54
  surface cracks, 391
Fracture toughness, 165
  biaxial effect, 242
  cleavage, 183
  constraints, 183
  dynamic evaluation, 271
  testing, 183
  transition behavior, 318
  transition testing, 305

H

Haynes 188, cumulative fatigue behavior, 94
High cycle fatigue threshold, 427
Hybrid material adherends, 526
Hydrostatic stress criterion, 242

I

Inclusions, 110
In-phase, 67
Inverse problem, 128
Irwin, George R.
  contributions to elastic-plastic fracture mechanics, 54
  stress intensity factor, 39, 54

J

J-A_2 curve, 165
J-R curve, 165

K

Kandil-Brown-Mill parameters, 79
Kinked cracks, 110, 331
  stress intensity predictions, 371

L

Lap-splice joints, 486
Life prediction
  basic methodology, 3
  cumulative cyclic loading, 94
  kinked cracks, 110
Linear damage rule, 94
Linear elastic fracture mechanics methods, 405
Loading
  cumulative cyclic, 94
  history, 427
  program, 457
  variable amplitude, 79
Local approach, 271
Low cycle fatigue, 110
  cracks, 427

M

Master curve, 318
Microcracking, directionality, 143
Miner-Palmgren rule, 79
Mode 1 fracture, 526
Moisture effect, 526
Multiaxial rainflow, 67
Multiple site dama, 486

N

Nickel alloy, 445
Nickel base alloys, time-dependent crack growth, 405
Nondestructive evaluation, computer-aided, 128
Notched round bars, transition fracture toughness testing, 305

O

Out-of-phase, 67
Overhead traveling crane, 457
Overloads, 427

P

Part-through cracks, 206, 221
Plasma-sprayed coatings, 143
Plasticity, 39
Plastic yielding, 391
Plastic zone, bolt hole, 391
Plastic zone size, 221
  surface-cracked plates, 206
Powder metallurgy, 110
Pressure vessels, 242
  fracture toughness transition, 318
Pressurized cylindrical shell, 505

R

Rainflow, 67, 457
Rainflow cycle counting, 79
Rate-temperature parameter, 271
Rayleigh-Ritz method, 526
Residual stress, 457
  welding, nondestructive evaluation, 128
Rivets, 486

S

Semi-elliptical surface flaw, 371
Shallow-flaw cruciform bend specimen, 242
Size requirements, 183
Slice synthesis methodology, 221
Smith-Watson-Topper parameter, 79, 94
S-N curves, 3
STAGS shell code, 486
Stainless steel 304
  biaxial fatigue, 79
Steel, structural, 271
Strain, 3
  mean, 94
Strain-life curves, 3
Stress, 3
  concentration, 457
  mean, 94
  nonlinear fields, 348
Stress effect, mean, 67
Stress intensity, 427
  ANSYS predictions, 371
  threshold, 445
Stress intensity factor, 331, 505
  cracks of complex geometry, 348
  effective, 457
  Irwin's, 39, 54
  surface cracks, 391
Strip-yield model, 221
Superalloy, 94, 110
Superposition, 331
Surface-cracked plates, under tension or bending loads, 206
Surface cracks, 206, 221
  compressor disks, 391
  small, 445
Surface flaw, semi-elliptical, 371
Swedlow Memorial lecture, 3

T

Tearing modulus, 165
Thermal barrier coating, bulk property evaluation, 143
Ti-6Al-4V, small, 427
Titanium alloy, 445
Transition fracture toughness testing, 305
T-stress, 39
Turbine engines, 427
  time-dependent crack growth, 405

U

U720, 110
Uniaxial rainflow counting algorithm, 67

W

Wedge, 331
Weibull stress, 242, 271
Weight functions, 221, 348, 391
Weld, reinforcement removal, 128
Welding residual stress, nondestructive evaluation, 128
Weld metals, 271
Weld repair specimens, fatigue strength, 457
Wood, 526

Z

Zirconia, 143

ISBN 0-8031-2868-1